ASME
SETTING THE STANDARD

Journal of Engineering for Gas Turbines and Power

Published Bimonthly by ASME

VOLUME 131 • NUMBER 3 • MAY 2009

Transactions of the ASME, Journal of Engineering for Gas Turbines and Power (ISSN 0742-4795) is published bimonthly (Jan., Mar., May, July, Sep, Nov.) by The American Society of Mechanical Engineers, Three Park Avenue, New York, NY 10016. Periodicals postage paid at New York, NY and additional mailing offices. POSTMASTER: Send address changes to Transactions of the ASME, Journal of Engineering for Gas Turbines and Power, c/o THE AMERICAN SOCIETY OF MECHANICAL ENGINEERS, 22 Law Drive, Box 2300, Fairfield, NJ 07007-2300.
CHANGES OF ADDRESS must be received at Society headquarters seven weeks before they are to be effective. Please send old label and new address.
STATEMENT from By-Laws. The Society shall not be responsible for statements or opinions advanced in papers or ... printed in its publications (B7.1, par. 3).

RESEARCH PAPERS

(Contents continued on inside back cover)

This journal is printed on acid-free paper, which exceeds the ANSI Z39.48-1992 specification for permanence of paper and library materials. ♾™
♻ 85% recycled content, including 10% post-consumer fibers.

(Contents continued)

Journal of Engineering for Gas Turbines and Power MAY 2009

Volume 131, Number 3

TECHNICAL BRIEFS

(Contents continued on facing page)

Journal of Engineering for Gas Turbines and Power **MAY 2009**

Volume 131, Number 3

The ASME Journal of Engineering for Gas Turbines and Power is abstracted and indexed in the following:

AESIS (Australia's Geoscience, Minerals, & Petroleum Database), Applied Science & Technology Index, Aquatic Sciences and Fisheries Abstracts, Civil Engineering Abstracts, Compendex (The electronic equivalent of Engineering Index), Computer & Information Systems Abstracts, Corrosion Abstracts, Current Contents, Engineered Materials Abstracts, Engineering Index, Enviroline (The electronic equivalent of Environment Abstracts), Environment Abstracts, Environmental Science and Pollution Management, Fluidex, INSPEC, Mechanical & Transportation Engineering Abstracts, Mechanical Engineering Abstracts, METADEX (The electronic equivalent of Metals Abstracts and Alloys Index), Pollution Abstracts, Referativnyi Zhurnal, Science Citation Index, SciSearch (The electronic equivalent of Science Citation Index), Shock and Vibration Digest

Performance of the Clean Exhaust Engine Concept

F. Noppel[1]
e-mail: f.g.noppel@cranfield.ac.uk

D. Lucisano

R. Singh

School of Engineering,
Cranfield University,
Bedfordshire MK43 0AL, UK

The climatic effects of air-traffic pollutants, such as carbon dioxide (CO_2) and mononitrogen oxides (NO_x), aerosols, contrails, and aviation induced cirrus clouds, are repeatedly stressed in assessment reports. It is therefore desired to reduce all aviation emissions simultaneously. In this paper, a novel propulsion concept, which has the potential to reduce all pollutants, is assessed regarding its performance. It is based on gas turbine technology, derived from the intercooled and recuperated engine cycle. Exhaust water condensation is facilitated inside the engine to avoid the formation of contrails. Particles and aerosols are scavenged from the exhaust gases during condensation. The condensed water is partially redirected into the combustion chamber to mitigate NO_x emissions via water injection technique. Calculations suggest that this new concept allows higher thermal efficiencies than conventional designs, yielding in better fuel economy and hence reduces greenhouse gas emissions. The corresponding design parameters for bypass ratio and fan pressure ratio suggest that this concept might be well suited for propfans or remotely driven fans. [DOI: 10.1115/1.3019142]

1 Introduction

The importance of air-traffic pollutants in the global climate, especially in the light of projected passenger numbers, is repeatedly stressed in aviation assessment reports. In the fourth assessment report on climate change by the Intergovernmental Panel on Climate Change (IPCC) [1], contrails and contrail cirrus clouds, which are contrails that spread in a highly ice-supersaturated environment, have been identified as the principle contributors to the total radiative forcing from commercial air-traffic.

In [1], aviation pollutants were compared in terms of radiative forcing, a metric for the steady-state response of the mean global temperature of a particular pollutant [2]. Although with some uncertainty at the current level of understanding, the radiative forcing from contrails and contrail cirrus combined could potentially represent 70.4% of the total radiative forcing from aviation, despite their much shorter life time than that of other aviation pollutants such as carbon dioxide.

The formation of contrails depends on many effects such as chemical reactions in the plume, aircraft wake dynamics, the state of the atmosphere, and engine technology. Several approaches for contrail avoidance are summarized and proposed in Ref. [3], of which the most cause an increase in fuel burn and hence carbon dioxide emissions. Although a change in cruise altitude could, for example, avoid the formation of contrails during flight, it is accompanied with an increase in fuel consumption.

Even though contrail avoidance strategies cause an increase in fuel burn considering current technology, synergies between future technologies could enable contrail avoidance and the reduction of other pollutants at the same time, potentially enabling a greener and more sustainable air-traffic.

A novel engine concept, the clean exhaust engine concept (CEEC), is proposed, offering the potential to reduce all pollutants simultaneously. It was presented for the first time in Ref. [4] and exhibits operation with significantly increased thermal efficiency compared to current engine designs, reduced water vapor, soot, and aerosol emissions to avoid the formation of contrails and cirrus clouds, and reduced NO_x emissions. Although theoretical approaches employing fuel cells and similar mechanisms may be feasible [5], they require significant deviation from current gas turbine practices. Hence, this novel engine concept was derived from existing gas turbine technology, which could operate with any available hydrocarbon based fuel or hydrogen.

2 Cycle Description

Figure 1 shows a graphical representation of the clean exhaust engine concept in a three spool arrangement. The improvement in thermodynamic work potential is realized by combining intercooling and exhaust regeneration. The intercooler (IC) is a heat exchanger placed between the intermediate pressure compressor (IPC) and the high pressure compressor (HPC). The flow on the cold side of the intercooler in the clean exhaust engine concept is the exhaust as opposed to bypass air. Intercooling reduces the work required for the compression of air in the HPC. The recuperator (REC), placed between the HPC and the combustion chamber (CC), recovers heat from the flow exiting the low pressure turbine (LPT) to increase the temperature of the precombustion chamber air. Hence, less heat energy, and hence fuel, is required in the CC.

Contrails form in the exhaust plume of an aircraft if saturation with respect to water occurs during the mixing process of the exhaust gases with ambient air. Considering current engine architecture, they form more likely with increasing overall engine efficiency [6]. Hence, fuel burn and contrail formation are in conflict with each other. However, the formation of contrails would not occur for low exhaust water content at relatively high temperatures.

The clean exhaust engine concept facilitates water condensation inside the engine, achieved through the reduction in flow temperature after the LPT. Therefore, the flow exiting the recuperator is further cooled by applying an additional heat exchanger: the condensation stage. Water condensation also occurs on particles and aerosols that are contained in exhaust gases. This effect is utilized to provoke the scavenging of particles and aerosols from the exhaust gases. Water from the condensation stage can be stored on the aircraft or released into the atmosphere in liquid or ice phase for precipitation.

NO_x emissions could be reduced by injecting water into the combustion chamber. According to Ref. [7], up to 80% reduction in NO_x is possible, as shown in Fig. 2, and the technology has been successfully demonstrated in the laboratory by Daggett [8]. Up to now, water injection is proposed for takeoff and climb only, due to weight penalties. With the clean exhaust engine concept, a fractional part of the condensed water could be redirected into the

[1]Corresponding author.

Manuscript received January 15, 2008; final manuscript received September 11, 2008; published online February 6, 2009. Review conducted by Dilip R. Ballal.

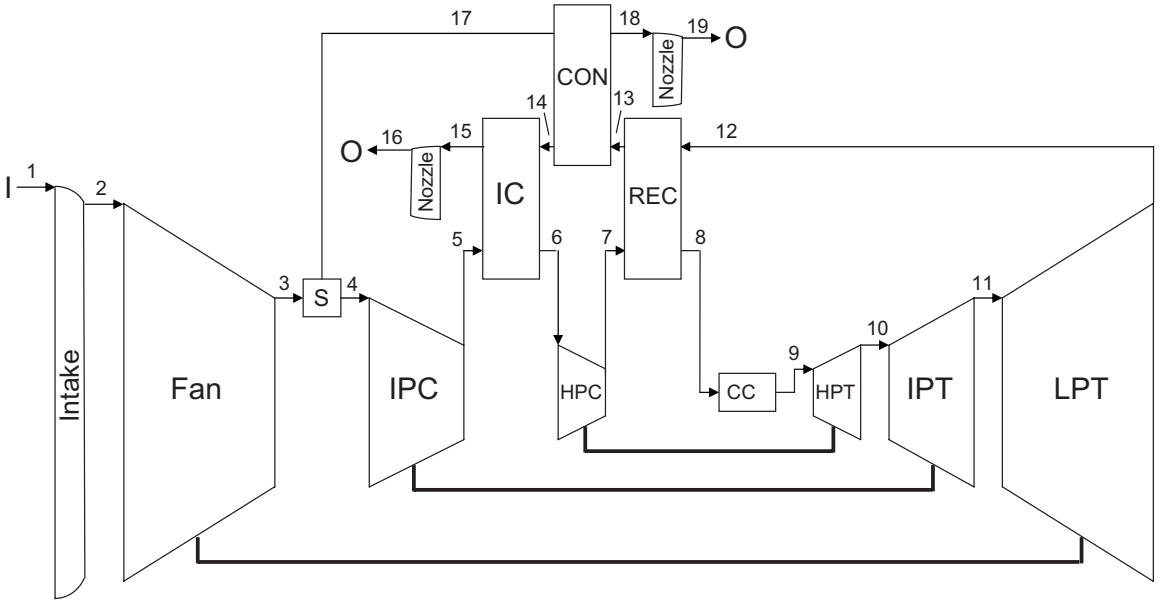

Fig. 1 Layout of the CEEC

combustion chamber to suppress the formation of NO_x during the entire flight without requiring additional water tanks.

The dry and cold air leaving the condensation stage is used to chill the compressor air flow in the intercooler. This causes an increase in the flow temperature of the core exhaust. Because contrails are less likely to form with increasing exhaust temperature, it has the effect of further reducing the potential for contrail formation.

Figure 3 shows the water partial pressure on a phase diagram of water for different stations within the engine and in the plume. The engine station numbers in Fig. 1 match with the station numbers in Fig. 3. Water saturation pressure is calculated from Ref. [9]. The water partial pressure in the flow exiting the hot side of the condensation stage is determined by the water saturation pressure at the given flow temperature. Static flow temperatures and pressures are considered for the stations within the engine, whereas stagnation properties relative to the atmosphere frame of reference are considered in the plume.

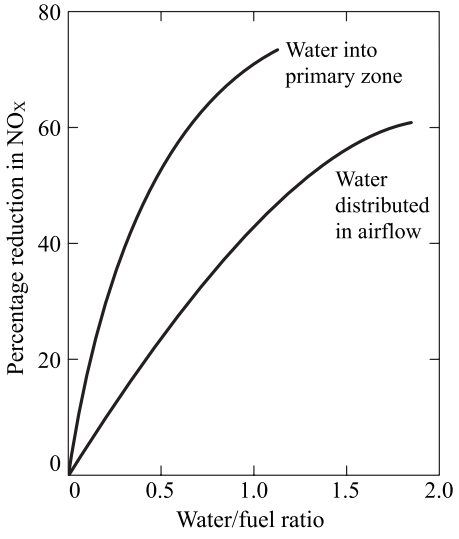

Fig. 2 NO_x reduction through water injection (adopted from Ref. [7])

The mixing of the exhaust gases with ambient air is represented by a straight line, assuming that the mixing of the flows takes place adiabatically and isobarically, and temperature and humidity mixing at an equal rate. The flows originating from the cold side of the condensation stage and from the bypass are assumed to mix prior to the mixing with ambient air. The actual mixing line represents the weight averaged mixing of the mixed exhausts with ambient air.

Furthermore, Fig. 3 shows also the critical mixing line, which is a tangent to the water saturation pressure line originating from the ambient state of the atmosphere. Together with the actual mixing line, it is used for contrail prediction. If the slope of the actual mixing line is lower than that of the critical mixing line, contrail formation is not facilitated. This is because contrails only form if the actual mixing line surpasses the region for which water is present in the liquid phase in a phase diagram [10].

Additionally, the theoretical mixing line is shown. It represents the mixing line of the mixed exhaust with ambient air if no dehumidification took place. Originating from the ambient state of the atmosphere, its slope is calculated from Ref. [6].

$$G = \frac{\mathrm{EI}_{\mathrm{H_2O}} p_a c_p}{(1 - \eta_0) q_{\mathrm{net}} \omega} \tag{1}$$

where c_p is the specific heat capacity of air, $\mathrm{EI}_{\mathrm{H_2O}}$ is the water emission index for a certain fuel, p_a is the ambient static pressure, η is the overall engine efficiency, q_{net} is the fuel net calorific value, and ω is the molar mass ratio of water to air. The slopes of the actual mixing line and of the theoretical mixing line coincide if water condensation is not facilitated within the engine.

3 Methodology

A one-dimensional mathematical model representing the thermodynamic cycle was combined with a commercially available genetic algorithm optimization package to investigate the performance of the clean exhaust engine concept. All calculations were carried out for a three spool turbofan configuration with separate exhausts, as shown in Fig. 1. The engine design variables for optimization were fan pressure ratio (FPR), bypass ratio (BPR), overall pressure ratio (OPR), turbine entry temperature (TET), and the ratio (R) of the IPC pressure ratio (PR) and the HPC PR.

All calculations were carried out with the same engine technology parameters, including turbomachinery isentropic efficiencies,

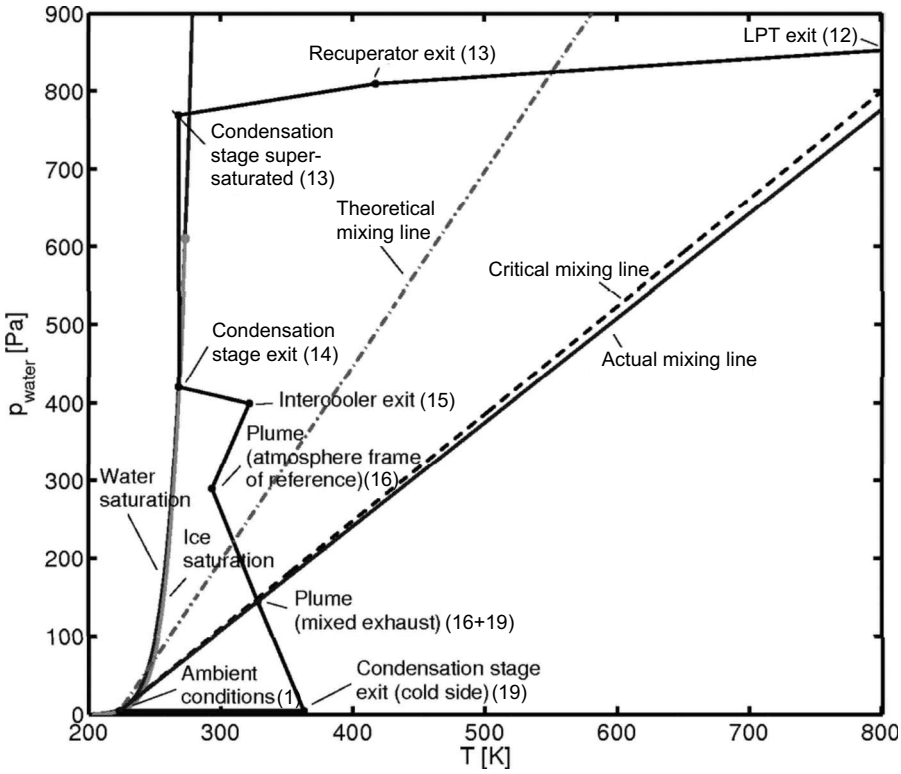

Fig. 3 The engine stations on a phase diagram of water

values for heat exchanger effectiveness, and pressure losses occurring in the heat exchangers and the CC. Pressure losses across the heat exchangers and the CC are expressed in terms of percentage differences between the ingoing and outgoing flows. The heat exchanger effectiveness, defined as the ratio between the heat transferred and the maximum transferable heat, was assumed to be 85% for the recuperator and the intercooler, while a 90% effectiveness was assumed for the condensation stage as temperatures close to ambient are required to facilitate water condensation inside the engine. Other technology parameters were based on industry forecasts and information available in the public domain. Bleed, power off take, and cooling flows are not considered in the model. Table 1 summarizes the technology parameters and their values used in the calculations.

Ambient conditions are defined by altitude, Mach number, and ambient ice-supersaturation (ISS). The standard atmosphere model was used to calculate ambient pressures and temperatures for a given altitude.

Table 1 Engine parameters and values

Parameter	Value
η_{intake}	0.99
η_{fan}	0.94
η_{IPC}	0.89
η_{HPC}	0.89
η_{LPT}	0.91
η_{IPT}	0.89
η_{HPT}	0.87
η_{nozzle}	0.98
$\varepsilon_{\text{intercooler}}$	0.85
$\varepsilon_{\text{recuperator}}$	0.85
$\varepsilon_{\text{condenser}}$	0.90
$\Delta P_{\text{heat exchanger, hot side}}$	3%
$\Delta P_{\text{heat exchanger,cold side}}$	6%
$\Delta P_{\text{combustion chamber}}$	5%

For contrail forecast, engine exhaust flow conditions were considered when the mixing line slope between the exhaust flow and ambient air on a water phase diagram was calculated. If the slope of the actual mixing line in the phase diagram, denoted by G_{real}, is lower than the slope of the critical mixing line G_{crit}, contrail formation is avoided, whereas contrail formation is facilitated for $G_{\text{real}} > G_{\text{crit}}$. The water partial pressure at the engine intake is calculated from the ambient conditions and a given ice-supersaturation. The theoretical mixing line G_{theo} is used to verify the performance model and is calculated from Eq. (1).

Genetic algorithms, performing an exploitation of random search to solve optimization problems, were chosen for optimization as they are robust and are able to find solutions where the search space is not fully understood or with discontinuities. The objective function was defined as $\text{OBJ} = 1/\eta_0$. Through the definition of constraints, only combinations of design parameters yielding $G_{\text{real}}/G_{\text{crit}} < 1$ were brought forward. Several sets of optimizations were carried out varying the TET from 1600 K to 2200 K in 100 K intervals. A reference case was calculated where constraints were disabled, and subsequent optimizations were performed for different TETs and ice-supersaturations of 115% and 130%. Equal altitudes and Mach numbers were used for each set of optimizations: 33,000 ft and 0.8, respectively.

4 Results

The objective of the first set of optimizations was to identify the most efficient cycle, regardless of its ability to avoid contrail formation. Following runs were performed with enabled constraints to calculate the performance of engines that do not facilitate contrail formation.

The results are shown in Figs. 4 and 5. In general, cycles with higher TET result in lower specific fuel consumption (SFC). For a

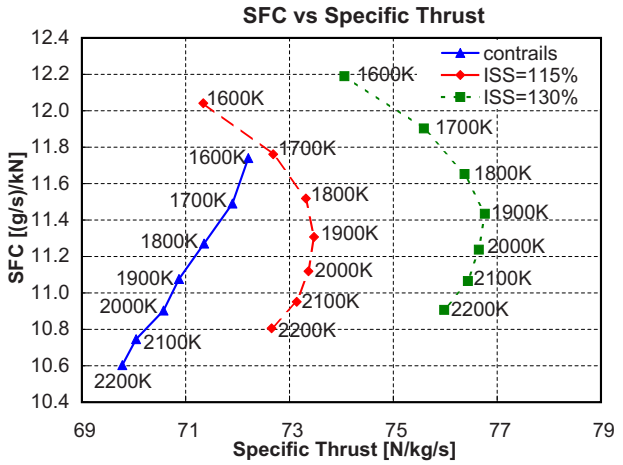

Fig. 4 SFC versus specific thrust of the clean exhaust engine concept for various TETs

given TET, a specific fuel consumption is higher if contrail suppression is considered, and specific fuel consumption penalties increase with higher levels of ice-supersaturation, as depicted in Fig. 4.

In terms of overall engine efficiency, cycles reach values between 0.44 and 0.52, as shown in the top left chart of Fig. 5; well above what is achievable with current engines, which is about 0.35.

No significant influence of ice-supersaturation could be found on the optimum bypass ratio, which increases with TET, as it can be seen in the top right chart of Fig. 5. The results suggest that the clean exhaust engine concept requires very high bypass ratios, exceeding 20, to achieve maximum efficiency, which is far more than conventional turbofan configuration values, which are about 11 for modern engines.

The optimum overall pressure ratio increases with TET, as shown in the bottom left chart of Fig. 5. It is lowest if contrail avoidance is not considered and increases for higher levels of ambient ice-supersaturation. The calculated OPRs are below that of modern engines, indicating that less turbomachinery is required in the clean exhaust engine concept, hence reducing the weight associated with turbomachinery.

The optimum fan pressure ratios are shown in the bottom right chart of Fig. 5. For the case of contrail avoidance not being considered during optimization, the optimum fan pressure ratio is

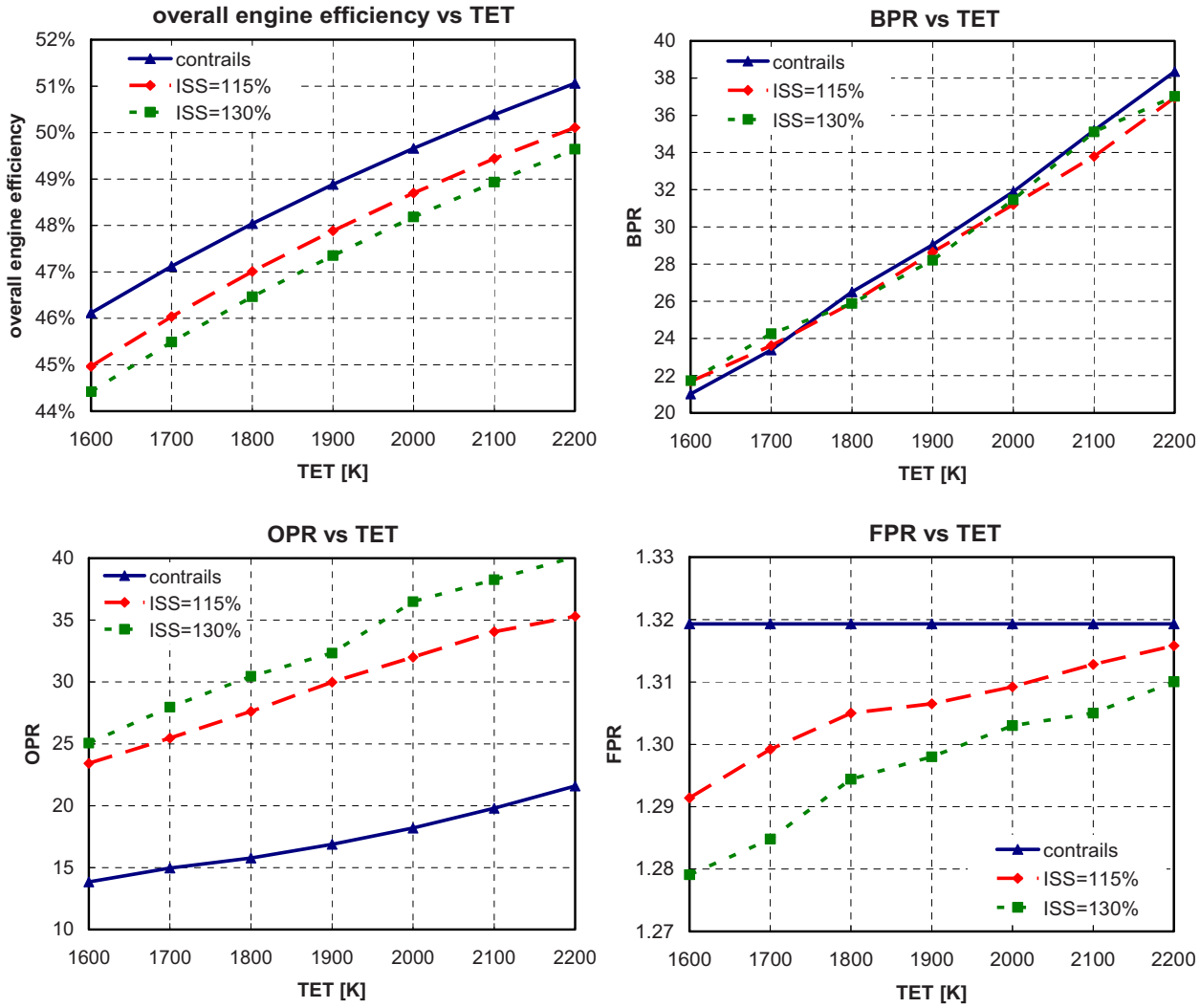

Fig. 5 Performance results and design variables of optimized clean exhaust engine cycles for a variety of TETs: overall engine efficiency (top left), bypass ratio (top right), overall pressure ratio (bottom left), and fan pressure ratio (bottom right)

independent from TET, with a value of 1.32. In other cases, the optimum fan pressure ratio is increasing with TET and is lower for higher levels of ice-supersaturation.

5 Discussion

In this study, it is shown that the clean exhaust engine concept exhibits a significant performance advantage over conventional engine architecture. Overall efficiencies in excess of 50% are possible, and at the same time, water condensation within the engine results in reduced water vapor emissions, and thus contrail avoidance. NO_x emissions could be reduced through direct water injection in the combustion chamber during the entire flight, and aerosols and soot could be scavenged from the exhaust gases.

The calculations suggest that the calculated optimum fan pressure ratios are below that of conventional engines. The clean exhaust engine concept would hence provide an attractive basis for the application of unducted fans or remotely driven fans, which have bypass ratios similar to what was obtained in this study.

Although heat exchanger technology is at a level where heat exchanger performance requirements could probably be met for this engine concept, weight and volume issues as well as pressure losses would probably require further advances in heat exchanger technology. Heat exchanger size and weight are dependent on mass flow and the required temperature change. As these parameters are determined by the cycle, the challenge is to design a heat exchanger with the required performance at low weight and volume, and pressure loss. Therefore, superconducting light heat transfer materials [11] and similar materials that might become available in the future could provide the necessary step required in the realization for the clean exhaust engine concept, at least to reduce weight. The remaining hurdle to take would then be pressure loss and volume. Usually, the pressure loss across a heat exchanger is in conflict with its volume; although compact designs with sophisticated surface structures may reduce the volume of heat exchangers due to better heat transfer rates, the associated turbulence in the flow imposes higher pressure losses. An optimum may be found trading off the two conflicting design parameters via novel design and optimization techniques, but it is questionable whether current heat exchanger technology would facilitate the clean exhaust engine concept, especially in the light of the additional ducting required in this engine.

Therefore, it is recommended to conduct further work on this engine concept, including detailed design and integration analysis and in-depth heat exchanger performance considerations. This would help to understand whether or not current heat exchanger technology is sufficient for this engine concept, and, if it is not, how to improve heat exchanger technology to enable the clean exhaust engine concept.

Nomenclature

BPR = bypass ratio
CC = combustion chamber
CON = condenser
c_p = specific heat capacity
EI = emission index (kg/kg fuel)
FPR = fan pressure ratio
G = mixing line slope
HPC = high pressure compressor
HPT = high pressure turbine
IC = inter cooler
IPC = intermediate pressure compressor
IPT = intermediate pressure turbine
ISS = ice supersaturation
LPT = low pressure turbine
OPR = overall pressure ratio
P,p = pressure
PR = pressure ratio
q_{net} = fuel net calorific value
R = ratio of IPC PR and HOC PR
REC = recuperator
SFC = specific fuel consumption (g/s kN)
TET = turbine entry temperature (K)
ε = effectiveness
η = isentropic efficiency
ω = molar mass ratio water to air

References

[1] Solomon, S., Qin, D., Manning, M., Chen, Z., Marquis, M., and Averyt, K. B., 2007, *Climate Change 2007: The Physical Science Basis. Contribution of Working Group I to the Fourth Assessment Report of the Intergovernmental Panel on Climate Change, (IPCC, 2007)*, M. Tignor and H. L. Miller, eds., Cambridge University Press, New York.
[2] Hansen, J., Sato, M., and Ruedy, R., 1997, "Radiative Forcing Climate Response," J. Geophys. Res., **102**(D6), pp. 6831–6864.
[3] Noppel, F., and Singh, R., 2007, "Contrail and Cirrus Cloud Avoidance Technology," J. Aircr., **44**(5), pp. 1721–1726.
[4] Noppel, F., Singh, R., and Taylor, M., 2006, "Novel Engine Concept to Suppress Contrail and Cirrus Cloud Formation," *Proceedings of the International Conference on Transport, Atmosphere and Climate (TAC)*, DLR, Oxford, UK, June.
[5] Alexander, D., Lee, Y.-M., Guynn, M., and Bushnell, D., 2002, "Emissionless Aircraft Study," Paper No. AIAA 2002-4056.
[6] Schumann, U., 2000, "Influence of Propulsion Efficiency on Contrail Formation," Aerosp. Sci. Technol., **4**(6), pp. 391–401.
[7] Lefebvre, A. H., 1983, *Gas Turbine Combustion*, Hemisphere, New York.
[8] Daggett, D. L., 2002, "Ultra Efficient Engine Technology Systems Integration and Environmental Assessment," Boeing Commercial Airplane Group, Report No. NASA/CR-2002–211754.
[9] Flatau, P. J., Walko, R. L., and Cotton, W. R., 1992, "Polynomial Fits to Saturation Pressure," J. Appl. Meteorol., **31**(12), pp. 1507–1513.
[10] Jensen, E. J., Toon, O. B., Kinne, S. K., Sachse, G. W., Anderson, B. E., Chan, K. R., Twohy, C. H., Gandrud, B., Heymsfield, A., and Miake-Lye, C., 1998, "Environmental Conditions Required for Contrail Formation and Persistence," J. Geophys. Res., **103**(D4), pp. 3929–3936.
[11] Qu, Y., 2000, "Superconducting Heat Transfer Medium," U.S. Patent No. 6,132,823.

Secondary Air System Component Modeling for Engine Performance Simulations

A. Alexiou
Research Associate
e-mail: a.alexiou@ltt.ntua.gr

K. Mathioudakis
Professor
e-mail: kmathiou@central.ntua.gr

Laboratory of Thermal Turbomachines,
National Technical University of Athens,
P.O. Box 64069,
Athens 15710, Greece

This paper describes the modeling of typical secondary air system elements such as rotating orifices, seals, and flow passages with heat and work transfer from the surrounding surfaces. The modeling is carried out in an object-oriented simulation environment that allows the creation of different configurations in a simple and flexible manner. This makes possible to compare the performance between different designs of individual components or complete secondary air systems as well as integrate them directly in whole engine performance models. The modeling is validated against published experimental data and computational results. An example of implementation in an engine model is also presented. [DOI: 10.1115/1.3030878]

Keywords: secondary air system, orifice discharge coefficient, rotating cavity, preswirl system, labyrinth seal, performance

1 Introduction

The gas turbine secondary air system performs a variety of functions that are critical for the safe operation of the engine such as ventilation (mostly cooling but sometimes components are heated), sealing and purging air to disks, shafts, cavities, and bearing chambers. The use of this air is parasitic to the overall engine performance cycle (up to 6% of specific fuel consumption in a modern turbofan engine), since it is bled from appropriate compressor stages where work has been done to raise its pressure. Furthermore, its quality degrades as it flows through a complex network of orifices, cavities, component interfaces, and passages. For accurate engine performance calculations, these losses must be accounted for through an air system model. This is not simple as secondary air systems can be found in a wide variety of configurations, depending on engine architecture, performance requirements, manufacturing, safety, and financial constraints. A typical secondary air system, with some of its main components identified [1], is depicted in Fig. 1.

The fact that the capability of development of cycle gas path components has reached a high level, leaving small margins for further developments has made secondary air systems an area where comparable gains can be achieved and thus promoted the interest in their studies to a front line level. This can be seen from the emergence of many studies in recent years, ranging from simple semi-empirical models for individual components and their interconnections [2,3], to detailed computational fluid dynamics (CFD) flow studies for individual component characteristic prediction [4].

Air system losses (mass flow, pressure, temperature, and swirl velocity changes) are calculated by dedicated air system models (typically 1D flow network solvers) over a range of engine operating conditions, and the results are transferred into a whole engine performance model through bleeds and returns [5]. This approach makes the secondary air system a "black-box" for the performance engineer while the air system designer cannot assess autonomously the system performance as part of the whole engine model. Additionally, any changes either at the air system or engine cycle level must be communicated between the various specialists, thus increasing the scope for errors during this process.

In this paper, an approach based on object-oriented simulation technologies is proposed to model various secondary air system components, such as the ones shown in Fig. 1. This allows for constructing, evaluating, and comparing the performance of different air system design configurations in a generic, flexible, and intuitive manner. Individual components or entire air systems can then be integrated transparently in whole engine performance models created in the same simulation environment. The user can modify the attributes of the air system within the engine model or the modeling of an air system component or even use a completely different air system without making any changes to the rest of the engine model. Finally, configuration management and version control capabilities make component changes visible during model exchanging.

The modeling methodology of some typical secondary air system components is described in Sec. 2.

2 Air System Component Modeling

In order to make possible the modeling of any secondary air system layout, the typical flow configurations are identified and modeled as individual components. Appropriate design of the models produced allows then their interconnection for creating overall secondary air system models for a large variety of engine configurations. A study of the configurations encountered today in many engines in service has led to the definition of three main components: generic, orifice, and labyrinth seals. For a specified component geometry, the inlet flow conditions ($\dot{m}$, P_t, T_t, and V_φ) are linked to the outlet flow ones through the conservation equations for mass, energy, and axial and angular momenta. The object-oriented modeling allows the component's performance to be calculated using any valid combination of input/output variables and component characteristics.

2.1 Generic Component. This component is used to describe an arbitrary geometry consisting of J input flows and N output flows. The input flows are mixed together and the fully mixed flow undergoes both work and heat transfer from the surrounding K surfaces. The chamber of the preswirl system, the interdisk cavities in the compressor, and the drive cone cavity, depicted in Fig. 1, are some areas of the secondary air system that can be modeled using this component. Figure 2 shows an example of the component with two input and two output flows and four surfaces,

Manuscript received June 30, 2008; final manuscript received July 9, 2008; published online February 13, 2009. Review conducted by Dilip R. Ballal. Paper presented at the ASME Turbo Expo 2008: Land, Sea and Air (GT2008), June 9–13, 2008, Berlin, Germany.

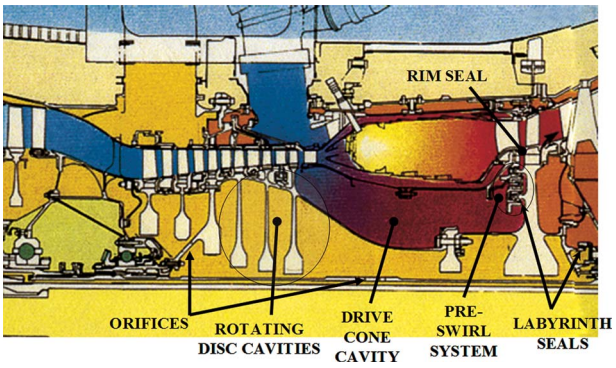

Fig. 1 Secondary air system

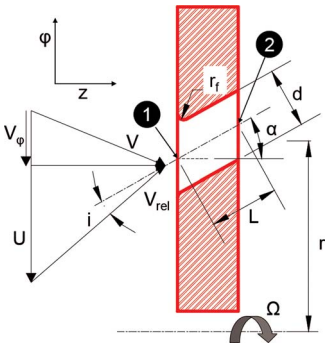

Fig. 3 Orifice component model

two of which are rotating.

The modeling approach is similar to the simple or drag model proposed in Ref. [2]. The fully mixed value of the tangential velocity, $V_{\varphi,\mathrm{mix}}$, at the component mean radius, r_m, is found from the angular momentum conservation equation

$$\dot{m}_{\mathrm{mix}} \cdot r_m \cdot V_{\phi,\mathrm{mix}} - \sum_{j=1}^{J} (\dot{m}_{\mathrm{in},j} \cdot r_{\mathrm{in},j} \cdot V_{\phi,\mathrm{in},j}) = \sum_{k=1}^{K} M_k \tag{1}$$

where the moment, M, exerted by the fluid on each surrounding surface, is obtained from

$$M_k = 0.5 \cdot C_{m,k} \cdot r_k \cdot A_k \cdot \rho_{\mathrm{mix}} \cdot |\Omega \cdot r_k - V_{\phi,\mathrm{mix}}| \cdot (\Omega \cdot r_k - V_{\phi,\mathrm{mix}}) \tag{2}$$

The friction coefficient, C_m, depends on both the surface configuration (disk, cone, or cylinder) and the flow conditions represented by the rotational Reynolds number [6] (see Appendix). The total temperature at the fully mixed conditions, $T_{t,\mathrm{mix}}$, can then be estimated from the energy conservation equation

$$\dot{m}_{\mathrm{mix}} \cdot C_{p,\mathrm{mix}} \cdot T_{t,\mathrm{mix}} - \sum_{j=1}^{J} (\dot{m}_{\mathrm{in},j} \cdot C_{p,j} \cdot T_{t,\mathrm{in},j}) = Q + \sum_{k=1}^{K} \Omega \cdot M_k \tag{3}$$

The mixing total pressure, $P_{t,\mathrm{mix}}$, is

$$P_{t,\mathrm{mix}} = P_{s,\mathrm{mix}} \cdot \left[(1-\zeta) \cdot \left(\frac{T_{t,\mathrm{mix}} - (Q/(\dot{m}_{\mathrm{mix}} \cdot C_P))}{T_{s,\mathrm{mix}}} \right)^{\gamma/(\gamma-1)} + \zeta \right] \tag{4}$$

where ζ is a mixing pressure loss coefficient, which takes into account the losses due to the mixing process, and the mixing static pressure, $P_{s,\mathrm{mix}}$, is determined from the axial momentum conservation equation

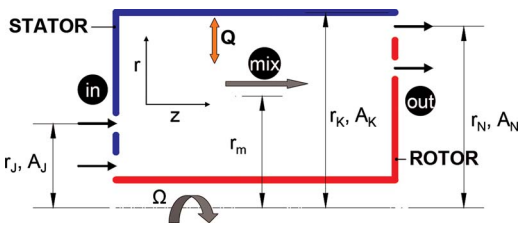

Fig. 2 Generic component model

$$P_{s,\mathrm{mix}} = \frac{\sum_{j=1}^{J} (\dot{m}_{\mathrm{in},j} \cdot V_{z,\mathrm{in},j} + P_{s,\mathrm{in},j} \cdot A_{\mathrm{in},j}) - \dot{m}_{\mathrm{mix}} \cdot V_{z,\mathrm{mix}}}{A_{\mathrm{mix}}} - (P_{t,\mathrm{mix,is}} - P_{t,\mathrm{mix}}) \tag{5}$$

The tangential velocity at each outlet is found assuming free vortex flow from the component mean radius to the outlet radius. The convective heat transfer is calculated from

$$Q = h_{\mathrm{av}} \cdot A_S \cdot (T_S - T_{\mathrm{ref}}) \tag{6}$$

where T_S is an area-weighted average surface temperature, T_{ref} is the appropriate fluid reference temperature, and h_{av} is a surface average heat transfer coefficient, calculated from empirical correlations depending on geometry and flow conditions.

2.2 Orifice Component. This component is used to simulate the flow of secondary system air through the various configurations of orifices and covers orifices located on disk, drum, and shaft surfaces. A thorough understanding of the discharge behavior of all types of orifices is required to guarantee that the right amount of air, at the appropriate level of pressure and temperature, will reach its destination, during the complete range of engine operating conditions. Figure 3 shows the model of an axial rotating orifice with the main parameters affecting the discharge behavior, namely, the orifice geometry and the flow conditions at its inlet.

The discharge behavior of an orifice is expressed in terms of the discharge coefficient, C_D, defined as the ratio of the actual mass flow rate through the orifice $\dot{m}_h$ to the ideal (isentropic) value $\dot{m}_{\mathrm{is}}$ as follows:

$$C_D = \frac{\dot{m}_h}{\dot{m}_{\mathrm{is}}} \tag{7}$$

Assuming a one-dimensional, isentropic compressible expansion of a perfect gas from the upstream total pressure, $P_{t,1}$, to the downstream static pressure, $P_{s,2}$, and considering the work transferred to the fluid (for rotating orifices), it can be shown that [7]

$$\dot{m}_{\mathrm{is}} = A_h \cdot \rho_{t,1} \cdot \left(\frac{P_{s,2}}{P_{t,1}} \right)^{1/\gamma} \cdot \left\{ \left(\frac{2 \cdot \gamma}{\gamma - 1} \right) \cdot \frac{P_{t,1}}{\rho_{t,1}} \cdot \left[1 - \left(\frac{P_{s,2}}{P_{t,1}} \right)^{(\gamma-1)/\gamma} \right] + 2 \cdot \Omega \cdot (r_2 \cdot V_{\phi,2} - r_1 \cdot V_{\phi,1}) - V_{\phi,2}^2 \right\}^{1/2} \tag{8}$$

When $V_{\varphi,1} = V_{\varphi,2} = 0$, the above equation reduces to the standard result for flow through a stationary nozzle.

If C_D is known, Eqs. (7) and (8) can be used to either calculate the pressure loss incurred for a given flow through an orifice or, if the pressure ratio across the orifice is known, calculate the flow though it. The value of C_D depends on a number of geometric and flow parameters and there are different methods for evaluating it, as described in Ref. [8]. The approach followed in this work is to

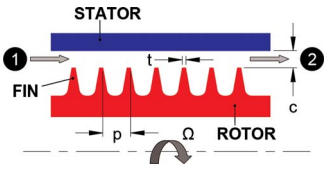

Fig. 4 Labyrinth seal component model

use the correlations presented in Ref. [9], which are based on the incidence angle, i, of the flow into the orifice and allow the effects of various parameters to be considered (Reynolds number, corner radius, length, chamfering, pressure ratio, pumping, rotation, and orifice angle of orientation). The value of C_D is then obtained from

$$C_D = 1 - f_1 \cdot f_{2,r_f/d} \cdot f_{2,L/d'} \cdot f_3 \cdot (1 - C_{D:\mathrm{Re}}) + \Delta C_{D:i} \tag{9}$$

where f_1, f_2, and f_3 are, respectively, the corner radius, length, and pressure ratio effect functions (chamfering and pumping effects were not considered in this work), $C_{D:\mathrm{Re}}$ is the basic discharge coefficient corrected for Reynolds number effects, and the term $\Delta C_{D:i}$ depends both on the incidence angle due to orifice rotation and the corner radius (see Appendix for equations). For the case of a rotating *axial* orifice, the incidence angle is defined here as the angle between the inlet relative tangential velocity of the orifice and the ideal axial velocity of the flow minus the orifice orientation angle, α,

$$i = \tan^{-1}\left(\frac{U - V_{\phi,1}}{V_{\mathrm{is}} \cos \alpha}\right) - \alpha \tag{10}$$

where V_{is} is equal to the term inside the curly brackets of Eq. (8), U is the rotational speed of the orifice, and $V_{\varphi,1}$ is the tangential velocity of the flow at the orifice inlet. Although the term $(V_{\mathrm{is}} \cos \alpha)$ does not represent an exact description of the flow at the orifice inlet, its use has been adopted here as it is used extensively in literature to describe the effect of rotation on C_D. For *radial* orifices, the incidence angle is defined as

$$i = \tan^{-1}\left(\frac{\sqrt{(U - V_{\phi,1})^2 + V_{z,1}^2}}{V_{\mathrm{is}} \cos \alpha}\right) - \alpha \tag{11}$$

where $V_{1,z}$ is the axial velocity of the crossflow.

2.3 Labyrinth Seal Component. This component simulates the flow through straight, staggered, and stepped labyrinth seals. These are all common in gas turbine secondary air systems. Figure 4 illustrates the main features of the straight-through seal model.

The component is structured so that one from mass flow rate, $\dot{m}$, or total pressure ratio ($\mathrm{PR}_t = P_{t,2}/P_{t,1}$) can be calculated, if the other is known. According to Ref. [10], the relationship between these two variables is

$$\dot{m} = A \cdot C_D \cdot \Gamma \cdot \frac{P_{t,1}}{\sqrt{R \cdot T_{t,1}}} \cdot \sqrt{\frac{1 - \mathrm{PR}_t^2}{n + \ln(1/\mathrm{PR}_t)}} \tag{12}$$

where A is the annular area between the fin tip and the casing. For the C_D Ref. [11] recommends a value of 0.71 when the clearance-to-thickness ratio, c/t, is between 1.3 and 2.3. Γ is the carry-over coefficient and for a straight-through seal can be determined from the following equation, proposed in Ref. [10]:

$$\Gamma = \sqrt{\frac{1}{1 - \dfrac{n-1}{n} \cdot \dfrac{c/p}{c/p + 0.02}}} \tag{13}$$

where n is the number of fins and p is the pitch. For stepped and staggered seals, $\Gamma = 1$. The last term in Eq. (12) is the expansion ratio.

3 Component Model Implementation and Validation

A brief overview of the simulation environment used to implement the modeling is presented in Sec. 3.1. Various test cases for these components are then described to demonstrate the effectiveness of the proposed modeling. Finally, an example is given of integrating an air system in a whole engine performance model.

3.1 Simulation Environment Overview. The tool used to implement the modeling is PROOSIS (PRopulsion Object-Oriented SImulation Software). It is a standalone, multiplatform, object-oriented simulation environment [12]. It shares the philosophy of the commercial simulation tool described in Refs. [13] and [14]. It uses a high-level object-oriented language (EL) for modeling engine systems. EL offers all the benefits of this type of programming: encapsulation, inheritance, aggregation, abstraction, polymorphism, etc. The most important concept in EL is the component (equivalent to a class in C++); it contains a mathematical description of the corresponding real-world engine component. Components communicate with each other through their ports. Ports define the set of variables to be interchanged between connected components. Components and ports are stored in a library.

The tool comes with a standard library of engine components and ports [15]. Their modeling is based on industry accepted standards and respects the international standards with regard to nomenclature, interface, object-oriented environment, and standard performance methodology. However, the use of the standard library is not compulsory and the user can build custom components and/or libraries. Components from different libraries can be combined in constructing a model as long as connected components share the same communication interface (e.g., ports).

A model, be it a single component, a subassembly, or a complete engine, can be constructed graphically by "drag-and-drop" icons from one or more library palettes to the schematic window.

The model's mathematical description (called a partition) is set with the help of wizards. Built-in mathematical algorithms process the equations symbolically, resolve high index problems, solve algebraic loops, suggest boundary conditions, and finally sort the equations for efficient calculation. The simulation tool allows for noncausal modeling; the order and form of equations do not matter.

Different simulation cases (experiments) can be performed for a partition. Within the experiment window and using the object-oriented language EL, one can initialize variables, set the values of boundary condition variables and component data, run single and multiple steady state simulations, integrate the model over time (transient operation), and generate reports (write results to file or screen). With the help of internal (EL) or external (C, C++, and FORTRAN) functions it is possible to create very complicated simulations (e.g., multipoint design, optimization, test analysis, etc.). Experiments can run either in batch mode or graphically.

The tool is also capable of performing multifidelity, multidisciplinary, and distributed simulations [16].

A new custom library is created in PROOSIS containing various secondary air system components. The components use the ports of the standard library so that they can connect to components from this library. The two libraries share also the same fluid model and thermodynamic functions.

3.2 Test Cases. In the following, results from single and aggregate components of the secondary air system library are compared against publicly available experimental or computational results.

3.2.1 Preswirl Chamber. The generic component can be used to model the wheel space between the stator carrying the preswirl nozzles and the rotor containing the receiver holes of a direct-transfer preswirl system. The main purpose of this system is to reduce the relative total temperature of the turbine blade cooling

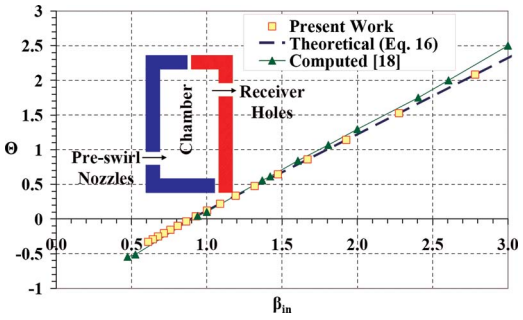

Fig. 5 Variation of Θ with β_{in}

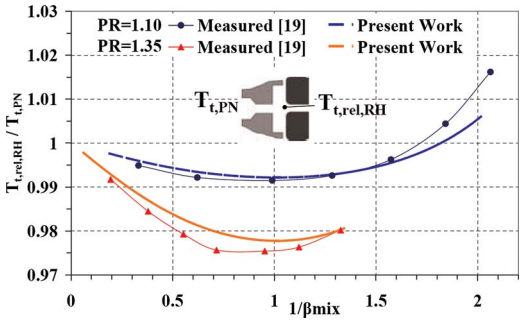

Fig. 7 Nondimensional temperature reduction

air. The adiabatic effectiveness, Θ, is described in terms of the maximum achievable temperature drop and is defined as

$$\Theta = \frac{2 \cdot C_P \cdot (T_{t,\mathrm{PN}} - T_{t,\mathrm{rel,RH}})}{\Omega^2 \cdot r_{\mathrm{RH}}^2} \tag{14}$$

where $T_{t,\mathrm{PN}}$ is the total temperature at the inlet to the preswirl nozzles and $T_{t,\mathrm{rel,RH}}$ is the total temperature at the entrance of the receiver holes in a frame of reference rotating with the rotor,

$$T_{t,\mathrm{rel,RH}} = T_{t,\mathrm{mix}} + \frac{(\Omega \cdot r_{\mathrm{RH}})^2 - 2 \cdot \Omega \cdot r_{\mathrm{RH}} \cdot V_{\phi,\mathrm{mix,RH}}}{2 \cdot C_P} \tag{15}$$

A theoretical value for Θ that accounts for the moment on the stator, M_S, can be obtained by applying the first law of thermodynamics and an angular momentum balance across the preswirl chamber [17] as follows:

$$\Theta = 2 \cdot \beta_{\mathrm{in}} \cdot \left(\frac{r_{\mathrm{PN}}}{r_{\mathrm{RH}}}\right)^2 - 1 - \frac{2 \cdot M_S}{\dot{m} \cdot \Omega \cdot r_{\mathrm{RH}}^2} \tag{16}$$

where β_{in} is the inlet swirl ratio defined as

$$\beta_{\mathrm{in}} = \frac{V_{\phi,\mathrm{in}}}{\Omega \cdot r_{\mathrm{PN}}} \tag{17}$$

Figure 5 shows a comparison between predicted (using the generic component), computed (from CFD in Ref. [18]), and theoretical (from Eq. (16)) values of Θ, for the preswirl chamber described in Ref. [18]. The predictions are in excellent agreement with the theoretical values of Θ and in line with the computations. Θ increases as β_{in} increases and becomes positive (indicating cooling) for $\beta_{\mathrm{in}} > 0.9$.

As it will be shown later for the receiver holes of this system, there is a critical value of the inlet swirl ratio β_{in} above which the flow rate of the blade cooling air will decrease. This value occurs when the effective swirl ratio at the receiver hole inlet, $\beta_{\mathrm{mix}} = V_{\phi,\mathrm{mix,RH}}/\Omega \cdot r_{\mathrm{RH}}$, is 1. For this system, the value (which strongly depends on the system geometry) is ~1.8, as can be seen in Fig. 6.

Additionally, the maximum temperature reduction is achieved when the effective swirl ratio is 1, as illustrated in Fig. 7, where the temperature ratio $T_{t,\mathrm{rel,RH}}/T_{t,\mathrm{PN}}$ is plotted against the inverse of the effective swirl ratio, $1/\beta_{\mathrm{mix}}$, for the preswirl system presented in Ref. [19].

For both nozzle pressure ratios, the curves decrease until a minimum is reached at $\beta_{\mathrm{mix}} = 1$. Further reduction of β_{mix} causes an increase in the temperature ratio, which reaches 1 at $1/\beta_{\mathrm{mix}} = 1.7$ from the experiments and 1.8 from the model predictions. As noted in Ref. [19], this is lower than the ideal value of 2.0. This is caused by the frictional heating of the air due to the work done by the rotor. Figure 8 shows the rotor moment becoming positive for $1/\beta_{\mathrm{mix}} > 1$, thus causing the heating of the air.

A further assessment of the model's accuracy is given in Fig. 9. The fully mixed tangential velocity is compared with circumferentially averaged measured tangential velocities. It is interesting to observe that the measured ones are approximately 50% lower than the values calculated assuming isentropic flow.

3.2.2 Rotating Cavities. A generic component is used to model each of the rotating cavities of the multicavity rig described in Ref. [20]. The rig simulates the secondary air system within a high pressure compressor where the cooling air flows axially in the annular space between the disk bores and the enclosed drive shaft. Heat transfer from the rotating surfaces causes a tempera-

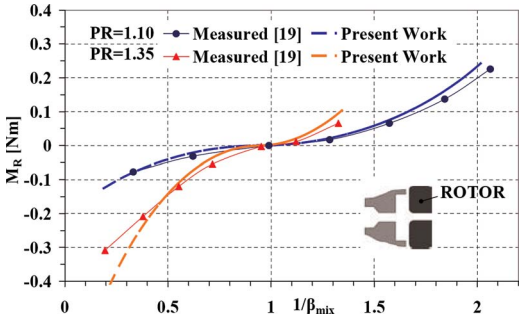

Fig. 8 Rotor moment

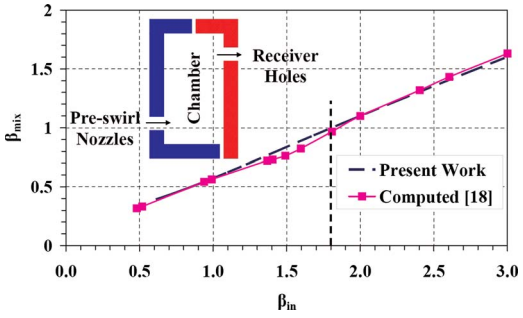

Fig. 6 Variation of β_{mix} with β_{in}

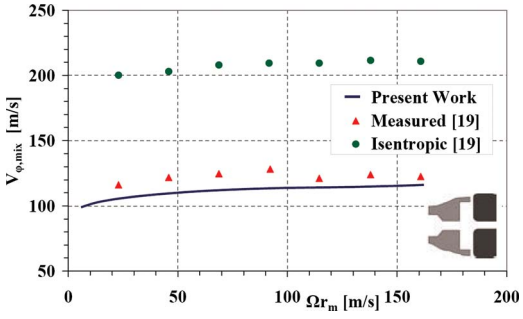

Fig. 9 Tangential velocity variation with disk speed

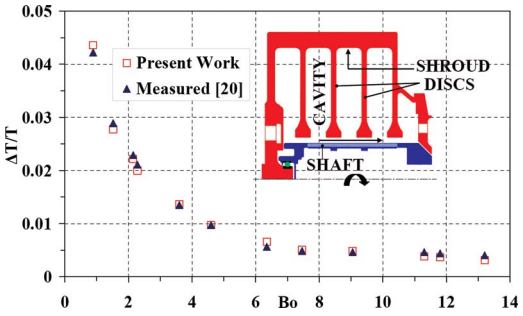

Fig. 10 Variation of nondimensional temperature change with buoyancy number

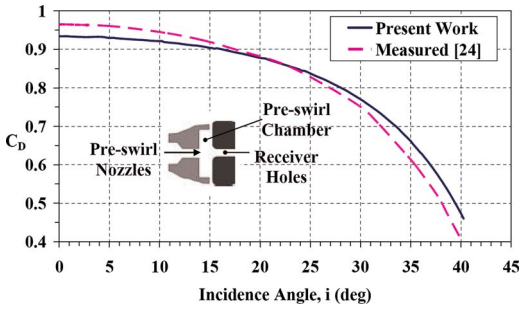

Fig. 11 Variation of C_D with i

ture rise in the air with important consequences to its cooling potential further downstream in the engine. The heat transfer measurements from the rig revealed two regimes of heat transfer depending on the value of the buoyancy number, Bo, which indicates the relative strengths of the axial inertia of the cooling jet to the centrifugal buoyancy of the flow [21]. Hence, at low values of Bo (<6), the heat transfer is governed by rotation while at larger values of this parameter the heat transfer is controlled by the action of the throughflow.

Figure 10 shows the variation of the nondimensional air temperature rise across the rotor against Bo. The two regimes can be clearly seen. Also plotted in the figure are the model predictions. Following Ref. [22], free convection from a horizontal plate is assumed for the peripheral shroud, a correlation for natural convection from a vertical plate is used for each disk, and a flat plate forced convection heat transfer coefficient for the shaft surfaces. The correlations are taken from Ref. [23] and are included in the Appendix. A relative total temperature (see Eq. (15)) is used as T_{ref} for the disks and shrouds while the total temperature at each cavity inlet is used for the shafts. The same average surface temperature is assumed for each disk surface, calculated as the average of the radially weighted average temperatures measured from the upstream and downstream surfaces of the second and third disks. The average temperature measured at the shrouds of the second and third cavities is used for all the shrouds. Finally, an average of the temperatures measured along the shaft is used for each shaft's T_S. As can be seen in the figure, the model is an accurate representation of the real situation both in terms of the physics of the flow and the absolute values of temperature rise.

3.2.3 Rotating Holes. The orifice component was used to model the rotating receiver holes of the direct-transfer preswirl system described in Ref. [24], where $L/d=5.66$, $r/d=0.2$, $\alpha=0$, and $N_{\text{RH}}=24$. These holes supply cooling air to the turbine blades. The air is delivered through a rotor-stator cavity from nozzles angled to the tangential direction, thus reducing the relative total temperature of the air entering the receiver holes. The experimentally derived values of C_D take into account the work done by the rotor and the change in total enthalpy of the cooling air. The inlet conditions (total pressure and temperature, mass flow, and swirl angle) for the orifice component are predicted from the corresponding model of the preswirl cavity described in Sec. 3.2.1. Figure 11 shows a comparison of experimental and predicted values of C_D against the incidence angle. The highest value of C_D is reached when $i=0$ (minimum separation at the inlet) and decays away from this position. The correlations accurately capture the holes' discharge behavior.

The same approach was used to model the receiver holes from the preswirl rotor-stator configuration of Ref. [18] where $L/d=1.25$, $r/d=0$, $\alpha=0$, and $N_{\text{RH}}=60$. Figure 12 shows the variation of C_D with the effective swirl ratio β_{mix}, based on the effective swirl velocity of the air at the inlet to the receiver holes.

As expected, the maximum value of C_D occurs when $\beta_{\text{mix}}=1$ corresponding to synchronous rotation of the fluid core adjacent to the receiver holes. Hence, there is an upper limit for the flow rate of the blade cooling air and this has important practical implications since, as it was shown in Sec. 3.2.1, cooling effectiveness increases monotonically with β. The model overpredicts the computational results although it is interesting to note that the measurements are consistently higher from both the correlations and computational predictions, but they are limited to $\beta_{\text{mix}}<0.6$.

Figure 13 shows the predicted variation of the receiver holes C_D with β_{mix} for the midradius preswirl cooling air delivery system reported in Ref. [2], where $L/d=0.86$, $r/d=0$, $\alpha=0$, and $N_{\text{RH}}=72$. No measurements were presented due to the loss of the rotating pressure transducers. The same discharge behavior is observed also in this case as in the previous ones, but with a lower value for the maximum C_D that could be attributed to the smaller value of L/d.

Finally, the orifice component was used to model the configuration described in Ref. [25], which simulates the part of the secondary air system where cooling air from the high pressure (HP) compressor rotor is bled through radial holes in the intermediate pressure (IP) drive shaft. In the experiments the rotor and shaft were independently driven and it was found that when the rotor and shaft are stationary or corotate at the same speed ($\Delta\Omega=0$) then the discharge coefficients agree with established experimen-

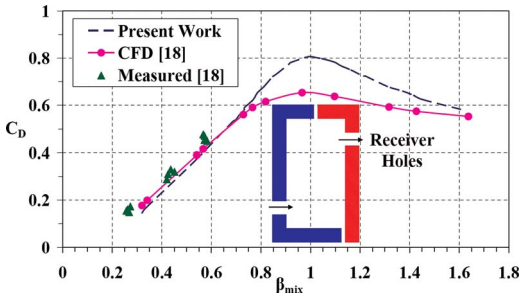

Fig. 12 Variation of C_D with β_{mix}

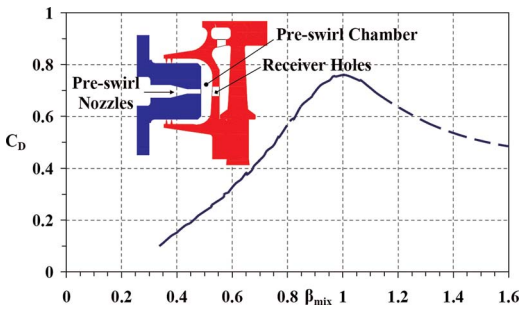

Fig. 13 Variation of C_D with β_{mix} for midradius preswirl system

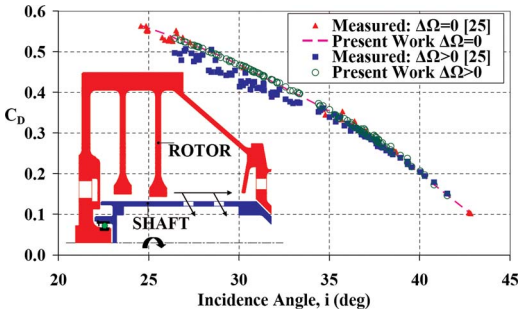

Fig. 14 Variation of C_D with i for radial rotating holes

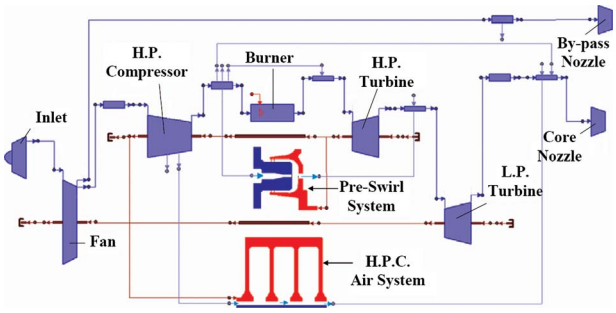

Fig. 16 Engine performance model with secondary air system

tal data for nonrotating holes in the presence of crossflow. When the rotor speed is greater than that of the shaft (including contrarotation) there is a significant decrease in the discharge coefficient ($\Delta\Omega > 0$).

In Fig. 14 the variations of both the experimentally derived and orifice component model predicted values of C_D are plotted against the incidence angle.

For $\Delta\Omega = 0$, the predicted values are within 3% of the measured ones. This is within the 4% uncertainty in the measured discharge coefficient values quoted in Ref. [25]. Although the correlations were derived for rotating axial holes they are also valid for nonrotating radial holes with crossflow since in principle the flows are similar [26]. When $\Delta\Omega > 0$, the model predictions overestimate the measurements by up to 7% at the lower incidence angles. This is expected as there is no correction in the correlations for taking into account both crossflow and preswirl effects. The orifice component modeling allows the addition of new corrections, when these become available. It should be noted also that there is less than 2% difference between the measured and model predicted values of static pressure at the orifice exit.

3.2.4 Preswirl System With Labyrinth Seals. An aggregate component was created to simulate the preswirl system of Ref. [2]. A generic component was used for the chamber, orifice components were used for the preswirl nozzles, and receiver holes and two labyrinth seal ones for the inner and outer seals. Figure 15 shows the variation of Θ with the effective swirl ratio β_{mix}. The model accurately reproduces the system's measured performance.

3.3 Whole Engine Model. In Sec. 3.2, discrete areas of the secondary air system have been modeled using components from a custom library and predictions were compared with available experimental and computational results. By combining appropriate components from this library together, an entire secondary air system, such as the one depicted in Fig. 1, could be constructed. Both individual and complete systems could then be added in a corresponding whole engine model to study their effect on overall engine performance and vice versa.

An example is illustrated in Fig. 16, where a preswirl system and part of the HP compressor internal air system are added in a model of a two-shaft, unmixed turbofan gas turbine engine. This is a virtual engine developed in Ref. [27]. The preswirl system consists of the nozzles, the chamber, and the receiver holes while the HP compressor internal air system comprises three rotating disk cavities. Since flow and heat transfer in these elements depend on geometry, their basic dimensions (e.g., disk and shaft radii, number of nozzles and receiver holes, etc.) had to be determined from the dimensions of the main annulus and best judgment for this type of engine. The surface temperatures inside the compressor disk cavities are determined from the compressor main flow air temperature at the inlet and exit, assuming forced convection in a duct to get the temperatures at the outer drum surface, radial conduction through the shroud to obtain the temperatures at the inner drum surface, and quadratic radial temperature distribution between the disk tip and bore. Although these assumptions are critical for the performance of these systems, the main purpose of this study is to demonstrate the ease of integrating these components in the engine model and the potential for design improvements through optimization at the system or global level.

In the original engine performance model, the HP turbine blade cooling air is simulated by extracting some air from the HP compressor delivery and returning it after the HP turbine. The preswirl system is added between these two locations. An HP compressor interstage bleed provides cooling and sealing air to the low pressure (LP) turbine and this is where the HP compressor internal air system is introduced. No other changes were made to the original model.

Figure 17 shows the effect on relative total temperature and receiver hole discharge coefficient of varying the HP turbine rotor cooling air by $\pm 2\%$ from the design value of $\sim 17\%$ of the compressor exit flow. At design, the effective swirl ratio β_{mix} is 0.94 (underswirled) and increasing the cooling air flow rate by $\sim 1\%$ will give the optimum preswirl system performance for the geometry and operating conditions considered. This increase though has a negative impact on the overall engine performance, increasing the specific fuel consumption by 0.43% and reducing the net

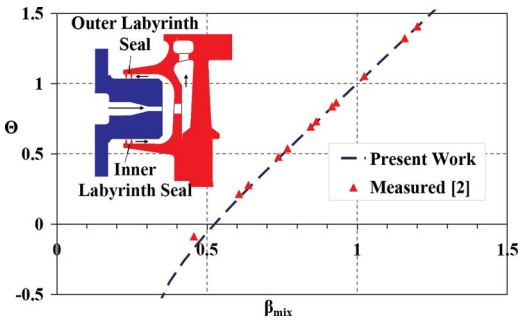

Fig. 15 Variation of Θ with β_{mix} for midradius preswirl cavity

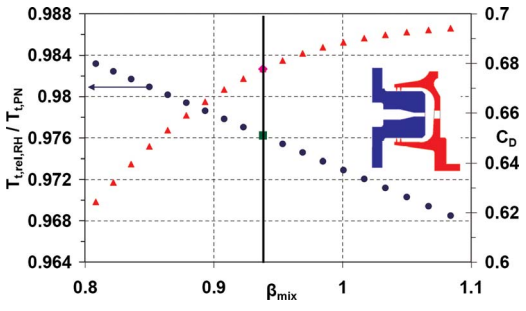

Fig. 17 Effect of turbine rotor cooling air mass flow rate variation on preswirl system performance

thrust produced by almost the same amount. Increasing the preswirl nozzles angle by 5 deg will need only half of the mass flow rate increase to achieve pure axial flow in the receiver holes, minimizing the impact on global performance. The addition of the HP compressor internal air system results in 2.5% temperature increase in the air delivered to the LP turbine, compared with the base model. Changing the preswirl mass flow rate also affects this system as the boundary conditions change resulting in different heat transfer rates from the surfaces to the air.

Given the assumptions made in constructing the model and the lack of data for validation, the values stated are only indicative. On the other hand, the validation carried out at the component level in Sec. 3.2 is an indication for the accuracy of the physical trends observed.

A multi-objective, multiconstraint optimization scheme, like the one described in Ref. [28], could be used to determine the geometric and flow conditions of main and secondary components, for best performance over a range of engine operating conditions.

Finally, it should be emphasized that although the present modeling approach is based mainly on semi-empirical models, it is also possible to integrate higher fidelity, physics-based computations (e.g., a CFD model), by exploiting the benefits of object-oriented simulation technologies. An example of this approach for a main flow component was demonstrated in Ref. [16].

4 Summary and Conclusion

An approach for modeling secondary air systems within an object-oriented environment for gas turbine engine performance simulations is presented. A custom library of typical secondary air system components is created in a specific modeling environment. The modeling of selected components from this library is presented in detail. The components are used to simulate various air system configurations and the predicted results are consistent with available experimental data and computational results. Finally, an example of adding parts of an air system to a whole engine performance model is given to demonstrate the benefits of this approach.

The flexibility of the simulation environment and the generality of the component modeling approach allow easily different air system configurations to be constructed and evaluated, both on their own and as part of a complete engine performance model. Since the approach presented allows components to be represented in varied levels of detail, it is possible to create more realistic models early in the engine design process.

Acknowledgment

The work described in this paper has been carried out as part of the EU Integrated Project VIVACE (AIP3-CT-2003-502917) and financial support of the European Union Commission is gratefully acknowledged. The authors would like also to express their thanks to the partners involved in Work Package 2.4 of VIVACE for the development of PROOSIS. The contribution of P. Dewallef in parts of the work is greatly appreciated.

Nomenclature

A = area
Bo = buoyancy number
C_D = discharge coefficient
CFD = computational fluid dynamics
C_m = friction factor
C_P = specific heat capacity at constant pressure
c = clearance
d = diameter
f = correction function
Gr = Grashof number
h = heat transfer coefficient
HP = high pressure
i = incidence angle
IP = intermediate pressure
k = thermal conductivity
L = length
LP = low pressure
M = moment
$\dot{m}$ = mass flow rate
n = number of labyrinth seal fins
P = pressure
p = pitch
PR = pressure ratio
$\mathrm{Pr}=\mu \cdot Cp/k$ = Prandtl number
Q = heat transfer
R = gas constant
r = radius
$\mathrm{Ra}=\mathrm{Pr} \cdot \mathrm{Gr}$ = Rayleigh number
Re = Reynolds number
T = temperature
t = thickness
U = rotational speed
V = velocity

Greek Symbols

α = orifice orientation angle
β = swirl ratio
Γ = carry-over coefficient
γ = ratio of specific heats
ζ = pressure loss coefficient
Θ = adiabatic effectiveness
μ = dynamic viscosity
ρ = density
Ω = angular velocity

Subscripts

1 = upstream of the component
2 = downstream of the component
av = average
h = hole
in = inlet
is = isentropic
mix = mixing
PN = preswirl nozzles
ref = reference
rel = relative
RH = receiver hole
S = surface, stator
s = static
t = total
z = axial
φ = tangential

Appendix

1 Discharge Coefficient Correlations. (See Ref. [9]). The effect of Reynolds number, Re_d, on C_D is

$$C_{D:\mathrm{Re}} = 0.5885 + \frac{372}{\mathrm{Re}_d} \tag{A1}$$

where $\mathrm{Re}_d = m_h \cdot d / A_h \cdot \mu$. The corner radius effect function is

$$f_1 = 0.008 + 0.992 \exp[-5.5 \cdot (r_f/d) - 3.5 \cdot (r_f/d)^2] \tag{A2}$$

When both corner radius and length effects occur together, the total length of the orifice is reduced by the presence of the radius and an additional correction function is introduced as follows:

$$f_{2,r/d} = [1 + 1.3 \exp(-1.606 \cdot (r_f/d)^2)] \cdot (0.435 + 0.021 \cdot (r_f/d)) \tag{A3}$$

The orifice length effect function is then calculated, using the reduced length, from

$$f_{2,L/d'} = \left[1 + 1.3\exp\left(-1.606\cdot\left(\frac{L-r_f}{d}\right)^2\right)\right] \cdot \left(0.435 + 0.021\cdot\left(\frac{L-r_f}{d}\right)\right) \quad \text{(A4)}$$

The pressure ratio effect function is given from

$$f_3 = \left(\frac{C_{D:\mathrm{Re},r,L} - 0.6}{0.263}\right)\cdot(C_{1,\mathrm{PR}} - C_{2,\mathrm{PR}}) + C_{2,\mathrm{PR}} \quad \text{(A5)}$$

where

$$C_{1,\mathrm{PR}} = 0.8454 + 0.3797\exp(-0.9083\cdot\mathrm{PR})$$
$$C_{2,\mathrm{PR}} = 6.6687\exp(0.4619\cdot\mathrm{PR} - 2.367\cdot\sqrt{\mathrm{PR}}) \quad \text{(A6)}$$

Finally, the incidence correction term is given by

$$\Delta C_{D,i} = 4\cdot\left(\frac{r_f}{d} - 0.25\right)\cdot(C_{r/d} - C_{\text{sharp-edge}}) + C_{r_f/d} \quad \text{(A7)}$$

where

$$C_{r_f/d} = -3.061\times10^{-3}\exp(0.1239\cdot i)$$
$$C_{\text{sharp-edge}} = -3.638\times10^{-4}\cdot i^2 \quad \text{(A8)}$$

2 Friction Coefficients. (See Ref. [6]). For free disks with nonzero inner radius and half angle θ, the moment coefficient for one side of a disk is

$$C_m = 0.07288\cdot(\sin\theta)^{-0.8}\cdot\left[1 - \left(\frac{r_i}{r_o}\right)^5\right]\cdot\mathrm{Re}_\varphi^{-0.2} \quad \text{(A9)}$$

where r_i and r_o are, respectively, the inner and outer radii of the disk. For a smooth cylinder of length L, the friction moment coefficient is defined as (for turbulent flow)

$$C_m = \frac{2\cdot\pi\cdot L}{r}\cdot C_f \quad \text{(A10)}$$

where $C_f = [4.07\log_{10}(\mathrm{Re}_\varphi\cdot\sqrt{C_f}) - 0.6]^{-2}$

3 Heat Transfer Coefficient Correlations. (See Ref. [23]). A correlation for natural convection from a vertical plate is used to model the heat transfer from the rotating cavity disk surfaces

$$h_{\mathrm{av}} = 0.68 + \frac{0.67\cdot\mathrm{Ra}^{0.25}}{\left[1 + \left(\frac{0.492}{\mathrm{Pr}}\right)^{9/16}\right]^{4/9}}\cdot\frac{k}{L} \quad \text{for} \quad \mathrm{Ra} < 10^9$$
$$h_{\mathrm{av}} = 0.1\cdot\mathrm{Ra}^{1/3}\cdot\frac{k}{L} \quad \text{for} \quad \mathrm{Gr} > 10^9 \quad \text{(A11)}$$

For the peripheral shroud, a correlation for natural convection from the upper surface of a heated plate is used as follows:

$$h_{\mathrm{av}} = 0.54\cdot\mathrm{Ra}^{0.25}\cdot\frac{k}{L} \quad \text{for} \quad 10^4 \le \mathrm{Ra} < 10^7$$
$$h_{\mathrm{av}} = 0.15\cdot\mathrm{Ra}^{1/3}\cdot\frac{k}{L} \quad \text{for} \quad 10^7 \le \mathrm{Ra} < 10^{11} \quad \text{(A12)}$$

Finally forced convection from a flat plate was assumed for the shaft surfaces as follows:

$$h_{\mathrm{av}} = 0.662\cdot\mathrm{Pr}^{1/3}\cdot\mathrm{Re}_z^{0.5}\cdot\frac{k}{L} \quad \text{for} \quad \mathrm{Re}_z < 5\times10^5$$
$$h_{\mathrm{av}} = 0.036\cdot\mathrm{Pr}^{1/3}\cdot\mathrm{Re}_z^{0.8}\cdot\frac{k}{L} \quad \text{for} \quad \mathrm{Re}_z \ge 5\times10^5 \quad \text{(A13)}$$

where $\mathrm{Gr} = \rho^2\cdot(T_S - T_{\mathrm{ref}})\cdot g\cdot L^3/T_{\mathrm{av}}\cdot\mu^2$, $\mathrm{Re}_z = \dot{m}\cdot L/\mu\cdot A$, g is acceleration due to gravity (9.81) or rotation ($\Omega^2\cdot L$), and the fluid properties (μ,ρ,k,Cp) are calculated at the mean film temperature $T_{\mathrm{av}} = (T_S + T_{\mathrm{ref}})/2$.

References

[1] Smout, P. D., Chew, J. W., and Childs, P. R. N., 2002, "ICAS-GT: A European Collaborative Research Programme on Internal Cooling Air Systems for Gas Turbines," ASME Paper No. GT-2002-30479.

[2] Chew, J. W., Hills, N. J., Khalatov, S., Scanlon, T., and Turner, A. B., 2003, "Measurement and Analysis of Flow in a Pre-Swirled Cooling Air Delivery System," ASME Paper No. GT-2003-38084.

[3] Bohn, D., and Wolff, M., 2003, "Improved Formulation to Determine Minimum Sealing Flow—$C_{w,\min}$—for Different Sealing Configurations," ASME Paper No. GT-2003-38465.

[4] Chew, J. W., and Hills, N. J., 2007, "Computational Fluid Dynamics for Turbomachinery Internal Air Systems," Philos. Trans. R. Soc. London, Ser. A, **365**, pp. 2587–2611.

[5] Foley, A., 2001, "On the Performance of Gas Turbine Secondary Air Systems," ASME Paper No. GT-2001-0199.

[6] Theodorsen, T., and Regier, A., 1945, "Experiments on Drag of Revolving Discs, Cylinders and Streamline Rods at High Speeds," NACA Report No. 793.

[7] Yan, Y., Farzaneh-Gord, M., Lock, G., Wilson, M., and Owen, J. M., 2003, "Fluid Dynamics of a Pre-Swirled Rotor-Stator System," ASME J. Turbomach., **125**, pp. 641–647.

[8] Hay, N., and Lampard, D., 1998, "Discharge Coefficient of Turbine Cooling Holes: A Review," ASME J. Turbomach., **120**, pp. 314–319.

[9] Idris, A., and Pullen, K. R., 2005, "Correlations for the Discharge Coefficient of Rotating Orifices Based on the Incidence Angle," Philos. Trans. R. Soc. London, Ser. A, **219**, pp. 333–352.

[10] Morrison, G. L., Rhode, D. L., Cogan, K. C., Chi, D., and Demko, J., 1983, "Labyrinth Seals for Incompressible Flow," Final Report No. NASA-CR-170938.

[11] Childs, P. R. N., 1998, *Mechanical Design*, Arnold, London.

[12] http://www.vivaceproject.com/ and http://www.proosis.com/.

[13] Alexiou, A., and Mathioudakis, K., 2005, "Development of Gas Turbine Performance Models Using a Generic Simulation Tool," ASME Paper No. GT-2005-68678.

[14] Alexiou, A., and Mathioudakis, K., 2006, "Gas Turbine Engine Performance Model Applications Using an Object-Oriented Simulation Tool," ASME Paper No. GT-2006-90339.

[15] Bala, A., Sethi, V., Lo Gato, E., Pachidis, V., and Pilidis, P., 2007, "PROOSIS—A Collaborative Venture for Gas Turbine Performance Simulation Using an Object Oriented Programming Schema," Report No. ISABE-2007-1357.

[16] Alexiou, A., Baalbergen, E. H., Kogenhop, O., Mathioudakis K., and Arendsen, P., 2007, "Advanced Capabilities for Gas Turbine Engine Performance Simulations," ASME Paper No. GT-2007-27086.

[17] Farzaneh-Gord, M., Wilson, M., and Owen, J. M., 2005, "Numerical and Theoretical Study of Flow and Heat Transfer in a Pre-Swirl Rotor-Stator System," ASME Paper No. GT-2005-68135.

[18] Lewis, P., Wilson, M., Lock, G., and Owen, J. M., 2006, "Physical Interpretation of Flow and Heat Transfer in Pre-Swirl Systems," ASME Paper No. GT-2006-90132.

[19] Geis, T., Dittmann, M., and Dullenkopf, K., 2004, "Cooling Air Temperature Reduction in a Direct Transfer Pre-Swirl System," ASME J. Eng. Gas Turbines Power, **126**(4), pp. 809–815.

[20] Long, C. A., Alexiou, A., and Smout, P. D., 2003, "Heat Transfer in H. P. Compressor Gas Turbine Internal Air Systems: Measurements From the Peripheral Shroud of a Rotating Cavity With Axial Throughflow," 2nd International Conference on Heat Transfer, Fluid Mechanics and Thermodynamics, HEFAT-2003.

[21] Alexiou, A., Hills, N. J., Long, C. A., Turner, A. B., and Millward, J. A., 2000, "Heat Transfer in H. P. Compressor Gas Turbine Internal Air Systems: A Rotating Disc-Cone Cavity With Axial Throughflow," Exp. Heat Transfer, **13**, pp. 299–328.

[22] Alexiou, A., Long, C. A., Turner, A. B., and Barnes, C. J., 2001, "Thermal Modelling of a Rotating Cavity Rig to Simulate the Internal Air System of a Gas Turbine H. P. Compressor," 5th World Conference on Experimental Heat Transfer, Fluid Mechanics and Thermodynamics, ExHFT-5, III, pp. 2387–2392.

[23] Long, C. A., 1999, *Essential Heat Transfer*, Longman, London.
[24] Dittmann, M., Dullenkopf, K., and Wittig, S., 2005, "Direct-Transfer Pre-Swirl System: A One-Dimensional Modular Characterization of the Flow," ASME J. Eng. Gas Turbines Power, **127**, pp. 383–388.
[25] Alexiou, A., Hills, N. J., Long, C. A., Turner, A. B., Wong, L. S., and Millward, J. A., 2000, "Discharge Coefficients for Flow Through Holes Normal to a Rotating Shaft," Int. J. Heat Fluid Flow, **21**, pp. 701–709.
[26] Idris, A., Pullen, K. R., and Read, R., 2004, "The Influence of Incidence Angle on the Discharge Coefficient for Rotating Radial Orifices," ASME Paper No. GT-2004-53237.
[27] http://www.poa-project.com/.
[28] Filomeno Coelho, R., Pierret, S., and Cobas, P., 2006, "Multi-Objective Evolutionary Algorithms Applied to Aircraft Engine Design," 25th Congress of the International Council of Aeronautical Sciences, ICAS-2006.

Transient Development of Flame and Soot Distribution in Laminar Diffusion Flame With Preheated Air

Bijan Kumar Mandal
Department of Mechanical Engineering,
Bengal Engineering and Science University,
Shibpur, Howrah, 711109, India

Amitava Sarkar
Department of Mechanical Engineering,
Jadavpur University,
Kolkata 700032, India

Amitava Datta
Department of Power Engineering,
Jadavpur University,
Salt Lake Campus,
Kolkata 700098, India

A numerical investigation of the transient development of flame and soot distributions in a laminar axisymmetric coflowing diffusion flame of methane in air has been carried out considering the air preheating effect. The gas phase conservation equations of mass, momentum, energy, and species concentrations along with the conservation equations of soot mass concentration and number density are solved simultaneously, with appropriate boundary conditions, by an explicit finite difference method. Average soot diameters are then calculated from these results. It is observed that the soot is formed in the flame when the temperature exceeds 1300 K. The contribution of surface growth toward soot formation is more significant compared with that of nucleation. Once the soot particles reach the high temperature oxygen-enriched zone beyond the flame, the soot oxidation becomes important. During the initial period, when soot oxidation is not contributing significantly, some of the soot particles escape into the atmosphere. However, under steady condition the exhaust product gas is nonsooty. Preheating of air increases the soot volume fraction significantly. This is both due to more number of soot particles and the increase in the average diameter. However, preheating of air does not cause a qualitative difference in the development of the soot-laden zone during the flame transient period.
[DOI: 10.1115/1.3018978]

1 Introduction

Diffusion flame is one of the most commonly seen flames in practical combustion chambers, such as gas turbine combustors, internal combustion engines, and industrial furnaces. Diffusion flames are generally free from the problems associated with stability, autoignition, flashback, etc. But unfortunately, soot formation in practical hydrocarbon based diffusion flames has become a matter of concern over the past few decades because of its adverse environmental effect. The emission norms are getting stricter day by day, resulting in the search for better combustion strategies with reduced levels of pollutant formation. Soot formation in flame is the result of the incomplete combustion of hydrocarbons in the reducing atmosphere, where enough oxygen is not available to completely convert the fuel to carbon dioxide and water vapor. Soot particles play a major role in heat transfer from the flame. Therefore, better understanding and control of soot forming processes in hydrocarbon combustion are required.

Wey et al. [1], Santoro et al. [2], Smooke et al. [3], Lee et al. [4], and Xu et al. [5] performed experiments in laminar diffusion flames, using various hydrocarbon fuels, for the determination of soot. Wey et al. [1] found that the soot volume fraction and the aggregate diameters increased with the height above the burner, while the opposite was the case with number densities. Santoro et al. [2] experimented with various fuels and observed that the increase in soot formation is primarily due to an increase in the residence time in the annular region of the diffusion flame. Smooke et al. [3] measured the soot volume fraction as well as the concentrations of fuel (methane), acetylene, and benzene within the flame zone of a coflowing laminar jet diffusion flame. Lee et al. [4] observed that the rate of soot inception became stronger with the oxygen-enriched oxidizer stream. Xu et al. [5] studied the soot surface growth and oxidation in laminar hydrocarbon-air diffusion flames at atmospheric pressure with several fuels. It was found that the fuel type did not affect the soot surface oxidation rates.

Different semiempirical soot models were proposed by Smith [6], Gore and Faeth [7], Kennedy et al. [8], Leung et al. [9], Syed et al. [10], Moss et al. [11], and Said et al. [12]. The results from those models showed good agreement with the experiments of Santoro et al. [2]. Soot oxidation plays an important role in controlling emission level. Different oxidation models were proposed by Lee et al. [13], Nagle and Strickland-Constable [14], and Najjar and Goodger [15].

The works conducted in laminar diffusion flames for the prediction of formation and distribution of soot used steady flames under different operating conditions and fuels. In coflowing gas burners having diffusion flames, a transient situation arises during ignition and initial lighting up of the flame, when the combustion phenomenon differs from the subsequent steady situation. There is a lack of understanding on soot formation in a transient flame. There are practical applications, e.g., in diesel engines or during extinction and reignition of turbulent flame in a gas turbine, when the flame is not steady. The combustion of fuel is simulated by a two-step equation for simplification. The soot models of Syed et al. [10] and Moss et al. [11] are employed with some minor adjustments for the sake of compatibility with the present combustion model. When preheated air is used, significant changes in the velocity and temperature fields are observed [16]. Hence the soot formation and its oxidation during the transient phase, subsequent to ignition, in a nonpremixed flame with preheated air are also studied.

2 Model Formulation

An axisymmetric confined laminar diffusion flame is modeled with fuel (methane) admitted as a central jet and with air as a coflowing annular jet. The diameters of the inner fuel tube and outer tube are 12.7 mm and 50.4 mm, respectively, and the length

Manuscript received September 21, 2007; final manuscript received August 27, 2008; published online January 29, 2009. Review conducted by Thomas Sattelmayer.

of the computational domain is 0.3 m. These dimensions are the same as those used in the earlier experimental work of Mitchell et al. [17].

The combustion process is simulated with a detailed numerical model, solving the governing equations for a laminar axisymmetric reacting flow with the appropriate boundary conditions. The flow is vertical through the reaction space, and the gravity effect is included in the momentum equation. Radiation heat transfer from the flame is neglected considering the methane flame to be predominantly nonluminous. The conservation equations for mass, radial momentum, and axial momentum in cylindrical coordinates for axisymmetric geometry considered here are as follows.

For mass,

$$\frac{\partial \rho}{\partial t} + \frac{1}{r}\frac{\partial}{\partial r}(r\rho v_r) + \frac{\partial}{\partial z}(\rho v_z) = 0 \tag{1}$$

For radial momentum,

$$\begin{aligned}\frac{\partial}{\partial t}(\rho v_r) + \frac{1}{r}\frac{\partial}{\partial r}(r\rho v_r^2) + \frac{\partial}{\partial z}(\rho v_r v_z) \\ = -\frac{\partial p}{\partial r} + \frac{2}{r}\frac{\partial}{\partial r}\left(r\mu\frac{\partial v_r}{\partial r}\right) - \frac{2}{r}\mu\frac{v_r}{r^2} + \frac{\partial}{\partial z}\left\{\mu\left(\frac{\partial v_z}{\partial r} + \frac{\partial v_r}{\partial z}\right)\right\} \\ - \frac{2}{3}\frac{\partial}{\partial r}\left(\mu\left(\frac{\partial v_r}{\partial r} + \frac{v_r}{r} + \frac{\partial v_z}{\partial z}\right)\right)\end{aligned} \tag{2}$$

For axial momentum,

$$\begin{aligned}\frac{\partial}{\partial t}(\rho v_z) + \frac{1}{r}\frac{\partial}{\partial r}(r\rho v_r v_z) + \frac{\partial}{\partial z}(\rho v_z^2) \\ = -\frac{\partial p}{\partial z} + \frac{1}{r}\frac{\partial}{\partial r}\left\{r\mu\left(\frac{\partial v_z}{\partial r} + \frac{\partial v_r}{\partial z}\right)\right\} + 2\frac{\partial}{\partial z}\left(\mu\frac{\partial v_z}{\partial z}\right) \\ - \frac{2}{3}\frac{\partial}{\partial z}\left\{\mu\left(\frac{\partial v_r}{\partial r} + \frac{v_r}{r} + \frac{\partial v_z}{\partial z}\right)\right\} + \rho g\end{aligned} \tag{3}$$

The combustion reaction of methane and air is assumed to proceed through simplified two-step global reaction chemistry as

$$CH_4 + 1.5O_2 \rightarrow CO + 2H_2O \tag{4}$$

$$CO + 0.5O_2 \rightarrow CO_2 \tag{5}$$

The reaction rates ($\dot{\omega}$) for the above reactions are obtained following an Arrhenius type rate equation from the work of DuPont et al. [18]. The density of the species mixture is calculated using the equation of state considering all the species as ideal gases.

The conservation equation for chemical species is solved for five gaseous species, viz., CH_4, O_2, CO_2, CO, and H_2O. The concentration for N_2 is obtained by difference. The governing equation for the gaseous species conservation is as follows:

$$\begin{aligned}\frac{\partial}{\partial t}(\rho C_j) + \frac{1}{r}\frac{\partial}{\partial r}(r\rho v_r C_j) + \frac{\partial}{\partial z}(\rho v_z C_j) \\ = \frac{1}{r}\frac{\partial}{\partial r}\left(r\rho D_{jm}\frac{\partial C_j}{\partial r}\right) + \frac{\partial}{\partial z}\left(\rho D_{jm}\frac{\partial C_j}{\partial z}\right) + \dot{S}_{cj}\end{aligned} \tag{6}$$

where C_j is the mass fraction of the respective species, and D_{jm} is the diffusion coefficient of the species j in the binary mixture of that species and nitrogen. The source term $\dot{S}_{cj}$ is the rate of production or destruction of jth species per unit volume due to chemical reactions calculated as

$$\dot{S}_{cj} = \sum_{k=1}^{2} (\gamma''_{jk}\dot{\omega}_k - \gamma'_{jk}\dot{\omega}_k)M_j \tag{7}$$

where M_j is the molecular weight of the jth species. γ''_{jk} and γ'_{jk} are the stoichiometric coefficients on the product side and reactant side, respectively, for the jth species and in the kth reaction. Obviously, k is either 1 for the reaction given by Eq. (4) or 2 for the reaction given by Eq. (5).

The conservation of energy equation for reactive flow is written as

$$\begin{aligned}\frac{\partial}{\partial t}(\rho h) + \frac{1}{r}\frac{\partial}{\partial r}(r\rho v_r h) + \frac{\partial}{\partial z}(\rho v_z h) \\ = \frac{1}{r}\frac{\partial}{\partial r}\left(r\frac{\lambda}{c_p}\frac{\partial h}{\partial r}\right) + \frac{\partial}{\partial z}\left(\frac{\lambda}{c_p}\frac{\partial h}{\partial z}\right) \\ + \frac{1}{r}\frac{\partial}{\partial r}\left[r\frac{\lambda}{c_p}\sum_{j=1}^{n} h_j(\mathrm{Le}_j^{-1} - 1)\frac{\partial C_j}{\partial r}\right] \\ + \frac{\partial}{\partial z}\left[\frac{\lambda}{c_p}\sum_{j=1}^{n} h_j(\mathrm{Le}_j^{-1} - 1)\frac{\partial C_j}{\partial z}\right]\end{aligned} \tag{8}$$

where Le_j is the local Lewis number of the jth species defined as

$$\mathrm{Le}_j = \frac{\lambda}{c_p}\frac{1}{\rho D_{jm}} \tag{9}$$

The enthalpy of the mixture, obtained as the mass weighted average of each individual species contribution, is as follows:

$$h = \sum_{j=1}^{n} C_j h_j = \sum_{j=1}^{n} C_j\left(h_{fj}^0 + \int_{T_0}^{T} c_{pj}dT\right) \tag{10}$$

where h_{fj}^0 is the heat of formation of the jth species at the reference temperature T_0 and the integral part is the contribution of the sensible heat.

The temperature of the gas mixture is implicitly calculated by solving Eq. (10) using the Newton–Raphson method. The transport of momentum, energy, and species mass in the calculation of a reacting flow involve transport coefficients such as viscosity (μ), thermal conductivity (λ), and mass diffusivity (D_{jm}) for the solution. The local variations in viscosity, thermal conductivity, and mass diffusivity with temperature have been taken into consideration with suitable correlations found in the literature. The mixture properties of viscosity and thermal conductivity are evaluated using the semiempirical method of Wilke, as described in Ref. [19].

3 Soot Model

The formation of soot is modeled along the line prescribed by Syed et al. [10] and Moss et al. [11]. The soot volume fraction (f_v) and number density (n) are considered to be the important variables. Nucleation, surface growth, coagulation, and oxidation effects are taken into account in the formation of the model equations. Following Syed et al. [10], the surface growth rate is evaluated considering the surface area of the soot particles into account. The soot oxidation is calculated using the model of Lee et al. [13] and is accounted in the equation for volume fraction as was done by Moss et al. [11]. The respective source terms for the conservation equations for soot mass concentration ($\rho_s f_v$) and number density (n/N_o) are as follows:

$$\frac{d}{dt}(\rho_s f_v) = \gamma(\rho_s f_v)^{2/3} n^{1/3} + \delta - \left(\frac{36\pi}{\rho_s^2}\right)^{1/3}(n\rho_s^2 f_v^2)^{1/3}\omega_{\mathrm{ox}} \tag{11}$$

$$\frac{d}{dt}\left(\frac{n}{N_0}\right) = \alpha - \beta\left(\frac{n}{N_0}\right)^2 \tag{12}$$

where

$$\alpha = C_\alpha \rho^2 T^{0.5} X_c \exp\left(-\frac{T_\alpha}{T}\right), \quad \beta = C_\beta T^{0.5}$$

$$\gamma = C_\gamma \rho T^{0.5} X_c \exp\left(-\frac{T_\gamma}{T}\right), \quad \delta = C_\delta \alpha$$

In the above equations, N_o is Avogadro's number; ρ_s is the soot particulate density (=1800 kg/m^3); T_α and T_γ are the activation temperatures (in K) for nucleation and surface growth, respectively; C_α, C_β, C_γ, and C_δ are model constants; and ρ and T are the local mixture density and temperature, respectively. The model constants and activation temperatures are taken from Syed et al. [10] for methane fuel. In the works of Syed et al. [10] and Moss et al. [11], X_c was referred to as the mole fraction of the parent fuel species.

In Eq. (11), the first and second terms on the right hand side are the contributions of the soot surface growth and soot nucleation, respectively, while the third term pertains to the depletion of soot due to oxidation. The terms on the right hand side of Eq. (12) are due to the contribution of nucleation and coagulation, respectively.

Conservation equations for the soot mass concentration and number density are solved in the present model along with the gaseous species in the solution domain. As soot particles do not follow the molecular diffusion theory, the diffusion velocities in the soot conservation equations are replaced by the corresponding thermophoretic soot particle velocities. Therefore, the conservation equations, in general, can be expressed as

$$\frac{\partial \varphi}{\partial t} + \frac{1}{r}\frac{\partial}{\partial r}(r v_r \varphi) + \frac{\partial}{\partial z}(\rho v_z \varphi) = \frac{1}{r}\frac{\partial}{\partial r}(r V_{t_r} \varphi) + \frac{\partial}{\partial z}(V_{t_z} \varphi) + \dot{S}_\varphi \tag{13}$$

The above equation is applicable both for the soot mass concentration ($\rho_s f_v$) and number density (n/N_0), and accordingly φ will assume the respective variable value. The thermophoretic velocity vector ($\boldsymbol{V}_t$) has been calculated following Santoro et al. [2] as

$$V_t = \frac{3}{4(1+\pi\xi/8)}\frac{\upsilon}{T}\nabla T \tag{14}$$

where the accommodation factor (ξ) has been taken as unity. Equations (11) and (12) form the source terms ($\dot{S}_\varphi$) of the conservation equations of the soot mass concentration and number density, respectively. The soot volume fraction is obtained from the mass concentration solution.

It has been observed that the use of the local mole fraction of the parent fuel species (i.e., methane) as X_c, following Syed et al. [10] and Moss et al. [11], predicts very high values of the soot volume fraction in the flame. Many studies concluded that the soot formation is proportional to the concentration of soot precursor such as acetylene. Smooke et al. [3] observed that the acetylene concentration inside the flame annulus is almost two orders of magnitude less than that of methane. On the other hand, in the modeling of soot, Kennedy et al. [8] used a reaction efficiency, which was varied from 5% low in the flame to 20% in the tip region. Smooke et al. [3] used a similar factor, coined as collision efficiency, for which a constant value of 13% had been adopted by them. In the present work, a similar constant reaction efficiency or collision factor term is adopted, whose value is taken as 7.5% after extensive trial and error.

4 Boundary Conditions

Boundary conditions at the inlet plane are given separately for the fuel stream at the central jet and the air stream at the annular coflow. The streams are considered to enter the computational domain with plug velocity profiles, calculated from their respective flow rates. The inlet fuel mass flow rate is taken as 3.71×10^{-6} kg/s and the inlet air mass flow rate as 2.214×10^{-4} kg/s, in conformation with the values used by Mitchell et al. [17]. The inlet temperatures of fuel and air are specified at the inlet plane. No soot is considered to enter the domain through the inlet plane. At the outlet the axial gradient of all the variables have been set to zero. However, in the case of reverse flow at the outlet plane, which occurs in the case of buoyant flame, the stream coming in from the outside is considered to be atmospheric air. Axisymmetric condition is applied at the central axis, while a no-slip, adiabatic, and impermeable boundary condition is adopted at the wall.

5 Solution Methodology

The gas phase conservation equations of mass, momentum, energy, and species concentrations along with the conservation equations of soot mass concentration and number density are solved simultaneously, with their appropriate boundary conditions, by an explicit finite difference computing technique taking into account the transient terms in the equations. The algorithm is primarily based on the SOLA scheme proposed by Hirt and Cook [20], which was modified on certain aspects, as described in Ref. [16]. The variables are defined following a staggered grid arrangement. The advection terms are discretized following a hybrid differencing scheme, based on cell Péclet number, while the diffusion terms are discretized by the central differencing scheme. The solution is explicitly advanced in time until the final steady state convergence is reached. The time increment for the explicit advancement is done by satisfying the stability criteria and the Courant–Friedrichs–Lewy criteria ensuring that a fluid particle never crosses a complete cell, in either direction, in one time step. In every time step, first the axial and radial momentum equations are solved. Pressure corrections and the associated corrections of velocities to satisfy the conservation of mass are then done using an iterative scheme. The enthalpy transport and the species transport equations, including those of soot variables, are subsequently solved within the same time step. The temperature is decoded from the enthalpy and species concentration values by the Newton–Raphson method.

The ignition is simulated by increasing the temperature (to 1000 K) of a few cells a little above the burner tip and at the interface of the two jets. This criterion, simulating the spark, is withdrawn once the flame has been established. After the flame is ignited, the time step is further reduced to avoid divergence of the results due to the increased number of source terms in the conservation equations.

A variable size adaptive grid system is considered with higher concentration of nodes near the axis. An extensive grid independence test is carried out and an optimized numerical mesh with 85×41 (in $z \times r$ directions) grid nodes is selected.

6 Results and Discussion

6.1 Validation of the Numerical Code. The predictions from the numerical model are validated against the experimental results available in the literature at steady state. The radial distributions of the steady state temperature (Fig. 1(*a*)) and product species (CO_2 and H_2O) concentrations (Fig. 1(*b*)) at an axial height of 12 mm above the burner tip have been compared against the corresponding experimental results [17], for the same burner geometry and inlet conditions. The model predicts the radial flame position fairly well, while the predicted peak temperature is higher than the measured value by about 125 K. This difference in temperature can be attributed to the simplified kinetics adopted in the model and also due to neglecting the effect of radiation from the flame. The peak concentrations of CO_2 and H_2O match well with the experiments, but the centerline concentrations are somewhat underpredicted.

The soot model employed in the present work is calibrated against the experimental results of Smooke et al. [3] for the same burner configuration and input conditions. Though the present code is found to be qualitatively capable of describing the flame conditions measured by Smooke et al. [3], the flame height pre-

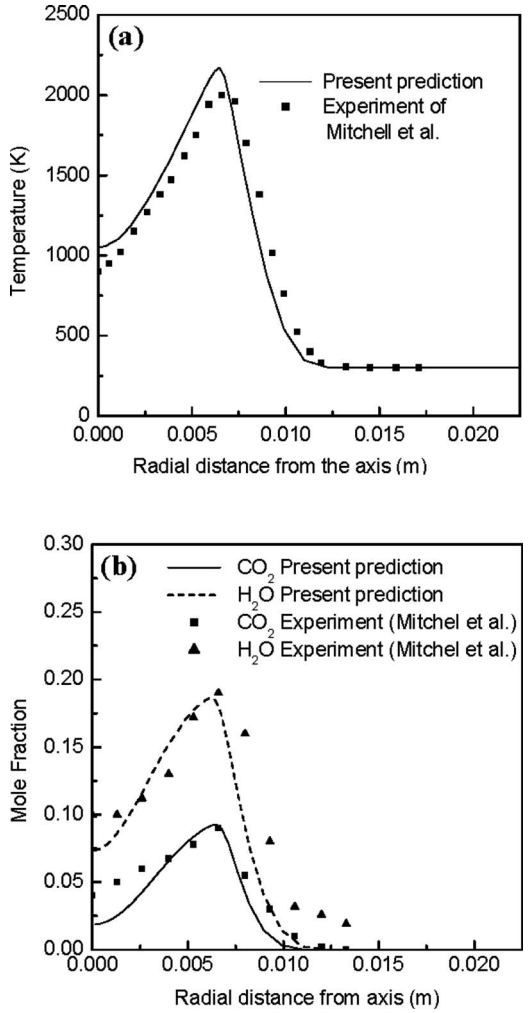

Fig. 1 Comparison of the radial distributions of (*a*) temperature and (*b*) CO_2 and H_2O predicted by the present model against the experimental data of Mitchell et al. [17] at 12 mm above the burner

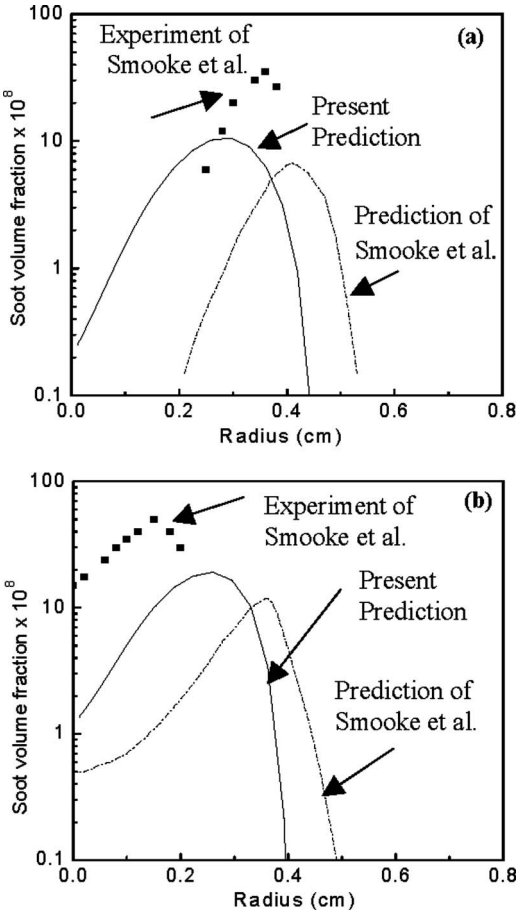

Fig. 2 Radial distribution of the soot volume fraction in diffusion flame at nondimensional axial heights (*a*) $z/H_F=0.5$, and (*b*) $z/H_F=0.69$; comparison of the present prediction (solid line) against Smooke et al. [3]

dicted by the present code is about 25% higher than that of the experiment. The reason for this variation is primarily attributed to the simplified chemical kinetics adopted in the present work. Therefore, we have compared the soot volume fraction described by the present model against the experiments of Smooke et al. at the same nondimensional axial height z/H_F, where H_F is the flame height. Figures 2(*a*) and 2(*b*) show the radial distributions of the soot volume fraction at two axial positions inside the flame. The figures reveal that the present code is capable of predicting the soot distribution quite well. The soot distributions show that the peak soot concentration is found away from the center at both heights. However, with the increase in height, the radius with the maximum soot concentration has shifted toward the axis, and the centerline concentration of soot has also increased.

6.2 Steady State Temperature and Velocity Fields. The temperature and velocity distributions, vis-a-vis the flame region for the steady jet diffusion flame, have been shown in Fig. 3 as a contour plot and a vector plot, respectively, with nonpreheated air. The steady condition in the entire computational domain is reached 0.8 s after the ignition is given. The flame region is described by the volumetric heat release rate contour whose value is 1% of the maximum local volumetric heat release rate due to chemical reaction. The flame surface clearly shows the overventilated structure achieved with the flow conditions. It almost entirely passes through the maximum temperature region. A very high temperature gradient is observed at the base of the flame. Inside the flame contour, the temperature first increases rapidly and then gradually in the axial direction as the flame surface is approached. Away from the flame, the temperature drops due to heat transfer and near the outside wall the gas temperature is low.

The flame structure can be further illustrated from the velocity field. An entrainment of flow from the coflowing air into the flame zone is clearly indicated in the figure. The figure also reveals the acceleration in the central region due to the effects of high temperature and gravity, which further augments the entrainment process. Therefore, very high velocities are observed in the central region within the flame surface. As a result of this, the pressure near the periphery drops and results in the ingress of atmospheric air from the outer surface giving rise to a recirculating zone.

The flame tip is reached at a height of 11.8 cm above the burner tip. This height is higher than the height of laminar diffusion flame predicted with detailed chemical kinetics under similar flow conditions in the literature [17]. The discrepancy is attributed to the simplified reaction kinetics adopted in the present work.

6.3 Transient Soot Distribution With Nonpreheated Air. Figures 4(*a*)–4(*f*) show the distributions of soot volume fractions along with the flame contour at different times after ignition. It is seen in Fig. 4(*a*) that though a thin flame is established at 0.05 s after ignition, the soot volume fraction at this time is very low. With increasing time, the soot formation process accelerates with the increase in the rates of nucleation and surface growth. The increase in temperature plays a major role in achieving this. The

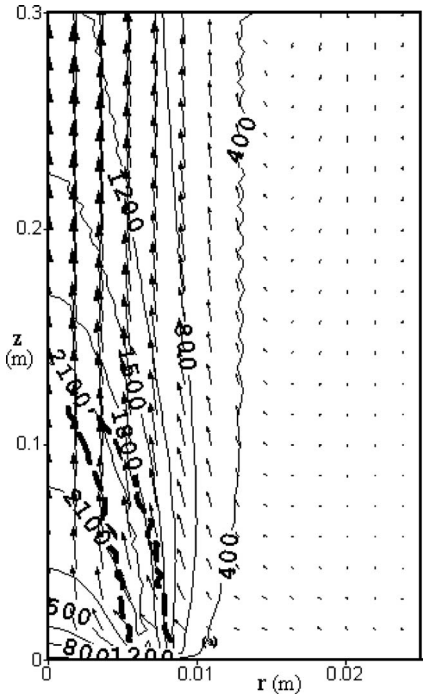

Fig. 3 Flame front surface (thick dashed line) along with temperature (K) and velocity distributions for the steady diffusion flame with nonpreheated air

corresponding temperature data in the soot-laden zone shows that the soot formation in a methane diffusion flame hardly initiates below a temperature of about 1300 K. At 0.1 s, the maximum soot volume fraction reaches a value of 60×10^{-8}. A high contour value of 40×10^{-8} occurs inside the flame (Fig. 4(*b*)). The high soot concentration zone is observed inside the flame surface because of the high fuel concentration there. Beyond the flame, the soot particles are oxidized due to the presence of oxygen at high temperature. Therefore, the soot concentration drops down quite sharply across the flame region and the volume fraction of soot becomes low. As the flame develops with time and elongates downstream, the soot-containing zone also shifts axially above the burner tip. The maximum soot volume fraction at 0.15 s after ignition is 120×10^{-8}, which is much more than the peak values of the earlier time. A high soot concentration contour of 60×10^{-8} is shown in Fig. 4(*c*). The region over which the soot particles are found to exist in good proportion has also increased along with the increase in the volume fraction, indicating an increase in the overall quantity of soot particles formed in the flame. Subsequent to this time, the peak soot concentration falls, and at 0.2 s the highest soot volume fraction is 67×10^{-8} (Fig. 4(*d*)). The higher soot formation during the earlier time was due to the accumulated fuel in the chamber that remained unburnt due to the absence of the flame front surface. Once the accumulated fuel is burnt, the conditions tend toward the steady state, and maximum soot volume fraction comes down.

The flame structure and soot distributions at 0.4 s and 0.8 s after ignition are similar (Figs. 4(*e*) and 4(*f*)). It shows that the flame reaches its steady state at 0.4 s. However, further changes in species concentration, velocity, and temperature occur in the postflame region due to transport of mass, momentum, and energy. Therefore, the velocity, temperature, and species concentration distributions modify in the postflame zone, though the flame remains unaltered. The entire computational domain reaches steady state at 0.8 s. The soot formation primarily occurs inside the flame region. Therefore, the soot distribution does not change much once the flame becomes stable at 0.4 s.

Figures 5(*a*) and 5(*b*) show the variation in the total soot volume and cumulative soot particle number within the solution domain at different times after ignition. It is observed from the figures that both the soot volume and soot particle number first increase to reach a peak and subsequently decrease and finally reach a steady value. However, the two quantities reach their peak values at different times. Accordingly, five time zones can be identified as follows:

(i) 0–0.15 s, when both the soot volume and particle number increase with time
(ii) 0.15–0.2 s, when the soot volume decreases but the particle number increases
(iii) 0.2–0.275 s, when the soot volume remains constant but the particle number still increases
(iv) 0.275–0.6 s, when soot volume remains constant but the particle number decreases

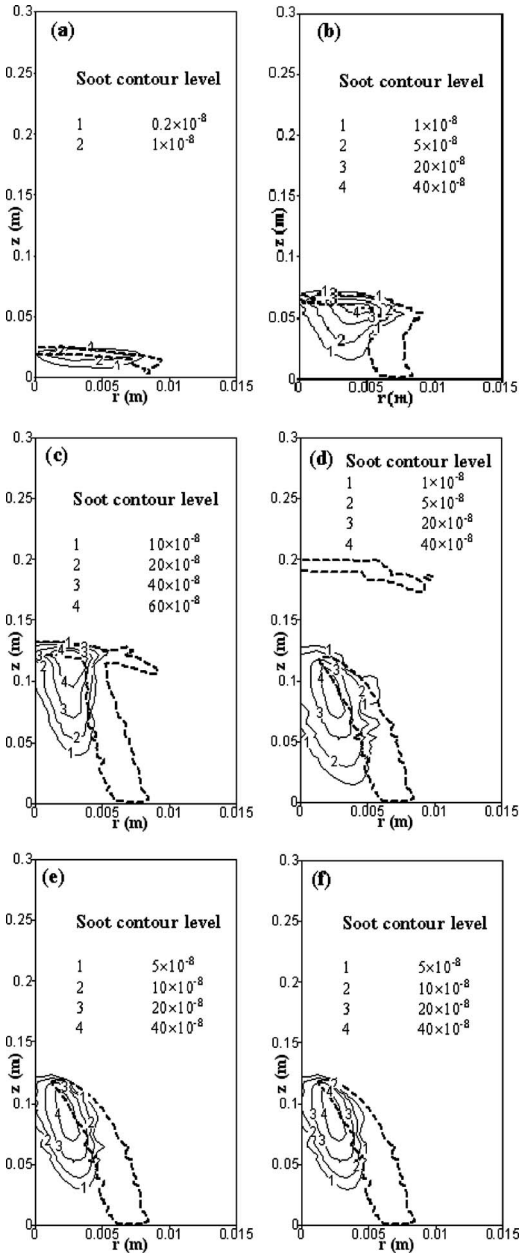

Fig. 4 Flame front surface (thick dotted line) and soot volume fraction contours at different times after ignition with nonpreheated air: (*a*) $t=0.05$ s, (*b*) $t=0.10$ s, (*c*) $t=0.15$ s, (*d*) $t=0.20$ s, (*e*) $t=0.4$ s, and (*f*) $t=0.8$ s

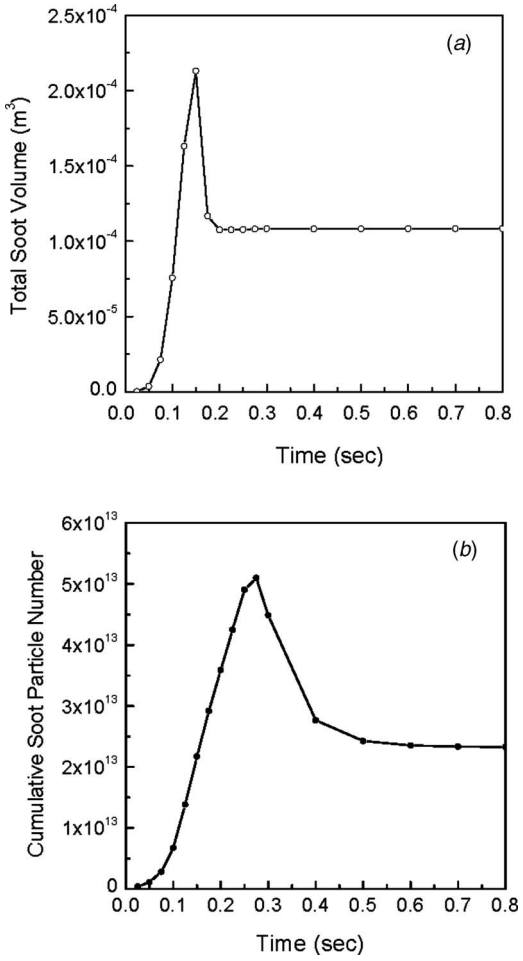

Fig. 5 Variation of (*a*) total soot volume and (*b*) cumulative soot particle number in the computational domain with time after ignition with normal air

(v) beyond 0.6 s, when both the soot volume and particle number remain constant

The activation temperature for the surface growth process ($T_\gamma = 12.6 \times 10^3$ K) is lower than that of soot nucleation ($T_\alpha = 46.1 \times 10^3$ K). Therefore, the surface growth rate dominates over the rate of nucleation in the soot formation process. It is observed from the numerical data that the surface growth rate is three orders of magnitude higher than the soot nucleation rate in the formation of soot mass in steady flame. However, during the early period just after ignition, when the high temperature zone is very limited, both the nucleation and surface growth rates of soot particles are equally low. The surface growth begins to increase at a much rapid rate than soot nucleation with the flame development. For example, the surface growth rate in the domain at 0.1 s is about 2.5×10^4 times of that at 0.01 s, while the increase in the rate of nucleation over the same time is about 25 times. As a result, the soot volume fraction builds up faster than the number density during the early period of flame development (Zone (i)). When the high temperature region spreads with time, the rate of soot nucleation increases to a higher value compared with its value during the initial time (the soot nucleation rate in the domain at 0.15 s is almost 40 times that at 0.01 s). As a result, the cumulative soot particle number in the domain also increases with time. The soot oxidation plays a very important role after 0.15 s, as the oxygen-enriched zone beyond the flame reaches a high temperature. Though the number of soot particles increases due to further nucleation of particles, oxidation overcomes the surface growth to cause a decrease in the total soot volume (Zone (ii)). The surface growth rate finally equals the soot oxidation rate, and the soot volume reaches a steady value (Zone (iii)). When many soot particles are formed in the domain, the increased coagulation of soot particles results in the formation of larger particles. The maximum rate of coagulation is observed at about 0.275 s. At this time the contribution of coagulation toward the rate of change of particle number density is 4×10^3 times its contribution at 0.01 s. Coagulation does not change the soot volume in the domain but reduces the number of particles within it (Zone (iv)). Finally, all the processes attain a state such that both the total soot volume and aggregate soot particle number reach their steady values.

The numerical prediction of the flame has an effect on the value of steady state soot volume fraction. It is already shown that the present model has overpredicted the flame length. As the formation process of soot occurs inside the flame zone (Fig. 4(*f*)), an increase in the flame length increases the available time for the soot particles to grow in size as well as number. Therefore, the corresponding soot volume fraction will also be somewhat overpredicted.

6.4 Soot Particle Size. The average soot particle diameter is calculated from the local values of soot volume fraction and number density as

$$d_s = \left(\frac{6 f_v}{\pi n} \right)^{0.33} \tag{15}$$

The distributions of the average soot particle diameters in the solution domain at different times are plotted in Figs. 6(*a*)–6(*f*). The maximum soot particle diameter, at steady condition, is obtained as 10 nm. However, the largest soot particle size is only about 4 nm after 0.05 s of ignition (Fig. 6(*a*)). This may be attributed to the low temperature and the insufficient time for growth of the particle during the initial period. The maximum soot particle size at $t = 0.1$ s is 10 nm (Fig. 6(*b*)), and the largest soot particles occur within the flame. At this time the peak temperature has already increased to above 2000 K, which augments the soot growth kinetics. The average soot diameter at the exit plane during this time is 2 nm. This reveals that following ignition and before the flame gets completely stabilized, some soot particles of small size escape into the atmosphere. The situation further worsens at 0.15 s after ignition, when the soot particle size escaping into the atmosphere grows to about 8 nm (Fig. 6(*c*)). Subsequently, the gases in the post flame region get heated, which increase the rate of soot oxidation beyond the flame (Fig. 6(*d*)). However, the soot particles near the exit plane still remain of considerable size and escape into the atmosphere. Therefore, it is clear that immediately after the ignition of a diffusion flame in a confined burner, the soot particles will escape into the atmosphere for some time causing pollution. Subsequently, the oxidation process will consume the soot particles above the flame zone, and the soot particles get restricted within the flame zone only (Figs. 6(*e*) and 6(*f*)).

6.5 Effect of Air Preheat on Soot Formation. The effect of air-preheat on soot formation has been studied by increasing the temperature of coflowing air from 300 K to 400 K. The velocity and temperature distributions along with the flame front for the steady flame are shown in Fig. 7, when preheated air is used. It is observed from the figure that the temperature and flow characteristics undergo extensive modifications due to air preheating. The factors, which lead to the changes in the temperature and velocity distributions (in the case of preheating), have been discussed in detail in our earlier work [16]. In case of preheated air, the steady state flame temperature increases due to the increase in air temperature. Nevertheless, a more uniform radial temperature variation is obtained beyond the flame region at steady state, when preheated air is used. The velocity field plays a major role in achieving such uniform temperature distribution. When the air is preheated, the coflowing air tends to move up more rapidly, due to

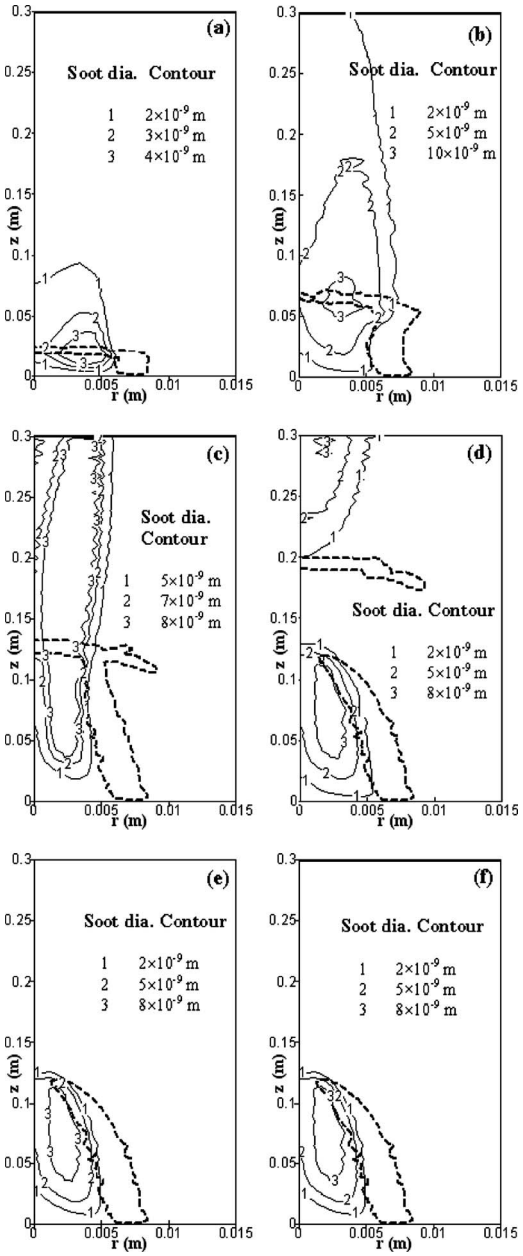

Fig. 6 Flame front surface (dotted thick line) and soot diameter contours at different times after ignition with nonpreheated air: (*a*) *t*=0.05 s, (*b*) *t*=0.10 s, (*c*) *t*=0.15 s, (*d*) *t*=0.20 s, (*e*) *t*=0.40 s, and (*f*) *t*=0.80 s

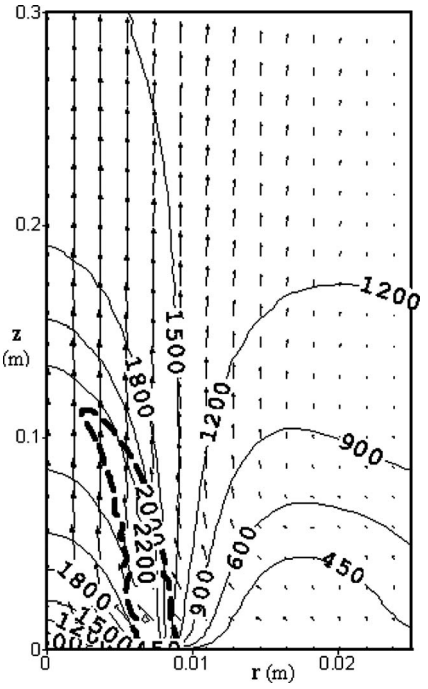

Fig. 7 Flame front surface (thick dashed line) along with temperature (K) and velocity distributions for the steady diffusion flame with preheated air

buoyancy, compared with when there is no preheat. As a result, the entrainment rate from the coflow toward the flame core becomes less. Moreover, the steady ingress of air through the outlet plane and along the wall, which is observed when the coflowing air enters at 300 K, is absent when preheated air is used. The air ingress through the outlet plane forms a recirculation zone adjacent to the wall, for air flow without preheat, which keeps the temperature low near the wall. However, such cold (ambient) air cushion, offered by the recirculating zone, on the wall is not realized when the coflowing air is preheated. In the absence of the recirculation zone on the wall, the flow dilates radially outward, advecting additional energy over that transported through conduction. As a result, the temperature reduces at the core and increases near the periphery. Figures 8(*a*) and 8(*b*), which show the steady state centerline temperature and the axial velocity distributions, respectively, without and with air-preheat, clearly depict the differences in the central region. Due to comparatively lower velocities on the centerline with preheated air, the residence time of the gas mixture increases. This along with the higher temperature creates favorable conditions for higher soot nucleation and surface growth.

The development of the soot profile during the transient development of the flame does not show much qualitative difference from the nonpreheat case. In the case of air-preheat, the complete steady state is attained after a considerable delay, mainly because of the complex postflame transport processes. Therefore, though the flame front does not reflect much change after 0.4 s from ignition, an additional 2.8 s is required to reach the final steady condition in the entire computational domain. The soot loading and the soot particle size in steady flame with preheated air are shown in Figs. 9(*a*) and 9(*b*), respectively. The soot volume fraction distribution (Fig. 9(*a*)) shows a fivefold increase in its maximum value compared with that in nonpreheated air combustion. The distribution of average soot diameter for the steady situation (Fig. 9(*b*)) reveals that despite the increase in the soot volume fraction, the average soot particle diameter experiences much less change with preheat compared with the nonpreheat case. The maximum soot diameter is calculated to be 13.6 nm. This indicates an increase of 2.5 times in the maximum soot volume due to increased surface growth. The peak soot number density, increased by two times indicating an increase in the soot nucleation rate too.

Figures 10(*a*)–10(*d*) illustrate the soot volume fraction distributions at intermediate times of 0.1 s, 0.2 s, 0.4 s, and 1.6 s after the ignition, respectively. It is clearly evident from the figures that the qualitative trends remain similar to that without air-preheat. The only difference is in the magnitude of the soot volume fraction, which is higher for all the corresponding times. The flame at 0.1 s (Fig. 10(*a*)) shows a diverging nature first before the rapid inward turn near the tip. However, at this time a large opening in the tip is observed. The soot concentration is high in the core of the flame. However, near the flame tip the concentration drops very rapidly. The flame at 0.2 s (Fig. 10(*b*)) is highly irregular owing to the flow pattern. The tip seems to be flickering at this state. The

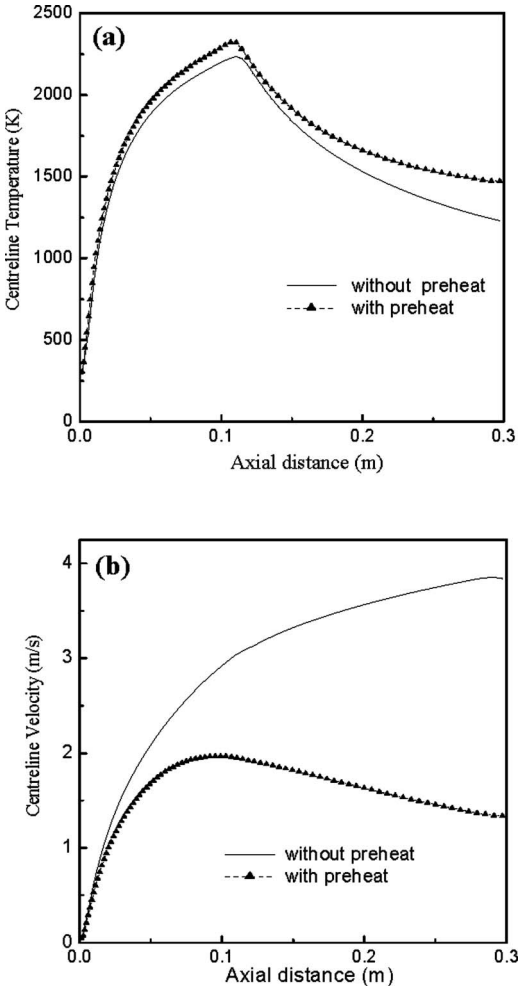

Fig. 8 (*a*) Centerline temperature and (*b*) centerline velocity distribution for the diffusion flame with and without air-preheat

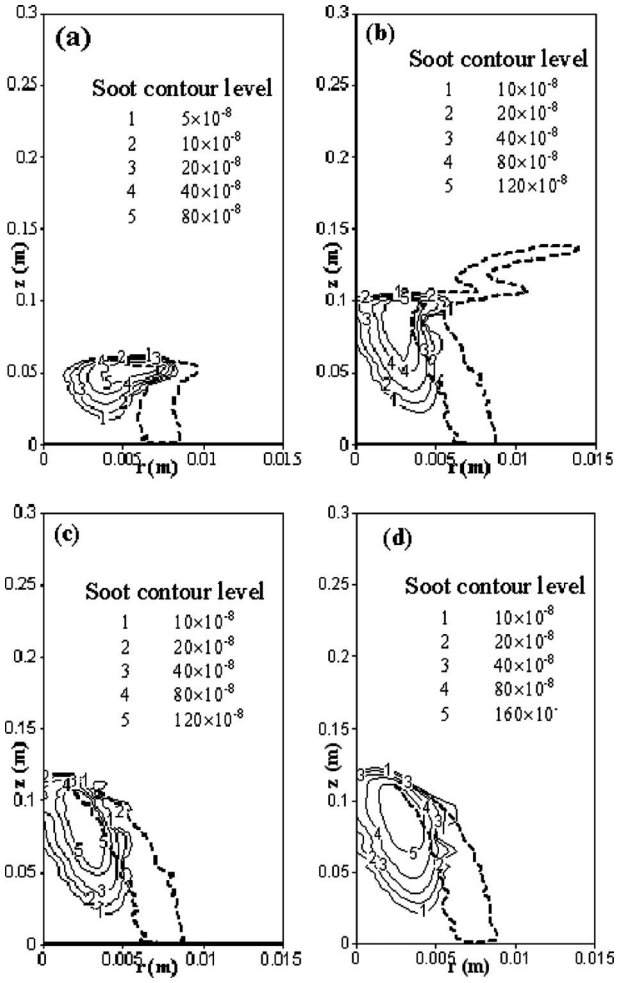

Fig. 10 Flame front surface (thick dotted line) and soot volume fraction contours at various times after ignition with preheated air: (*a*) *t*=0.10 s, (*b*) *t*=0.20 s, (*c*) *t*=0.40 s, and (*d*) *t* =1.60 s

soot loading has increased much compared with the earlier time shown. At 0.4 s (Fig. 10(*c*)), an overventilated steady flame structure is seen, with a small tip opening. The soot loading remains almost the same as in the previous time. As the soot formation takes place within the flame core and the soot oxidizes quite rapidly beyond the flame surface, not much change in the qualitative soot profiles are observed in the following times as well. However, a little change in the soot volume fraction value is noted. At 1.6 s, the soot volume fraction increases marginally (Fig. 10(*d*)). After 1.6 s, not much change is observed even in the quantitative value of the volume fraction until the final steady state is reached at 3.2 s.

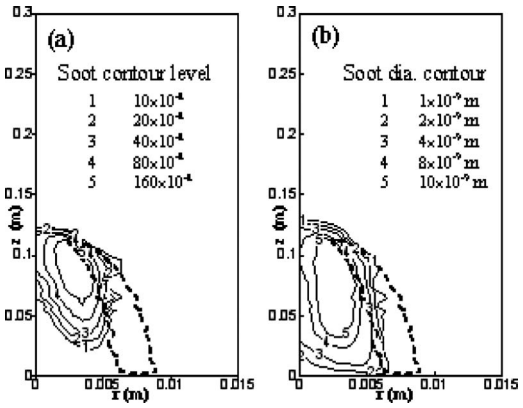

Fig. 9 Flame front surface (dashed thick line) and (*a*) soot volume fraction contours; and (b) soot diameter contours with preheated air under steady state

7 Conclusions

The effect of air-preheat on the flame development and soot distribution in a methane-air laminar coflowing diffusion flame during transient period just after ignition has been investigated numerically. With nonpreheated air, it is observed that 0.05 s after the ignition, a thin flame front is established and only a small amount of soot is formed due to lower temperatures in the flame front. Following this, as the temperature in the flame front increases, the soot volume fraction increases due to soot nucleation and surface growth (up to 0.15 s). Subsequently, the oxidation of soot particles plays a major role and controls the growth of soot volume. The number of soot particles also reaches a peak and then drops down due to coagulation of the particles to reach a steady level. The values of soot volume and particle number do not reach their peak simultaneously.

Initially, when the oxidization of the soot is not significant, some of the soot particles of smaller diameters are seen to escape into the atmosphere. However, under steady conditions, the soot, which is formed within the flame zone, gets totally oxidized beyond the flame and the product gas escapes with no soot.

When the air is preheated (400 K), the qualitative trend in the build up of the soot-laden zone remains similar. However, the peak concentration of soot is much more in the steady flame (five times compared with that without preheat). This is due to the increased rates of soot nucleation and surface growth. The peak soot number density is twice of that without preheat and the volume of the maximum soot particle is found to increase by 2.5 times. All the soot particles get oxidized in the postflame region and no soot particle escapes the exit plane.

Nomenclature

C_j = concentration of the jth species
c_p = specific heat
D = mass diffusivity
f_v = soot volume fraction
g = acceleration due to gravity
h = enthalpy
Le = Lewis number
N_0 = Avogadro's number
n = soot particle number density
p = pressure
r = radial distance
T = temperature
t = time
v = velocity
V_t = thermophoretic velocity
z = axial distance

Greek Symbols

μ = viscosity
ρ = density
λ = thermal conductivity
ω_{OX} = soot oxidation rate

Subscripts

a = air
f = fuel species
j = species identification
r = radial direction
z = axial direction

References

[1] Wey, C., Powell, E. A., and Jagoda, J. I., 1984, "The Effect of Temperature on the Sooting Behaviour of Laminar Diffusion Flames," Combust. Sci. Technol., **41**, pp. 173–190.

[2] Santoro, R. J., Yeh, T. T., Horvathand, J. J., and Semerjian, H. G., 1987, "The Transport and Growth of Soot Particles in Laminar Diffusion Flames," Combust. Sci. Technol., **53**, pp. 89–115.

[3] Smooke, M. D., McEnally, C. S., Pfefferle, L. D., Hall, R. J., and Colket, M. B., 1999, "Computational and Experimental Study of Soot Formation in a Coflow, Laminar Diffusion Flame," Combust. Flame, **117**, pp. 117–139.

[4] Lee, K. O., Megaridis, C. M., Zelepouga, S., Saveliev, A. V., Kennedy, L. A., Charon, O., and Ammouri, F., 2000, "Soot Formation Effects of Oxygen Concentration in the Oxidizer Stream of Laminar Co-Annular Non-Premixed Methane/Air Flames," Combust. Flame, **121**, pp. 323–333.

[5] Xu, F., El-Leathy, A. M., Kin, C. H., and Faeth, G. M., 2003, "Soot Surface Oxidation in Hydrocarbon/Air Diffusion Flames at Atmospheric Pressure," Combust. Flame, **132**, pp. 43–57.

[6] Smith, G. M., 1982, "A Simple Nucleation/Depletion Model for the Spherule Size of Particulate Carbon," Combust. Flame, **48**, pp. 265–272.

[7] Gore, J. P., and Faeth, G. M., 1986, "Structure and Spectral Radiation Properties of Turbulent Ethylene/Air Diffusion Flames," Proc. Combust. Inst., **21**, pp. 1521–1531.

[8] Kennedy, I. M., Kollmann, W., and Chen, J. Y., 1990, "A Model for the Soot Formation in Laminar Diffusion Flame," Combust. Flame, **81**, pp. 73–85.

[9] Leung, K. M., Lindstedt, R. P., and Jones, W. P., 1991, "A Simplified Reaction Mechanism for Soot Formation in Non-Premixed Flames," Combust. Flame, **87**, pp. 289–305.

[10] Syed, K. J., Stewart, C. D., and Moss, J. B., 1990, "Modelling Soot Formation and Thermal Radiation in Buoyant Turbulent Diffusion Flames," Proc. Combust. Inst., **23**, pp. 1533–1539.

[11] Moss, J. B., Stewart, C. D., and Young, K. J., 1995, "Modelling Soot Formation and Burnout in a High Temperature Laminar Diffusion Flame Burning Under Oxygen-Enriched Conditions," Combust. Flame, **101**, pp. 491–500.

[12] Said, R., Garo, A., and Borghi, R., 1997, "Soot Formation Modeling for Turbulent Flames," Combust. Flame, **108**, pp. 71–86.

[13] Lee, K. B., Thring, M. W., and Beer, J. M., 1962, "On the Rate of Combustion of Soot in a Laminar Soot Flame," Combust. Flame, **6**, pp. 137–145.

[14] Nagle, J., and Strickland-Constable, R. F., 1962, Fifth Carbon Conference, Vol. 1, pp. 154–164.

[15] Najjar, Y. S. H., and Goodger, E. M., 1981, "Soot Oxidation in Gas Turbines Using Heavy Fuels. 2," Fuel, **60**, pp. 987–990.

[16] Mandal, B. K., Datta, A., and Sarkar, A., 2005, "Transient Development of Methane-Air Diffusion Flame in a Confined Geometry With and Without Air-Preheat," Int. J. Energy Res., **29**, pp. 145–176.

[17] Mitchell, R. E., Sarofim, A. F., and Clomburg, L. A., 1980, "Experimental and Numerical Investigation of Confined Laminar Diffusion Flames," Combust. Flame, **37**, pp. 227–244.

[18] DuPont, V., Pourkashanian, M., and Williams, A., 1993, "Modelling of Process Heaters Fired by Natural Gas," J. Inst. Energy, **73**, pp. 20–29.

[19] Reid, R. C., Prausnitz, J. M., and Poling, B. E., 1988, *The Properties of Gases & Liquids*, McGraw-Hill, New York.

[20] Hirt, C. W., and Cook, J. L., 1972, "Calculating Three-Dimensional Flows Around Structures and Over Rough Terrain," J. Comput. Phys., **10**, pp. 324–338.

A Time-Domain Network Model for Nonlinear Thermoacoustic Oscillations

Simon R. Stow[1]
e-mail: simon.stow@rolls-royce.com

Ann P. Dowling

Department of Engineering,
University of Cambridge,
Cambridge CB2 1PZ, UK

Lean premixed prevaporized (LPP) combustion can reduce NO_x emissions from gas turbines but often leads to combustion instability. Acoustic waves produce fluctuations in heat release, for instance, by perturbing the fuel-air ratio. These heat fluctuations will in turn generate more acoustic waves and in some situations linear oscillations grow into large-amplitude self-sustained oscillations. The resulting limit cycles can cause structural damage. Thermoacoustic oscillations will have a low amplitude initially. Thus linear models can describe the initial growth and hence give stability predictions. An unstable linear mode will grow in amplitude until nonlinear effects become sufficiently important to achieve a limit cycle. While the frequency of the linear mode can often provide a good approximation to that of the resulting limit cycle, linear theories give no prediction of its resulting amplitude. In previous work, we developed a low-order frequency-domain method to model thermoacoustic limit cycles in LPP combustors. This was based on a "describing-function" approach and is only applicable when there is a dominant mode and the main nonlinearity is in the combustion response to flow perturbations. In this paper that method is extended into the time domain. The main advantage of the time-domain approach is that limit-cycle stability, the influence of harmonics, and the interaction between different modes can be simulated. In LPP combustion, fluctuations in the inlet fuel-air ratio have been shown to be the dominant cause of unsteady combustion: These occur because velocity perturbations in the premix ducts cause a time-varying fuel-air ratio, which then convects downstream. If the velocity perturbation becomes comparable to the mean flow, there will be an amplitude-dependent effect on the equivalence ratio fluctuations entering the combustor and hence on the rate of heat release. Since the Mach number is low, the velocity perturbation can be comparable to the mean flow, with even reverse flow occurring, while the disturbances are still acoustically linear in that the pressure perturbation is still much smaller than the mean. Hence while the combustion response to flow velocity and equivalence ratio fluctuations must be modeled nonlinearly, the flow perturbations generated as a result of the unsteady combustion can be treated as linear. In developing a time-domain network model for nonlinear thermoacoustic oscillations an initial frequency-domain calculation is performed. The linear network model, LOTAN, is used to categorize the combustor geometry by finding the transfer function for the response of flow perturbations (at the fuel injectors, say) to heat-release oscillations. This transfer function is then converted into the time domain through an inverse Fourier transform to obtain Green's function, which thus relates unsteady flow to heat release at previous times. By combining this with a nonlinear flame model (relating heat release to unsteady flow at previous times) a complete time-domain solution can be found by stepping forward in time. If an unstable mode is present, its amplitude will initially grow exponentially (in accordance with linear theory) until saturation effects in the flame model become significant, and eventually a stable limit cycle will be attained. The time-domain approach enables determination of the limit cycle. In addition, the influence of harmonics and the interaction and exchange of energy between different modes can be simulated. These effects are investigated for longitudinal and circumferential instabilities in an example combustor system and the results are compared with frequency-domain limit-cycle predictions. [DOI: 10.1115/1.2981178]

1 Introduction

LPP combustion is a method of reducing NO_x emissions from gas turbines by mixing the fuel and air more evenly before combustion. However, LPP combustion is highly susceptible to thermoacoustic oscillations. The interaction between sound waves and combustion can lead to large pressure fluctuations, resulting in structural damage. Linear models can give predictions for the frequency and linear stability of oscillations, and thus indicate possible modes. However, they do not give predictions of oscillation amplitude. Ideally one would wish to design a combustion system that is linearly stable; however, this may not be possible. Thus models that can predict limit-cycle amplitude are required to help design combustors that oscillate within acceptable bounds. Furthermore, such models can be used to investigate the potential amplitude reduction from damping devices.

We present a low-order theory to predict limit cycles in LPP combustors, which is based in the time domain and combines a linear thermoacoustic model with a nonlinear combustion model.

[1]Present address: Rolls-Royce plc, Derby DE24 8BJ, UK.

Contributed by the International Gas Turbine Institute of ASME for publication in the JOURNAL OF ENGINEERING FOR GAS TURBINES AND POWER. Manuscript received March 28, 2008; final manuscript received April 25, 2008; published online February 3, 2009. Review conducted by Dilip R. Ballal. Paper presented at the ASME Turbo Expo 2008: Land, Sea and Air (GT2008), Berlin, Germany, June 9–13, 2008.

Previously, we presented a frequency-domain method [1] using a describing-function approach, which was only valid when a single frequency dominated. The time-domain approach can be used to investigate limit-cycle stability, the influence of harmonics, and the interaction between different modes.

The thermoacoustic model, described in Sec. 2, is formulated in terms of a network of modules describing the features of the geometry. This model can be applied either to long combustors (typical of industrial gas turbines) where the perturbations can be treated as one dimensional, or to thin-annular combustors (typical of aeroengines) where the perturbations can be treated as circumferential and longitudinal waves. There have been several studies on linear combustion-instability models in literature. For example, Paschereit et al. [2] described an approach in which the premixer and combustion zone are modeled by a single transfer matrix. The coefficients of the matrix were found experimentally by using a loud-speaker forcing in a test rig. Krüger et al. [3,4] have used networks of one-dimensional modules linked together in both axial and circumferential directions to model annular combustors. Oscillations in annular combustors have also been computed by Hsiao et al. [5,6] using a hybrid computational fluid dynamics (CFD)/acoustics-based model on a three-dimensional grid of cells. A review of linear modeling of combustion instability is given in Refs. [7,8]. Nonlinear modeling of thermoacoustic oscillations was first motivated by instability in rocket engines (see, for example, Refs. [9,10]). For LPP combustion, nonlinear time-domain models have been developed to calculate limit cycles [11–14].

There is much evidence that equivalence ratio fluctuations are the dominant cause of heat-release oscillations in LPP combustors (see, for example, Refs. [15,16]). As described in Sec. 3, a simple saturation model (similar to that in Ref. [14]) is used to model the unsteady combustion. However, a more complex flame model, such as that developed in Ref. [1], can be used. It is assumed that this is the main source of nonlinearity determining the amplitude of the limit cycle. An initial calculation using the linear frequency-domain model categorizes the combustor geometry by finding the transfer function for the response of flow perturbations (at the fuel injectors, say) to heat-release oscillations; see Sec. 4. This transfer function is converted to a Green's function, which thus relates unsteady flow to heat release at previous times. In Sec. 5, we show that by combining this with a nonlinear flame model (relating heat release to unsteady flow at previous times) a solution can be found by stepping in time. Thus, whereas in Ref. [1] a time-domain nonlinear flame model was converted to the frequency domain then combined with the linear acoustic model, here the acoustic model is converted to the time domain then combined with the flame model. If an unstable mode is present, its amplitude will initially grow exponentially (in accordance with linear theory) until saturation effects in the flame model become significant, and eventually a stable limit cycle will be attained. In Sec. 6, the model is applied to an example geometry and the results are compared with limit-cycle predictions from the frequency-domain model. Finally, our conclusions are presented in Sec. 7.

2 Linear Thermoacoustic Network Model

Before investigating the nonlinear effects, we give a brief description of the linear combustion-instability model. We use cylindrical polar coordinates x, r, and θ and write the pressure, density, temperature, and velocity as p, ρ, T, and (u,v,w), respectively. We will assume a perfect gas, $p=R_{\text{gas}}\rho T$. The flow is taken to be composed of a steady axial mean flow (denoted by bars) and a small perturbation (denoted by dashes). We make one of the two assumptions about the combustor geometry: either we assume it is axially long (typical of industrial gas turbines) or that it has a narrow annular gap compared with its circumference (typical of aeroengines). The mean flow for either cases can be assumed to be one dimensional. For the former case, the perturbations will also be one dimensional (at least at frequencies of practical interest). In the latter case, circumferential and axial variations of the perturbation could be important but radial variation can be neglected. We consider perturbations with complex frequency ω, i.e., we have $p=\bar{p}(x)+p'(x,\theta,t)$ with $p'=\text{Re}[\hat{p}(x,\theta)e^{i\omega t}]$ (and similarly for the other flow variables). We may consider the perturbations as a sum of circumferential modes by writing $\hat{p}(x,\theta)=\Sigma_{n=-N}^{N}\hat{p}^n e^{in\theta}$ and so on (where N is sufficiently large that the higher-order modes can be neglected). If the geometry is axisymmetric throughout then the circumferential modes can be considered independently. However, if the symmetry is broken (for instance, by a Helmholtz resonator being present [17]) the modes can become coupled and must be calculated together. Note that for the case of a one-dimensional geometry, only the plane waves are present and we simply have $N=0$.

The geometry is composed of a network of modules describing its features, such as straight ducts, area changes, and combustion zones. For the straight duct modules, wave propagation is used to relate the perturbations at one end of the duct to those at the other. The rest of the modules are assumed to be acoustically compact. Here quasisteady conservation laws for mass, momentum, and energy are used to relate the flow at the inlet and exit of the module, accounting for any force or heat input applied within the module. At a combustion zone, the unsteady heat release is related to the flow disturbances by a (linear) flame transfer function. Acoustic boundary conditions are assumed to be known at the inlet and outlet of the geometry. The procedure to find the resonant modes is to guess an initial value for ω and calculate the perturbations, starting at the inlet and stepping through the modules to the outlet. In general this solution will not match the outlet boundary condition. ω is then iterated to satisfy this constraint. (For coupled circumferential modes, the relative phase and magnitude of the modes at the inlet must also be calculated.) The frequency of the mode is then $\text{Re}(\omega)/(2\pi)$, and we define the growth rate as $-\text{Im}(\omega)$. If the growth rate is negative the mode is linearly stable and would not be expected to be seen in practice, whereas if the growth rate is positive the mode is unstable and would grow in amplitude until nonlinear effects become important and a limit cycle is achieved. More details on this linear model are given in Ref. [18], with the procedure for coupled circumferential modes described in Ref. [17].

The above references only consider geometries with a single flow-pathway from the inlet to the outlet; however, it is possible to extend the model to have multiple pathways. These additional "secondary paths" may originate by splitting of the flow or from secondary inlets to the geometry. The paths can later terminate as dead ends or by joining into other paths. Flow from one path to another through holes can also be incorporated. This means that cooling flows and staged combustion can be modeled. Schematics of a possible application and modeling approach are shown in Fig. 1. At the start of each secondary path there is an unknown parameter for the perturbation (such as the ratio of the mass-flux perturbations at a flow split), and at the end of each path there is a boundary condition (such as $\hat{u}=0$ at a dead end). However, due to the linearity of the model, calculation of these simply involves the solution of a $(P+1)$-dimensional complex matrix equation (or $(P+1)(2N+1)$-dimensional for coupled circumferential modes), where P is the number of secondary paths.

A general review of linear methods for combustion instability in LPP gas turbines is given Refs. [7,8].

3 Nonlinear Flame Model

We assume that combustion takes place at a single combustion zone, i.e., there is no radial or axial staging (however, this constraint can be relaxed; see Sec. 5.3). This combustion zone is assumed to be acoustically compact in the axial direction (i.e., short compared with the wavelength of flow perturbations). We assume that a ring of D premix ducts or burners is present. For simplicity, we take these to be identical and uniformly spaced

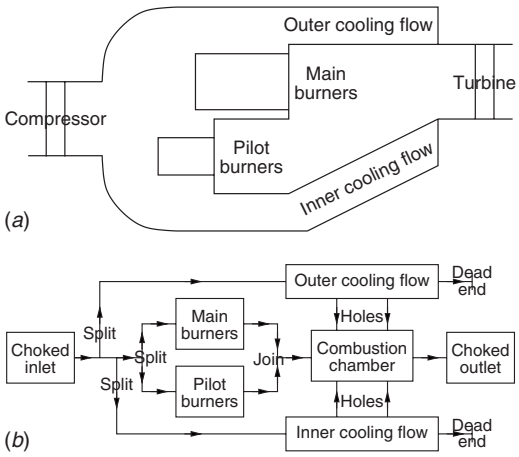

Fig. 1 Schematics of possible application of thermoacoustic network model (top) and modeling approach (bottom)

around the circumference, although this need not be the case. We denote the heat release from duct d by $Q_d(t)$. A flame model relates $Q_d(t)$ to the unsteady flow at previous times. In the examples in Sec. 6, we will use the following simple saturation model:

$$Q_d'^L(t) = -k\frac{m_d'(t-\tau)}{\bar{m}_d}\bar{Q}_d \tag{1a}$$

$$Q_d'(t) = \begin{cases} Q_d'^L(t) & \text{for} |Q_d'^L(t)| \le \alpha\bar{Q}_d \\ \alpha\bar{Q}_d \,\text{sgn}(Q_d'^L(t)) & \text{for} |Q_d'^L(t)| > \alpha\bar{Q}_d \end{cases} \tag{1b}$$

where m_d denotes the (air) mass flow at the fuel injection point in duct d, τ is the convection time from there to the combustion zone, k is a constant associated with the low-amplitude behavior, and α is a constant associated with the saturation ($0<\alpha\le 1$). (This nonlinear flame model is very similar to that used in Ref. [14].) The overbars denote unperturbed steady-state values and the primes denote the perturbation; hence, $Q_d(t)=\bar{Q}_d+Q_d'(t)$. (Note that for small oscillations the unperturbed value is the same as the time-averaged mean, but for larger amplitudes this is not necessarily the case.) A more complex nonlinear flame model is described in Ref. [1]. Like Eqs. (1*a*) and (1*b*), this model relates heat release to a single flow variable in each duct, but models involving more than one variable could also be used. However, to maintain causality in the time-domain calculation, the model must give $Q_d(t)$ in terms of flow variables evaluated at earlier times, not the current time.

3.1 Flame Transfer Function. We now convert the flame model in Eqs. (1*a*) and (1*b*) into the frequency domain. This is not required in the time-domain calculations, but gives insight into the effect of the flame model and is required for frequency-domain calculations of linear modes and limit cycles. We aim to find the response from Eqs. (1*a*) and (1*b*) to a harmonic input

$$m_d'(t) = \text{Re}(\hat{m}_d e^{i\omega t}) \tag{2}$$

For small disturbances, the heat release is also harmonic and can be written as

$$Q_d'(t) = \text{Re}(\hat{Q}_d e^{i\omega t}) \tag{3}$$

The (linear) flame transfer function used in linear-mode calculations is then defined by

$$T_{\text{flame}}^L(\omega) = \frac{\hat{Q}_d/\bar{Q}_d}{\hat{m}_d/\bar{m}_d} = -ke^{-i\omega\tau} \tag{4}$$

(For a discussion of flame transfer functions, see, for example, Refs. [19,20].)

For finite disturbances, $Q_d'(t)$ may not be harmonic but is still periodic (with the same period as $m_d'(t)$) and hence it can be described by a Fourier series

$$Q_d'(t) = \text{Re}\left(\sum_{m=0}^{\infty} \hat{Q}^{(m)} e^{im\omega t}\right) \tag{5}$$

In frequency-domain limit-cycle calculations, we ignore the higher-frequency harmonics generated and take $\hat{Q}_d=\hat{Q}^{(1)}$. From this we define a nonlinear flame transfer function, which is a function of frequency and amplitude, $A=|\hat{m}_d|/\bar{m}_d$. Evaluating the first Fourier coefficient

$$\hat{Q}^{(1)} = \frac{\omega}{\pi}\int_0^{2\pi/\omega} Q_d'(t)e^{i\omega t}dt \tag{6}$$

with $Q_d'(t)$ and $m_d'(t)$ as in Eqs. (1*a*), (1*b*), and (2), it can be shown that

$$\frac{T_{\text{flame}}(\omega,A)}{T_{\text{flame}}^L(\omega)} = \frac{\hat{Q}^{(1)}}{\hat{Q}^L} = \begin{cases} 1 & \text{for } \beta \le 1 \\ 1 - \dfrac{2\psi}{\pi} + \dfrac{2(1-1/\beta^2)^{1/2}}{\pi\beta} & \text{for } \beta > 1 \end{cases} \tag{7}$$

where $\beta=|k|A/\alpha$ and $\psi=\cos^{-1}(1/\beta)$, with $\hat{Q}^L$ being the value from the linearized flame model. Although they are not used in any of the calculations, it is interesting to consider the values of the other terms in the expansion equation (5). For a sinusoidal input, the flame model produces a bounded sinusoid (see, for example, the dashed line in the third plot of Fig. 5). From the symmetry of this, it is easily seen that no mean or even harmonics are produced, i.e., $\hat{Q}^{(m)}=0$ for even $m\ge 0$. Furthermore, it can be shown that the odd harmonics are given by

$$\frac{\hat{Q}^{(m)}}{\hat{Q}^L} = \begin{cases} 0 & \text{for } \beta \le 1 \\ \dfrac{4}{\pi(n^2-1)}\left(\cos(n\psi)(1-1/\beta^2)^{1/2} - \dfrac{\sin(n\psi)}{n\beta}\right) & \text{for } \beta > 1 \end{cases} \tag{8}$$

for odd $m\ge 3$. Figure 2 shows the variation of $\hat{Q}^{(m)}/\hat{Q}^L$ with β for this flame model. For $\beta\le 1$, there are no nonlinear effects and so the values are the same as for the linearized flame model. As β is increased, the saturation causes the gain of the nonlinear flame transfer function to decrease, with the harmonic terms becoming more significant relative to this.

4 Flow-Response Transfer Function

Before beginning the time-domain calculation, an initial frequency-domain calculation is required in order to describe the response of flow variables to heat-release fluctuations. We expand the flow variables in circumferential modes, writing the heat release as

$$Q(\theta,t) = \text{Re}(\hat{Q}(\theta)e^{i\omega t}) \tag{9a}$$

$$\hat{Q}(\theta) = \sum_{n=-N}^{N} \hat{Q}^n \Theta_1^n(\theta) \tag{9b}$$

where

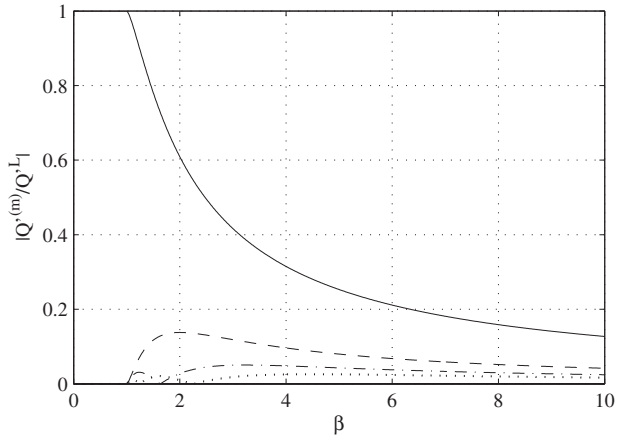

Fig. 2 Variation of $\hat{Q}^{(m)}/\hat{Q}^L$ with β. The solid, dashed, dashed-dotted, and dotted lines denote m=1, 3, 5, and 7, respectively (the value being zero for even m). Note that $\hat{Q}^{(1)}/\hat{Q}^L$ is equivalent to the nonlinear flame transfer function relative to the linearized version, $T_{\text{flame}}(\omega, A)/T^L_{\text{flame}}(\omega)$.

$$\Theta_1^n(\theta) = \begin{cases} 1 & \text{for } n = 0 \\ \cos(n\theta) & \text{for } n > 0 \\ \sin(n\theta) & \text{for } n < 0 \end{cases} \tag{9c}$$

and similarly for the other flow variables. $\hat{Q}^n$ represent the components of $\hat{Q}$ in terms of circumferential standing modes and N is the maximum mode number of interest. Previously, we have decomposed into spinning modes by taking $\Theta_1^n(\theta)=e^{in\theta}$ (see Ref. [17]). Using standing modes instead is only a minor change to the frequency-domain analysis, but is essential when moving to a time-domain solution (see Sec. 5). We assume a thin-annular combustor, or else we consider only plane waves by taking $N=0$. To proceed, we also need information about the azimuthal distribution of the heat-release perturbations. Here we will assume that combustion is localized to the outlet of each premix duct, and so take

$$\hat{Q}(\theta) = \sum_{d=1}^{D} 2\pi\delta(\theta - \theta_d)\hat{Q}_d \tag{10}$$

where $\theta_d=\theta_1+2\pi(d-1)/D$ are the azimuthal locations of the premix ducts. (We could consider other distributions, such as $\hat{Q}_d$ uniformly distributed over the sector. However, since the circumferential mode-number of interest is typically much less than the number of premix ducts, the particular distribution is unlikely to have a big effect.) Comparing Eqs. (9*b*) and (10) gives

$$\hat{Q}^n = \frac{1}{2\pi}\int_0^{2\pi} \hat{Q}(\theta)\Theta_2^n(\theta)d\theta = \sum_{d=1}^{D} \hat{Q}_d\Theta_2^n(\theta_d) \tag{11a}$$

where

$$\Theta_2^n(\theta) = \begin{cases} 1 & \text{for } n = 0 \\ 2\cos(n\theta) & \text{for } n > 0 \\ 2\sin(n\theta) & \text{for } n < 0 \end{cases} \tag{11b}$$

The nonlinear flame model requires certain flow variables as inputs. For definiteness, we suppose that only m'_d is required (as in the model in Eqs. (1*a*) and (1*b*)). In the frequency domain this is $\hat{m}_d$ and may be written as

$$\hat{m}_d = \hat{m}(\theta) = \sum_{n=-N}^{N} \hat{m}^n\Theta_1^n(\theta_d) \tag{12}$$

(see Ref. [1]). The frequency-domain calculation is then as follows. The flow response to unsteady combustion is identified by forcing the components of the heat release. The response to unsteady heat release in mode n^* is determined by setting $\hat{Q}^n/\bar{Q} = \delta^{n,n^*}$. The frequency-domain model (see Sec. 2) is used to calculate the perturbations in the flow for this forced rate of heat release in the combustor geometry, for a fixed value of ω. Due to the linearity of the problem, this amounts to solving a matrix equation. We define $T^{n,n^*}(\omega)=\hat{m}^n/\bar{m}$ for this solution. Linearity in the flow response then gives that for any set of values of $\hat{Q}^{n^*}$,

$$\frac{\hat{m}^n}{\bar{m}} = \sum_{n^*=-N}^{N} T^{n,n^*}(\omega)\frac{\hat{Q}^{n^*}}{\bar{Q}} \tag{13}$$

T^{n,n^*} is thus a matrix of transfer functions describing the linear response of the flow variable to heat-release fluctuations. It gives no information about the flame but instead categorizes the linear waves generated in the geometry by unsteady combustion. Note that if the geometry is axisymmetric, the matrix is diagonal with $T^{-n,-n} \equiv T^{n,n}$.

4.1 Green's Function. To use the transfer functions in the time-domain calculation, they are converted into Green's functions, G^{n,n^*}, by taking the inverse Fourier transform

$$G^{n,n^*}(t) = \frac{1}{2\pi}\int_{-\infty}^{\infty} T^{n,n^*}(\omega)e^{i\omega t}d\omega = \frac{1}{\pi}\text{Re}\int_0^{\infty} T^{n,n^*}(\omega)e^{i\omega t}d\omega \tag{14}$$

In practice, $T^{n,n^*}(\omega)$ is calculated at a discrete set of frequencies, $f=\omega/(2\pi)=0,\Delta f, 2\Delta f, \ldots, f^*_{\max}$. The integral is thus approximated by the corresponding inverse discrete Fourier transform, with $G^{n,n^*}(t)$ being evaluated at $t=0,\Delta t, 2\Delta t, \ldots, t_{\max}$, where $\Delta t = 1/(2f^*_{\max})$ and $t_{\max}=1/\Delta f$. Δt will also be the time step used in the time-domain calculation. In order to remove the possibility of high-frequency oscillations, while keeping Δt small, we may wish to set T^{n,n^*} to be zero for $f>f_{\max}$, say.

5 Time-Domain Solution

The flame model and the flow-response transfer function developed in Secs. 3 and 4 model the physics of the flow phenomena that lead to self-excited combustion oscillations. Green's function (see Eq. (14)) describes the flow fluctuations generated by unsteady heat release, including the reflection and transmission of sound throughout the combustor geometry. The flame model describes how the flow perturbations lead to further combustion unsteadiness. By combining the two, the development of an oscillation can be predicted. The time-domain calculation proceeds as follows. For $t\le 0$, m'_d and Q'_d are set to low-amplitude random noise. This encourages any instabilities in the system to initiate themselves, in the same way as background turbulent noise would in a real engine. The solution is then stepped forward in time, using a time step of Δt (see Sec. 4.1). For each duct, $Q'_d(t)$ at the new time value is found from m'_d at previous times using the nonlinear flame model (suitably discretized if necessary). In a similar way to Eqs. (9*a*)–(9*c*) and (10), we write

$$Q'(t,\theta) = \sum_{n=-N}^{N} Q'^n(t)\Theta_1^n(\theta) = \sum_{d=1}^{D} 2\pi\delta(\theta - \theta_d)Q'_d(t) \tag{15}$$

Note that in the time domain, we cannot decompose into a sum of circumferential spinning modes. This is why a standing-wave decomposition was chosen in Eq. (9*b*). We can then find $Q'^n(t)$ from

$Q'_d(t)$ using the equivalent to Eq. (11*a*) as follows:

$$Q'^n(t) = \frac{1}{2\pi}\int_0^{2\pi} Q'(t,\theta)\Theta_2^n(\theta)d\theta = \sum_{d=1}^{D} Q'_d(t)\Theta_2^n(\theta_d) \quad (16)$$

It is thought that the combustion zone is the main source of nonlinearity, and we therefore assume that the flow response in the rest of the geometry can be treated as linear. (This is the same assumption previously used when calculating limit cycles in the frequency domain in Ref. [1].) Hence the linear frequency-domain calculation in Sec. 2 still applies at finite amplitude. This means that Green's functions can now be used to find $m'^n(t)$ from $Q'^n(t)$, using the time-domain version of Eq. (13), which is the convolution

$$\frac{m'^n(t)}{\bar{m}} = \sum_{n^*=-N}^{N}\int_0^{\infty} G^{n,n^*}(t^*)\frac{Q'^{n^*}(t-t^*)}{\bar{Q}}dt^* \quad (17)$$

Finally, $m'_d(t)$ is found from $m'^n(t)$ using the equivalent to Eq. (12) as follows:

$$m'_d(t) = m'(t,\theta) = \sum_{n=-N}^{N} m'^n(t)\Theta_1^n(\theta_d) \quad (18)$$

The time stepping can then be repeated in this manner until either the initial disturbances decay away or a stable limit cycle is achieved. The mode shape for the limit cycle can be found by taking the Fourier transform of $Q'^n(t)$ to find its frequency components, $\hat{Q}^n(\omega)$, and then using these in forced frequency-domain calculations of the type described in Sec. 2.

Note that if we are only considering plane waves (i.e., $N=0$), we only need to calculate the solution for one duct, since the solution in the others is identical; $m'_d \equiv m'^0 \equiv m'$ and $Q'_d \equiv Q'^0 \equiv Q'$. Also, in this case we clearly have only a single transfer function and corresponding Green's function.

In the above analysis, we have chosen to use Green's functions relating the circumferential modes. We could instead have found Green's functions, G_{d,d^*}, relating the flow variable in duct d to heat release in duct d^* at earlier times. If the geometry is axisymmetric, by symmetry we have

$$T_{d,d^*} \equiv T_{1+(d-d^*)\bmod D,1} \equiv T_{1+(d^*-d)\bmod D,1} \quad (19)$$

Therefore, in this case, a single forced perturbation solution per frequency is required and $(\text{floor}(D/2)+1)$ Green's functions must be calculated, as opposed to $(N+1)$ perturbation solutions and $(N+1)$ Green's functions if using circumferential modes. Hence this may require more or less computational time than the circumferential-mode approach, depending on the number of modes of interest and on the relative effort of calculating the perturbation solutions compared with computing the inverse Fourier transforms when finding Green's functions. If there is asymmetry in the geometry and hence modal coupling, D perturbation solutions and D^2 Green's functions are needed, instead of $(2N+1)$ and $(2N+1)^2$, respectively. For an aeroengine, the number of ducts might be around 20–30 while we may only be interested in the first or second circumferential mode; hence, calculating the duct Green's functions requires much more effort.

5.1 Single Circumferential Spinning Mode. The results from the time-domain model suggest that the final limit-cycle solution is always dominated by single-frequency circumferential spinning mode (see Sec. 6). This is in agreement with numerical simulations by Schuermans [21] (see also Ref. [22]), who also gave an analytical proof that the spinning-mode limit cycle was stable, while the standing mode was not, for a simplified example. Hence we now describe a special case where a solution of this form is assumed, thus reducing the computation required.

In Eq. (9*b*), only a single value of n is now considered, with $\Theta_1^n(\theta) = \Theta_2^n(\theta) = e^{in\theta}$. Hence only a single transfer function and corresponding Green's function are calculated. In the time domain, we only calculate the solution in a single duct, say duct 1. The solutions for the other ducts are assumed to be identical except for a phase difference corresponding to the assumed circumferential mode, i.e., duct d has a phase shift of $2\pi n(d-1)/D$, and so we take $Q^n = Q_1$. Note that it is implicit in this assumption that a single frequency must be dominant; otherwise, the spinning-wave pattern cannot be present. Therefore, if harmonics are present, this method provides only an approximation.

5.2 Sector Rigs. The approach is easily adapted for a thin-annular sector rig, $0 < \theta < \theta_{\max}$, instead of a full annulus. In the decomposition into circumferential mode in Eq. (9*b*), n is replaced with $n\pi/\theta_{\max}$, with the modes for negative n no longer present. This leads to minor changes in the frequency-domain analysis, such as the values of the axial wave numbers.

5.3 Multiple Combustion Zones. In the method described above, we assumed a single combustion zone, although the method can still be used if we assume that any additional combustion zones respond linearly so that they can be included in the initial frequency-domain calculation. For multiple nonlinear combustion, the approach can be extended to the following. Suppose that there are Z nonlinear combustion zones. Let $Q'_{d,z}(t)$ denote the heat-release perturbation from duct d at zone z, which is related to a flow perturbation, $m'_{d,z}(t)$, by a nonlinear flame model. (The flame model and the number of ducts, D_z, need not be the same at each combustion zones.) In the initial frequency-domain calculation, we set circumferential components $\hat{Q}_z^n = \delta_{z,z^*}^{n,n^*}$ and find the forced perturbation solution, defining $T_{z,z^*}^{n,n^*}(\omega) = \hat{m}_z^n$ for this solution. The general result is then

$$\hat{m}_z^n = \sum_{z^*=1}^{Z}\sum_{n^*=-N}^{N} T_{z,z^*}^{n,n^*}(\omega)\hat{Q}_{z^*}^{n^*} \quad (20)$$

As before, these transfer functions can be converted into Green's functions. In the time domain, at each time step we calculate the heat-release perturbation from each duct in each combustion zone using the corresponding flame model, and find the flow perturbations using Green's functions.

6 Results

We now apply the method described above to find time-domain solutions for an example geometry. The geometry is intended to be representative of an aeroengine combustor. It consists of an annular plenum chamber, a ring of 20 identical premix ducts, and an annular combustion chamber, and each of these is modeled as a uniform axial duct. The plenum inlet and combustor outlet are assumed to be choked, to model the turbine outlet and compressor inlet, respectively. The fuel injection point (where m_d is measured) is halfway along the premix ducts, and the combustion zone is assumed to be concentrated at the start of the combustor. Details of the geometry and flow conditions are given in Table 1 (the relevance of the long-combustion version is explained in Sec. 6.2).

6.1 Single Unstable Circumferential Mode. Before calculating a time-domain solution for the geometry, we use the frequency-domain model (Sec. 2) to calculate the linear modes. Note that the axisymmetry of the geometry means that there is no circumferential modal coupling for linear calculations, and that positive and negative values of n are equivalent. There are several stable linear modes for the geometry; however, only one unstable mode is present (for frequencies less than 3 kHz). This is a first-order circumferential mode, i.e., $n = \pm 1$. Its frequency is 521.4 Hz and its growth rate is 56.3 s^{-1}. There is relatively little axial variation of the pressure perturbation for this mode, except that it

Table 1 Geometry and flow conditions for original and long-combustor examples

Choked inlet, pressure	5 MPa
Choked inlet, temperature	1000 K
Choked inlet, mass flow rate	100 kg s^{-1}
Plenum, cross-sectional area	0.3 m^2
Plenum, mean radial location	0.3 m
Plenum, length	0.1 m
Premix ducts, number of ducts	20
Premix ducts, combined area	0.02 m^2
Premix ducts, mean radial location	0.3 m
Premix ducts, length before fuel	0.05 m
Premix ducts, length after fuel	0.05 m
Combustor, cross-sectional area	0.2 m^2
Combustor, mean radial location	0.3 m
Flame model, convection time τ	1.5 ms
Flame model, linear constant k	4
Flame model, saturation constant α	0.4
Combustor, temperature	2500 K
Combustor, length (original)	0.3 m
Combustor, length (long version)	0.707 m
Choked outlet	-

is at a lower level in the plenum compared with the premix ducts and combustor. (Note that typically we would take $k=1$ in the flame model; however, $k=4$ was chosen here in order for an unstable mode to be present.)

In the time-domain calculations, we take $N=1$, i.e., second- and higher-order circumferential waves are ignored. We take $f_{\max}=1$ kHz with $\Delta f=1$ Hz. The time step used is $\Delta t=0.1$ ms. Figure 3 shows the transfer functions and Green's functions for the (original) example geometry. Note that the values for $n=\pm 1$ are equal and no coupling terms are present (i.e., $T^{n,n^*}\equiv 0$ and $G^{n,n^*}\equiv 0$ for $n^*\neq n$). The results from a time-domain calculation are shown in Fig. 4. As we would expect from the linear predictions, the initial random noise induces an instability in both m'^{-1} and m'^{1}, while m'^{0} decays away. To begin with, these instabilities grow exponentially. During this initial linear phase ($t<0.3$ s), the amplitude of m'^{-1} was found to be larger for this simulation. This is simply because the random noise excited this mode more. As the amplitude of m'^{-1} becomes larger, nonlinear effects become important and its rate of growth diminishes. At around $t=0.35$ s, it appears that a limit cycle for m'^{-1} may have been achieved; however, meanwhile m'^{1} has grown and nonlinear coupling between the two modes is now important. Between $t=0.35$ s and 0.4 s, m'^{1} continues to grow, while m'^{-1} decays slightly, until for $t>0.4$ s a stable coupled limit cycle is achieved, which appears to continue indefinitely (the simulation was continued beyond $t=10$ s). From the third plot of Fig. 4, we can see that in the final limit cycle m'^{-1} and m'^{1} have the same amplitude but differ in phase by 90 deg. This corresponds to a spinning mode, spinning in the positive-θ direction (i.e., having the form $e^{-i\theta}$ in the frequency domain). The amplitude of m'^{-1} and m'^{1} was $0.152\bar{m}$, with the frequency found to be 519.8 Hz (close to the frequency of the unstable linear mode, as we might expect). Note that since the transfer function was only calculated up to $f_{\max}=1$ kHz, harmonics of 519.8 Hz are not seen and only a single frequency is present. The same calculation was conducted several times. Due to the initial random noise differing, in different calculations the amplitude of m'^{-1} was initially larger, smaller, or very similar to that of m'^{1}. In each case, however, the final limit cycle was a spinning wave of the same frequency and amplitude (the direction of spin varying from one calculation to another). A standing-wave limit cycle was never found in the calculations. This is because the standing-wave form is unstable, as can be explained as follows. Suppose a large-amplitude standing wave were present, say of the cosine form ($n=1$). The instability would be strong near to $\theta=0$ deg and 180 deg and the flame response saturated there. Now suppose that a small perturbation of the sine form ($n=-1$) were added. Near to $\theta=90$ deg and 270 deg the instability would still be weak, meaning that the sine form would see little saturation in the flame response and hence it would grow in amplitude, thus destroying the standing-wave structure (see also Refs. [21,22]). Decreasing Δf and Δt had a very little effect on the solution, indicating that the values used were sufficiently small. The effect of increasing $f_{\max}$ is discussed in Sec. 6.3.

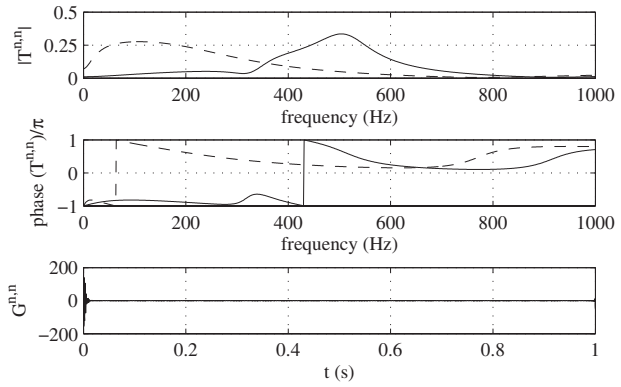

Fig. 3 Transfer functions, $T^{n,n}(\omega)$, and Green's functions, $G^{n,n}(t)$, for original geometry. The solid and dashed lines denote $n=\pm 1$ (these being equivalent) and $n=0$, respectively.

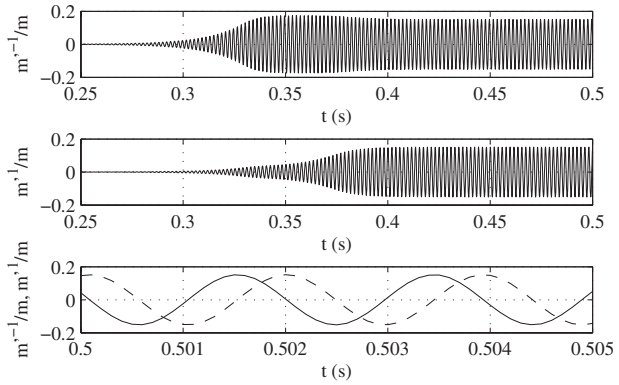

Fig. 4 Time-domain solution for original geometry. $m'^{-1}(t)/\bar{m}$ and $m'^{1}(t)/\bar{m}$ are shown; in the third plot, the solid line denotes the former while the dashed lines denotes the latter. ($m'^{0}(t)$ is negligible for this solution.)

As the limit cycle has the form of a single-frequency spinning wave, the approach described Sec. 5.1 should be applicable. Figure 5 shows the results for this simplified method for $n=1$. Note that here $m'^{1}\equiv m'_1$ and $Q'_1\equiv Q'^{1}$. In the third plot of Fig. 5 we see that, as dictated by the flame model, the heat-release oscillation in duct 1 is out of phase with the mass flow perturbation with a lag of 1.5 ms, and bounded between ± 0.4. Although the interplay between the two circumferential modes is now lost, the growth and saturation of the instability are representative of the coupled solutions calculated previously, and the final spinning-wave limit cycle has frequency and amplitude identical to those before.

The results were compared with frequency-domain limit-cycle predictions by using Eq. (7). These predictions assume that the limit cycle has a single dominant frequency, with harmonics being ignored (details of the technique are given in Refs. [1,8]). The method predicts a first-order circumferential spinning-wave limit cycle with frequency 519.8 Hz and amplitude $0.151\bar{m}$, this being virtually the same as the time-domain result. If modal coupling is included, the method also admits standing-wave solutions at the same frequency. One of the benefits of the time-domain approach

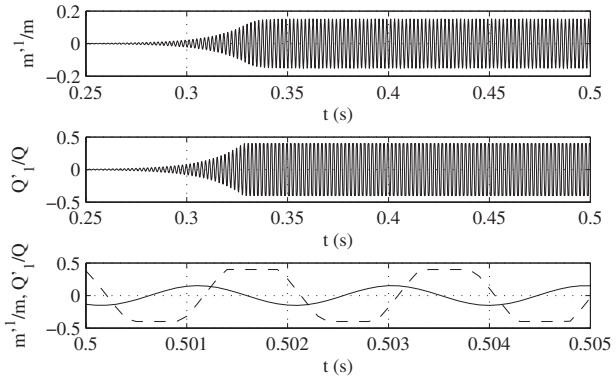

Fig. 5 Time-domain solution for original geometry, assuming a single-spinning wave, $n=1$. $m'^1(t)/\bar{m}$ and $Q'_1(t)/\bar{Q}$ are shown; in the third plot, the solid line denotes the former while the dashed lines denotes the latter.

is that it reveals that only the spinning-wave limit cycles are stable (although it may be possible to adapt the frequency-domain method to give stability predictions).

6.2 Interaction Between Two Unstable Modes. In order to investigate interaction between different modes, the geometry was modified by lengthening the combustion chamber (see Table 1). For this geometry there are now two unstable linear modes (below 3 kHz). One is a first-order circumferential mode ($n=\pm1$) at 510.7 Hz, which is very similar to the unstable mode for the original geometry, while the other is a plane wave mode ($n=0$) at 618 Hz, this being approximately a half-wave resonance of the combustion chamber. In order to maximize the chances of these modes interacting in the time domain, as opposed to one mode dominating the other, the combustor length was specifically chosen to give the same growth rate for the two modes, the value being 11.6 s^{-1}. The numerical parameters were taken to be the same as before (i.e., $N=1$, $\Delta f=1$ Hz, $f_{max}=1$ kHz, and $\Delta t=0.1$ ms). The results from four time-domain calculations are shown in Figs. 6–9. The different results are entirely due to differences in the random noise used to start the solution. In each case, there is an initial linear phase where an exponentially growing instability is seen in all three circumferential components. In Calculation 1 (Fig. 6), initially m'^{-1} and m'^1 have similar amplitudes while m'^0 is larger. At around $t=1.7$ s nonlinear interaction between the modes causes m'^{-1} and m'^1 to begin to decay. Beyond $t=2$ s these components become negligible and a stable plane wave limit cycle is established, the amplitude of m'^0, $0.116\bar{m}$, with frequency 619.5 Hz (close to the frequency of the linear plane wave mode). In Calculation 2 (Fig. 7), m'^0 and m'^1 initially have similar amplitudes while m'^{-1} is larger. Eventually m'^0 decays away and a stable spinning-wave limit cycle is set up. This has a frequency of 509.6 Hz (close to that of the linear mode for $n=\pm1$) and amplitude $0.123\bar{m}$. In Calculation 3 (Fig. 8), m'^{-1} and m'^0 initially have similar amplitudes while m'^1 is much smaller. In this case, at around $t=1.7$ s, it appears that a limit cycle in m'^{-1} and m'^0 may have been achieved; however, m'^1 continues to grow until modal interactions cause m'^0 to decay and a spinning limit cycle is formed, which is identical to that in Calculation 2. In Calculation 4 (Fig. 9), the amplitude of m'^{-1} is initially slightly larger than for m'^1 while m'^0 is slightly larger

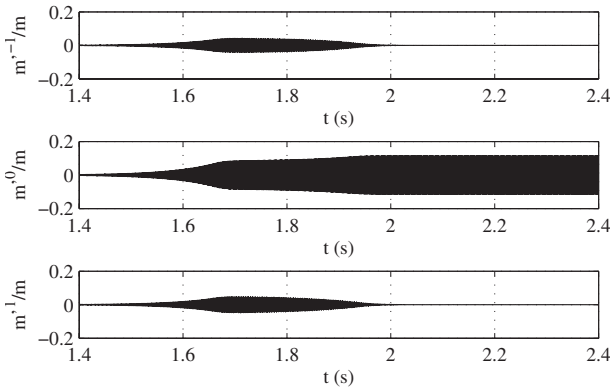

Fig. 6 $m'^n(t)/\bar{m}$ for time-domain solution for long-combustor geometry (Calculation 1)

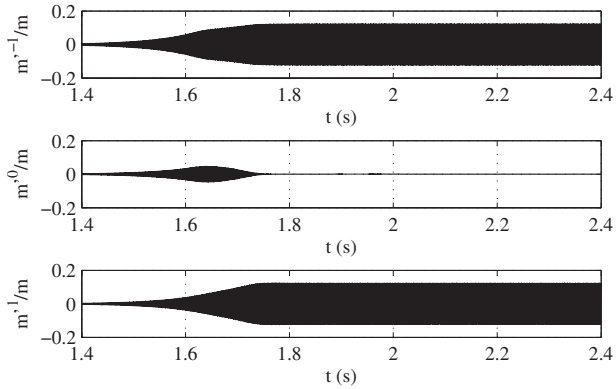

Fig. 7 $m'^n(t)/\bar{m}$ for time-domain solution for long-combustor geometry (Calculation 2)

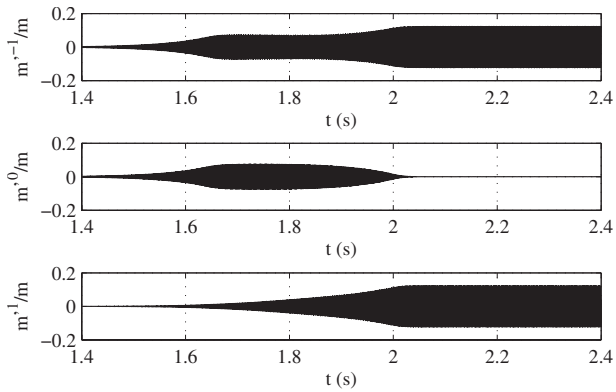

Fig. 8 $m'^n(t)/\bar{m}$ for time-domain solution for long-combustor geometry (Calculation 3)

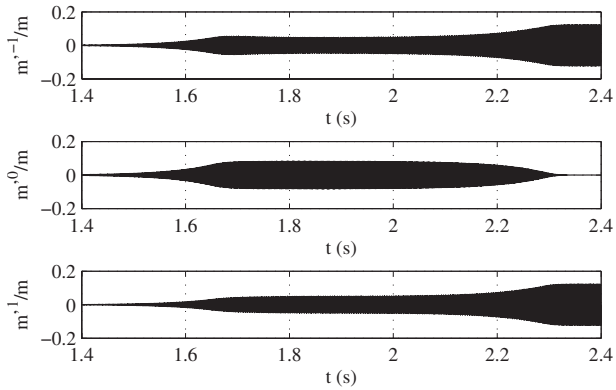

Fig. 9 $m'^n(t)/\bar{m}$ for time-domain solution for long-combustor geometry (Calculation 4)

still. Between $t=1.8$ s and 2 s it appears that limit cycle is established in which a spinning wave and a plane wave coexist. However, this is found to be transient and the solution eventually becomes the same purely spinning limit cycle as in Calculations 2 and 3. Other calculations were conducted and in each case either the plane wave limit cycle or the spinning limit cycle (spinning in one direction or the other) was eventually formed.

Frequency-domain limit-cycle predictions were also calculated for the long-combustor geometry. The solutions found were a plane wave limit cycle, frequency 619.6 Hz, and amplitude $0.116\bar{m}$, and a first-order circumferential spinning-wave limit cycle, frequency 509.7 Hz, and amplitude $0.124\bar{m}$. Again, these are virtually the same as the two limit cycles found in the time-domain calculations. As before if modal coupling is included, standing-wave solutions were also found at the same frequency as the spinning wave.

6.3 Effect of Including Harmonics. In the previous calculations, $f_{\max}$ was always set to be less than twice the limit-cycle frequencies, and so harmonics could not be present in m'. The effect of allowing harmonics to be present is now investigated. We first consider the plane wave limit cycle in the long-combustor geometry, setting $N=0$ so that only plane waves are present, and so $Q'_d \equiv Q'^0$. Using the same numerical coefficients as before, time-domain calculations resulted in a limit cycle in which m'^0 was sinusoidal with frequency 619.5 Hz and amplitude $0.116\bar{m}$, identical to the final limit cycle in Calculation 1 in Sec. 6.2. Of course, m'^0 is not sinusoidal, but a bounded sinusoid (similar to the dashed line in the third plot of Fig. 5). As shown in Sec. 3.1, this contains only odd harmonics. A calculation was then conducted for $f_{\max}=2$ kHz (with $\Delta f=1$ Hz and $\Delta t=0.05$ ms). As expected, m'^0 in the final limit cycle contained a component at the third-harmonic frequency (1858.8 Hz). However, the amplitude of this component was very low, 0.0006, and it had a negligible affect on the fundamental (first harmonic), the limit-cycle solution being virtually identical to that before. There are two reasons for this: First, the amplitude of the limit cycle is not especially high meaning that saturation effects are moderate and the third harmonic of Q'^0 is not large (see Fig. 2), and second, the flow-response transfer function has low gain at 1858.8 Hz. It is likely that a harmonic of an instability could play a significant role if it was close to a resonant frequency of the geometry, and especially if it was close to another unstable mode or a weakly stable mode of the system.

We now consider harmonics for the circumferential mode in the original geometry. Increasing $f_{\max}$ (with $N=1$), we might expect to find harmonics present in $m'^{\pm 1}$; however, this was not seen, the limit cycle being sinusoidal and virtually identical to that before. This is because, although harmonics are present in Q'_d, when the contributions from the ducts are combined (through Eq. (16)), for a spinning wave, $Q'^{\pm 1}$ become very close to sinusoidal. (This particularly so since n is small compared with D and saturation is moderate.) The effect of Eq. (16) is to instead transfer disturbances at the harmonic frequencies to the higher circumferential modes. The results for a time-domain calculation for $N=3$ and $f_{\max}=2$ kHz (with $\Delta f=1$ Hz and $\Delta t=0.05$ ms) are shown in Fig. 10. We see that $m'^{\pm 3}$ are negligible during the linear phase and start to grow in amplitude once nonlinear effects appear in $m'^{\pm 1}$. The final limit cycle consists of a sinusoidal spinning wave in $m'^{\pm 1}$ with frequency 520.2 Hz and amplitude $0.152\bar{m}$ (very close to the result before), with additionally a sinusoidal spinning wave in $m'^{\pm 3}$ with frequency 1560.4 Hz (the third harmonic) and very small amplitude $0.004\bar{m}$.

The effect of increasing $f_{\max}$ for the single-spinning-mode approximation (Sec. 5.1) was also investigated. In a calculation for $f_{\max}=2$ kHz (with $\Delta f=1$ Hz and $\Delta t=0.05$ ms), m'^1 had a component at the third-harmonic frequency. This is incorrect because, as we have seen above, the third harmonic should only be present in $m'^{\pm 3}$. However, its amplitude was very low (0.001) and the limit-cycle solution was virtually the same as before. This demonstrates that the single-spinning-mode approximation can give good results, but must be used with caution since the harmonics are treated incorrectly and potentially this could lead to an inaccurate solution.

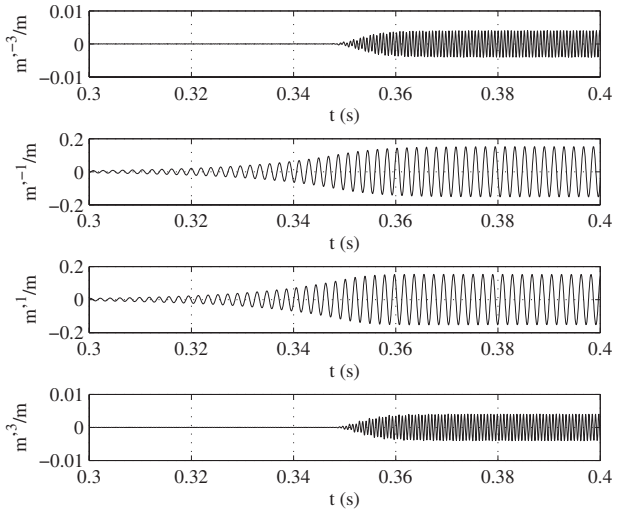

Fig. 10 Time-domain solution for original geometry, with $N=3$ and $f_{\max}=2$ kHz. $m'^n(t)/\bar{m}$ is shown for $n=-3$, -1, 1, and 3. ($m'^n(t)$ is negligible for even n.)

6.4 Helmholtz Resonators. We now investigate the effect of adding Helmholtz resonators to the geometry. Helmholtz resonators are damping devices consisting of a large volume connected to the combustor via a short neck. The modeling of these is described in Ref. [17]. Attaching a Helmholtz resonator destroys the axisymmetry of the geometry, leading to modal coupling, and hence a matrix of Green's functions is required. We first consider attaching a single resonator to the (original) geometry. The resonator is placed just before the choked outlet at 0 deg azimuthally. The resonator neck is taken to radius 7 mm and length 30 mm, with a through flow of 10 m s^{-1} into the combustor. The resonator volume is set to 1.3×10^{-4} m^3, and the temperature inside is assumed to be at 1000 K. (This corresponds to a resonator frequency of 522.7 Hz.) As discussed in Ref. [17], for linear theory (i.e., small oscillations) a single resonator does not provide damping for a circumferential mode. The effect instead is to couple the two spinning waves to produce a standing wave with a pressure node at the resonator neck. A time-domain solution was calculated, taking $N=1$ (with $f_{\max}=1$ kHz, $\Delta f=1$ Hz, and $\Delta t=0.1$ ms). m'^0 and m'^1 were found to be negligible, while m'^{-1} grew in amplitude until a stable limit cycle was achieved, in a similar way to before. Hence the limit cycle was a standing wave with a node at 0 deg (and therefore also at 180 deg). The frequency was 519.8 Hz, identical to the case without the resonator, and the amplitude was $0.179\bar{m}$. (This limit cycle is, in fact, the same as the standing-wave solution found in the frequency-domain calculations in Sec. 6.1.) As in linear theory, the resonator does not provide any damping (since the pressure oscillation at the neck is zero) but adjusts the circumferential-mode shape. Note that the peak amplitude is, in fact, higher than without the resonator, although the circumference average is $(2/\pi)\times 0.179\bar{m}=0.114\bar{m}$, which is lower than before. In practical applications, the peak amplitude is likely to be the more critical in terms of the structural damage caused; hence, the results indicate that using a single Helmholtz resonator for a circumferential mode can potentially make the situation worse. The calculation was repeated with the resonator at 45 deg azimuthally. In this case, m'^0 was negligible, while both m'^{-1} and m'^1 grew to form a limit cycle of

frequency 519.8 Hz. The amplitudes of m'^{-1} and m'^{1} were both $0.126\bar{m}$, and they were in phase. This indicates a standing wave of amplitude $\sqrt{2}\times 0.126\bar{m}=0.178\bar{m}$, with a node at 45 deg. Hence, as we would expect, the solution is virtually identical to that before but rotated by 45 deg. This provides a good check that coupled Green's functions are working correctly in the numerical scheme.

Calculations were then conducted using two Helmholtz resonators for different azimuthal separations (both resonators having the same specifications and axial location as before). With both resonators at the same azimuthal location, as we would expect, the results were the same as for a single resonator. For a separation of 180 deg, the results were again the same (the symmetry of the standing wave giving nodes at both 0 deg and 180 deg). For a 45 deg separation, the Helmholtz resonators can give damping. For linear calculations there is still a single unstable mode. Its frequency is slightly shifted (to 522.3 Hz), while its growth rate is significantly reduced (to 31.3 s^{-1}) indicating a reduction in the strength of the instability as a result of damping by the resonators. (The presence of the resonators also introduces additional linear modes; however, these modes are stable and therefore of little interest.) The resulting limit cycle still has the standing-wave form, with a node halfway between the resonators (to within 0.5 deg). The frequency is now 521.6 Hz and damping from the resonators reduces the amplitude to $0.139\bar{m}$. The results for a separation of 135 deg were very similar (the unstable mode having frequency 522.0 Hz and growth rate 30.1 s^{-1}, and the limit-cycle having frequency 520.9 Hz and amplitude $0.137\bar{m}$, with now an antinode halfway between the resonators). For a 90 deg separation, the damping is sufficient for there to be no linearly unstable modes (the largest growth rate being -6.1 s^{-1}) and so no instability is seen in the time-domain calculations, the initial random noise simply decaying away. (Note that the results in Ref. [17] indicate that the best resonator separation for an $n=1$ mode is approximately 90 deg.) Increasing N (i.e., including more circumferential modes in the calculation) had a small but noticeable effect. For instance, taking $N=4$ in the 45 deg separation case, the frequency became 522.9 Hz and the amplitude (of m'^{-1}) became $0.144\bar{m}$ (with the amplitude of m'^{-2} being $0.002\bar{m}$, and the other components being smaller still). In all cases, the time-domain calculations were in very good agreement with frequency-domain limit-cycle predictions.

7 Conclusions

A time-domain network model for nonlinear thermoacoustic oscillations has been developed. In previous work, a time-domain nonlinear flame model was converted to the frequency domain then combined with the linear acoustic model. Here, the acoustic model is converted to the time domain then combined with a flame model. Unlike the frequency-domain method, which assumes a single dominant frequency, in the time domain the effect of harmonics and the interaction between different unstable modes can be investigated.

Time-domain calculations have been conducted on an example geometry using a simple saturation flame model. These were compared with frequency-domain results, and in all cases good agreement was found. Harmonics were not significant for this geometry and flame model, although if a harmonic happened to be close to another unstable mode it could have an important effect. Where more than one unstable mode was present (and provided one mode was not a harmonic of another) the interaction was such that the final limit cycle corresponded to one or other of the modes alone, never a combination of modes. Additionally, for a circumferential instability in an axisymmetric geometry, the spinning-wave form was always preferred to the standing mode.

Acknowledgment

This work was funded by the European Commission, whose support is gratefully acknowledged. It is part of the GROWTH program, research projects ICLEAC: Instability Control of Low Emission Aero Engine Combustors (G4RD-CT-2000-0215) and LOPOCOTEP: Low Pollutant Combustor Technology Programme (G4RD-CT-2001-00447).

Nomenclature

G^{n,n^*} = flow-response Green's function, relating m'^n to Q'^{n^*}
m = mass flow
p = pressure
Q = heat release
t = time
T_{flame} = nonlinear flame transfer function, relating $\hat{Q}_d$ to $\hat{m}_d$
T^{n,n^*} = flow-response transfer function, relating $\hat{m}^n$ to $\hat{Q}^{n^*}$
u = axial velocity
w = circumferential velocity
x = axial coordinate
θ = circumferential coordinate
ρ = density
ω = complex frequency

Subscripts

$()_d$ = value for premix duct d

Superscripts

$\bar{()}$ = unperturbed value
$()'$ = perturbation
$\hat{()}$ = complex perturbation, assuming factor of $e^{i\omega t}$
$()^{(m)}$ = frequency harmonic m
$()^n$ = circumferential mode n

References

[1] Stow, S. R., and Dowling, A. P., 2004, "Low-Order Modelling of Thermoacoustic Limit Cycles," ASME Paper No. GT2004-54245.
[2] Paschereit, C. O., Schuermans, B., Polifke, W., and Mattson, O., 2002, "Measurement of Transfer Matrices and Source Terms of Premixed Flames," ASME J. Eng. Gas Turbines Power, **124**, pp. 239–247.
[3] Krüger, U., Hürens, J., Hoffmann, S., Krebs, W., and Bohn, D., 1999, "Prediction of Thermoacoustic Instabilities With Focus on the Dynamic Flame Behavior for the 3A-Series Gas Turbine of Siemens KWU," ASME Paper No. 99-GT-111.
[4] Krüger, U., Hürens, J., Hoffmann, S., Krebs, W., Flohr, P., and Bohn, D., 2000, "Prediction and Measurement of Thermoacoustic Improvements in Gas Turbines With Annular Combustion Systems," ASME Paper No. 2000-GT-0095.
[5] Hsiao, G. C., Pandalai, R. P., Hura, H. S., and Mongia, H. C., 1998, "Combustion Dynamic Modeling for Gas Turbine Engines," AIAA Paper No. 98-3380.
[6] Hsiao, G. C., Pandalai, R. P., Hura, H. S., and Mongia, H. C., 1998, "Investigation of Combustion Dynamics in Dry-Low-Emission (DLE) Gas Turbine Engines," AIAA Paper No. 98-3381.
[7] Dowling, A. P., and Stow, S. R., 2003, "Acoustic Analysis of Gas Turbine Combustors," J. Propul. Power, **19**(5), pp. 751–764.
[8] Dowling, A. P., and Stow, S. R., 2005, "Acoustic Analysis of Gas Turbine Combustors," *Combustion Instabilities in Gas Turbine Engines: Operational Experience, Fundamental Mechanisms, and Modeling* (Progress in Astronautics and Aeronautics Vol. 210), T. C. Lieuwen and V. Yang, eds., AIAA, New York, Chap. 13, pp. 369–414.
[9] Culick, F. E. C., 1971, "Non-Linear Growth and Limiting Amplitude of Acoustic Oscillations in Combustion Chambers," Combust. Sci. Technol., **3**(1), pp. 1–16.
[10] Culick, F. E. C., 1989, "Combustion Instabilities in Liquid-Fueled Propulsion Systems: An Overview," *AGARD Conference Proceedings No. 450*, Bath, UK, Oct. 6–7, Paper No. 1, AGARD, Neuilly-sur-Seine, France.
[11] Peracchio, A. A., and Proscia, W. M., 1999, "Nonlinear Heat-Release/Acoustic Model for Thermoacoustic Instability in Lean Premixed Combustors," ASME J. Eng. Gas Turbines Power, **121**(3), pp. 415–421.
[12] Pankiewitz, C., and Sattelmayer, T., 2003, "Time Domain Simulation of Combustion Instabilities in Annular Combustors," ASME J. Eng. Gas Turbines Power, **125**(3), pp. 677–685.
[13] Schuermans, B., Bellucci, V., and Paschereit, C. O., 2003, "Thermoacoustic Modeling and Control of Multi Burner Combustion Systems," ASME Paper No. GT2003-38688.

[14] Bellucci, V., Schuermans, B., Nowak, D., Flohr, P., and Paschereit, C. O., 2004, "Thermoacoustic Modeling of a Gas Turbine Combustor Equipped With Acoustic Dampers," ASME Paper No. GT2004-53977.
[15] Richards, G. A., and Janus, M. C., 1998, "Characterization of Oscillations During Premix Gas Turbine Combustion," ASME J. Eng. Gas Turbines Power, **120**(2), pp. 294–302.
[16] Lieuwen, T., and Zinn, B., 1998, "The Role of Equivalence Ratio Oscillations in Driving Combustion Instabilities in low NO_x Gas Turbines," *Proceedings of the 27th International Symposium on Combustion*, Boulder, CO, Aug. 2–7, The Combustion Institute, Pittsburgh, PA.
[17] Stow, S. R., and Dowling, A. P., 2003, "Modelling of Circumferential Modal Coupling Due to Helmholtz Resonators," ASME Paper No. GT2003-38168.
[18] Stow, S. R., and Dowling, A. P., 2001, "Thermoacoustic Oscillations in an Annular Combustor," ASME Paper No. 2001-GT-0037.
[19] Cheung, W. S., Sims, G. J. M., Copplestone, R. W., Tilston, J. R., Wilson, C. W., Stow S. R., and Dowling, A. P., 2003, "Measurement and Analysis of Flame Transfer Function in a Sector Combustor Under High Pressure Conditions," ASME Paper No. GT2003-38219.
[20] Armitage, C. A., Riley, A. J., Cant, R. S., Dowling, A. P., and Stow, S. R., 2004, "Flame Transfer Function for Swirled LPP Combustion From Experiment and CFD," ASME Paper No. GT2004-52830.
[21] Schuermans, B., 2003, "Modeling and Control of Thermoacoustic Instabilities," Ph.D. thesis, École Polytechnique Fédérale de Lausanne, Lausanne, Switzerland.
[22] Schuermans, B., Paschereit, C. O., and Monkewitz, P., 2006, "Non-Linear Combustion Instabilities in Annular Gas-Turbine Combustors," AIAA Paper No. AIAA-2006-0549.

Combustion Performance of Biodiesel and Diesel-Vegetable Oil Blends in a Simulated Gas Turbine Burner

Heena V. Panchasara

Benjamin M. Simmons

Ajay K. Agrawal

Department of Mechanical Engineering,
University of Alabama,
Tuscaloosa, AL 35487

Scott K. Spear

Daniel T. Daly

Alabama Institute for Manufacturing Excellence,
University of Alabama,
Tuscaloosa, AL 35487

Recent increases in fuel costs, concerns for global warming, and limited supplies of fossil fuels have prompted wide spread research on renewable liquid biofuels produced domestically from agricultural feedstock. In this study, two types of biodiesels and vegetable oil (VO) are investigated as potential fuels for gas turbines to generate power. Biodiesels produced from VO and animal fat were considered in this study. The problems of high viscosity and poor volatility of VO (soybean oil) were addressed by using diesel-VO blends with up to 30% VO by volume. Gas chromatography/mass spectrometry, thermogravimetric analysis, and density, kinematic viscosity, surface tension, and water content measurements were used to characterize the fuel properties. The combustion performance of different fuels was compared experimentally in an atmospheric pressure burner with an air-assist injector and swirling primary air around it. For different fuels, the effect of the atomizing airflow rate on Sauter mean diameter was determined from a correlation for air-assist atomizers. Profiles of nitric oxides (NO_x) and carbon monoxide (CO) emissions were obtained for different atomizing airflow rates, while the total airflow rate was kept constant. The results show that despite the compositional differences, the physical properties and emissions of the two biodiesel fuels are similar. Diesel-VO fuel blends resulted in slightly higher CO emissions compared with diesel, while the NO_x emissions correlated well with the flame temperature. The results show that the CO and NO_x emissions are determined mainly by fuel atomization and fuel/air mixing processes, and that the fuel composition effects are of secondary importance for fuels and operating conditions of the present study. [DOI: 10.1115/1.2982137]

1 Introduction

In recent years, two important factors have influenced the world's energy market. First, the increased demand for petroleum fuels has steadily raised their price to impose economic burden on importing nations. Second, the concerns for global warming have increased scrutiny on emissions of greenhouse gases such as carbon dioxide (CO_2) formed by the combustion of fossil fuels. The depletion of conventional fossil fuels is also a cause for concern. The above factors have prompted research on alternative energy sources. Biofuels derived from agricultural products (i.e., biomass) offer the potential for a sustainable energy future. Unlike nonrenewable fossil fuels, the CO_2 emitted from the combustion of biofuels is recycled during cultivation of the biomass. Biofuels can increase energy security since the biomass feedstock is domestic, diffuse, and hence, secure. However, for commercial viability, the land usage and fossil energy input for biofuel production must be reduced through process integration/optimization and/or specialty energy crops such as microalgae [1].

Ethanol and biodiesel are the two commonly available liquid biofuels in the United States. These fuels are currently mixed with gasoline or diesel fuel in small amounts (up to 10% for ethanol and up to 20% for biodiesel) to reduce the demand for fossil fuels for vehicular transportation. Accordingly, several studies have been performed to evaluate performance of these fuels for automotive internal combustion engines [2–4]. Although market demand currently favors the use of liquid biofuels mainly for vehicles, biodiesel could also serve as an alternative fuel for the power generation industry, for example, by replacing the fuel in diesel or gas turbine engines.

Biodiesel is obtained from vegetable oils (VO) or animal fats through a process known as transesterification. In this process, the vegetable oil or animal fat (triglyceride) reacts with an alcohol in the presence of a catalyst such as sodium or potassium hydroxide to produce glycerol and biodiesel [5]. The most common form of biodiesel in the United States is made from soybean (vegetable oil) and methanol, and it is known as soy methyl ester (SME) or methyl soyate, which is one of the fuels of interest in the current study. The transesterification process improves the physical properties of the original VO, and, in particular, decreases the viscosity to improve fuel atomization in the combustion system. This process however incurs a cost penalty and hence, the price of biodiesel exceeds that of the VO used to produce it. Furthermore, glycerol, coproduced with biodiesel, is often a waste product since it is yet to find a commercial market. Thus, the direct use of VO in a gas turbine to generate power can offer economic benefits, especially if the problem of fuel atomization associated with high viscosity can be alleviated by blending VO with diesel or biodiesel fuels.

The continuous flow operation of gas turbines offers greater flexibility, unlike the unsteady processes of internal combustion engines imposing constraints on fuel chemistry in terms of octane and/or cetane numbers. Field tests in recent years have demonstrated the technical feasibility of gas turbine engine operation on fuels such as bio-oil, ethanol, and biodiesel [6–9]. However, these tests have produced limited data on emissions of nitric oxides (NO_x) and carbon monoxide (CO). Detailed NO_x and CO emission measurements in an atmospheric pressure burner simulating typical features of a gas turbine combustor were reported by

Contributed by the International Gas Turbine Institute of ASME for publication in the JOURNAL OF ENGINEERING FOR GAS TURBINES AND POWER. Manuscript received March 30, 2008; final manuscript received May 17, 2008; published online February 6, 2009. Review conducted by Dilip R. Ballal.

Table 1 List of fuels used in the study

Fuel	Description
Diesel	Commercial Grade No. 2
Biodiesel No. 1 (BD-1)	Methyl soyate made from soybean oil
Biodiesel No. 2 (BD-2)	Methyl soyate made from chicken fat
Vegetable oil (VO)	100% refined soybean oil
90–10 blend	90% diesel–10% VO
80–20 blend	80% diesel–20% VO
70–30 blend	70% diesel–30% VO

Sequera et al. [10] for flames of diesel, biodiesel, emulsified bio-oil, and diesel-biodiesel fuel blends. Sequera et al. [10] found that the NO_x and CO emissions are determined mainly by the fuel atomization process. Although fuel properties are important, the atomization process itself could be tailored to minimize the emissions for a given fuel.

The objective of the current paper is to document fuel properties and combustion performance of biodiesel and diesel-VO blends. Biodiesels produced from vegetable oil (soybean) and animal fat (chicken) are considered in this study. In the case of VO, the fuel must be heated to reduce its kinematic viscosity so that the pressure drop in the fuel supply line is reasonable, atomization occurs with fine droplets, and combustion emissions are acceptable. To circumvent the need for heating the VO, and thus, to avoid hardware changes to the fuel supply system, we have investigated diesel-VO blends in this study.

Table 1 lists the fuels used for the experiments. The physical and chemical properties of fuel are characterized by gas chromatography and mass spectrometry (GC-MS), thermogravimetric (TGA) analysis, and kinematic viscosity, surface tension, density, and water content measurements. Combustion performance is characterized by predictions of the Sauter mean diameter (SMD), and measurements of NO_x and CO emission profiles within the combustor. For a fixed total airflow rate, the split between the atomizer air and primary combustion air was varied to document fluid dynamic effects on emissions. The volume flow rate of the fuel was either constant or adjusted to achieve a specified heat release rate for different fuels. In the following sections, fuel property measurements are reported before discussing the results from the combustion experiments.

2 Fuel Property Measurements

It is important to characterize chemical and physical properties of various fuels because they were obtained from different sources. First, the fuel composition was determined using the GC-MS technique. The GC-MS analysis of biodiesel fuels (BD-1 and BD-2) was used to determine the fuel's low heating value (LHV) and an equivalent chemical formula. The TGA analysis was performed to characterize the fuel volatility. Fuel kinematic viscosity and surface tension measurements were obtained to determine an acceptable operational range and to compute the Sauter mean diameter. In addition, density and water content measurements were taken for reference.

2.1 GC-MS Analysis. The GC-MS analysis technique combines gas chromatography and mass spectrometry to determine mass % (or vol %) of species present in a chemical (by gas chromatography) together with the elemental composition of each species (by mass spectrometry). The analysis was carried out at UA's GC-MS Facility using HP 6890 GC connected with a micromass AutoSpec-Ultima^{TM} NT mass spectrometer. GC was performed with Column DB-1, with inlet temperature of 225°C, split ratio of 30, oven temperature of 100°C, heating rate of 10°C/min, hold time of 25 min. The GC column did not produce any peaks for the VO sample because of the low column temperature. Table 2 presents the analysis results for the two biodiesel fuels. In BD-1, linoleic methyl ester is the major component, while that in BD-2 is oleic methyl ester. The last two esters, i.e., tetradecanoic methyl ester and 9-hexadecenoic methyl ester were found in small amounts in BD-2, but they were not present in BD-1. Table 2 also lists the enthalpy of formation of each component taken from Ref. [11]. This information was used to compute fuel component's LHV assuming complete combustion. Evidently, the LHV of different components is within 2% of each other. For reference, the equivalent chemical formulas for BD-1 and BD-2 are $C_{18.71}H_{34.71}O_2$ and $C_{18.47}H_{35.10}O_2$, respectively.

2.2 Thermogravimetric Analysis. Thermogravimetric analysis is an experimental approach to determine a material's thermal stability and/or its fraction of volatile components by monitoring the weight change as a specimen is heated. A volatile sample loses mass with an increase in temperature, and after a certain temperature it loses maximum of its mass and what remains is the residue mass. The volatility has a significant effect on fuel vaporization, which in turn affects fuel-air mixing and combustion processes. For example, poor vaporization can result in fuel droplets burning in the diffusion mode. The resulting high flame temperatures are known to produce high concentrations of NO_x, CO, and soot emissions [12]. The fuel samples (8–17 mg) were characterized using TA 2950 analyzer from TA instruments. The maximum temperature was set at 600°C, and testing was conducted from the ambient temperature to 600°C with a heating rate of 5°C/min in an atmosphere of air supplied at the rate of 90 cm^3/min. Before starting the experiment, the sample loading pan was flame cleaned and tared to zero. The microbalance was calibrated with standard weights varying from 1 mg to 100 mg. Figure 1 shows the TGA profiles for diesel, BD-1, BD-2, and VO. The results show that diesel is the most volatile fuel among all the fuels listed in Fig. 1. Diesel evaporated rapidly when heated to 80°C, and it completely vaporized at approximately 180°C. Both biodiesel fuels show similar volatility characteristics: negligible mass loss when heated below 100°C, rapid mass loss (or vaporization) at temperatures above 150°C, and nearly complete vaporization approximately at 225°C. The vegetable oil is the least volatile fuel, showing negligible mass loss at 225°C. In this case, much of the mass loss occurs at temperatures between 250°C and 500°C. Clearly, VO will require significantly higher thermal feedback from the flame to the fuel droplets to fully prevaporize the fuel, and thus, to create a homogenous fuel-air mixture prior to combustion. Results in Fig. 1 explain our choice of diesel-VO fuel blends: Blending a

Table 2 Results of GC-MS analysis

Fatty acid methyl esters	Formula	% Mass BD-1	% Mass BD-2	Molecular weight	Enthalpy of formation (kJ/kmol) [11]	LHV (kJ/kg)
Linoleic methyl ester	$C_{19}H_{34}O_2$	50.1	20.3	294.3	−513,000	37,634
Oleic methyl ester	$C_{19}H_{36}O_2$	35.8	45.0	296.3	−643,250	37,756
Palmitic methyl ester	$C_{17}H_{34}O_2$	10.3	19.3	270.2	−727,500	37,284
Stearic methyl ester	$C_{19}H_{38}O_2$	3.4	8.6	298.3	−787,400	38,314
Tetradecanoic methyl ester	$C_{15}H_{30}O_2$	0.0	0.2	242.2	−684,300	36,526
9-hexadecenoic methyl ester	$C_{17}H_{32}O_2$	0.0	6.6	268.2	−587,000	37,184

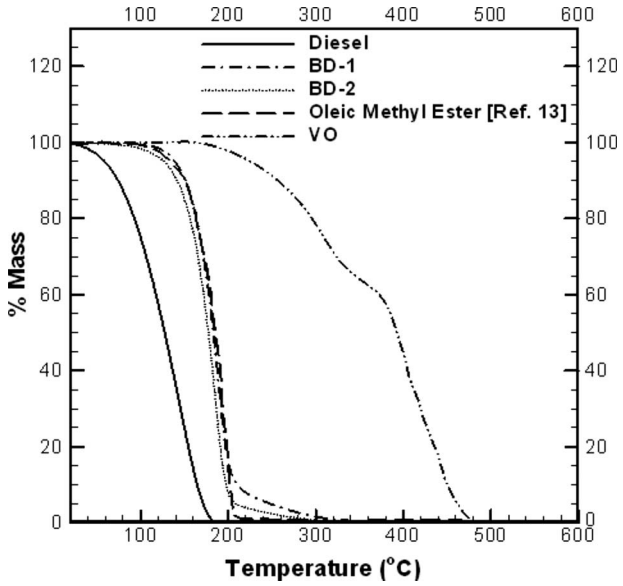

Fig. 1 Results of thermogravimetric analysis

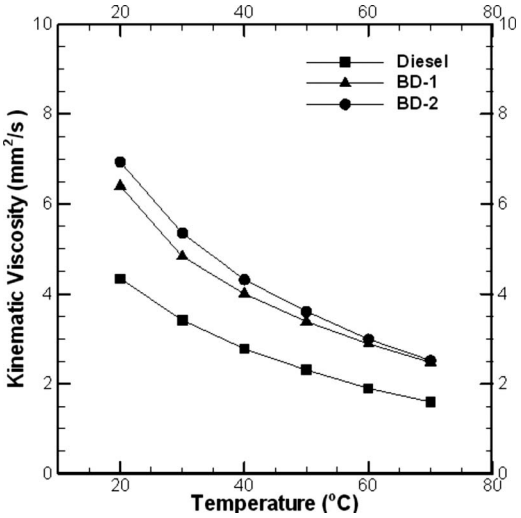

Fig. 2 Kinematic viscosity of diesel and biodiesel fuels

high volatility fuel (diesel) with a low volatility fuel (VO) would improve fuel vaporization, which can result in lower combustion emissions. Figure 1 includes TGA data for oleic methyl ester (the main component of BD-2) from Ref. [13]. The results show an excellent agreement between present results and data reported in the literature. Minor differences are attributed to the presence of an oxidizing environment in this study (as apposed to an inert gas), which tends to increase the oxidation of the fuel, especially at higher temperatures.

2.3 Density, Viscosity, and Surface Tension. Table 3 lists the measured physical properties of various fuels together with the relevant measurement uncertainties. The density measurements were performed gravimetrically at 25°C using volumetric glassware. Three test runs were taken to ensure the repeatability and accuracy of the data. Diesel is a lighter fuel compared with both biodiesels, while the density of the VO is the highest. Density measurements are important to determine the volumetric flow rate of the fuel to obtain a specified heat release rate in the combustor. Table 3 also lists the LHV of fuels on a volumetric basis. The LHV of the two biodiesel fuels was determined from component analysis presented in Table 1, while data from existing literature were used for the remaining fuels. For a given heat release rate, biodiesel fuels will require nearly 13% higher volume flow rate compared with the diesel fuel.

Kinematic viscosity is an important physical property affecting pressure drop in the fuel line as well as the fuel atomization in the combustor. High fuel viscosity results in excessive pressure drop and a spray with large droplets, which lowers combustion performance. The kinematic viscosity was measured by Cannon-Fenske Type 200 viscometer (Cannon Instrument Co., State College, PA) with a viscosity range of 20–100 mm^2/s (cSt). The viscometer was immersed in a water bath connected to a temperature controlled heat exchanger. The temperature was controlled using a Fisher Scientific Isotemp 1016 S recirculating water bath (Pittsburgh, PA). The kinematic viscosity was measured for a temperature range from 20°C to 70°C. Table 3 lists the viscosity values at 25°C and detailed profiles are shown in Figs. 2 and 3.

Table 3 and Fig. 2 show that the viscosity of biodiesels is 45–55% higher compared with that of diesel. The viscosity of both biodiesels is nearly the same over the entire temperature range. The higher fuel viscosity will require higher pumping power for biodiesel compared with diesel to overcome the pressure drop in the fuel supply line. Furthermore, the high fuel viscosity of biodiesel can also negatively impact fuel atomization, an effect that will be quantified later on by droplet size predictions.

Table 3 and Fig. 3 show that the kinematic viscosity of vegetable oil is higher than that of diesel by more than an order of magnitude. Fuels with such high viscosity do not produce acceptable atomization, which was also verified experimentally. Hence, blends of VO with diesel were prepared to reduce the fuel viscosity. Figure 3 shows the measured and computed kinematic viscosity of the 70–30 diesel-VO blend (by volume). The viscosity of the blend was calculated for a mixture [14] from

$$\ln \nu = \sum_{i=1}^{n} x_i \ln \nu_i \tag{1}$$

where x_i is the volume fraction of the species i, and ν_i is the kinematic viscosity of the species i. The excellent agreement between measured and computed values for the 70–30 diesel-VO blend in Fig. 3 verifies Eq. (1). Subsequently, Eq. (1) was used to predict the kinematic viscosity of the 80–20 and 90–10 diesel-VO blends, as shown in Fig. 3. The results show that the diesel vis-

Table 3 Physical properties of fuels

	Fuel			
Property	Diesel	BD-1	BD-2	VO
Mol. weight (kg/kmol)	142.2	291.45	289.06	–
Density at 25°C (kg/m^3)	834.0 ± 9.2	880.0 ± 8.3	868.0 ± 8.8	925.0 ± 8.6
Viscosity at 25°C (mm^2/s)	3.88 ± 0.016	5.61 ± 0.016	6.14 ± 0.016	53.74 ± 0.220
Surface tension at 25°C (mN/m)	28.2 ± 0.6	31.1 ± 0.6	30.7 ± 0.6	30.1 ± 0.6
LHV (kJ/kg)	44,601.7	38,002.3	37,659.7	37,000 [4]
LHV (MJ/m^3)	37,198 [12]	33,442	32,689	34,225 [4]

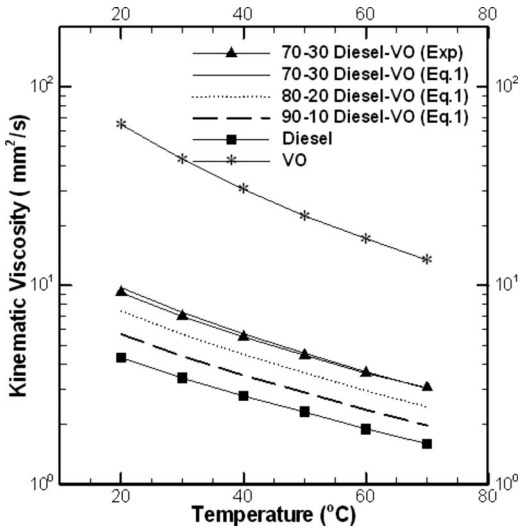

Fig. 3 Kinematic viscosity of diesel-VO blends

cosity at 25°C matches the viscosity of the 90–10 blend at 40°C, the 80–20 blend at 50°C, and the 70–30 blend at 60°C. At 25°C, the biodiesel viscosity is nearly the same as that of the 80–20 diesel-VO blend. Furthermore, vegetable oil will require temperature above 80°C to replicate the room temperature viscosity of diesel. For a given temperature, the viscosity of the 70–30 blend is more than twice that of the diesel. Hence, this blend was considered as the upper operating limit for VO content in the diesel fuel. The blends remained miscible for all volume ratios. Accordingly, the present combustor system was operated with a variety of fuels in the viscosity range of 3.9–8.1 cSt at room temperature.

A "Kruss" K-12 model processor tensiometer with a platinum ring was used to measure the surface tension of the fuel samples at 25°C. Three test runs were taken for each fuel to ensure the repeatability of the results. The surface tension was also calculated theoretically from the surface tension data of individual methyl esters listed in Table 2. The surface tension for the fuel blends was evaluated from [14]

$$\sigma_m = \left[\sum_{i=1}^{n} y_i (\sigma_i)^{1/4} \right]^4 \tag{2}$$

where σ_m is the surface tension of the blend, y_i is the mass fraction of the species i, and σ_i is the surface tension of species i. For biodiesel fuels, we compared measurements with computations using Eq. (2) and published surface tension data [15] for esters in Table 2, and two results were within 0.4 % of each other.

2.4 Water Content. The water content of the fuels was measured to observe the percent volume of water present in the fuels. The water content of each fuel (as received) was determined using a volumetric Aquastar Karl Fischer titrator (EM Science, Gibbstown, NJ) with Composite 5 solution as the titrant and anhydrous methanol as the solvent. Each sample was at least 0.1 g and triplicate measurements were performed on each sample at 25°C. The equilibrium water content for each sample was determined by first contacting equal volumes of fuel and de-ionized water for 24 h followed by titration of the fuel sample using the above method. De-ionized water was obtained from a commercial deionizer (Culligan, Northbrook, IL). Table 4 summarizes the results from the water content analysis.

3 Combustion Experiments

A test setup was designed to obtain spray characteristics and detailed emissions data for different fuels for a range of operating conditions.

Table 4 Water content in the fuel

Fuel	% Mass of water in fuel	% Mass of water in equilibrated fuel
Diesel	0.06 ± 0.01	0.06 ± 0.02
BD-1	0.11 ± 0.02	0.17 ± 0.04
BD-2	0.09 ± 0.04	0.16 ± 0.01
VO	0.05 ± 0.04	0.20 ± 0.02

3.1 Experimental Setup. The test apparatus shown schematically in Fig. 4 consists of the combustor assembly and the injector assembly. The primary air enters the system through a plenum filled with marbles to breakdown the large vortical structures. The air passes through a swirler into the mixing section, where the gaseous fuel is supplied during the startup. The reactants or primary-air enter the combustor through a swirler section shown schematically in Fig. 5(*a*). The swirler is used to enhance fuel-air mixing, and it also helps to stabilize the flame. The swirler has six vanes positioned at 28 deg to the horizontal to produce swirl number of about 1.5. The bulk axial inlet velocity of the primary air is

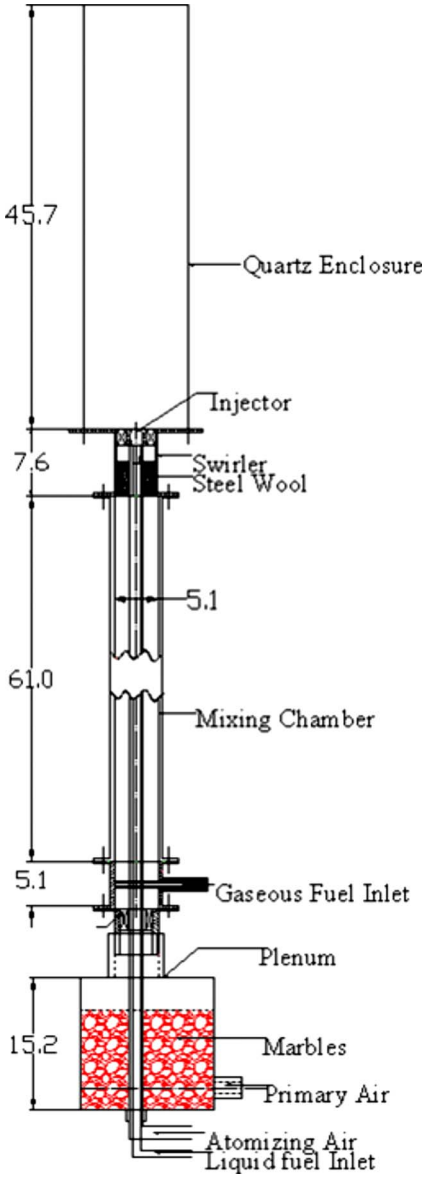

Fig. 4 Schematic of the experimental setup; all dimensions are in cm

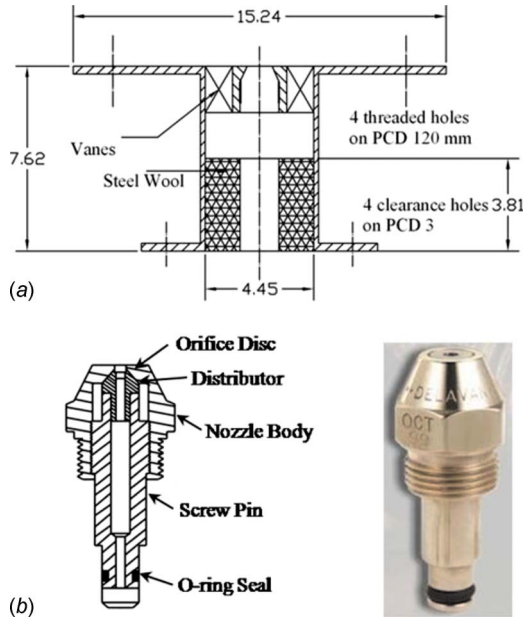

Fig. 5 (*a*) Schematic of a swirler; (*b*) air assist injector schematic and picture

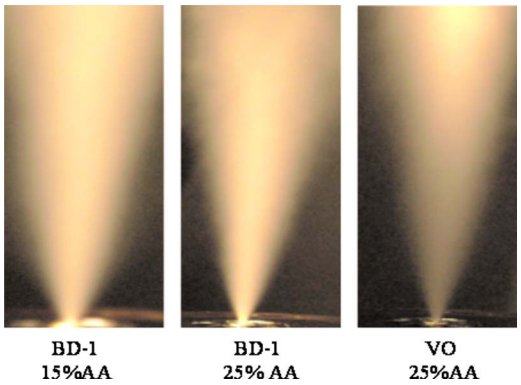

Fig. 6 Spray visualization photographs

1.9–2.1 m/s, which resulted in Reynolds number (based on the equivalent diameter of the injector) varying from 5960 to 6750. The combustor is enclosed within an 8.0 cm inside diameter, 46 cm long quartz tube, and it is back-side cooled by natural convection. The liquid fuel is supplied to the injector with separate concentric tube inlets for fuel and atomization air.

The injector system runs through the plenum and the mixing chamber. An *O*-ring within a sleeve is located at the bottom of the plenum to prevent air leakage. A commercial air-blast atomizer (Delavan Siphon type SNA nozzle) with its details shown schematically and photographically in Fig. 5(*b*) was used for the experiments. This commercial version creates a swirling flow of atomizing air to breakdown the fuel jet as the fluids exit the orifice plate. The liquid fuel was supplied by a peristaltic pump with reported calibration error of $\pm 0.25\%$ of the flow rate reading ranging from 12 ml/min to 130 ml/min in steps of 2 ml/min. Viton tubes were used to prevent degradation of the fuel lines. A 25 μm filter was placed in the fuel supply line to prevent dirt and foreign particles from entering into the injector.

The primary and atomizing air was supplied by an air compressor. The air passed through a pressure regulator, and a dehumidifier and water traps to remove the moisture. Then, the air was split into primary air supply and atomizing air supply lines. The primary air flow rate was measured by a laminar flow element (LFE) with reported calibration error of ± 5 lpm. The pressure drop across the LFE was measured by a differential pressure transducer. An absolute pressure transducer was used to measure air pressure in the LFE. The flow rate measured by the LFE is corrected for temperature and pressure as specified by the manufacturer. The atomizing airflow rate was measured by calibrated mass flow meter with measurement uncertainty of ± 1.5 lpm. The product gas was sampled continuously by a quartz probe (OD $=7.0$ mm) attached to a three-way manual traversing system. The upstream tip of the probe was tapered to 1 mm ID to quench reactions inside the probe. The probe was traversed in the axial direction at the center of the combustor and in the radial direction at the combustor exit plane. The gas sample passed through an ice bath and water traps to remove moisture upstream of the gas analyzers. The dry sample entered the electrochemical analyzers to measure concentrations of CO and NO_x in ppm. The analyzer also measured oxygen and carbon dioxide concentrations, which were used to cross-check the equivalence ratio computed from the measured fuel and air flow rates. The uncorrected emissions data on dry basis are reported with uncertainty of ± 2 ppm.

The experiment was started by supplying gaseous methane and then igniting the methane-air reactant mixture in the combustor. Next, the liquid fuel flow rate was gradually increased to attain the desired value, while the methane flow rate was slowly decreased to zero. In this study, the volume flow rate of total air (primary + atomizing) was constant at 150 standard lpm. Experiments were conducted for fixed volume flow rate of fuel and for fixed heat release rate in the combustor. For the latter case, the volume flow rate of biodiesel fuels was increased to match the heat release rate of the diesel fuel according to the LHV data in Table 3. In case of diesel-VO blends, the fuel volume flow rate approximated the heat release rate and hence, no flow rate adjustment was necessary. Previous studies have shown significant effect of atomizing airflow (AA) rate on emissions of NO_x and CO [10]. Hence, atomizing airflow rates of 15% and 25% of the total air flow rate were used for experiments with all fuels considered in this study. The spray was also photographed without the flame to determine the cone angle for different fuels.

3.2 Spray Angle and Droplet Size Characteristics. Figure 6 shows photographs of BD-1 spray for two different atomizing airflow rates. A photograph of the VO spray is also shown for comparison. Visually, biodiesel produced a fine spray, while the VO spray contained large droplets around the outer edge. These large droplets give the appearance of a larger cone angle with VO, a problem that was addressed during data analysis using intensity profile to compute the cone angle. Figure 7 shows similar spray cone angles for diesel and biodiesel fuels. The cone angle for VO is smaller by about 5 deg. For all cases, the cone angle increased with increasing atomizing air flow rate, signifying increased penetration of fuel into the combustor.

Detailed characterization of the fuel spray requires measurements of drop size distributions, for example, using phase Doppler particle analyzer and/or laser diffraction techniques. Such analysis is beyond the scope of the present work. Instead, we performed droplet size calculations using the following correlation of Rizk and Lefebvre [16] for the Sauter mean diameter produced by a plane air-blast injector:

$$\frac{\mathrm{SMD}}{d_o} = 0.48\left(\frac{\sigma}{\rho_A U_R^2 d_o}\right)^{0.4}\left(1+\frac{1}{\mathrm{ALR}}\right)^{0.4} + 0.15\left(\frac{\mu_L^2}{\sigma\rho_L d_o}\right)^{0.5}\left(1+\frac{1}{\mathrm{ALR}}\right) \quad (3)$$

where SMD is the Sauter mean diameter (μm), d_o is the liquid discharge orifice diameter (m), σ is the surface tension (N/m), μ_L is the liquid fuel viscosity (m^2/s), ρ_A is the density of air (kg/m^3), ρ_L is the liquid fuel density (kg/m^3), U_R is the coflowing air

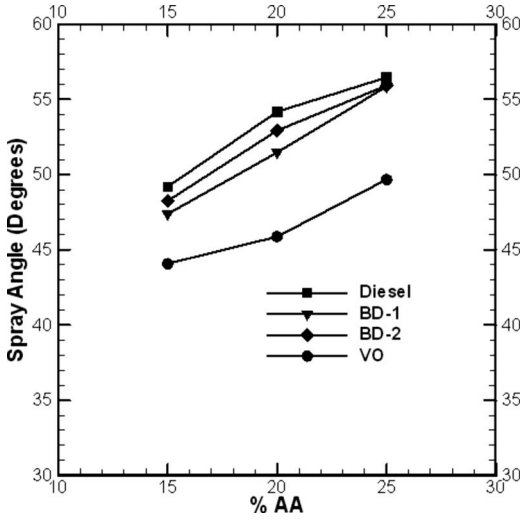

Fig. 7 Spray cone angle versus atomizing airflow rate

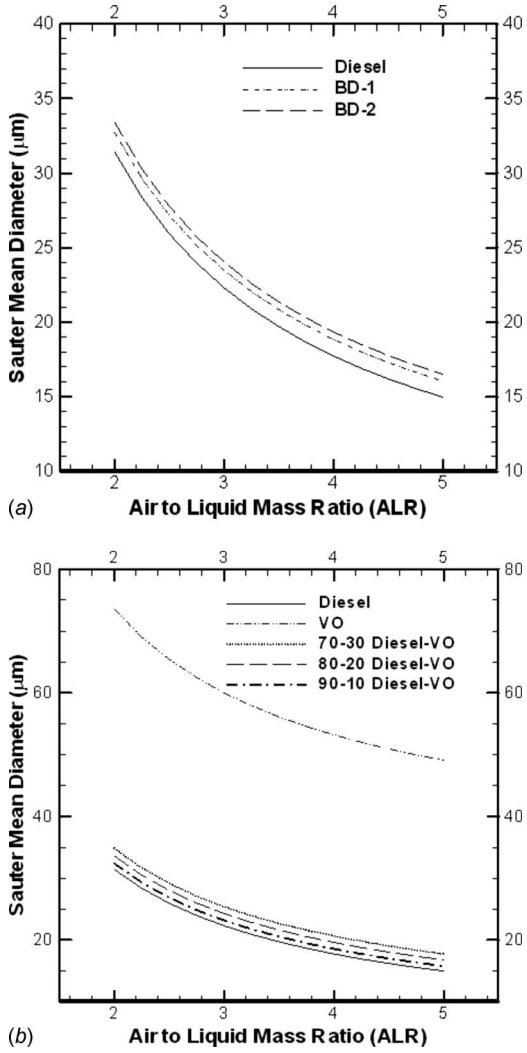

Fig. 8 (*a*) SMD versus ALR for Diesel, BD-1 and BD-2; and (*b*) SMD versus ALR for diesel, VO, and diesel-VO blends

velocity relative to fuel velocity (m/s), and ALR is the air to liquid mass flow ratio.

Figure 8(*a*) presents the Sauter mean diameter versus the air to liquid mass flow ratio (ALR) for diesel and biodiesel. Note that 15% AA pertains to ALR of 2.65 and 2.52, respectively, for diesel and biodiesel fuels. The corresponding values for 25% AA are 4.35 and 4.12. Figure 8(*a*) shows that increasing the atomizing airflow rate (for a fixed fuel flow rate) improves atomization by decreasing the SMD of the droplets produced. For a given ALR, the biodiesel droplets are larger than diesel droplets by only about 2 μm. The SMD of the two biodiesel fuels is nearly the same for all ALR values. Figure 8(*b*) presents the SMD for diesel, VO, and diesel-VO blends. For VO, the 15% AA and 25% AA correspond to ALR of 2.40 and 3.92, respectively. For the entire range of ALR, the SMD of VO is two to three times higher than that of the diesel. However, the SMD of diesel-VO blends is only moderately higher than that of the diesel. Interestingly, the 70–30 diesel-VO blend produces nearly the same droplet diameter at different ALR values as the biodiesels (see Fig. 8(*a*)). The results in Fig. 8 have provided a quantitative assessment of atomization behavior of different fuels, but an accurate knowledge of the droplet size requires direct measurements in the spray as noted previously.

3.3 Emissions Measurements. Figures 9(*a*) and 9(*b*) present radial profiles of CO and NO_x emissions at the combustor exit plane, i.e., z=46 cm, when 15% of the total airflow rate (AA =15%) is used for fuel atomization. The results are shown for diesel and both biodiesel fuels, with the diesel serving as the reference fuel. In case of biodiesels, data are reported for a fixed fuel volume flow rate (same as that of diesel, constant V) and for a fixed heat input rate (same as that of diesel, constant Q). Figure 9(*a*) shows a typical parabolic profile with higher CO emissions near the center and decreasing values near the combustor wall. This trend is caused by the fuel-air mixing processes, which confine the flame to the center region and shield it from the combustor wall. Minor asymmetry in radial profiles is attributed to minor imperfections in the injector/swirler geometry and large turbulent flame fluctuations.

For a fixed fuel flow rate (constant V), the CO emissions for diesel are higher than those for biodiesel fuels. The two biodiesel CO emission profiles overlap, indicating negligible effect of the fatty oil source (vegetable oil or animal fat). For a fixed heat input rate (constant Q), the CO emissions for biodiesels are higher than those for diesel. Again, the CO profiles for the two biodiesel fuels are similar. These results illustrate that biodiesel can be incorrectly characterized as cleaner fuel compared with diesel, based on data obtained for a fixed fuel flow rate. Since the gas turbine must generate the same power regardless of the fuel, the comparison based on fixed heat input rate is more appropriate. In this case, biodiesel CO emissions exceed those for diesel. Higher CO emissions for biodiesel do not pertain to the fuel chemistry effects alone. Later on, it will be shown that the flow effects such as fuel atomization (intimately related to fuel kinematic viscosity and injector design) can dominate emissions from the combustor. Overall, the CO emissions for all of the cases are within 30 ppm.

Radial profiles of NO_x emissions shown in Fig. 9(*b*) provide support to the above discussion. For constant V, the NO_x emissions for both biodiesels are lower than those for diesel. The profiles for the two biodiesels are nearly identical, indicating negligible effect of the fatty oil source on NO_x emissions. Interestingly, for constant Q, the NO_x profiles for all three fuels overlap each other. The NO_x emissions are relatively high, approximately 150 ppm. If the thermal mechanism is dominant, the NO_x emissions can be correlated with the flame temperature, which remains constant for constant Q. These results suggest that the NO_x is formed mainly by the thermal mechanism, and that the fuel chemistry has a negligible effect on NO_x emissions.

The superiority of flow effects in comparison to chemical effects is illustrated by the result presented in Figs. 9(*c*) and 9(*d*). In this case, the total air and fuel flow rates are identical to those in Figs. 9(*a*) and 9(*b*). However, a larger percentage of the total

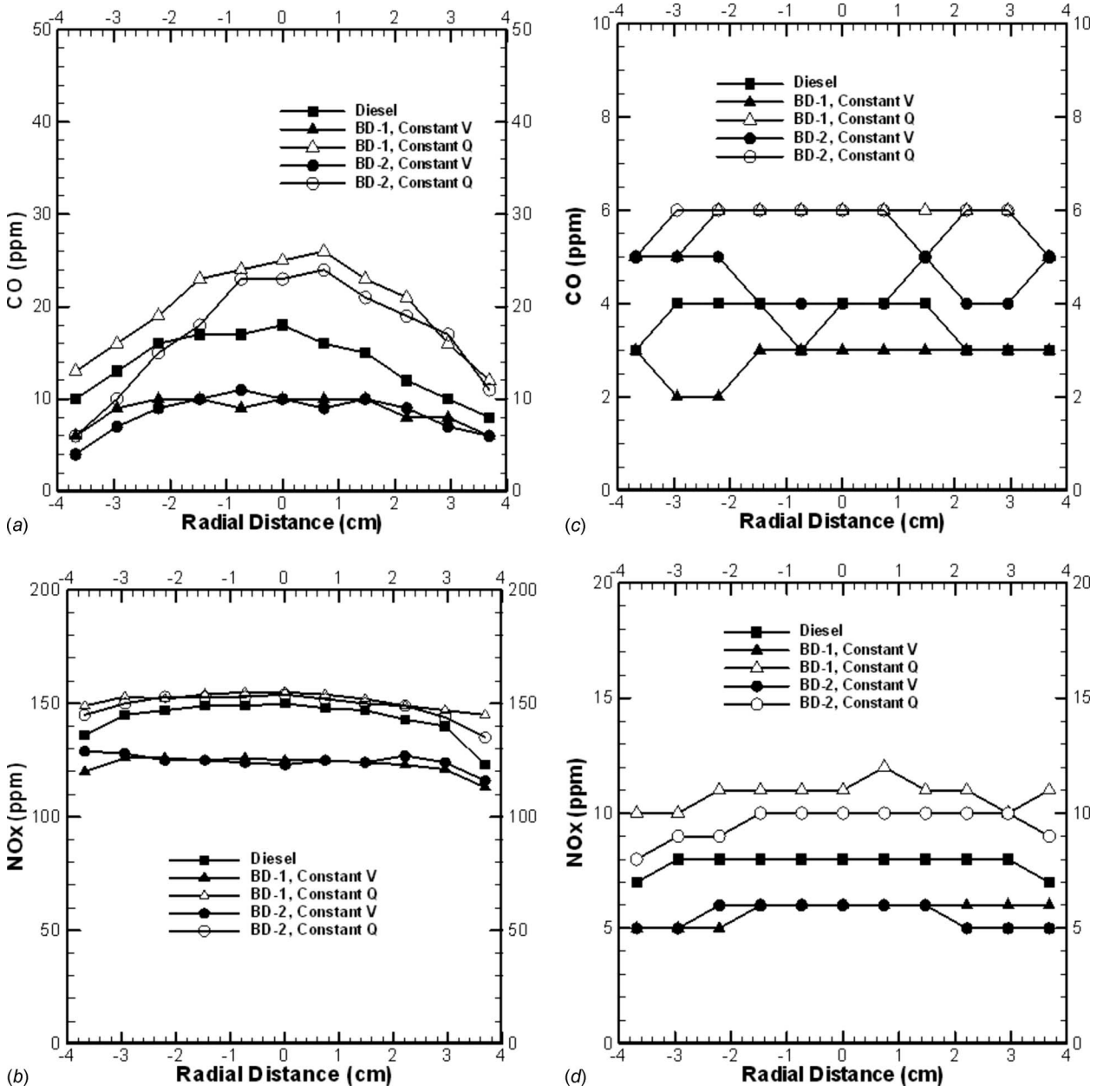

Fig. 9 Radial profiles of CO and NO_x emissions at the combustor exit plane for diesel and biodiesel fuels; (*a*) and (*b*), profiles for 15% AA; (*c*) and (*d*) profiles for 25% AA

airflow rate (AA=25%) is routed through the fuel injector to improve atomization, and hence, the fuel-air mixing processes. The results show that improved atomization associated with higher AA leads to dramatic reductions in CO and NO_x emissions for diesel and biodiesel fuels. The CO emissions show nearly fivefold decrease, with single digit CO concentrations measured for all of the cases. In Fig. 9(*c*), the CO profiles for different fuels are within the measurement uncertainty of the gas analyzer.

The radial profiles in Fig. 9(*d*) show more than 15-fold decrease in NO_x emissions compared with the data for AA=15% presented in Fig. 9(*b*). The NO_x emissions for diesel are higher than those with biodiesels for constant *V* and lower than those with biodiesels for constant *Q*. However, the difference among various cases is rather small. The maximum NO_x concentration is only about 11 ppm compared with the maximum of about 150 ppm for AA =15%.

Clearly, the fuel atomization and associated flow processes dominate emissions from the combustor. Thus, in principle, one can optimize the fuel injector to overcome the negative effects of the fuel chemistry, for example, by adjusting the atomizing airflow rate and/or injector geometry for each fuel.

Figure 10 presents CO and NO_x emissions profiles at the centerline of the combustor. The axial distance in these profiles is measured from the combustor inlet plane. Figure 10(*a*) shows a decrease in CO emissions in the axial direction. Initially, the fuel decomposes in the flame region to produce high CO concentrations. Subsequently, the CO decreases as the products pass through the combustor to attain the residence time needed to complete the oxidation reactions. The overall trends for various cases are similar to those presented in Fig. 9(*a*): The CO emissions for biodiesel fuels with constant *V* are lower and with constant *Q* are higher than those with diesel fuel. Higher measurement uncertainties can be expected for the data in Fig. 10(*a*), because of the large turbulent fluctuations in the flame region, i.e., $z<25$ cm. Axial

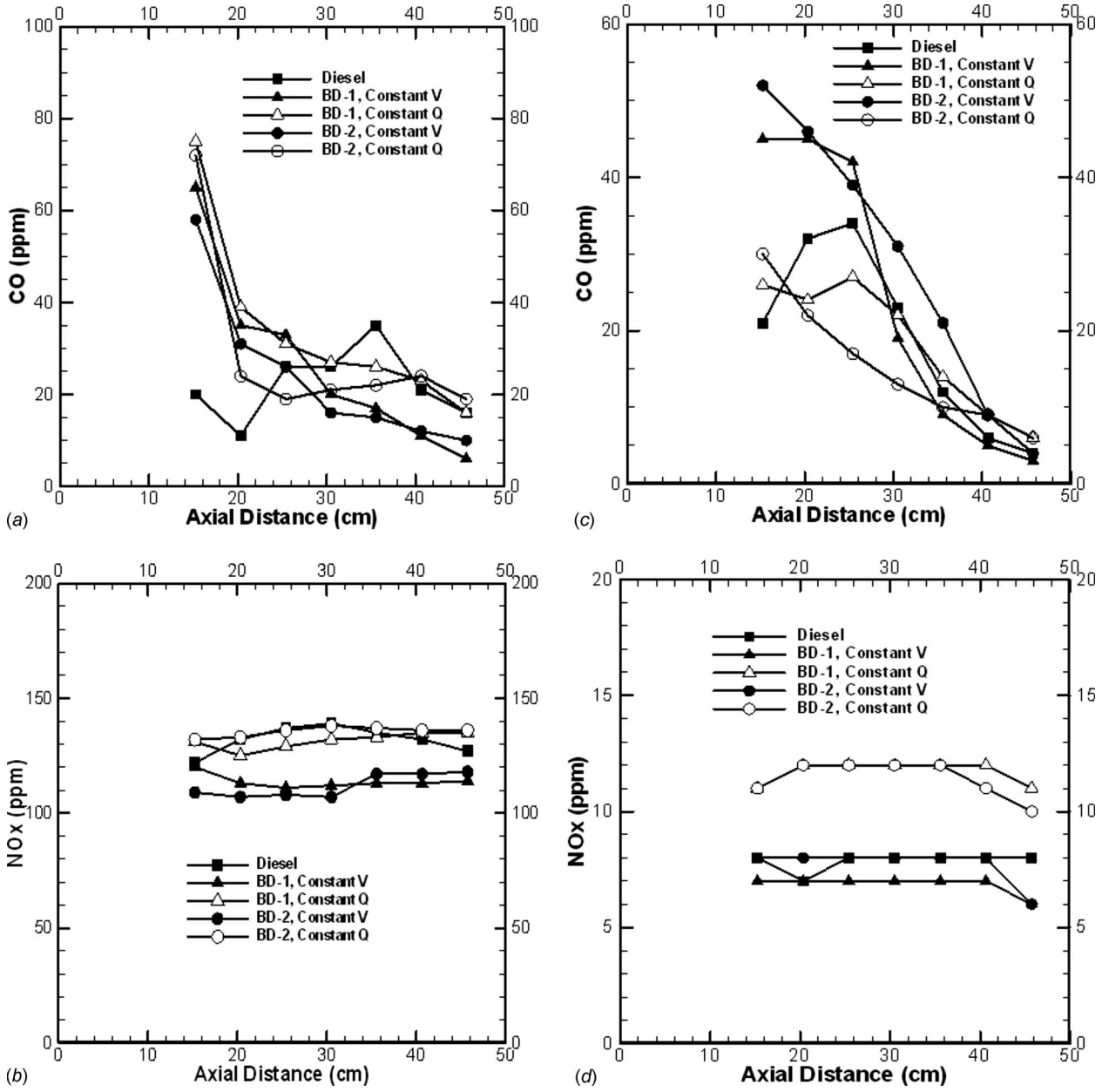

Fig. 10 Axial Profiles of CO and NO_x emissions at the combustor exit plane for diesel and biodiesel fuels; (*a*) and (*b*), profiles for 15% AA; (*c*) and (*d*), profiles for 25% AA

profiles in Fig. 10(*b*) show that the NO_x emissions are nearly constant in the axial direction for $z > 15$ cm. Thus, NO_x is formed within $z = 15$ cm or in a short reaction zone. The NO_x emissions for both biodiesel fuels are nearly the same, and for constant *V*, they are lower than the NO_x emissions for diesel. Axial profiles in Fig. 10(*c*) and 10(*d*) were taken for the higher atomizing airflow rate (AA=25%), and they represent the trends discussed previously, i.e., CO and NO_x emissions decrease dramatically for higher atomizing airflow rate. Overall, results illustrate the significance of fluid dynamic effects on emissions from combustion of diesel and biodiesel fuels in the present burner replicating continuous flow operation of gas turbines for power generation.

Figure 11 presents radial profiles of CO and NO_x emissions at the combustor exit plane for diesel and diesel-VO blends. Because of the high diesel concentration in blends, constant *V* and constant *Q* cases were essentially equivalent, and hence, experiments were conducted for constant *V* only. Figure 11(*a*) shows that the diesel-VO blends produced slightly higher CO emissions compared with diesel. Higher viscosity of the blends and deterioration in fuel atomization associated with it are the likely cause for this result. The low volatility of VO is another factor, since the droplets of the blended fuels will be more difficult to vaporize compared with diesel. Although the relative importance of these factors cannot be ascertained, data suggest that the fuel chemistry effects on CO emissions are minor. This result is supported by radial profiles of NO_x emissions in Fig. 11(*b*). The NO_x emissions for diesel-VO blends are slightly higher than those for diesel. For all cases, the NO_x emission is high, approximately 150 ppm, which matches NO_x values for biodiesel fuels. The results suggest that the flame temperature or the heat input rate is the determining factor affecting NO_x emissions for all fuels in this study. Similar to biodiesel fuels, the CO and NO_x emissions for diesel-VO blends decrease dramatically with an increase in the atomizing airflow rate (see Figs. 11(*c*) and 11(*d*)). The CO emissions decreased by a factor of 5 and the NO_x emissions decreased by a factor of 15 as AA was changed from 15% to 25%. In spite of the

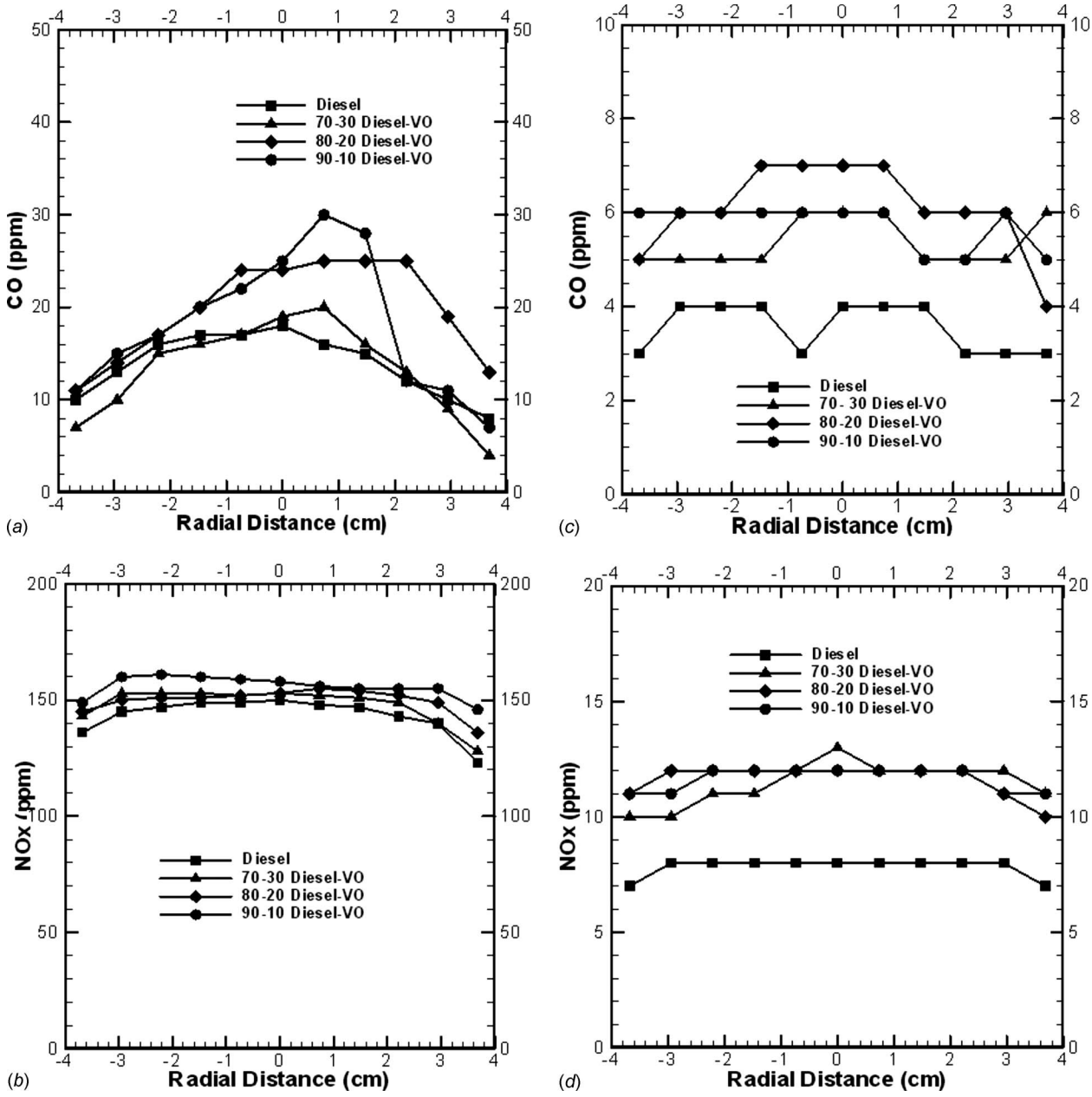

Fig. 11 Radial Profiles of CO and NO_x emissions at the combustor exit plane for diesel and diesel-VO blends; (*a*) and (*b*), profiles for 15% AA; (*c*) and (*d*), profiles for 25% AA

different physical and chemical properties of diesel, biodiesels, and diesel-VO blends, CO and NO_x emissions for all fuels are nearly the same for AA=25%.

The axial profiles of CO and NO_x emissions at the combustor centerline are presented in Fig. 12. After the CO is formed in the reaction zone, it is oxidized along the length of the combustor, especially in the post flame region around $z=20$ cm. The NO_x emissions are independent of the axial location, suggesting that NO_x is formed within the reaction zone located at $z<15$ cm. The data suggest that CO and NO_x emissions for diesel-VO blends are slightly higher than those for diesel.

4 Conclusions

In this study, the fuel properties and combustion emissions were measured for diesel, two types of biodiesel, and diesel-VO blends. The composition of biodiesel fuels was determined using the GC-MS technique, which also allowed us to compute the low heating value of the fuel. The main constituent of VO biodiesel was linoleic methyl ester while that for animal fat biodiesel was oleic methyl ester. In spite of the compositional differences, the volatility, kinematic viscosity, and surface tension properties of the two biodiesel fuels were similar. The kinematic viscosity of biodiesel fuels was about 50% higher than that of diesel. The kinematic viscosity of VO was more than ten times that of diesel, and hence, VO could be used only if it was blended with a low viscosity fuel. Diesel-VO blends with up to 30% VO (by volume) were used in this study to achieve an acceptable range of fuel viscosity which is about twice that of the diesel. The TGA analysis indicated diesel to be the most volatile, while VO was the least volatile fuel. The Sauter mean diameter of biodiesel fuel droplets was estimated to be only slightly larger than that of diesel. The estimated SMD of biodiesel and 70–30 diesel-VO blends was nearly the same.

The CO and NO_x emissions for both biodiesels were similar at

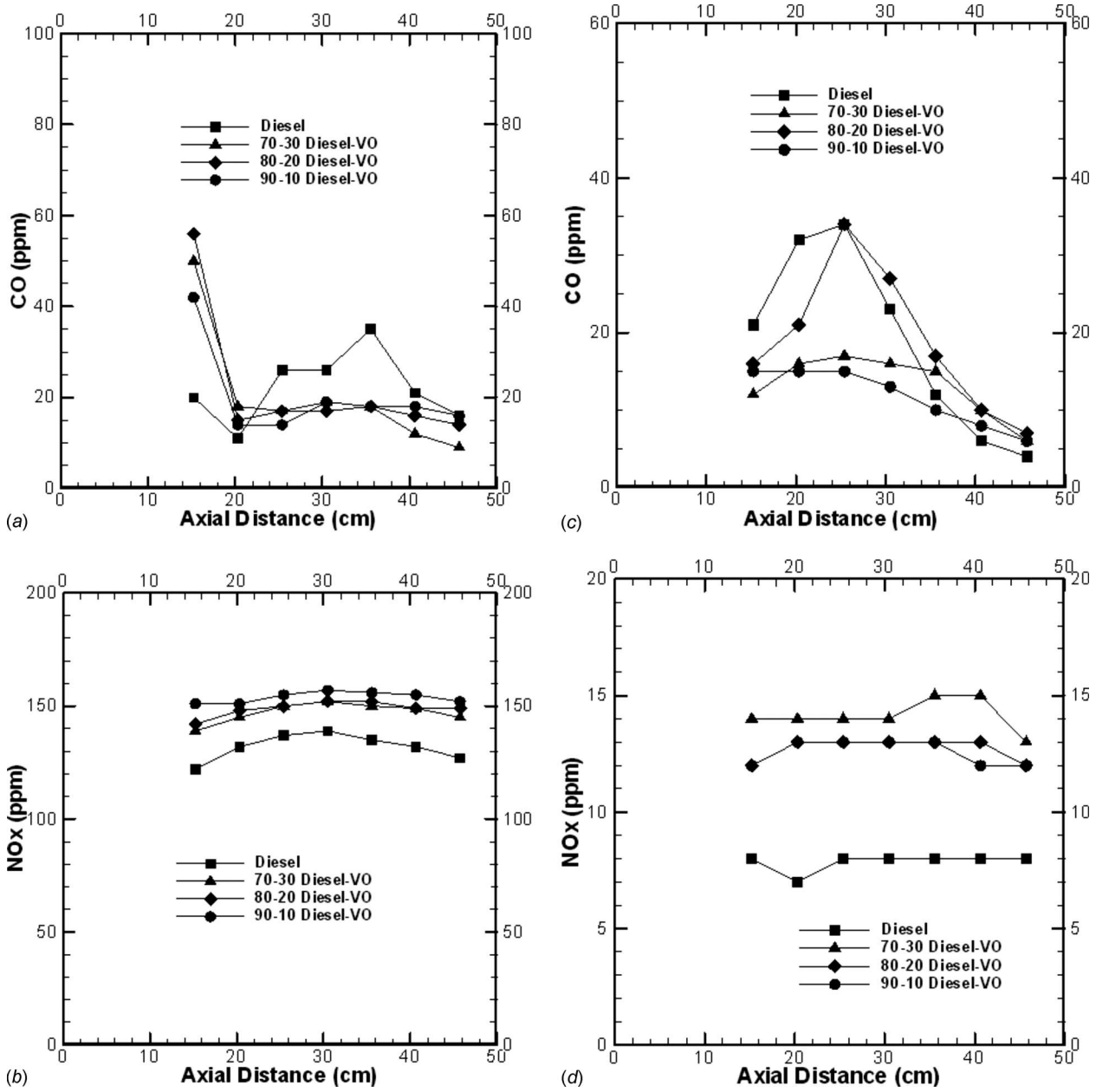

Fig. 12 Axial Profiles of CO and NO_x emissions at the combustor exit plane for diesel and diesel-VO blends; (a) and (b), profiles for 15% AA; (c) and (d), profiles for 25% AA

various operating conditions. For constant V, the heat release rate with biodiesel fuels is lower than that for diesel, which translates to lower CO and NO_x emissions for the former. For constant Q, the CO emissions for both biodiesels and 70–30 diesel-VO blend were similar, but they were slightly higher than the CO emissions for diesel. The NO_x emissions for all of the fuels in this study depended on flame temperature or the heat release rate. The results show that the atomization and fuel-air mixing processes have a major impact on CO and NO_x emissions for all fuels. For example, a 67% increase in the atomizing airflow rate decreased CO emissions by a factor of 5 and NO_x emissions by a factor of 10. Within the range of the present experiments, the fuel composition or chemistry effects are of secondary importance, since one could minimize the combustion emissions for a given fuel by controlling the fuel atomization and related flow processes. Moreover, the 70–30 diesel-VO blend was equivalent to biodiesel fuels in terms of droplet size and emissions.

Acknowledgment

This work was supported in part by the Southern Co. with Elizabeth Philpot serving as the technical liaison. We would like to thank Dr. Qiaoli Liang for assistance with GC-MS analysis and Meghna Dilip for assistance with the TGA analysis.

References

[1] Chisti, Y., 2007, "Biodiesel for Microalgae," Biotechnol. Adv., **25**, pp. 294–306.
[2] Agarwal, A. K., 2007, "Biofuels (Alcohol and Biodiesel) Application as Fuels for Internal Combustion Engines," Prog. Energy Combust. Sci., **33**, pp. 233–271.
[3] Monyem, A., and Germen, J. H. V., 2001, "The Effect of Biodiesel Oxidation on Engine Performance and Emissions," Biomass Bioenergy, **20**, pp. 317–325.
[4] Rakopoulos, C. D., Antonopoulos, K. A., Rakopoulos, D. C., Hountalas, D. T., and Giakoumis, E. G., 2006, "Comparative Performance and Emissions Study of a Direct Injection Diesel Engine Using Blends of Diesel Fuel With Veg-

etable Oils or Bio-Diesels of Various Origins," Energy Convers. Manage., **47**, pp. 3272–3287.
[5] Demirbas, A., 2005, "Biodiesel Production From Vegetable Oils Via Catalytic and Non-Catalytic Supercritical Methanol Transesterification Methods," Prog. Energy Combust. Sci., **31**, pp. 466–487.
[6] Lupandin, V., Thamburaj, R., and Nikolayev, A., 2005, "Test Results of the OGT2500 Gas Turbine Engine Running on Alternative Fuels: Biooil, Ethanol, Biodiesel, and Crude Oil," ASME Paper No. GT2005-68488.
[7] Chiang, H.-W., Ching, I.-C., and Li, H.-L., 2007, "Performance Testing of Microturbine Generator System Fueled by Biodiesel," ASME Paper No. GT2007-28075.
[8] Moliere, M., Panarotto, E., Aboujaib, M., Bisseaud, J. M., Cambell, A., Citeno, J., Maire, P-A, and Ducrest, L., 2007, "Gas Turbine in Alternative Fuel Applications: Biodiesel Field Test," ASME Paper No. 2007-27212.
[9] Bolszo, C., McDonell, V., and Samuelsen, S., 2007, "Impact of Biodiesel on Fuel Preparation and Emissions for a Liquid Fired Gas Turbine Engine," ASME Paper No. GT2007-27652.
[10] Sequera, D., Agrawal, A. K., Spear, S. K., and Daly, D. T., 2007, "Combustion Performance of Liquid-Biofuels in a Swirl Stabilized Burner," ASME Paper GT2007-2838.
[11] http://webbook.nist.gov/chemistry.
[12] Turns, S. R., 2000, *An Introduction to Combustion-Concepts and Applications*, 2nd ed., McGraw-Hill, New York.
[13] Cayli, G., and Kusefoglu, S., 2008, "Increased Yields in Biodiesel Production From Cooking Oils by a Two Step Process: Comparison With One Step Process Using TGA," Fuel Process. Technol., **89**, pp. 118–122.
[14] Ejim, C. E., Fleck, B. A., and Amirfazli, A., 2007, "Analytical Study for Atomization of Biodiesels and Their Blends in a Typical Injector: Surface Tension and Viscosity Effects," Fuel, **86**, pp. 1534–1544.
[15] http://www.chemspinder.com
[16] Rizk, N. K., and Lefebvre, A. H., 1984, "Spray Characteristics of Plain-Jet Airblast Atomizers," ASME J. Eng. Gas Turbines Power, **106**, pp. 634–638.

A. Lacarelle[1]
e-mail: arnaud.lacarelle@tu-berlin.de

T. Faustmann

Institut für Strömungsmechanik
und Technische Akustik,
Technische Universität Berlin,
Müller-Breslau-Strasse 8,
10623 Berlin, Germany

D. Greenblatt
Faculty of Mechanical Engineering,
Technion-Israel Institute of Technology,
Technion City, Haifa 32000, Israel

C. O. Paschereit

O. Lehmann

D. M. Luchtenburg

B. R. Noack

Institut für Strömungsmechanik
und Technische Akustik,
Technische Universität Berlin,
Müller-Breslau-Strasse 8,
10623 Berlin, Germany

Spatiotemporal Characterization of a Conical Swirler Flow Field Under Strong Forcing

In this study, a spatiotemporal characterization of forced and unforced flows of a conical swirler is performed based on particle image velocimetry (PIV) and laser Doppler anemometry (LDA). The measurements are performed at a Reynolds number of 33,000 and a swirl number of 0.71. Axisymmetric forcing is applied to approximate the effects of thermoacoustic instabilities on the flow field at the burner inlet and outlet. The actuation frequencies are set at the natural flow frequency (Strouhal number $St_f \approx 0.92$) and two higher frequencies ($St_f \approx 1.3$ and 1.55) that are not harmonically related to the natural frequency. Phase-averaged measurement are used as a first step to visualize the coherent flow structures. Second, proper orthogonal decomposition (POD) is applied to the PIV data to characterize the effect of the actuation on the fluctuating flow. Measurements indicate a typical natural flow instability of helical nature in the unforced case. The associated induced pressure and flow oscillations travel upstream to the swirler inlet where generally fuel is injected. This observation is of critical importance with respect to the stability of the combustion. Harmonic actuation at different frequencies and amplitudes does not affect the mean velocity profile at the outlet, while the coherent velocity fluctuations are strongly influenced at both the inlet and outlet. On one hand, the dominant helical mode is replaced by an axisymmetric vortex ring if the flow is forced at the natural flow frequency. On the other hand, the natural flow frequency prevails at the outlet under forcing at higher frequencies and POD analysis indicates that the helical structure is still present. The presented results give new insight into the flow dynamics of a swirling flow burner under strong forcing. [DOI: 10.1115/1.2982139]

Keywords: swirling flows, PIV, LDA, POD, coherent structures, flow instability, flow forcing

1 Introduction

For the past decades, lean premixed combustion has become a standard feature in gas turbine engines and is expected to be implemented in aircraft engines. The main advantage of this combustion technique is that the low fuel/air ratio results in a lower burning temperature and produces relatively low NO_x emissions. One of the main disadvantages of lean premixed combustion is that it is susceptible to combustion instabilities that produce large-amplitude pressure oscillations that can damage the combustor and turbine. The mechanisms leading to thermoacoustic instabilities are numerous and closely related to each other: fuel/air ratio oscillations [1], acoustics boundary conditions [2], and flame surface oscillations induced by coherent structures [3,4].

These coherent flow structures are present in most combustors (jet flames, bluff body, and swirling flows) and lead to periodical oscillations of the velocity and mixing profile. This results in oscillations of the flame, which can excite acoustic modes of the combustor and in turn generate combustion instabilities. Particularly in swirling combustors, different coherent structures have been identified in experimental and numerical studies of isothermal flows [5–10]. Most of these investigations revealed a precessing vortex core (PVC) and a helical mode. The typical frequencies of these two phenomena were generally not related but some investigations showed that the frequency of the PVC was very closed or equal to the frequency of the helical mode [7] and particularly in a downscaled model of the burner used in this investigation [10]. In the shear layer of the flow, Kelvin–Helmholtz instabilities have also been observed [3,5,9]. The influence of the burner geometry, swirl number, expansion ratio, and boundary conditions on the flow field have also been investigated by many authors [11–13].

To avoid combustion instabilities induced by coherent structures, it is essential to understand their generation mechanism, as well as their evolution in the case of forced flows. The forcing, which is applied in the current investigation, approximates the impact of axial acoustic modes of combustion instabilities on the flow field in the burner.

Numerous experimental investigations on the excitation of simple jets have been reported in literature [14,15]. The forcing of those jets with different excitation modes generated axisymmetric or helical structures. Literature dealing with the experimental forcing of swirling jets is rare, and even rarer are studies carried out on swirl burners. One of the main reasons is that actuators may not have sufficient authority to excite the flow with an amplitude that is comparable to the oscillation amplitude that is attained under full-scale operating conditions ($\pm 10\%$ of the mean flow velocity).

Nevertheless, Paschereit et al. [3] investigated the flow in reacting and non-reacting flows on a model premixed burner. They observed that axisymmetrical and helical modes could be excited by changing the boundary conditions downstream of the combustion chamber. Cold flow investigations of the same burner in a water test rig showed that the helical mode found in the reacting experiments corresponded to a helical mode of the burner flow. Using the same burner type, Lacarelle et al. [16] showed that forcing at the frequency of the helical mode led to an increase in scalar mixing at the burner outlet. Phase-averaged measurements

[1]Corresponding author.

Contributed by the International Gas Turbine Institute of ASME for publication in the JOURNAL OF ENGINEERING FOR GAS TURBINES AND POWER. Manuscript received March 31, 2008; final manuscript received April 21, 2008; published online February 6, 2009. Review conducted by Dilip R. Ballal. Paper presented at the ASME Turbo Expo 2008: Land, Sea and Air (GT2008), Berlin, Germany, June 9–13, 2008.

from PIV data showed that axial forcing at the natural flow frequency replaced a helical mode with an axisymmetric mode at the burner outlet. Khalil et al. [17] also investigated the impact of forcing on the flow field of a generic swirler. They found that forcing frequency and amplitude have an influence on both the vortex shedding and mean-field of the flow. Pulsing at the natural flow frequency caused the development of axisymmetric vortex rings in the shear layer, while the unforced flow showed a $m=+2$ helical structure. Forcing at frequencies lower than two times the natural frequency resulted in a lock-in phenomenon of the vortex shedding frequency on the excitation, which disappeared for higher frequencies. The amplitude of the excitation had a significant impact on the breakdown position, which moved downstream as the amplitude increased.

As it is difficult to experimentally actuate the flow at a high amplitude over a wide frequency range, numerical simulations are often employed as these actuation boundary conditions can be relatively easily implemented. Wang and Yang [9] performed a large-eddy-simulation (LES) of the axially forced flow of a swirl injector with radial entry. They focused on forcing frequencies remaining below or equal to the natural flow frequencies of the PVC (4 kHz). One simulation was performed at the natural frequency of the shear layer (13 kHz). The amplitude of forcing was set to 10%. They showed that the forced axial disturbance may be split into two parts at the burner outlet: The propagation of the waves in the streamwise direction followed an acoustic wave, propagating at the speed of sound. On the other hand, the azimuthal oscillations were convected downstream with the local flow velocity. The excitation of the flow had a small impact on the mean flow properties, except when the forcing was applied at a frequency matching the natural flow frequency of the outer shear layer region. In this case mixing was dramatically enhanced.

The goal of this work is to understand the impact of strong forcing on the flow field at the inlet and outlet of a swirl burner. This is achieved by initially studying the unforced natural burner flow field and then comparing this to the forced case. Two measurement techniques (PIV and laser Doppler anemometry (LDA)) and postprocessing tools (phase averaging and proper orthogonal decomposition (POD)) are combined to characterize the unforced and forced flows. In Sec. 2, the experimental setup (water test rig with excitation mechanism) is presented. Then the measurement technique and the postprocessing tools used are described. Section 4 shows the results obtained with PIV and LDA at the burner outlet and inlet for the unforced flow of the burner. A typical helical structure is observed in this case and a physical explanation of the observed phenomenon is advanced. Section 5 focuses on the impact of axial forcing on the flow field at the inlet and outlet of the burner. Two excitation frequencies are chosen and show remarkable properties concerning the flow structures. The POD analysis of the PIV snapshots presented in Sec. 6 reveals the shape of the dominant structures for all forcing cases investigated, and a sensitivity analysis of the number of PIV snapshots needed to resolve the modes is shown. The results demonstrate the effectiveness of POD for the analysis of complex turbulent flows.

2 Experimental Setup

2.1 The Burner. The burner that is employed in this investigation is a full-size conical swirler, normally used in gas turbine engines. It consists of two halves of a cone that are shifted with respect to each other in the radial direction, such that two inlet slots of constant width are formed. The diameter of each cone-half at the outlet is $D=82$ mm. This diameter is used as a reference length for all characteristic numbers.

The airflow through the lateral slots generates a strong azimuthal velocity component. This component produces a flow with a high degree of swirl, which results in vortex breakdown near the burner outlet followed by a recirculation zone where the flame stabilizes. The recirculation of hot combustion gas, inside the flame, leads to a second oxidation and to a reduction in carbon monoxide gas. The disadvantages of this type of flame stabilization are flow instabilities and complex three-dimensional coherent structures. A detailed description of the burner under running conditions is presented by Sattelmayer et al. [18] or Döbbeling et al. [19].

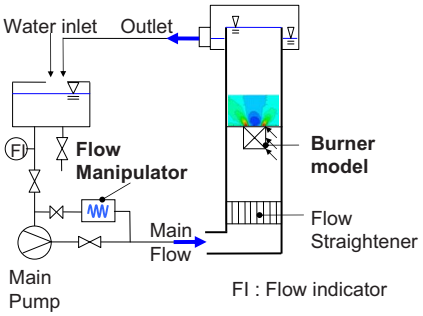

Fig. 1 Principle sketch of the water test rig illustrating the excitation mechanism

2.2 The Test Rig. The conical swirler was mounted in the square test section of a specially designed water test rig, which allows for full optical access to the burner from all four sides (see Fig. 1). The burner was secured to a plate, and this assembly was mounted in the center of the test section. The dump plane thus created had an expansion ratio burner/test section of 0.033.

The water test rig volume flow was set to 7.75 m^3/h, which corresponds to a Reynolds number of 33,000. One of the main features of the test rig was the forcing mechanism, which was located upstream of the test section, in the bypass of the pump. It consisted simply of a standard rotating valve driven by an electric motor. Depending on the parameters set (valve position, volume flow, and frequency of forcing and rotation of the pump), strong forcing amplitudes were achievable (up to $\pm 90\%$ for some configurations). All the measurement points chosen exhibited an almost sinusoidal excitation, which could be acquired using a hydrophone (Bruel & Kjaer, type 8103) that was fixed on the burner outlet above slot S1 as shown in Fig. 2 (center of hydrophone located at $x/D=0.05$). The hydrophone was used to synchronize the triggering of the measurement equipment described below. A second hydrophone was also used to determine the rotational sense of the natural coherent structure.

The first PIV measurements made in planes containing the streamwise axis x for different burner angles θ showed that the flow at the burner outlet was not fully rotational symmetric, which can be explained by the lack of rotational symmetry of the burner geometry. The reference plane for the measurement was thus cho-

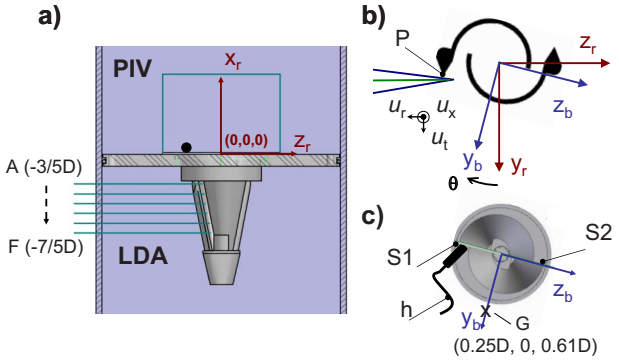

Fig. 2 Mounted burner in the test rig, side (*a*) and top views ((*b*) and (*c*)). The figures show the PIV and LDA measurement positions. S1 and S2 are the two slots of the burner. The hydrophone *h* was fixed on S1. For the LDA measurement in the slot, the angle θ was set equal to −20 deg.

sen to be the axial plane containing the two injection slots (x_b, z_b). With this definition and the two velocity components (u_x, u_t) (i.e., the streamwise and azimuthal components) recorded by the LDA at the burner exit $(x/D=0.25)$, it was possible to obtain an evaluation of the degree of swirl at the outlet. In our case, the swirl number S is defined as the ratio of azimuthal to streamwise momentum from $z=0$ to $z_s=50$ mm

$$S = \frac{2\pi \int_0^{z_s} \rho \bar{u}_x \cdot \bar{u}_t z^2 \cdot dz}{z_s \cdot 2\pi \int_0^{z_s} \rho \bar{u}_x^2 z \cdot dz} \tag{1}$$

For the present Reynolds number Re=33,000, the swirl number S was calculated to be $S \approx 0.71$, consistent with the presence of a strong recirculation zone at the burner outlet.

3 Measurement Techniques

A main aim of these investigations is to characterize the flow instabilities occurring in swirling flows when forcing is applied to the flow. As instabilities could be also evidenced in the unforced case, it is appropriate to characterize the flow following the triple decomposition technique [20], where turbulent fluctuations u_{fluc} are split into a coherent part $\tilde{u}$ and a random part u'. Both parts are then added to the time-averaged velocity $\bar{u}$ to build the instantaneous velocity u

$$u = \bar{u} + u_{\text{fluc}} \tag{2}$$

$$u_{\text{fluc}} = \tilde{u} + u' \tag{3}$$

Thus, phase triggered PIV and phase-averaged velocities of the 2D LDA were used to capture the evolution of coherent structures characterized by $\tilde{u}$ in the unforced and forced cases. Both measurement techniques used the signal of the hydrophone (h) as a trigger signal to allow for the reconstruction of the triple decomposition. To reduce noise and avoid filter phase shifting, this signal was bandpass filtered with a single cutoff frequency corresponding to the dominant frequency observed.

3.1 PIV Measurement. PIV measurements were performed at the burner outlet in the (x_b, z_b)-plane. For this a standard PIV installation was used (Nd:YAG laser, 20 mJ per pulse, associated with a PCO Sensicam, 1024×1024 pixels, two image pairs per second). Seeding of water was achieved with 5 μm spherical silver coated particles. Data were processed in 32×32 pixel interrogation areas with 50% overlap. Interrogation areas were cross-correlated and a local median filter was used to eliminate spurious vectors. The eliminated data were replaced via interpolation from adjacent interrogation areas. The resulting vector field was used for an adaptive cross-correlation of the data, spurious data were filtered again and adaptive cross-correlation in 16×16 pixel interrogation areas was reapplied. The percentage of spurious vectors never exceeded 2% for any measurement plane.

The mean velocity profiles were computed with 500 image-pairs taken randomly. For the phase triggered acquisitions 60 image-pairs per phase were taken and averaged. This number was found to be high enough to capture the flow structure of interest but was not sufficient to obtain reliable statistical values of the flow as suggested by Wernert and Favier [21].

3.2 LDA Measurements. 2D LDA measurements were made using a Dantec two component system (Model No. 5500A-00 with BSA F60). The "sample and hold" acquisition of the bursts was set (2 ms dead time between two valid bursts, i.e., maximal data rate of 500 Hz), and the two velocity measurements were noncoincident. Data rates ranging from 100 Hz up to 500 Hz were achieved, depending on the location of the measurement probe. These values were sufficient to obtain a good resolution of the dominant frequencies of interest ranging below 10 Hz. The positioning of the LDA optic was ensured by a traversing system and positioning correction due to the different refraction indices (air, glass, and water) was applied.

LDA measurements were mainly used to investigate the flow in the inlet slots. Measurements were performed at five axial positions from $x/D=-7/5D$ to $-3/5D$ in steps of $1/5D$ (Fig. 2(*a*)). Due to the complex geometry of the slot, which cannot be considered as a translated 2D profile with an increasing axial position x, a positioning procedure was defined. The burner angle was first set to $\theta=-20$ deg to ensure optical access into the inlet slot. The outer edge of the slot was used to position the measurement volume (point P in Fig. 2(*b*)). Then a translation along $\boldsymbol{y_r}$ and $\boldsymbol{z_r}$ (1 mm and 4 mm) positioned the measurement probe in the flow. The same procedure was repeated to define the points A to F shown in Fig. 2(*a*).

3.3 LDA Phase Averaging Processing. The velocity samples acquired by the LDA were first phase sorted in reference to the filtered reference signal, with a phase resolution of 1 deg (resulting in 360 *bins*). About 15,000 valid samples for each measurement point were taken. As the number of samples per bin did not allow for reliable statistical results, an estimate of the mean phase-averaged profile was obtained by fitting a Fourier series to the bin averaged profile, as described by Sonnenberger et al. [22]. Five harmonics were used and ensured a higher stability of the obtained profile against outliers resulting from the measurement. The formulation of the Fourier estimation of the mean velocity $u_{F,t}$ (here for the azimuthal velocity) was therefore

$$u_{F,t}(\phi) = \bar{u}_t + \sum_{m=1}^{5} a_m \cos(2\pi m f_0 \phi) + b_m \sin(2\pi m f_0 \phi) \tag{4}$$

where $\bar{u}_t$ is the mean velocity at the considered point, f_0 is the dominant frequency, and a_m and b_m are the Fourier coefficients of the harmonic m. To allow for a direct comparison of the amplitude and phase shift relationship between measurement points and hydrophone signal, the expression (4) was reformulated as follows:

$$u_{F,t}(\phi) = \bar{u}_t + \sum_{m=1}^{5} |\tilde{u}_{t,m}| \cos(2\pi m f_0 \phi + \angle(\tilde{u}_{t,m})) \tag{5}$$

with

$$\tilde{u}_{t,m} = a_m - i b_m \tag{6}$$

With this definition, the amplitude $|\tilde{u}_{t,m}|$ and the phase $\angle(\tilde{u}_{t,m})$ of the harmonic m are directly obtained. The same processing was also applied to the hydrophone signal as data of the hydrophone were sampled with a valid burst of the streamwise velocity and not continuously sampled. Figure 3 illustrates the effectiveness of the Fourier estimation in comparison to the bin averaging method. Measurements were performed at the position G at the burner outlet for the unforced flow (see position in Fig. 2). The left figure shows the phase sorted samples of the u_t component and the resulting bin averaging. It illustrates the strength of the random component u_t' in comparison to the coherent motion $\tilde{u}_t$. The Fourier estimation on the right figure smoothes the profile and allows for obtaining a better estimate of $\tilde{u}_t$.

In Fig. 3, it is also noticeable that the phase-averaged signal at the burner outlet is not sinusoidal but reproduces qualitatively the signal obtained in other experimental configurations [6].

The Fourier estimation was then used to calculate the phase shift between the first harmonic of the phase-averaged velocity at a chosen point i and the first harmonic of the signal of the hydrophone located above slot 1, which was calculated as follows:

$$\angle\varphi = \angle\tilde{u}_{t,1,i} - \angle\tilde{h}_1 \tag{7}$$

3.4 Definition of the Forcing Amplitude. The amplitude of the excitation showed a nonlinear response to the frequency and the different settings of the water test rig, such as the valve position. No global actuation amplitude could be satisfyingly defined

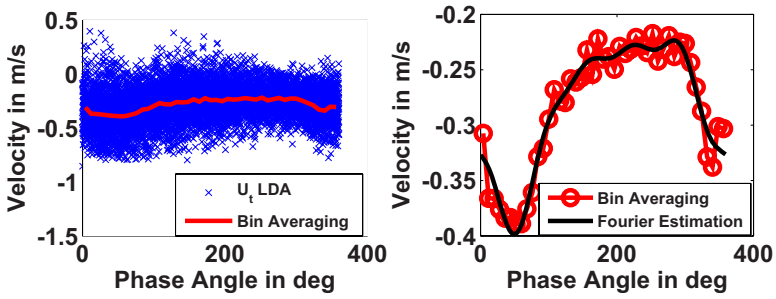

Fig. 3 Scatter plot of the phase-sorted azimuthal velocity u_t, bin averaging of the velocity (left) and comparison of the bin averaging with the Fourier estimation of the bin averaged velocity (right), $u_{F,t}$ for the unforced flow

from these settings, as resonance phenomena of the hydraulic pump with the piping system also occurred. Thus a local definition F_a of the forcing amplitude was chosen. It was constructed using the ratio of the first harmonic amplitude of the azimuthal velocity to its mean value at the arbitrarily chosen position C $(x/D=1)$ in the slot S1

$$F_a = \left(\frac{|\tilde{u}_{t,1}|}{\bar{u}_t} \right)_C \tag{8}$$

With this definition, forcing amplitudes of up to $\pm 90\%$ for selected frequencies were achievable. The corresponding forcing Strouhal number St_f was based on the forcing frequency f, the burner outlet diameter D, and the mean bulk streamwise velocity U_0 based on this diameter.

3.5 Proper Orthogonal Decomposition. A low-dimensional characterization of the fluctuating velocity field is obtained by proper orthogonal decomposition. POD decomposes the flow in spatial dependent modes and time-dependent mode coefficients. The POD modes are sometimes referred to as coherent structures of the flow field. The decomposition represents the flow field in an optimally compact fashion in the sense that $\overline{\|\mathbf{u}_{\mathrm{fluc}}(\mathbf{x},t) - \Sigma_{j=1}^{N} a_j(t)\mathbf{u}_j(\mathbf{x})\|^2}$ is minimal for any N over the class of all orthonormal bases. The fluctuating velocity field is decomposed as follows:

$$\mathbf{u}_{\mathrm{fluc}}(\mathbf{x},t) \approx \mathbf{u}_{\mathrm{fluc}}^{(N)}(\mathbf{x},t) = \sum_{j=1}^{N} a_j(t)\mathbf{u}_j(\mathbf{x}) \tag{9}$$

where N is the number of modes, $\mathbf{u}_j$ are the POD modes, and the mode coefficients are labeled a_j.

The optimality condition leads to the following eigenproblem:

$$\int_{\Omega} \overline{\mathbf{u}_{\mathrm{fluc}}(\mathbf{x}) \otimes \mathbf{u}_{\mathrm{fluc}}(\mathbf{x}')}\mathbf{u}_j(\mathbf{x}')d\mathbf{x}' = \lambda_j \mathbf{u}_j(\mathbf{x}) \tag{10}$$

where Ω is the considered flow domain. The λ_j are the eigenvalues corresponding to the eigenfunctions $\mathbf{u}_j$, which are called POD modes. $\overline{\mathbf{u}_{\mathrm{fluc}}(\mathbf{x}) \otimes \mathbf{u}_{\mathrm{fluc}}(\mathbf{x}')}$ is the two-point space-time correlation tensor ($\otimes$ is the dyadic product). The eigenvalues λ_j represent the contribution of the mode j to the mean turbulent kinetic energy (TKE). The modes are ordered by decreasing energy contribution (optimality condition). The time coefficients can be obtained by taking the inner product with the corresponding mode

$$a_j(t) = \int_{\Omega} \mathbf{u}_{\mathrm{fluc}}(\mathbf{x},t)\mathbf{u}_j(\mathbf{x})d\mathbf{x} \tag{11}$$

A full discussion of the POD framework may be found in Holmes et al. [23].

4 Unforced Flow of the Burner

4.1 Natural Coherent Structure Visualization. The first step of the investigation is to characterize the unforced flow field, as well as the dominant structures and their characteristic frequencies. Figure 4 shows the PIV results of the mean unforced flow $(\mathrm{St}_f=0)$ at the burner outlet in the (x_b,z_b)-plane. The contour plot of the streamwise velocity u_x on which the vector plot (u_x,u_r) is superposed, shows a central recirculation zone surrounded by a conical jet, which is typical for this kind of swirling flow. The signal of the hydrophone showed a dominant frequency corresponding to $\mathrm{St}_n \approx 0.92$. This frequency could also be observed in the u_x and u_t components of the LDA in the shear layer, as shown by the power spectrum densities (PSD) of their fluctuating parts, $\tilde{u}_{x,\mathrm{fluc}}$ and $\tilde{u}_{t,\mathrm{fluc}}$, in Fig. 5. Further measurement showed that the dimensionless frequency St_n of the helical structure was also independent of the Reynolds number, confirming that this instability

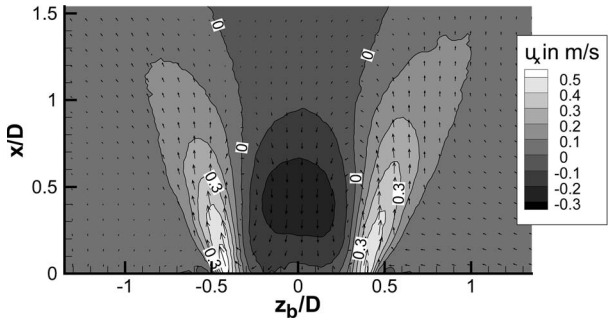

Fig. 4 Contour plot of the mean streamwise velocity $\bar{u}_x$ in m/s with the vector plot of the velocity in the (x_b,z_b)-plane, unforced flow

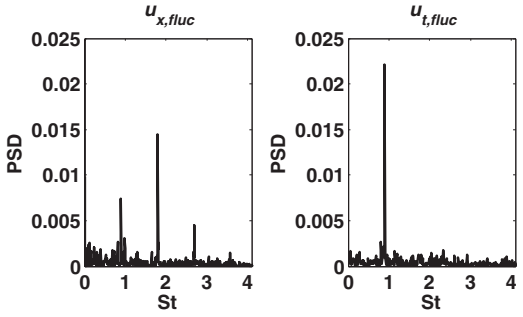

Fig. 5 Frequency spectra of the $u_{x,\mathrm{fluc}}$ (left) and $u_{t,\mathrm{fluc}}$ (right) components for the unforced flow, in the shear layer at the burner outlet (G position, $x=D/4$, $y=0$, and $z=-50$ mm)

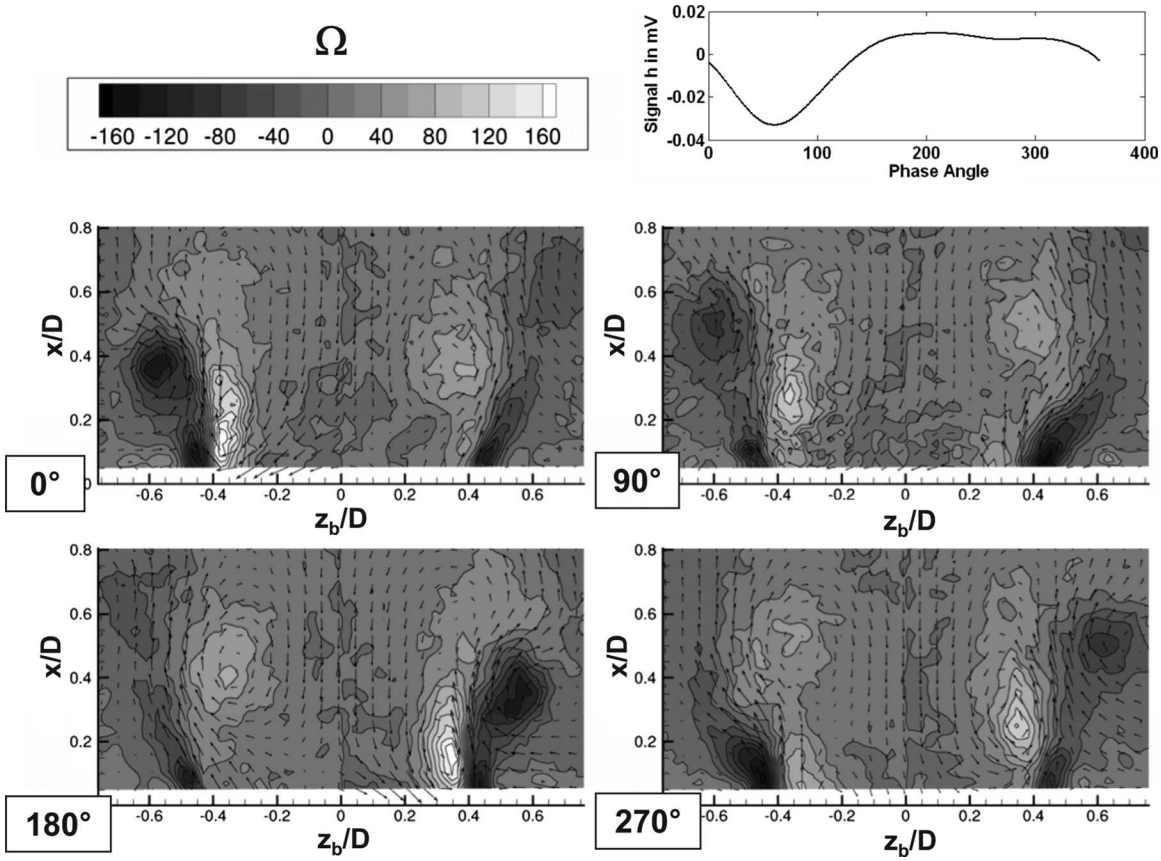

Fig. 6 Phase-averaged color maps of the azimuthal vorticity Ω (in s^{-1}) in the (x_b, z_b)-plane of the unforced flow, which evidences the natural helical mode. Four phases of the hydrophone signal (top right) were used to trigger the acquisition. The arrows represent the velocity vectors.

is related to a flow instability.

To visualize this flow structure, phase triggered PIV measurements were performed as described in Sec. 3. The azimuthal vorticity Ω defined as

$$\Omega = \frac{\partial u_x}{\partial r} - \frac{\partial u_r}{\partial x} \tag{12}$$

was used to plot the data, with r corresponding to the distance of a considered point to the centerline of the flow. This definition characterizes more easily rotational systems, as a rotational structure centered on $r/D=0$ will have the same vorticity sign (and hence the same color in the color maps) in the positive ($z_b/D \geq 0$) or negative ($z_b/D \leq 0$) axial half planes. Four of the eight phase angles acquired, which are presented in Fig. 6, clearly show the streamwise evolution of one helical structure. The phase angle 0 deg appears indeed to be the axial symmetric picture of the phase angle 180 deg. This helical structure is made up of two counter rotating vortices, which evolve downstream as the phase angle increases.

As the helical structure could be detected at the burner outlet, the question of what happen to the slot needs to be answered. To this end, LDA measurements were performed in slot 1 at the previously defined axial positions. Then, the complete system hydrophone/burner was rotated by 180 deg allowing for an access to the second slot.

The power spectrum densities presented in Fig. 7 clearly show that an oscillation at the same frequency ($St \approx 0.92$) is also present upstream within the slots. This oscillation can be found back near the burner apex (position E). Furthermore, the relative amplitude of the oscillation in both slots for the azimuthal velocity $\tilde{u}_t$ is plotted along the axial position. The amplitude of the fundamental frequency is calculated following Eq. (8), this time applied at the considered point. This amplitude increases as a power 4 of the axial position, but remains still lower than the amplitude observed in the shear layer at position G.

The evolution of the phase shift between the azimuthal velocities in the two slots and the hydrophone is shown in Fig. 8. A phase shift of about 180 deg is visible, confirming the helical nature of the oscillations in the burner slots. This plot facilitates an estimation of the axial wavelength λ of the instability into the burner, which is $\lambda = 2.25D$.

This wavelength decreases strongly to $\lambda \approx 0.5D$ at the burner outlet, as can be seen in Fig. 6, where a half wavelength of 0.25D can be estimated at each phase angle presented. This decrease is mainly due to the change in the flow field induced by the geometry of the dump section.

4.2 Determination of the Mode Sign and Phase Equation. As the PIV phase locked measurement showed that the structure is traveling downstream, only the sense of rotation (i.e., clockwise or counterclockwise rotation) determined at one axial position is necessary to fully characterize the structure (see Ref. [8] or Ref. [24] for more details). The determination of the sign of the helical mode was performed by introducing a second hydrophone probe. One hydrophone (h_2) was fixed over slot 1, while the angle β of the other hydrophone (h_1) was varied on the circumference of the burner (see sketch in Fig. 9). The cross-correlation R_{h1h2} of both signals gives then the resulting time lag and hence phase lag $\angle h_1 h_2$ depending on the angle β. Figure 9 shows that both angles have the same sign and, regarding the common definition of R_{h1h2}, this means that the signal h_1 precedes the signal h_2 when $\beta \in [0, 180]$ and follows h_2 when $\beta \in [-180, 0]$. The helix is thus wind-

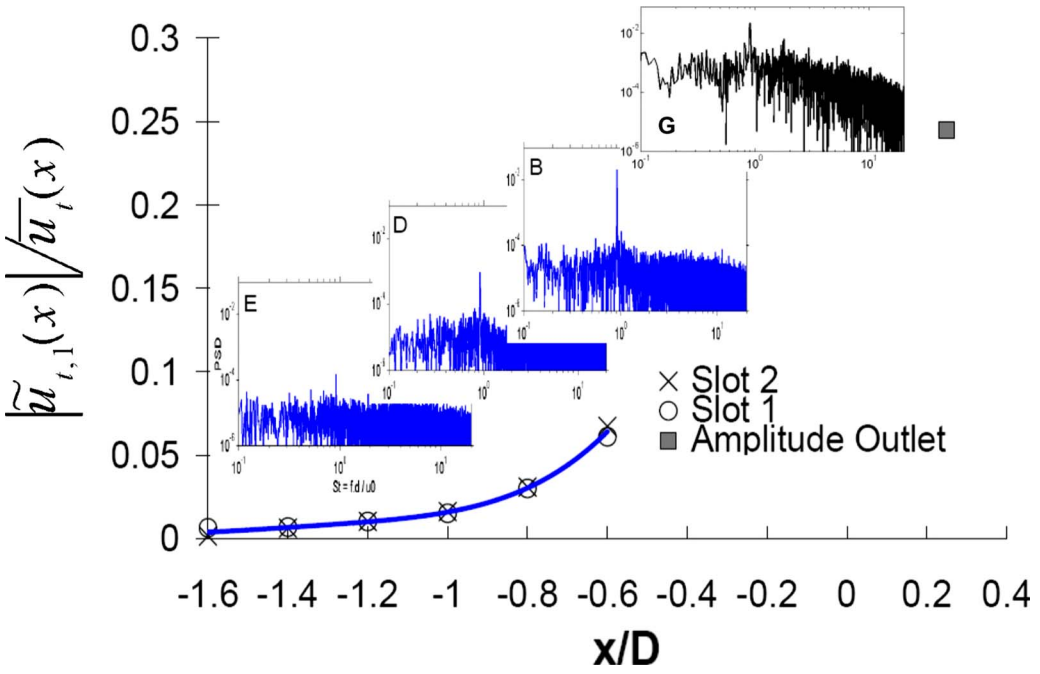

Fig. 7 Relative oscillation amplitude of the natural frequency for u_t over the axial position for the unforced flow. Spectrum of the signal at the different locations (E, D, B, and shear layer G) is shown. A best fit power four polynomial is applied to the data.

ing in the same sense as the swirling motion, and the mode sign is positive ($m=1$), confirming the results of the LES simulation on the same burner model presented by Duwig et al. [10].

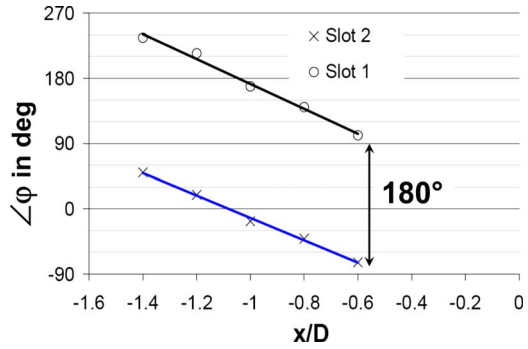

Fig. 8 Phase relationship between the tangential velocity $\tilde{u}_t$ and the hydrophone signal h within Slots 1 and 2 of the burner depending on the axial position x/D for the unforced flow

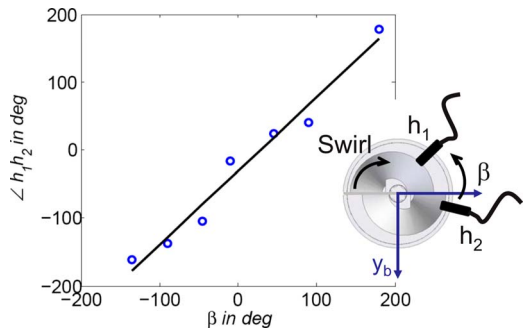

Fig. 9 Phase angle $\angle h_1 h_2$ of the hydrophone signals as a function of the angle β

With the data acquired, as discussed above, it is possible to reconstruct the phase relation φ_{hel} of the helical wave into the burner.

$$\varphi_{\text{hel}}(x,\theta,t) = (kx + m\theta - \omega t) \tag{13}$$

with the measured parameter, $k=2\pi/(2.25D)$, $m=1$, and $\omega=2\pi\,\text{St}_n\,U_0/D$. This relation may be taken from Ref. [8] or Ref. [24] and is valid for a flow rotating counterclockwise when viewed from the downstream x-direction, as is the case here.

4.3 Transposition of the Water Experiment to Gaseous Experiment. To verify that the results of the water test rig could be transposed to real gas flow conditions, similar tests were conducted on a similar burner in an air test rig [25]. A dominant frequency corresponding to the same Strouhal number St=0.92 was measured in the inlet slot, confirming that the water laboratory experiments catch the same dominant flow phenomena as in the gaseous case.

4.4 Explanation of the Origins of Flow Oscillations in the Slot. The previous results demonstrate that the helical instability, which was observed at the burner outlet, is also present upstream of the inlet slot. In order to explain the phenomena observed, information on the flow field inside the burner was needed. Some of the required information was obtained from a steady computational fluid dynamics (CFD) simulation of the flow field performed by the authors but, as yet, is still unpublished. The domain extending between $x/D=-2.8$ and $x/D=4$ was calculated using a first order Reynolds average Navier–Stokes (RANS) solver in CFX 10.0. A k-ε turbulence model was employed together with an unstructured mesh that was refined in regions containing large velocity gradients. They showed that the vortex breakdown (VBD) already occurs in the burner and the stagnation point of the recirculation zone narrows the apex of the burner. In other words, the recirculation zone is already present in the burner. As the helical instability is closely related to the VBD phenomenon, the steady numerical simulation confirms also the experimental observation

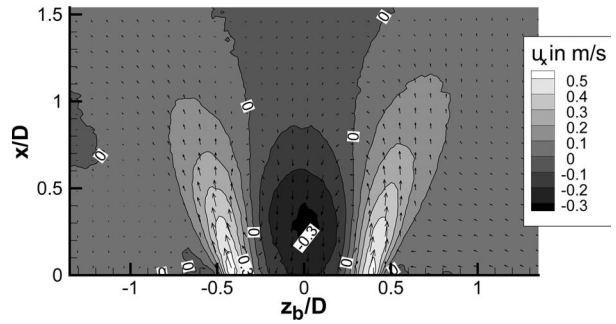

Fig. 10 Contour plot of the mean streamwise velocity $\overline{u}_x$ in m/s with the vector plot of the velocity in the (x_b, z_b)-plane, forced flow at $St_f \approx 0.92$

of Sec. 4.1.

The first explanation of the velocity oscillations at the burner inlet presupposes that the helical structure is directly responsible for pressure and velocity oscillations at the inlet. This helical structure may be seen by the slots as a rotating pressure field, which changes periodically the local pressure loss coefficient over the slot length. As the overall pressure drop over the burner remains constant, this is also the case of the pressure drop along a streamline of the mean flow. An increase in the local pressure drop coefficient will thus lead to a reduction in the velocity to keep the mean total pressure constant. Thus, the velocity oscillations will also follow the periodic motion of the helical instability.

Another explanation deals directly with the nature of the flow. The VBD is related to a change in the flow nature and can be explained by a transition from a supercritical state to a subcritical one [13]. The subcritical nature of the flow is a necessary condition to obtain an absolute instability, which allows for the pressure field oscillation associated with the coherent structures to propagate upstream of the perturbation or VBD location. These pressure oscillations would also lead to velocity oscillations. As the VBD already occurs in the burner, there is no chance for the flow to be supercritical in the burner, as suggested by Keller et al. [26], which is a necessary condition to avoid oscillations in the slots.

These results are important for the understanding of the mixing process fuel/air of the burner as the injection of fuel is performed in the slots. In fact, Flohr et al. [27] underlined that the turbulent scalar transport induced by coherent motion may have a dominant contribution to the global turbulent transport for the same burner. The natural velocity oscillations evidenced here will lead to fuel/air ratio oscillations, which may excite unstable modes of the combustor.

5 Impact of Axial Forcing on the Flow Field

5.1 Forcing at the Natural Frequency ($St_f \approx 0.92$). First, the flow was excited at the natural frequency previously measured ($St_f \approx 0.92$), and the same measurements as in the unexcited case were performed. The amplitude F_a of forcing was set to 50%. Figure 10 shows the resulting flow field at the burner outlet. Compared with the unforced case presented in Fig. 4, it clearly shows that the forcing has a negligible impact on the mean velocity field at the burner outlet. This is confirmed by the radial profiles of the axial and radial velocities presented in Fig. 11, which show little changes between the two cases. The inner recirculation zone slightly decreases when forcing is applied and the axial velocity on the centerline near the burner outlet also decreases. Beside those minor changes, the mean flow field remains mostly unchanged. It is not the case of the coherent motion which shows completely different patterns with forcing at the natural flow frequency as shown by the phase-averaged vorticity plots in Fig. 12. For this forcing frequency, the helical structure is replaced by an axially symmetric vortex ring.

As for the unforced flow, the phase relationship between velocity in the slot and the hydrophone was recorded for three forcing amplitudes F_a and is presented in Fig. 13. The forcing completely eliminates the phase shift existing between the different axial positions in the unforced configuration as the phase angle $\angle\varphi$ remains constant. The phase shift of 60 deg obtained for the three forcing amplitudes is due to a phase shift between the hydrophone and velocity, as pressure oscillations coming from the excitation are not in phase with the velocity oscillation in the shear layer.

The observation of the oscillation amplitude along the slot for the three forcing amplitudes is shown in Fig. 14. An increase in the axial position leads also to a slight increase in the oscillation amplitude in the slot. This observation may be of interest regarding the control of combustion by fuel injection. On one hand, one would prefer a steady fuel injection at the bottom of the burner, where flow oscillations and hence fuel mixing oscillations are lower than near the burner outlet. On the other hand, an unsteady

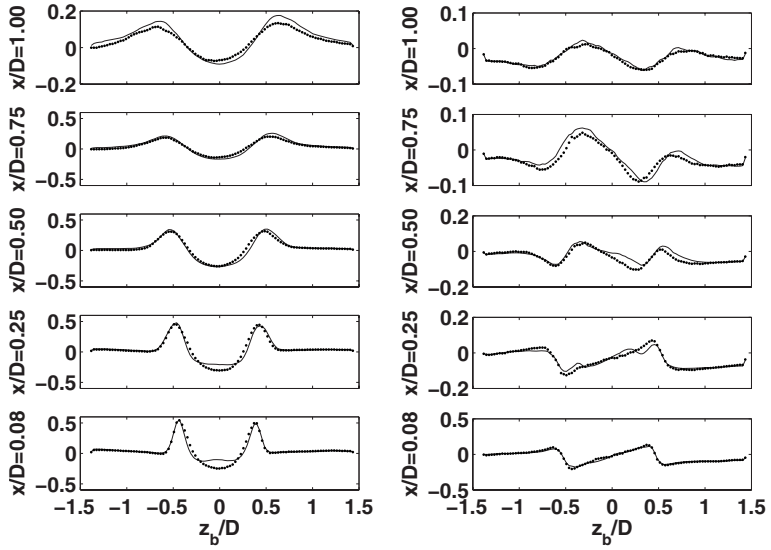

Fig. 11 Line plot of the mean streamwise velocity $\overline{u}_x$ (left) and radial velocity $\overline{u}_r$ (right), in m/s, for the unforced ($St_f = 0$, –) and forced ($St_f \approx 0.92$, ●) cases

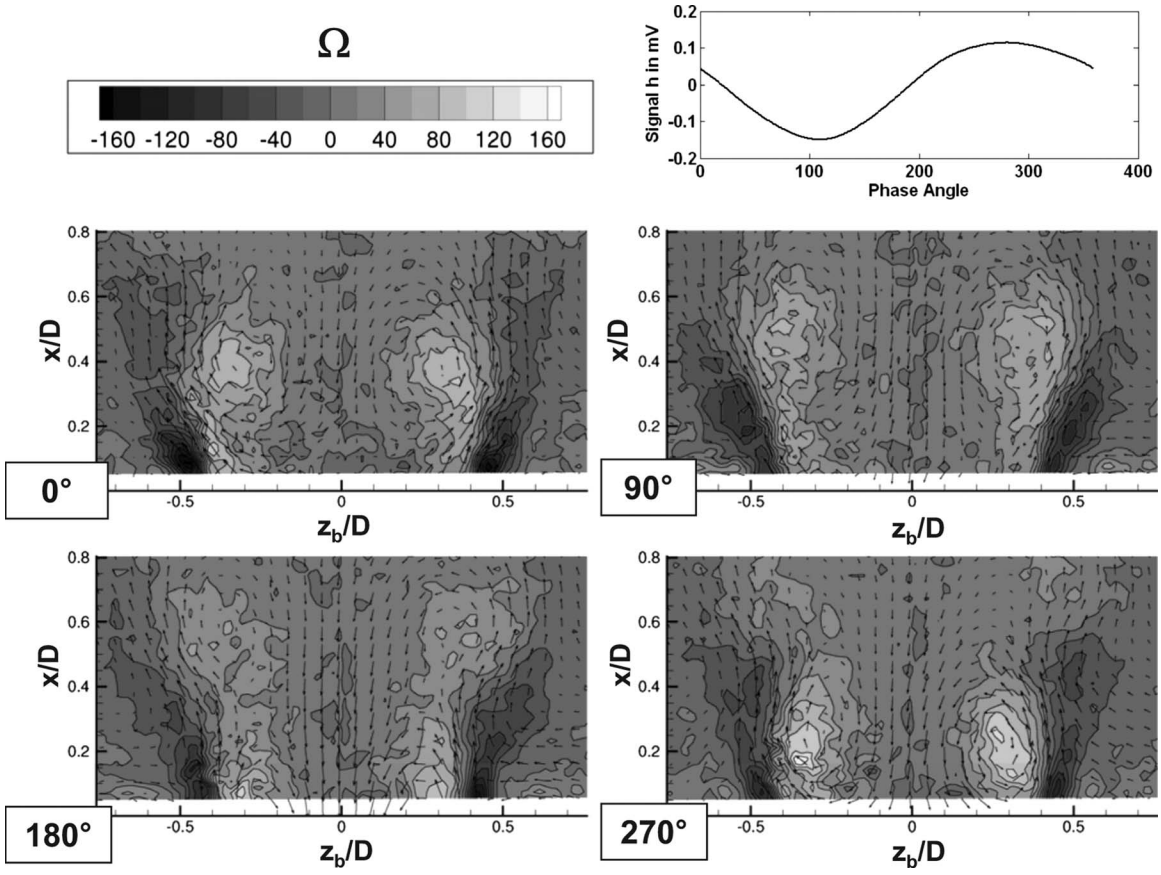

Fig. 12 Phase-averaged azimuthal vorticity Ω (in s^{-1}) in the (x_b, z_b)-plane of the forced flow at $St_f \approx 0.92$, which shows the axisymmetric structure. Four phases of the hydrophone signal (top right) were used to trigger the acquisition. The arrows represent the velocity vectors.

injection of fuel at the frequency of the instability (active control) may be more effective near the burner outlet if the phase between the fuel injection and the main flow is properly adjusted.

Furthermore, except for the extremely strong forcing amplitude (F_a=90%) where back flow occurs, the profiles of the mean velocity (Fig. 15) and oscillation amplitude appear similar from the apex of the burner to $x/D \approx -0.8$. Mean radial profiles across the slots of the axial and tangential velocities showed also the same results. Thus, except for a deviation in the profiles at $x/D > -0.8$ and $F_a > 50\%$, the mean distribution of the flow in the burner inlet slots is only slightly influenced by the forcing.

5.2 Forcing at a Frequency Not Related to the Natural Flow Frequency($St_f \approx 1.3$). The impact of an excitation, which did not correspond to any harmonic of the unforced flow was investigated. For this, the PSD spectra of the LDA measurements in the slot ($x/D = -4/5D$, point B) and in the shear layer (x

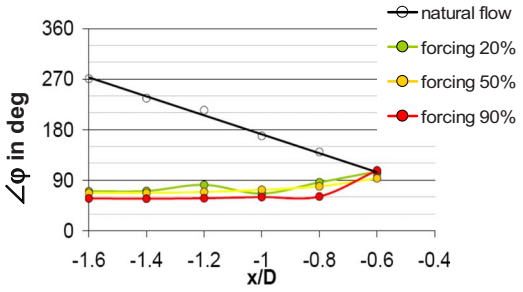

Fig. 13 Phase relationship between the tangential velocity $\tilde{u}_t$ and the hydrophone signal h within slot 1, for three forcing amplitudes at $St_f \approx 0.92$

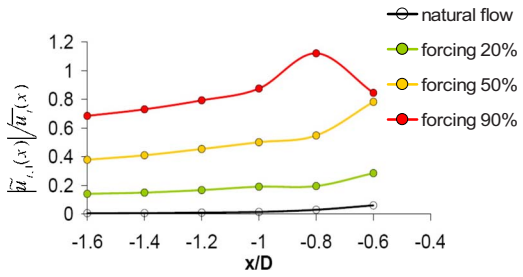

Fig. 14 Relative oscillation amplitude of $\tilde{u}_t$ depending on the axial position x/D for three forcing amplitudes at $St_f \approx 0.92$

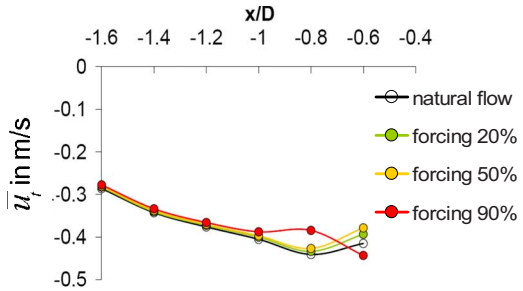

Fig. 15 Impact of the excitation on the mean flow velocity $\bar{u}_t$ in slot 1 at $St_f \approx 0.92$

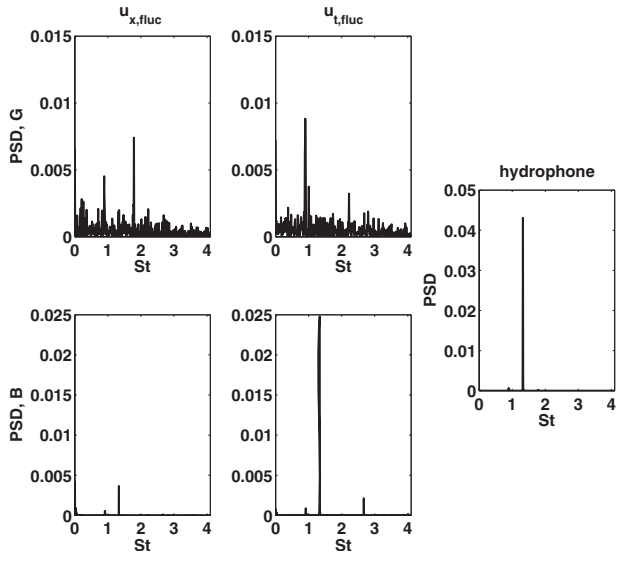

Fig. 16 Spectra of $u_{x,\mathrm{fluc}}$ and $u_{t,\mathrm{fluc}}$ in the shear layer (G) and in Slot (B) for $\mathrm{St}_f \approx 1.3$ and $F_a = 10\%$. The spectrum of the hydrophone is shown in the right plot.

$= D/4$, $y = 0$, $z = -50$ mm, point G) were compared. The results for the streamwise and azimuthal turbulent velocities at $\mathrm{St}_f \approx 1.3$ are presented in Fig. 16. They show that the dominant frequency in the shear layer is equal to $\mathrm{St} \approx 0.9$ even if the forcing is applied at a higher frequency.

The jet is thus not receptive to this forcing frequency, and no lock-in of the vortex shedding can be achieved at the burner outlet. These results show the same trends as those of Khalil et al. [17], with the difference that the lock-in of the vortex shedding occurred in their study at frequencies of up to $\mathrm{St}_f = 2\ \mathrm{St}_n$. As their experimental setup is totally different, one cannot expect the same results to be obtained in the present case. Thus the lock-in phenomenon, if present, may occur over a narrower frequency bandwidth.

With the measurement setup used, the phase-averaged PIV measurement did not reveal any flow structure when forcing was applied at higher frequencies than the natural instability frequency. The signal of the hydrophone recorded mainly the pressure oscillations induced by the forcing at $\mathrm{St} \approx 1.3$ and was not appropriate to be used as a trigger signal at $\mathrm{St} \approx 0.9$ for the phase-averaged PIV (see Fig. 16). POD analysis of the PIV snapshots was thus performed to obtain the missing information, particularly when forcing is applied at higher frequencies than the natural one.

6 Analysis of Flow Structures With POD

6.1 Turbulent Kinetic Energy Distribution. The POD analysis of the velocity vector field (u_x, u_r) was performed for the three cases: $\mathrm{St}_f = 0$, $\mathrm{St}_f \approx 0.92$, and $\mathrm{St}_f \approx 1.55$. In all cases, at least 200 modes were necessary to resolve 90% of the turbulent kinetic energy, which confirms the complexity of the unforced as well as the forced flows. However, the first POD modes still represent a significant fraction of the TKE, as shown in Fig. 17. Regarding the unforced flow, the first five modes resolve 25% of the TKE, i.e., important flow features are captured with a relatively small number of modes. The normalized modal TKE of the first mode matches also well with the POD results from the numerical simulation of Duwig et al. [10] (6.2% compared with 5.7%).

As we compare the TKE distribution of the three flow cases presented in Fig. 17, it is apparent that the natural flow and the flow forced at $\mathrm{St}_f \approx 1.55$ are similar, except for the differences in the second mode. Actuation with the natural flow frequency ($\mathrm{St}_f \approx 0.92$) presents a more significant change in the energy repartition, as the first mode contains twice as much energy as the first mode of the unforced flow. Hence this explains partly why the $\mathrm{St}_f \approx 0.92$ case will show a stronger change in the structures than the $\mathrm{St}_f \approx 1.55$ case when compared with the unforced flow.

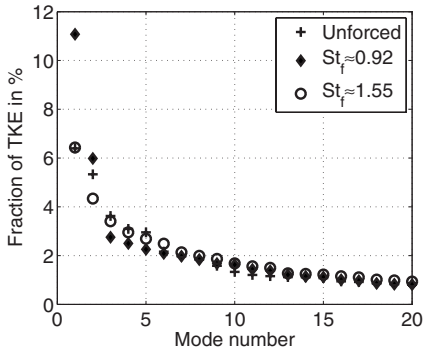

Fig. 17 Repartition of the turbulent kinetic energy within the POD modes for the three with PIV investigated cases

6.2 Mode Shape. The resulting modes of the above mentioned POD method are defined in the velocity (u_x, u_r). As the mode structures are of interest, the modes are rewritten in the azimuthal vorticity $\Omega(\mathbf{x})$, which is shown in Fig. 18. For each case (from left to right), the mean flow and the first four POD modes are presented (from top to bottom). Antisymmetric structures can be observed for the unforced and the forced case $\mathrm{St}_f \approx 1.55$ (modes 1–3), whereas the forced case corresponding to $\mathrm{St}_f \approx 0.92$ shows axisymmetric structures. A helical mode can be associated with the antisymmetric structures, which confirms that a helical structure is present at the burner outlet for the case $\mathrm{St}_f \approx 1.55$. The main difference between both helical structures is that the helix of the unforced flow is more stretched in the $\boldsymbol{x}$ and $\boldsymbol{r}$ directions than for the $\mathrm{St}_f \approx 1.55$ case. For the latter, almost one revolution period of the helix is visible, and the axial wavelength is smaller. The radial stretching is due to the jet opening angle, which is lower for the forced case. Forcing at $\mathrm{St}_f \approx 1.55$ leads to a small jet opening angle and promotes a lower axial decay of the coherent structures.

POD modes 2 and 3 of the $\mathrm{St}_f \approx 0.92$ case form a pair, exhibiting strong similarities and a phase shift with respect to each other in the axial direction. They indicate two counter-rotating vortices at $|r/D| \approx 0.5$ and an axial displacement of the structure. Since the snapshots are not correlated in time, it is not possible to track with the POD analysis the evolvement of this structure. The first mode of this case describes a mean flow correction of the velocity flow field, which may correspond to a slow variation in the central recirculation zone. A similar analysis can be done with the first two POD modes of the case $\mathrm{St}_f \approx 1.55$ or modes 1 and 3 of the unforced flow.

The fourth mode of case $\mathrm{St}_f \approx 1.55$ is axially symmetric, showing that a low energy axial symmetric structure is present at the burner outlet. On the contrary, mode 4 of case $\mathrm{St}_f \approx 0.92$, exhibits an antisymmetric structure, while the three first modes are symmetric. Thus, the forcing does not necessarily suppress some structures, but redistributes the modal contribution on the TKE.

6.3 Sensitivity Analysis. A sensitivity analysis was performed in order to see how many snapshots are needed for a good representation of the dominant coherent structures. Therefore, the POD framework was applied on $M = 63$, 125, 250, and 500 snapshots. The unforced flow was chosen for this analysis and modes 1, 3, 7, and 9 are presented in Fig. 19. As expected, an increase in the number of snapshots smoothes the shape of the POD modes. Especially, for modes 1–7, the shape of the modes obtained with 500 snapshots is already recognizable in the modes obtained with four times less snapshots. Mode 9 shows also strong similarities in

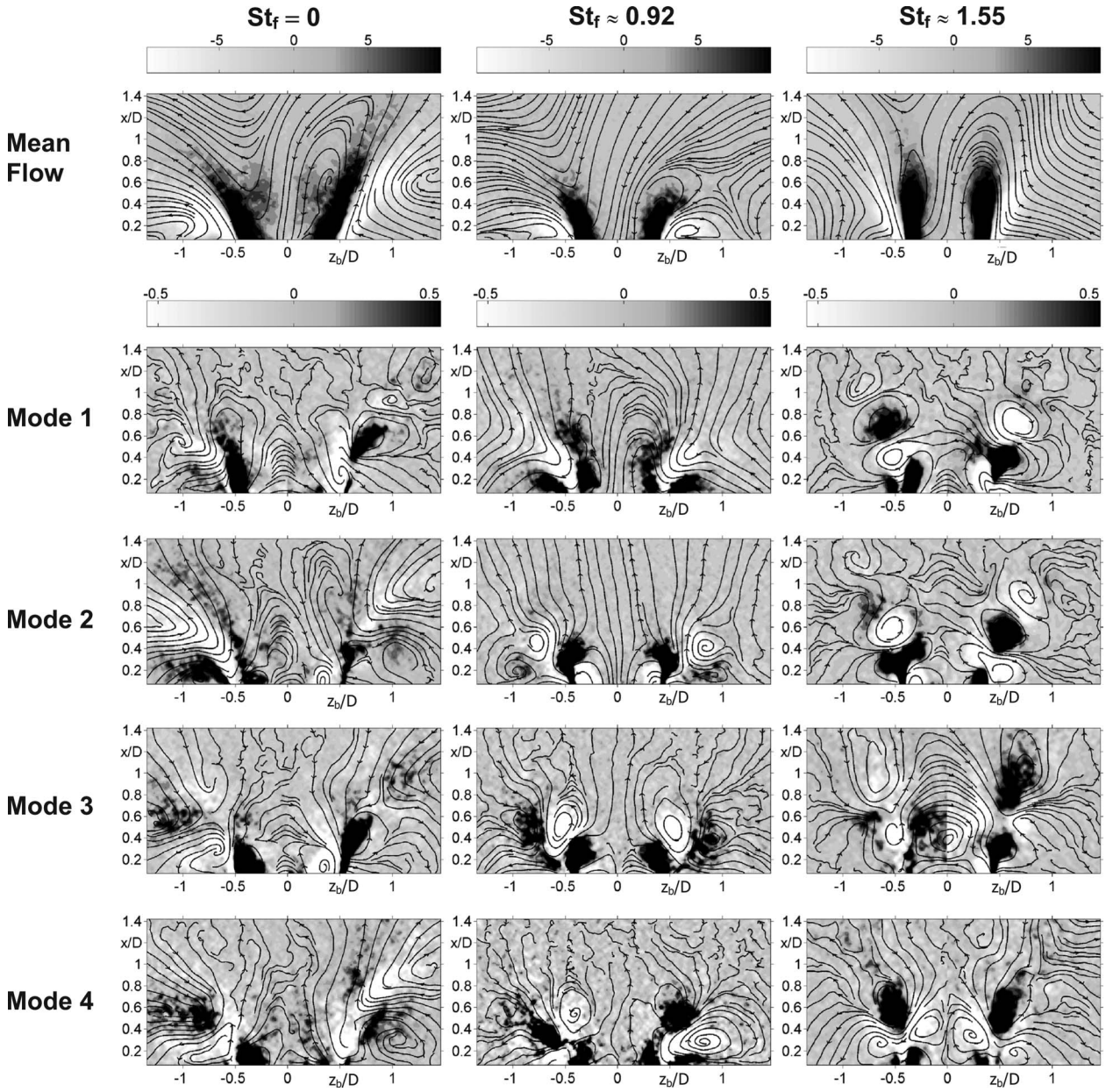

Fig. 18 Contour plot of the azimuthal vorticity Ω resulting from the POD analysis of the snapshots in the (x_b, z_b)-plane. The mean vorticity and the first four (1–4) dominant modes for all three investigated cases are presented and show the dominant coherent flow structures. The limits of the gray scale are set to emphasize the vorticity sign of the structures, as absolute vorticity values are not of interest. Superposed are streamline representations of the corresponding modes.

structures resulting from 500 and 250 snapshots. Thus, 500 snapshots are sufficient if one is only interested in the dominant flow structures.

7 Conclusion and Outlook

The impact of axial forcing on the flow field of a swirl burner was investigated and compared with its unforced counterpart. The impact of different oscillation frequencies and amplitudes on the flow at the inlet and outlet of the burner was documented.

The natural helical mode ($m=+1$) typical for those types of flows could be captured by phase-averaged LDA and PIV at the burner outlet. The helical wave could be also found in the inlet slots of the burner, upstream of the stagnation point located in the burner. Thus the flow from the inlet of the burner is subject to an absolute instability, which needs to be taken into account for further modeling of the fuel/air mixing.

The forcing frequencies and amplitudes had little impact on the mean velocity field at the burner inlet and outlet, but had a stronger influence on the coherent flow motion. Axisymmetrical forcing of the flow leads to a lock-in of the oscillation in the slot onto the forcing frequency. However, the response of the flow at the burner outlet is dependent on the forcing frequency as follows.

- Forcing at the natural frequency leads to a switch of the helical structure to an axisymmetric one.
- Forcing at a higher frequency than the natural frequency ($St_f \approx 1.3$) shows no lock-in of the vortex shedding frequency onto the applied frequency. The POD analysis of PIV snapshots shows clearly that a helical structure is still present at the burner outlet even if the forcing applied is axially symmetric ($St \approx 1.55$).

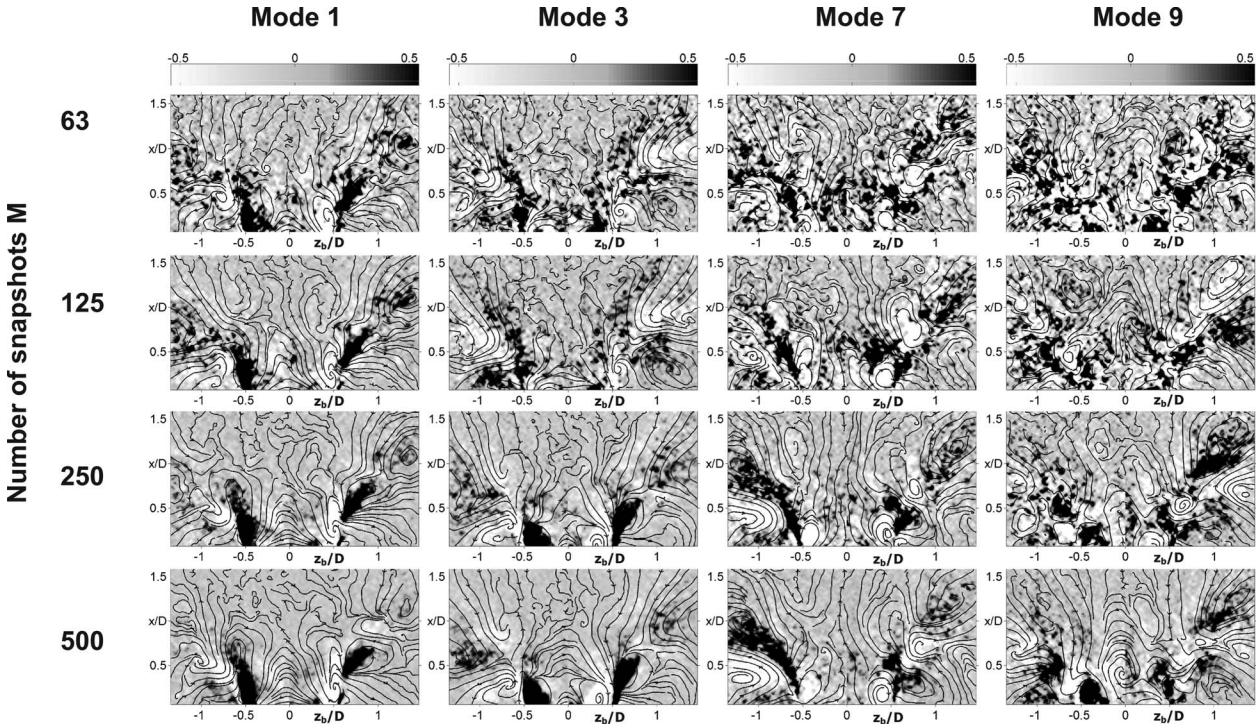

Fig. 19 Sensitivity of the POD to the number *M* of PIV snapshots (63, 125, 250, and 500) taken for the analysis. Modes 1, 3, 7, and 9 of the unforced flow are presented.

The proper orthogonal decomposition performed on experimental data appears to be an appropriate tool to capture physical properties of the flow, which cannot be easily and directly measured by the present measurement configuration. Even if the flow is quite complex, as more than 200 modes were needed to resolve 90% of the total kinetic energy, the five dominant modes of the unforced and forced flows still represented 25% of the TKE. Low order modeling, based on the approach described in Ref. [28], may represent the physical mechanisms sufficiently for further work related to closed-loop control.

Acknowledgment

The authors would like to thank Y. Singh for helping to perform the LDA measurements and would also like to thank the German Science Foundation (DFG) for the financial support as part of the Collaborative Research Center (SFB) 557 "Control of Complex Turbulent Shear Flows."

Nomenclature

a_j = mode coefficients from POD
a_m = Fourier series coefficient
b_m = Fourier series coefficient
D = burner diameter
f = excitation frequency
F_a = forcing amplitude
h = hydrophone signal
$r=\sqrt{(y^2+z^2)}$ = radius
$\mathbf{u}_j$ = POD modes
u_x = streamwise velocity
u_r = radial velocity
u_t = azimuthal velocity
U_0 = bulk velocity at the burner outlet
x = streamwise axis
(x_b, y_b, z_b) = coordinate system of the burner
(x_r, y_r, z_r) = coordinate system of the test rig
$\boldsymbol{R}_{h1,h2}$ = cross-correlation function
$\mathrm{Re}=U_0 D/\nu$ = Reynolds number
$\mathrm{St}=fD/U_0$ = Strouhal number
$\mathrm{St}_f=f_{\mathrm{forcing}}D/U_0$ = Strouhal number of the forcing
$\angle\varphi$ = phase angle between the hydrophone and LDA signal
φ_{hel} = phase function of the helical wave
λ = axial wavelength
λ_j = eigenvalues of the POD Analysis
ν = kinematic viscosity
ω = precessing frequency
$\Omega=\partial u_x/\partial r-\partial u_r/\partial x$ = azimuthal vorticity
$\overline{(\cdot)}$ = time-averaged quantity
$\widetilde{(\cdot)}$ = coherent part of the turbulent motion
$(\cdot)'$ = turbulent quantity

References

[1] Lieuwen, T., and Zinn, B. T., 1998, "The Role of Equivalence Ratio Oscillations in Driving Combustion Instabilities in Low NO*x* Gas Turbines," *Proceedings of the 27th Symposium (International) on Combustion*, Combustion Institute, Boulder, CO, Aug. 2–7, pp. 1809–1816.
[2] Bothien, M. R., Moeck, J. P., Lacarelle, A., and Paschereit, C. O., 2007, "Time Domain Modelling and Stability Analysis of Complex Thermoacoustic Systems," Proc. Inst. Mech. Eng., Part A, **221**(5), pp. 657–668.
[3] Paschereit, C. O., Gutmark, E. J., and Weisenstein, W., 1999, "Coherent Structures in Swirling Flows and Their Role in Acoustic Combustion Control," Phys. Fluids, **11**, pp. 2667–2678.
[4] Poinsot, T., Trouvé, A., Veyante, D., Candel, S., and Esposito, E., 1987, "Vortex Driven Acoustically Coupled Combustion Instabilities," J. Fluid Mech., **177**, pp. 265–292.
[5] Panda, J., and McLaughlin, D. K., 1994, "Experiments on the Instabilities of a Swirling Jet," Exp. Fluids, **6**, pp. 263–276.
[6] Syred, N., 2006, "A Review of Oscillation Mechanisms and the Role of the Precessing Vortex Core (PVC) in Swirl Combustion Systems," Prog. Energy Combust. Sci., **32**, pp. 93–161.
[7] Lucca-Negro, O., and O'Doherty, T., 2001, "Vortex Breakdown: A Review," Prog. Energy Combust. Sci., **27**, pp. 431–481.
[8] Fernandes, E. C., Heitor, M. V., and Shtork, S. I., 2006, "An Analysis of Unsteady Highly Turbulent Swirling Flow in a Model Vortex Combustor," Exp. Fluids, **40**, pp. 177–187.
[9] Wang, S., and Yang, V., 2005, "Unsteady Flow Evolution in Swirl Injectors With Radial Entry. II. External Excitations," Phys. Fluids, **17**, p. 045107.

[10] Duwig, C., Fuchs, L., Lacarelle, A., Beutke, M., and Paschereit, C. O., 2007, "Study of the Vortex Breakdown in a Conical Swirler Using LDV, LES and POD," ASME Paper No. GT2007-27006.
[11] Paschereit, C. O., and Gutmark, E. J., 2004, "The Effectiveness of Passive Combustion Control Methods," ASME Paper No. 2004-GT-53587.
[12] Rodriguez-Martinez, V. M., Dawson, J. R., Syred, N., and O'Doherty, T., 2003, "The Effect of Expansion Plane Geometry on Fluid Dynamics Under Combustion Instability in a Swirl Combustor," AIAA Paper No. 2003-116.
[13] Escudier, M. P., and Keller, J. J., 1985, "Recirculation in Swirling Flow: A Manifestation of Vortex Breakdown," AIAA J., **23**, pp. 111–116.
[14] Paschereit, C. O., Oster, D., Long, T. A., Fiedler, H. E., and Wygnanski, I., 1992, "Flow Visualization of Interactions Among Large Coherent Structures in an Axisymmetric Jet," Exp. Fluids, **12**, pp. 189–199.
[15] Suzuki, H., Kasagi, N., and Suzuki, Y., 2004, "Active Control of an Axisymmetric Jet With Distributed Electromagnetic Flap Actuators," Exp. Fluids, **36**, pp. 498–509.
[16] Lacarelle, A., Moeck, J. P., Konle, H. J., Vey, S., Nayeri, C. N., and Paschereit, C. O., 2007, "Effect of Fuel/Air Mixing on NO*x* Emissions and Stability in a Gas Premixed Combustion System," AIAA Paper No. 2007-1417.
[17] Khalil, S., Hourigan, K., and Thompson, M. C., 2006, "Response of Unconfined Vortex Breakdown to Axial Pulsing," Phys. Fluids, **18**, p. 038102.
[18] Sattelmayer, T., Felchlin, M. P., Haumann, J., Hellat, J., and Styner, D., 1990, "Second Generation Low-Emissions ABB Combustors for Gas Turbines: Burner Development and Tests at Atmospheric Pressure," ASME Paper No. 1990-GT-192.
[19] Döbbeling, K., Knopfle, H. P., and Polifke, W., 1994, "Low NO*x* Combustion of MBTU Fuels Using the ABB Double Cone Burner (EV Burner)," ASME Paper No. 94-GT-394.
[20] Matsumura, M., and Antonia, R. A., 1993, "Momentum and Heat Transport in the Turbulent Intermediate Wake of a Circular Cylinder," J. Fluid Mech., **250**, pp. 651–666.
[21] Wernert, P., and Favier, D., 1999, "Considerations About the Phase Averaging Method With Application to ELDV and PIV Measurements Over Pitching Airfoils," Exp. Fluids, **27**, pp. 473–483.
[22] Sonnenberger, R., Graichen, K., and Erk, P., 2000, "Fourier Averaging: A Phase-Averaging Method for Periodic Flow," Exp. Fluids, **28**, pp. 217–222.
[23] Holmes, P., Lumley, J., and Berkooz, G., 1998, *Turbulence, Coherent Structures, Dynamical Systems and Symmetry*, Cambridge University Press, Cambridge, England.
[24] Gallaire, F., and Chomaz, J. M., 2003, "Mode Selection in Swirling Jet Experiments: A Linear Stability Analysis," J. Fluid Mech., **494**, pp. 223–253.
[25] Roessler, M., 2006, "Experimentelle Bestimmung des Akustisch Angeregten Strömungsfeldes an Einem Drall-Brennermodell für Industrielle Gasturbinen," Studienarbeit, Technische Universität Berlin.
[26] Keller, J. J., Sattelmayer, T., and Thüringer, F., 1991, "Double Cone Burner for Gas Turbine Type 9 Retrofit Application," *Proceedings of the CIMAC 19th International Congress on Combustion Engines*, Florence, Italy.
[27] Flohr, P., Schmitt, P., and Paschereit, C. O., 2002, "Mixing Field Analysis of a Gas Turbine Burner," Paper No. IMECE 2002-39317.
[28] Li, F., Banaszuk, A., Tadmor, G., Noack, B. R., and Mehta, P. G., 2006, "A Reduced Order Galerkin Model for the Reacting Bluff Body Flame Holder," AIAA Paper No. 2006-3487.

Simulation of Turbulent Lifted Flames Using a Partially Premixed Coherent Flame Model

Yongzhe Zhang

Rajesh Rawat

CD-adapco,
60 Broadhollow Road,
Melville, NY 11747

Partially premixed combustion occurs in many combustion devices of practical interest, such as gas-turbine combustors. Development of corresponding turbulent combustion models is important to improve the design of these systems in efforts to reduce fuel consumption and pollutant emissions. Turbulent lifted flames have been a canonical problem for testing models designed for partially premixed turbulent combustion. In this paper we propose modifications to the coherent flame model so that it can be brought to the simulation of partially premixed combustion. For the primary premixed flame, a transport equation for flame area density is solved in which the wrinkling effects of the flame stretch and flame annihilation are considered. For the subsequent nonpremixed zone, a laminar flamelet presumed probability density function (PPDF) methodology, which accounts for the nonequilibrium and finite-rate chemistry effects, is adopted. The model is validated against the experimental data on a lifted H_2/N_2 jet flame issuing into a vitiated coflow. In general there is fairly good agreement between the calculations and measurements both in profile shapes and peak values. Based on the simulation results, the flame stabilization mechanism for lifted flames is investigated.
[DOI: 10.1115/1.3026559]

1 Introduction

In a lifted diffusion flame, the flame lifts off and stabilizes itself further downstream instead of attaching to the fuel nozzle exit. Understanding the stabilization mechanism in turbulent lifted flames is helpful for the design of highly stable combustion systems of practical interest, such as gas-turbine combustors. Despite the apparent simplicity of the flow, modeling the stabilization processes in lifted flames is still an outstanding difficulty. Different theories and assumptions have been proposed. A comprehensive review can be found in Peters [1]. The approach of solely considering premixed flame propagation, in which flame stabilizes itself at the position where the mean flow velocity is equal to the turbulent burning velocity of the premixed mixture [2,3], or the approach of diffusion flame quench solely due to high scalar dissipation rates (SDRs) [4] could not fully explain the findings in experiments, and the conclusion was that neither can satisfactorily predict the lift-off behavior [5]. Triple flames have been considered as a key element in turbulent lifted jet flames. At the base of the lifted flame, a premixed flame propagates along a surface that is in the vicinity of a stoichiometric mixture. Behind the leading edge of the flame, a diffusion flame develops into which unburned intermediates such as H_2 and CO diffuse from the rich premixed flame branch and the leftover oxygen diffuses from the lean premixed flame branch [1]. Thus a partially premixed combustion formulation combining the premixed combustion and nonpremixed combustion is required to correctly represent the physics behind lifted flames. Lifted flames have been a canonical problem for testing models for partially premixed turbulent combustion.

One modeling approach for partially premixed combustion is to extend the existing premixed combustion models by considering effects of the variation of the local equivalence ratio. The coherent flame model (CFM) has been one of the models developed and applied for premixed combustion [6]. It assumes that chemical reaction takes place in a relatively thin layer that separates pockets of unburned and fully burned gas. By this flamelet assumption CFM decouples the combustion problem from the analysis of the turbulent flow field. The effects of turbulence on combustion are modeled by a flame area density (FAD) (defined as the flame surface per unit volume). Recent direct numerical simulation (DNS) work [7–9] has clarified the inhomogeneity effects on the flame area density in turbulent combustion. Extensions of CFM to partially premixed combustion have been proposed in the literature. Usually a mixture fraction is introduced to describe the inhomogeneous fuel distribution in the unburned mixture. Helie and Trouve [10] described the reaction zone as a combination of one premixed and one nonpremixed flame. The premixed stage is modeled using CFM, while the nonpremixed postflame uses a classical eddy dissipation model (EDM). Two mean fuel mass fraction equations, corresponding to the two combustion stages, are solved. However, the whole system is formulated based on an irreversible single-step chemistry. Bondi and Jones [11] designed a model for premixed flames with varying stoichiometry. A detailed chemical mechanism is incorporated for generating the burned state look-up table and laminar flame speed. It implicitly assumes that all the fuel is consumed in the premixed stage; thus it cannot be employed to the case where highly rich-lean conditions exist. Scalar dissipation effects are not included when calculating the burned state.

In this paper we propose a partially premixed coherent flame model (PCFM), which accounts for the detailed finite-rate chemistry effects and local heat losses while being computationally efficient by using a precalculated table. Instead of solving two fuel mass fraction equations as in Ref. [10], we derive a progress variable equation, which can describe the two-stage combustion in partially premixed flames. The model is thus applicable to highly stratified fuel/oxidizer mixtures. It is used to simulate a lifted H_2/N_2 jet flame issuing into a vitiated coflow. The stabilization mechanism is studied.

This paper is organized as follows: first is a description of the CFM, then the PCFM model is proposed and the methodology details are listed. Next, the lifted burner for simulation is introduced, and the numerical setup is explained. Then the simulation results are compared to the experimental measurements. Finally, the conclusions and future research directions are discussed.

Manuscript received April 4, 2008; final manuscript received August 25, 2008; published online February 10, 2009. Review conducted by Dilip R. Ballal. Paper presented at the ASME Turbo Exop 2008: Land, Sea and Air (GT2008), June 9–13, Berlin, Germany.

2 Coherent Flame Model

In CFM a transport equation for flame area density, Σ, is given by

$$\frac{\partial \Sigma}{\partial t} + \frac{\partial u_i \Sigma}{\partial x_i} = \frac{\partial}{\partial x_i}\left(\Gamma_\Sigma \frac{\partial \Sigma}{\partial x_i}\right) + \alpha K_t \Sigma - D\Sigma^2 \tag{1}$$

where Γ_Σ is the diffusion coefficient that includes both the molecular and turbulent parts, K_t is the turbulent stretch, i.e., the mean stretch rate averaged along the flame, D is the consumption coefficient, and α is a model parameter. This equation is a simplified form of the exact equation derived by Pope [12], Candel and Poinsot [13], and Trouve [14].

References [15,16] review formulations for K_t and D that have been used in the literature. Simple estimates for K_t include the small scale strain rate $\sqrt{\epsilon/\mu}$ (ϵ is the turbulent dissipation rate and μ is the viscosity) or the large scale strain, ϵ/k (k is the turbulent kinetic energy). They fail to reproduce effects of chemistry or of turbulence length scales on the turbulent burning velocity [15]. Here we adopted the intermittent turbulence net flame stretch (ITNFS) model developed in Ref. [17]. This model states that small scale eddies do not have effects on the flame front as much as the value of their high theoretical strain suggests, which is due to the viscous effects, curvature effects, or the geometry effects. For example, the Kolmogorov scale is believed to have no effect on the flame front because it is too small and too easily dissipated before affecting the flame front. An efficiency correction function is defined to have the correct relation between the theoretical strain of a structure and the actual stretch which this structure induces on a flame. This efficiency function approaches 1 when the I_l/δ_l (I_l is the eddy length scale and δ_l is the flame thickness) increases. ITNFS uses detailed experimental data about intermittency turbulence to determine the distribution of stretch along the flame front. Effects of a complete turbulence flow field are considered by taking into account the existence of a wide range of scales as well as the statistical distribution of the velocity of each scale. Then the stretch effects are integrated over each turbulence scale, from the smallest scale at which the eddies can stretch the flame to the large scale along the flame front. ITNFS also considers the flame quenching by high stretch. Quenching conditions include not only the length and velocity scales needed to quench a flame front but also how long such perturbation scales must be applied on the flame front before actual quenching takes place. In other words, in order to quench a flame, an eddy must have a large velocity as well as a time scale that is larger than flame-time scale to complete the quenching. Reference [17] curve fitted their results in the form of a dimensionless net flame stretch function, Γ_k, with the following form:

$$\Gamma_k = \frac{K_t}{\epsilon/k} = f\left(\frac{u'}{S_L}, \frac{I_l}{\delta_l}\right) = \Gamma_p - b\Gamma_q \tag{2}$$

Here u' is the turbulence intensity, S_L is the laminar flame speed, and Γ_p and Γ_q are the flame production and quench due to the stretch. b is a model parameter. Γ_p has been shown only strongly dependent on I_l/δ_l and weakly on u'/S_L.

The consumption term in the Σ equation is due to the flame surface consumption of the intervening reactants and by mutual interaction of flame fronts [15]. It is proportional to the square of the flame area density. It does not include the quenching effects by the high stretch since it has been included in the K_t term (Eq. (2)). It is modeled as

$$D = \frac{\rho_u (S_L + a\sqrt{k})}{\rho Y_F / Y_{Fu}} \tag{3}$$

Here ρ_u and ρ are densities in unburned mixture and fluid, and Y_F and Y_{Fu} are fuel mass fractions in unburned mixture and fluid. a is a model parameter.

A progress variable equation is also solved in the CFM. Equivalently one can also solve a transport equation for fuel mass fraction,

$$\frac{\partial \langle\rho\rangle \tilde{c}}{\partial t} + \frac{\partial \langle\rho\rangle \tilde{u}_i \tilde{c}}{\partial x_i} = \frac{\partial}{\partial x_i}\left(\Gamma_c \frac{\partial \tilde{c}}{\partial x_i}\right) + \tilde{\omega}_c \tag{4}$$

In this paper two averaging methods are used: conventional Reynolds averaging is denoted by the angle brackets $\langle\ \rangle$, and Favre averaging (a mass-averaging) by the tilde $\tilde{}$ operators. For any quantity Q, the relationship between them is $\tilde{Q} = \langle\rho Q\rangle/\langle\rho\rangle$. A progress variable increases monotonically from zero in unburned mixture to unity in fully burned products. It is usually defined as the following:

$$\tilde{c} = \frac{\tilde{Y}_{Fu} - \tilde{Y}_F}{\tilde{Y}_{Fu} - \tilde{Y}_{Fb}} \tag{5}$$

Here $\tilde{Y}_{Fu}$ is the fuel mass fraction in unburned gas and $\tilde{Y}_{Fb}$ is in burned gas. For one irreversible single-step reaction, $\tilde{Y}_{Fb}$ equals 0 in lean and stoichiometric mixtures and is positive in rich mixtures.

With the assumption of thin-layer combustion, the source term $\tilde{\omega}_c$ is

$$\tilde{\omega}_c = \rho_u S_L \Sigma \tag{6}$$

3 Partially Premixed Coherent Flame Model

In partially premixed combustion, a mixture fraction, z, may be introduced to account for the inhomogeneous fuel mass fraction in the unburned mixture. z, with a value of zero in the oxidizer stream and unity in the fuel stream, is a conserved scalar when there is no phase change,

$$\frac{\partial \langle\rho\rangle \tilde{z}}{\partial t} + \frac{\partial \langle\rho\rangle \tilde{u}_i \tilde{z}}{\partial x_i} = \frac{\partial}{\partial x_i}\left(\Gamma_z \frac{\partial \tilde{z}}{\partial x_i}\right) \tag{7}$$

Then the Favre-average of any quantity Q, such as species mass fractions and temperature, can be fully described by z and c as

$$\tilde{Q}(\tilde{z},\tilde{c};\underline{x},t) = \int_0^1 \int_0^1 Q(z,c) P(z,c;\underline{x},t)\, dz\, dc \tag{8}$$

Here $P(z,c;\underline{x},t)$ is the joint probability density function (PDF). It can be decomposed to a conditional PDF $P_z(z|c;\underline{x},t)$ and a marginal PDF $P_c(c;\underline{x},t)$,

$$P(z,c;\underline{x},t) = P_z(z|c;\underline{x},t) P_c(c;\underline{x},t) \tag{9}$$

By assuming the thin flame at high Damköhler number, we can choose a bimodal form for $P_c(c;\underline{x},t)$,

$$P_c(c;\underline{x},t) = \tilde{c}\,\delta(1-c) + (1-\tilde{c})\,\delta(c) \tag{10}$$

We then have

$$\tilde{Q}(\tilde{z},\tilde{c};\underline{x},t) = (1-\tilde{c}) \int_0^1 Q(z,0) P_z(z|c=0;\underline{x},t)\, dz + \tilde{c} \int_0^1 Q(z,1) P_z(z|c=1;\underline{x},t)\, dz \tag{11}$$

By assuming statistical independence of z and c for $c=0$ and $c=1$, we can obtain

$$\tilde{Q}(\tilde{z},\tilde{c};\underline{x},t) = (1-\tilde{c}) \int_0^1 Q(z,0) P_z(z;\underline{x},t) + \tilde{c} \int_0^1 Q(z,1) P_z(z;\underline{x},t) \tag{12}$$

$$\tilde{Q}(\tilde{z},\tilde{c};\underline{x},t) = (1-\tilde{c})\tilde{Q}_u(\tilde{z};\underline{x},t) + \tilde{c}\tilde{Q}_b(\tilde{z};\underline{x},t) \tag{13}$$

Apparently, one Favre-averaged quantity can be expressed as a linear combination of the Favre-averaged quantities in the unburned and burned states. The unburned state corresponds to the situation where fuel and oxidizer only convect and diffuse but no chemical reaction takes place. Any quantity under this state can be written as a function of the quantity values in the fuel and oxidizer streams, Q_F and Q_O, respectively,

$$\tilde{Q}_u(\tilde{z};\underline{x},t) = Q_O + \tilde{z}(Q_F - Q_O) \tag{14}$$

The turbulent flame under the burned state can be regarded as an ensemble of laminar flamelets [1], and the Favre-averaged quantity is

$$\tilde{Q}_b(\tilde{z},\widetilde{z''^2},\tilde{\chi};\underline{x},t) = \int_0^\infty \int_0^1 Q(z,\chi)P(\tilde{z},\widetilde{z''^2},z;\underline{x},t)P(\chi;\underline{x},t)dzd\chi \tag{15}$$

This is usually tabulated as functions of $\tilde{z}$, $\widetilde{z''^2}$, and $\tilde{\chi}$. Here $\widetilde{z''^2}$ is the mean variance of mixture fraction, and it is obtained from the solution of the transport equation,

$$\frac{\partial\langle\rho\rangle\widetilde{z''^2}}{\partial t} + \frac{\partial\langle\rho\rangle\tilde{u}_i\widetilde{z''^2}}{\partial x_i} = \frac{\partial}{\partial x_i}\left(\Gamma_{z''^2}\frac{\partial\widetilde{z''^2}}{\partial x_i}\right) + 2\Gamma_{z''^2}\frac{\partial\tilde{z}}{\partial x_i}\frac{\partial\tilde{z}}{\partial x_i} - c_\chi\frac{\tilde{\varepsilon}}{\tilde{k}}\widetilde{z''^2} \tag{16}$$

The scalar dissipation of mixture fraction $\tilde{\chi}$ is defined as

$$\tilde{\chi} = c_\chi\frac{\tilde{\varepsilon}}{\tilde{k}}\widetilde{z''^2} \tag{17}$$

Usually a β PDF function is employed for $P(\tilde{z},\widetilde{z''^2},z)$ and a log-normal or a δ function is used for $P(\chi)$.

It is straightforward to extend the tabulation to include the local heat loss by using a heat loss ratio [18],

$$\gamma = \frac{h_a - \tilde{h}}{C_P(T_a - T_u)} \tag{18}$$

where h_a is the adiabatic enthalpy, $\tilde{h}$ is the mean enthalpy, T_a is the adiabatic temperature, and T_u is the unburned temperature. γ is bounded between -1 and 1. In this case an enthalpy equation needs to be solved.

Although Eq. (13) is derived for partially premixed combustion, it can be immediately applied to premixed combustion where z is uniform and χ equals 0. Now if $\tilde{c}$, $\tilde{z}$, and $\widetilde{z''^2}$ are known, Favre-average for quantities such as species mass fraction and temperature can be obtained from Eq. (13). Next we derive the $\tilde{c}$ equation for partially premixed flames starting from a fuel mass fraction equation, while Eq. (4) is only valid for premixed combustion.

In a partially premixed flame, there exist a premixed combustion zone and a nonpremixed combustion zone. Thus, for a transport equation for fuel mass fraction, the source terms include the contributions from both combustion zones. It can be written as

$$\frac{\partial\langle\rho\rangle\tilde{Y}_F}{\partial t} + \frac{\partial\langle\rho\rangle\tilde{u}_i\tilde{Y}_F}{\partial x_i} = \frac{\partial}{\partial x_i}\left(\Gamma_{Y_F}\frac{\partial\tilde{Y}_F}{\partial x_i}\right) - \langle\rho_u\rangle\tilde{S}_L\Sigma(\tilde{Y}_{Fu} - \tilde{Y}_{Fb}) + \tilde{\omega}_{\text{diff}} \tag{19}$$

Here, the first source term is due to the premixed combustion, and the second is due to the nonpremixed combustion. The second term is omitted in Ref. [11]. The contribution of nonpremixed combustion on the fuel mass fraction can be obtained from the look-up flamelet table with ease. However, in order to solve this equation we need to reconstruct the source term $\tilde{\omega}_{\text{diff}}$ from the look-up table. In the following, we will show that this equation can be converted to a progress variable equation where this source from the nonpremixed flame disappears.

From Eq. (5) the Favre-averaged fuel mass fraction is

$$\tilde{Y}_F = \tilde{Y}_{Fu} - \tilde{c}(\tilde{Y}_{Fu} - \widetilde{Y_{Fb}}) \tag{20}$$

The unburned and burned fuel mass fractions follow these two transport equations,

$$\frac{\partial\langle\rho\rangle\tilde{Y}_{Fu}}{\partial t} + \frac{\partial\langle\rho\rangle\tilde{u}_i\tilde{Y}_{Fu}}{\partial x_i} = \frac{\partial}{\partial x_i}\left(\Gamma_{Y_{Fu}}\frac{\partial\tilde{Y}_{Fu}}{\partial x_i}\right) \tag{21}$$

$$\frac{\partial\langle\rho\rangle\tilde{Y}_{Fb}}{\partial t} + \frac{\partial\langle\rho\rangle\tilde{u}_i\tilde{Y}_{Fb}}{\partial x_i} = \frac{\partial}{\partial x_i}\left(\Gamma_{Y_{Fb}}\frac{\partial\tilde{Y}_{Fb}}{\partial x_i}\right) + \tilde{\omega}_{Fb} \tag{22}$$

Equation (13) implies that

$$\tilde{\omega}_{\text{diff}} = \tilde{c}\cdot\tilde{\omega}_{Fb} \tag{23}$$

Combining Eqs. (19)–(23), we can have

$$\frac{\partial\tilde{c}}{\partial t} + u_i\frac{\partial\tilde{c}}{\partial x_i} = \frac{1}{\langle\rho\rangle}\frac{\partial}{\partial x_i}\left(\Gamma_c\frac{\partial\tilde{c}}{\partial x_i}\right) + \frac{\langle\rho_u\rangle}{\langle\rho\rangle}\tilde{S}_L\Sigma + 2\frac{\Gamma_c}{\langle\rho\rangle(\tilde{Y}_{Fu} - \tilde{Y}_{Fb})}\frac{\partial\tilde{c}}{\partial x_i}\frac{\partial(\tilde{Y}_{Fu} - \tilde{Y}_{Fb})}{\partial x_i} \tag{24}$$

This equation is similar to that in Ref. [7]. However, that is derived based on the assumption of a lean mixture and one global reaction, where $\tilde{Y}_{Fb}=0$. This equation is applicable for a more general condition. It can incorporate detailed chemical mechanisms and can be used under lean/rich conditions and with local heat losses.

Equation (24) can be converted to the following form, which is more amenable to most CFD solvers:

$$\frac{\partial\langle\rho\rangle\tilde{c}}{\partial t} + \frac{\partial\langle\rho\rangle\tilde{u}_i\tilde{c}}{\partial x_i} = \frac{\partial}{\partial x_i}\left(\Gamma_c\frac{\partial\tilde{c}}{\partial x_i}\right) + \langle\rho_u\rangle\tilde{S}_L\Sigma + 2\frac{\Gamma_c}{(\tilde{Y}_{Fu} - \tilde{Y}_{Fb})}\frac{\partial\tilde{c}}{\partial x_i}\frac{\partial(\tilde{Y}_{Fu} - \tilde{Y}_{Fb})}{\partial x_i} \tag{25}$$

In this equation the source term due to the nonpremixed flame disappears. It is mainly because this effect has been reflected in the definition of $\tilde{c}$ (Eq. (5)). The salient advantage of using the $\tilde{c}$ equation instead of the $\tilde{Y}_F$ equation is that reconstruction of the diffusion source term is not needed.

4 Experiments and Case Setup of a Lifted H_2/N_2 Jet Flame in a Vitiated Coflow

Figure 1 shows a schematic of the burner [19,20] used in the current simulation. It consists of a jet flame in a coaxial flow of hot combustion products from a lean premixed flow (vitiated flow). Thus, the flame stabilization in hot combustion products can be addressed while the chemical kinetics is decoupled from the complex recirculating flow. The central fuel jet with a diameter $D=4.57$ mm, an averaged velocity of 107 m/s, a temperature of 305 K, and a Reynolds number of 23,600 is surrounded by a slow and hot coflow with a diameter of 210 mm and a velocity of 3.5 m/s. The central fuel is a 25%/75% (by volume) H_2/N_2 mixture. The vitiated coflow with a temperature of 1045 K is products from a H_2/air flame with a mixture fraction of 0.25. Rayleigh measurements were performed for the temperature and Raman and LIF measurements for the mixture fraction and mass fractions of chemical species including O_2, N_2, H_2, H_2O, OH, and NO. Centerline measurements were taken from $x/D=1$ to 38 downstream of the nozzle exit, and the radial profiles were obtained at seven axial locations ($x/D=1$, 8, 9, 10, 11, 14, and 26). The data for a nonreacting jet of air and a lifted flame, both issuing in a

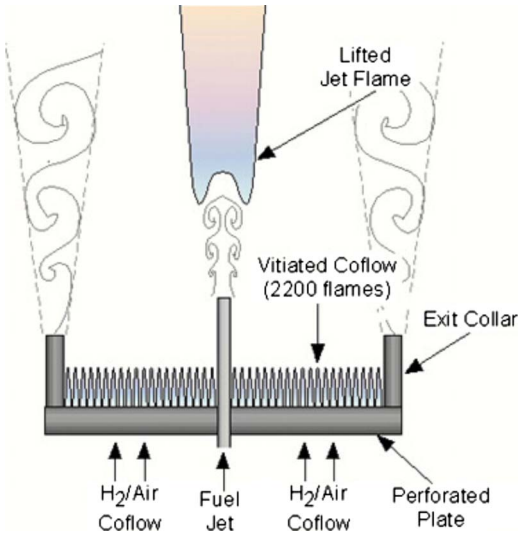

Fig. 1 Schematic of the burner

vitiated coflow, are available. No measurements for velocity field have been made. Further details of the experiments and data may be found in Ref. [19]. Experimental conditions for velocity, temperature, and species mass fractions are shown in Table 1 for both reacting and nonreacting jets.

Table 1 Experimental boundary conditions for the nonreacting and reacting jets

	Nonreacting		Reacting	
	Jet	Coflow	Jet	Coflow
Velocity (m/s)	170	4.4	107	3.5
T (K)	310	1190	305	1045
H_2	0	0	0.02326	0
O_2	0.233	0.1582	0	0.1709
N_2	0.767	0.76	0.97674	0.7643
H_2O	0	0.0818	0	0.0645
OH	0	0	0	0.0003

In this study, the computational domain is 0.07 m long in the fuel jet and 0.2285 m long in the vitiated coflow. Although air is surrounding the vitiated coflow in the experiments, it is not included in the simulation domain since it has been shown that the integrity of the coflow is maintained in the entire test region [20]. An axisymmetric nonuniform grid is used with around 15,000 cells. Finer meshes also have been used, with little difference in the results regarding the species compositions and temperature.

The PCFM model has been implemented in the commercial software STAR-CCM+ [21]. In this investigation a segregated flow solver is employed, which handles the velocity and pressure coupling using a SIMPLE algorithm. An alternative to this in STAR-CCM+ is the coupled flow solver, which solves the conservation equations for mass and momentum simultaneously using a time- (or pseudo-time-) marching approach, and it is more necessary for high speed flows. A second-order scheme is used to treat all the convective terms in the equations. A two-equation k-ε model with standard wall functions has been used for turbulence, and standard values have been used for model coefficients; there has been no "tuning." Radiation is omitted. However, it is straightforward to include radiative heat losses under PCFM methodology.

Digital analysis of reaction systems (DARS) from DigAnaRS LLC (Melville, NY) [22] was used to calculate the laminar flame speed and to generate the laminar flamelet library. DARS calculates the laminar flame speed using a freely propagating 1D laminar flame. For partially premixed combustion, DARS can loop through the equivalence ratio to generate a laminar flame speed table. These are inputs required by the PCFM model in STAR-CCM+. The generation of the laminar flamelet table follows the methodology developed in Ref. [23]. The table is a function of mixture fraction, its variance, and scalar dissipation. When considering radiation, a fourth parameter is included, indicating the amount of heat losses. For both the laminar flame speed and laminar flamelet table, the mechanism developed in Ref. [24] was adopted, which included nine species (H, O, OH, HO_2, H_2O_2, H_2, O_2, H_2O, and N_2) and 19 reactions. Studies of sensitivity to chemical mechanisms are not performed in current work.

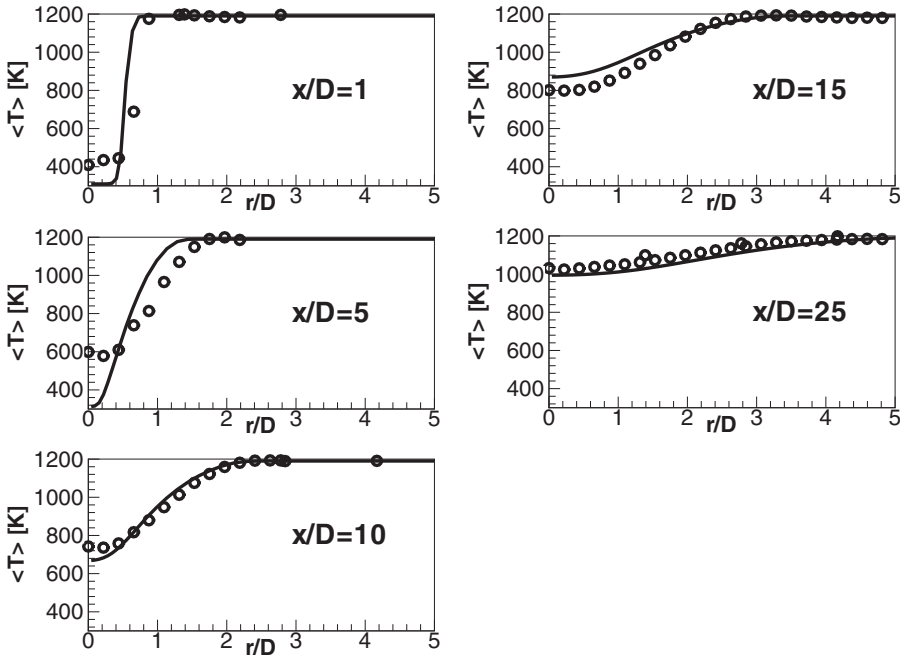

Fig. 2 Computed and measured radial profiles of mean temperature in the nonreacting jet. Symbols: experimental measurements. Lines: computation.

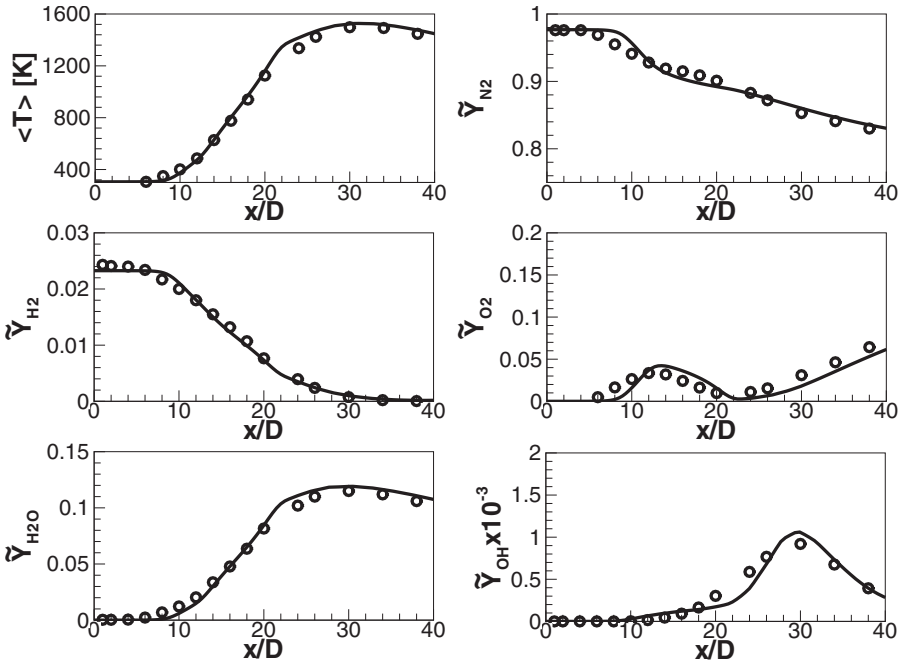

Fig. 3 Computed and measured axial profiles of mean temperature and mean mass fractions of H_2, H_2O, N_2, O_2, and OH at the centerline. Symbols: experimental measurements. Lines: computation.

5 Results and Discussion

First, a nonreacting jet is simulated where the FAD is kept as zero in the PCFM by assigning zero to the boundary condition, initial condition, and source term of the FAD. This reproduces a pure mixing process between the fuel and oxidizer streams. Thus the temperature, density, and species mass fractions are a linear combination of conditions of the fuel jet and the coflow based on the mixture fraction. Figure 2 shows the mean temperature profiles at five locations along the axial direction, $x/D=1$, 5, 10, 15, and 25, respectively. Overall, reasonable agreements between measurements and computations can be observed. This indicates that the current model can predict the mixing process, which is also important in a reactive jet, fairly well. Improvements might be obtained by the standard adjustments of increasing one of the parameters in the k-ε model, $C_{\varepsilon 1}$, from 1.44 to 1.6, as performed in Ref. [25], due to the fact that the k-ε model, with its standard constants, is known to overpredict the spreading rate of round jets. The centerline measurement error due to the thermocouple calibration as acknowledged in Ref. [19] might contribute to the discrepancy of measured and computed temperatures at the centerline.

Next, we present the results for the lifted flame. Simulation results are compared with those from experiments at the jet centerline and axial locations at $x/D=1$, 8, 10, 11, 14, and 26. Figure 3 shows profiles of temperature and mass fractions of species H_2, H_2O, N_2, O_2, and OH at the centerline, while Figs. 4–9 are the radial profiles at six axial locations. In general there is fairly good agreement between the calculations and measurements both in profile shape and peak values, even for composition of minor species OH. There is no combustion at upstream locations (as shown at $x/D=1$, 8, and 10), and temperature and species simply follow a pure mixing process. At the inner region (r/D around 0.5) of these locations, the temperature and compositions of O_2 and H_2O are overpredicted more or less, which is consistent with the underpredictions of compositions of N_2 and H_2. This clearly indicates that the spreading rate of the jet is overpredicted, as also being found out in previous work [25]. Combustion can be observed at location $x/D=11$, from where the agreement between simulation results and experimental measurements starts to deteriorate slightly. We can still see overpredictions of temperature and compositions of O_2 and H_2O, and underpredictions of compositions of H_2 and N_2, at the inner zone of the jet. An opposite trend can be observed at the outer region at $x/D=11$. This again might be related to the shortcomings of the k-ε model used. The OH species shows the biggest discrepancy between the simulation and measurements. In the simulation, the OH composition is set to 300 ppm in the coflow, consistent with the experimental measurements. However, from the experimental data it seems that OH might be oxidized by O_2 in the hot coflow, and the composition of OH at outer region is almost zero. In the simulation a composition of 300 ppm for OH is kept at the coflow and most of the outer region of the jet. Except for this, OH prediction and measurements are in reasonably good agreement. The OH mass fraction has been used as a marker of the average flame lift-off height in both measurements and modeling [20]. The lift-off height was taken to be the location where the mass fraction of OH species reaches 600 ppm. Using this criteria, the lift-off height in our simulation is around $x/D=10.5$, very close to the measurements $x/D=10$.

Now based on the simulation results, we investigate the flame stabilization mechanism of the PCFM for lifted flames. Computed contours of progress variable, flame area density, mixture fraction, and scalar dissipation rate are shown in Fig. 10. The flame starts to develop and stabilizes itself at the location where the progress variable and the flame area density become nonzero (Fig. 11). Combustion occurs where the progress variable is nonzero, as indicated by Eq. (13). The source term of the conservation equation for the progress variable (Fig. 12) is proportional to the flame area density and laminar flame speed (Eq. (6)). Regions where the mixture fraction is close to the stoichiometric state (around 0.4789) exist even far upstream, as shown in the contour of mixture fraction (Fig. 10) and the radial profiles (Fig. 13). These locations will have a laminar flame speed much higher than zero, given the fact that the high temperature in the coflow can even elevate the laminar flame speed. So the only reason for zero progress variable before the flame edge is the zero FAD. FAD evolves according to the balance of convection, diffusion, produc-

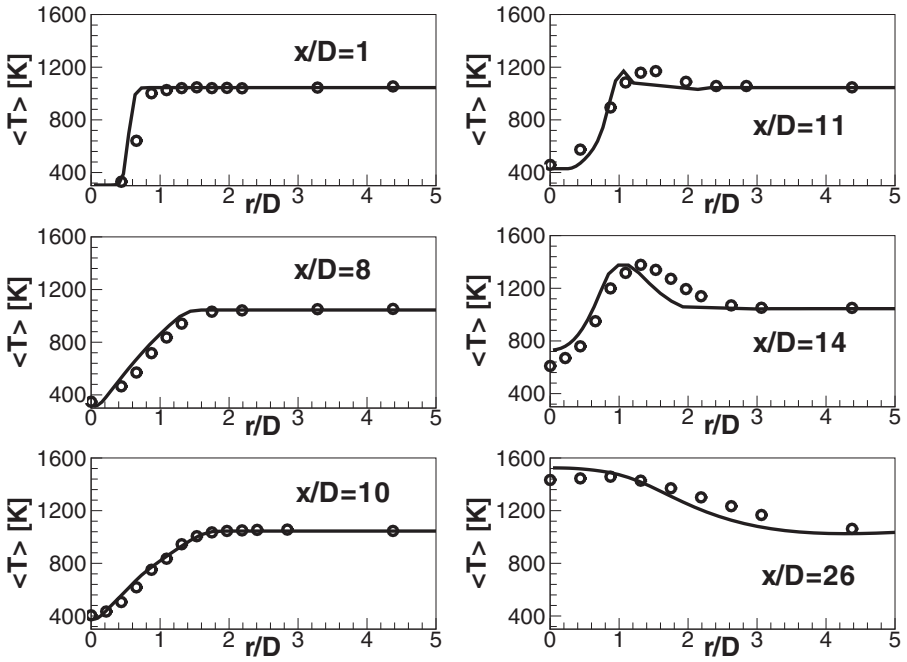

Fig. 4 Computed and measured radial profiles of mean temperature. Symbols: experimental measurements. Lines: computation.

tion, and consumption, as shown in Eq. (1). The turbulent stretch K_t in the production term is dependent on the turbulent time scale, nondimensional velocity ratio u'/S_L, and length ratio I_l/δ_l. At location $x/D=10$, a small amount of FAD has been developed, which results in a nonzero value for the progress variable. Then it increases to a high value at $x/D=11$, which turns the progress variable to nearly 1.0 very quickly. This apparently shows a triple flame configuration. A premixed flame is formed at the flame edge and is stabilized based on the turbulence and chemical reaction. Then a diffusion flame develops between the leftover fuel at the rich side and the leftover oxidizer at the lean side. The diffusion flame determines the burned state, while the progress variable indicates how far a partially premixed mixture is to the burned state and to the unburned state. It is also worth noting that SDR cannot be the sole reason for the lifted-off behavior. DARS calculation shows that only a SDR of more than 2362 can lead to the extinction of the nonpremixed flame. As illustrated in Fig. 14, a high SDR (around 2000 [1/s]) exists at $x/D=1$. At $x/D=8$ it reduces to only 300 [1/s] at maximum. This SDR cannot extinguish a nonpremixed flame, but it certainly affects the diffusion flame behind the flame edge.

Even though a relatively detailed chemical mechanism is em-

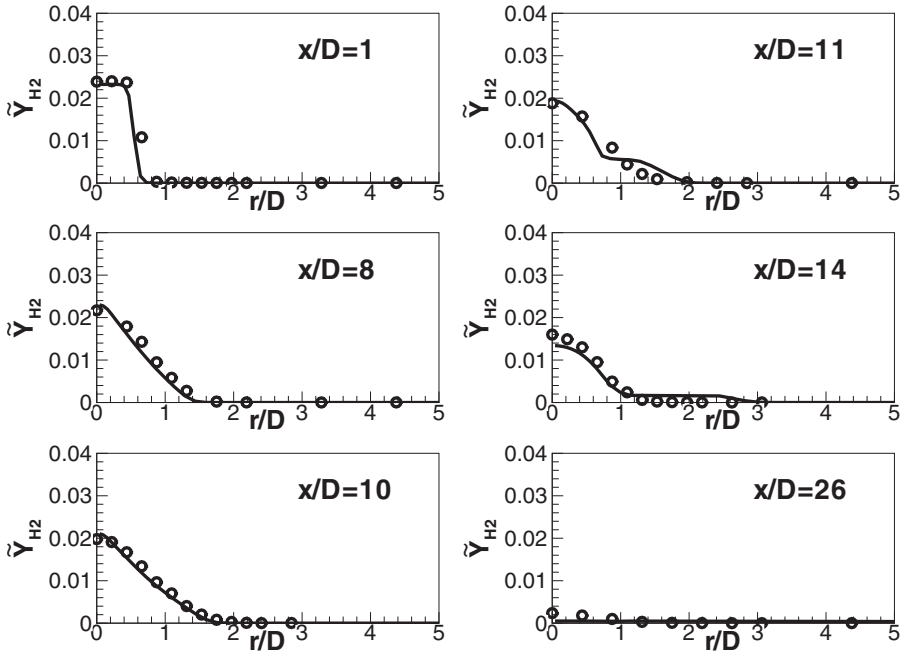

Fig. 5 Computed and measured radial profiles of mean mass fraction of H_2. Symbols: experimental measurements. Lines: computation.

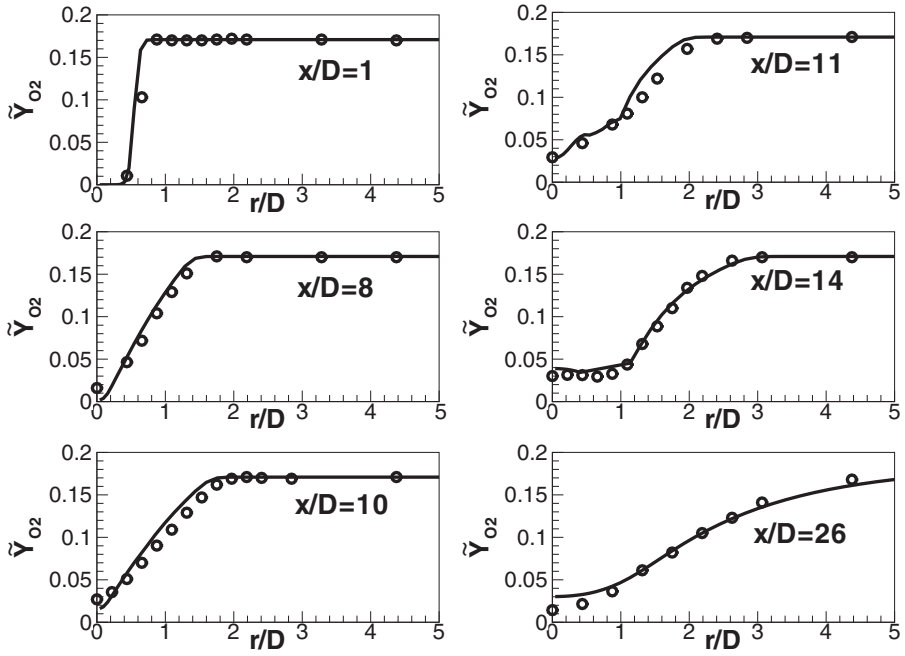

Fig. 6 Computed and measured radial profiles of mean mass fraction of O_2. Symbols: experimental measurements. Lines: computation.

ployed in the simulation, it does not increase computational cost significantly due to the precomputation of a laminar flamelet library and a laminar flame speed table. Compared to earlier numerical investigations performed on this flame using an eddy-dissipation concept (EDC) model [20] and a transported probability density function (TPDF) model [20,25], PCFM offers a salient advantage of high efficiency since it completely separates the detailed chemistry from flow fields based on the flamelet assumption. Thus it can be applied with very large chemical mechanisms without greatly increasing the computational cost.

Modeling parameters in the simulation presented above have the default values from the literature; no sensitivity study is performed in this paper. It has been shown that the k-ε model might be responsible for the overprediction of the spreading rate observed in the simulation, and adjustments of one parameter might improve the prediction [25]. Since the values of FAD mainly control the location of flame stabilization, its modeling parameters (α in Eq. (1), b in Eq. (2), and a in Eq. (3)) might have strong effects on the simulation results. For example it has been shown that the

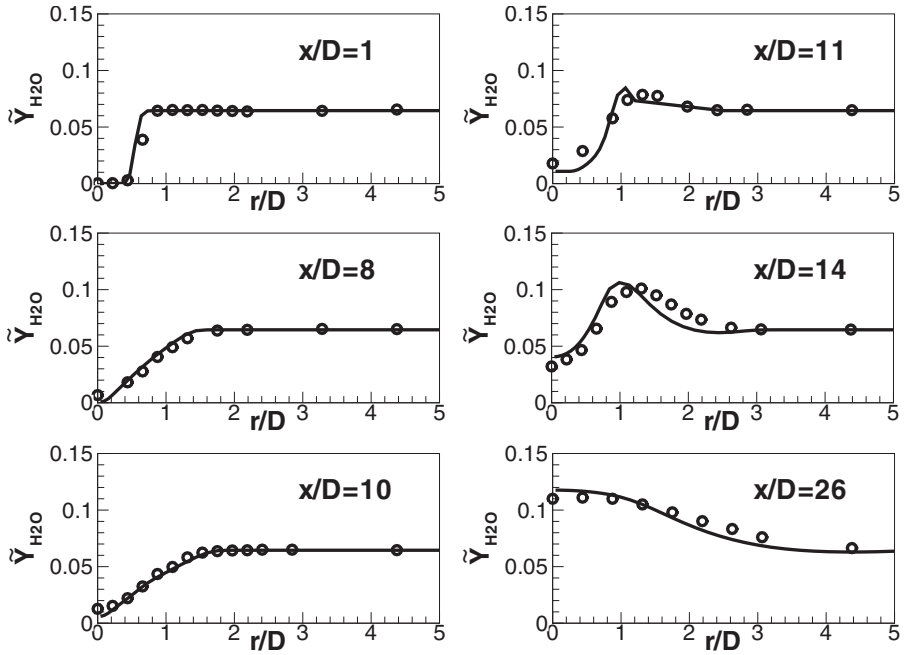

Fig. 7 Computed and measured radial profiles of mean mass fraction of H_2O. Symbols: experimental measurements. Lines: computation.

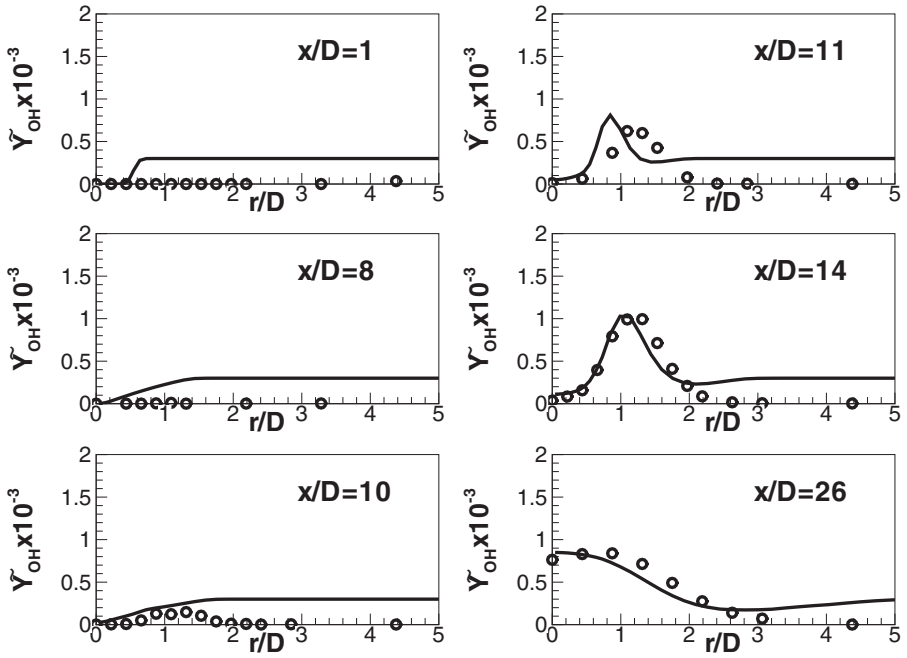

Fig. 8 Computed and measured radial profiles of mean mass fraction of OH. Symbols: experimental measurements. Lines: computation.

turbulent burning velocity is proportional to the square root of α [6]. Different values of α will inevitably change the lift-off height. Different formulations for K_t and D (in Eq. (1)) have been proposed in the literature. Here we only adopted the ITNFS. It might be worthwhile to compare with other formulations. Similar work in the literature is limited to premixed combustion [26]. Finally, influences of chemical mechanism in the PCFM is still an open question. Sensitivity studies of the chemical mechanism on TPDF methods are performed in Ref. [25]. All these can serve as the directions for subsequent studies.

6 Conclusions

In this paper we propose a PCFM model for partially premixed combustion that is seen in many practical combustion systems, such as gas-turbine combustors. By assuming the thin flame at high Damköhler number, it is shown that one Favre-averaged quantity can be expressed as a linear combination of the Favre-averaged quantities in the unburned and burned states. Starting from a transport equation for fuel mass fraction, a progress variable equation is derived, which has the salient advantage that

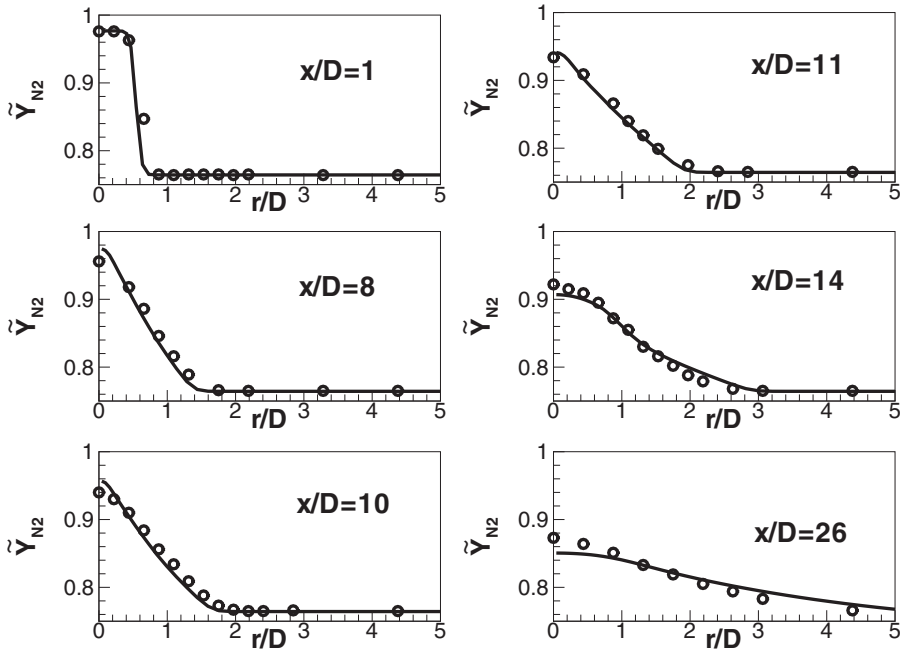

Fig. 9 Computed and measured radial profiles of mean mass fraction of N_2. Symbols: experimental measurements. Lines: computation.

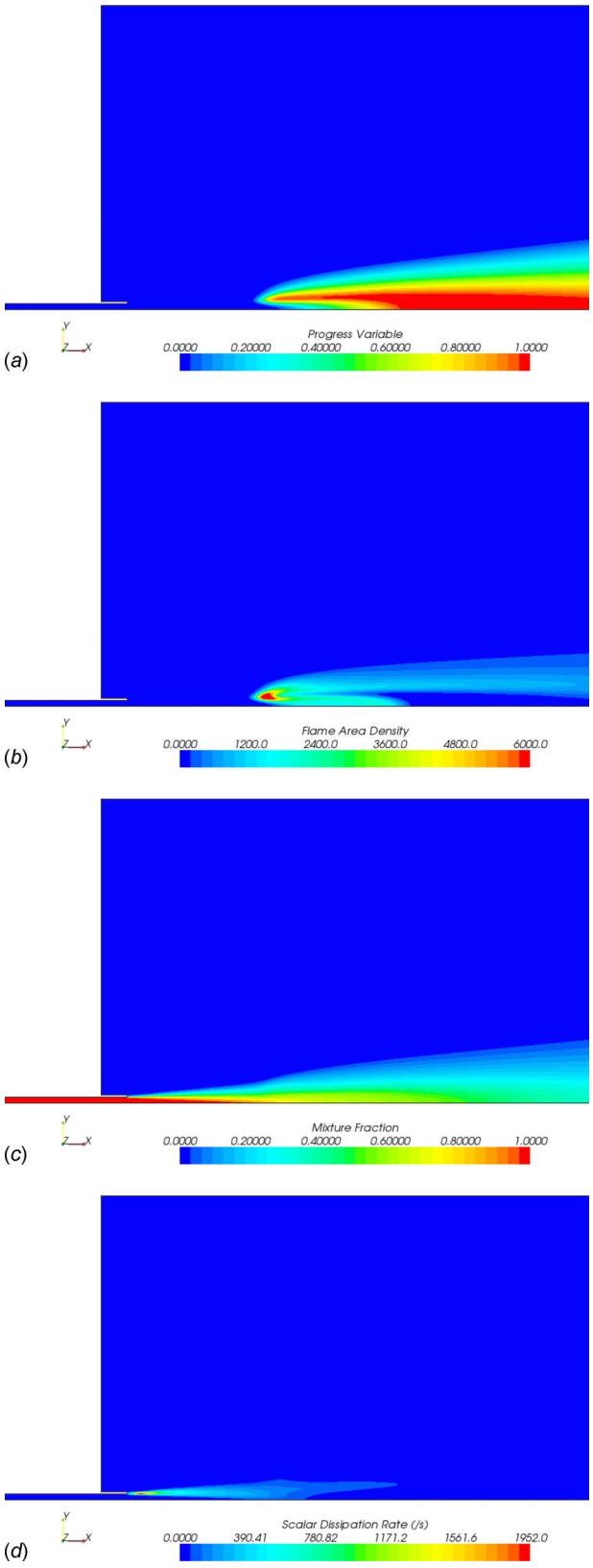

Fig. 10 Computed contours of progress variable, flame area density, mixture fraction, and scalar dissipation rate

reconstruction of the diffusion source term is not needed, while it can fully describe the premixed combustion zone and the nonpremixed combustion zone in partially premixed combustion. PCFM can account for the detailed finite-rate chemistry effects and local

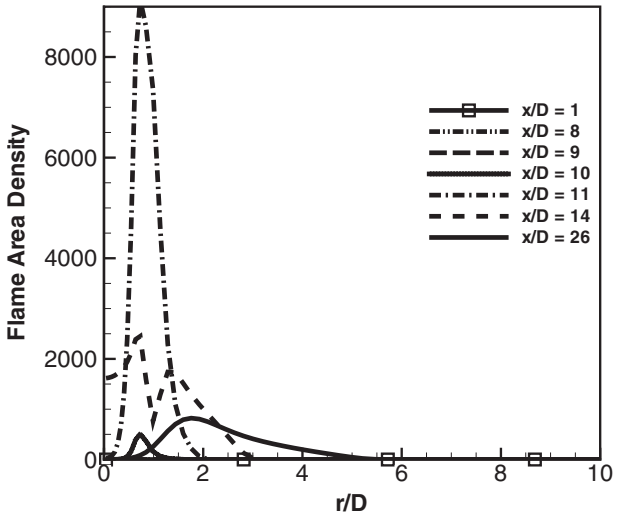

Fig. 11 Computed radial profiles of mean flame area density

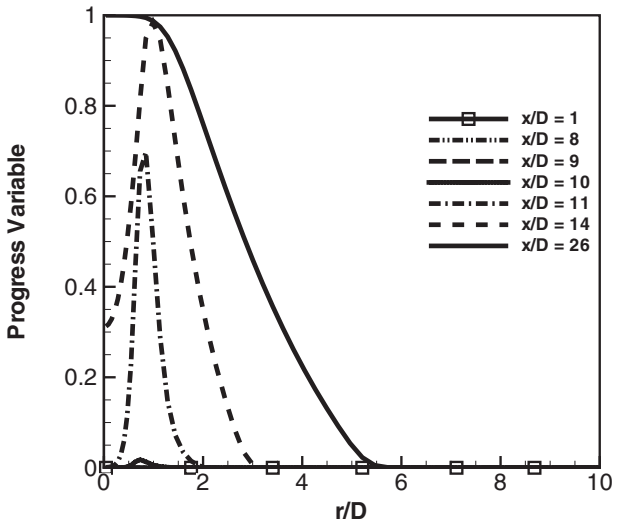

Fig. 12 Computed radial profiles of mean progress variable rate

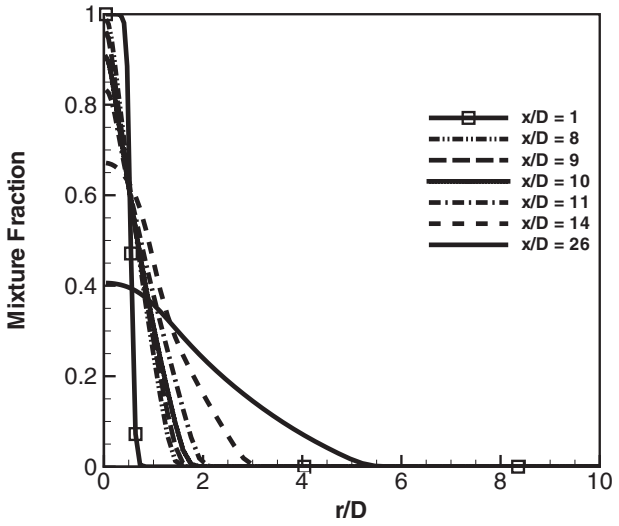

Fig. 13 Computed radial profiles of mean mixture fraction

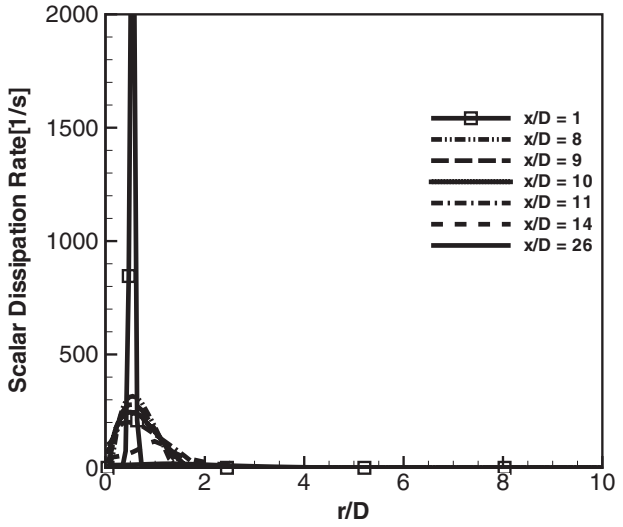

Fig. 14 Computed radial profiles of mean scalar dissipation rate

heat losses while still being computationally efficient by using a precalculated laminar flame speed table and a laminar flamelet library. It is also applicable to highly stratified fuel/oxidizer mixtures. The model is applied to simulate a lifted H_2/N_2 jet flame issuing into a vitiated coflow. Comparison with experimental data shows a good agreement for the temperature and compositions of species. The predicted lift-off height is close to the experimental measurements. The investigation on the flame stabilization mechanism shows that the flame stabilizes at the location where the flame area density starts to develop and is balanced by the convection, diffusion, production, and consumption. It is also found that the scalar dissipation rate is not the sole reason for lift-off behavior. Future research directions on PCFM include sensitivity studies on modeling parameters, formulations for turbulent stretch and consumption terms, and chemical mechanisms.

References

[1] Peters, N., 2000, *Turbulent Combustion*, Cambridge University Press, Cambridge, UK.

[2] Vanquickenborne, L., and Tiggelen, A. V., 1966, "The Stabilization Mechanism of Lifted Diffusion Flames," Combust. Flame, **10**, pp. 59–69.

[3] Eikhoff, H., Lenze, B., and Leukel, W., 1984, "Experimental Investigation on the Stabilization Mechanism of Jet Diffusion Flames," Sym. (Int.) Combust., [Proc.], **20**, pp. 311–318.

[4] Peters, N., and Williams, F. A., 1983, "Liftoff Characteristics of Turbulent Jet Diffusion Flames," AIAA J., **21**, pp. 423–429.

[5] Pitts, W. M., 1988, "Assessment of Theories for the Behavior and Blowout of Lifted Turbulent Jet Diffusion Flames," Sym. (Int.) Combust., [Proc.], **22**, pp. 809–816.

[6] Poinsot, T., and Veynante, D., 2001, *Theoretical and Numerical Combustion*, Edwards, Philadelphia, PA.

[7] Poinsot, T., Veynante, D., Trouve, A., and Ruetsch, G., 1996, "Turbulent Flame Propagation in Partially Premixed Ames," *Proceedings of the Summer Program*, Center for Turbulence Research, pp. 111–141.

[8] Helie, J., and Trouve, A., 1998, "Turbulent Flame Propagation in Partially Premixed Combustion," Sym. (Int.) Combust., [Proc.], **27**, pp. 891–898.

[9] Haworth, D. C., Blint, R. J., Cuenot, B., and Poinsot, T., 2000, "Numerical Simulation of Turbulent PropaneÂcair Combustion With Nonhomogeneous Reactants," Combust. Flame, **121**, pp. 395–417.

[10] Helie, J., and Trouve, A., 2000, Proc. Combust. Inst., **28**, pp. 193–201.

[11] Bondi, S., and Jones, W. P., 2002, "A Combustion Model for Premixed Flames With Varying Stoichiometry," Proc. Combust. Inst., **29**, pp. 2123–2129.

[12] Pope, S. B., 1988, "The Evolution of Surfaces in Turbulence," Int. J. Eng. Sci., **26**, pp. 445–469.

[13] Candel, S. M., and Poinsot, T., 1990, "Flame Stretch and the Balance Equation for the Flame Area," Combust. Sci. Technol., **70**, pp. 1–15.

[14] Trouve, A., 1992, "The Evolution Equation for the Flame Surface Density," Center for Turbulence Research Annual Research Briefs, pp. 393–409.

[15] Duclos, J. M., Veynante, D., and Poinsot, T., 1993, "A Comparison of Flamelet Models for Premixed Turbulent Combustion," Combust. Flame, **95**, pp. 101–118.

[16] Choi, C. R., and Huh, K. Y., 1998, "Development and Validation of a Coherent Flamelet Model for a Spark-Ignited Turbulent Premixed Flame in a Closed Vessel," Combust. Flame, **114**, pp. 336–348.

[17] Meneveau, C. and Poinsot, T., 1991, "Stretching and Quenching of Flamelets in Premixed Turbulent Combustion," Combust. Flame, **86**, pp. 311–332.

[18] Smoot, D., and Smith, P., 1985, *Coal Combustion and Gasification*, Plenum, New York.

[19] Cabra, R., http://me.berkeley.edu/cal/VCB/Data/.

[20] Cabra, R., Myhrvold, T., Chen, J. Y., and Dibble, R. W., 2002, "Simultaneous Laser Raman-Rayleigh-Lif Measurements and Numerical Modeling Results of a Lifted Turbulent H_2/N_2 Jet Flame in a Vitiated Coflow," Proc. Combust. Inst., **29**, pp. 1881–1887.

[21] CD-adapco, http://www.cd-adapco.com/

[22] DARS, http://www.DigAnaRS.com/

[23] Mauss, F., 1998, "Entwicklung eines kinetischen Modells der Russbildung mit schneller Polymerisation," Ph.D. thesis, RWTH Aachen, Aachen, Germany.

[24] Warnatz, J., 1979, "Combustion Chemistry," Ber. Bunsenges. Phys. Chem. **83**, pp. 950–957.

[25] Masri, A. R., Cao, R., Pope, S. B., and Goldin, G. M., 2004, "PDF Calculations of Turbulent Lifted Flames of H_2/N_2 Issuing Into a Vitiated Co-Flow," Combust. Theory Modell., **8**, pp. 1–22.

[26] Prasad, R. O. S., and Gore, J. P., 1999, "An Evaluation of Flame Surface Density Models for Turbulent Premixed Jet Flames," Combust. Flame, **116**, pp. 1–14.

The Influence of Dump Gap on External Combustor Aerodynamics at High Fuel Injector Flow Rates

A. Duncan Walker

Jon F. Carrotte
e-mail: j.f.carrotte@lboro.ac.uk

James J. McGuirk

Department of Aeronautical and Automative Engineering,
Loughborough University,
Loughborough LE11 3TU, UK

The increasing demand to reduce fuel burn, hence CO_2 emissions, from the gas turbine requires efficient diffusion to reduce the system pressure loss in the combustor. However, interactions between prediffuser and combustor can have a significant effect on diffuser performance. For example, the consequence of increased fuel injector flow at a dump gap set using conventional design guidelines has been shown (Walker, A. D., Carrotte, J. F., and McGuirk, J. J., 2007. "Compressor/Diffuser/Combustor Aerodynamic Interactions in Lean Module Combustors," ASME Turbo Expo 2007—Power for Land Sea and Air, Paper No. GT2007-27872) to introduce a destabilizing interaction between fuel injector and upstream components. The present paper concentrates on examining the effects of increased dump gap. Dump gap ratios of 0.8, 1.2, and 1.6 were employed, with each test utilizing the same inlet guide vane, compressor rotor, integrated outlet guide vane (OGV)/prediffuser, and dump geometry. The flow fraction of compressor efflux entering the combustor cowl was set to be representative of lean combustors (50–70%). Measurements were made on a fully annular rig using a generic flame tube with metered cowl and inner/outer annulus flows. The results demonstrate that, with fixed cowl flow, as the dump gap increases, component interactions decrease. At a dump gap ratio of 0.8, the proximity of the flame tube influences the prediffuser providing a beneficial blockage effect. However, if increased to 1.2, this beneficial effect is weakened and the prediffuser flow deteriorates. With further increase to 1.6, the prediffuser shows strong evidence of separation. Hence, at the dump gaps probably required for lean module injectors, it is unlikely the prediffuser will be influenced beneficially by the flame tube blockage; this must be taken into account in the design. Furthermore, with small dump gaps and high cowl flow fraction, the circumferential variation in cowl flow can feed upstream and cause OGV/rotor forcing. At larger dump gaps, the circumferential variation does not penetrate upstream to the OGV, and the rotor is unaffected. The optimum dump gap and prediffuser design for best overall aerodynamic system performance from rotor through to feed annuli is a compromise between taking maximum advantage of upstream blockage effects and minimizing any 3D upstream forcing. [DOI: 10.1115/1.3028230]

Introduction

In future aeroengine gas turbine combustor designs, lean module combustion will be essential in order to achieve required NO_x targets. Consequently, up to 70% of the flow issuing from the compressor may be required to enter the combustor cowl, compared with (typically) 30% in current combustor designs. To accommodate this increased mass flow requirement while maintaining an acceptable pressure drop, lean module fuel injectors will be significantly larger than their conventional air-spray counterparts. This will necessitate geometric changes to the combustor external aerodynamic layout, such as a deeper flame tube and larger dump gaps, potentially increasing the aerodynamic loss due to increased turning within the dump region. Additionally, these geometry and flow split changes and the strongly 3D (circumferential) distribution of the flow into the combustor head compared to current practice are likely to increase the coupling or interaction between the combustor external aerodynamics and upstream components such as the compressor outlet guide vane (OGV)/prediffuser combination and possibly even lead to forcing of the final compressor rotor stage. Indeed previous work by Walker et al. [1] showed that it may be necessary to adopt an integrated design approach in order reduce the aerodynamic loss. By integrating the design of the OGV into the prediffuser and by introducing lean and sweep, the secondary flow structure at exit from the OGV was manipulated promoting radial transfer of higher momentum fluid into the diffuser end wall boundary layers. Not only did this enable the prediffuser area ratio to be increased to 1.8 from a conventional nonintegrated design of 1.6 but it also improved the prediffuser exit profile. The net result was an improvement in the overall flow uniformity and an estimated reduction in the system total pressure loss of approximately 20%. However, although this work was conducted using a generic lean module combustor geometry, the flow split was still typical of conventional systems. In a further piece of work, Walker et al. [2] investigated the effect of increasing the cowl flow from typical air-spray levels to those required for lean combustion (30% and 50–70% of compressor efflux, respectively). The results demonstrated that, with fixed geometry, as the injector flow increases, the performance of the prediffuser and feed annuli suffers. Prediffuser losses increased and at higher cowl flow rates the diffuser moved close to separation. Furthermore, the substantial circumferential variation in cowl flow fed upstream causing notable differences in performance to be observed inline and between injectors at OGV exit, ultimately causing rotor forcing.

The present investigation extends the studies of Walker et al. [1,2] to consideration of the dump gap. The earlier studies em-

Manuscript received April 21, 2008; final manuscript received May 8, 2008; published online February 11, 2009. Review conducted by Dilip R. Ballal.

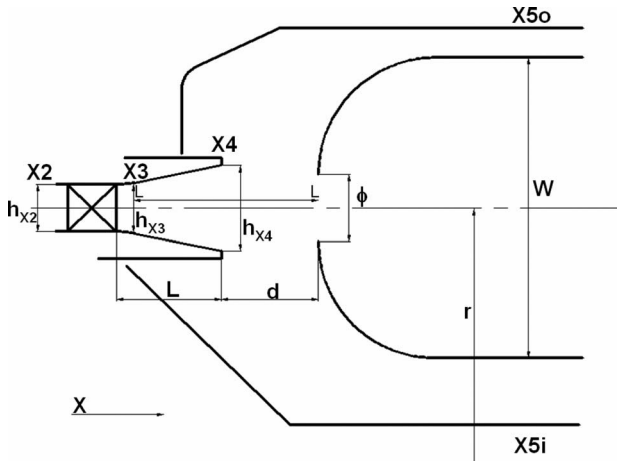

Fig. 1 Geometrical notation

ployed a fixed dump gap typical of conventional combustors. However, it is unlikely that dump gaps defined using existing design rules will be sufficient to accommodate the increased size of lean module fuel injectors. The dump gap is defined as the axial distance (d) from the prediffuser exit plane to the flame tube and is usually expressed as a fraction of the diffuser exit height, d/h_{X4} (for a definition of geometric parameters, see Fig. 1). As this ratio reduces, the proximity of the flame tube induces flow curvature within the prediffuser and a migration of flow toward the end walls. Hestermann [3] showed that this results in a more uniform diffuser exit profile and can suppress flow separation due to the introduction of higher momentum fluid into the boundary layers. Fishenden and Stevens [4] demonstrated that optimizing the dump gap also increases prediffuser pressure recovery but stated that it does not necessarily follow that this will result in lower losses to the feed annuli. Initially, as the dump gap reduces, the beneficial blockage effect increases diffuser performance and reduces the annulus losses. However, as the dump gap reduces beyond a certain point, the annulus loss begins to increase rapidly as the diffuser efflux must now turn in a much shorter space hence incurring a higher loss. Hestermann [3], Fishenden and Stevens [4], and Carrotte and Barker [5] all attempted to optimize the dump gap, in terms of diffuser and annulus performance, but for flame tube depths appropriate to traditional and not lean module combustors. Expressing the flame tube depth as a ratio of diffuser inlet height (W/h_{X3}), their results are summarized in Table 1 and it is noticeable that the optimum dump gap increases with flame tube depth. It is difficult to say how applicable these data are to lean module combustors, hence the current study was undertaken to characterize the extent that the inevitable change in dump gap will alter the external combustor aerodynamics. The experimental study utilizes the same rig as used by Walker et al. [1,2], which comprises a fully annular generic combustor downstream of a single stage axial compressor. The OGV/prediffuser coupling is effected via an advanced integrated OGV/prediffuser geometry [1]. Several traverse planes are used to gather five-hole probe data, which allow the flow structure to be examined through the rotor, OGV, prediffuser, and in the inner/outer annulus supply ducts, quantifying the extent of the component interactions and associated system performance. Several configurations have been investigated where the cowl mass flow has been set at typical lean combustion levels (50–70% of compressor efflux) and the dump gap ratio (d/h_{X4}) varied from 0.8 to 1.6.

Table 1 Optimum dump gap [3–5]

Flame tube depth (W/h_{X3})	Dump gap (d/h_{X4})
3.5	0.6
4.8	0.7–0.8
5.5	0.8–1.0
Lean module combustor >6.0	>1.0?

Experimental Facility

During this project, all experimental data were obtained on a low speed isothermal test facility operating at nominally atmospheric conditions. Figure 2 provides an illustrative sketch, and full details are provided in Ref. [1]. The working section (Fig. 3) comprises a single stage axial compressor (IGV and rotor), an OGV/prediffuser assembly, and a generic representation of a downstream combustion system. Geometric details of the IGV, rotor, and OGV rows are also given in Ref. [1]. The rotor is operated at a fixed nondimensional speed ($N\pi D/\sqrt{(\gamma RT)}$) and mass flow ($\dot{m}\sqrt{(RT)}/AP$), the mass flow being derived from measurements in the calibrated inlet section located upstream of the compressor. The operating conditions corresponded to a fixed flow coefficient $\phi(=V_a/U)$ of 0.403 and a mass flow of approximately 4 kg s^{-1} resulting in an axial velocity through the blade rows of approximately 40 m s^{-1} (Mach number 0.12) and a Reynolds number (based on OGV chord) of approximately 1.6×10^5. The downstream flow distribution to the feed annuli and combustor cowl is controlled by a system of throttles, and a centrifugal fan is utilized as a further throttle to ensure that the axial compressor maintains the desired operating condition. It should be noted that for all the geometry and flow split conditions studied experimentally here, the overall nondimensional rotor speed and mass flow operating conditions remained unchanged.

Test Geometry

Integrated OGV/Prediffuser. The OGV row has 160 vanes, whose geometry includes specific lean, sweep, and camber characteristics that were determined in Ref. [6] by a process of manual computational fluid dynamics (CFD) optimization. This achieves a spanwise blade loading variation that creates secondary flows, which transport higher momentum fluid toward the walls, thus offloading the end wall boundary layers within the prediffuser. Hence, as reported in Ref. [1], this integrated OGV (IOGV) design was able to achieve a prediffuser area ratio of 1.8 without separation while maintaining the same nondimensional length ($L/h_{\text{in}}=2.23$). According to the standard diffuser loading chart of Howard et al. [7], a conventionally designed diffuser would have resulted in separation.

Generic Flame Tube, Cowl, and "Fuel Injectors". The same simple flame tube geometry as used previously by Walker et al. [1,2] was retained in the present work. This presents the IOGV/prediffuser with a representative downstream blockage. Lean module combustors may not feature air admission ports in the annuli, hence no holes were included in the flame tube liner walls. The resultant generic flame tube, illustrated in Fig. 4, has 20 simulated "fuel injectors" represented for convenience by 20 simple holes. The initial area of these holes was set in Ref. 2 to match the effective area of a traditional air-spray injector. As the mass flow through the cowl was increased, the ratio of cowl mass flow to hole area was maintained by increasing the size of the holes. This means that as the mass flow increased the relative acceleration of the dump flow into the cowl did not change. In the current study, cowl flows relevant to lean module levels were employed (50–70% of compressor efflux) with the remaining flow split equally between the annuli. Three dump gaps ratios (d/h_{X4}) were employed beginning with a value of 0.8 as employed in Refs. [1,2]. However, it is unlikely that such a dump gap would provide enough space for a lean module injector. Thus, the dump gap ratio was increased to 1.2 and 1.6 representing values that are large enough to accommodate a typical lean module injector.

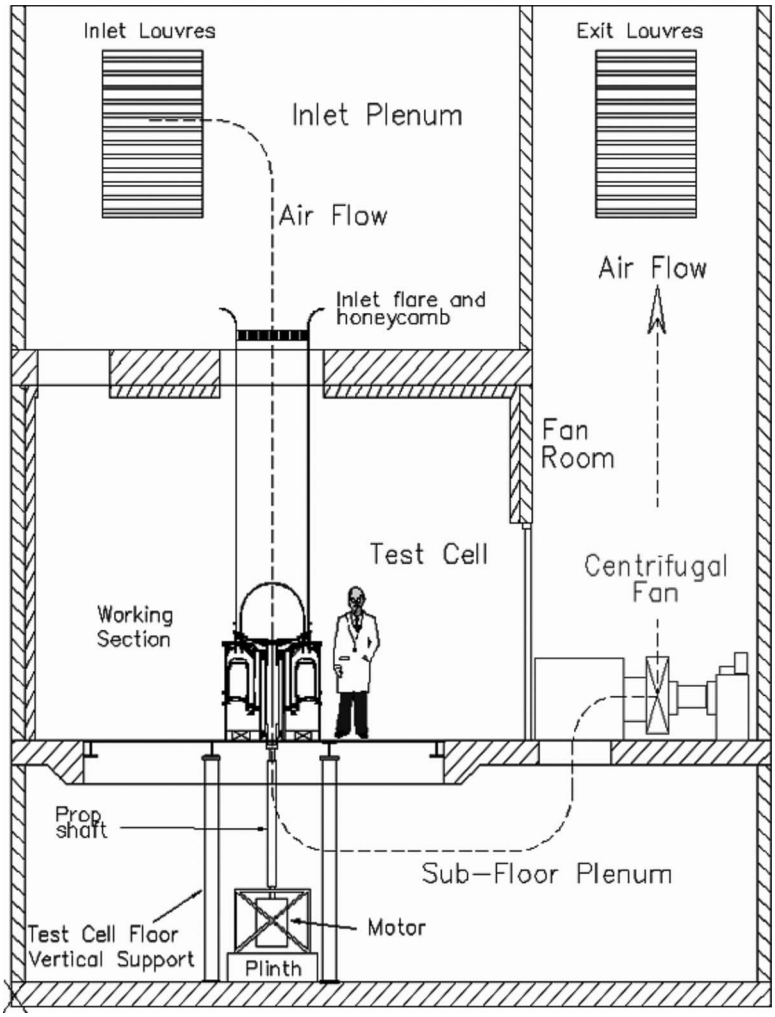

Fig. 2 Test facility

Instrumentation

Probes. Aerodynamic performance was assessed using suitably calibrated miniature five-hole probes as described by Wray and Carrotte [8] and employed in a non-nulled mode to determine the local flow vector and total and static pressures. As indicated in Fig. 3, five-hole probe area traverses could be conducted at rig inlet ($X1$), rotor exit ($X2$), OGV exit ($X3$), prediffuser exit ($X4$), within the inner ($X5_i$) and outer ($X5_o$) feed annuli and at various axial locations within the dump. The probes were traversed in the radial direction using a stepper motor powered linear guide attached to the external casings of the test section. Circumferential traversing was achieved by rotation of the casing or rotation of the IGV, OGV, and flame tube. The flow passage area traversed typically consisted of two OGV passages at stations close to the compressor (e.g., $X2$ and $X3$) but as whole combustor sector information was required further downstream (e.g., at prediffuser exit and within each feed annuli), the traverse area was typically increased to eight OGV passages (one combustor sector).

Data Reduction and Errors. Overall aerodynamic performance is quantified in terms of total pressure loss and static pressure recovery coefficients derived from the five-hole probe area traverses data, corrected to ICAO standard day conditions. Thus, at any measurement plane the mass flow rate and bulk average velocity are defined via

$$\dot{m} = \int \rho U dA = \rho \bar{U} A \tag{1}$$

The mass flow balance on area traverse planes was within $\pm 1\%$ of the rig mass flow entering the test facility measured via a five-hole probe traverse at plane ($X1$). Spatially averaged values of total and static pressures at each plane were derived using the mass-weighted technique described by Klein [9], e.g.,

$$\tilde{P} = \frac{1}{\dot{m}} \int P d\dot{m} = \frac{1}{\rho \bar{U} A} \int P \rho U dA \tag{2}$$

The mass-weighted total pressure loss (λ) and static pressure rise (Cp) coefficients are then defined as

$$\lambda_{1-2} = \frac{\tilde{P}_1 - \tilde{P}_2}{\tilde{P}_1 - p_1}, \quad Cp_{1-2} = \frac{\tilde{p}_2 - \tilde{p}_1}{\tilde{P}_1 - \tilde{p}_1} \tag{3}$$

The mass-weighted total pressures were repeatable to within ± 1 mm H_2O, which amounts to less than $\pm 0.5\%$ of the dynamic pressure at OGV exit. Thus, the repeatability of the derived total pressure loss and static pressure rise coefficients was better than ± 0.005 of the values presented.

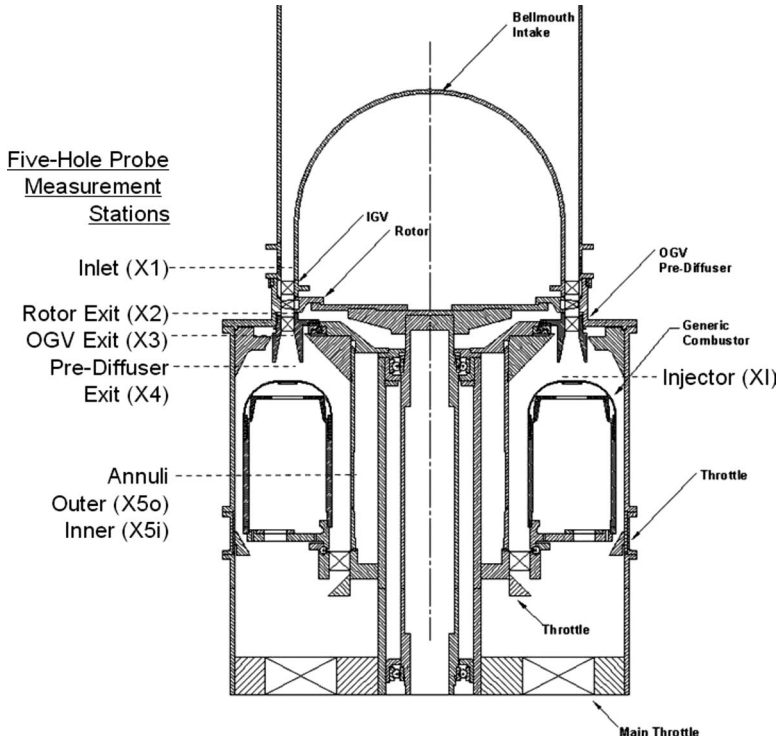

Fig. 3 Measurement planes

Results and Discussion

Prediffuser Exit (*X*4) and Dump Flow. Figure 5 presents normalized axial velocity contours over a full injector sector for dump gap ratios of 0.8, 1.2, and 1.6 and with the flow split entering the cowl set at 70% of the compressor efflux. OGV wakes are still clearly visible at prediffuser exit and exhibit only subtle differences as the dump gap ratio increases. However, the most notable change is the deterioration of the end wall boundary layer flow, particularly on the inner wall. The OGV/prediffuser was optimized for a conventional combustor, with a 30% cowl flow, in the previous study by Barker et al. [6]. Certainly it is shown here not to be the optimum design for the current configuration. With an increase in the cowl flow to 70%, while maintaining the dump gap (Fig. 5(*a*)), the inner wall shows some low velocity regions. But, as the flame tube moves away from diffuser exit, its influence reduces and the low velocity regions become larger and more distinct. Indeed, at the highest dump gap (Fig. 5(*c*)), the inner wall flow shows strong evidence of separation. The changing character of the flame tube blockage effect (acting to stabilize the prediffuser flow) as the cowl flow fraction increases is clearly illustrated in Fig. 6. This displays the prediffuser exit static pressure profile for a fixed dump gap (d/h_{X4}=0.8) for varying cowl flow (30%, 50%, and 70%). At the smallest cowl flow, the pressure profile has the expected "n" shape indicating a positive blockage effect—increasing the pressure at diffuser center relative to the walls, hence driving flow toward the end wall boundary layers. As the cowl flow increases, the suction effect eventually turns the pressure profile into a "u" shape (low pressure at diffuser center relative to the walls), which is not beneficial for end wall boundary layers to remain attached. Pitch-averaged profiles generated from sector data at the highest cowl flow (Fig. 7) further highlight the deterioration of the prediffuser flow with the end wall velocity dropping to less than 10% and 40% of the bulk mean for the inner and outer walls, respectively, at the larger dump gap. Given the data are time averaged it is thought that to avoid any transient separation within the prediffuser a value at the location nearest to the wall of above 40% is desirable. The pitch-averaged static pressure profiles demonstrate that, at this cowl flow, any beneficial back pressure generated by the flame tube is so weak relative to the suction effect that the u shaped pressure profile is present for all dump gaps. Static pressure contours (Fig. 8) also show this trend but reveal, at the smallest dump gap ratio of 0.8, a high

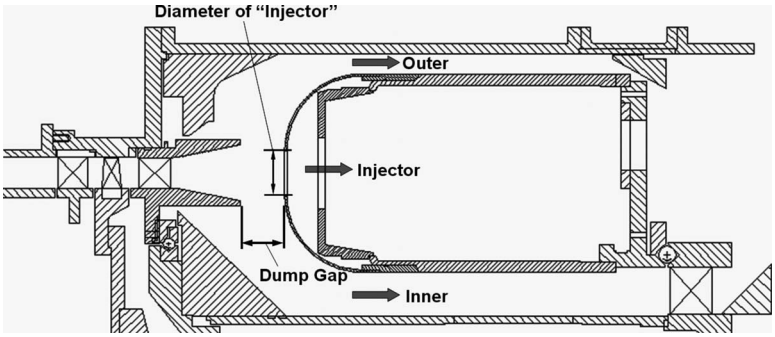

Fig. 4 Combustor details

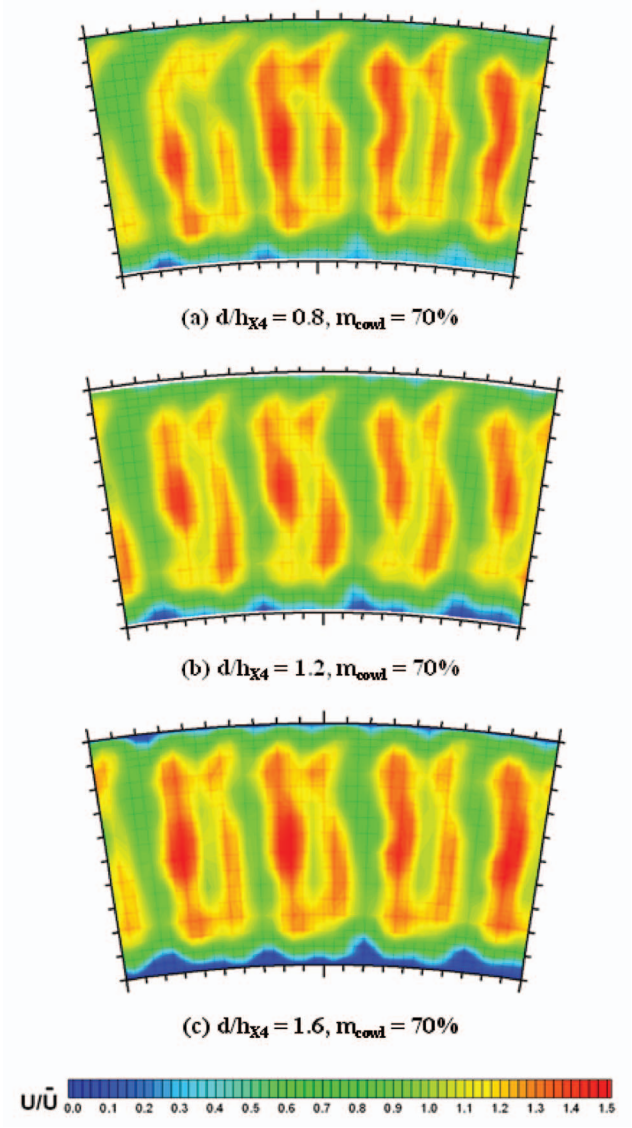

Fig. 5 Axial velocity contours at prediffuser exit (*X4*) (height 65.9 mm, sector angle $\Delta\theta$=18 deg, 8-OGV passages)

azimuthal variation caused by the circumferentially varying downstream pressure field on the combustor head from a high impingement value between cowl holes to a low suction value in line with the holes caused by the high (70%) cowl flow. Velocity data show that, with respect to the overall rig mass flow rate, the indicated mass flow per sector varies from inline to between injectors by $\pm 10\%$. However, as the dump gap ratio increases beyond 1.2, the circumferential static pressure variation decreases suggesting the prediffuser no longer feels any influence of the flame tube. In order to examine this phenomenon, further axial traverses were performed along the prediffuser centerline (line L-L in Fig. 4) inside the prediffuser and dump region at 50% and 70% cowl flows. Figure 9 plots the normalized static pressure for the three dump gap ratios both inline and between the injectors. Also shown on each plot is a numerically generated prediction for the prediffuser with no flame tube which provides data in which the prediffuser flow develops with no influence from flame tube blockage or circumferential variation due to cowl flow. For a dump gap ratio of 0.8, the static pressure inline and between injectors begins to diverge from the data at $d/h_2 \approx -0.35$, suggesting the flow within the prediffuser is influenced by the flame tube. As the dump gap ratio increases to 1.2 and 1.6, the static pressure

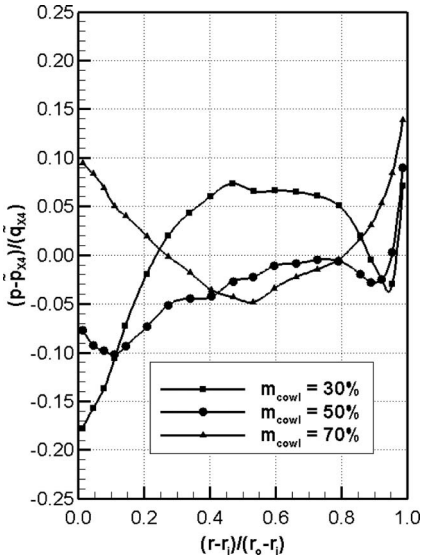

Fig. 6 Pitch average static pressure at prediffuser exit (*X4*), fixed dump (d/h_{X4}), varying flow

only begins to deviate downstream of diffuser exit at $d/h_2 \sim 0.1$ and 0.25, respectively, suggesting that the prediffuser, at least on its centerline, does not feel the any influence from the flame tube blockage. Figure 9 also serves to illustrate the circumferential variation caused by the flow through the injectors and the fact that

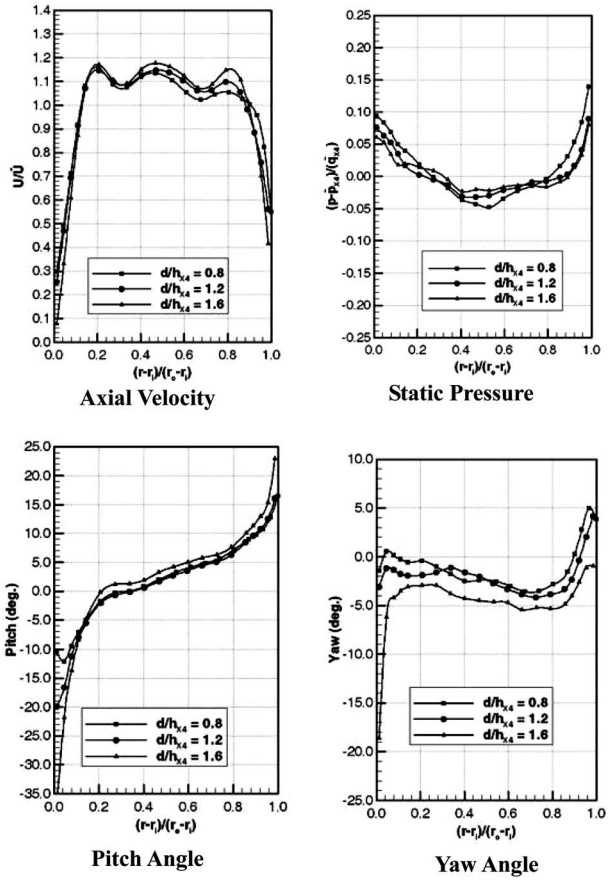

Fig. 7 Pitch averaged profiles at prediffuser exit (*X4*) injector mass flow, m_{cowl}=70%

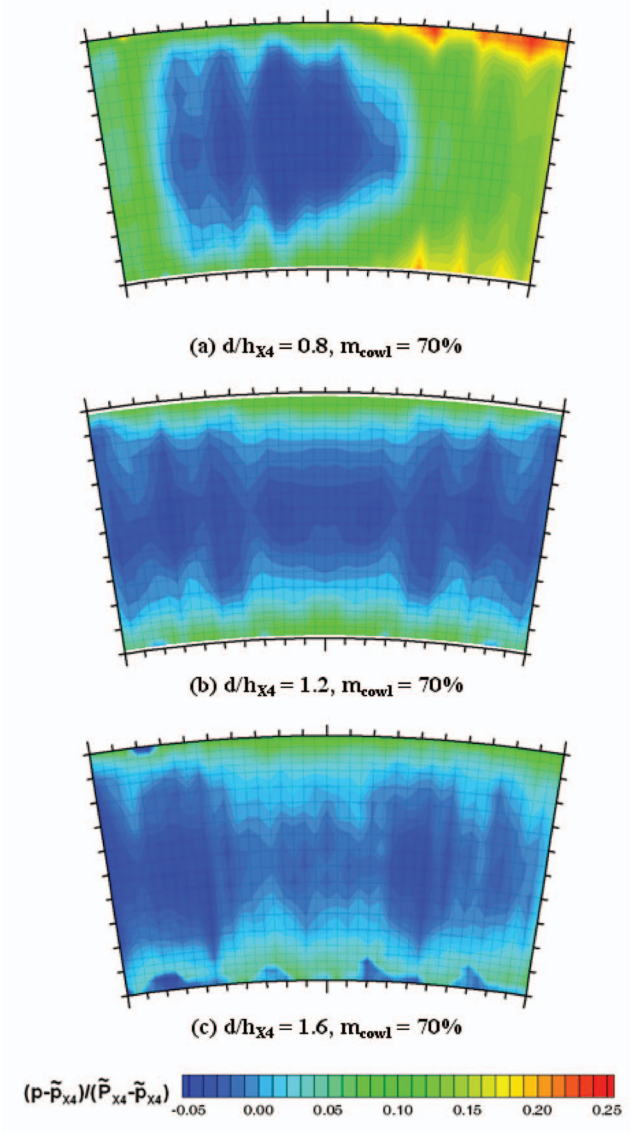

Fig. 8 Static pressure contorus at prediffuser exit (*X4*), (height 65.9 mm, sector angle $\Delta\theta$=18 deg, 8-OGV passages)

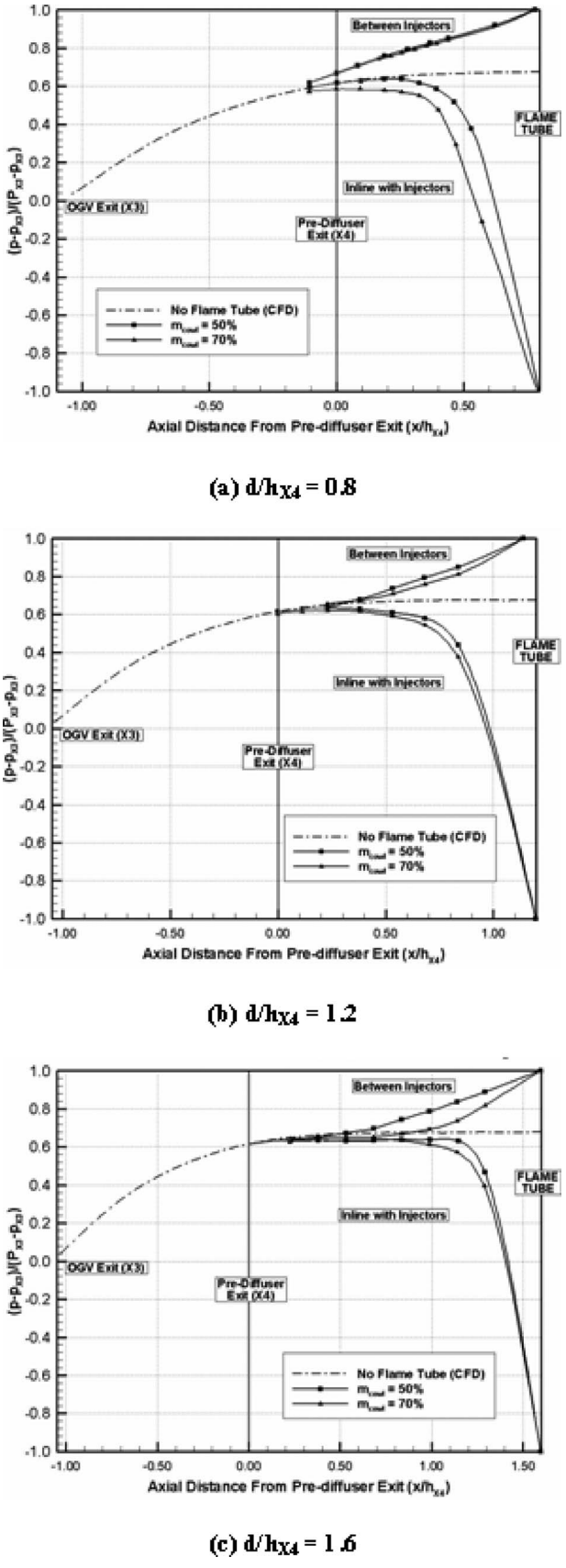

Fig. 9 Dump static pressure (on line L-L in Fig. 3)

this penetrates further upstream at reduced dump gaps with a larger circumferential difference inline and between at the higher flow rates.

Mass-weighted static pressure recovery and total pressure loss coefficients (Table 2) for a complete injector sector with respect to rotor exit do not show a noticeable difference in performance for the two smaller dump gaps due to the fact that the low mass-flow near wall regions do not contribute significantly in the mass-weighted averaging process. However, at the larger dump gap, the near wall flow deterioration is indicated by a clear increase in λ and a decrease in *Cp*.

OGV Exit (*X3*). Axial velocity contours at a cowl mass flow of 70% are plotted for each dump gap in Fig. 10. Data were taken over a two OGV sector both inline and between injectors. Adjacent OGV wakes differ because there is one IGV per two OGV and the IGV wakes persists through the rotor, deepening one of the OGV wakes. Note that the OGV downstream of an IGV wake is the right-hand vane for the inline sector, but the left-hand vane for the between sector. For the two larger dump gaps, where the results above showed that the presence of the flame tube is not felt at the prediffuser exit, there is nominally no difference between the flow field inline and between the injectors. However, Fig. 10 shows that with the smallest dump gap there is a notable differ-

Table 2 Prediffuser performance data (m_{cowl}=70%)

Dump gap (d/h_{X4})	λ_{X2-X4}	Cp_{X2-X4}
0.8	0.163	0.660
1.2	0.165	0.660
1.6	0.179	0.648

Table 3 OGV performance data (m_{cowl}=70%)

Dump gap (d/h_{X4})	λ_{X2-X3}	Cp_{X2-X3}
0.8 (2-OGV sector inline)	0.097	0.39
0.8 (2-OGV sector between)	0.153	0.36
0.8 (injector sector)	0.129	0.38
1.2	0.127	0.38
1.6	0.126	0.38

ence. Indeed the velocity data show that with respect to the overall rig mass flow rate, the indicated mass flow per sector varies form inline to between injectors by 10%. Table 3 details the total pressure loss and static pressure recovery across the OGV.

For the two larger dump gap ratios, performance is maintained. Over a whole injector sector, it would appear that the smallest dump gap produces a similar level of OGV performance. However, if separate 2-OGV sectors are considered, this is not the case. Between injectors, where there is a flow deficit, λ increases from 0.13 to 0.15, whereas inline with injectors, where there is increased flow, λ falls to 0.1.

It is clear therefore that at the smallest dump gap, the circumferential variation generated by the injectors can modify the flow field as far upstream as the OGV. This is also confirmed by Fig. 11, which shows the circumferential variation of a single OGV exit (*X*3) total pressure measurement located at midannulus height between two OGVs as the combustor is rotated through one injector sector. With a dump gap ratio of 0.8 and a cowl flow of 70%, the measured pressure at OGV exit varies significantly and periodically with the injector location. The magnitude of this variation is relatively large at 7% of the local dynamic pressure. At all other dump gaps and flow rates measured, the pressure is constant to within measurement accuracy. Caution must be exercised here in that this measurement is only at midblade passage, midannulus height, so it cannot be unequivocally concluded that the OGV row does not see the variation in circumferential blockage provided by the combustor at other dump gaps and cowl flows, but it is likely to be the case as the midpassage region is probably the least sensitive to downstream conditions.

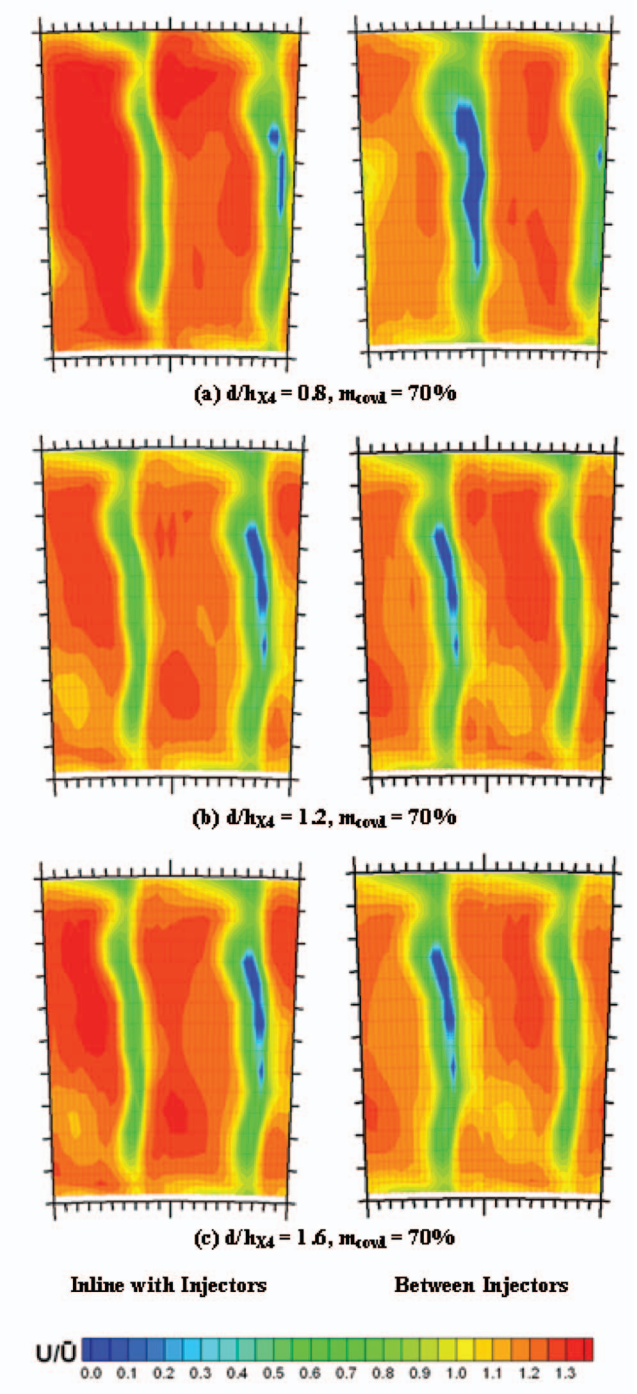

Fig. 10 Axial velocity contours at OGV exit (*X*3) (height =36.6 mm, sector angle $\Delta\theta$=4.5 deg, 2-OGV passages)

Rotor Exit (*X*2)

Figure 12 illustrates clearly that the circumferential variation seen at OGV exit persists into the rotor for a dump gap ratio of 0.8 and a cowl flow of 70%. The plot shows data from a fixed wall static tapping at rotor exit as the combustor was rotated though two sectors. At dump gap ratios of 1.2 and 1.6, there are only slight variations in the measured pressure circumferentially (eight

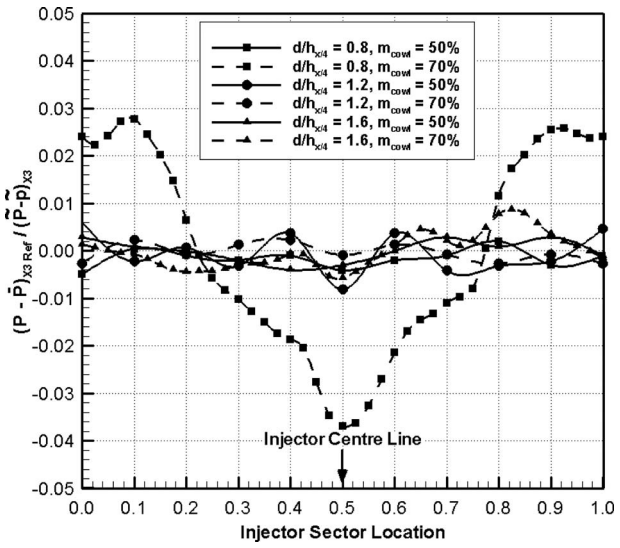

Fig. 11 OGV exit (reference) total pressure

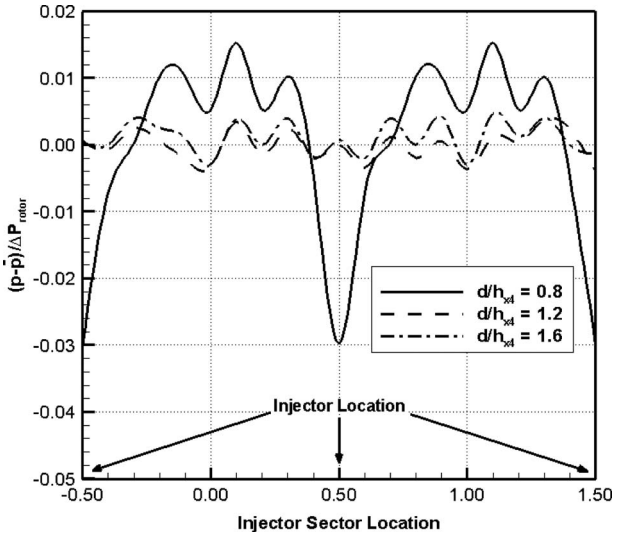

Fig. 12 rotor exit static pressure (m_{cowl}=70%)

peaks and troughs can be seen), with the circumferential resolution in the data being just sufficient to pick up these changes in static pressure, which are associated with the potential field of the OGVs. However, the static pressure for the 0.8 case can be seen to vary significantly from inline to in between injectors, showing a low pressure inline. The variation caused by the cowl flow suction field is much larger than the OGV potential disturbance and is equivalent to approximately 5% of the rotor total pressure rise. This is enough to force the rotor to move locally up or down its characteristic, a fact that is confirmed in the pitch-averaged velocity and total pressure profiles presented in Fig. 13. The forced profiles exhibit a velocity deficit at the tip, a feature not seen in any of the other configurations where the profiles remain unchanged (see also Walker et al. [2]). It is emphasized again that upstream of the rotor, at rig inlet ($X1$) for all configurations, the conditions remained constant.

The fact that the changes in dump gap and downstream flow split can penetrate as far upstream as the rotor and affect its operation is significant, and shows that dump gap design rules to achieve optimum stability and performance for prediffusers will clearly not be transferable between conventional and lean module combustors.

Table 4 Inner annulus performance data (m_{cowl}=70%)

Dump gap (d/h_{X4})	λ_{X2-X5i}	Cp_{X2-X5i}
0.8	0.262	0.71
1.2	0.265	0.72
1.6	0.290	0.70

Annuli ($X5_{i/o}$) and Overall System Performance. Overall system performance was established from measurements in both feed annuli. Traditionally, as the dump gap increases, it would be expected that the turning loss within the dump and hence the annulus loss would reduce. However, at annulus flow splits as low as 15%, the flow entering the annulus is almost entirely comprised of prediffuser boundary layer flow. Already of low quality, this flow is seen to further deteriorate as the dump gap increases and the beneficial blockage effect offered by the flame tube is removed. Indeed, the boundary layers show evidence of separation, which would undoubtedly produce higher levels of turbulence, which would, in turn, increase losses in the shear layer passing around the flame tube head. Tables 4 and 5 detail the mass-weighted performance and confirm that as the dump gap ratio increases from 0.8 to 1.6, the loss increases in both the inner and outer annuli from 26% to 29% of rotor exit dynamic. Further the flow becomes much less uniform as illustrated by normalized axial velocity contours plotted in Figs. 14 and 15. However, associated with the low flow rate, the velocity in the annuli is low (Mach number ~0.02) and consequently the absolute magnitude of the variation is not excessive. For example, Fig. 16 plots contours of total pressure loss coefficient (with respect to rotor exit ($X2$)) at a dump gap ratio of 1.6. This configuration results in the greatest nonuniformity in the velocity field but the figure shows that the total pressure loss varies by less than 2% of its mean value.

Conclusions

The effect on combustion system external aerodynamics of increasing the dump gap from a typical air-spray injector value to

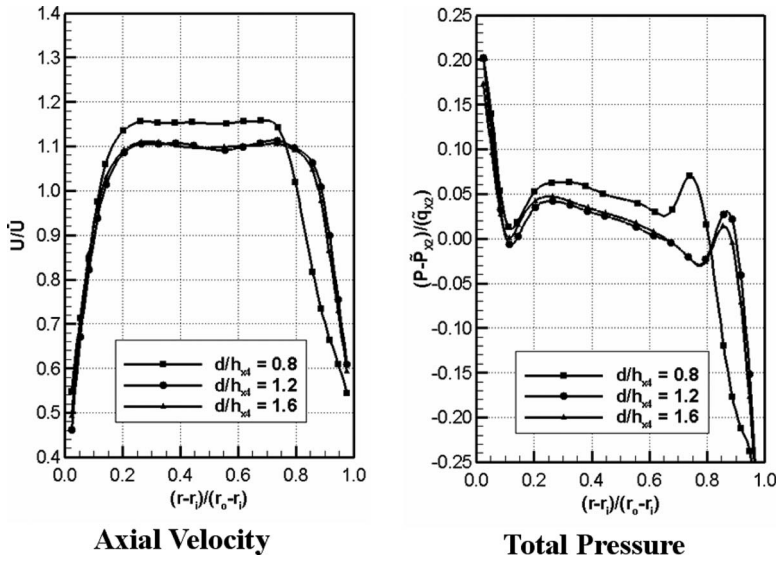

Fig. 13 Pitch averaged profile at rotor exit ($X2$) cowl mass, flow, m_{cowl} =70%

Table 5 Outer annulus performance data (m_{cowl}=70%)

Dump gap (d/h_{X4})	λ_{X2-X5o}	Cp_{X2-X5o}
0.8	0.263	0.72
1.2	0.268	0.72
1.6	0.291	0.69

values typical of lean module injectors has been studied. Dump gap ratios of 0.8, 1.2, and 1.6, were employed with each test utilizing the same inlet section, IGV, rotor and integrated OGV/prediffuser. The flow fraction of compressor efflux entering the combustor cowl was set to representative lean module levels (50–70%). From the results presented here, the following conclusions can be made.

- At a dump gap ratio (d/h_{X4}) of 0.8, typical of an optimum value for conventional combustor systems, the proximity of the flame tube influences the flow within the prediffuser providing a beneficial blockage effect. However, with an increase to 1.2, possibly needed for access reasons for a lean module injector, the effect is negligible and the prediffuser flow deteriorates. With a further increase to 1.6, the prediffuser no longer feels any influence from the flame tube and shows strong evidence of separation. Hence, at the magnitude of dump gap required for lean module injectors, it is unlikely the prediffuser will "feel" any benefit from the flame tube blockage. This will certainly influence prediffuser design rules, perhaps enforcing more conservative designs.
- The high cowl flow rates of lean module combustors generate a strong circumferential variation in the flame tube head static pressure field. At small dump gaps, this is strong enough to feed upstream through the prediffuser affecting OGV performance and ultimately forcing the rotor. Note that this implies in the present experiment that the compressor moves locally up/down its characteristic as a result of the downstream pressure changes, while keeping the overall flow coefficient constant. However, at larger lean module

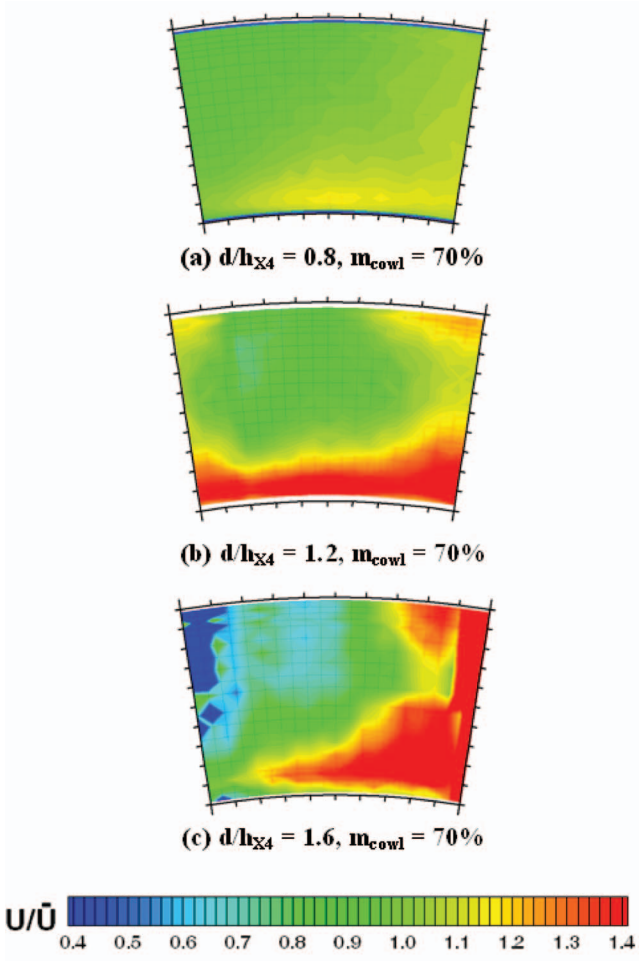

Fig. 14 Axial velocity contours in inner annulus ($X5_i$) (sector angle $\Delta\theta$=18 deg)

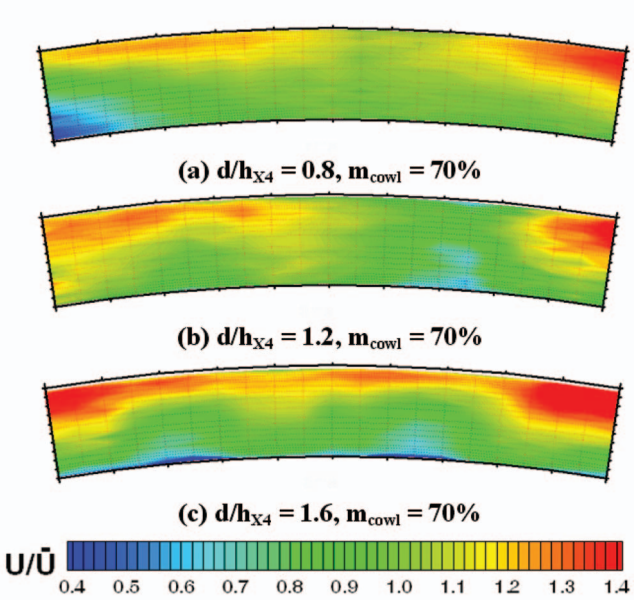

Fig. 15 Axial velocity contours in outer annulus ($X5_o$) (sector angle $\Delta\theta$=18 deg)

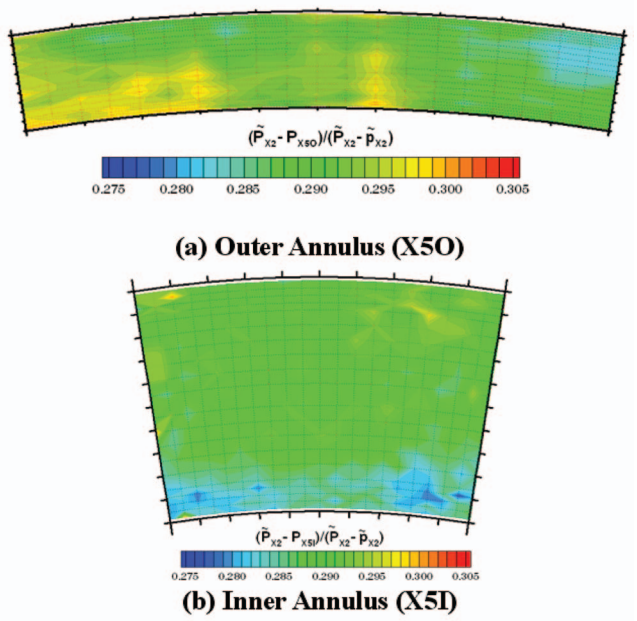

Fig. 16 Loss contours in the feed annuli ($X5$) (d/h_{X4}=1.6, m_{cowl}=70%, sector angle $\Delta\theta$=18 deg)

dump gaps, the circumferential variation does not penetrate as far upstream as the OGV and the rotor operating condition is unaffected.
- System performance from rotor through to feed annuli is a function of the amount of turning in the dump in conjunction with the condition of the flow at prediffuser exit, particularly the boundary layer. As the dump increases, the turning loss should reduce but here degradation in the prediffuser flow negates this causing a slight increase in loss and a decrease in flow uniformity.
- The present set of experiments has concentrated on a constant flow coefficient case corresponding to the deign condition of the system. It would also be of interest to know the sensitivity of optimum dump gap to off-design operating conditions, and this should be the subject of future work.

Acknowledgment

The financial support of the European Union under Contract No. F-AST3-CT-2003-502961 (INTELLECT_DM) is gratefully acknowledged. The authors would also like to express their appreciation to A. Fardoe, L. Monk, and W. Niven for their help in the construction of the test facility.

Nomenclature

A = passage area
AR = area ratio
Cp = static pressure rise coefficient
d = distance, dump gap
h = annulus passage height
L = diffuser length
$\dot{m}$ = mass flow rate
N = rotor speed
P, p = local total or static pressure
R = gas constant (perfect gas law)
r = radius relative to rig centerline
r_i, r_o = inner casing, outer casing radius
T, t = total or static temperature
U = rotor midpassage blade speed
V_a = midpassage axial velocity
x = axial distance
W = flame tube depth
α = kinetic energy flux coefficient
ϕ = flow coefficient (va/U)
ρ = density
λ = total pressure loss coefficient

Subscripts

$X1$ = rotor inlet traverse plane
$X2$ = rotor exit/OGV inlet traverse plane
$X3$ = OGV exit traverse plane
$X4$ = prediffuser exit traverse plane
$X5_{i/o}$ = inner/outer annulus traverse plane

Superscripts

$-$ = area weighted spatially averaged mean value
$\sim$ = mass-weighted spatially averaged mean value

References

[1] Walker, A. D., Carrotte, J. F., and McGuirk, J. J., 2007, "Enhanced External Aerodynamic Performance of a Generic Combustor Using an Integrated OGV/Pre-Diffuser Design Technique," ASME J. Eng. Gas Turbines Power, **129**(1), pp. 80–87.
[2] Walker, A. D., Carrotte, J. F., and McGuirk, J. J., 2007, "Compressor/Diffuser/Combustor Aerodynamic Interactions in Lean Module Combustors," ASME Paper No. GT2007–27872.
[3] Hestermann, R., Kim, S., and Wittig, S., 1991, "Geometrical Dependence of the Fluid Dynamic Parameters of Plane Combustor Model Diffusers," *Proceedings of the International Symposium on Air Breathing Engines*, Paper No. ISABE 91-7105, pp, 995–1001.
[4] Fishenden, C. R., and Stevens, S. J., 1977, "Performance of Annular Combustor-Dump Diffusers," J. Aircr., **14**, pp. 60–67.
[5] Carrotte, J. F., and Barker, A. G., 1994, "Annular Dump Diffuser Systems, Part II: The Combined Effects of Shortened Pre-Diffusers and Dump Gap Variation," Loughborough University, Internal Report No. TT94R07.
[6] Barker, A. G., Carrotte, J. F., Luff, J., and McGuirk, J. J., 2003, "D1.1 Design of an Integrated OGV/Diffuser System," Loughborough University, Report No. TT03R01.
[7] Howard, J. H. G., Henseler, H. J., and Thornton-Trump, A. B., 1967, "Performance and Flow Regimes for Annular Diffusers," ASME New York, 67-WA/FE-2.
[8] Wray, A. P., and Carrotte, J. F., 1993, "The Development of a Large Annular Facility for Testing Gas Turbine Combustor Diffuser Systems." Paper No. AIAA-93-2546.
[9] Klein, A., 1995, "Characteristics of Combustor Diffusers," Prog. Aerosp. Sci., **31**(9), pp. 171–271.

Analysis of NO_x Formation in a Hydrogen-Fueled Gas Turbine Engine

Peter Therkelsen
Tavis Werts
Vincent McDonell
Scott Samuelsen

UCI Combustion Laboratory,
University of California,
Irvine, CA 92697-3550

A commercially available natural gas fueled gas turbine engine was operated on hydrogen. Three sets of fuel injectors were developed to facilitate stable operation while generating differing levels of fuel/air premixing. One set was designed to produce near uniform mixing while the others have differing degrees of nonuniformity. The emission performance of the engine over its full range of loads is characterized for each of the injector sets. In addition, the performance is also assessed for the set with near uniform mixing as operated on natural gas. The results show that improved mixing and lower equivalence ratio decrease NO emission levels as expected. However, even with nearly perfect premixing, it is found that the engine, when operated on hydrogen, produces a higher amount of NO than when operated with natural gas. Much of this attributed to the higher equivalence ratios that the engine operates on when firing hydrogen. However, even the lowest equivalence ratios run at low power conditions, higher NO was observed. Analysis of the potential NO formation effects of residence time, kinetic pathways of NO production via NNH, and the kinetics of the dilute combustion strategy used are evaluated. While no one mechanism appears to explain the reasons for the higher NO, it is concluded that each may be contributing to the higher NO emissions observed with hydrogen. In the present configuration with the commercial control system operating normally, it is evident that system level effects are also contributing to the observed NO emission differences between hydrogen and natural gas. [DOI: 10.1115/1.3028232]

Introduction

Gas turbine engines designed to operate on various fuel stocks are available commercially. Most commonly natural gas and liquid kerosene are used to fuel gas turbine engines [1]. Opportunity fuels such as gases produced from landfills and anaerobic digesters have become popular recently due to both increased criteria pollutant control that restricts the ability to simply vent these gases to the atmosphere and the economic benefits of their conversion to useful electricity and waste heat [2]. Often, the quantities of these fuels available warrant relatively small engines. As a result, engines producing 30 to 250 kW ("microturbines" (MTGs)) are of interest for many of these applications. These fuels typically contain large quantities of carbon dioxide and nitrogen compared to natural gas. Studies of MTGs operated with these low energy-containing fuels have shown that emission levels of criteria pollutants including carbon monoxide and oxides of nitrogen are influenced by the same control techniques developed for engines fueled with natural gas.

With economic and political drivers in place, hydrogen has seen an increase in applications to a wide range of power generation devices. These include both large-scale gasification/power generation plants and distributed generation devices. Historically hydrogen has seen limited use in gas turbine engines though research has been documented.

The National Advisory Committee for Aeronautics conducted tests of a kerosene-fueled engine with hydrogen [3]. These tests were conducted with an aero-engine onboard an aircraft at altitude. These tests focused on engine efficiency and relight abilities with regard to altitude. The hydrogen engines were better able to maintain a reaction and restart after blowout at high altitudes. The superior combustion properties of hydrogen were exploited to reduce the combustor length by 40% compared to the kerosene combustor.

Nomura et al. [4] conducted atmospheric testing of a liquid fired can combustor with hydrogen. These tests utilized a 202 kW gas turbine combustor. The kerosene fuel supply system was removed, and a hydrogen flow metering system was installed. Data were obtained on pressure losses of the fuel system, ignition performance, temperature distributions, combustion efficiency, liner wall temperature distributions, NO_x emission levels, noise levels, and operating performance. The conversion from liquid fuel system to hydrogen was not found to be complicated. A swirler type injector, as well as an angled cone injector with small holes, was used. The cone type injector was found to degrade quickly due to its protrusion into the combustion chamber. Combustor efficiency was not reduced with hydrogen operation. While noise levels did not increase with hydrogen, emissions of NO_x were found to be greater than those produced with kerosene combustion. To reduce NO_x emission levels new fuel nozzles were recommended.

Pratt and Whitney Canada tested two liquid fired can combustors in laboratory bench tests with hydrogen [5]. This work extended that done by Nomura et al. by elevating the pressure of the combustors up to 1.0 MPa. For each combustor liner two different types of injectors were used. The research showed that a liquid fired can combustor could be retrofitted with a different injector to operate with hydrogen. Issues of uneven liner temperatures and increased NO_x levels compared to liquid Jet-A operation were noted. The benefits of increased combustion efficiency and ease of ignition were also seen. Liner geometry modifications to reduce reaction zone temperatures and residence times were suggested as next steps to reduce NO_x emissions.

The utilization of pure hydrogen in a gas turbine poses certain challenges that have been outlined [6,7]. The nature of hydrogen to react easily and quickly has led to concern of flashback and autoignition for premixed systems. In addition hydrogen reacts on average 126 K hotter than natural gas for an equal equivalence

Manuscript received April 25, 2008; final manuscript received April 28, 2008; published online February 19, 2009. Review conducted by Dilip R. Ballal. Paper presented at the ASME Turbo Expo 2008: Land, Sea and Air (GT2008), June 9–13, 2008, Berlin, Germany.

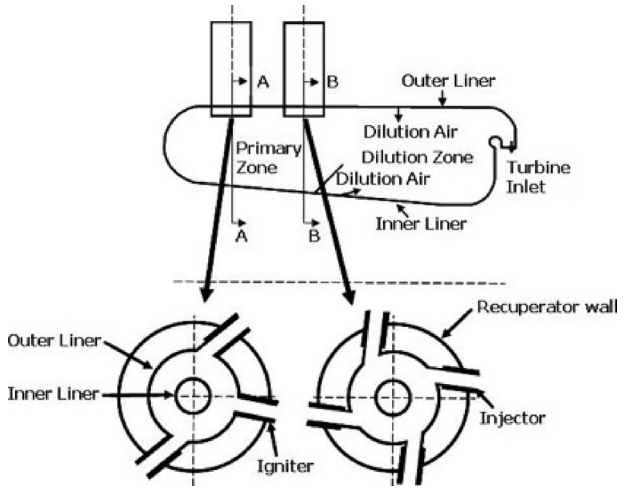

Fig. 1 C60 combustor outline with injector plane cross section

ratio [7]. Emissions of NO_x from a stoichiometric hydrogen reaction have been shown to exceed current regulatory limits [6].

Measurements of NO have been reported for a retrofitted natural gas MTG operated on hydrogen [7]. The emission levels were found to be 10–100 times greater than those produced by the commercial MTG operating on natural gas. Equivalence ratio and fuel/air mixing were both shown to play a role in the generation of relatively high NO levels. This study went on to conclude that further improved mixing should result in further NO emission reductions. The present work extends this earlier work by achieving the refined mixing, characterizing the subsequent emissions, and also discusses in detail the NO emission characteristics observed.

Approach

To accomplish this, the following steps are taken:

- characterize three unique injection systems for fuel/air mixing at various power loads
- operate the MTG with each of the injection systems over the full load range measuring performance characteristics and stack emission levels
- operate the MTG on natural gas using the injector set resulting in the lowest emissions when operated on hydrogen
- evaluate the effect of residence time, chemistry, and overall combustor configuration on the relative levels of NO_x formation observed.
- operate the MTG on a varying mixture of natural gas and hydrogen at full load to measure the effects on stack emission levels.

Experiment

A brief overview of the experimental apparatus and numerical methods used in this study is provided below.

Capstone C60 Microturbine. The Capstone C60 is a commercially available natural gas fueled recuperated Brayton cycle engine. It has been extensively studied when operating with natural gas as well as other fuels such as digester gas and landfill gas [2,7,8].

Air enters the C60 and is passed through a recuperator. It is then compressed via a radial compressor to a pressure of approximately 4 atm. The air enters the engine in one of three ways—as primary zone combustion air and as part of two dilution zones. The manufacturer quantified this flow split, allowing calculation of combustor primary zone equivalence ratio. The quantified flow split information is proprietary. The combustor, diagramed in Fig. 1, contains six injectors tangentially inserted on two planes. The six injectors are fuel staged throughout the operational load of the engine. All injectors flow air regardless of fuel flow. The first plane contains two injectors. These injectors are always fueled during engine operation. The remaining four injectors are located on the second plane. These injectors are fueled based on engine power demand. This fuel staging creates a quench effect when some injectors are not fueled. Previous work [8] showed that this effect will aid in the formation of carbon monoxide when the engine is fueled with natural gas. Relatively cool air enters the combustion chamber through these injectors such that the injectors act as large-scale dilution ports.

Carbon monoxide formation was not a problem with hydrogen operation in this experiment due to the lack of carbon in the system. Control of the primary zone fueling was necessary, however, to ensure that all six injectors were equal in their contribution to the combustion reaction. Having six equal injectors over the full power load of the engine allowed for better comparisons of equivalence ratio and emissions.

It is noted that the engine control system is working from set points on turbine exhaust temperature and shaft speed. The engine varies shaft speed to meet the power demand and it adds fuel accordingly. The exhaust temperature limit point precludes overheating of the engine and will limit fuel flow and therefore power if necessary.

Simultaneous onboard and external data acquisition systems provided engine operational data during testing. As part of the C60 fuel staging, engine shaft speed and airflow data were recorded. Fuel flow rate was measured externally to the engine using a positive displacement gas meter (Roots). Delivered power from the engine as well as fuel pressure and temperature were also measured external to the engine. Ambient conditions were recorded as well.

Emission Console. A gas analyzer (Horiba PG 250) was used to measure emission levels. A continuous gas sample was drawn from the MTG exhaust stack with a vacuum pump connected to a stainless steel probe. The analyzer draws from this gas line and measures the stream for levels of NO, CO, CO_2, SO_2, and O_2. At 30 s intervals these data were electronically logged. The analyzer was zeroed and spanned before each test. Drift checks showed less than 1% variation for all channels.

Injector Test Rig. An atmospheric test rig was used to simulate airflow distribution to a single injector. The C60 utilizes tangential injection that produces unique flow fields that are inherently asymmetric. By using the actual C60 injector bellows assembly the complex series of airflow turns in an actual engine is properly simulated. A more detailed description of the injector test rig operation is documented in previous work [7].

Gas Chromatograph. A SRI gas chromatograph (GC) was used to measure mixing profiles generated by the hydrogen injectors. The GC was calibrated using a certified sample gas mixture to ensure its accuracy. The GC was calibrated and checked before each test with drift remaining under 1% during all testing. Further details about the operation of the GC are found in previous work [7].

Chemical Kinetics Code. CHEMKIN [9] was used to model kinetics behavior using the GRI 3.0 mechanism [10] as well as that of Konnov et al. [11]. While other mechanisms [12] are available that are more directed at modeling the hydrogen/air reaction, for the present work it was helpful to use a common mechanism that can simulate both hydrogen and methane air reactions. Both mechanisms used have low temperature NO formation reactions that are investigated as part of the study.

Modified Injector Design

Several modifications were made to the commercial C60 injector (Fig. 2) to ensure safe, stable operation of the engine when operated on hydrogen [7].

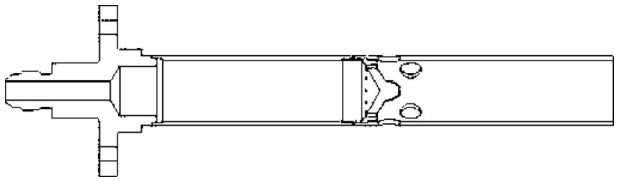

Fig. 2 Fuel injector, OEM natural gas C60 injector

Designs to generate differing fuel/air profiles for a given equivalence ratio were developed. To help mitigate flashback concerns [7], the fuel injection point within the mixing tube was moved closer to the injector exit plane, downstream of where air enters the injector. The commercial C60 injectors utilize a fuel distributor located approximately halfway down the mixing tube. Moving the fuel entry point forward nearly 90% of the injector length, the total volume of the injector exposed to a combustible mixture was significantly reduced. By introducing the fuel to the injector downstream of where air enters the injector, the possibility of a combustible mixture located in a wake or other aerodynamic feature associated with air entry into the injector was also reduced.

An insert was placed into the injector exit plane to further reduce the likelihood of flashback. The insert extends inside the injector from the exit plane to the point of fuel injection. This insert contains one 1.78 cm diameter center hole in which all of the fuel and most of the air are mixed and released to the combustion chamber. The remainder of the injector air is distributed to six cooling slots that run along the inner wall of the injector. These slots comprise about 17% of the total injector airflow area.

The hydrogen injectors are designed to operate fuel lean to reduce reaction temperature and minimize pollutant emissions. For a given equivalence ratio, hydrogen reacts at a temperature approximately 126 K higher than methane. However, the wide hydrogen stability limits allow the reaction to be sustained at much lower equivalence ratios (and correspondingly lower temperatures) than natural gas (as low as 0.09 versus 0.48 for natural gas) [7]. To take advantage of this attribute, the airflow into the injectors was increased, resulting in equivalence ratios ranging from 0.21 to 0.7 across the 0–60 kW power load range.

Three injector sets were fabricated, each designed to flow the same amount of air and fuel across the power load range, but providing differing degrees of fuel/air mixing to allow the influence of mixing on emissions to be studied. Each design releases fuel to a mixing length via a 6.35 mm tube. In one case the fuel enters the air stream coflowing with the air. This injector type is denoted as an "axial injector" (Fig. 3).

Two injectors feature two rows of six 1 mm holes on the side of the capped tube, which provide radial fuel injection. The two radial injectors differ in the mixing length afforded to the fuel/air mixture prior to injection into the combustor. The first has a mixing length of 19 mm (the same length as the axial injector) and is labeled the "radial injector." The third injector is called the "early radial injector" due to its 63.5 mm mixing length. The two radial injectors are shown in Figs. 4 and 5.

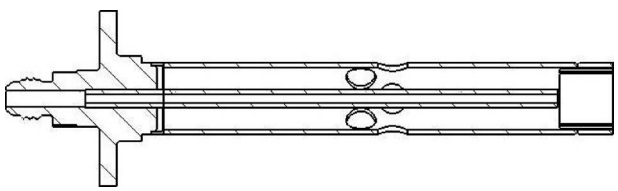

Fig. 3 Fuel injector, axial hydrogen injector

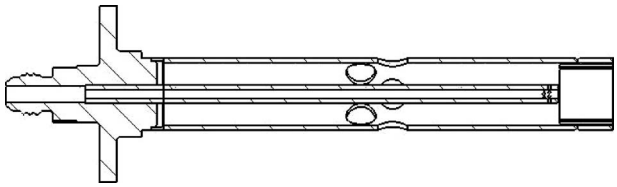

Fig. 4 Fuel injector, radial hydrogen injector

Modified Injector Mixing Results

The fuel distribution across the exit plane was measured for each injector type. Engine conditions were approximated at 1 atm and 300 K by matching momentum. Three power settings, 5 kW, 30 kW, and 60 kW, were tested. Measurements were taken as a single line across the diameter of the injectors.

Measurements of hydrogen concentration were taken by GC and reported as volumetric percentages. These volumetric concentrations for all three injector types can be seen in Fig. 6. These volumetric concentration values were then equated to equivalence ratio, as shown in Fig. 7. In both graphs the x-axis indicates location along the injector exit diameter with 0.0 being the middle of the injector. All three injector exit planes are 17.78 mm in diameter. Lines indicating upper and lower flammability limits are included in Fig. 7 for Ref. [13].

Integration of the measured profiles shows less than 3% variation in total hydrogen between radial and axial hydrogen injectors for each power load tested, indicating consistent fuel flows for each configuration. The asymmetry of the concentration peaks has been observed in other tests [8] of OEM Capstone injectors and is due to the complex airflow that develops in the injector feed annulus.

Each injector type creates a unique mixing profile, as seen in Figs. 6 and 7. The axial injector produces peaks between 55% and 39% for the different power loads. The radial injector produces a maximum concentration of 25% at 60 kW and 22% at 5 kW. In addition, differences as a function of load are reduced with the radial injector. The early radial injector produced the most uni-

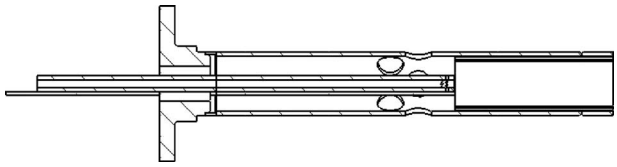

Fig. 5 Fuel injector, early radial hydrogen injector

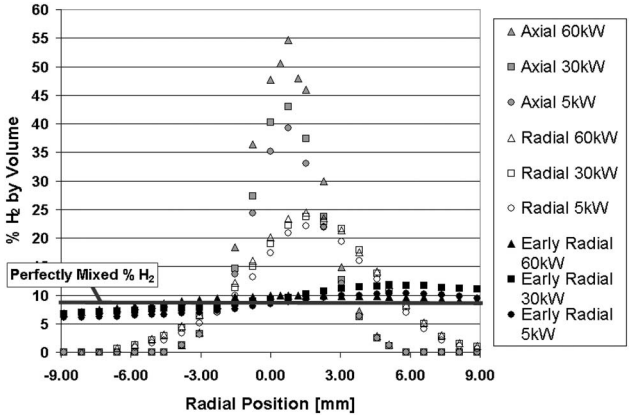

Fig. 6 Radial, axial, and early radial hydrogen injector mixing profiles for multiple power loads, volumetric concentration comparison

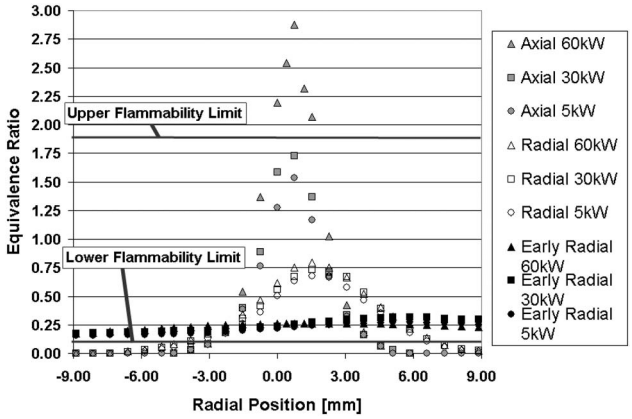

Fig. 7 Radial, axial, and early radial hydrogen injector mixing profiles for multiple power loads, equivalence ratio comparison

form concentration profile of the three. The profile still exhibits the modest asymmetry but approaches uniform mixing (Fig. 6). The early radial injector also exhibits smaller differences as a function of load.

When examined as a function of equivalence ratio the axial injector creates a mixture at 60 kW that exceeds the upper flammability limit. This indicates that a diffusion flame will be produced, resulting in high reaction temperatures and high NO_x formation rates. The radial or early radial injector does not exceed the upper flammability limit. Both the axial and radial injectors do not have a combustible mixture present at the injector walls by design. The early radial injector does have a combustible mixture present at the walls, which could be a concern from a flashback viewpoint.

Engine Operation and Emission Results

The MTG was started and operated on pure hydrogen for all tests. Previous work conducted accounts for startup procedures and experiences [7]. Four tests each were conducted for the axial, radial, and early radial hydrogen injectors. These tests were done at slightly different ambient temperatures, as summarized in Tables 1–3.

Calculation of equivalence ratio requires knowledge of the engine airflow. Capstone provided an equation relating engine shaft speed and turbine exit temperature to total airflow. This equation was developed with the commercially available natural gas engine. Tests conducted with hydrogen demonstrated that, for all power loads, shaft speed and turbine exit temperature values were the same as those with natural gas fueled engine [7], confirming applicability of the expression for the current work. Primary zone airflow was determined from this total airflow. Engine airflow splits for the natural gas engine were provided. By creating ratios

Table 1 Test numbers and ambient temperatures (K) for axial hydrogen injectors

	Axial 1	Axial 2	Axial 3	Axial 4
Ambient temperature	292.6	297.3	293.7	293.2

Table 2 Test numbers and ambient temperatures (K) for radial hydrogen injectors

	Radial 1	Radial 2	Radial 3	Radial 4
Ambient temperature	292.6	291.7	291.3	290.7

Table 3 Test numbers and ambient temperatures (K) for early radial hydrogen injectors

	Early radial 1	Early radial 2	Early radial 3	Early radial 4
Ambient temperature	292.4	291.1	291.7	292.2

of effective area measurements for natural gas injectors to hydrogen injectors, new primary zone air splits were calculated.

Emissions were measured from the engine operated using each injector set run over the full operational load range with hydrogen. For each injector four separate tests were conducted to ensure repeatability. NO and O_2 emission levels were measured. Emission values of NO were corrected to 15% O_2. A correlation of NO to NO_x can be found in other work [7].

Figure 8 shows the NO emission levels as a function of load for each injector type. Each injector type produces a near linear relation between NO emission and power load. For all power settings the axial injector produces the most NO with the radial and early radial producing less each. The slope of the emissions versus load line differs for each injector, ordered by axial, radial, and early radial. At a power level of 5 kW both the axial and radial injectors produce just below 70 ppm NO. The early radial injectors produce just over 25 ppm NO at 5 kW. At the full load point of 60 kW the axial injectors produce between 313 ppm and 360 ppm of NO depending on ambient temperature. The radial injectors produce 243–269 ppm NO at 60 kW. The early radial injectors produce between 92 ppm and 110 ppm NO at 60 kW.

The effect of ambient temperature has been discussed in earlier experiments with hydrogen MTGs [7]. The effects of ambient conditions are most noticeable when the engine is operated with the axial injectors. Ambient temperature effects are noted with the radial and early radial injectors but to a lesser degree.

A relation between emissions and equivalence ratio is shown in Fig. 9. For all injector types equivalence ratio varies between 0.2 and 0.7 for hydrogen. A vertical line has been inserted in Fig. 9 to indicate the lean flammability limit of hydrogen. As equivalence ratio decreases NO emission decreases for all injector types. Similar trends between NO emissions and power load are seen between NO emissions and equivalence ratio.

Axial 1, Radial 1, and Early Radial Test 1 can be directly compared for their levels of NO. The three sets of data have been taken with an ambient temperature difference of less than 0.4%. A distinct correlation between injector type (i.e., fuel mixing) and NO emission level can be seen. At an equivalence ratio of 0.7 a NO emission jump of 39% is seen between the axial and radial

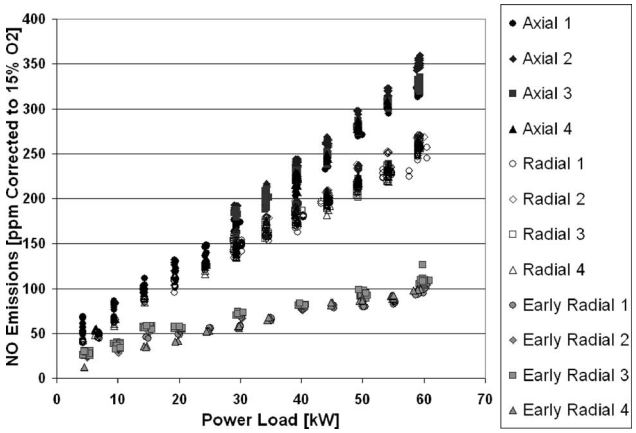

Fig. 8 Axial, radial, and early radial injection NO emissions versus power load (full load range)

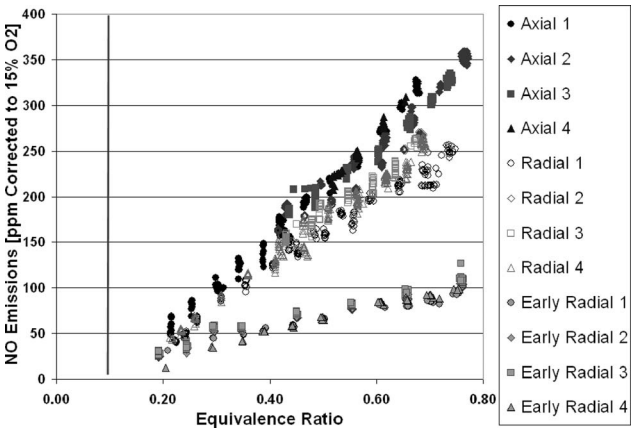

Fig. 9 Axial, radial, and early radial injector NO emissions versus equivalence ratio (full load range)

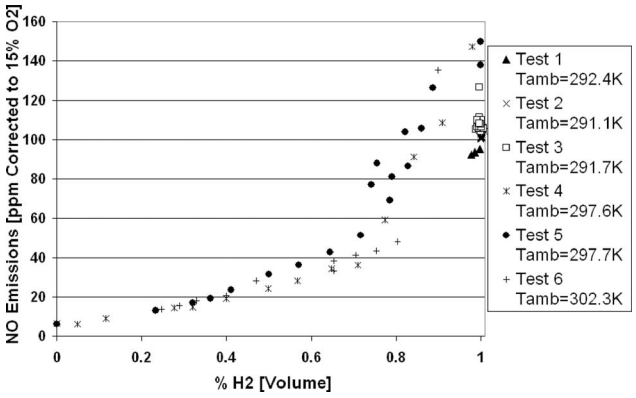

Fig. 11 NO emissions for early radial injectors operated on a mixture of hydrogen and natural gas

injectors. A 169.5% variation is seen between the early radial and radial injectons. This extreme jump in emission level indicates a strong relation of NO emission level to fuel/air mixing.

The early radial injectors were fueled with natural gas and emission levels of NO taken in order to confirm that differences between the mixing for the OEM injector and the early radial injectors were not giving rise to significantly different NO_x emissions. This injector was chosen because it produced a near uniform mixing profile (see Fig. 6). In order to maintain stability with natural gas operation, the engine *must be* fuel staged. As power load increased, the number of injectors that were fueled increased. Hydrogen operation does not require fuel staging. The natural gas operation produced emissions of NO between 3.5 ppm and 31 ppm. The results are seen in Fig. 10. Note that the staging occurs at different power loads for the two fuels. This is attributed to differences in the flame temperatures and inlet temperatures during the tests.

Overall the geometry changes made to the fuel injection system did not affect the engine's performance when fueled with natural gas. For all power settings the engine fueled with hydrogen produced significantly higher NO than it does when fired on natural gas.

To help further understand the behavior of the engine as fuel type is changed, additional tests that were run at full load using a varying mixture of natural gas and hydrogen demonstrate an exponential increase in NO emission as the percentage of hydrogen increases. Shown in Fig. 11 the results show that there is a substantial jump in NO production from 60% hydrogen to 100% hydrogen.

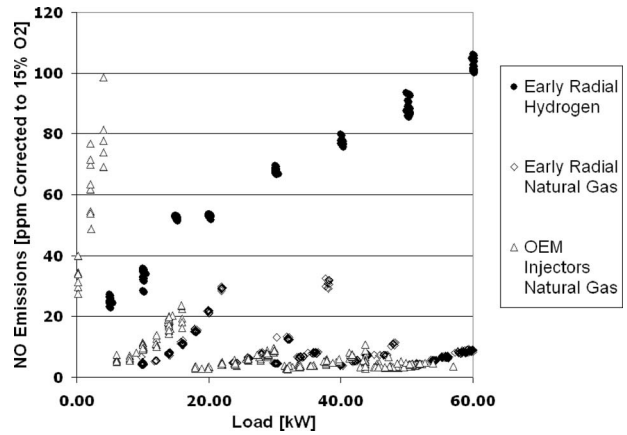

Fig. 10 NO emissions for early radial injector operated on hydrogen and natural gas

Discussion

Though the increase in NO emission from a retrofitted gas turbine is consistent with historical work [3,5] an understanding of why an increase is seen is desired. In the present case, two different issues are noted. First, at full power, the engine primary zone equivalence ratio when operated on hydrogen is much higher than it is for natural gas. This leads to significant thermal NO formation. However, because of the turbine exit temperature limit point, this presents a paradox regarding heat transfer within the system because the exhaust must reach the relatively cool turbine exit temperature regardless of the temperature it starts from in the primary zone. Apparently, for hydrogen, a much higher primary zone temperature results than it does for natural gas. Second, even at the very low equivalence ratios found at low power, the NO levels are still higher than they are for natural gas. Four potential effects leading to higher NO emissions in these two cases are explored in this section.

MTG Control Strategy. The MTG used in this experiment controls the amount of fuel added to the reaction based on the turbine exit temperature. At full load on hydrogen, running at an equivalence ratio of 0.70 (based on metered air and fuel flows), the flame temperature in the combustor primary zone will be several hundred degrees higher than the equivalent full load condition running on natural gas at an equivalence ratio of 0.49. This higher flame temperature explains the much higher overall NO emission at full load as a result of the thermal formation of NO in the combustor. What is perplexing is how the exhaust gases for hydrogen can be so hot in the primary zone compared to natural gas yet still reach the same turbine exit temperature set point. Several experiments were done to try to explain how the temperature between the combustor and the turbine exit could vary so greatly for the two fuels. At this point, additional information regarding relative heat transfer to the liner is needed to fully explain what is going on.

At the low power end of the spectrum, the equivalence ratio is relatively low and the apparent reaction temperatures are also low. As a result, other factors may be contributing to the differences in NO emission.

Effect of Residence Time. The MTG used in this study was designed to operate on natural gas. It is surmised that the combustion chamber of the original engine has been optimized to minimize pollutant formation when operated on natural gas. This optimized configuration may lead to higher NO emission levels when the engine is run with hydrogen. Previous work has indi-

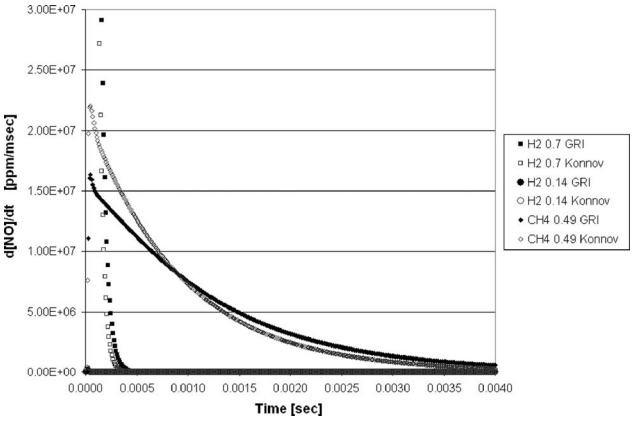

Fig. 12 NO formation rate for methane and hydrogen at given equivalence ratios

cated that gas turbines operated on hydrogen could use a shorter combustor compared to those used for conventional fuels due to the relative fast reaction rate of hydrogen [3]. Use of an oversized geometry creates an unnecessarily long residence time. To further explore this, NO formation rates were modeled at engine inlet conditions of 832.75 K and 3.599 atm in a simplistic single perfectly stirred reactor model. An equivalence ratio of 0.49 for methane was used to represent the 60 kW point of engine operation. Hydrogen was modeled with 0.70 and 0.14 equivalence ratios. The 0.70 point represents the 60 kW operation point measured in the operational engine with the current injector modifications while the 0.14 point represents the lowest possible equivalence ratio the engine could theoretically achieve with a complete reconfiguration of the airflow splits. Initial reactor temperatures were set to the adiabatic flame temperature levels of the corresponding fuel and equivalence ratio levels. Both the GRI 3.0 and Konnov mechanisms were used. This was done in part to help understand the sensitivity of the conclusions regarding low temperature NO formation to the mechanism used.

The results of this modeling are shown in Fig. 12. Though the exact residence time of the primary zone of the combustor is not known it is estimated based on combustor geometry to be between 7.8 ms and 8.8 ms over the load range of the engine. At comparable 60 kW points the hydrogen reaction with an equivalence ratio of 0.70 has a greater NO formation rate for a shorter amount of time. Unless a combustor could be made that would terminate a reaction in under a millisecond at this equivalence ratio, large amounts of NO will be formed. The hydrogen reaction with an equivalence ratio of 0.14, however, shows that, at a reduced equivalence ratio, the magnitude of the NO formation rate can be reduced. The length of time during which NO is being formed, however, is significantly larger. A short yet realistic combustor could take advantage of this longer reaction time and prematurely quench NO formation. By shortening the combustor length and lowering equivalence ratio the formation of NO in a hydrogen-fueled MTG can be reduced.

NO is formed considerably faster with hydrogen at operational engine condition equivalence ratio of 0.70 than when operating on methane at an equivalence ratio of 0.49. In addition, the equilibrium amount of NO produced in the hydrogen engine is 2.3 times higher than that of methane at an equivalence ratio of 0.49. By dropping the equivalence ratio of hydrogen to 0.14 the initial formation rate of NO drops well below that for methane at 0.49. The equilibrium value of NO from hydrogen at an equivalence ratio of 0.14 is 15 times less than that from methane at 0.49.

From this analysis, two possible NO reduction methods are apparent. Clearly, lowering the equivalence ratio reduces both the formation rate and the total amount of NO formed. In addition if the residence time during which species exist at elevated temperatures is reduced the formation of NO could be extinguished before reaching equilibrium. However, the high NO levels measured from the engine operated on hydrogen at an equivalence ratio of 0.14 observed in engine measurements (Figs. 9 and 10) are in contrast to this simplified reactor analysis. Hence further investigation into possible NO formation paths is warranted.

NO Formation Analysis

Traditional NO formation routes including thermal, prompt, and N_2O may not fully account for all NO produced in hydrogen fired systems. In addition to these pathways, as first suggested by Miller et al. [14], NNH is another intermediate species contributor to NO formation and may be important in the current system. NNH has been shown to explain discrepancies between NO concentrations from hydrogen reactions measured by laser induced fluorescence and modeling of traditional (thermal, N_2O, and prompt) NO formation mechanisms [11].

Bozzelli and Dean [15] used this idea when introducing the $O+NNH=NO+NH$ pathway as an important part of NO production models. This pathway is shown to be an important contributor to NO_x production including cases where large concentrations of H and O molecules are present. Combustion of hydrogen and air in a gas turbine engine provides large amounts of dissociated H_2 and O_2. NNH dissociation to H and N_2 is shown to be expected under all conditions; yet due to the nearly thermoneutral nature of $NNH=H+N_2$ at high temperatures, NNH formation from H and N_2 is also rapid. Bozzelli and Dean also suggested that of the several bimolecular reactions associated with NNH the most important is that with O atoms. Additionally by appropriately adding the NNH formation reactions to a kinetics model predicted concentrations of NO may be increased by an order of magnitude.

The formation of NO via the NNH pathway occurs in both hydrogen and methane flames for all equivalence ratios [16]. The amount of NO produced that is attributed to the NNH pathway, however, depends greatly on temperature, equivalence ratio, and pressure. Hayhurst and Hutchinson [17] are also supportive of the importance the NNH pathway plays in NO formation. Their work also shows that the NNH pathway will form NO in both hydrogen and methane flames.

NNH is also shown to be the dominant route of NO formation in systems with short residence times in the order of 1–25 ms for all temperatures [11]. For systems exceeding this residence time window NNH still plays a role in the formation of NO yet primarily at low temperatures. At higher temperatures the Zel'dovich mechanism is dominant [17]. For hydrogen/air systems Konnov et al. [16] stated that the flames above 2100 K are dominated by thermal NO and below that value by NNH.

Low temperature shows greater sensitivity to NNH for lean flames [16]. Under fuel-rich conditions, however, a large discrepancy between the Arrhenius plot of the third equation in the Zel'dovich mechanism ($N+O_2 \rightarrow NO+O$) and experimental measurements of NO was found. This discrepancy is attributed to the formation of NO via the NNH pathway that is not described by Zel'dovich [16]. In fuel-rich systems an abundance of free H atoms accelerates the formation of NNH via the reaction $H+N_2=NNH$ [17]. Others also found that while NNH is present for all situations that during fuel-rich conditions thermal NO dominates NO formation [16,18,19].

In addition to the arguments by Bozzelli and Dean [15] other work has shown discrepancies in the modeling of NNH NO with kinetics codes. The GRI 2.11 mechanism was shown to overpredict NO levels formed due to NNH in methane flames at high pressures [20]. Simultaneously Konnov et al. [11] stated that the GRI 2.11 mechanism shows that NNH is a viable explanation for ppm levels of NO found in hydrogen/air flames. Hughes et al. showed an improvement in the NNH portion of the GRI code since versions 2.11 with the release of version 3.0. More experimental work is needed to accurately model the formation of NO via NNH [21]. Even with discrepancies it is noted that the GRI 3.0 mecha-

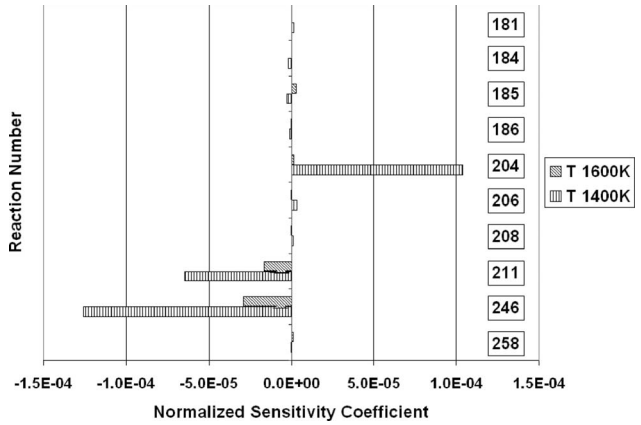

Fig. 13 Normalized sensitivity coefficients for methane; run at engine inlet conditions and various reactor temperatures

nism is improved in its ability to show the formation of NO from NNH. Using the GRI 3.0 mechanism to show relative reaction activity in a hydrogen-fueled MTG compared to a natural gas fueled MTG would not quantitatively prove the level of NO being produced by NNH but give a strong qualitative comparison.

The GRI 3.0 mechanism was used to determine if the NNH reaction pathways were more sensitive during a hydrogen reaction than with a methane reaction. For each fuel type engine condition of pressure 3.559 atm, inlet temperature 832.75 K and equivalence ratio 0.20 for hydrogen and 0.49 for methane were used. Initial reactor temperatures of 1000 K, 1200 K, 1400 K, and 1600 K were investigated. Sensitivity values were taken at the point when 5–80% of the fuel was consumed [22]. After executing the code all reactions involving NNH or NO were extracted. The ten most sensitive reactions from each fuel were collected and plotted. The sensitivity results for methane can be seen in Fig. 13 and for hydrogen in Fig. 14. Table 4 lists the reactions found in Figs 13 and 14. Reactions listed in italic and bold are common to both methane and hydrogen reactions. Those reactions underlined are only found in the hydrogen reactions.

Initial reactor temperatures of 1400 K and 1600 K only appear when methane is used as the fuel. At temperatures of 1000 K and 1200 K no methane reaction occurs. At an initial reactor temperature of 1400 K methane shows great sensitivity to reactions 204, 211, and 246. Reaction 204 is driven in the forward reaction while reactions 211 and 246 in the reverse. The reverse of reaction 211 leads to the formation of NNH while the forward 204 consumes the produced NNH forming monatomic hydrogen and diatomic

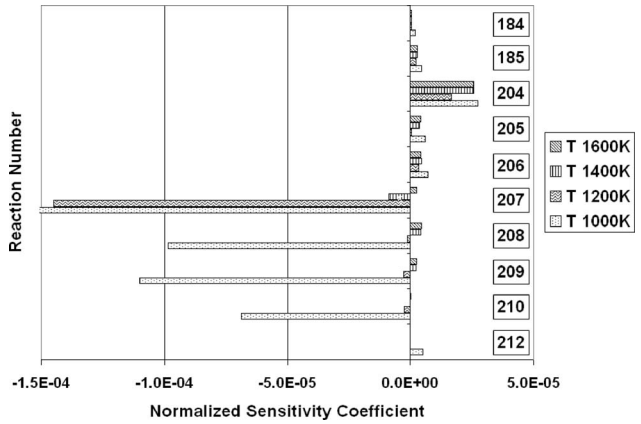

Fig. 14 Normalized sensitivity coefficients for hydrogen; run at engine inlet conditions and various reactor temperatures

Table 4 Reaction numbers and statements taken from GRI 3.0 [10]

No.	Reaction	No.	Reaction
181	$N_2O+O \leftrightarrow N_2+O_2$	**208**	**$NNH+O \leftrightarrow NH+NO$**
184	**$N_2O+OH \leftrightarrow N_2+HO_2$**	209	$NNH+H \leftrightarrow H_2+N_2$
185	***$N_2O(+M) \leftrightarrow N_2+O(+M)$***	210	$NNH+OH \leftrightarrow H_2O+N_2$
186	$HO_2+NO \leftrightarrow NO_2+OH$	211	$NNH+CH_3 \leftrightarrow CH_4+N_2$
204	**$NNH \leftrightarrow N_2+H$**	212	$H+NO+M \leftrightarrow HNO+M$
205	$NNH+M \leftrightarrow N_2+H+M$	246	$CH+NO \leftrightarrow HCN+O$
206	**$NNH+O_2 \leftrightarrow HO_2+N_2$**	258	$HCNN+O \leftrightarrow HC*N*+NO$
207	$NNH+O \leftrightarrow OH+N_2$		

nitrogen. Reaction 246 in the reverse direction directly forms NO from the intermediate HCN and O in no way participating in NO formation from NNH. Changing the initial temperature of the reactor to 1600 K results in the same reactions being the most sensitive though less so in magnitude.

The response of hydrogen was more varied than that of methane. When the reactor had an initial temperature of 1000 K reactions 207, 208, 209, and 210 are found to be very sensitive in the reverse direction. These four reactions all lead to the formation of NNH when in the reverse direction. Reactions 204, 205, and 206 that consume NNH but at low initial reactor temperature are considerably less sensitive than the four reactions mentioned before that are producing NNH. When initial reactor temperature increases to 1400 K the same reactions still show sensitivity and form NNH yet as with methane to a much lesser degree. As the temperature is increased further to 1400 K and 1600 K the NNH forming reactions reverse and start consuming NNH.

Both methane and hydrogen show an affinity to produce NNH at lower initial reactor temperatures. This follows with the discussion in the introduction that NO produced via NNH is more viable at lower temperatures. Hydrogen does not require a large amount of energy to react and can maintain a reaction at very low temperatures due to its large flammability limit. This allows for a greater potential of NO formation from NNH with hydrogen at low equivalence ratios than fuels that cannot sustain such low reaction temperatures.

In addition to GRI 3.0 a specific hydrogen mechanism was used to investigate the potential effect of NNH on NO formation with hydrogen. The mechanism is a combination of work done by Li et al. [23] and Mueller et al. [22]. It combines the hydrogen air reaction with all forms of NO_x formation pathways. The NO_x formation predictions the code generates have not been compared against any NO_x flame production data. The code is used nonetheless due to a lack of alternatives combined with the desire to have a counterpart to the GRI 3.0 tests.

The hydrogen specific code showed nearly no NO formation via NNH. The most active reactions were four to six orders of magnitude less active than what GRI 3.0 predicted. While this directly contradicts the idea that NO is being formed via NNH the lack of validation in the hydrogen specific code points to the need for a strong mechanism if modeling is to be used to predict NO emissions from hydrogen gas turbines.

Though not proven, the formation of NO via NNH may explain why all three injectors produced approximately 50 ppm NO at a lean equivalence ratio of 0.20. The adiabatic flame temperature of hydrogen at an equivalence ratio of 0.20 is approximately 1400 K, which effectively eliminates any thermal NO. At higher power loads the higher adiabatic flame temperature indicates that NO formation via the Zel'dovich pathway should be dominant.

Dilute Combustion Analysis

The Capstone C60 operated on natural gas produces very little criteria pollutant emissions. Past studies of the engine show that, at full load, emissions of CO and NO corrected to 15% O_2 do not

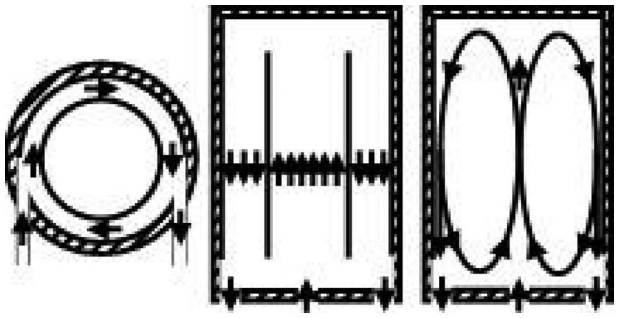

Fig. 15 Diagram of "loop reactors" presented for flameless oxidation [26]

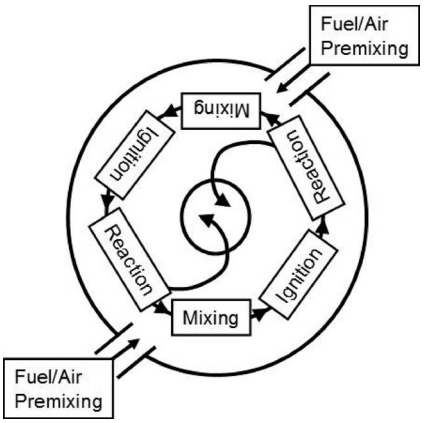

Fig. 16 Recreated NO_x reburn engine pathway diagram [27]

exceed 5.7 ppm and 4.9 ppm, respectively [8]. These low emissions have been attributed to near perfect premixing of fuel and air along with ultrafuel lean equivalence ratios. Additionally the geometry of the engine and the flow conditions entering the combustion chamber may be leading to the low emission values.

A technique used to lower NO emissions from a combustor involves injecting partially combusted products that would contain NO into a fresh stream of fuel and oxidant. This paper will refer generally to this idea as dilute combustion though other unique names for the various configurations of combustors that use this principle exist.

This technique has been presented historically for different combustion technologies. The first application of this idea has been to furnaces. The first such furnace combustor was named a low NO_x regenerative burner [24]. This dilute combustion device used a diffusion pilot flame to create partially combusted gases. These gases were then fed directly into the reaction zone of a larger secondary diffusion reaction. The heat from the pilot flame preheated the incoming main air, which in turn increased flame stability. By introducing the combusted gases to the main reaction NO_x levels were reduced by 50% compared to traditional furnace burners.

Another furnace application [25] of dilute combustion focused on the air preheat gains of exhaust gas recirculation. This study showed that burner configurations that directly interacted product gas with reaction zones reduced emission levels of both CO and NO_x. Additionally noncombustion product diluents N_2 and CO_2 were injected with the oxidant stream. While both diluents caused a reduction in reaction temperature the use of CO_2 created a larger reduction in criteria pollutants. This suggested that not only does the diluent effect lower emission levels through reaction temperature changes but the chemistry of the added diluent impacts emission levels.

The idea of using partially oxidized gases to stabilize a reaction and reduce NO_x emissions has been outlined for other combustors [26]. One type dubbed a "flameless oxidation combustor" due to the "invisible flame" it generates utilizes partially combusted products to reduce NO_x levels and stabilize the reaction. A distinction is made with exhaust gas recirculation, which utilizes combusted products from the exhaust stack that are brought into the oxidant stream before combustion occurs. Instead, the flameless combustor recycles combustion products internally to the combustion chamber. In order to obtain a flameless oxidation reaction a "loop reactor" is necessary. The three loop reactors diagramed and reproduced in Fig. 15 all incorporate a geometry that returns combustion product to the combustion zone.

The leftmost loop reactor diagram in Fig. 15 uses nearly the same tangential injection and annular configuration as the Capstone C60. The concept of a burner that would utilize exhaust gas as a way to stabilize a reaction and reduce emissions has been proposed for a similar combustor geometry [27], which is also similar to the leftmost loop reactor of Fig. 15. As the reactants from one injector enter the combustor and begin the oxidation process traditionally modeled in plug flow reactors, they are prematurely interrupted and encounter the relatively cool reactants from the second reactor. The combined partially combusted products from the first injector and fresh reactants from the second injector combine and react on their path to the first injector where fresh reactants wait to continue the process. This process is diagramed in Fig. 16. A fraction of the combusted products enter a burnout zone and exit the combustor axially. There are two important requirements for this process to take place: A certain fraction of the combustion products must enter the fresh reactant stream and they must enter at the right time during the kinetic process.

The momentum of the flow field will dictate the transit of species from the injector to their ignition through the kinetic process and into the next injector's path. If the magnitude of momentum is not great enough the reacting fuel and air will not reach the second injector and simply be transported from the combustion chamber. Low momentum will result in the dilute combustion strategy not occurring.

Atmospheric testing of a dilute combustion system with similar geometry to the Capstone C60 has been reported [28]. The experimentation showed that the addition of partially oxidized gases could help stabilize a reaction of fresh reactants and decrease the lean blowout limit of a fuel. The combustor contained two injectors that could be adjusted to allow for different angles of injection into the combustor. As this angle was changed emissions of CO and NO_x changed as well. By changing this angle the residence time of the path from injector exit to the second injector can be manipulated. As this residence time increased and decreased with the injector angle, the kinetic reaction taking place had a longer or shorter period of time to be driven toward equilibrium. Optimization of the time a reaction is allowed to exist before introduction to the new reactant stream can maximize the NO mitigation potential. This optimization led to sub-ppm levels of NO_x and CO in the combustor tested when operated on natural gas.

This strategy of a dilute combustion engine using partially combusted products combining with fresh reactants to produce low emissions has been proven through experimentation [29,30]. The stagnation point reverse flow type combustor injects fuel and air from an open end of a tube toward a closed end. This combustor geometry is analogous to the rightmost diagramed loop reactor described for flameless oxidation reprinted in Fig. 15. The reacting fuel and air entering the chamber are sheared by the partially combusted products returning from the stagnation plane at the other end of the tube. This shearing effect and combination of partially combusted products along with fresh reactants resulted in low emissions of CO and NO_x.

The chemistry behind dilute combustion has been investigated [31]. A counterflow laminar flat flame burner was used to deter-

mine the effect of different diluents on emission levels of NO. Varying amounts of CO_2, N_2, and burned gas containing NO were injected to the oxidant inlet stream. Reductions in the output levels of NO were seen when diluents CO_2 and N_2 were added to the oxidant stream. The effect of adding these species lowered the reaction temperature and reduced thermal NO_x production. When NO laden burned gas was introduced to the oxidant stream the initial concentration of NO increased but postcombustion the amount of NO was lower than precombustion. The introduction of NO to the combustion region was shown to reduce the amount of NO that would have been produced without diluent. Kinetic modeling of the reaction showed a considerable increase in N_2 production from N and as well as NO destruction when burned gas was used for dilution. NO destruction reactions are listed that are of primary importance when burned gas is added to the reaction.

The Capstone C60 contains a geometry that may be promoting dilute combustion when operated with natural gas. Modification to the injector hardware did not affect the effectiveness of this strategy when fueled with natural gas, as seen in Fig. 10. Changing fuel stocks from natural gas to hydrogen does not affect the momentum in the engine. This constant momentum coupled with the greatly differing reaction rates may be giving rise to mismatched time scales associated with the mixing, ignition, and reaction zones. Additionally the time necessary to drive a hydrogen reaction to equilibrium is considerably less than that of natural gas. This time difference is shown in Fig. 12. With the preclusion of NO_x reburn due to the change from natural gas to hydrogen, NO emissions generated in the engine could increase.

Conclusions

Multiple modifications to the fuel injectors of a commercial natural gas fired MTG have been made to allow the engine to operate on pure hydrogen. These modifications created three unique fuel/air mixing profiles while maintaining similar equivalence operational ranges. The injectors were characterized in an atmospheric test rig for their mixing profiles. Emission performance of each injector type was tested in a MTG over its full range. Each injector type was tested four times. The data gathered from the engine were compared to power load, equivalence ratio, and mixing level. Emission levels dropped as the mixing profile of the injector became more uniform. Lower equivalence ratios uniformly produced less NO.

Compared to natural gas operation the engine run on hydrogen produced larger volumes of NO. This follows the precedent set by previous work when engines are retrofitted to operate with hydrogen. Four potential effects that would lead to higher NO emissions from the engine when fueled with hydrogen are presented.

- The control strategy of the MTG is not optimized for hydrogen and is causing a large volume of thermal NO production in the combustor at full load.
- Residence time analysis was conducted for hydrogen at multiple equivalence ratios. By utilizing lower equivalence ratios along with early termination of the reaction emissions of NO could be reduced.
- Kinetics modeling of NO formation was conducted. Specifically the residence time of combustible species at engine conditions was examined to see the rate of formation of NO. NO formation is much slower when methane is used as a fuel stock compared to hydrogen. By lowering the equivalence ratio of hydrogen a similar NO formation rate to that of methane can be obtained. Sensitivity studies were conducted to examine the role of NNH in the production of NO. Hydrogen showed a greater affinity to produce NO via the NNH formation route when modeled with the GRI 3.0 mechanism. NO is more likely to be produced at lower temperatures via NNH than at higher temperatures. Hydrogen at low equivalence ratios has a low adiabatic flame temperature conducive to NO being formed by NNH.
- The concept of dilute combustion in the commercial natural gas Capstone C60 may be leading to the engine's low emission values when operating with natural gas. When the fuel type is changed to hydrogen without changing the combustor, geometry dilution may not be occurring. This could lead to the increase in NO observed.

Acknowledgment

The support of the California Energy Commission (Contract No. 500-00-020) is gratefully acknowledged. The support of Richard Hack and discussions with Mark Mitchell of Capstone Turbine Corporation are appreciated.

References

[1] Lefebvre, A. H., 1999, *Gas Turbine Combustion*, 2nd ed., Taylor & Francis, Philadelphia, PA.
[2] Effinger, M. W., Mauzey, J. L., and McDonell, V. G., 2005, "Characterization and Reduction of Pollutant Emissions from a Landfill and Digester Gas Fired Microturbine Generator," ASME Paper No. GT2005–68520.
[3] Conrad, W. E., and Corrington, L. C., 1957, "NACA Research Memorandum: Hydrogen for Turbojet and Ramjet Powered Flight," Report No. NACA RM E57D23.
[4] Nomura, M., Tamaki, H., Morishita, T., Ikeda, H., and Hatori, K., 1981, "Hydrogen Combustion Test in a Small Gas Turbine," Int. J. Hydrogen Energy, **6**(4), pp. 397–412.
[5] Sampath, P., and Shum, F., 1985, "Combustion Performance of Hydrogen in a Small Gas Turbine Combustor," Int. J. Hydrogen Energy, **10**(2), pp. 829–837.
[6] Chiesa, P., Lozza, G., and Mazzocchi, L., 2005, "Using Hydrogen as Gas Turbine Fuel," ASME J. Eng. Gas Turbines Power, **127**, pp. 73–80.
[7] Therkelsen, P. L., Mauzey, J. L., McDonell, V. G., and Samuelsen, S., 2006, "Evaluation of a Low Emission Gas Turbine Operated on Hydrogen," ASME Paper No. GT2006–90725.
[8] Phi, V. M., Mauzey, J. L., McDonell, V. G., and Samuelsen, G. S., 2004, "Fuel Injection and Emissions Characteristics of a Commercial Microturbine Generator," ASME Paper No. GT2004–54039.
[9] Reaction Design, 2006, CHEMKIN, Version 4.0.2.
[10] GRI-MECH 3.0, http://www.me.berkeley.edu/gri_mech/.
[11] Konnov, A. A., Dyakov, I. V., and De Ruyck, J., 2002, "Nitric Oxide Formation in Premixed Flames of $H_2+CO+CO_2$ and Air," Proc. Combust. Inst., **29**, pp. 2171–2177.
[12] Mueller, M. A., Kim, T. J., Yetter, R. A., and Dryer, F. L., 1999, "Flow Reactor Studies and Kinetic Modeling of the H_2/O_2 Reaction," Int. J. Chem. Kinet., **31**(2), pp. 113–125.
[13] Reed, R. J., 1985, *North American Combustion Handbook*, Vol. 1, 3rd ed., North American Mfg. Co., Cleveland, OH.
[14] Miller, J. A., Branch, M. C., and Kee, R. J., 1981, "A Chemical Kinetic Model for the Selective Reduction of Nitric Oxide by Ammonia," Combust. Flame, **43**, pp. 81–98.
[15] Bozzelli, J. W., and Dean, A. M., 1995, "O+NNH: A Possible New Route for NO_x Formation in Flames," Int. J. Chem. Kinet., **27**, pp. 1097–1109.
[16] Konnov, A. A., Colson, G., and De Ruyck, J., 2001, "NO Formation Rates for Hydrogen Combustion in Stirred Reactors," Fuel, **80**, pp. 49–65.
[17] Hayhurst, A. N., and Hutchinson, E. M., 1998, "Evidence for a New Way of Producing NO via NNH in Fuel-Rich Flames as Atmospheric Pressure," Combust. Flame, **114**, pp. 274–279.
[18] Baulch, D. L., Cobos, C. J., Cox, R. A., Esser, C., Frank, P., Just, Th., Kerr, J. A., Pilling, M. J., Troe, J., Walker, R. W., and Warnatz, J. J., 1992, "Evaluated Kinetic Data for Combustion Modeling," J. Phys. Chem. Ref. Data, **21**(3), pp. 411–734.
[19] Michael, J. V., and Lim, K. P., 1992, "Rate Constants for the N_2O Reaction System: Thermal Decomposition of N_2O; $N+NO \rightarrow N_2+O$; and Implications for $O+N_2 \rightarrow NO+N$," J. Chem. Phys., **97**(5), pp. 3228–8234.
[20] Charlston-Goch, D., Chadwick, B. L., Morrison, R. J. S., Campisi, A., Thomesn, D. D., and Laurendeau, N. M., 2001, "Laser-Induced Fluorescence Measurements and Modeling of Nitric Oxide Premixed Flames of $CO+H_2+CH_4$ and Air at High Pressures," Combust. Flame, **125**, pp. 729–743.
[21] Hughes, K. J., Tomlin, A. S., Hampartsoumain, E., Nimmo, W., Zsely, I. G., Ujvari, M., Turanyi, T., Glague, A. R., and Pilling, M. J., 2001, "An Investigation of Important Gas-Phase Reactions of Nitrogenous Species from the Simulation of Experimental Measurements in Combustion Systems," Combust. Flame, **124**, pp. 573–589.
[22] Mueller, M. A., Yetter, R. A., and Dryer, F. L., 2000, "Kinetic Modeling of the $CO/H_2O/O_2/NO/SO_2$ System: Implications for High-Pressure Fall-Off in the $SO_2+O(+M)=SO_3(+M)$ Reaction," Int. J. Chem. Kinet., **32**(6), pp. 317–339.
[23] Li, J., Zhao, Z., Kazakov, A., and Dryer, F. L., 2004, "An Updated Comprehensive Kinetic Model of Hydrogen Combustion," Int. J. Chem. Kinet., **36**(10), pp. 566–575.
[24] Suzukawa, Y., Sugiyama, S., Hino, Y., Ishioka, M., and Mori, I., 1997, "Heat Transfer Improvement and NO_x Reduction by Highly Preheated Air Combustion," Energy Convers. Manage., **38**(10–13), pp. 1061–1071.
[25] Hasegawa, T., Tanaka, R., and Niloka, T., 1997, "High Temperature Air Combustion Contributing to Energy Saving and Pollutant Reduction in Industrial

Furnace," *International Joint Power Generation Conference*, Vol. 1, pp. 259–266.
[26] Wünning, J. A., and Wünning, J. G., 1997, "Flameless Oxidation to Reduce Thermal NO-Formation," Prog. Energy Combust. Sci., **23**, pp. 81–94.
[27] Kalb, J. R., and Sattelmayer, T., 2004, "Lean Blowout Limit and NO_x Production of a Premixed Sub-ppm NO_x Burner With Periodic Flue Gas Recirculation," ASME Paper No. GT2004–53410.
[28] Brückner-Kalb, J. R., Hirsch, C., and Sattelmayer, T., 2006, "Operation Characteristics of a Premixed Sub-ppm NO_x Burner With Periodical Recirculation of Combustion Products," ASME Paper No. GT2006–90072.
[29] Neumerier, Y., Weksler, Y., Zinn, B., Seitzman, J., Jagoda, J., and Kenny, J., 2005, "Ultra Low Emissions Combustor With Non-Premixed Reactants Injection," 41st AIAA/ASME/SAE/ASEE Joint Propulsion Conference, Tuscon, AZ, Jul., Paper No. AIAA-2005–3775.
[30] Bobba, M. K., Gopalakrishna, P., Seitzman, J. M., and Zinn, B. T., 2006, "Characteristics of Combustion Processes in a Stagnation Point Reverse Flow Combustor," ASME Paper No. GT2006–91217.
[31] Choi, G.-M., and Katsuki, M., 2002, "Chemical Kinetic Study on the Reduction of Nitric Oxide in Highly Preheated Air Combustion," Proc. Combust. Inst., **29**, pp. 1165–1171.

Steady State Off-Design and Transient Behavior of a Solid Oxide Fuel Cell/Gas Turbine Hybrid Power Plant With Additional Firing of the Gas Turbine Combustor

Christian Wächter
e-mail: waechter@hsu-hh.de

Franz Joos
e-mail: joos@hsu-hh.de

Power Engineering Laboratory of Turbomachinery,
Helmut-Schmidt-University (University of the Federal Armed Forces Hamburg),
Holstenhofweg 85,
D-22043 Hamburg, Germany

The purpose of the current work is to analyze and also to verify the operating behavior of a solid oxide fuel cell/gas turbine (GT) hybrid system in order to derive necessary requirements for an appropriate control system. The studies are carried out with a control oriented simplified dynamic model of a 25 MW_e hybrid system based on a conceptual design previously presented in literature. As a specific feature additional firing of the GT combustor is investigated. First the design point is defined. Then the off-design performance is presented in terms of characteristic performance maps. Based on operating map investigations an appropriate part-load operating curve is defined with considerations given to constraints (e.g., stack temperature or surge margin), efficiency, and operational flexibility. The load range goes from 40% part-load to 105% overload. To investigate the transient behavior five open loop simulations are carried out changing different model inputs, as well as all model inputs applying a 30% load change according to the operating curve. The simulated behavior reveals that the inputs should be changed with specific care to avoid critical situations during load change. [DOI: 10.1115/1.2981176]

Keywords: SOFC, GT, hybrid system, off-design transient model

1 Introduction

High temperature solid oxide fuel cells (SOFCs) in combination with gas turbines (GTs) offer potential for increasing state-of-the-art efficiencies over 60% [1]. Another advantage of a SOFC is its ability to quickly change the delivered electrical power [2]. However, commercial usage still faces some elaborate challenges.

In recent years many papers have been published dealing with modeling and analyzing the operating behavior of SOFC/GT hybrid systems (HSs). Kemm et al. [3] built up a one-dimensional steady state model of the integrated planar SOFC and enhanced it to a transient model. Simulating a load change they found that because of the thermal inertia there is a time window, within that the airflow has to be readjusted to control the stack temperature. Then they concluded that in HSs without additional firing of the GT combustor this time window is smaller, as via the recuperator the turbine outlet temperature influences the SOFC inlet temperature. Next they defined a part-load operational window for a HS taking into account SOFC minimum and maximum temperatures as well as the maximum temperature rise over the fuel cell. Therefore they used the steady state SOFC model, which is upgraded to a HS model. Then they suggested an adaptation of the SOFC size or inlet guide vanes to enlarge the operating range of the HS.

Another constraint for the HS off-design operation is the surge margin (SM), which was investigated by Hildebrandt et al. [4]. In steady state operation the surge and the choke limit border the compressor operational lines. An extension is possible using an air bypass or air bleed of or by means of an adjustment of turbine inlet temperature (TIT) or turbine swallowing capacity. In transient operation surge is mainly dependent on the mechanical inertia of turbomachinery, the volume, and the thermal inertia of the SOFC. For fast load decrease the authors recommended a surge control system.

Costamagna et al. [5] used a steady state nondimensional tubular SOFC model to analyze the design and part-load performance of a HS. The authors found out that keeping the fuel utilization constant and increasing the stack temperature lead to higher efficiency and voltage. At the same time lower air utilization causes lower stack temperatures because cooling is increased. Keeping this in mind it becomes obvious that good part-load efficiencies of the HS can only be achieved by reducing the air mass flow and the shaft speed, respectively. So variable shaft speed operation is essential. In other papers the same institute compared a simplified nondimensional HS model with a detailed one-dimensional one [6] and developed a transient HS model in lumped volume technique [7–9] for testing a control system using an air bypass for regulating the shaft speed [10]. There they defined the differential pressure across the electrolyte as another critical parameter because it causes mechanical stress in the electrolyte assembly.

Miller et al. [1] also used a steady state nondimensional tubular SOFC model to investigate the off-design behavior of a HS. With an iterative scheme they calculated more than 1000 off-design operating points. In performance maps each for constant shaft speed the HS power and the efficiency are plotted versus current density. Partly they contain isolines for stack temperature, voltage, and fuel flow. Unlike Ref. [4] the SM does not restrict the operational range. Future studies will base on this knowledge to develop a control strategy.

Stiller et al. [11,12] presented an all-embracing analysis of a

Contributed by the International Gas Turbine Institute of ASME for publication in the JOURNAL OF ENGINEERING FOR GAS TURBINES AND POWER. Manuscript received March 28, 2008; final manuscript received May 18, 2008; published January 29, 2009. Review conducted by Dilip R. Ballal. Paper presented at the ASME Turbo Expo 2008: Land, Sea and Air (GT2008), Berlin, Germany, June 9–13, 2008.

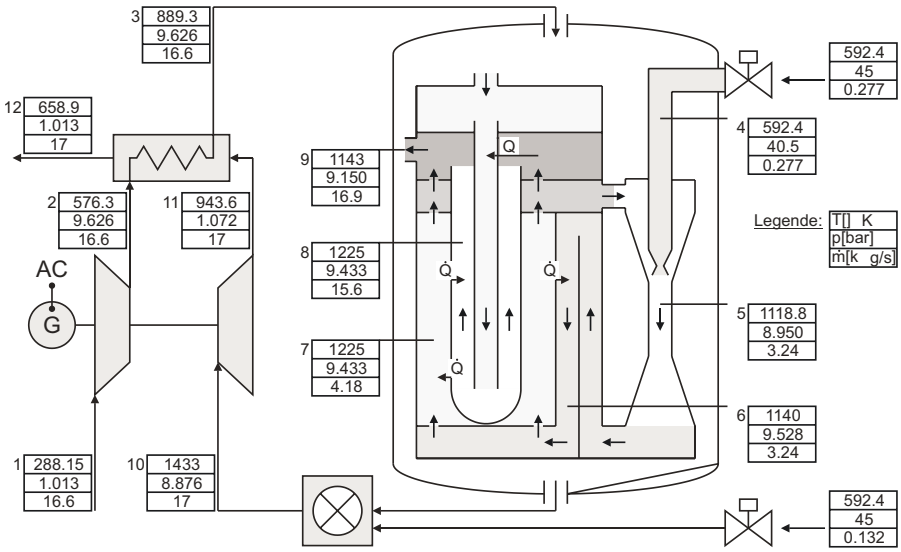

Fig. 1 Hybrid system configuration with design point data (for one power block)

HS. First they calculated the part-load behavior using a detailed HS model. Keeping the FU constant there are two degrees of freedom in defining an operating point: shaft speed and fuel flow. So important parameters are presented in two-dimensional performance maps. Then an operation line is defined, in which the mean stack temperature is as constant as possible because this speeds up load changes and enhances cell lifetime. At last they tested successfully a control strategy that is a combination of several feedback loops and map-based pilot controls. However, they warned of fast load increase because backflow of gas from the burner into the anode may arise.

Stiller et al. [11,12] identified several critical parameters that have to be considered in an appropriate HS operation strategy and suggested different promising approaches.

In the work presented here a steady state and dynamic nondimensional model of a large scale HS (25 MW_e) based on a conceptual design study [13] is developed; its design point is defined in accordance with given data. Unlike other proposed HSs this study assumed firing of the GT combustor in order to maintain the design conditions of the GT. Although this deteriorates the HS efficiency, some advantages arise. This secondary fuel flow represents an additional degree of freedom, which can be used to affect the stack temperature, the SM, and the HS power. Under these conditions the steady state off-design behavior is calculated and the results are presented in performance maps similar to those used in Refs. [11,12]. Also an operating line is deduced. Finally, the transient behavior is investigated. Therefore five open loop simulations are carried out changing different model inputs, as well as all model inputs applying a 30% load change according to the operating curve.

2 SOFC/GT Hybrid Plant

Within the U.S. Department of Energy high efficiency fossil power plant program Siemens Westinghouse (SW) and Caterpillar developed a 20 MW_e-class power plant concept combining the recuperated Mercury 50 GT with the SW pressurized tubular SOFC generator module [13]. To generate the desired electrical power with high efficiency and at the same time low COE the system comprises two independent power blocks; each contains one single-shaft GT with axial impellers and 80 576-cell substacks delivering 4.5 MW_e and 8 MW_e, respectively, to the grid. The system layout is shown in Fig. 1. It resembles that of the first operating SOFC/GT HS [14].

The compressor (2) provides pressurized air to the SOFC stack. On its way into the cathode (8) it is first preheated in an external recuperator (3) and then in an air supply tube located inside the fuel cell tube. The flow in the anode recirculation section (5–7) is driven by an ejector (5) with pressurized methane. In the reformer (6) the water content and the thermal energy of the recirculated anode exhaust prevent carbon deposition and ensure a high conversion rate of methane to hydrogen according to the chemical reactions

$$CH_4 + H_2O \rightarrow CO + 3H_2 \tag{1}$$

$$CO + H_2O \rightarrow CO_2 + H_2 \tag{2}$$

A proper fuel mixture then reaches the anode (7), where the electrochemical reactions

$$H_2 + 0.5O_2 \rightarrow H_2O \tag{3}$$

$$CO + 0.5O_2 \rightarrow CO_2 \tag{4}$$

take place and electrical power is generated. In the combustion plenum (9) downstream of the anode/cathode assembly the excess air and the depleted fuel flow mix while the remaining fuel is combusted completely. Secondary fuel is injected into the GT combustor (10) to reach a TIT of 1433 K, which is the design case for the stand-alone Mercury 50. The turbine (11) expands the hot exhaust to power the compressor and a generator before it enters the recuperator (12) to heat the fresh air.

The design point of the plant is defined with data given in Ref. [13] or in other published literature dealing with HS [5,8,14–16]. Figure 1 and Table 1 contain the most important specifications. Because of uncertain or missing data that are completed with reasonable assumptions (see Sec. 3) some information differs from those presented in Ref. [13]. However, this is not decisive as the general operating behavior of a HS is of interest here.

3 System Model

The presented model is based on that described in Ref. [17]. It is a simple nondimensional model and uses lumped volumes to simulate the gas dynamics. The fast dynamics of electrolyte and electrode processes as well as the slow dynamics of diffusive material transport and cell degradation are not included. To calculate the steady state behavior of the HS the differential equations of the transient model are substituted by iteration loops. Figure 2 shows the information flow and the single components of the model.

Specifications and additional information about the components are given in the following listing.

Table 1 Design point data for one power block

SOFC	
FU	0.85(0.62)[a]
AU	0.24
Current density	2960 A/m^2
Cell voltage	0.742 V
Power, dc	8.4 MW$_e$
GT	
Isentropic efficiency, compressor	87.5%
Isentropic efficiency, turbine	87.6%
Mechanical efficiency	98.7%
Power[b]	5.3 MW$_e$
Rotational speed	14,000 rpm
Ejector	
Mass flow ratio	10.7
Pressure rise	94 mbars (1%)
STCR	2.5
Recuperator	
Effectivity	85.2%
ΔT_{min}	54.3 K
Heat transfer	5.7 MW$_t$
Hybrid system	
Power, ac[b]	12.9 MW$_e$
Efficiency	62.4%

[a]Global FU (single passage FU).
[b]Power consumption for fuel compression: 0.3 MW; generator efficiency: 0.97%; inverter efficiency: 0.94%.

Table 2 Estimated geometrical dimensions

Volumes (per power block)*	
Compressor with recuperator (air side)	3.66 m^3
Fuel cell (cathode)	17.73 m^3
Combustion plenum	7.28 m^3
GT combustor*	0.72 m^3
Fuel cell (anode)	14.96 m^3
Ejector	2.86 m^3
Reformer	35.28 m^3
Masses (per power block)*	
Recuperator	1,275 kg
Upper stack	6,000 kg
Lower stack	123,840 kg
Surfaces (per power block)*	
Recuperator	797 m^2
Air supply/combustion plenum	296 m^2
Cathode	9152 m^2
Anode	6599 m^2
Reformer	1352 m^2

[a]Based on the drawings in Refs. [13,18].
[b]With turbine and recuperator gas side.

- The supplied fuel is pure methane.
- Besides secondary fuel flow and primary fuel pressure the shaft speed as well as the voltage are model inputs. However, in an extended model that simulates the behavior of HS in a distribution grid (subject of another paper) they are state variables controlled by the power electronics.
- Two first-order lag elements account for the dynamics of the fuel supply.
- The HS is divided into seven lumped volumes represented by (1) the compressor with the air side of the recuperator, (2) the cathode, (3) the combustion plenum, (4) the GT combustor, (5) the anode, (6) the ejector, and (7) the reformer. The gas dynamics are simulated by nondimensional unsteady conservation equations for mass and energy. The equation of momentum is only necessary for calculating the mass flow in the diffusor section of the ejector to prevent instabilities; otherwise, it is neglected and the mass flows are simply proportional to pressure differences.
- The geometrical dimensions of the modeled HS (e.g., volumes or surface areas) are estimated based on the drawing in Ref. [18]; decisive data are given in Table 2.
- The different gas compositions inside the HS are evaluated using steady state conservation equations.
- Within the SOFC the model allows for heat transfer between combustion plenum and air supply tube and for heat removal of the electrolyte/electrode assembly into the anode, the cathode and the reformer. In doing so convective heat transfer coefficients are variable using different Nusselt correlations. In the air supply tube, cathode, anode, and reformer, the Nusselt numbers are assumed to be constant because of a laminar flow regime [19]; in the combustion plenum the Nusselt number is calculated under the assumption of a cross blown shell tube [20]. After merging the solid parts of the stack its thermal inertia is represented by two

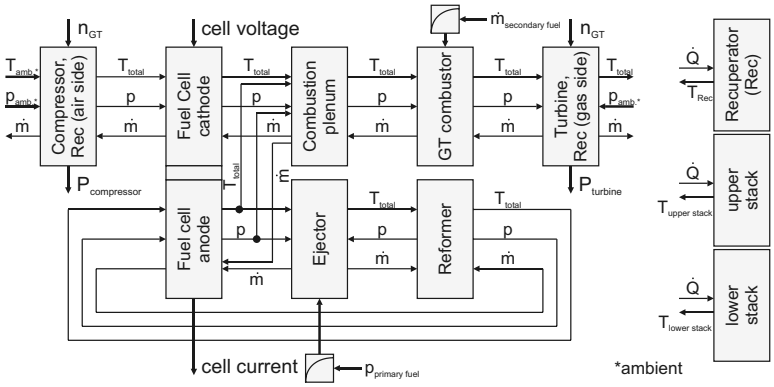

Fig. 2 Information flow of the model

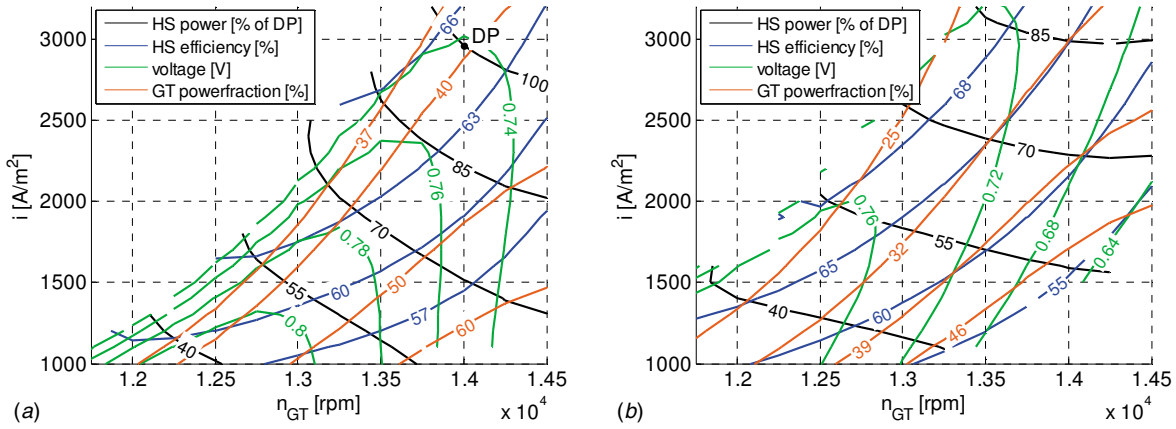

Fig. 3 Steady state performance parameters for (*a*) TIT=1433 K (left) and (*b*) 1183 K (right)

temperatures belonging to the lower and the upper stack casing (see Fig. 2). They are computed in an unsteady way by summing up the heat fluxes.

- The (primary surface) recuperator is dimensioned according to Ref. [21]. Heat transfer and friction coefficients are calculated as functions of Reynolds number [21], whereas the model neglects the pressure loss on the air side. The thermal inertia of the recuperator components is handled analogous to that of the SOFC by using one averaged temperature for the casing (see Fig. 2).
- Turbomachinery performance maps of midsize axial turboengines [22] are used to specify the operation behavior of the compressor and the turbine. To match the design of the Mercury 50 GT the map data (reduced mass flow $\dot{m}_{red}$ and shaft speed n_{red}, pressure ratio π, and isentropic efficiency η_s) are scaled. The maps are integrated into the model as continuous functions

$$\dot{m}_{red} = k_1(1 - e^{k_2((\pi/k_3)-1)}) \tag{5}$$

$$\eta_s = k_4(\pi/n_{red})^2 + k_5(\pi/n_{red}) + k_6 \tag{6}$$

whose parameters k_i are polynomial functions of the shaft speed. The calculation of the SM considers both steep and flat sections of the speed lines.

- In the anode the assumption of full methane conversion and equilibrium of the shift reaction defines the chemical conversion. The electrochemical conversion rate of hydrogen and carbon monoxide, thus the cell current, is determined by means of Nernst potential, cell voltage, and voltage losses (including Ohmic resistance, activation, and concentration polarization). The latter are nonlinear functions of cell current. So to avoid time consuming iterations a small inductive reactance is added to the voltage equation.
- The ejector comprises a simple nozzle, a Laval nozzle, and a mixing section followed by a diffusor (see Fig. 1). To ensure an appropriate recirculation ratio of the anode exhaust in the complete operational range, the fuel flow has to be accelerated to supersonic speed. So it can be controlled by the nozzle input pressure. The flow inside both ducts and the diffusor is simulated using one-dimensional polytropic steady state flow equations. The assumed component efficiencies are 100%, 92%, and 88%, respectively. Additionally a reduction of fuel momentum by 4% accounts for the mixing losses of both mass flows.
- The pre- and the internal reformer are treated as one component. Minimizing the Gibbs free energy results in the chemical gas composition.
- In the combustion plenum the cathode and anode exhaust mix and complete combustion of the residual fuel is applied. Because of the heat transfer the exit temperature is less than the temperatures at the inlet.
- In the GT combustor the supplied fuel is completely combusted.
- Some model constants are adjusted to compensate for the inaccuracy arising from the nondimensional approach and to set up the model with regard to the desired design point data.
- The electrical conversion losses are not considered.

The model is implemented in MATLAB®/SIMULINK®; the single components are written as *M*-file *S*-functions.

4 Steady State Off-Design Behavior

Compared with Ref. [11] the HS design presented here has four degrees of freedom: (1) shaft speed, (2) primary fuel flow, (3) voltage (or current), and (4) secondary fuel flow (or TIT). However, since lowering the FU results in a lower STCR (and thus possibly carbon deposition), and high FU evokes destructive temperature gradients inside the fuel cell, the FU will be kept constant here. This reduces the degrees of freedom by one. The remaining free parameters span a three-dimensional operating space that has to be displayed in a suitable manner. In the steady state model current and TIT are independent parameters. However, in the dynamic model voltage and secondary fuel flow are the inputs. According to the proceeding in Ref. [11] two-dimensional maps are chosen showing meaningful parameters as a function of current and shaft speed and the third free parameter is accounted for by plotting each map twice, each with constant but different values for TIT.

4.1 Operating Map Results. Figures 3–5 show the results of the analysis. The design point is marked in the upper right corner of the left hand side figures. The left figures are for a TIT of 1433 K that is close to the upper limit for the turbine and the right figures are for a TIT of 1183 K that requires less fuel flow. Because of constructive constraints TIT and shaft speed are assumed to be limited to 1450 K and 14,500 rpm, respectively. The lower bound of TIT is variable and obtained with zero secondary fuel flow. The other bounds are defined in order to realize power outputs between 40% and 105% of nominal power.

However, not every possible combination of the independent parameters results in physical operating points (see the empty regions in the upper left and lower right corners of the figures). This is because the stack temperature exceeds tolerable limits. So the calculations are stopped if the lower stack temperature falls below 950 K or goes beyond 1400 K.

As seen in Fig. 3 reducing only the current density leads to

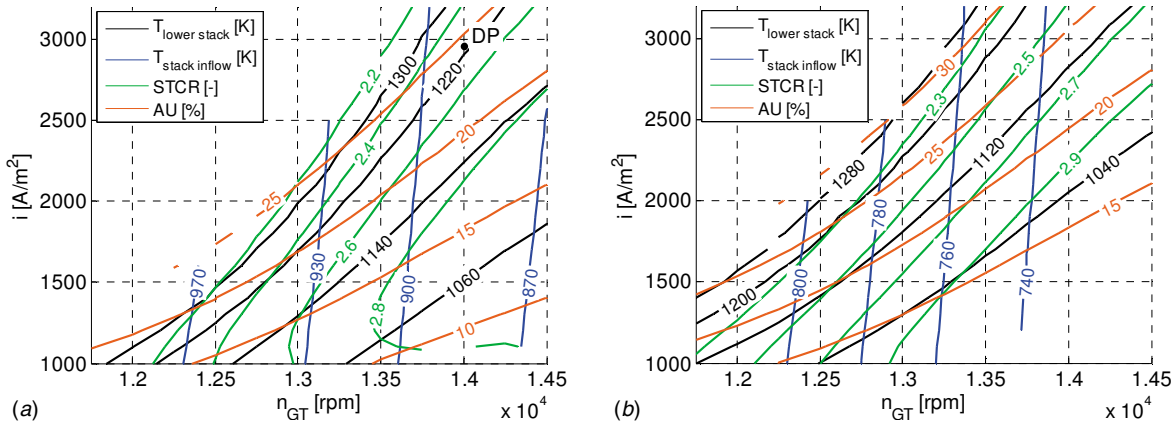

Fig. 4 Meaningful temperatures, STCR, and AU for (*a*) TIT=1433 K (left) and (*b*) 1183 K (right)

lower HS power. Owing to lower stack temperatures (Fig. 4) and greater GT power fraction the HS efficiency decreases as seen in Fig. 3. The lower stack temperature is in turn a result of constant stack inlet temperature, constant air mass flow, and decreasing waste heat.

Lowering the shaft speed reduces air mass flow (Fig. 5) and for this reason GT power. Although greater stack temperatures (Fig. 4) and (for the most part) voltages partly compensate for this, HS power sinks, too (Fig. 3). However, HS efficiency gets better because GT power fraction reduces (Fig. 3).

Decreasing the TIT from 1433 K (Figs. 3(*a*), 4(*a*), and 5(*a*)) to 1183 K (Figs. 3(*b*), 4(*b*), and 5(*b*)) causes the following: Given the same current and speed point, the stack temperature decreases (Fig. 4) because stack inlet temperature and TIT are coupled via the recuperator. So the tolerable operating range expands into the upper left region of the map. Due to lower cell voltage and GT power, the HS power drops (Fig. 3). SM and HS efficiency level also increase. The latter is evident since the GT power fraction (and the secondary fuel flow) sinks and the GT efficiency is worse compared with the SOFC efficiency.

Additional calculations show that HS operation with constant TIT, which means a controllable secondary fuel flow, is less sensible to variations of current density and shaft speed than HS operation with zero secondary fuel flow because there is no feedback from the recuperator's thermal capacitance.

4.2 Defining the Operating Curve. The challenge of a power plant is to deliver a certain power to the customer ensuring minimization of fuel demand, safe operation, and fast response times. So the definition of an appropriate operating curve requires many constraints to be considered.

First of all it must cover the desired range of performance with high efficiency. Figure 3 shows that reducing every free parameter simultaneously can fulfill this specification.

Since neither the STCR nor the temperature difference across the SOFC tube length exceeds any critical values in the entire operating range, they do not restrict the definition of the operating curve. According to literature [6,11] common limitations for STCR and temperature difference are 2 and 300 K, respectively. Because of the nondimensional approach spatial temperature gradients cannot be evaluated.

Further constraints represent the lower stack temperature and the differential pressure across the electrolyte. Since low stack temperatures decrease cell voltage and temporal temperature changes degrade cell lifetime, it is recommendable to maintain constant stack temperatures on the entire operating curve. In addition temperature changes will negatively impact the temporal load response due to the high thermal inertia of the stack. Unlike the results in Ref. [11] here it is possible to keep the lower stack temperature constant by controlling the TIT (see Fig. 4). Anyway, a reduction of AU is also required because decreasing fuel flow and shaft speed improve the recuperator effectiveness [5] and lead to minor pressure and thus to increased turbine outlet temperature and stack inlet temperatures.

Comparing Figs. 4 and 5 it can be seen that the isolines of AU and differential pressure are almost parallel (due to the same pressure inside the combustion plenum), so a conflict arises between constant stack temperature and zero differential pressure. Here the

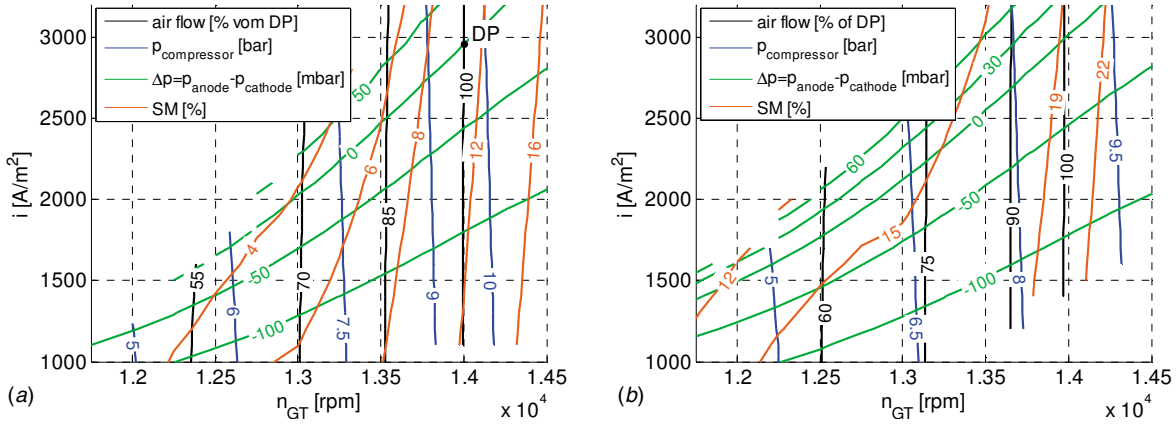

Fig. 5 Turbomachinery parameters: differential pressure for (*a*) TIT=1433 K (left) and (*b*) 1183 K (right).

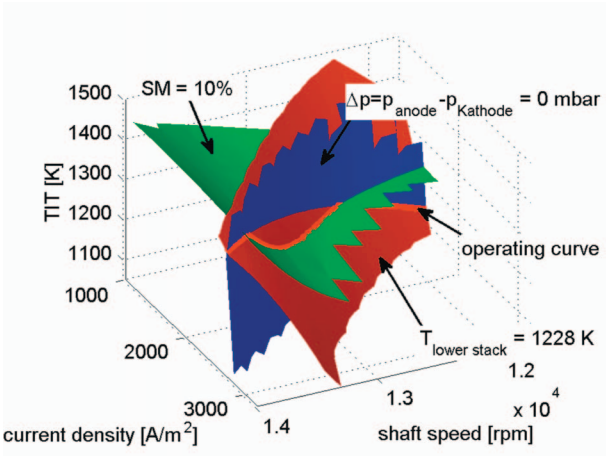

Fig. 6 Definition of the operating curve

third free parameter, thus the TIT, is beneficial. Instead of lowering the AU the TIT can be decreased improving the cell cooling via lower stack inlet temperatures.

At last SM must be mentioned. Considering steep as well as flat speed lines SM is defined as

$$\mathrm{SM} = \left(1 - \frac{\pi}{\pi_{\mathrm{SM}}}\frac{\dot{m}_{\mathrm{SM}}}{\dot{m}}\right)\frac{1}{\mathrm{SM}_{\max}} \tag{7}$$

with the pressure ratio π. From Figs. 4 and 5 it can be seen that SM declines along the isolines of stack temperature, especially for great TIT. Hildebrandt et al. [4] observed a similar behavior in their studies. It is not universal and depends strongly on the used turbomachinery maps. Again reduction of TIT can enlarge the operating range (see Fig. 5).

After these preliminary considerations the operating curve is defined by the intersections of the isoareas of SM (10%), differential pressure (0 mbar), and lower stack temperature (1228 K) in the three-dimensional operating space. In doing so the isoareas are fitted with complete bicubic trial functions. Then the intersections are cubic functions that are analytically calculated using Cardanic formulas. The resulting operating curve consists of three sections (see Fig. 6). The middle section lasts from 56% to 97% part-load and is characterized by the minimal allowable SM and constant lower stack temperature. Differential pressures of up to 17 mbars have to be tolerated there. In contrast stack temperature and differential pressure are constant in the other sections, since there SM is above 10%. Figure 7 shows the actuating values along the operating curve as functions of dimensionless HS power. One can see that the variation range is quite different: e.g., it constitutes 6% points for the cell voltage and almost 100% for the secondary fuel flow. The HS power range lasts from below 40% to above 105%. Additional significant parameters are reported in Fig. 8. So,

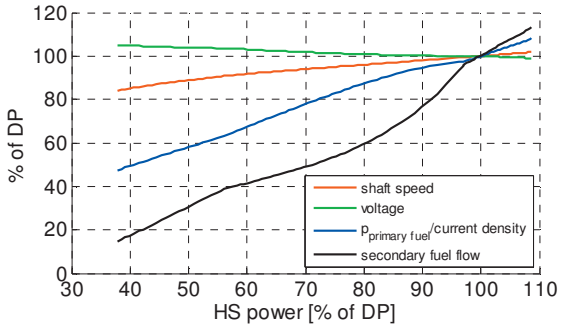

Fig. 7 Actuating values on the operating curve

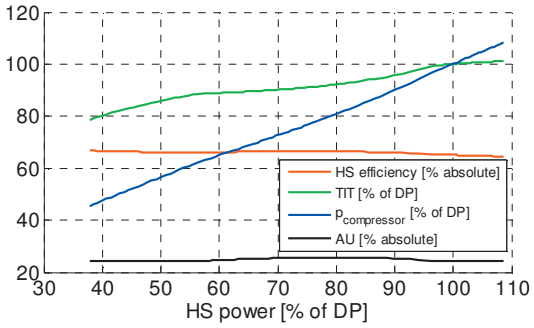

Fig. 8 Additional significant parameters

the HS efficiency features values over 64% along the entire operating range, while the TIT decreases monotonically from 101% down to 79%.

This operating curve can be used in different control studies, e.g., as a map-based pilot control or to calculate secondary setpoint values of inner control loops as a function of the primary setpoint value HS power.

5 Transient Behavior

This section reveals the causal progress and also the critical incidents during transient load changes. To improve the insight into the HS first four simulation runs are carried out changing only one actuating value and keeping the residual constant. After listing the identified characteristic effects a fifth simulation is described in more detail (Figs. 9–11). There each actuating value is changed according to the previously defined operating curve given a 30% load reduction step change.

For these theoretical studies step functions are applied to voltage, fuel flow, and fuel pressure. Allowing for its inertia shaft speed is always varied along a ramp function.

The general results are given as follows.

- The behaviors of the three heat storing elements and the affected temperatures are coupled and characterized by different relaxation times. The recuperator reaches its new steady state first, and the lower stack last.
- The long-term behavior of the HS is dominated by the lower stack temperature. If the thermal balance of the lower stack is positive (e.g., because its cooling is worse due to a reduction of shaft speed), the temperatures and pressures of the entire HS will increase and thus SM will decrease. On the other hand, if the thermal balance is negative (e.g., owing to a reduction of cell current), the temperatures and pressures

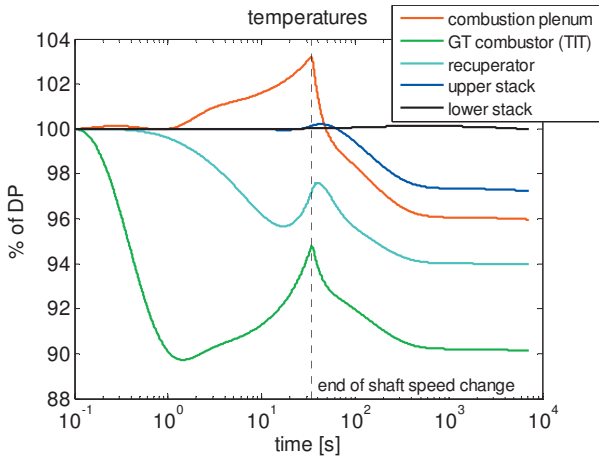

Fig. 9 Temperatures during load decrease (100%→70%)

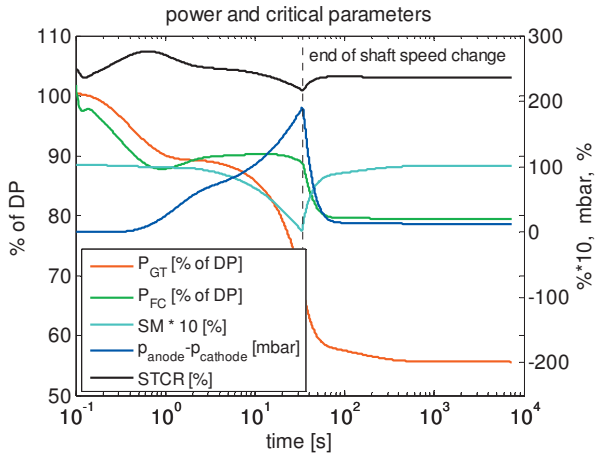

Fig. 10 Power and critical parameters during load decrease (100%→70%)

of the entire HS will decrease. Then cell current continues to decrease and in certain circumstances the unused fuel may rise the temperatures again.

A change of shaft speed (rate of change: −100 rpm/s) exhibits some interesting and maybe critical impacts as follows.

- Reduction of shaft speed can lead to compressor surge, because due to large SOFC volumes the pressure decreases slowly.
- The pressure changes induced into the cathodic cycle result in temporary high pressure differences between the cathode and the anode since the pressure change of the anode is delayed. Thereby its behavior is probable dependent on the size of the plenum volumes concerned.
- In the case of a shaft speed increase, the same time delay involves temporarily small differential pressures between the anode and the combustion plenum and the danger of oxygen flow into the anode.
- Depressurization of the anode cycle conveyed additional fuel into the anode. Despite increasing cell current FU declines and causes low STCR and high temperatures inside the combustion plenum and the GT combustor.
- Simultaneously the recycled mass flow decreases.

A step change in cell voltage affects the HS as follows.

- A voltage rise forces the cell current to decrease almost instantly. Simultaneously FU drops so that STCR and the temperatures inside the combustion plenum and the GT combustor can reach unfavorable values.
- Because of the model approach the gas density inside the anode and thus the mass flow also drops instantly.
- In contrast large voltage drops force cell current and FU to rise. This might lead to an undersupply of fuel inside the anode.
- Due to critical turbine flow greater TIT pressurizes the cathodic cycle, which takes back time-delayed effect onto the anodic cycle (see above).
- The lower stack reaches its steady state temperature comparatively fast since current reduction and stack inlet temperature rise compensate each other.

A reduction of primary fuel pressure has the following effects.

- Like the fuel flow itself the momentum is proportional to the fuel pressure. Since it is the actuation of the flow inside the anodic cycle, there the mass flows as well as the pressures are reduced.
- However, for the first 10 s the ejector pressure rises because the law of conservation of momentum forces the mass outflow to sink faster than the inflow.
- Less fuel arrives at the anode and cell current declines. Thereby FU and STCR increase, which lead to sinking temperatures downstream the cathode.
- In contrast to the first two cases here the depressurization begins in the anodic cycle and is transmitted into the cathodic side via a declining anode outflow.
- Due to minor reforming conversion the lower stack temperature increases first (for about 1 s) and then it begins to fall because of decreasing stack inlet temperatures.

Decreasing secondary fuel flow results in the following.

- TIT declines. Owing to critical turbine flow this leads to minor pressures and rising mass flows in the cathodic cycle followed by a greater SM.
- The depressurization of the anodic cycle is delayed compared with the cathodic cycle and exhibits the same effects already mentioned in case of the shaft speed change.

The results of the 30% load step change are shown in Figs. 9–11, featuring several effects previously described. For example, one can identify the decrease in the TIT (see Fig. 9, due to the reduction of secondary fuel flow), the decline of the fuel cell power (see Fig. 10, due to voltage rise, primary fuel pressure drop, and shaft speed reduction), or the decrease in mass flows in

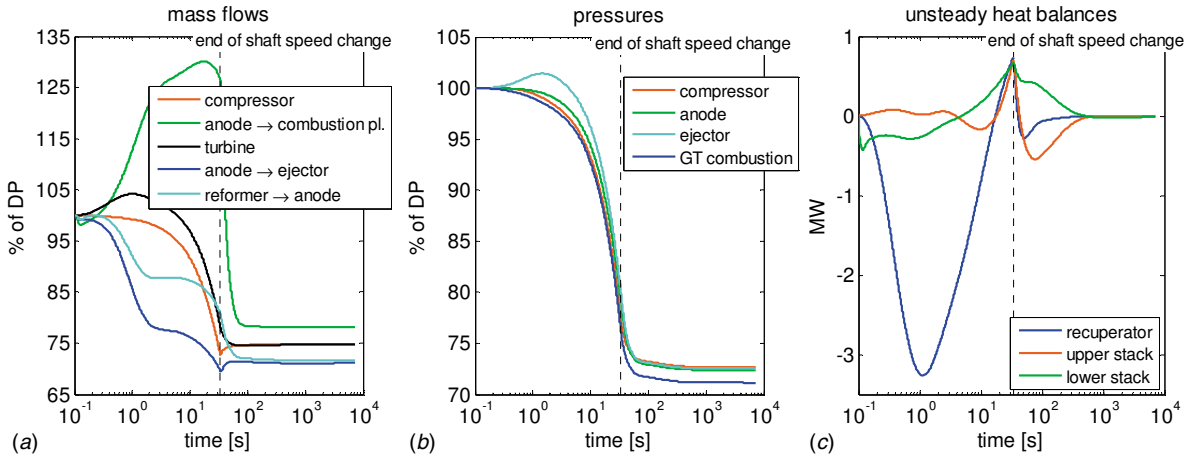

Fig. 11 (*a*) Mass flows, (*b*) pressures, and (*c*) heat balances during load decrease (100%→70%)

the anodic cycle and the temporary rise of the ejector pressure (see Figs. 11(*a*) and 11(*b*), due to primary fuel pressure drop). However, the negative effects are not critical. So the danger of running into surge because of shaft speed reduction is prevented (see Fig. 10) by the simultaneous reduction of the TIT and additionally by a smaller rate of change of shaft speed (−25 rpm/s). As another example the depressurization of the cathodic cycle (see Fig. 11(*b*), due to reduction of shaft speed and secondary fuel flow) is partially compensated for by the depressurization of the anodic cycle (see Fig. 11(*b*), due to primary fuel pressure drop). So peak differential pressure between the anode and the cathode decreases to 200 mbars. Again the depressurization is accompanied by temporary extra fuel flow into the anode leading to less FU, smaller STCR (see Fig. 10), and temperature peaks at 34 s (see Fig. 9). However, no critical values are overshot as prior STRC has gone up and most temperatures have declined. Of course, the temperatures affect the heat balances. Thus they exhibit peaks at 34 s, too (see Fig. 11(*c*)). However, it is more noteworthy even though intended that the lower and the upper stack reach its steady state at the same time. This is because the variations of the actuating values are adjusted according to the specifications of the operating curve. As a consequence the temperature of the lower stack is quasiconstant. Although its heat balance is distorted, it balances relatively fast since the reduction of heat supply (due to cell current reduction) and the decrease in cooling air (due to the reduction of mass flow) compensate each other.

So the relaxation time of system power that is most important for power plants decreases significantly down to 500 s compared with the first simulations (above 5000 s). However, this is still quite long for a plant connected to the grid or even for a plant in isolated operation [11]. A suitable control system might decrease the relaxation times further. The challenge is to adjust and to time the variations of the actuating values in such a way that its different effects onto the system behavior are used to prevent critical situations. The analysis of the simulated load change has already revealed some possibilities to do so.

6 Conclusions

A model of a SOFC/GT-HS has been presented to investigate the steady state as well as the dynamic behavior of the HS. As a special feature a secondary fuel flow supplied to the GT combustor is considered.

The calculation of the entire steady state operating behavior reveals the advantages of a controllable TIT. It permits the definition of a steady state operating curve, whose operating points are all characterized by constant lower stack temperature, high efficiency, tolerable SM, and small differential pressures between the anode and the cathode.

However, there is a disadvantage of secondary fuel flow, too. It decreases the HS efficiency due to worse efficiency of the GT. Comparing both maps in Fig. 3 they show that lowering the TIT and rising the cell current can result in operating points with equal power but better efficiency.

In accordance to Ref. [11] the operating area still exhibits regions where no stable operation is possible, since the stack temperature exceeds its tolerable limits.

The dynamic simulations expose several critical aspects that have to be cared for. Again the TIT can help to overcome some of these. For example, it can be decreased to sustain a tolerable SM. A further conclusion is that the variations of the actuating values must and can be adjusted and timed in such a way that its different effects onto the system behavior are used to ease or even prevent critical situations.

The last comments concern the model quality. Since the estimation of the geometrical data is very uncertain and the actual model was not validated against true measurements, the quantitative data presented here are also uncertain. However, the qualitative trends are assumed to have a more general meaning, so that the model can be used to develop a general control strategy. This assumption is confirmed by a comparison with the data presented in Ref. [11].

Future investigations will deal with controlling the power output of the HS. Then possible load ramp rates will be given and also suitable current, fuel flow, and shaft speed ramp rates. However, they refer solely to the system modeled since they depend strongly on the geometrical data used. Their interaction with critical parameters will be part of the investigation, too.

Merely the importance of the calculation of the gas compositions with steady state conservation equations for the dynamic behavior of the HS should be investigated further.

Nomenclature

Abbreviation

AU = air utilization
ac = alternating current
COE = cost of electricity
dc = direct current
DP = design point
FC = fuel cell
FU = fuel utilization
G = generator
rec = recuperator
STCR = steam-to-carbon ratio

Variables

i = current density
k_1–k_6 = polynomial functions of the shaft speed
$\dot{m}$ = mass flow
n = rotational speed
P = power
p = pressure
$\dot{Q}$ = heat flux
T = temperature

Greek Symbols

π = pressure ratio
η_s = isentropic efficiency

Subscripts

max = maximum
min = minimum
red = reduced

References

[1] Miller, A., Milewski, J., and Salacinski, J., "Off-Design Operation of Fuel Cell-Gas Turbine Hybrid System," Institute of Heat Engineering, Warsaw University of Technology, Warsaw, Poland.

[2] Sedghisigarchi, K., and Feliachi, A., 2006, "Impact of Fuel Cells on Load-Frequency Control in Power Distribution Systems," IEEE Trans. Energy Convers., **21**(1), pp. 250–256.

[3] Kemm, M., Hildebrandt, A., and Assadi, M., 2004, "Operation and Performance Limitations for Solid Oxide Fuel Cells and Gas Turbines in a Hybrid System," ASME Paper No. GT2004-53898.

[4] Hildebrandt, A., Genrup, M., and Assadi, M., 2004, "Steady-State and Transient Compressor Surge Behavior Within a SOFC-GT-Hybrid System," ASME Paper No. GT2004-53892.

[5] Costamagna, P., Magistri, L., and Massardo, A. F., 2001, "Design and Part-Load Performance of a Hybrid System Based on a Solid Oxide Fuel Cell Reactor and a Micro Gas Turbine," J. Power Sources, **96**, pp. 352–368.

[6] Magistri, L., Bozzo, R., Costamagna, P., and Massardo, A. F., 2002, "Simplified Versus Detailed SOFC Reactor Models and Influence on the Simulation of the Design Point Performance of Hybrid Systems," ASME Paper No. GT-2002-30653.

[7] Magistri, L., Trasino, F., and Costamagna, P., 2004, "Transient Analysis of Solid Oxide Fuel Cell Hybrids Part A: Fuel Cell Models," ASME Paper No. GT2004-53842.

[8] Ferrari, M. L., Traverso, A., and Massardo, A. F., 2004, "Transient Analysis of Solid Oxide Fuel Cell Hybrids Part B: Anode Recirculation Model," ASME Paper No. GT2004-53716.

[9] Magistri, L., Ferrari, M. L., Traverso, A., Costamagna, P., and Massardo, A. F., 2004, "Transient Analysis of Solid Oxide Fuel Cell Hybrids Part C: Whole-Cycle Model," ASME Paper No. GT2004-53845.

[10] Ferrari, M. L., Magistri, L., Traverso, A., and Massardo, A. F., 2005, "Control System for Solid Oxide Fuel Cell Hybrid Systems," ASME Paper No. GT2005-68102.
[11] Stiller, C., Thorud, B., and Bolland, O., 2005, "Safe Dynamic Operation of a Simple SOFC/GT Hybrid System," ASME Paper No. GT2005-68481.
[12] Stiller, C., Thorud, B., Bolland, O., Kandepu, R., and Imsland, L., 2006, "Control Strategy for a Solid Oxide Fuel Cell and Gas Turbine Hybrid System," J. Power Sources, **158**, pp. 303–315.
[13] Lundberg, W. L., Veyo, S. E., and Moeckel, M. D., 2003, "A High-Efficiency Solid Oxide Fuel Cell Hybrid Power System Using the Mercury 50 Advanced Turbine Systems Gas Turbine," ASME J. Eng. Gas Turbines Power, **125**, pp. 51–58.
[14] Veyo, S. E., Lundberg, W. L., Vora, S. D., and Litzinger, K. P., 2003, "Tubular SOFC Hybrid Power System Status," ASME Paper No. GT2003-38943.
[15] Campanari, S., 2001, "Thermodynamic Model and Parametric Analysis of a Tubular SOFC Module," J. Power Sources, **92**, pp. 26–34.
[16] Song, T. W., Sohn, J. L., Kim, J. H., Kim, T. S., Ro, S. T., and Suzuki, K., 2004, "Parametric Studies for a Performance Analysis of a SOFC/MGT Hybrid Power System Based on a Quasi-2D Model," ASME Paper No. GT2004-53304.
[17] Wächter, C., Lunderstädt, R., and Joos, F., 2006, "Dynamic Model of a Pressurized SOFC/Gas Turbine Hybrid Power Plant for the Development of Control Concepts," J. Fuel Cell Sci. Technol., **3**, pp. 271–279.
[18] Veyo, S. E., Shockling, L. A., Dederer, J. T., Gillet, J. E., and Lundberg, W. L., 2000, "Tubular Solid Oxide Fuel Cell/Gas Turbine Hybrid Cycle Power Systems—Status," ASME Paper No. 2000-GT-550.
[19] Campanari, S., and Iora, P., 2004, "Definition and Sensitivity Analysis of a Finite Volume SOFC Model for a Tubular Cell Geometry," J. Power Sources, **132**, pp. 113–126.
[20] Gnielinski, V., 1997, *VDI-Wärmeatlas: Wärmeüber-Tragung bei der Querströmung um Einzelne Rohrreihen und Durch Rohrbündel (8. Auflage)*, Springer, Berlin.
[21] Utriainen, E., and Sundén, B., 2002, "Evaluation of the Cross Corrugated and Some Other Candidate Heat Transfer Surfaces for Microturbine Recuperators," ASME J. Eng. Gas Turbines Power, **124**, pp. 550–560.
[22] Kurzke, J., 2001, "GasTurb 9—A Program to Calculate Design and Off-Design Performance of Gas Turbines," Germany, http://www.gasturb.de

Steady-State and Transient Performance Modeling of Smart UAV Propulsion System Using SIMULINK

Jayoung Ki
Easy Gas Turbine R&D Co., Ltd.,
1112-Ho, Cention Building, 1
412 Dunsan-dong, Seo-gu,
Daejeon 301-120, Republic of Korea
e-mail: young@ezgtc.com

Changduk Kong
e-mail: cdgong@chosun.ac.kr

Seonghee Kho
e-mail: habari@paran.com

Department of Aerospace Engineering,
Chosun University,
375 Seosuk-dong, Dong-gu,
Gwangju 501-759, Republic of Korea

Changho Lee
Smart UAV Development Center,
Korea Aerospace Research Institute,
45 Eoeun-dong, Yuseong-gu,
Daejeon 305-333, Republic of Korea
e-mail: leech@kari.re.kr

Because an aircraft gas turbine operates under various flight conditions that change with altitude, flight velocity, and ambient temperature, the performance estimation that considers the flight conditions must be known before developing or operating the gas turbine. More so, for the unmanned aerial vehicle (UAV) where the engine is activated by an onboard engine controller in emergencies, the precise performance model including the estimated steady-state and transient performance data should be provided to the engine control system and the engine health monitoring system. In this study, a graphic user interface (GUI) type steady-state and transient performance simulation model of the PW206C turboshaft engine that was adopted for use in the Smart UAV was developed using SIMULINK for the performance analysis. For the simulation model, first the component maps including the compressor, gas generator turbine, and power turbine were inversely generated from the manufacturer's limited performance deck data by the hybrid method. For the work and mass flow matching between components of the steady-state simulation, the state-flow library of SIMULINK was applied. The proposed steady-state performance model can simulate off-design point performance at various flight conditions and part loads, and in order to evaluate the steady-state performance model their simulation results were compared with the manufacturer's performance deck data. According to comparison results, it was confirmed that the steady-state model agreed well with the deck data within 3% in all flight envelopes. In the transient performance simulation model, the continuity of mass flow (CMF) method was used, and the rotational speed change was calculated by integrating the excess torque due to the transient fuel flow change using the Runge–Kutta method. In this transient performance simulation, the turbine overshoot was predicted. [DOI: 10.1115/1.2982141]

1 Introduction

Since an aircraft gas turbine operates under different flight conditions that change with altitude, flight velocity, and ambient temperature, the performance estimation considers that the flight conditions must be known before developing or operating the gas turbine. In the early stage of gas turbine development this gas turbine performance could be obtained from the experimental tests performed in a simulated environmental test chamber, although recent technological advancement proves that computer performance models may be used to simulate engine performance.

The computer performance model can reduce greatly the engine development cost and risk.

The steady-state performance simulation also can be divided into a design point performance analysis that can estimate each component performance through the cycle analysis to meet the engine design requirements, including thrust and specific fuel consumption, into an off-design point performance simulation that considers various ambient and flight conditions at performance estimation, and into a part-load performance simulation that is analyzed at different rotational speeds from the design point.

The transient performance simulation can estimate the time dependent dynamic performance by the engine state change, such as fuel throttling. Hence it can estimate temperature overshoot that may give fatal failure of the gas generator turbine, or the compressor stall at the transient state. The transient performance simulation can be built based on the knowledge of the steady-state performance model. Therefore the steady-state performance modeling should be done prior to having the transient performance model.

Performance simulation programs have been developed by the text programming languages, such as FORTRAN, PASCAL, etc. [1,2]. However, there is a growing tendency for these to transform into a graphic user interface (GUI) program [3]. A good example is the commercial program MATLAB/SIMULINK, which can apply various numerical analysis techniques and has the capability of adding control functions now widely used in propulsion system modeling. A dynamic nonlinear model of a single-shaft industrial gas turbine using SIMULINK was developed by Bettocchi et al. [3]. This model is composed of modular structures representing individual engine components in their simplified form. A 65 MW heavy-duty gas turbine plant model was also built using SIMULINK by Crosa et al. [7].

In this study, a GUI type steady-state and transient performance simulation model of the PW206C turboshaft engine for the Smart unmanned aerial vehicle (UAV) that was developed by the Korea Aerospace Research Institute (KARI) was developed using SIMULINK, and the performance analysis was performed by this performance simulation model.

The steady-state analysis results were compared with the performance deck data provided by engine manufacturer to evaluate

Contributed by the International Gas Turbine Institute of ASME for publication in the JOURNAL OF ENGINEERING FOR GAS TURBINES AND POWER. Manuscript received March 31, 2008; final manuscript received April 9, 2008; published online February 10, 2009. Review conducted by Dilip R. Ballal. Paper presented at the ASME Turbo Expo 2008: Land, Sea and Air (GT2008), Berlin, Germany, June 9–13, 2008.

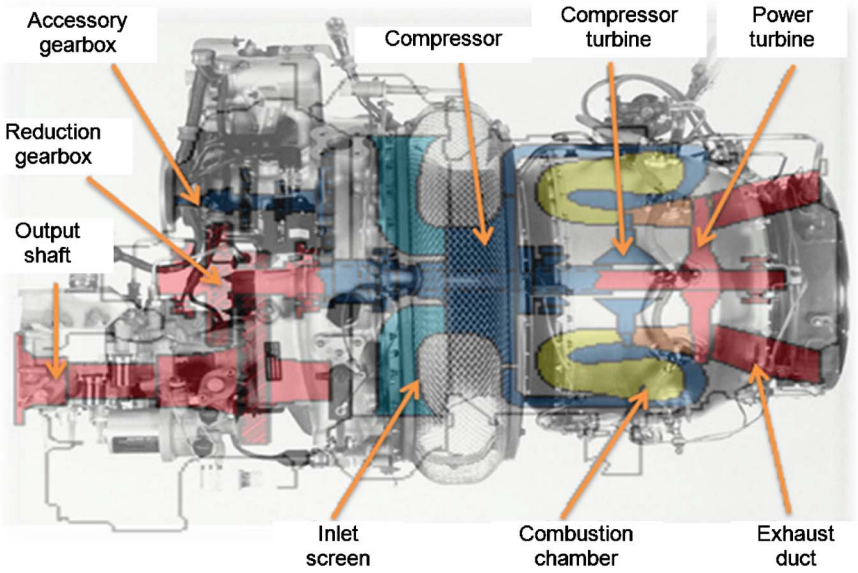

Fig. 1 Engine schematic of the PW206C turboshaft engine

the developed performance model, and the dynamic performance parameters, such as the transient torque and compressor exit pressure and the gas generator turbine temperature, was simulated by the transient performance model.

2 Engine Specification

A performance simulation program for the PW206C turboshaft engine that was selected as a power plant for the tilt rotor type Smart UAV developed by KARI was developed. Figure 1 shows the schematic engine layout.

As seen in Fig. 1, the engine has a gas generator composed of a single stage centrifugal compressor, a reverse flow annular type combustion chamber, a single stage compressor turbine, and a power section composed of a single stage free power turbine, an exhaust duct, a reduction gear box, and an output drive shaft. The System Integration Group of the Smart UAV R&D Center of KARI provided the required operating range for the propulsion system, as shown in Table 1.

Table 1 Operating range of the propulsion system Smart UAV

Ambient temp.	ISA ± 30
Altitude (km)	0–5
Flight velocity (km/h)	0–500

Table 2 Design performance data

Variable	Values
Atmospheric condition	S/L, static STD condition
Mass flow rate (kg/s)	2.004
Fuel flow rate (kg/s)	0.0392
Compressor pressure ratio	7.912
Exhaust gas temperature (K)	865
Power (kW)	416
SFC (kg/kW h)	0.34
Gas generator rotational speed (100% rpm)	54,751
Propeller rotational speed (100% rpm)	6,000

Table 2 shows design performance data at the maximum take-off condition, which were provided by the engine manufacturer (EEPP Manual), and Table 3 explains the engine operation limit [4].

3 Component Map Generation Using Hybrid Intelligent Method

If real component maps cannot be obtained from the engine manufacturer, they can generally be scaled based on the design point data from similar component maps using the well known scaling method. Although the generated maps by this method have a similar performance behavior around the design point, they have a much bigger error if the performance analysis point is located farther away from the design point. Prior to building the performance model, major component maps, such as compressor, gas generator compressor, and turbine maps, should be known.

In order to generate much closer component maps, a new intelligent method was proposed instead of the traditional scaling method. The used component map generation scheme in this study is a hybrid method that is a combination of the previously developed "system identification method" and "genetic algorithm method [5]." The brief view of this hybrid intelligent method is as follows.

First the scaling is performed at each engine rotational speed with some limited performance data provided by the engine manufacturer, and then the component characteristic equations are obtained at each engine rotational speed using the system identification method.

Table 3 Engine operating limit

Variable	Values
Torque (N m)	759.26
Power (kW)	418
Bleed air (%)	5
Compressor speed (rpm)	58,900
Fuel flow (kg/h)	192.78
Comp. delivery pressure (kPa)	1,034.2
Power limit (kW)	5.96

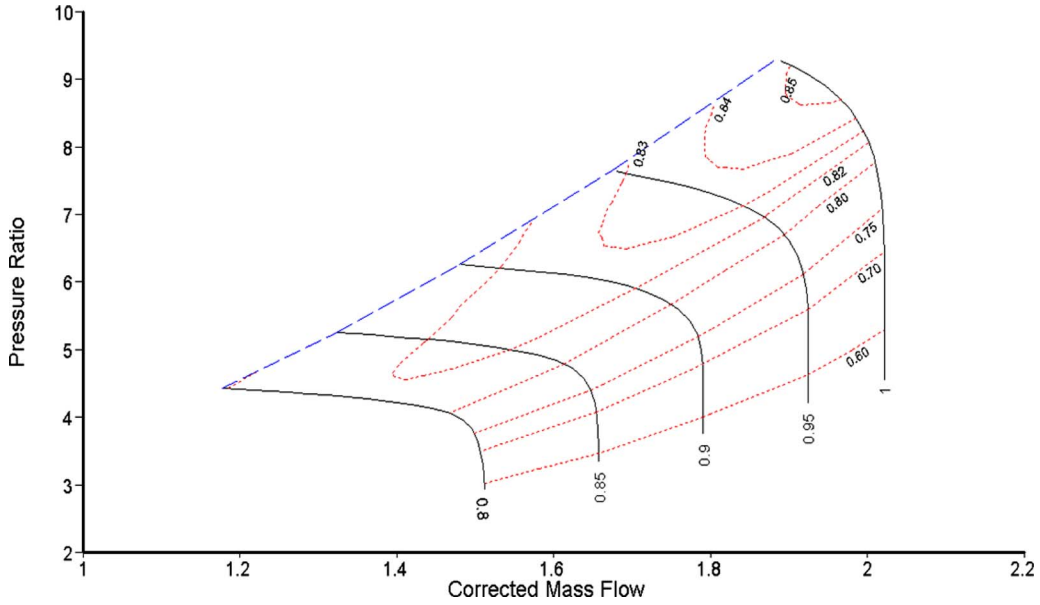

Fig. 2 Generated compressor map by the hybrid intelligent method

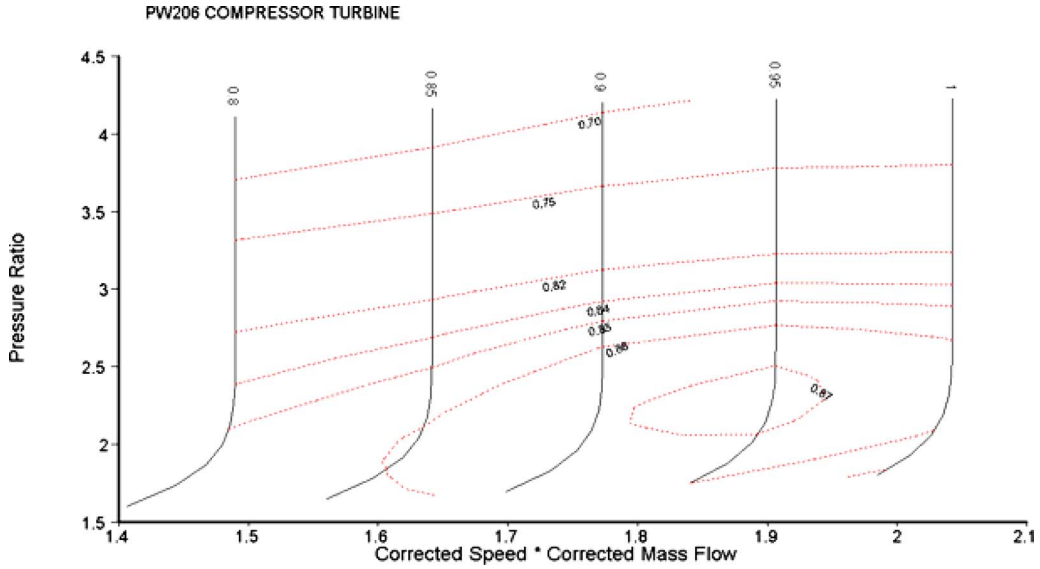

Fig. 3 Generated compressor turbine map by the hybrid intelligent method

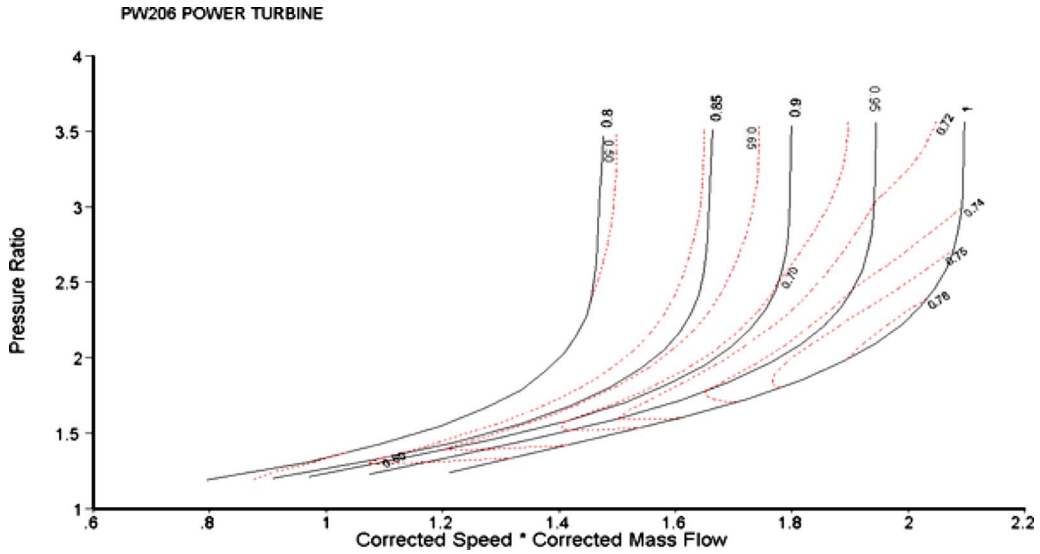

Fig. 4 Generated power turbine map by the hybrid intelligent method

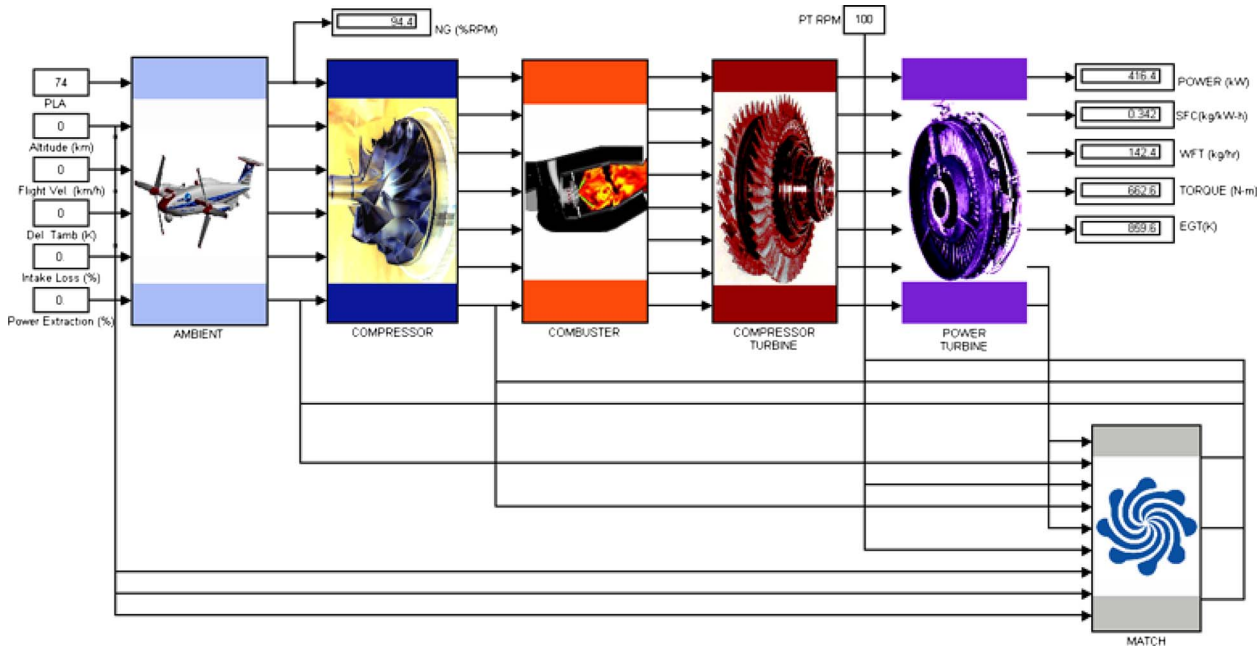

Fig. 5 Steady-state performance model using SIMULINK®

Second the initially obtained component characteristics are modified by considering the engine component behaviors for various operational conditions, such as the flight Mach number, altitude, and atmospheric temperature, using genetic algorithms (GAs). In the modification by the GA, component characteristics obtained by the system identification are used as initial data to reduce the calculation time.

Finally the component map is generated by integrating the component characteristic equations taken at each engine rotational speed. Resulting generated component performance maps by the hybrid intelligent method are illustrated in Figs. 2–4.

4 Steady-State Performance Modeling

The overall the SIMULINK® model for the PW206C turboshaft engine is expressed in Fig. 5 [6]. The overall model is composed of modular blocks representing individual components, such as the ambient subsystem for the flight environment condition, the intake subsystem, the compressor subsystem, the combustor subsystem, the compressor turbine subsystem, the power turbine subsystem, and the match subsystem for work and mass flow matching between components.

In this SIMULINK model, the β-line method was used for rapid convergence, and Reynold's effect was considered for precise calculation. For work matching between the compressor and compressor turbine and mass flow matching between the gas generator and power turbine, the subsystem "state flow" was proposed. After this subsystem calculates the error in mass flow and work matching, it searches repeatedly the updated β values until the matching error reaches 0.5%. Figure 6 shows the flowchart for the steady-state performance simulation model.

After carrying out the performance analysis at off-design point conditions, such as various gas generator rotational speeds, flight velocities, and ambient temperatures, the analysis results were compared with the manufacturer's performance deck data. Figure 7 shows the comparison result. Because the maximum performance of the Smart UAV propulsion system is limited to 94.4% gas generator speed due to the UAV system's performance requirement (i.e., power limit), the comparison was carried out at the gas generator speed range from 70% to 94.4% speed. The slightly large deviation of the top line (cold ambient temperature condition at sea level) at 94.4% speed may be caused by the consideration of the torque limit in the manufacturer's performance deck.

According to comparison results, analysis results of the proposed model were well agreed with the performance deck data within a 3% error. At specific operation regions, because the engine performance exceeds the engine operation limit, the engine operator must give attention when handling the engine in these regions.

5 Transient Performance Modeling

When fuel input is rapidly increased or decreased, the engine runs in the transient state, and the transient power output produced by the rotor shaft is surpassed or insufficient for the required work

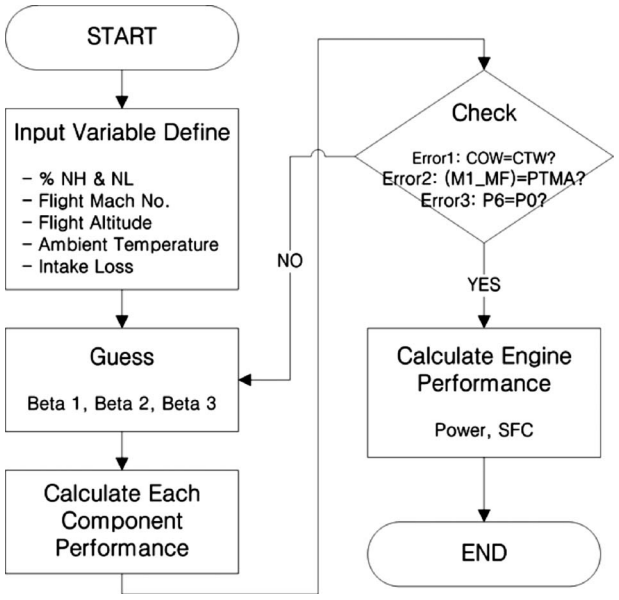

Fig. 6 Flowchart for the steady-state performance simulation

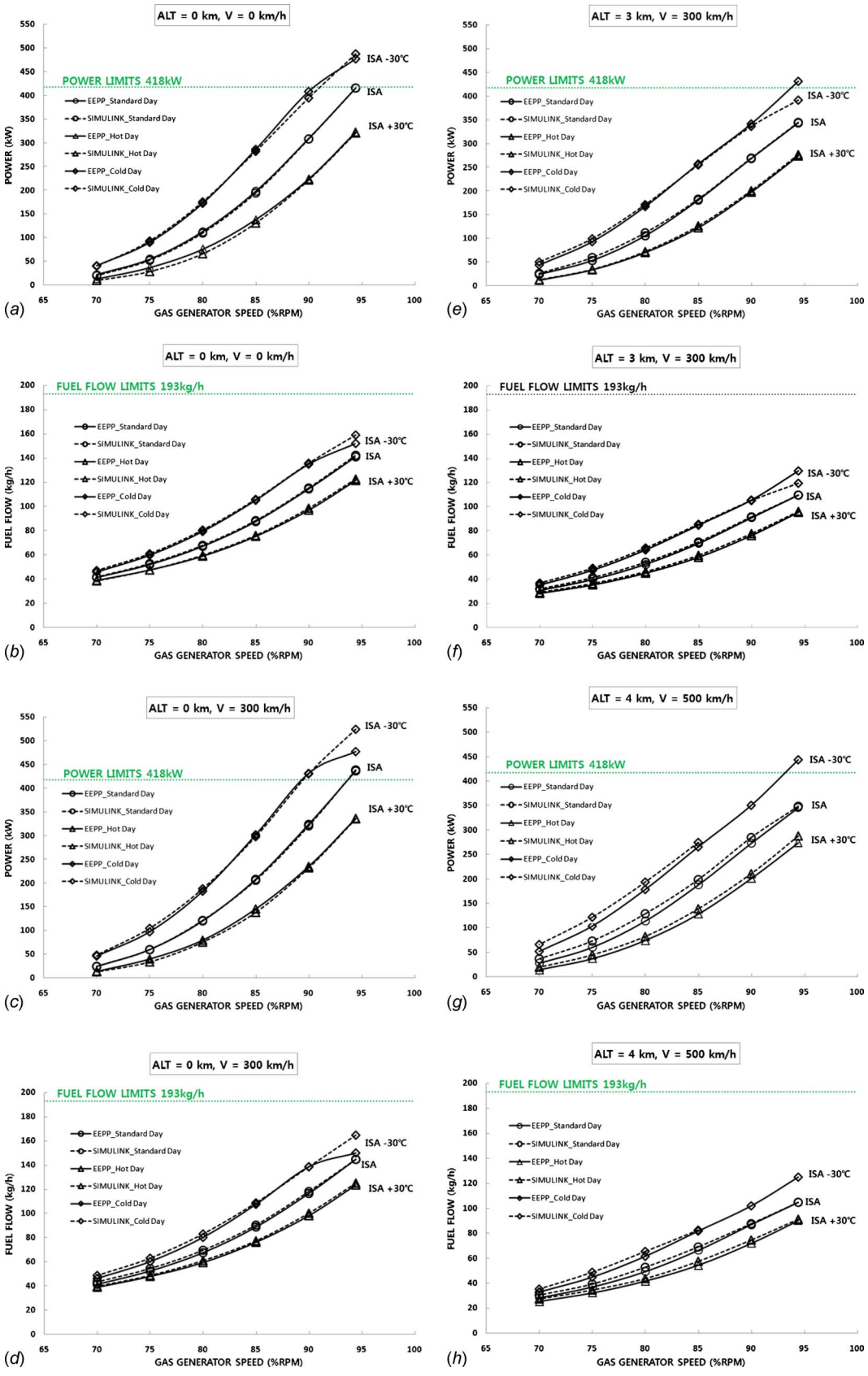

Fig. 7 Results of the steady-state performance analysis

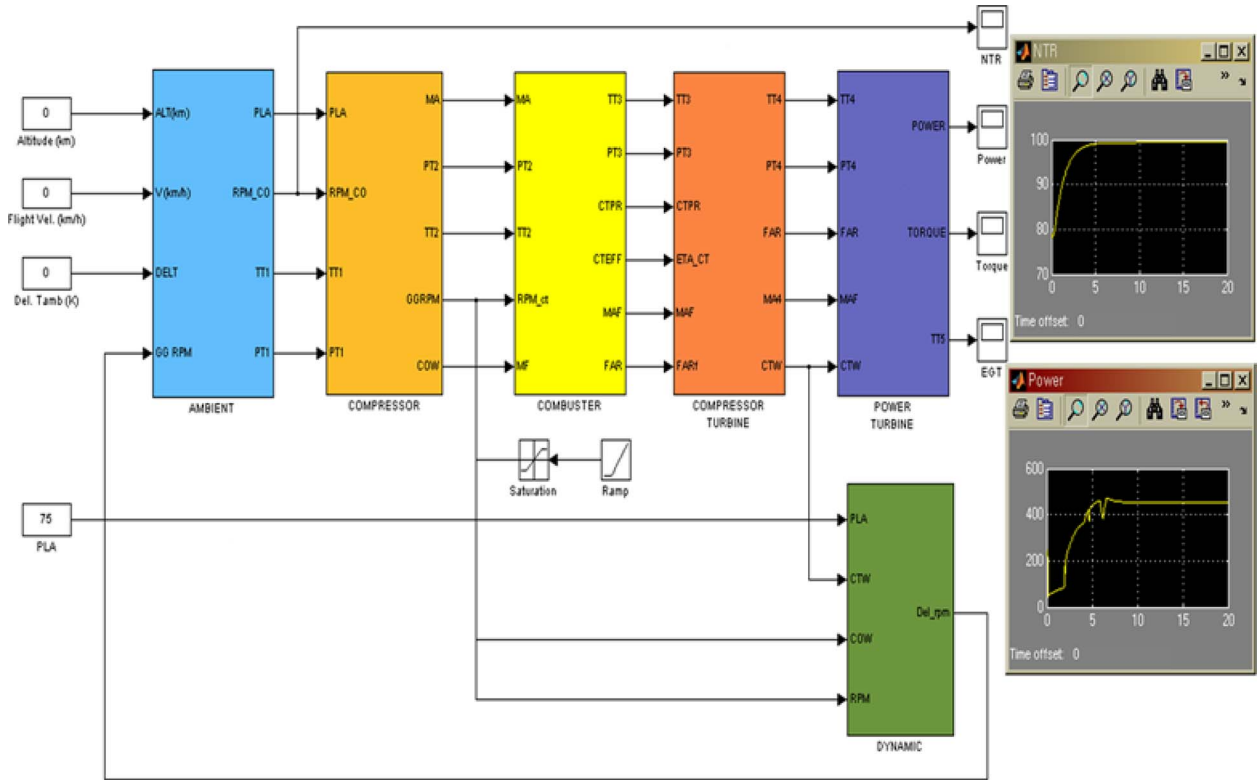

Fig. 8 Transient performance model using SIMULINK®

balance between the compressor and the compressor turbine. Consequently, the engine is frequently beyond the operational range, which may damage the engine or shorten its lifetime.

When the engine is operated in rapid acceleration, the overshoot of the compressor turbine inlet temperature may exceed frequently the thermal stress limit produced in the turbine blade. Therefore it is very important that the dynamic characteristics of the engine should be correctly simulated or anticipated when improving the reliability of the engine during the transient operation of an engine.

In this study, the transient simulation model of the PW206C turboshaft engine was constructed using SIMULINK®, shown in Fig. 8, and the acceleration and deceleration performance was simulated by this transient model.

For this transient performance simulation algorithm, the continuity mass flow (CMF) method was adopted to limit the tedious calculation brought about as a result of large changes in rotational speed [8]. The concept of the CMF method means that the stored mass flow between engine components is ignored. In other words, since the mass flow passed through then each component must be constant; the iteration process for mass flow matching is needed. Figure 9 shows the flowchart for the transient performance simulation.

The work difference between the compressor and the gas generator turbine in the transient state can be expressed in the following equation:

$$\dot{m}_{CT}\Delta H_{CT} = \dot{m}_C \Delta H_C + \left(\frac{2\pi}{60}\right)^2 I \cdot N \cdot \frac{dN}{dt} \tag{1}$$

In the transient performance simulation, the increase or decrease in the gas generator rotor shaft rotational speed can be calculated by integrating the surplus torque of the second term on the right hand side equation. In this study, the Runge–Kutta method was used for integration.

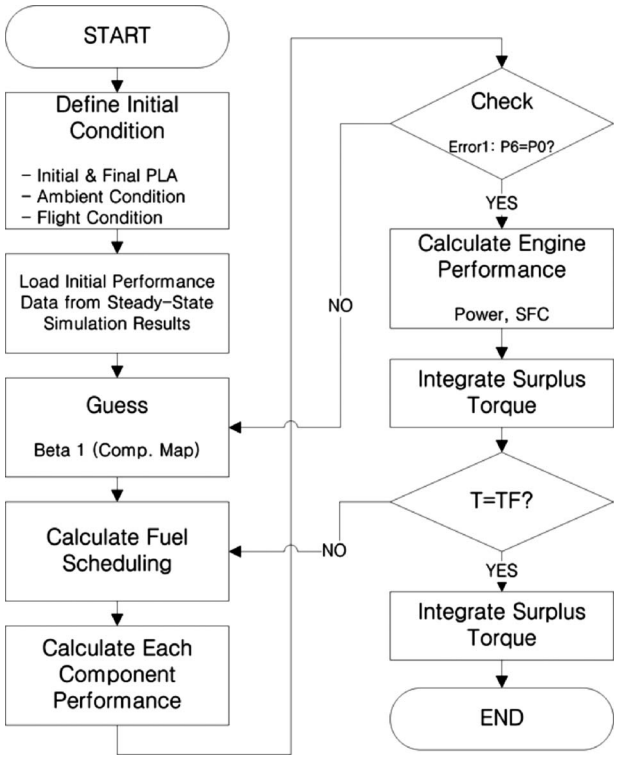

Fig. 9 Flowchart for the transient performance simulation

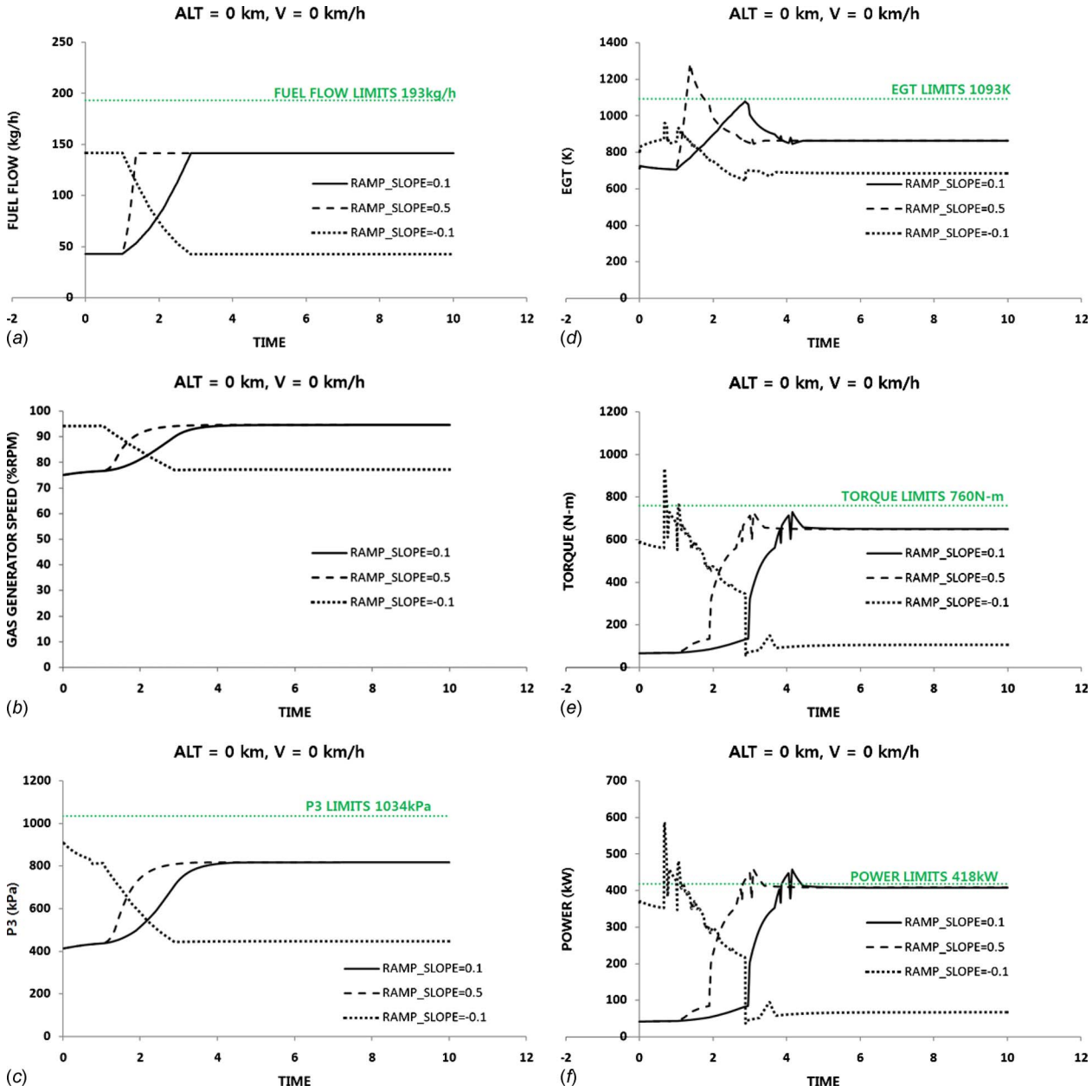

Fig. 10 Results of the transient performance simulation

The transient performance analysis results that were performed by accelerating and decelerating the gas generator rotational speed from 75% to 94.48% according to three types of fuel schedules are shown in Fig. 10.

According to analysis results, if the fuel flow increases rapidly at the acceleration schedule, it was found that the exhaust gas temperature, torque, and power exceed the operational limits. In case of a deceleration schedule, the torque and the power exceed the operational limits even in a short operation period. Therefore, in order to prevent this circumstance, proper fuel control is needed. However, in these acceleration and deceleration fuel schedules, no compressor surge phenomenon was found.

Because the propulsion system of the Smart UAV is under development, the experimental data are not obtained yet. Therefore the validation of the estimated transient performance will be carried out later.

6 Conclusion

In this study, a GUI type steady-state and transient performance simulation model of the PW206C turboshaft engine for the Smart UAV was developed using SIMULINK.

Performance analysis at off-design point conditions under various gas generator rotational speeds, flight velocities, and ambient temperatures was performed, and the analysis results were compared with the manufacturer's performance deck data.

Through this evaluation, the reliability of the proposed performance model was confirmed because the analysis results using the developed model agreed well with the performance deck data within a 3% error. At specific operation regions, it was found that the engine performance exceeds partly the engine operation limits, and therefore the analysis results can be used for basic data to set the engine operational envelope.

The transient simulation model of the PW206C turboshaft engine was constructed based on the steady-state performance simulation model using SIMULINK, and the transient performance analysis was performed by accelerating and decelerating fuel schedules.

According to analysis results, it was found that the performance parameters, such as the gas generator rotational speed, the power, the exhaust gas temperature, and the compressor exit pressure, converge to steady-state values after 4–5 s, and in addition the exhaust gas temperature, torque, and power exceed the operational limits at the beginning of the fuel schedules. A remedial corrective action would be a proper fuel control algorithm.

Nomenclature

alt = altitude
H = enthalpy
I = polar momentum of inertia
N = percentage nondimensional rotational speed
m = mass flow rate

Subscripts

C = compressor
CT = compressor turbine

References

[1] Sellers, J. F., and Daniele, C. J., 1975, "DYNGEN—A Program for Calculating Steady-State and Transient Performance of Turbojet and Turbofan Engines," NASA Technical Report No. TN D-7901.
[2] Palmer, J. R., and Yan, C. Z., 1985, "TURBOTRANS—A Programming Language for the Performance Simulation of Arbitrary Gas Turbine Engines With Arbitrary Control Systems," Int. J. Turbo Jet Engines, **2**, pp. 19–28.
[3] Bettocchi, R., Spina, P. R., and Fabbri, F., 1996, "Dynamic Modeling of Single-Shaft Industrial Gas Turbine," ASME Paper No. 96-GT-332.
[4] *EEPP (Estimated Engine Performance Program) Manual*, Pratt-Whiteny, Canada.
[5] Kong, C. D., Ki, J. Y., and Lee, C. H., 2006, "Components Map Generation of Gas Turbine Engine Using Genetic Algorithms and Engine Performance Deck Data," ASME Paper No. GT-2006-90975.
[6] Kong, C. D., and Ki, J. Y., 2001, "Performance Simulation of Turboprop Engine for Basic Trainer," ASME Paper No. 2001-GT-391.
[7] Crosa, G., Pittaluga, F., Trucco, A., Beltrami, F., Torelli, A., and Traverso, F., 1998, "Heavy-Duty Gas Turbine Plant Aerothermodynamic Simulation Using SIMULINK," ASME J. Eng. Gas Turbines Power, **120**, pp. 550–556.
[8] Pilidis, P., 1996, "Gas Turbine Performance," Cranfield Short Course Note, UK.

Computational Study of the Effects of Shock Waves on Film Cooling Effectiveness

C. X.-Z. Zhang

I. Hassan[1]
e-mail: IbrahimH@alcor.concordia.ca

Concordia University,
Montréal, QC,
H3G 1M8, Canada

The performance of a louver cooling scheme on a transonic airfoil has been studied numerically in this paper. Film cooling holes are located near the passage throat. The Mach number at the location of the jet exit is close to unity. A comparison of film cooling effectiveness between numerical prediction and experimental data for a circular hole shows that the numerical procedures are adequate. In addition to the shock-wave effects and compressibility, curvature effect was also studied by comparing cooling effectiveness on the airfoil surface with that on a flat plate. Substantially higher cooling effectiveness for the louver cooling scheme on the airfoil was predicted at blowing ratios below 1 in comparison to other cooling configurations. At higher blowing ratios than 2 the advantages of the louver cooling scheme become less obvious. It was also found that for the same cooling configuration the cooling effectiveness on the transonic airfoil is slightly higher than that on a flat plate at moderately low blowing ratios below 1. At high blowing ratios above 2 when the oblique shock becomes detached from the leading edge of the hole exits, dramatic reduction in cooling effectiveness occurs as a result of boundary layer separation due to the strong shock waves. A coolant-blockage and shaped-wedge similarity was proposed and found to be able to qualitatively explain this phenomenon satisfactorily. [DOI: 10.1115/1.3026568]

Keywords: film cooling, louver cooling scheme, shaped holes, transonic airfoil, shock-wave reflection, flow past a wedge, CFD, gas turbines

1 Introduction

Film cooling is a technique that is widely used in the aerospace industry to provide cooling protection for gas turbine engines operating under extremely harsh thermal environment. More efficient engines demand more efficient cooling techniques for the gas turbine blades. Early studies on film cooling concentrated on circular holes on a flat plate under incompressible flow conditions. Although there are quite a few studies of film cooling on a curved surface in literature within the past ten years, most of them are under incompressible flow conditions [1–10]. Only a few studies of film cooling involve a high speed test at Mach number higher than 0.5 [11–13] when compressibility of fluid cannot be neglected.

Reiss and Bolcs [14] found that film cooling effectiveness is slightly lower for high Mach number with the onset of flow separation occurring at smaller blowing ratios. It was proposed that an increased Mach number reduces the boundary layer thickness, which in turn causes a stronger jet penetration and a smaller quantity of coolant remaining in the boundary layer while a bigger portion of the coolant was lost to the freestream. Gritsch et al. [15] measured film cooling effectiveness for shaped holes under supersonic flow conditions with mainstream Mach number up to 1.2. It was found that the laterally averaged film cooling effectiveness was hardly affected by the mainstream Mach number for the subsonic test cases. For supersonic cases, however, the laterally averaged effectiveness increases in comparison to the subsonic cases. This is because the jet liftoff is impeded by the shock-induced pressure field. Due to the test section being a flat plate, the effect of surface curvature was not addressed.

Study of the effect of shock-wave interaction on supersonic film cooling was done by Juhany and Hunt [16]. Coolant was injected into a mainstream of Mach 2.4 through a slot parallel to the mainstream and shock wave was induced by placing a variable angle wedge on the top wall of the test section. Contrary to the study of Gritsch et al. [15], shock impingement was found to decrease film cooling effectiveness. Ligrani et al. [17] studied shock-wave interactions with film cooling from a row of cylindrical holes with a simple angle on a flat plate. Freestream Mach numbers of 0.8 and 1.12 were used and it was demonstrated that the cooling effectiveness is generally higher when shock waves are present. Strong oblique shock waves were found to form at the immediate vicinity of the film hole exits and reflect back and forth between the top and the bottom walls. The configurations, locations, and character of these oblique shock waves vary significantly as the blowing ratio is changed. The static pressure can increase by as much as 50% after strong shock waves, which, coupling with mainstream flow deflections, forces larger quantities of cooling film near the surface compared to a situation without shock waves.

The flow behaviors and performance of film cooling in supersonic mainstream flow are significantly different from those when the mainstream flow is subsonic. Both film cooling and shock-wave interaction have been studied heavily in literature. However, combined studies of the two are rare. To the authors' knowledge, the only two of these are Refs. [16] and [17], both of which are experimental studies. A combined numerical study of the two has not been done. If carried out properly, a numerical study could shed new light on this phenomenon as it affords us to examine the solution in great detail that an experimental study would not permit. This paper presents the performance of a louver cooling scheme on a transonic airfoil. The benchmark case [18] is a symmetrical transonic airfoil tested in a wind tunnel with the Mach number, airfoil suction surface geometry, freestream pressure gradient, and boundary layer development matching transonic engine operating conditions. The effects of curvature and compressibility of the working fluid on the performance of different film cooling schemes were examined. Specifically, film cooling behaviors under the mainstream flow condition of Mach number greater than 1

[1]Corresponding author.

Manuscript received April 13, 2008; final manuscript received July 9, 2008; published online February 10, 2009. Review conducted by Dilip R. Ballal.

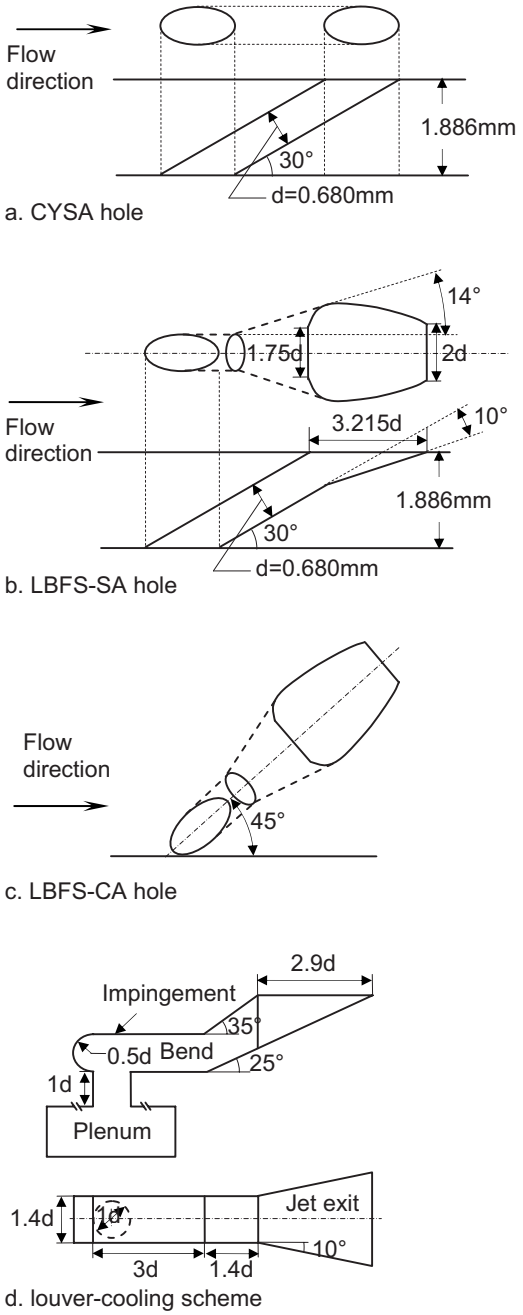

Fig. 1 Geometries of the cooling schemes (a. b. c. reproduced from [18])

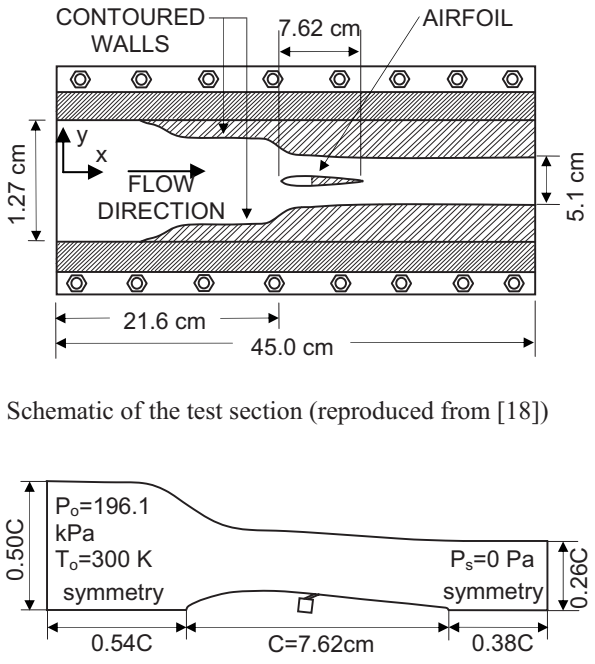

Fig. 2 Test section and computational domain with boundary conditions

were analyzed from a gasdynamics perspective. This study predicted that a dramatic losing of cooling effectiveness caused by boundary layer separation due to the presence of a strong detached shock at very high blowing ratios on a curved surface would occur. A new coolant-blockage and shaped-wedge similarity was also proposed to qualitatively explain this unusual event.

2 Simulation Details

The film cooling configurations are shown in Fig. 1. Film cooling configurations in Figs. 1(*a*)–1(*c*) were based on Ref. [18] and configuration in Fig. 1(*d*) was designed by the authors to be tested numerically on the same airfoil for a comparison. The first three film cooling configurations on an airfoil were tested in a wind tunnel and local film cooling effectiveness and Mach number were measured during a steady state flow condition in a blowdown-type facility in the experimental study [18]. Mach numbers along the airfoil surface range from 0.4 to 1.24, which match values on the suction surface of an airfoil under operating condition. Film cooling holes were located near the passage throat of the air flow passage. A single row of holes was employed on the suction surface with the density ratios about 1.4–1.6 over a range of blowing ratios. The detailed geometries of the test section of the experimental study are presented in Figs. 2(*a*) and 2(*b*) shows the detailed computational domain along with the boundary conditions. To save computational resources, only half of the test section was modeled. The chord length of the airfoil is 7.62 cm. The diameter of the circular hole is 0.680 mm oriented 30 deg toward the airfoil surface. The length of the hole is 5.5*d* with a pitch/diameter ratio of 3.5. A total pressure of 196.1 kPa and a total temperature of 300 K were held at the upstream inlet, and static atmospheric condition was applied at the downstream outlet. Mass flow at the plenum inlet is used as a boundary condition. Periodic boundary conditions were applied on the two faces in the spanwise direction. All the other walls are adiabatic with no-slip boundary conditions. Different blowing ratios were achieved by keeping the mainstream condition constant and changing the mass flow rate at the plenum inlet. Those conditions were based on Refs. [18,19].

The Reynolds number based on the chord length is 1.8×10^6 at the nose of the airfoil and 3.2×10^6 at the throat. Therefore, turbulent flow prevails in the flow passage. Assume the flow is steady state and there is no source of fluid or heat generation in the domain with the gravitational force neglected. The flow was governed by conservation equations of continuity, momentum, and energy.

$$\frac{\partial \rho}{\partial t} + \nabla \cdot (\rho \bar{v}) = 0 \tag{1}$$

$$\frac{\partial}{\partial t}(\rho \bar{v}) + \nabla \cdot (\rho \bar{v} \bar{v}) = -\nabla p + \nabla \cdot \left(\mu \left[(\nabla \bar{v} + \nabla \bar{v}^T) - \frac{2}{3} \nabla \cdot \bar{v} I \right] \right) \tag{2}$$

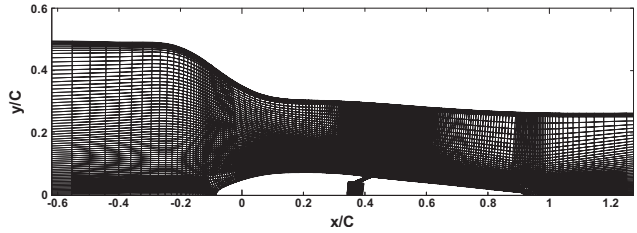

Fig. 3 Multi-block structured mesh

$$\frac{\partial}{\partial t}(\rho E) + \nabla \cdot [\bar{v}(\rho E + p)] = \nabla \cdot \left[k_{\text{eff}} \nabla T + \left(\mu_{\text{eff}} \left((\nabla \bar{v} + \nabla \bar{v}^T) - \frac{2}{3} \nabla \cdot \bar{v} I \right) \cdot \bar{v} \right) \right] \quad (3)$$

As turbulent flows are characterized by fluctuating fields of small scale and high frequency, which are computationally expensive, the instantaneous governing equations have been time-averaged to remove the small scales. As a result, new unknown variables have been created. These unknown variables have been defined differently in terms of known quantities, and have given rise to various turbulence models. The Reynolds-averaged Navier–Stokes equations were solved using computational fluid dynamics (CFD) solver FLUENT 6 by Fluent Inc. The realizable k-ε model in combination with standard wall functions was selected for turbulence closure. The transport equations for k and ε in the realizable k-ε model are as follows:

$$\frac{\partial}{\partial t}(\rho k) + \frac{\partial}{\partial x_j}(\rho k u_j) = \frac{\partial}{\partial x_j}\left[\left(\mu + \frac{\mu_t}{\sigma_k} \right) \frac{\partial k}{\partial x_j} \right] + G_k + G_b - \rho\varepsilon - Y_M + S_k \quad (4)$$

$$\frac{\partial}{\partial t}(\rho \varepsilon) + \frac{\partial}{\partial x_j}(\rho \varepsilon u_j) = \frac{\partial}{\partial x_j}\left[\left(\mu + \frac{\mu_t}{\sigma_\varepsilon} \right) \frac{\partial \varepsilon}{\partial x_j} \right] + \rho C_1 S_\varepsilon - \rho C_2 \frac{\varepsilon^2}{k + \sqrt{\nu\varepsilon}} + C_{1\varepsilon} \frac{\varepsilon}{k} C_{3\varepsilon} G_b + S_\varepsilon \quad (5)$$

Detailed information of the realizable k-ε model can be found in Ref. [20]. In this study, the realizable k-ε model was selected to perform the simulations since a previous study [21] has shown the superiority of this turbulence model over the other models in film cooling applications. The wall function approach was chosen to avoid using a very fine mesh close to walls to resolve the boundary layer. Thus, smaller meshes can be used with more efficient computation and faster and better convergence. The test of different wall treatments in film cooling application [22] showed that both the wall function approach and the two-layer based wall treatment approach, supposedly capable of resolving the boundary layer all the way to the wall, yield essentially the same results as long as the near wall mesh is appropriate. Multiblock mostly structured meshes were created to fully resolve the features of the flow field with most of the cells concentrated in areas of large variable gradients, since a hexahedron is more efficient to fill a volume than a tetrahedron, Fig. 3. When used appropriately, this method successfully captured the jet liftoff effect in traditional circular jet-in-cross flow over a flat plate. Details of this methodology can be found in Refs. [21,22]. It should be noted that this is probably the only numerical study clearly demonstrating the successful capturing of the jet liftoff effect in the circular hole on a flat plate under incompressible flow conditions. This numerical procedure was extended to study film cooling holes on a curved surface in high speed compressible flow.

As the Mach number is more than 1 and compressibility cannot be neglected, the density was defined as ideal gas according to the ideal gas law

$$\rho = \frac{p}{RT} \quad (6)$$

Turbulence intensity of the flow at the inlet was set at 0.5% as in the experimental study. A total temperature of 150 K at the plenum inlet was specified, which gives a range of coolant to mainstream density ratios around 1.3–2.0 depending on the blowing ratios. For the circular film hole on a flat plate case with a 35 deg inclined angle, the mainstream velocity is 20 m/s corresponding to a Mach number of less than 0.05. Therefore, fluid compressibility can be neglected. The density of the working fluid air was defined as incompressible. The mainstream part of the computational domain for the flat plate case is a rectangle of $20d \times 60d$ with $20d$ in the upstream of the film hole exit. The temperatures at the mainstream and plenum inlets were specified at 300 K and 150 K, respectively, which give a coolant to mainstream density ratio of 2.

The grids contain between 0.8 and 1.5×10^6 cells, which took roughly 24 h of computing time to reach convergence using a workstation with a CPU of 3 GHz and a RAM of 3 Gbytes. In this study, a multiblock structured mesh was used, which means a structured mesh was created wherever possible. The majority of cells are concentrated in the boundary layer regions close to wall surfaces as well as the jet exit area. It is highly important to ensure an efficient use of grid/cells in CFD simulation, a critical factor determining the accuracy of numerical results. Besides residuals going down several orders of magnitude, mass and energy were also checked to ensure they were conserved throughout the computational domain before declaring convergence. Steady state flow condition was assumed for all the cases in the numerical simulations. Second order discretization scheme was used in solving the flow, turbulence, and energy differential equations.

3 Results and Discussion

The louver cooling scheme was first introduced by Immarigeon and Hassan [23]. However, the performance of the cooling scheme was not compared with other schemes and the advantages of it were not fully shown. In the subsequent studies [21,22], the scheme was modified and simplified. Comparison with other known film cooling schemes in literature has shown its superior performance in terms of both cooling effectiveness and heat transfer coefficient. Nonetheless, all the studies of this louver cooling scheme so far have been done on a flat plate under incompressible flow conditions. It is known that the flow will behave quite differently under supersonic flow conditions than under subsonic or incompressible conditions. The airfoil presented by Furukawa and Ligrani [18], in which three cooling schemes were tested in a wind tunnel, was chosen to test the performance of the louver cooling scheme. Shock-wave dynamics analysis was also done to understand the transonic film cooling phenomenon. Firstly, simulations of the flow without a film cooling hole were performed and the prediction of Mach numbers compared with the available experimental data. Then, the simulations of a circular hole at different blowing ratios were carried out and predictions of cooling effectiveness were compared with the experimental data. Those two steps were used to validate the numerical procedure. After that, the louver cooling scheme on the transonic airfoil was tested numerically and its performance compared with the other three cooling configurations. An extensive grid independence test was also carried out during the study. It was found that when the size of mesh increases to 1.5×10^6 cells the solution is almost the same as that of a 0.8×10^6 cell mesh. Different meshing strategies of decomposing the computation domain for structured meshing were tried with a similar result. When the size of the mesh was reduced to below half a million, the accuracy will suffer. Finally, it was determined that the optimum mesh size is around $0.8-1.2 \times 10^6$ cells given the computational domain and flow conditions, which is a compromise between computing power, accuracy, and converging rate.

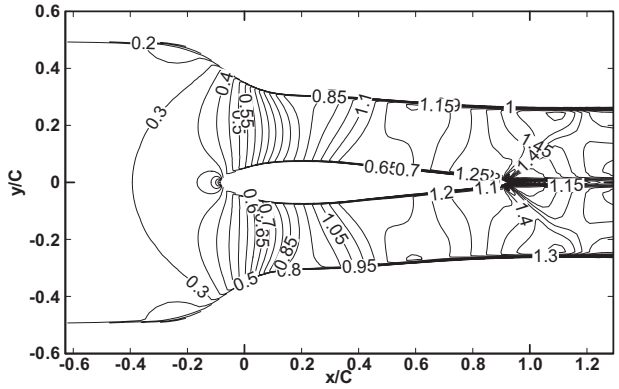

Fig. 4 Contours of Mach number on the cross section without film cooling hole

The calculated Mach number distribution on the center-plane without a film cooling hole is shown in Fig. 4. It can be seen that the Mach number increases from 0.4 at the nose to 1 in the middle then 1.35 at the passage exit with an oblique shock wave at the trailing edge. It is evident that there is no shock wave occurring in the passage between the leading edge and the trailing edge when film cooling jet is absent. It also can be seen that the Mach number at the location of the jet exit is between 1.05 and 1.1, which matches the experimental data [18] of 1.07 very well. Figure 5 shows the good agreement of Mach number around the airfoil surface between the prediction and the experimental data. This indicated that the geometries and boundary conditions shown in Fig. 2(*b*) are appropriate with reasonable accuracy.

Figure 6 shows the comparison of laterally averaged cooling effectiveness at different moderately low blowing ratios between the louver cooling scheme and the other shaped holes as well as the circular hole. For the circular hole case very good agreement between the predictions and experimental data exists, indicating the consistency of the numerical procedures on handling film cooling applications. The louver cooling scheme was predicted to have the highest cooling effectiveness among the three configurations compared, namely, circular hole with a simple angle (CYSA), layback-fan-shaped hole with a simple angle (LBFS-SA), and layback-fan-shaped hole with a compound angle (LBFS-CA). The geometries of those holes are shown in Fig. 1. An interesting phenomenon is that the difference in laterally averaged effectiveness between the circular hole and the louver scheme increases with blowing ratios while that difference between the louver scheme and the other two shaped hole schemes, LBFS-SA

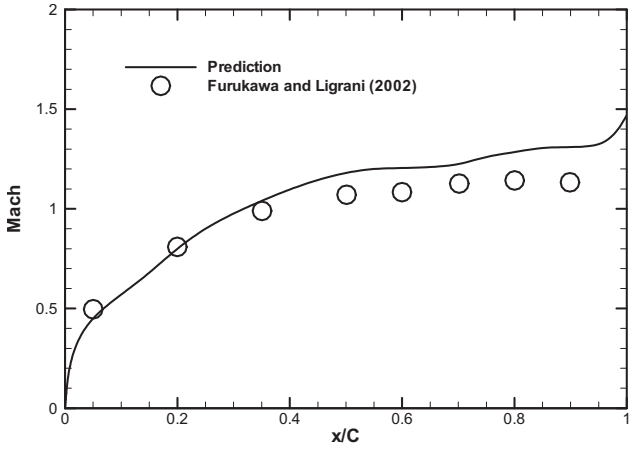

Fig. 5 Mach number distribution around the airfoil surface without film cooling hole

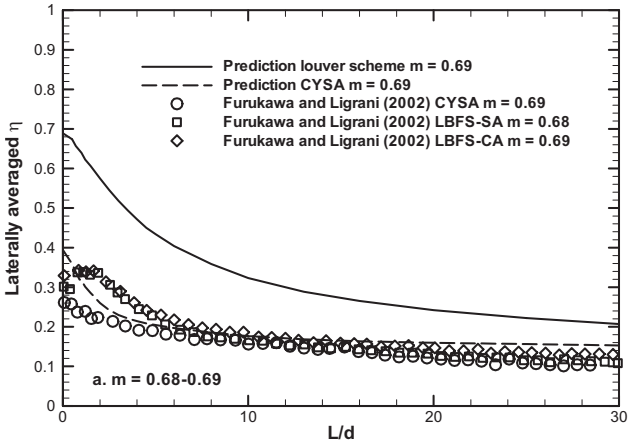

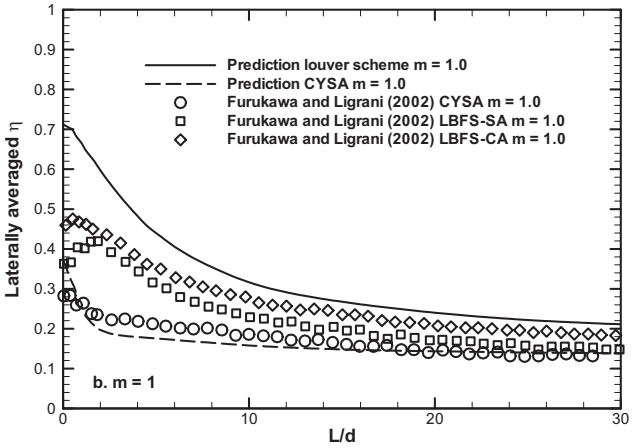

Fig. 6 Laterally averaged η for different cooling configurations

and LBFS-CA, decreases with increasing blowing ratio. This can be explained as the cooling effectiveness for the circular hole decreases with blowing ratio after the jet lifts off from the surface at high blowing ratios. The jet liftoff can be avoided or delayed for shaped holes since the jet momentum is reduced by the expanded exit before coolant injection. The advantages of the louver scheme were more noticeable at a low blowing ratio than at a high blowing ratio.

Figure 7 shows the comparison of laterally averaged effectiveness for the circular hole and the louver scheme at different high

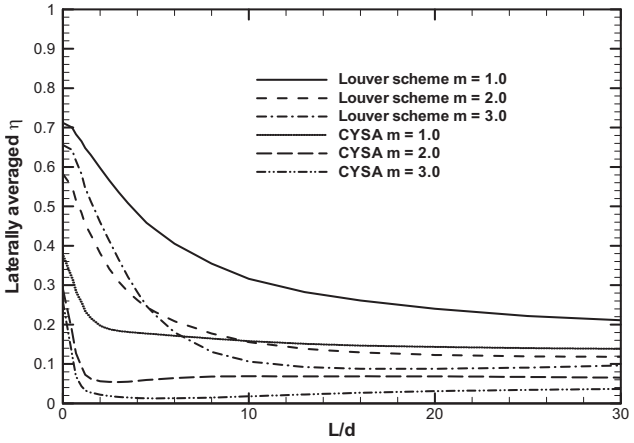

Fig. 7 Predicted laterally averaged η at high blowing ratios

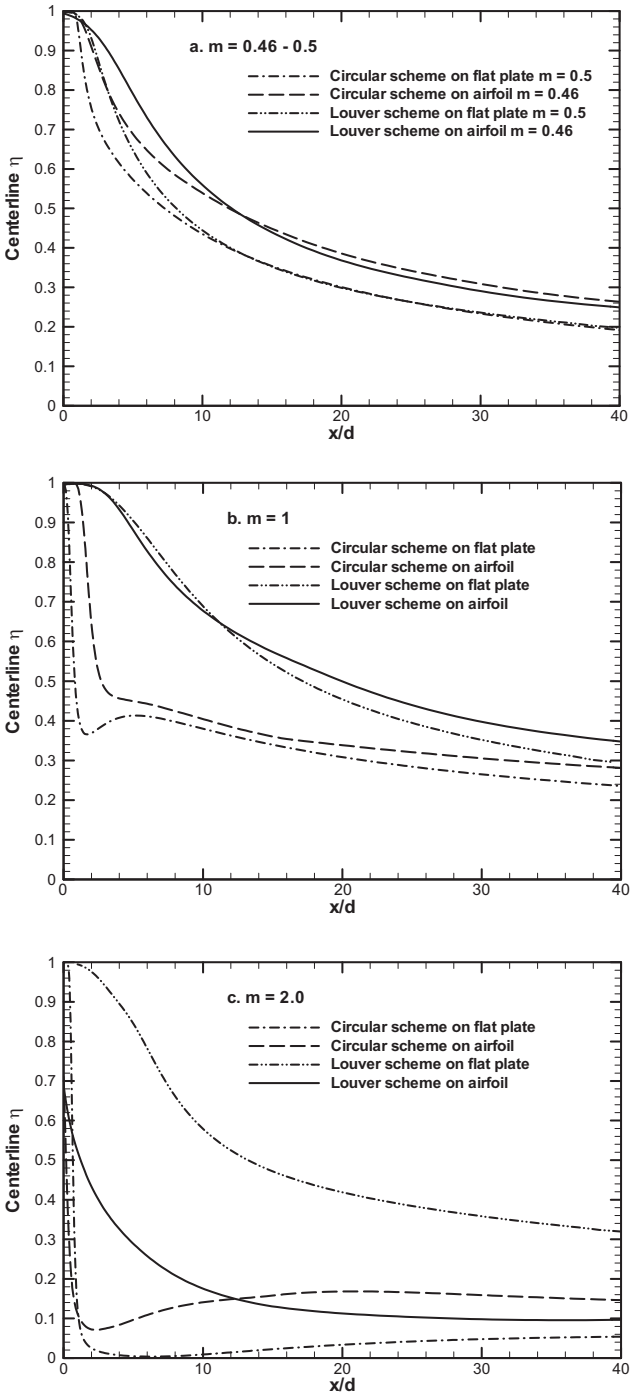

Fig. 8 Curvature effect at different blowing ratios

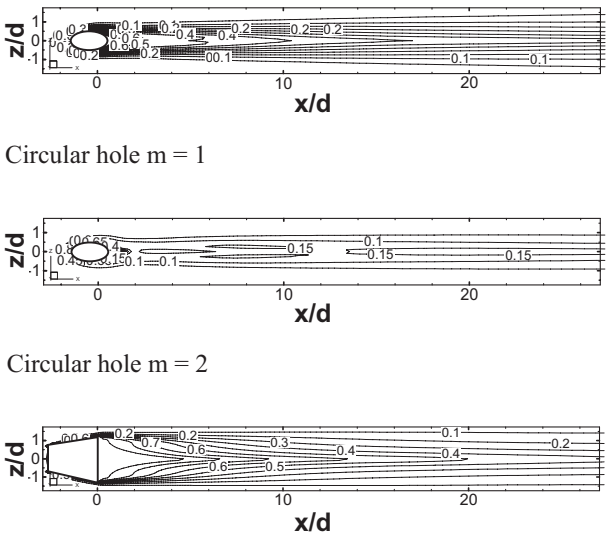

a. Circular hole m = 1

b. Circular hole m = 2

c. Louver scheme m = 1

Fig. 9 Contours of cooling effectiveness

blowing ratios on the airfoil. Cooling effectiveness decreases dramatically with blowing ratios when the blowing ratios are higher than 1 for both the circular hole and the louver scheme. This is in contrast to what happens at low blowing ratios where effectiveness slowly increases with blowing ratio, as shown in Fig. 6. In general, the louver scheme still gives higher laterally averaged effectiveness than the circular hole scheme. However, the effectiveness difference between the two schemes becomes less as blowing ratio is increased. At very high blowing ratios, namely, blowing ratios of 2 and 3, the cooling protection provided by the two schemes decreases quickly with blowing ratio and becomes almost ineffective and the louver cooling scheme is only effective in the area of L/d less than 6. In addition to the traditional jet liftoff such as happens with a circular jet on a flat plate at a blowing ratio of 1 under incompressible flow conditions, the shock wave generated as a result of jet-mainstream interaction contributes more in reducing cooling effectiveness, which will be analyzed in detail next.

Figure 8 presents the curvature effect and the comparison of centerline film cooling effectiveness between the circular hole and the louver scheme. At a low blowing ratio of around 0.5, where the circular jets do not lift off from the surface, the advantage of the louver scheme is apparent only at x/d less than 8, beyond which both schemes give the same level of effectiveness, Fig. 8(a). In either scheme, effectiveness is higher on an airfoil surface than on a flat plate due to the favorable pressure gradient created by flow acceleration and convex surface on the curved surface. At a higher blowing ratio of 1, Fig. 8(b), for the circular hole case the jet liftoff effect was evident on both the flat plate and the airfoil. The superiority of the louver cooling scheme is clearly demonstrated. As the blowing ratio is raised to 2, Fig. 8(c), dramatic decrease in effectiveness was observed for both cooling schemes on the airfoil. The louver scheme is effective only at x/d less than 8 although jet liftoff does not occur since there is no sudden drop in cooling effectiveness at the centerline. The circular holes lift off of both the flat plate and the airfoil surface completely, leading to poor cooling protection. The liftoff effect on the airfoil for the circular hole is less severe than on the flat plate as a result of favorable pressure gradient created by a curved surface and flow acceleration as already mentioned, Figs. 8(a) and 8(b); therefore, the effectiveness is slightly higher on an airfoil. Samples of contours of cooling effectiveness on the airfoil surface are presented in Fig. 9. The jet liftoff is apparent for the circular hole at a blowing ratio of 2, Fig. 9(b). A substantially higher cooling effectiveness exists on the airfoil surface for the louver cooling scheme than for the circular hole at a blowing ratio of 1, Figs. 9(a) and 9(c).

The detailed velocity profiles at different locations along the centerline are shown in Fig. 10. For film cooling on the airfoil in transonic flow conditions, Fig. 10(a) shows that at a blowing ratio of 1 the circular hole slightly lifts off from the surface due to high coolant momentum and reattachment occurs around L/d of 10. A small separation bubble appears downstream of the injection around L/d from 2 to 6. As the blowing ratio increases to 2, Fig. 10(b), the separation bubble becomes longer and deeper into the mainstream and reattachment did not occur. The separation bubble dissipates into the mainstream along with the injected coolant, and

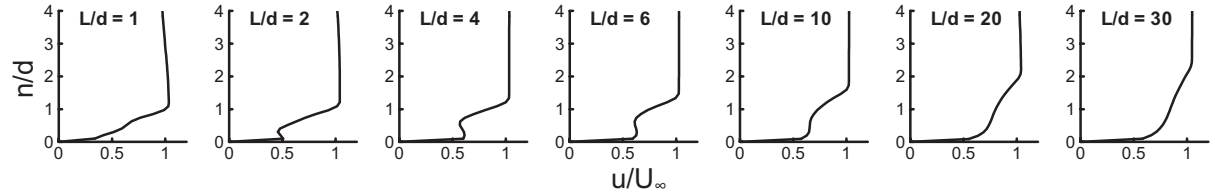

a. Circular hole on the airfoil at m = 1

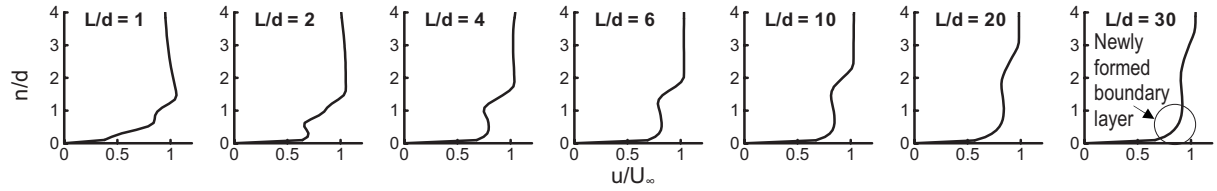

b. Circular hole on the airfoil at m = 2

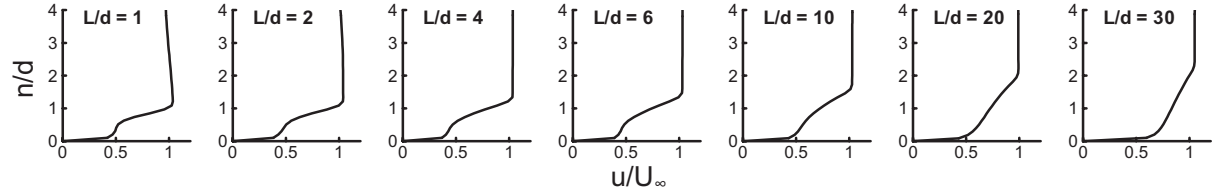

c. Louver scheme on the airfoil at m = 1

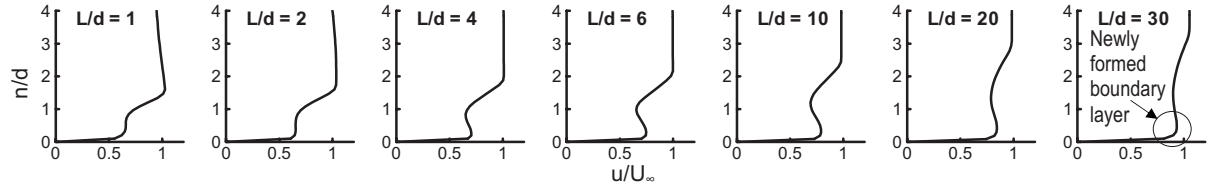

d. Louver scheme on the airfoil at m = 2

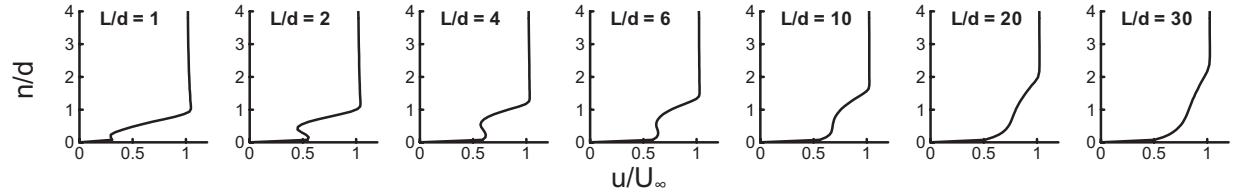

e. Circular hole on a flat plate at m = 1

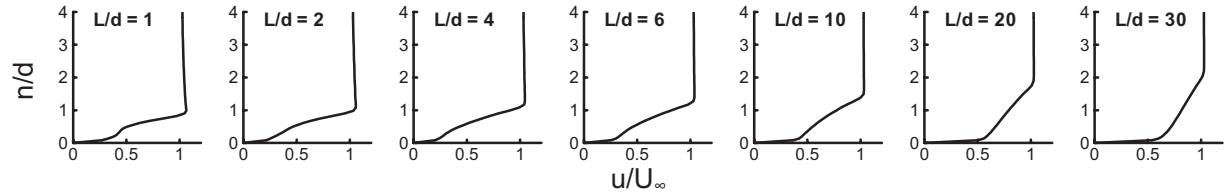

f. Louver scheme on a flat plate at m = 1

Fig. 10 Velocity profiles at different locations along the centerline

a new fully developed boundary layer forms after L/d of 20 close to the airfoil wall. For the louver scheme on the airfoil, Fig. 10(*c*) shows that at a blowing ratio of 1, no separation bubble occurs due to the reduced momentum because of the shaping of the exit, though the boundary layer profile was disturbed a little bit. When the blowing ratio increases to 2, Fig. 10(*d*), a big separation bubble appears, which dissipates into the mainstream. No jet reattachment occurs for the louver scheme, which is similar to what happens to the circular hole case at a blowing ratio of 2. To see the difference between high speed and low speed flows, the velocity profiles for both the circular hole and the louver scheme on a flat plate at a blowing ratio of 1 are also shown in Figs. 10(*e*) and

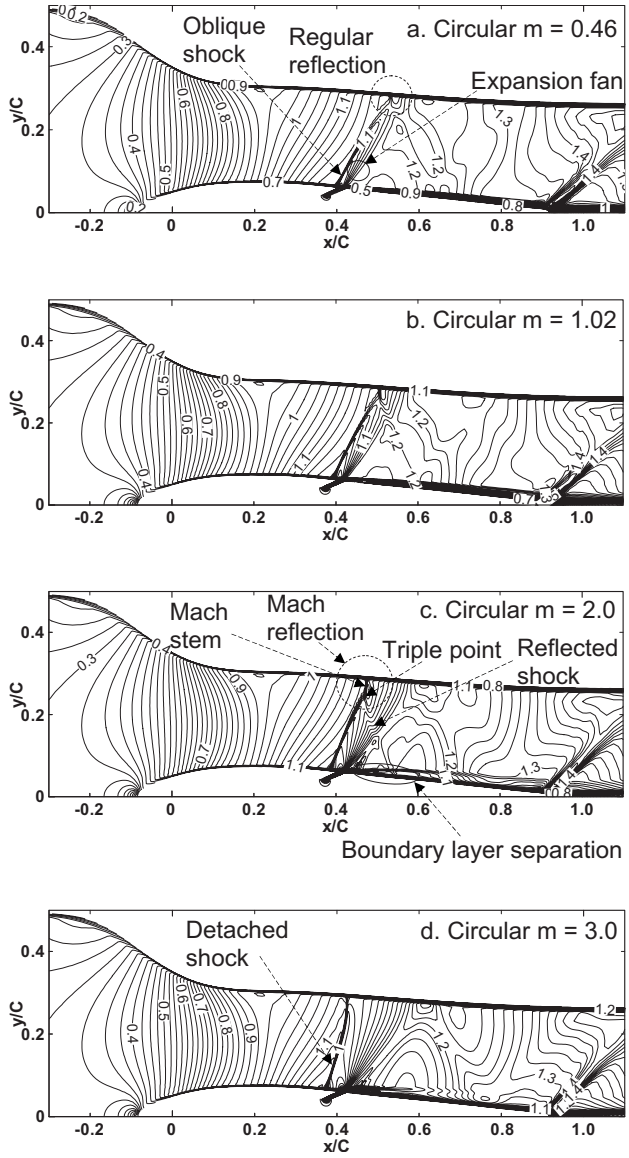

Fig. 11 Mach number distribution for the circular hole case at different blowing ratios

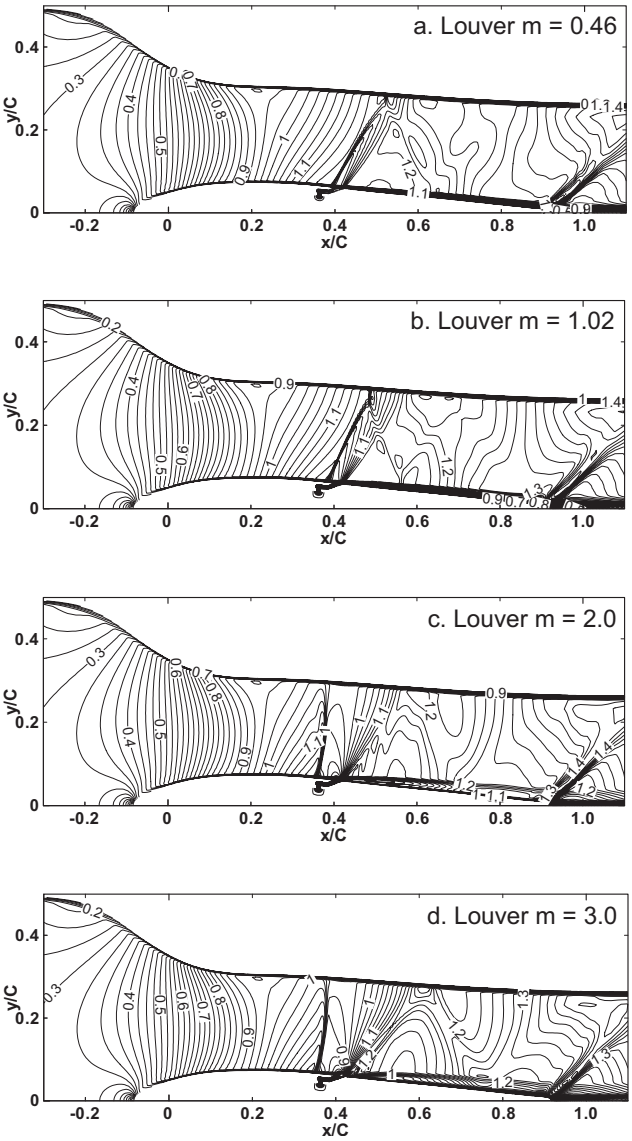

Fig. 12 Mach number distribution for the louver scheme at different blowing ratios

10(*f*), respectively. At low speed, when the flow can be considered as incompressible, the circular hole also lifts off from the surface at a blowing ratio of 1, Fig. 10(*e*). Nonetheless, the separation takes place a little earlier and the bubble is a little thinner and closer to the wall. A comparison between Figs. 10(*c*) and 10(*f*) reveals that at a blowing ratio of 1 there is no fundamental difference between on a curved airfoil and on a flat plate for the louver cooling scheme except that the boundary layer is a little thinner on a flat plate than on the airfoil.

Figures 11 and 12 show the Mach number distribution on the center-plane with film cooling for the circular hole and the louver scheme cases, respectively. At a low blowing ratio of 0.46, Figs. 11(*a*) and 12(*a*), an oblique shock wave is clearly observed right before the leading edge of the jet exit. This oblique shock emanating from the leading edge of the jet exit reaches the top wall and is reflected back to the bottom surface, known as a regular reflection. A series of expansion waves, also known as an expansion fan, is found around the center of the hole exit right above the shear layer formed by the injected coolant. As the blowing ratio increases, the oblique shock becomes stronger. At a blowing ratio of 2 for the circular hole, Fig. 11(*c*) and a blowing ratio of 1 for the louver cooling scheme, Fig. 12(*b*), a so-called Mach reflection results, which consists of three shock waves intersecting at a single point, known as the triple point. Still, at a higher blowing ratio of 3, Figs. 11(*d*) and 12(*d*), the shock in front of the jet exit is so strong that it detaches completely from the leading edge of the hole exit as a detached shock wave or as a bow shock. Comparing the shock structures at the same blowing ratios between the circular hole and the louver scheme shows that under the same flow conditions the louver scheme causes slight stronger shock-wave structures than the circular hole does, Figs. 11(*a*) and 12(*a*), and Figs. 11(*c*) and 12(*c*). At the blowing ratio of 1.0, the louver scheme causes a longer Mach stem on the top wall than the circular hole, Figs. 11(*b*) and 12(*b*), which means stronger shock structures and shock interactions for the louver scheme. At the same blowing ratio of 2, the shock associated with the louver scheme becomes the bow shock, in Fig. 12(*c*), while an attached oblique shock occurs with the circular hole, Fig. 11(*c*).

The contours of the coolant after injection are shown in Fig. 13 by plotting Mach number on the isosurface of constant temperature of 200 K. It can be seen that the coolant at a constant temperature forms a narrower band for the circular hole than for the louver scheme, as shown in the top views in Figs. 13(*a*) and 13(*c*). On the other hand, the angle the top layer of the injected coolant

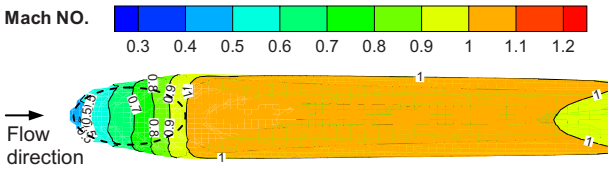

a. Top view for circular hole on the airfoil

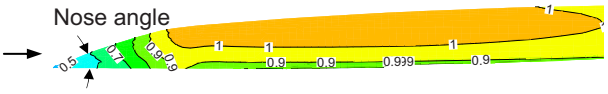

b. Side view for circular hole on the airfoil

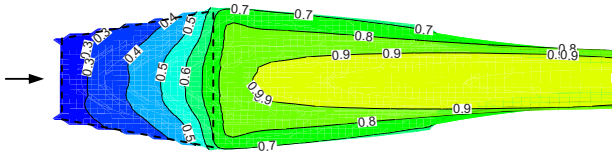

c. Top view for louver hole on the airfoil

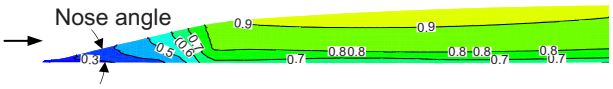

d. Side view for louver hole on the airfoil

Fig. 13 Contours of Mach number on iso-surfaces of constant temperature at m=1

at the same temperature makes with the wall surface—the nose angle—is sharper for the louver scheme, Figs. 13(*b*) and 13(*d*), as expected since the coolant is stretched in the spanwise direction by the exit shaping in the louver scheme. In this sense, the circular hole is like a three dimensional cone and the louver scheme is close to a two dimensional wedge. For the same flow conditions of mainstream Mach number and the same amount of coolant injected, a cone due to circular hole injection will cause less disturbance to and weaker reaction from the mainstream than a wedge due to the louver scheme injection. From the physics point of view, the flow can more easily pass around the sides of the three dimensional cone to negotiate the obstacle, so that the cone presents less overall disruption to the mainstream.

Figure 14 shows the schematics of a shaped wedge in a supersonic flow. Unlike in subsonic or incompressible flow conditions where the mainstream can sense the presence of an obstacle before reaching it, therefore, it can adjust itself to allow gradual changes in flow properties with continuous streamlines, in supersonic flow, as the mainstream cannot sense the presence of an obstacle, shock-wave result by which the flow adjusts rapidly to the obstacle through discontinuous changes in fluid properties. The presence of a coolant injection in supersonic flow generates the effect of a supersonic flow past a wedge. The interaction between the mainstream and the injected coolant can be simplified as a shaped wedge with a rounded top sitting on the surface, as shown in Fig. 14(*a*). The shape of the shaped wedge is based on the streamlines of the injected coolant. The wedge angle θ is related to the blowing ratio under the same jet injection angle. The higher the blowing ratio, the larger the wedge angle, and the stronger the shock-wave structures that will be generated. The rounded top is acting like a gradual convex turn by which an expansion fan is generated with gradual changes in flow properties; thus, isentropic expansion can be assumed for the flow going through the expansion fan [24]. Figure 14(*b*) represents the conditions of low

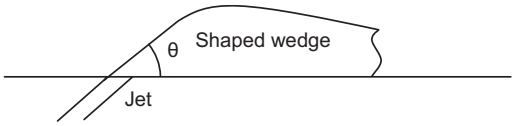

a. Shaped wedge

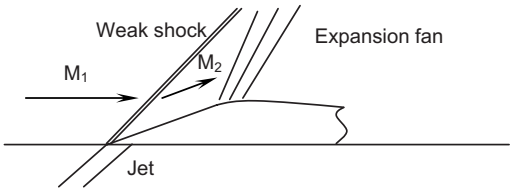

b. Weak shock at low blowing ratios

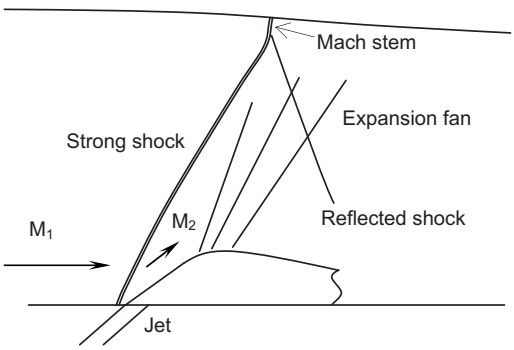

c. Strong shock at high blowing ratios

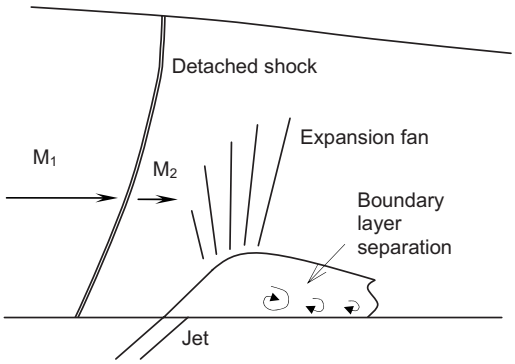

d. Detached shock at very high blowing ratios

Fig. 14 Schematic of shock wave structures at different blowing ratios

blowing ratios. At small wedge angles associated with low blowing ratios, an attached weak oblique shock occurs at the leading edge of the jet exit. A narrow expansion fan is also observed, as shown in Figs. 11(*a*) and 12(*a*). The flow properties across these weak shocks do not change much and the cooling effectiveness on the airfoil is close to that on a flat plate, as shown in Fig. 8(*a*). The slightly higher cooling effectiveness on the airfoil is the result of a favorable pressure gradient due to the curved surface that a flat plate does not have.

Under the same mainstream flow condition and Mach number, as the blowing ratio increases, the wedge angle becomes larger, resulting in a stronger, still attached, oblique shock and a wider expansion fan, Fig. 14(*c*). The strong oblique shock emanating from the leading edge reaches the top surface where Mach reflection occurs [25]. The length of the Mach stem increases with blowing ratios. Immediately after the Mach stem, the flow be-

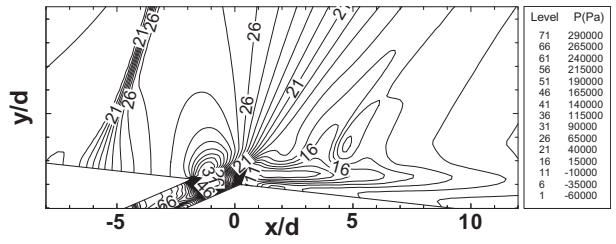

a. Circular hole

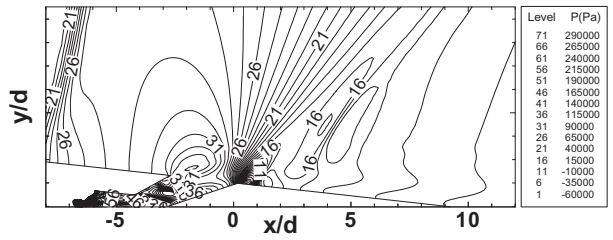

b. Louver scheme

Fig. 15 Static pressure distribution around the jet exit at m =3

comes subsonic, Figs. 11(*c*) and 12(*b*). After the strong oblique shock wave, the flow is deflected upward by a finite angle, usually in the direction parallel to the wedge surface, and the magnitude of the velocity is also reduced suddenly from supersonic to subsonic, leading to more jet liftoff in addition to the traditional liftoff at higher blowing ratios and reduced cooling effectiveness. Particularly, in the vicinity of the leading edge after the shock, the magnitude of the flow velocity is the lowest, typically in the subsonic flow regime. The flow accelerates to supersonic again across the ensuing expansion fan. But the small turning angle due to the expansion fan cannot make up the loss. Overall, the difference in film cooling effectiveness between on a flat plate and on the airfoil at a high blowing ratio is less than that at a lower blowing ratio for the same cooling scheme, Figs. 8(*a*) and 8(*b*). The advantages of the louver cooling scheme are more pronounced at moderately high blowing ratios, Fig. 8(*b*).

When the blowing ratio is too high a detached shock wave developed, Fig. 14(*d*). The supersonic flow is reduced to subsonic flow immediately after the detached shock because the detached shock behaves more like a normal shock. After the detached shock, the flow goes through a wide expansion fan through which the flow becomes supersonic again. The detached shock and expansion fan drastically change the flow field. Take blowing ratio of 3 as an example, as shown in Fig. 15, the static pressure increases by as much as 35% across the compressive detached shock, then decreases by 30% across the ensuring expansion fan. These sudden changes of pressure within a short distance cause boundary layer separation, Figs. 11(*c*), 11(*d*), 12(*c*), and 12(*d*), more pronouncedly Figs. 10(*b*) and 10(*d*), resulting in injected coolant dissipated into the mainstream and poor cooling protection. This coolant dissipation due to boundary layer separation should be distinguished from the traditional jet liftoff caused by the high jet momentum at high blowing ratios. In the traditional jet liftoff, the high momentum of the jet at high blowing ratios is solely responsible for the reduced cooling effectiveness. Once the boundary layer separates from the airfoil surface due to the shock waves, the injected coolant could not stick to the airfoil surface as it does when there is no boundary layer separation. Consequently, most of the coolant is dissipated into the mainstream no matter how much coolant is injected and how small the normal momentum of the jet is. In other words, jet reattachment does not occur once shock-wave-induced boundary layer separation takes place. This is totally different from what happens for film cooling under subsonic flow condition where there is no shock-wave-induced boundary layer separation.

4 Summary and Conclusions

The flow behaviors of the film cooling in transonic or supersonic flows are quite different from those in subsonic or incompressible flows. Convex surface on the airfoil in combination with flow acceleration due to compressibility of the fluid creates a favorable pressure gradient, which help press the injected coolant close to the targeted surface. When the blowing ratio is low and the oblique shock generated by the interaction between the jet and the mainstream stays attached, usually a weak shock, the cooling effectiveness is generally higher on a convex airfoil surface than on a flat plate. Shock waves were also found to be reflected back and forth between the upper and lower walls as weaker shocks depending on how strong the original shock wave is. The working fluid going through the oblique shock waves is compressed and the subsequent increased pressure may also help push the coolant toward the airfoil surface, increasing the cooling effectiveness. However, when the blowing ratio is too high, a strong detached shock occurs, which drastically changes the flow field. As a result, the boundary layer separates from the wall and the coolant becomes ineffective. The proposed coolant-blockage and shaped-wedge similarity qualitatively explains this phenomenon well and sheds light on the physics of supersonic film cooling.

1. In transonic or supersonic mainstream flow conditions, the blockage effect of the injected coolant makes the jet act like a shaped wedge. Under the same mainstream flow condition, the higher the blowing ratio, the larger the wedge angle and the stronger the shock waves that are generated.
2. When the oblique shock due to the coolant injection is weak and stays attached to the leading edge of the jet exit, a higher blowing ratio usually provides a higher cooling effectiveness than a low blowing ratio. When the shock becomes a detached shock, the cooling effectiveness is drastically reduced due to the boundary layer separation caused by shock waves regardless of cooling configurations.
3. The louver cooling scheme provides higher cooling effectiveness than the circular hole and the fan-shaped hole. The difference of laterally averaged effectiveness between the louver cooling scheme and the fan-shaped hole is reduced as blowing ratio increases.
4. Using extremely high blowing ratios should be avoided for any cooling schemes when the flow field in the mainstream at the location of the hole is supersonic, particularly for shaped holes, because at very high blowing ratios, a detached shock along with other strong shock-wave structures causes boundary layer separation, rendering the coolant virtually ineffective.

The focus of this study is the cooling effectiveness on an airfoil surface at supersonic flow conditions. Therefore, the cells were mostly concentrated on the airfoil surface in the boundary layer areas and the jet exit area. As a result, the detailed shock-wave structures may not have been resolved fully, particularly the shock-wave reflections and interactions. It should be noted that this is only the first attempt to study the shock-wave effects on the film cooling performance from a new perspective. There is conflicting information in literature as to whether the resulting shock waves increase the cooling effectiveness or decrease it. Currently, there are no experimental data of cooling effectiveness available in the open literature for holes on a curved surface at very high blowing ratios when a detached shock wave occurs. Therefore, experimental work of cooling effectiveness at higher blowing ratios under transonic or supersonic flow conditions is highly recommended, since low speed incompressible effectiveness data do not apply to high speed flow conditions.

Nomenclature

C = chord length of the airfoil (m)
d = diameter of the hole at the inlet (m)
E = total energy (J)
k = turbulent kinetic energy (m^2/s^2)
L = distance measured along the blade surface from the trailing edge of the hole exit (m)
m = blowing ratio, $\rho_j U_j/\rho_\infty U_\infty$
M = Mach number (Mach)
n = normal distance to the wall (m)
p = pressure (Pa)
R = gas constant (J/kg K)
T = temperature (K)
u = velocity component in the x direction (m/s)
U = velocity (m/s)
$\bar{v}$ = velocity vector (m/s)
x = streamwise coordinate (m)
y = vertical coordinate (m)
z = spanwise coordinate (m)

Greek Symbols

ε = dissipation rate of turbulent kinetic energy (m^2/s^3)
η = local adiabatic film cooling effectiveness, $(T_{o\mathrm{aw}}\text{-}T_{o\infty})/(T_{oj}-T_{o\infty})$
ρ = density (kg/m^3)

Subscripts and Superscripts

aw = adiabatic wall
j = refers to the jet
o = total condition
∞ = mainstream conditions
s = static condition

References

[1] Ito, S., Goldstein, R. J., and Eckert, E. R. G., 1978, "Film Cooling of a Gas Turbine Blade," ASME J. Eng. Power, **100**, pp. 476–481.
[2] Teng, S., Sohn, D. K., and Han, J.-C., 2000, "Unsteady Wake Effect on Film Temperature and Effectiveness Distribution for a Gas Turbine Blade," ASME J. Turbomach., **122**, pp. 340–347.
[3] Rutledge, J. L., Robertson, D., and Bogard, D. G., 2006, "Degradation of Film Cooling Performance on a Turbine Vane Suction Side Due to Surface Roughness," ASME J. Turbomach., **128**, pp. 547–554.
[4] Thakur, S. T., Wright, J., and Shyy, W., 1999, "Convective Film Cooling Over a Representative Turbine Blade Leading-Edge," Int. J. Heat Mass Transfer, **42**, pp. 2269–2285.
[5] Ethridge, M. I., Cutbirth, J. M., and Bogard, D. G., 2001, "Scaling of Performance for Varying Density Ratio Coolants on an Airfoil With Strong Curvature and Pressure Gradient Effects," ASME J. Turbomach., **123**, pp. 231–237.
[6] Colban, W., Gratton, A., Thole, K. A., and Haendler, M., 2006, "Heat Transfer and Film-Cooling Measurements on a Stator Vane With Fan-Shaped Cooling Holes," ASME J. Turbomach., **128**, pp. 53–61.
[7] Dittmar, J., Schulz, A., and Wittig, S., 2003, "Assessment of Various Film-Cooling Configurations Including Shaped and Compound Angle Holes Based on Large-Scale Experiments," ASME J. Turbomach., **125**, pp. 57–64.
[8] Lakehal, D., Theodoridis, G. S., and Rodi, W., 2001, "Three-Dimensional Flow and Heat Transfer Calculations of Film Cooling at the Leading Edge of Symmetrical Turbine Blade Model," Int. J. Heat Fluid Flow, **22**, pp. 113–122.
[9] Colban, W., Thole, K. A., and Haendler, M., 2007, "Experimental and Computational Comparison of Fan-Shaped Film Cooling on a Turbine Vane Surface," ASME J. Turbomach., **129**, pp. 23–31.
[10] Haas, W., Rodi, W., and Schonung, B., 1992, "The Influence of Density Difference Between Hot and Coolant Gas on Film Cooling by a Row of Holes: Predictions and Experiments," ASME J. Turbomach., **114**, pp. 747–755.
[11] Guo, S. M., Lai, C. C., Jones, T. V., Oldfield, M. L. G., Lock, G. D., and Rawlinson, A. J., 1998, "The Application of Thin-Film Technology to Measure Turbine-Vane Heat Transfer and Effectiveness in a Film-Cooled, Engine-Simulated Environment," Int. J. Heat Fluid Flow, **19**, pp. 594–600.
[12] Drost, U., and Bolcs, A., 1999, "Investigation of Detailed Film Cooling Effectiveness and Heat Transfer Distributions on a Gas Turbine Airfoil," ASME J. Turbomach., **121**, pp. 233–242.
[13] Guo, S. M., Lai, C. C., Jones, T. V., Oldfield, M. L. G., Lock, G. D., and Rawlinson, A. J., 2000, "Influence of Surface Roughness on Heat Transfer and Effectiveness for a Fully Film Cooled Nozzle Guide Vane Measured by Wide Band Liquid Crystals and Direct Heat Flux Gages," ASME J. Turbomach., **122**, pp. 709–716.
[14] Reiss, H., and Bolcs, A., 2000, "Experimental Study of Showerhead Cooling on a Cylinder Comparing Several Configurations Using Cylindrical and Shaped Holes," ASME J. Turbomach., **122**, 161–169.
[15] Gritsch, M., Schulz, A., and Wittig, S., 1998, "Adiabatic Wall Effectiveness Measurements of Film-Cooling Holes With Expanded Exits," ASME J. Turbomach., **120**, pp. 549–556.
[16] Juhany, K. A., and Hunt, M. L., 1994, "Flowfield Measurements in Supersonic Film Cooling Including the Effect of Shock-Wave Interaction," AIAA J., **32**, pp. 578–585.
[17] Ligrani, P. M., Saumweber, C., Schulz, A., and Wittig, S., 2001, "Shock Wave-Film Cooling Interactions in Transonic Flows," ASME J. Turbomach., **123**, pp. 788–797.
[18] Furukawa, T., and Ligrani, P., 2002, "Transonic Film Cooling Effectiveness From Shaped Holes on a Simulated Turbine Airfoil," J. Thermophys. Heat Transfer, **16**, pp. 228–237.
[19] Jackson, D. J., Lee, K. L., Ligrani, P. M., and Johnson, P. D., 2002, "Transonic Aerodynamic Losses Due to Turbine Airfoil, Suction Surface Film Cooling," ASME J. Turbomach., **122**, pp. 317–326.
[20] Shih, T.-H., Liou, W. W., Shabbir, A., Yang, Z. and Zhu, J., 1995, "A New k-ε Eddy-Viscosity Model for High Reynolds Number Turbulent Flows—Model Development and Validation," Comput. Fluids, **24**(3), pp. 227–238.
[21] Zhang, X. Z., and Hassan, I., 2006, "Film Cooling Effectiveness of an Advanced-Louver Cooling Scheme for Gas Turbines," J. Thermophys. Heat Transfer, **20**, pp. 754–763.
[22] Zhang, X. Z., and Hassan, I., 2006, "Numerical Investigation of Heat Transfer on Film Cooling With Shaped Holes," J. Thermophys. Heat Transfer, **16**, pp. 848–869.
[23] Immarigeon, A., and Hassan, I., 2006, "An Advanced Impingement/Film Cooling Scheme for Gas Turbines—Numerical Study," Int. J. Numer. Methods Heat Fluid Flow, **16**, pp. 470–493.
[24] John, J. E. A., 1969, *Gas Dynamics*, Allyn and Bacon, Boston, MA, 1969, pp. 120–123.
[25] Ben-Dor, G., 1992, *Shock Wave Reflection Phenomena*, Springer-Verlag, New York, pp. 10–16.

A Model of Nonlinear Fatigue-Creep (Dwell) Interactions

Xijia Wu
Institute for Aerospace Research,
National Research Council Canada,
Ottawa, ON, K1A 0R6, Canada

A nonlinear creep/dwell interaction model is derived based on nucleation and propagation of a surface fatigue crack and its coalescence with creep/dwell damages (cavities or wedge cracks) along its path inside the material, which results in the total damage accumulation rate as given by $da/dN = (1 + (l_c + l_z)/\lambda)\{(da/dN)_f + (da/dN)_{env}\}$, *where* $(da/dN)_f$ *is the pure fatigue crack growth rate,* $(da/dN)_{env}$ *is the environment-assisted crack growth rate,* l_c/l_z *is the cavity/wedge crack size, and* λ *is the average spacing between the internal cavities or cracks. Since wedge cracks are usually present in the form of dislocation pile-ups at low temperatures and cavitation usually occurs at high temperatures, the model attempts to reconcile the creep-/dwell-fatigue phenomena over a broad temperature range of engineering concern. In particular, the model has been used to explain the dwell fatigue of titanium alloys and high temperature creep-fatigue interactions in Ni-base superalloys under tensile cyclic creep rupture, compressive cyclic creep rupture, and tension/compression-hold strain controlled cyclic test conditions.*
[DOI: 10.1115/1.2982152]

1 Introduction

Prognostic health management (PHM) demands that effects of service (loading) history be accurately accounted for in assessing the current state and the remaining life of an engineering system. For gas turbine components, the loading profiles can be translated into combinations of cyclic loads and steady dwell periods with temperature variations. It has been known that depending on the operating temperature, load-holding periods could induce either dwell-fatigue or creep-fatigue interactions, which are detrimental to life.

Over the past half century, researchers have been actively developing more descriptive, more accurate, and more efficient analytical models for the dwell-/creep-fatigue phenomena, albeit they are largely empirical. Some basic approaches are briefly reviewed below.

One way to count the total accumulated damage during creep fatigue is to combine the rules of Miner [1] and Robinson [2] as follows:

$$\sum \frac{N_i}{N_{fi}} + \sum \frac{t_j}{t_{rj}} = 1 \tag{1}$$

where N_{fi} is the pure fatigue life at the ith cyclic stress or strain amplitude and t_{rj} is the creep rupture life at the jth holding stress level.

Another method—the so-called strain range partitioning (SRP) approach—was developed by NASA [3], where it was proposed that the entire inelastic cyclic strain range could be divided into a combination of plastic strain reversed by plasticity, $\Delta\varepsilon_{pp}$; creep strain reversed by creep, $\Delta\varepsilon_{cc}$; plastic strain reversed by creep, $\Delta\varepsilon_{pc}$; and creep strain reversed by plasticity, $\Delta\varepsilon_{cp}$. Then, the total failure life is expressed as

$$\frac{1}{N} = \frac{F_{pp}}{N_{pp}} + \frac{F_{cc}}{N_{cc}} + \frac{F_{pc}}{N_{pc}} + \frac{F_{cp}}{N_{cp}} \tag{2}$$

where F_{ij} is the fraction of the named strain component and N_{ij} is the number of cycles to failure if the entire inelastic strain is comprised of the named strain only. N_{ij} generally follows the Coffin–Manson relationship [4,5],

$$N_{ij} = D_{ij}\Delta\varepsilon_{ij}^{c_{ij}} \tag{3}$$

where D_{ij} and c_{ij} are empirical constants.

In addition to the two relationships above, which appear to be more generic, there are also about a hundred models proposed to deal with the time or frequency dependence of low cycle fatigue (LCF). Halford [6] provided a comprehensive review of those models developed up to 1991. This large suite of models reflects how complicated the problem is. However, it has been recognized that basically three processes—(i) cycle-dependent fatigue, (ii) time-dependent creep, and (iii) oxidation—play important roles in damage accumulation in materials at high temperatures. Therefore, more recent developments tend to formulate the total damage accumulation as the sum of the above three in a rate form as

$$\frac{da}{dN} = \left\{ \left(\frac{da}{dN}\right)_{\text{fatigue}} + \left(\frac{da}{dN}\right)_{\text{creep}} + \left(\frac{da}{dN}\right)_{\text{ox}} \right\} \tag{4}$$

and to substitute the appropriate rate equation for each damage component to compute the total life. Note that Eq. (4) also represents a linear summation rule, and it is equivalent to Eq. (1) if all damage components proceed at constant rates accordingly.

The above developments have given engineers a variety of choices to tackle specific dwell-/creep-fatigue problems they may encounter, but, on the other hand, some may just add more pieces to the puzzle because it has been lacking a consistent physics-based rationale, favoring one model or the other.

This paper presents a rational model of dwell/creep fatigue based on a holistic consideration of crack nucleation and propagation from a surface flaw coalescing with internal creep/dwell damage along the way, leading to final fracture. A nonlinear dwell/creep interaction model is derived and illustrated with experimental data.

Contributed by the International Gas Turbine Institute of ASME for publication in the JOURNAL OF ENGINEERING FOR GAS TURBINES AND POWER. Manuscript received April 1, 2008; final manuscript received April 2, 2008; published online February 10, 2009. Review conducted by Dilip R. Ballal. Paper presented at the ASME Turbo Expo 2008: Land, Sea and Air (GT2008), Berlin, Germany, June 9–13, 2008.

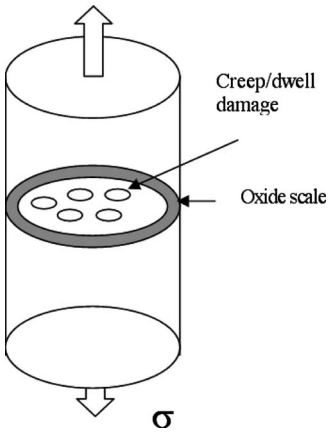

Fig. 1 A schematic of damage development in a specimen cross-section

2 The General Model

For generality, consider a polycrystalline material with multiple forms of damage developed under general thermomechanical fatigue (TMF) loading, as shown schematically in Fig. 1. Usually, fatigue damage initiates at surface flaws or as intrusion/extrusion of persistent slip bands. Oxidation also occurs first at the material surface or at existing crack surfaces or a crack tip. Oxidation damage penetrates the material inwardly through diffusion processes. In the meantime, creep cavities or wedge cracks may develop in the material interior, particularly along grain or interface boundaries. Subsurface cracks may also initiate at manufacturing flaws such as pores or inclusions, but they will quickly break into surface and become surface cracks. Therefore, the life evolution process can be envisaged as nucleation of surface cracks by fatigue and/or oxidation and inward propagation of the dominant crack, coalescing with internal cavities or cracks along its path, leading to a final rupture.

Fatigue damage can be regarded as an accumulation of irreversible slip offsets on preferred slip systems. These slip offsets may occur at the surface of grains or at grain boundaries or interface boundaries, which act as nuclei for cracks. Restricted slip reversal ahead of the crack tip is also recognized as the basic mechanism of transgranular fatigue crack propagation [7]. Therefore, in a holistic sense, we can use one term, da/dN, to represent both the rate of accumulation of irreversible slip offsets leading to crack nucleation as well as the fatigue crack growth rate, bearing in mind that the functional dependencies of da/dN on the loading parameters are different for crack nucleation and crack growth.

On the other hand, creep damage may develop in the forms of cavity and/or wedge cracks [8,9]. Cavity growth has been recognized as a diffusion phenomenon, whereas wedge cracking is a result of dislocation pile-up, also called Zener–Stroh–Koehler (ZSK) crack.

The coalescence of creep/dwell damage with a propagating fatigue crack will result in a total damage accumulation rate as expressed by

$$\frac{da}{dN} = \left(\frac{da}{dN}\right)_f + \frac{l_c + l_z}{\Delta N} \tag{5}$$

where l_c is the collective cavity size per grain boundary facet, l_z is the ZSK crack size, and ΔN is the number of cycles during which the fatigue crack propagates between two cavities or between two ZSK cracks separated by an average distance of λ ($\lambda \sim$ grain size or grain boundary precipitate spacing). Note that usually creep cavitation occurs at a high temperature and ZSK cracks occur at a relatively low temperature. These two types of damage usually do not occur at the same time. Here they are added together as competitive mechanisms over the entire temperature range from ambient temperature to near melting temperature.

Assume that during the period of ΔN, the dominant crack only propagates by pure fatigue, i.e., $da/dN \sim \lambda/\Delta N$. Then we can rewrite Eq. (5) as

$$\frac{da}{dN} = \left(1 + \frac{l_c + l_z}{\lambda}\right)\left(\frac{da}{dN}\right)_f \tag{6}$$

In the presence of environmental effects, which will contribute to the propagation of the dominant crack in a cycle-by-cycle manner, for simplicity, the total crack growth rate is

$$\frac{da}{dN} = \left(1 + \frac{l_c + l_z}{\lambda}\right)\left\{\left(\frac{da}{dN}\right)_f + \left(\frac{da}{dN}\right)_{\text{env}}\right\} \tag{7}$$

In the following, we will only discuss the application of Eq. (7) to dwell/creep fatigue, while ignoring oxidation.

3 Discussion

3.1 Dwell Fatigue. Dwell fatigue usually refers to fatigue with hold times at ambient temperatures, and it could cause significant LCF life reduction. Therefore, the phenomenon is often called the "cold dwell" effect, which is most pronounced in high strength titanium alloys such as IMI 685, IMI 829, and IMI 834 and Ti6242. The dwell fatigue of titanium alloys is often accompanied with a faceted fracture along the basal planes of the α phase, which is believed to be driven by dislocation pile-up [10].

Referring to Eq. (7), in order to understand the cold dwell effect, one needs to find the ZSK crack size as a function of dwell stress and dwell time. The relationship will be briefly described below, whereas a complete treatment is given in Ref. [11] based on the kinetics of dislocation pile-up.

First of all, it is recognized that the rate of dislocation pile-up accumulation is the net result of dislocation arriving by glide and leaving by climb in a unit time, which can be expressed as

$$\frac{dn}{dt} = \rho v s - \kappa n \tag{8}$$

where ρ is the dislocation density, v is the dislocation glide velocity, s is the slip bandwidth, κ is the rate of dislocation climb, and n is the number of dislocations in a pile-up at time t.

According to the Orowan relationship, $\dot{\gamma}_p = \rho b v (s \approx b)$, Eq. (8) can be rewritten as

$$\frac{dn}{dt} = \dot{\gamma}_p - \kappa n \tag{9}$$

The number of dislocations in a pile-up at a steady state can be obtained by the integration of Eq. (9) as

$$n = \frac{\dot{\gamma}_p}{\kappa}[1 - \exp(-\kappa t)] \tag{10}$$

Note that the energy release rate of a ZSK crack in an anisotropic material is given by [12]

$$G = \frac{1}{2} K_i F_{ij}^{-1} K_j = \frac{b_T^{(i)} F_{ij} b_T^{(j)}}{8\pi a} \tag{11}$$

where F_{ij} is an elastic matrix for anisotropic materials ($F_{11} = F_{22} = \mu/(1-\upsilon)$ and $F_{33} = \mu$, μ is the shear modulus, for isotropic materials) and $b_T = nb$ is the total Burgers vector in the pile-up group. Considering an average slip band angle of 45 deg, the dislocation pile-up may create a mix-mode I-II crack by Griffith's criteria,

$$\frac{\bar{F}_{22} b_T^2}{8\pi a} = 4 w_s \tag{12}$$

where w_s is the surface energy and $\bar{F}_{22} = (F_{11} + F_{22})/2$ is the average modulus.

Combining Eqs. (11) and (12), we can find the crack size $l(=2a)$ as

$$l = \frac{\bar{F}_{22} n^2 b^2}{16\pi w_s} \tag{13}$$

Substituting Eq. (10) into Eq. (13), we obtain

$$l_z = \frac{\bar{F}_{22} b^2}{16\pi w_s} \left(\frac{\dot{\gamma}}{\kappa}\right)^2 [1 - \exp(-\kappa\tau)]^2 \tag{14}$$

For a constant amplitude fatigue with a constant holding period, substituting Eq. (14) into Eq. (7) and neglecting cavity formation, integration leads to

$$N = \frac{N_f}{\left(1 + \frac{F_{22} b^2}{16\pi\lambda w_s} \left(\frac{\dot{\gamma}}{\kappa}\right)^2 [1 - \exp(-\kappa\tau)]^2\right)} \tag{15}$$

Equation (15) shows that the fatigue life is knocked down by a factor greater than 1 when a dwell period is imposed on fatigue loading. This "knockdown" factor depends on the material properties such as elastic constants, surface energy, and microstructure (λ), and most importantly it is controlled by the ratio of dislocation glide velocity to the climb rate in the material. This means that if damage occurs in the form of dislocation pile-up, the dwell effect will be more detrimental when the ratio of dislocation glide to climb is large, particularly in materials with fewer active slip systems at low temperatures. As temperature increases though, the climb will overwhelm the glide such that dislocation pile-up can hardly form, and hence the dwell damage becomes minimal, but cavities may start to grow. Basically, this is the essence of cold dwell versus "hot creep." Creep fatigue will be discussed later.

Bache et al. [10] studied IMI834 and plotted the dwell-fatigue life as a function of dwell time and stress, as shown in Figs. 2(*a*) and 2(*b*), respectively. The model, Eq. (9), describes the experimental behavior very well. It shows that the dwell sensitivity, in terms of the ratio of the dwell-fatigue life to the pure fatigue life, indeed follows an exponential function. Hence, given the pure fatigue life as the baseline, dwell-fatigue life can be predicted, as shown in Fig. 2(*b*), in the form of *S-N* curves.

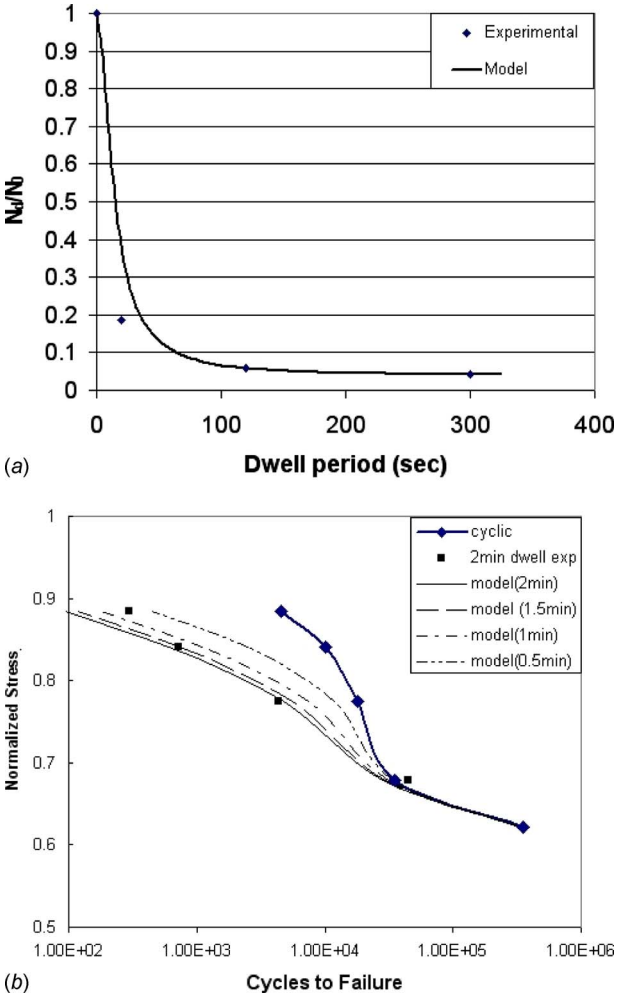

Fig. 2 Comparison of Eq. (15) with the experimental data on IMI 834 [10]: (*a*) normalized dwell-fatigue life as a function of dwell time and (*b*) *S-N* curves with different dwell times.

3.2 Creep Fatigue. The creep-fatigue interaction refers to the effect of cyclic-hold interactions at high temperatures where creep damage can be significant. NASA has developed a number of test methods (see the Appendix for details) to simulate the creep-fatigue interaction and has proposed the SRP approach to deal with the life prediction for a deformation process that may involve a combination of different strain components manifested from those tests [3]. In practice, however, it is always a challenge to quantify the four strain components, i.e., pp, cc, pc, and cp, from the material's complex hysteresis behavior, and all the four strain-life behaviors need to be characterized, which requires excessive testing. For a simplification of the matter, it is attempted to use Eq. (7) in combination with the basic deformation physics to reconcile the creep-fatigue behaviors observed from SRP associated tests, as discussed in the following.

At high temperatures, the inelastic strain, ε_{in}, is basically comprised of grain deformation, ε_g, and grain boundary sliding (GBS), ε_{GBS}, as

$$\varepsilon_{in} = \varepsilon_g + \varepsilon_{GBS} \tag{16}$$

Wu and Koul developed an entire-creep-curve model based on the above concept and the involved deformation mechanisms [13]. McLean and Pineau [14] used GBS as a correlating concept for the creep-fatigue interaction during tensile strain hold cycles. Without further digressing on the details of those deformation mechanisms, which have been discussed extensively [13–16], we propose the following hypotheses by the nature of the involved deformation processes:

- The grain deformation, which proceeds in a cyclic manner, leads to transgranular damage accumulation, such as persistent slip bands and fatigue cracking. Therefore, it is equivalent to the pp strain under cyclic conditions.
- For short-period holds, cc, pc, and cp types of inelastic strains are contributed mainly from GBS during the transient creep since purely tertiary creep would never start upon short cycle repeats. GBS mainly contributes to intergranular fracture.

When GBS operates, the accumulation of grain boundary damage, either in the form of cavity nucleation and growth or as grain boundary cracks, is proportional to the GBS displacement, such that

$$l_c = \varepsilon_{GBS} d \tag{17}$$

where d is the grain size.

Under cyclic creep conditions as imposed by strain controlled cycles, l_c can be stabilized once the entire hysteresis behavior is stabilized. Therefore, again under constant amplitude cycling conditions, Eq. (7) can be integrated to (in this case, neglecting dislocation pile-ups, i.e., let l_z=0):

Table 1 The new strain partitioning concept

Test type	$\Delta\varepsilon_g$	$\Delta\varepsilon_{GBS}$
HSRC	pp	0
CCCR	pp+pc	pc
TCCR	cp+cp	cp
BCCR	pp	cc
THSC	pp+cp+cc	$\Delta\sigma/E$ [a]
CHSC	pp+pc+cc	$\Delta\sigma/E$ [a]

[a]Note that $\Delta\sigma$ is the range of stress drop during stress relaxation in this test.

$$N = \frac{N_f}{1 + \frac{\varepsilon_{GBS} d}{\lambda}} \tag{18}$$

and, for now, the pure LCF life, N_f, is correlated with $\Delta\varepsilon_g$ through the Coffin–Manson relation with an exponent of $-1/2$ as

$$\Delta\varepsilon_g = DN_f^{-1/2} \tag{19}$$

This relationship can be established by high rate strain cycle (HRSC) tests.

For the application of Eq. (18) to the asymmetrical creep-fatigue interaction tests such as compressive cyclic creep rupture (CCCR), tensile cyclic creep rupture (TCCR), tensile hold strain cycle (THSC), and compressive hold strain cycle (CHSC), it should be recognized that due to reversed plasticity, each individual grain is fatigued by the entire inelastic strain range, but the GBS contributes to the effect of additional intergranular fracture. Since GBS operates in shear, it may produce grain boundary damage during either uniaxial tension or compression. Table 1 summarizes the new strain partitioning of $\Delta\varepsilon_g$ and $\Delta\varepsilon_{GBS}$ for the different creep-fatigue interaction tests.

Taking data from a NASA contract report [17] and reorganizing the strain partitioning data as outlined in Table 1, we have the creep-fatigue information for Rene 80 (in high vacuum) and IN100 (coated) as shown in Tables 2 and 3. For the bulk failure of these two materials under the test conditions, environmental effects can be neglected. Predictions with Eqs. (18) and (19) for Rene 80 and IN100 are also given in Tables 2 and 3, and the results are shown in Figs. 3 and 4, respectively.

Apparently, Eqs. (18) and (19) fit the observed behaviors very well (within a typical scatter factor of 2). The advantage of this physics-based rational model is that it simplifies very much the analytical procedure to characterize the creep-fatigue interaction, and it is rationalized with physical considerations of the damage accumulation processes, as discussed in the previous section. It unifies the SRP concept with the physics-based deformation decomposition rule, Eq. (16), taking note that in an asymmetrical cyclic deformation process, $\Delta\varepsilon_g$ is the total inelastic strain range that the grain body has to experience, and $\Delta\varepsilon_{GBS}$ contributes to the additional mode of intergranular fracture.

Table 2 Rene 80 at 871°C (D=0.08, d/λ=8)

Specimen ID	Test	$\Delta\varepsilon_g$	$\Delta\varepsilon_{GBS}$	N_f	N	Expt.
74-U-pp-13	HRSC	0.605	0	175	175	145
21U-pp-8	HRSC	0.322	0	617	617	642
41U-pp-10	HRSC	0.179	0	1997	1997	1410
22U-pp-9	HRSC	0.026	0	94,675	94,675	163,533
42U-pp-11	HRSC	0.051	0	24,606	24,606	217,620
92U-pc-13	CCCR	0.554	0.46	209	45	41
28U-pc-9	CCCR	0.378	0.283	448	137	149
91U-pc-12	CCCR	0.257	0.209	969	363	356
98U-pc-16	CCCR	0.258	0.183	961	390	396
29U-pc-10	CCCR	0.204	0.164	1538	665	1415
112U-cp-11	TCCR	0.385	0.308	432	125	101
86U-cp-9	TCCR	0.289	0.306	766	222	147
30U-cp-5	TCCR	0.289	0.254	766	253	193
31U-cp-6	TCCR	0.208	0.202	1479	565	530
36U-cp-7	TCCR	0.111	0.092	5194	2992	3705

Table 3 IN 100 (coated) at 900°C (D=0.0364, d/λ=50)

Specimen ID	Test	$\Delta\varepsilon_g$	$\Delta\varepsilon_{GBS}$	N_f	N	Expt.
7	HRSC	0.129	0	796	796	635
6	HRSC	0.121	0	905	905	900
1	HRSC	0.138	0	696	696	1260
2	HRSC	0.086	0	1792	1792	2120
3	HRSC	0.059	0	3806	3806	3670
4	HRSC	0.05	0	5300	5300	9460
5	HRSC	0.031	0	13,788	13,788	12,210
10	HRSC	0.026	0	19,601	19,601	17,340
8	HRSC	0.028	0	16,901	16,901	27,260
11	HRSC	0.014	0	67,602	67,602	48,320
N12	CHSC	0.196	0.03375	345	128	250
N10	CHSC	0.105	0.02	1202	601	764
N9	CHSC	0.102	0.019375	1274	647	944
39	THSC	0.18	0.026875	409	174	239
N8	THSC	0.08	0.016875	2070	1123	1495
54	BCCR	0.09	0.168	1636	174	159
N5	BCCR	0.085	0.16	1834	204	200
56	BCCR	0.054	0.11	4544	699	383

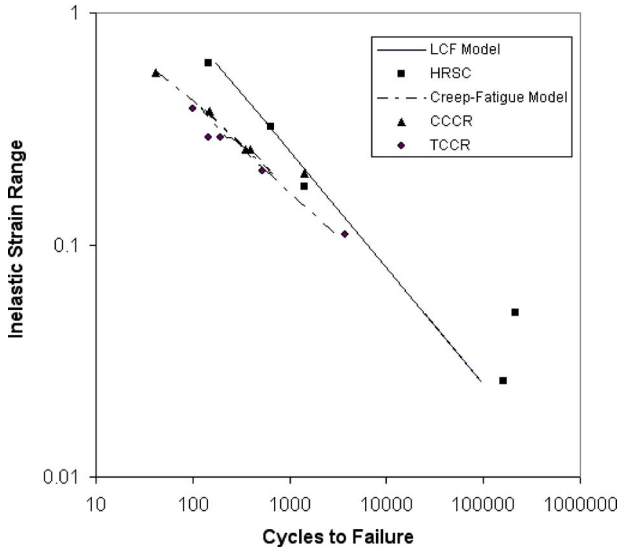

Fig. 3 Comparisons of Eqs. (18) and (19) with experimental data for Rene 80 at 871°C

4 Conclusions

A nonlinear creep-/dwell-fatigue interaction model is derived based on the nucleation and propagation of a surface fatigue crack and its coalescence with creep/dwell damages (cavities or wedge cracks) along its path inside the material.

The model has been shown to be successful in correlating both cold dwell fatigue and hot creep fatigue, as long as the respective damage accumulation processes are described based on the relevant deformation mechanism. In cold dwell, the damage is envisaged as dislocation pile-up, leading to the formation of ZSK cracks. In hot creep, the damage accumulation is related to grain boundary sliding. Particularly, for a creep-fatigue interaction, the model reconciles the SRP concept. Therefore, it provides a unified approach to deal with dwell-/creep-fatigue interactions.

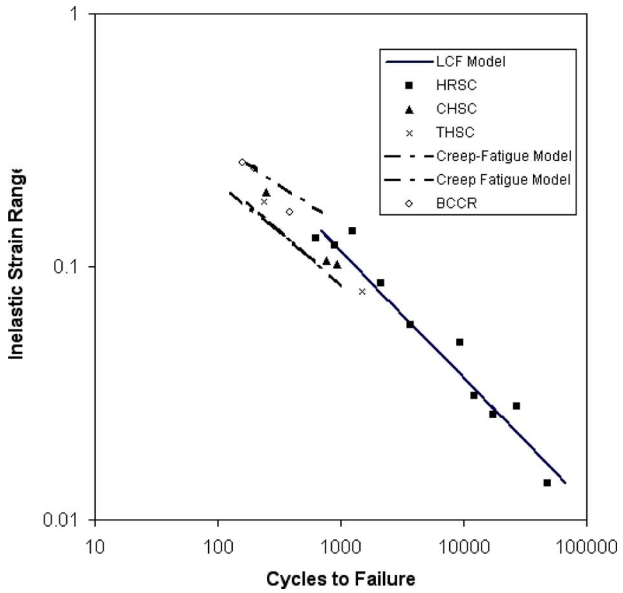

Fig. 4 Comparisons of Eqs. (18) and (19) with experimental data for IN 100 (coated) at 1000°C

Acknowledgment

The author would like to thank the Defense Research and Development Canada of the Department of National Defense, Canada for providing the financial support to projects related to prognosis and health management.

Nomenclature

- a = half crack size
- b = Burgers vector
- c = exponent in the Coffin–Manson relationship
- d = grain size
- D = empirical constant in the Coffin–Manson relationship
- da/dN = crack growth rate (subscript f indicates pure fatigue and "env" and "ox" indicates environmental and oxidation contributions
- F_{ij} = elastic matrix for anisotropic materials
- G = Griffith's energy release rate
- l_c = cavity size
- l_z = wedge crack size
- n = number of dislocations in a pile-up
- N = number of cycles to failure, subscript f specifies pure fatigue
- s = slip bandwidth
- v = dislocation velocity
- w_s = surface energy
- ε = strain
- κ = dislocation climb rate
- $\dot{\gamma}_p$ = strain rate
- λ = average spacing between internal creep damages
- μ = shear modulus
- ρ = dislocation density
- σ = stress
- τ = hold time

Appendix: Cyclic Tests to Generate SRP

1) High rate strain cycle (HRSC): constant ramping in tension and compression.

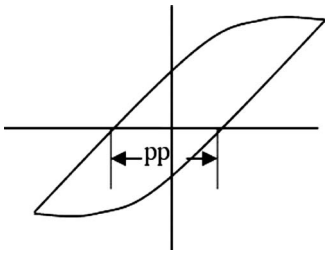

2) Compressive cyclic creep rupture (CCCR): ramped to a predetermined stress with compressive creep hold; reversed ramping to equal tensile strain.

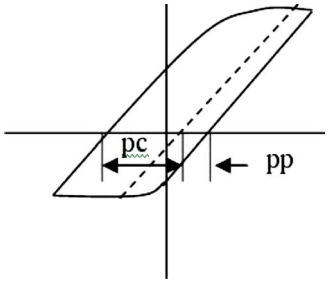

3) Balanced cyclic creep rupture (BCCR): creep holds in tension and compression at constant load until specific strain reached.

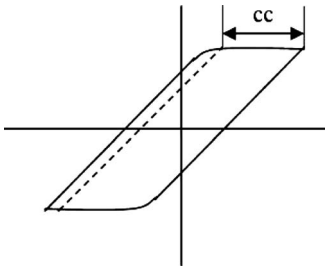

4) Tensile cyclic creep rupture (TCCR): opposite cycle to CCCR with tensile hold.

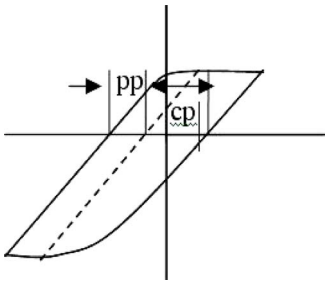

5) Tensile hold strain cycle (THSC): ramped to specific strain; stress relaxation followed by reversed ramping to equal compressive strain.

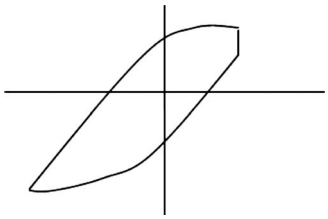

6) Compressive hold strain cycle (CHSC): opposite to THSC with compressive stress relaxation.

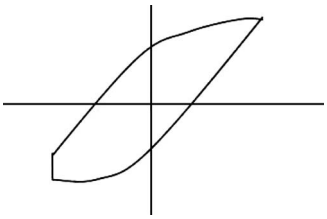

References

[1] Miner, M. A., 1945, "Accumulative Damage in Fatigue," ASME Trans. J. Appl. Mech., **67**, pp. A159–A167.

[2] Robinson, E. L., 1952, "Effect of Temperature Variation on the Long-Time Rupture Strength of Steels," Trans. ASME, **74**, pp. 777–780.

[3] Halford, G. R., Saltsman, J. F., and Hirschberg, M. H., 1977, "Ductility-Normalized Strain Range Partitioning Life Relations for Creep-Fatigue Life Predictions," NASA Report No. TM-73737.

[4] Coffin, L. F., 1954, "A Study of the Effects of Cyclic Thermal Stresses on a Ductile Metal," Trans. ASME, **76**, pp. 931–950.

[5] Manson, S. S., 1954, "Behavior of Materials Under Conditions of Thermal Stress," NACA Report No. TN-2933.

[6] Halford, G. R., 1991, "Evolution of Creep-Fatigue Life Prediction Models," *Proceedings of the Winter Annual Meeting of the American Society of Mechanical Engineers*, ASME AD-Vol. 21, pp. 43–57.

[7] Wu, X. J., Koul, A. K., and Krausz, A. S., 1993, "A Transgranular Fatigue Crack Growth Model Based on Restricted Slip Reversibility," Metall. Trans. A, **24**, pp. 1373–1380.

[8] Baik, S., and Raj, R., 1982, "Wedge Type Creep Damage in Low Cycle Fatigue," Metall. Trans. A, **13**, pp. 1207–1214.

[9] Baik, S., and Raj, R., 1982, "Mechanisms of Creep-Fatigue Interaction," Metall. Trans. A, **13**, pp. 1215–1221.

[10] Bache, M. R., Cope, M., Davies, H. M., Evans, W. J., and Harrison, G., 1997, "Dwell Sensitive Fatigue in a Near Alpha Titanium Alloy at Ambient Temperature," Int. J. Fatigue, **19**, pp. S83–S88.

[11] Wu, X. J., and Au, P., 2007, "Deformation Kinetics During Dwell Fatigue," Mater. Sci. Technol., **23**, pp. 1446–1449.

[12] Wu, X. J., 2005, "A Continuously Distributed Dislocation Model of Zener-Stroh-Koehler Cracks in Anisotropic Materials," Int. J. Solids Struct., **42**, pp. 1909–1921.

[13] Wu, X. J., and Koul, A. K., 1996, "Modeling Creep in Complex Engineering Alloys," *Creep and Stress Relaxation in Miniature Structures and Components*, H. Merchant, ed., TMS, Warrendale, PA, pp. 3–19.

[14] McLean, D., and Pineau, A., 1978, "Grain Boundary Sliding as a Correlating Concept for Fatigue-Hold Time," Meat Sci., **12**, pp. 313–316.

[15] Frost, H., and Ashby, M. F., 1982, *Deformation Mechanism Maps*, Pergamon, Elmsford, NY.

[16] Wu, X. J., and Koul, A. K., 1995, "Grain Boundary Sliding in the Presence of Grain Boundary Precipitates During Transient Creep," Metall. Mater. Trans. A, **26**, pp. 905–913.

[17] Romannoski, G. R., Jr., 1982, "Mechanisms of Deformation and Fracture in High Temperature Low-Cycle Fatigue of Rene 80 and IN 100," NASA Contractor Report No. 165498.

Fast Epitaxial High Temperature Brazing of Single Crystalline Nickel Based Superalloys

Britta Laux
e-mail: b.laux@tu-bs.de

Sebastian Piegert

Joachim Rösler

Technische Universität Braunschweig,
Institut für Werkstoffe,
38106 Braunschweig, Germany

A new high temperature brazing technology for the repair of turbine components made of single crystalline nickel based superalloys has been developed. It allows the repair of single crystalline parts by producing an epitaxially grown braze gap within very short times. In contrast to commonly used brazing technologies, the process is not diffusion based but works with consolute systems, particularly nickel-manganese alloys. Brazing experiments with 300 μm wide parallel braze gaps, as well as V-shaped gaps with a maximum width of 250 μm, were conducted. Furthermore, thermodynamic simulations, with the help of THERMOCALC software, Version TCR, were carried out to identify compositions with a suitable melting behavior and phase formation. With the new alloys complete, epitaxial bridging of both gap shapes has been achieved within brazing times as short as 10 min. [DOI: 10.1115/1.3026576]

1 Introduction

Since in aircraft engines, as well as in stationary gas turbines, enhanced efficiency requires increased combustion temperatures, nowadays turbine components are frequently made of single crystalline nickel based superalloys providing a good high temperature durability [1–5]. However, single crystalline components are very expensive so the repair of damaged parts is of special economical interest. Filling cracks by high temperature diffusion brazing is the most common repair technology [3,5,6].

The central idea of this method consists of a fast diffusing melting point depressant, which can cause solidification by diffusing into the base material [7–10]. Due to the high stresses in turbine components, the primary purpose of healing is to produce a single crystalline microstructure with the crystallographic orientation of the base material, which is called "epitaxial solidification." With regard to the mechanical properties, the absence of grain boundaries in the braze gap and the reproduction of the elastic anisotropy of the base material are important.

However, current technologies only produce epitaxially solidified braze gaps when the melting point depressant is entirely diffused out of the braze gap, which requires very long times [3,11–15]. Otherwise, because of the poor solubility of the melting point depressant in the solid phase and the resulting segregation in the liquid phase, brittle phase precipitates lead to nucleation sites for equiaxed grains. The solidification then terminates with an eutectic reaction, resulting in a polycrystalline microstructure with brittle phases in the center of the braze gap.

Even with fast moving elements such as boron and silicon used as melting point depressants and a brazing temperature in the range of 1423 K, complete isothermal solidification of a crack in the dimension of 300 μm requires a hold time of about 50 h [15].

In this study, new braze alloys have been developed for fast epitaxial high temperature brazing. The approach is the use of a nickel based alloying system with a melting point depressant, which allows single phase solidification, so that formation of a second phase as nucleation site of stray grains is entirely avoided.

One alloying system, which was found to be applicable, is the nickel-manganese system (Fig. 1): Manganese provides a good compatibility with nickel based superalloys and acts in nickel as an effective melting point depressant, whereby the azeotropic composition has a melting temperature of 1293 K. Furthermore, the system shows complete miscibility down to relatively low temperatures so even a fast cooling does not result in the formation of brittle phases. Additionally, the melting interval in the nickel-manganese system is very small and even becomes narrower with increasing amount of manganese. Therefore, a high solidus temperature is provided, which is, with regard to high temperature applications, important for the avoidance of remelting of the brazed gaps.

It can be taken from the phase diagram that at least 28 wt % of manganese are required to obtain a system with a liquidus temperature of about 1473 K, which is important for the avoidance of γ'-coarsening and too much dissolution of the base material during the brazing process [17]. Moreover, there are two interesting compositions: on the one hand, the eutectoid system with 36.7 wt % Mn and, on the other hand, the azeotropic system with 58.4 wt % Mn. In the first case, the formation of the βNi_2Mn-phase and the αNiMn-phase out of the γMn-phase occurs at relatively low temperatures and can possibly be avoided by fast quenching. The azeotropic system stands out due to its very low liquidus temperature allowing a significant reduction of the brazing temperature. However, since in both cases relatively high amounts of manganese are necessary, the addition of a second melting point depressant was also taken into account. It was found that the nickel-manganese system with small amounts of silicon (below the limit of solubility) forms alloys with a beneficial melting behavior. Additionally, silicon improves the wettability of the alloy, which is very important for a stable bonding to the base material.

2 Simulation

All thermodynamic simulations were performed with THERMOCALC, Version TCR, whereby the database TTNi7 particularly developed for nickel based superalloys was used. In THERMOCALC, diffusion based effects can only be taken into account by the Scheil–Gulliver module; otherwise, only systems in complete equilibrium can be computed. In this work, thermodynamic simulations, as well as kinetic ones, were carried out.

2.1 Thermodynamic Simulations. In addition to the binary compositions described above, special interest was directed toward the ternary system Ni–Mn–Si to find alloys with an applicable melting behavior, i.e., a maximum liquidus temperature in the range of 1473 K and a minimum solidus temperature of about

Manuscript received April 16, 2008; final manuscript received April 23, 2008; published online February 11, 2009. Review conducted by Dilip R. Ballal. Paper presented at the ASME Turbo Expo 2008: Land, Sea and Air (GT2008), June 9–13, 2008, Berlin, Germany.

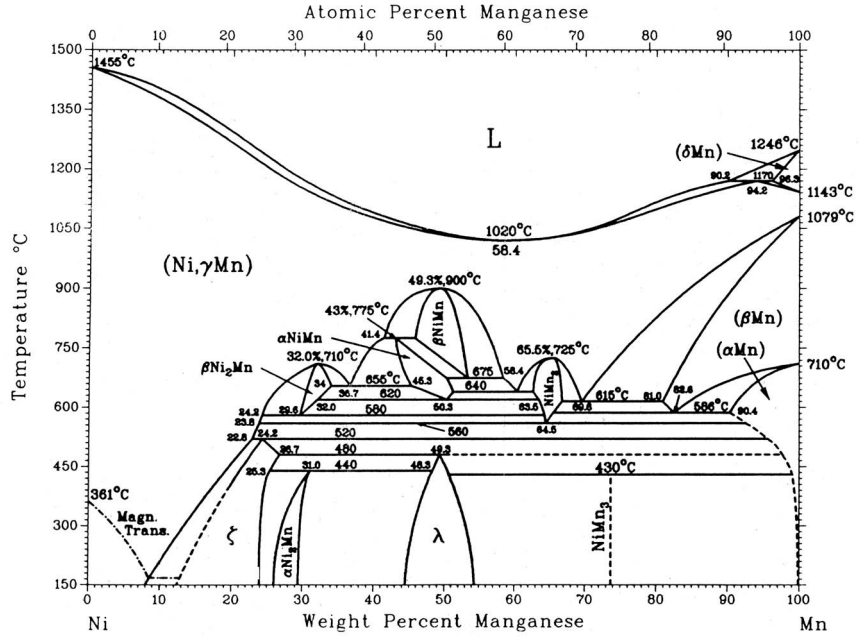

Fig. 1 Binary phase diagram of the system Ni–Mn [16]

1273 K. The lower boundary condition was chosen with regard to high application temperatures requiring a sufficiently high melting temperature. In first simulations, manganese fractions of 15 wt %, 20 wt %, 25 wt %, and 30 wt % were assumed and quasibinary phase diagrams with temperature versus fraction of silicon have been computed (Fig. 2). The plotted phase boundaries mark the appearance and the disappearance of the phases formed in the system. For example, in cases of low amounts of silicon, the γ-phase appears if the liquidus temperature of the composition is reached; the phase boundary L marks the disappearance of the liquid phase and therefore the solidus temperature. It can be seen in the calculated diagrams that in addition to the γ-phase the

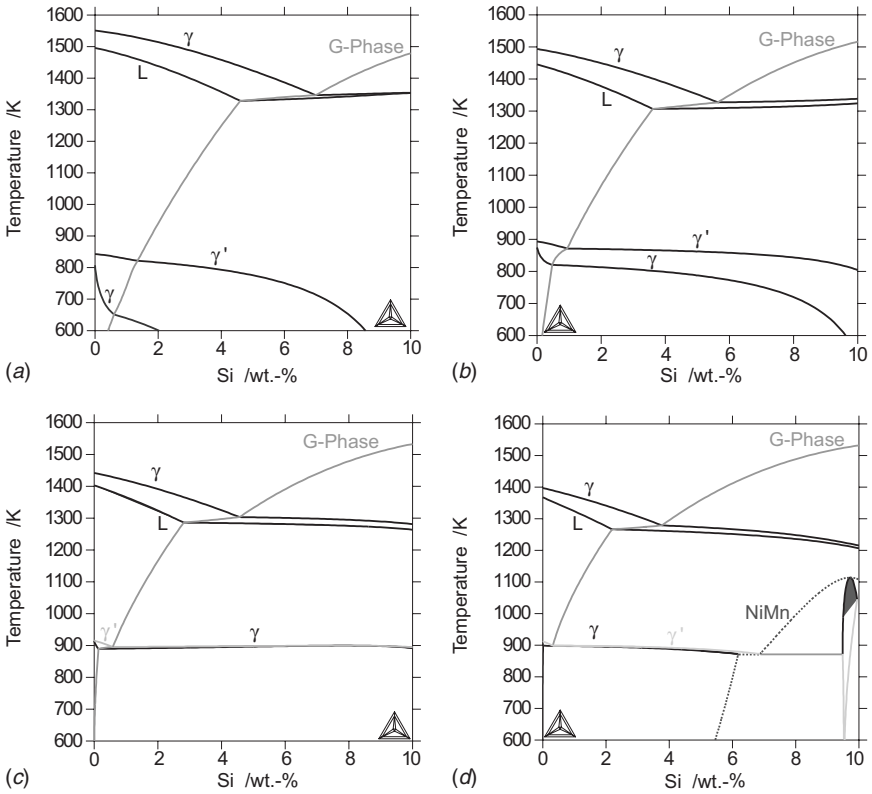

Fig. 2 Quasibinary phase diagrams with fixed fractions of manganese and varying fractions of silicon, simulated with THERMOCALC, Version TCR. (*a*) 15 wt % Mn, (*b*) 20 wt % Mn, (*c*) 25 wt % Mn, and (*d*): 30 wt % Mn

Table 1 Calculated solidus and liquidus temperatures as well as melting intervals in K for selected braze alloys (composition given in wt %)

Mn	Si	T_S	T_L	ΔT_{SL}
15	0	1496	1551	55
15	1	1470	1535	65
15	2	1438	1514	76
20	0	1446	1494	48
20	1	1415	1474	59
20	2	1377	1449	72
25	0	1403	1442	39
25	1	1366	1419	53
25	2	1324	1391	67
30	0	1367	1397	30
30	1	1324	1371	47
30	2	1276	1341	65

G-phase is formed, either as first solid phase or out of the solidified γ-phase. In previous study, the *G*-phase was identified as a cubic intermetallic with the stoichiometric composition $Ni_{16}Si_7Mn_6$ [18].

For several compositions, the solidus and liquidus temperatures, as well as the corresponding melting intervals, were calculated and listed in Table 1.

Following the calculations, the melting point depressing effect caused by the addition of silicon becomes stronger as the fraction of manganese increases, so the two melting point depressants reinforce their effects (Table 1). Furthermore, the melting interval becomes smaller in case of higher manganese fractions, whereby the addition of silicon causes a widening of the melting interval. The formation of the *G*-phase cannot be completely avoided; with higher amounts of silicon and manganese, the precipitation occurs at higher temperatures. However, it has to be assured that the solidification is completed before the *G*-phase precipitates. Therefore, the amount of silicon has to be restricted.

For temperatures in the range of 900 K, the formation of the γ'-phase is calculated: Higher amounts of manganese cause a higher γ' solvus temperature, whereby it is reduced by the addition of silicon. For the system with 30 wt % Mn, the formation of the NiMn-phase with the stoichiometric composition NiMn is predicted. From the thermodynamic simulations, it is suggested that the fraction of the melting point depressants has to be restricted to lower the amounts of the *G*-phase and to narrow the melting intervals. In addition, high amounts of the γ'-phase with a high solvus temperature are essential for a high temperature stability. Therefore, it is recommended that a manganese fraction in the range of 20–30 wt % and a silicon fraction up to 2 wt % is advantageous.

2.2 Kinetic Simulations. Scheil–Gulliver simulations for three braze alloys were carried out for kinetic simulation: The eutectoid binary NiMn-system with 36.7 wt % Mn, as well as two ternary alloys with a composition out of the advantageous range, i.e., 20 wt % and 25 wt % Mn combined with 2 wt % Si, was selected (Table 2). In the Scheil–Gulliver solidification model, infinite fast diffusion of components in the liquid phase and zero

Table 2 Selected braze alloys (composition in wt %) with their corresponding solidus and liquidus temperatures as well as melting intervals (in K) measured by DSC (heating curve)

Ni	Mn	Si	T_S	T_L	ΔT_{SL}
No. 1 bal.	36.7	0	1387	1423	36
No. 2 bal.	58.4	0	1295	1295	0
No. 3 bal.	20	2	1449	1523	74
No. 4 bal.	25	2	1412	1470	58

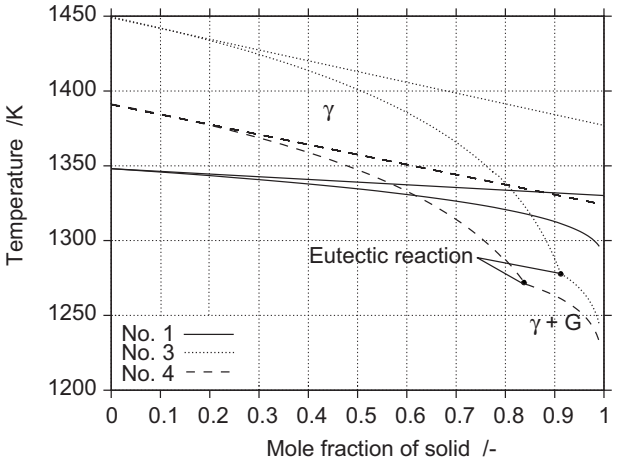

Fig. 3 Calculated fraction of solid versus temperature curves for the alloys listed in Table 2 with exception of the azeotropic system: complete equilibrium in comparison to Scheil calculations

diffusion coefficients in the solidified phases are assumed. The cooling simulation is computed stepwise by calculating the equilibrium at a certain temperature and setting the overall composition to the composition of the liquid phase. This is done for each step until the lowest temperature where the liquid phase can exist is reached.

In Fig. 3, mole fraction solid versus temperature curves for these alloy systems listed in Table 2 with exception of the azeotropic system are depicted. The simulations were computed by using the Scheil module with assumption of equilibrium condition (straight lines). Since the Scheil simulations are not finished until the liquid phase is completely consumed, the predicted solidus temperatures compared with the equilibrium assumed ones are very low.

In contrast to binary systems where the solidification ends with the binary eutectic reaction at a certain temperature, in multicomponent alloys, the eutectic reaction takes place over a temperature range [19]. This can be also observed in case of the two ternary systems: From the eutectic starting temperature marked in Fig. 3 by small black points, until the end of the solidification, the liquid phase, the γ-phase, and the *G*-phase are coexisting. Eutectic temperatures of 1278 K and 1271 K are predicted for alloys No. 3 and No. 4, respectively.

For the ternary Ni–Mn–Si systems, the change in the composition of the liquid phase during solidification is also visualized by plotting Scheil computed solidification paths into a ternary phase diagram (Fig. 4). In this case, the silicon fraction was plotted against the fraction of manganese. Contour lines for several temperatures indicate the slope of the surface, whereby two "liquidus plateaus" separated by a univariant liquidus line are visible. In case of low amounts of silicon and manganese, the solidification starts with the formation of the γ-phase; otherwise, the first solid phase formed during cooling is the *G*-phase. The two solidification paths indicate in accordance with Fig. 3 that in both cases an eutectic reaction occurs before the liquid phase is completely consumed. Corresponding to Fig. 3, the univariant liquidus line is reached at the temperature, which is marked as the eutectic start temperature. It can be noted that the amount of mangnese and silicon increases with decreasing temperature. Starting with their particular gross composition, the final eutectic compositions for alloys 3 and 4 were computed to 37.85 wt % of manganese, 3.04 wt % of silicon, and 40.91 wt % of manganese, 2.89 wt % of silicon, respectively.

From the thermodynamic and kinetic simulations, the simulation data provide beneficial solidus and liquidus temperatures as well as melting intervals for the ternary alloy systems except for

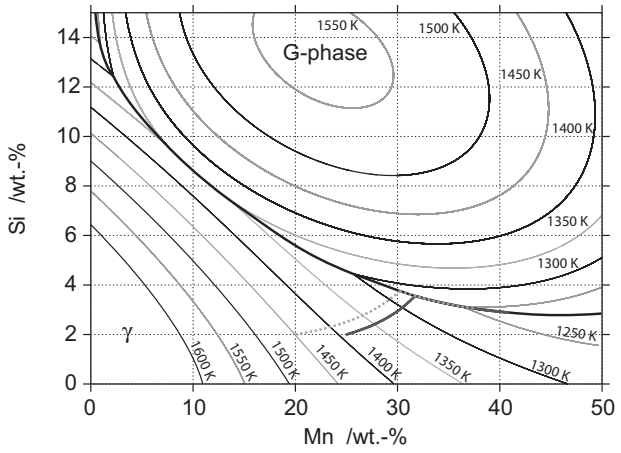

Fig. 4 Liquidus surface of the ternary system Ni–Mn–Si simulated by assuming complete equilibrium with the solidification paths of the two ternary systems, calculated by utilizing the Scheil module

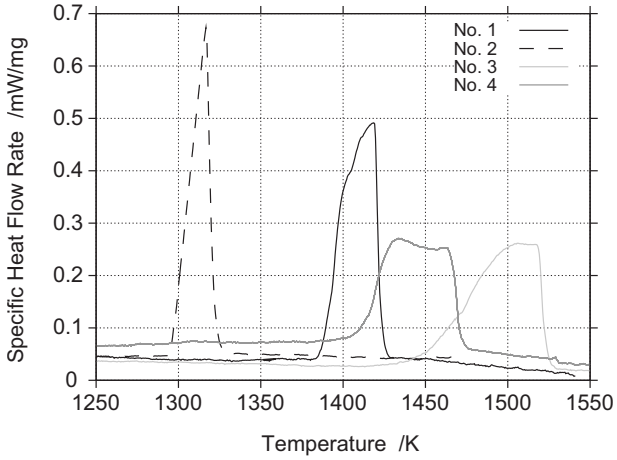

Fig. 6 DSC heating curves for the chosen braze alloys

the eutectic reaction at the end of the solidification. Therefore, two binary alloy systems, as well as two ternary alloy systems, were selected as candidate braze alloy systems for fast epitaxial high temperature brazing of single crystal nickel based superalloys. The detailed experimental method and results will be explained in Sec. 3.

3 Experiments

Various brazing experiments were conducted with the four selected nickel-manganese based alloys: The compositions and corresponding solidus and liquidus temperatures measured by differential scanning calorimetry (DSC) are listed in Table 2. As shown in Fig. 5, two gap geometries such as 300 μm wide parallel gap and V-shaped gap with a maximum width of 250 μm were used to measure the epitaxially grown gap width after several brazing cycles. All samples were machined from a single crystalline nickel based superalloy with the composition (in wt %): Ni–7.5Co–7.0Cr–1.5Mo–5.0W–6.5Ta–6.2Al–3.0Re.

The parallel gap samples were prepared from 1.9 mm thick sheets using a cutting machine with a 300 μm thick blade. Since crack formation within turbine components normally occurs perpendicular to the [001] direction of the single crystal, the cutting direction was also perpendicular to [001]. The V-shaped specimens were fabricated by cutting a sheet with a thickness of 2.5 mm into two halves that were joined by spot welding with the help of a 250 μm thick nickel spacer. In case of the V-shaped samples, the gap direction was also perpendicular to the [001] direction of the single crystal.

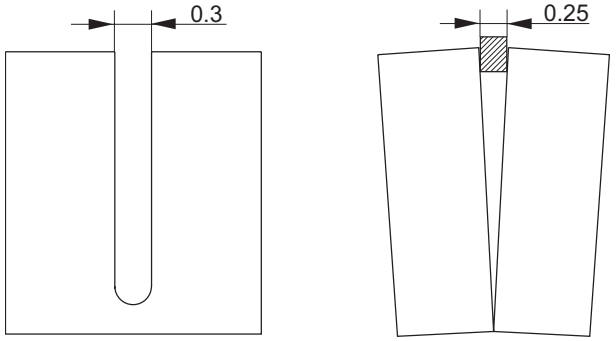

Fig. 5 Braze gap specimens: parallel gap, 300 μm (left), V-shaped gap, maximum width 250 μm (right)

The selected alloys were melted in a vacuum arc furnace and small lenses with about 10 g weight were produced. Small pieces were cut from these lenses for DSC analysis. Calorimetric analyses were conducted with a Netzsch DSC 404 C Pegasus© calorimeter by applying a heating and cooling rate of 10 K/min. The specific heat flow rate was plotted against the temperature in order to observe phase transformations as peaks in the curves (Fig. 6).

For evaluation, only the heating curves were taken into account, whereby tangents at the rising and falling slopes were used. The intersection of these tangents with the extrapolated base line was read off as solidus and liquidus temperatures, respectively. In case of the azeotropic system, only the rising edge was used. The corresponding melting temperatures of the chosen systems are listed in (Table 2).

Subsequent to calorimetric analysis, the braze alloy lenses were cut into thin bars that were placed on the braze gaps. All brazing experiments were conducted in a vacuum furnace with a residual pressure of less than 8×10^{-5} mbar. The first step of the brazing cycle was heating-up to a temperature of about 150 K below the solidus temperature with a gradient of 10 K/min, followed by 10 min hold time for homogenization (Fig. 7). Afterwards, the temperature was increased to the brazing temperature T_B with a gradient of 30 K/min. During the subsequent hold time of 30 min, the braze filler metal liquefies and flows into the braze gap. For cooling from brazing to final temperature T_F, different cycle shapes were applied: Ramp shaped cycles (No. 1) as well as cascaded shapes with one hold time (No. 2) and multiple hold times (No. 3). For T_B, several temperatures between 1313 K and 1533 K were

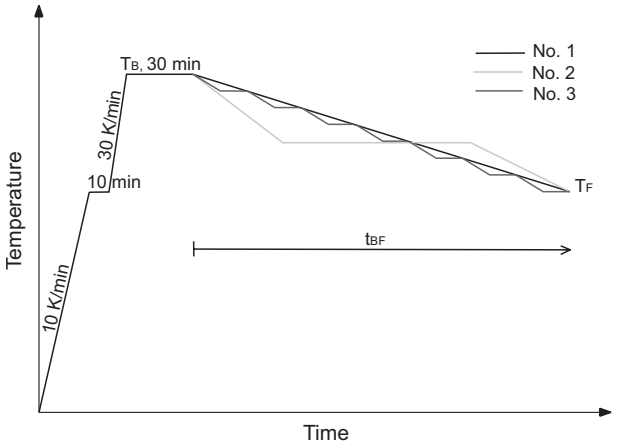

Fig. 7 Different brazing cycles

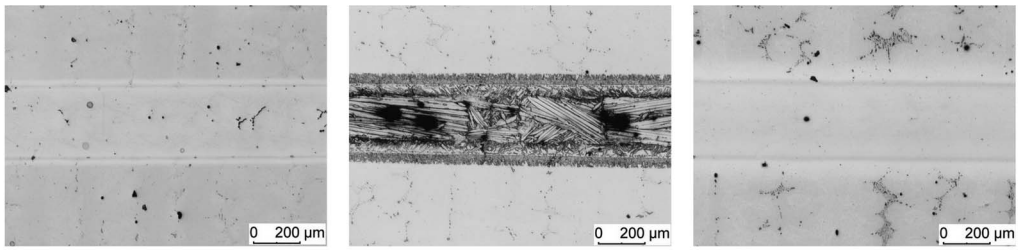

(a) Ni-36.6Mn, parallel gap, T_B=1433 K, T_F=1273 K, t_{BF}=300 min, ramp

(b) Ni-58.4Mn, V-shaped gap, T_B=1313 K, T_F=1273 K, t_{BF}=300 min, ramp

(c) Ni-20Mn-2Si, parallel gap, T_B=1533 K, T_F=1273 K, t_{BF}=60 min, ramp

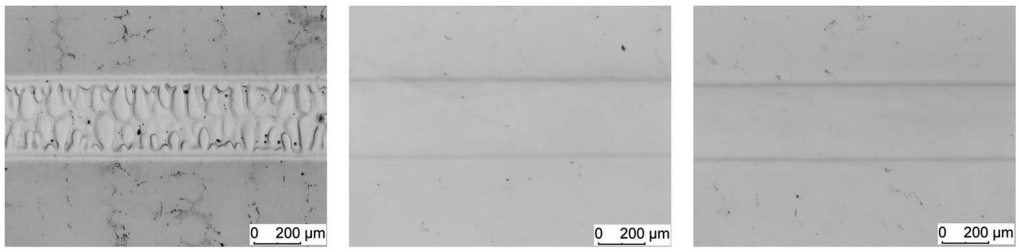

(d) Ni-20Mn-2Si, parallel gap, T_B=1533 K, T_F=1273 K, t_{BF}=10 min, ramp

(e) Ni-25Mn-2Si, parallel gap, T_B=1483 K, T_F=1373 K, t_{BF}=240 min, cascaded (one hold time)

(f) Ni-25Mn-2Si, parallel gap, T_B=1483 K, T_F=1273 K, t_{BF}=300 min, cascaded (five hold times)

Fig. 8 Light microscope images of the brazed gaps etched with V2A etchant

applied and T_F of 1273 K was selected for the final temperature. The time t_{BF} between T_B and T_F was varied between 10 min and 5 h. After reaching the T_F, the temperature was lowered to room temperature with a gradient of 1 K/min.

4 Results

In order to visualize grain boundaries by means of light microscopy, ground and polished specimens were etched with V2A etchant. Details from the brazed gaps taken by light microscope are depicted in Fig. 8. No grain boundaries except for the azeotropic system in Fig. 8(*b*) were observed within the brazed gaps. Even a brazing time t_{BF} of 10 min led to complete epitaxial solidification. Since also the V-shaped gaps are bridged without any stray grains, measurement of epitaxially filled gap width dependent on time, as planned, was impossible. As the brazing cycle with the azeotropic system has not been successful, it is concluded, that the amount of manganese has to be restricted. The addition of small amount of silicon does not influence the epitaxial growth; additionally, no secondary phases could be revealed. Further detailed microstructural analysis is necessary to verify if the predicted *G*-phase is not formed during brazing.

To assure the results from light microscopy, the samples were examined using a scanning electron microscope (SEM). In particular, electron backscatter diffraction (EBSD) analyses were conducted to detect the crystallographic orientation distribution within the brazed gaps.

All EBSD results were visualized by misorientation profiles and pole figures (Figs. 9–12). The misorientation profiles were measured perpendicular to the gap, labeled by a black line. All profiles were plotted relative to the first point, which was chosen in each

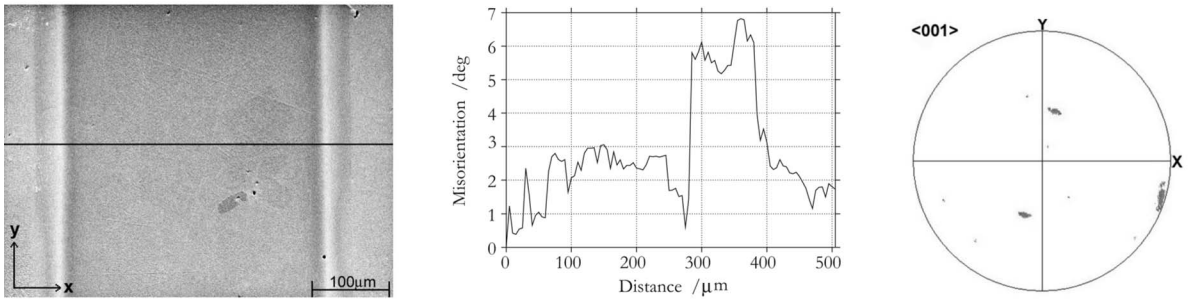

(a) SEM-image

(b) misorientation profile, relative to first point

(c) ⟨001⟩ pole figure

Fig. 9 EBSD analysis: Ni–36.7Mn, parallel gap, T_B=1433 K, T_F=1273 K, t_{BF}=300 min, ramp

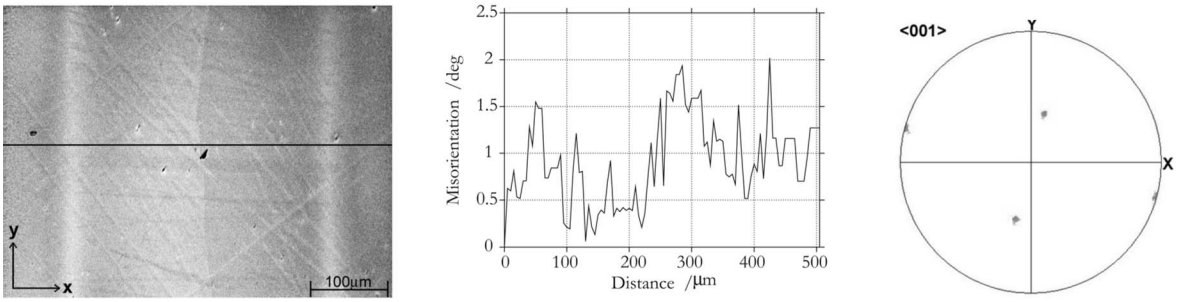

(a) SEM-image (b) misorientation profile, relative to first point (c) ⟨001⟩ pole figure

Fig. 10 EBSD analysis: Ni–20Mn–2Si, parallel gap, T_B=1533 K, T_F=1273 K, t_{BF}=300 min, ramp

case on the left boundary within the base material. As pole figures, the ⟨001⟩ ones were plotted, which means that the breakthrough points of the ⟨001⟩ directions are projected onto the equatorial plane of a projection globe. In case of a single crystalline orientation, three discrete projection points have to be visible in the pole figure; polycrystalline materials produce statistically distributed points. In this case, the primary orientation [001] is parallel to the *x*-axis, and the gap is perpendicular to this; therefore, all projection points should lie on the axes of the pole figure coordinate system. However, since the secondary orientations are not fixed, the position of the corresponding breakthrough points can be distributed over the whole *y*-*z*-plane; in the ⟨001⟩ pole figures, no exact *y*-position is fixed.

The misorientation profiles show that the maximum misorientation, measured relative to the first point, is in the range of 8 deg (Fig. 11(*b*)). No large angle grain boundaries could be identified within the brazed gaps [20]. All pole figures show three discrete projection areas. In Fig. 10(*c*), one area is divided into two parts, which appear in the second and fourth sectors of the projection plane, respectively. With exception of Fig. 11(*c*), each pole figure shows a small rotation of the projection points. Obviously, small orientation deviations of the [001] direction are at hand. However, for the analysis of epitaxial solidification, the exact sample orientation is not essential. Altogether, it is concluded from the results of the EBSD analysis that complete epitaxial solidification of the

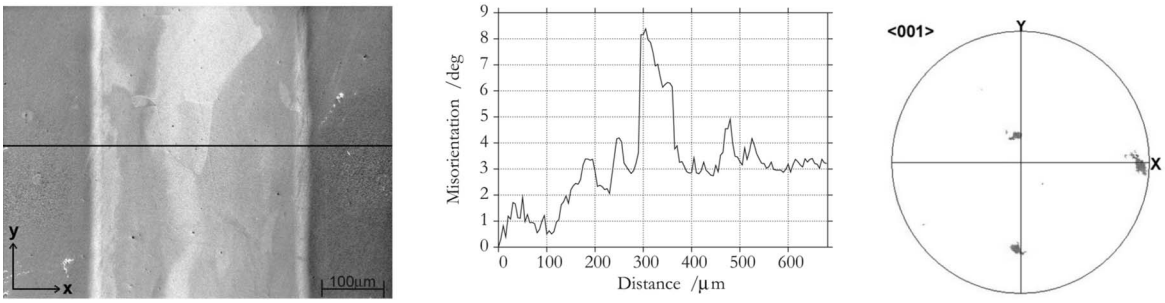

(a) SEM-image (b) misorientation profile, relative to first point (c) ⟨001⟩ pole figure

Fig. 11 EBSD analysis: Ni–25Mn–2Si, parallel gap, T_B=1483 K, T_F=1273 K, t_{BF}=300 min, cascaded (five hold times)

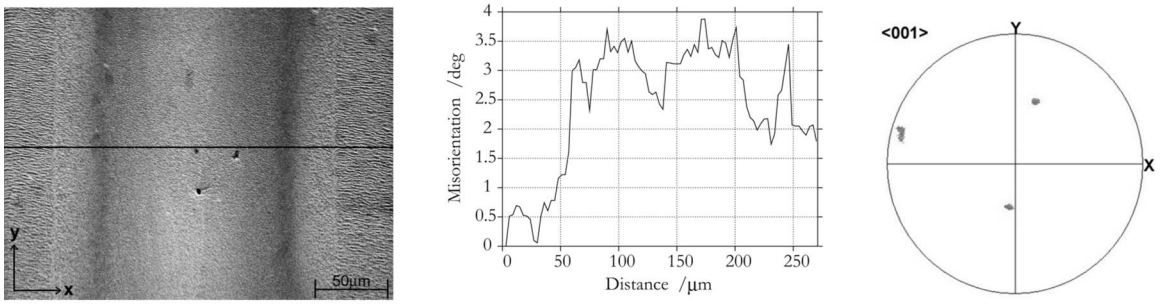

(a) SEM-image (b) misorientation profile, relative to first point (c) ⟨001⟩ pole figure

Fig. 12 EBSD analysis: Ni–25Mn–2Si, V-shaped gap, T_B=1483 K, T_F=1273 K, t_{BF}=300 min, ramp

parallel gaps as well as of the V-shaped ones was successful in case of the binary and also in case of the two ternary filler systems.

Additionally, SEM was used to find the *G*-phase predicted by THERMOCALC within the braze gaps. However, no second phase could be identified by means of SEM: Either the formation of the *G*-phase did not occur during brazing or the segregation morphology is very fine so it could not be detected. Nevertheless, even if a second phase is present in the brazed gaps, it obviously did not influence the epitaxial solidification.

5 Discussion

In conventional transient liquid phase (TLP) bonding technologies usually boron and/or silicon are used as melting point depressants [6,15]. Elements such as phosphorus, hafnium, and zirconium are also possible to lower the melting point in nickel based materials; however, the use of these elements is of lesser extent [15]. It is observed that an epitaxial bridging of braze gaps in single crystalline alloys can be achieved within long hold times in the range of several hours in combination with high temperatures. The braze gap's microstructure is similar to the base material's one consisting of γ' cubes in a γ matrix [6,17]. Furthermore, a homogenization between filler and surrounding base material takes place; hence a concentration of the melting point depressant below the solubility boundary is assured. Due to its high diffusivity in nickel, shortest brazing times are achieved with boron containing filler alloys. However, due to its poor solubility, insufficient hold times lead to brittle secondary phases, serving as nucleation sites for stray grains. Additionally, in case of incomplete epitaxial growth, solidification is finished by a eutectic reaction resulting in a multiphase and polycrystalline microstructure [6]. Furthermore, high temperatures and long hold times cause a coarsening of the base material with the result of deteriorating mechanical properties; especially the stress rupture behavior is influenced [6,17]. Altogether, the problem of conventional TLP is that either the base material loses its mechanical properties or insufficient hold times involve weak polycrystalline braze gaps [6].

In several publications; correlations between temperature, hold time and resulting microstructure within the braze gap have been reported for single crystalline nickel based superalloys.

In Ref. [5], gaps of 45 μm were brazed with an insert alloy containing 5.3% of silicon and 2.04% of boron. Temperatures between 1473 K and 1523 K, a bonding pressure of 5.58×10^{-3} MPa and hold times between 0.5 and 24 h were applied. It is suggested that in case of 1523 K, 8 h hold time are necessary to achieve complete epitaxial solidification.

In Ref. [6], 100 μm wide gaps in CMSX-4 were brazed by use of the commercial high temperature filler system D15 (composition: Ni–15Cr–10Co–3.4Ta–3.5Al–2.3B). Epitaxial solidification could be observed after 5 h; however, the high brazing temperature of 1553 K caused massive coarsening in the base material; an average γ' diameter of 0.8 μm was measured.

A similar correlation between hold time and brazing temperature was found by Kamohara et al. [21]. Rods from a nickel based superalloy with a diameter of 8 mm were brazed by applying a 50 μm thick filler insert containing nickel with 4.4 wt % silicon and 3.0 wt % boron. A temperature of $0.88T_m$ (base material's melting temperature) in combination with a bonding pressure of 0.98 MPa allowed epitaxial bridging of 50 μm within half an hour; with increasing temperatures the times required decreased. Compared with the results from Li et al. [5], it is concluded that the high bonding pressure of almost 1 MPa, which is 180 times higher than the pressure applied in Ref. [5], involves a reduced effective gap width and, thus, a decreased solidification time.

The kinetics of the epitaxial solidification of D15 applied to CMSX-4 has been investigated in Ref. [15]. It is reported that at higher temperatures the diffusion coefficient increases resulting in faster solidification. However, at the same time more base material is dissolved during the brazing process leading to an increased effective gap width. Furthermore, the boron solubility in nickel diminishes above the eutectic temperature. Considering these effects, an optimum brazing temperature of about 1423 K was found [15]. The following correlation between gap width W_0 and hold time t_{iso} at 1423 K was derived from the experiments [15]:

$$W_0 = K \cdot \sqrt{t_{\mathrm{iso}}} \tag{1}$$

with

$$K \approx 6.9 \times 10^{-7} \ \mathrm{m/s^{0.5}}$$

Equation (1) shows that a hold time of about 50 h is necessary for complete epitaxial solidification of gaps in the range of 300 μm.

In Refs. [12,13], CMSX-2 and CMSX-4 rods in combination with the braze filler materials MBF-80 (composition: Ni–15.5Cr–3.7B) and F-24 (composition: Ni–8.8Cr–8.0Co–10.8Mo–3.7W–2.9Al–3.0Ta–2.8B) were investigated. In agreement to Refs. [5,6,21], no optimum brazing temperature was found, rather a decrease of the required hold time with increasing temperature was observed. Epitaxial bridging of 40 μm wide braze gaps was achieved within 1 h, 3.4 h, and 5.5 h at temperatures of 1523 K, 1453 K, and 1373 K, respectively.

Compared with current TLP bonding, the Ni–Mn filler systems developed here permit solidification times being 100 times shorter, which gives the possibility of brazing even large gaps within economically justifiable times. This is primarily caused by the high solubility of manganese in the solid phase and the low segregation tendency to the liquid phase. For this reason, epitaxial solidification can be accomplished in very short times without the nucleation of stray grains. Additionally, as a result of the short hold times, the risk of coarsening of the base material is relatively low even in case of high brazing temperatures in the range of 1530 K. Complete epitaxial solidification of 300 μm wide gaps could be observed after only 10 min. In this case, dendritic growth is visible (Fig. 8(*d*)). It is concluded that a change from planar to dendritic solidification front took place, as it occurs during single crystalline fabrication (Bridgman process) in case of sufficiently high supercooling [17,22]. However, the dendritic solidified gap did not show grain boundary formation indicating that epitaxial bridging was successful. Furthermore, in spite of the prediction of a second phase (*G*-phase) by thermodynamic simulations, no additional phases could be observed. The microstructure of all epitaxially solidified samples with exception of the dendritic solidification was very homogeneous.

6 Conclusions

The epitaxial high temperature brazing of 300 μm wide gaps using very short brazing times was demonstrated. The following conclusions can be drawn.

1. A brazing process, which does not depend on the diffusion of the melting point depressant into the surrounding base material, was developed. Compared with commercially available braze filler metals, relying on boron and/or silicon as melting point depressants, an epitaxial healing of cracks in single crystalline materials is possible in brazing times being up to 100 times shorter.
2. Manganese was identified as ideal melting point depressant because it combines little segregation tendency with excellent solubility in the nickel-rich matrix. As a result, fast epitaxial solidification without formation of second phases or stray grains is possible.
3. The parameters controlling epitaxial solidification during brazing are the brazing temperature T_B, the final temperature T_F, and the time t_{BF} between these two temperatures. In contrast, different cycle shapes have little influence on the braze result.
4. The investigation of the azeotropic system containing 58.4 wt % of manganese showed that the amount of man-

ganese has to be restricted. With regard to the results of the simulations, it is assumed that the fraction of silicon also has to be restricted to a few percent: fractions of 30 wt % of manganese and 2 wt % of silicon should not be exceeded.

5. From this study, one binary and two ternary alloys, such as Ni–36.7Mn, Ni–20Mn–2Si, and Ni–25Mn–2Si, were found to be suitable for wide gap brazing of single crystalline nickel based superalloys.

References

[1] Antony, K. C., and Goward, G. W., 1988, "Repair of Air-Cooled Turbie Vanes of High-Performance Aircraft Engines—Problems and Experience," Sixth International Symposium on Superalloys, pp. 745–754.

[2] Brauny, P., Hammerschmidt, M., and Malik, M., 1985, "Repair of Air-Cooled Turbie Vanes of High-Performance Aircraft Engines—Problems and Experience," Mater. Sci. Technol., **49**(1), pp. 719–727.

[3] Idowu, O. A., Richards, N. L., and Chaturvedi, M. C., 2005, "Effect of Bonding Temperature on Isothermal Solidification Rate During Transient Liquid Phase Bonding of Inconel 738LC Superalloy," Mater. Sci. Eng., A, **397**(1-2), pp. 98–112.

[4] Idowu, O. A., Ojo, O. A., and Chaturvedi, M. C., 2006, "Microstructural Study of Transient Liquid Phase Bonded Cast Inconel 738LC Superalloy," Metall. Mater. Trans. A, **37**(9), pp. 2787–2796.

[5] Li, W., Jin, T., Sun, X., Guo, Y., and Guan, H., 2002, "Transient Liquid Phase Bonding of Ni-Base Single Crystal Superalloy CMSX-2," J. Mater. Sci. Technol., **18**(1), pp. 54–56.

[6] Hoppe, B., 2003, *Verhalten gelöteter Nickelbasis-Superlegierungen unter thermischer Ermüdungsbelastung*, Der Andere Verlag, Osnabrück.

[7] Duvall, D. S., Owczarski, W. A., and Paulonis, D. F., 1974, "TLP-Bonding: A New Method for Joining Heat Resisting Alloys," Weld. J. (Miami, FL, U.S.), **53**(4), pp. 203–214.

[8] Ellison, K. A., Lowden, P., and Liburdi, J., 1994, "Powder Metallurgical Repair of Turbine Components," ASME J. Eng. Gas Turbines Power, **116**, pp. 237–242.

[9] Heikinheimo, L. S. K., Laukkanen, A., and Veivo, J., 2005, "Joint Characterization for Repair Brazing of Superalloys," Weld. World, **49**(5/6), pp. 5–12.

[10] Heine, B., 1995, "Hochwarmfestigkeit von Nickelbasis-Superlegierungen für den Gasturbinenbau aus metallkundlicher Sicht," Z. Metallkd., **49**(6), pp. 393–400.

[11] Jung, J.-P., Lee, B.-Y., and Kang, C.-S., 1993, *International Trends in Welding Science and Technology: Proceedings of an International Conference*, pp. 1101–1105.

[12] Kim, D. U., 2001, "Isothermal Solidification and Single Crystallization Behaviors During TLP Bonding of a Ni-Base Single Crystal Superalloy," Journal of the Korean Institute of Metals and Materials, **39**(5), pp. 589–594.

[13] Nishimoto, K., Saida, K., Kim, D., and Nakao, Y., 1998, "Bonding Mechanisms of Ni-Base Single Crystal Superalloy During Transient Liquid Phase Bonding," Weld. World, **41**(2), pp. 121–131.

[14] Ramirez, J. E., and Liu, S., 1992, "Diffusion Brazing in the Nickel-Boron System," Weld. J. (Miami, FL, U.S.), **71**(10), pp. 365–375.

[15] Schnell, A., 2004, "A Study of the Diffusion Brazing Process Applied to the Single Crystal Superalloy CMSX-4," EPF de Lausanne.

[16] Massalski, T. B., 1988, *Binary Alloy Phase Diagrams*, American Society for Metals, Metals Park, OH, Vol. 1.

[17] Bürgel, R., 2001, *Handbuch Hochtemperatur-Werkstofftechnik*, Vieweg & Sohn Verlagsges mbH, Braunschweig, Wiesbaden.

[18] Villars, P., *Pearson's Handbook*, 1997, ASM International, Materials Park, OH, p. 44073.

[19] Meurer, B., Spencer, P. J., and Neuschütz, D., 2003, "Simulation of Solidification and Heat Treatment of Nickel-Base Superalloy SC-16," Z. Metallkd., **94**(2), pp. 139–143.

[20] Schatt, E., and Worch, H., 1996, *Werkstoffwissenschaft*, Deutscher Verlag für Grundstoffindustrie, Stuttgart.

[21] Kamohara, S., Funamoto, T., Yasuda, K., Yoshinari, A., and Shibayangi, T., 1993, "Liquid-Phase Diffusion-Welding of Single-Crystal Nickel-Base Superalloy," *International Trends in Welding Science and Technology: Proceedings of an International Conference*, pp. 1089–1093.

[22] Sahm, P. R., Egry, I., and Volkmann, T., 1999, *Schmelze, Erstarrung, Grenzflächen*, Vieweg & Sohn Verlagsgesellschaft mbH, Braunschweig, Wiesbaden.

Long-Term Microturbine Exposure of an Advanced Alloy for Microturbine Primary Surface Recuperators

Wendy J. Matthews
Capstone Turbine Corporation,
Chatsworth, CA 91311

Karren L. More

Larry R. Walker

Oak Ridge National Laboratory,
Oak Ridge, TN 37831

Haynes alloy HR-120 (Haynes and HR-120 are trademarks of Haynes International, Inc.) forms a protective oxide scale when exposed to the harsh operating environment of a microturbine primary surface recuperator. Primary surface recuperators manufactured from HR-120 are currently in use on the Capstone C65 MicroTurbine (MicroTurbine is a registered trademark of Capstone Turbine Corporation). Long-term microturbine tests of this alloy are currently being conducted at an elevated turbine exit temperature (~100°F higher than that in a normal operation) at Capstone Turbine Corporation. Alloy samples that have been tested under steady-state microturbine operating conditions are removed after predetermined exposure intervals for characterization by Capstone Turbine Corporation in collaboration with Oak Ridge National Laboratory. Such evaluations include the characterization of surface oxide scales and the associated alloy compositional changes following a steady-state operation ranging from 1800 h to 14,500 h. Results from the microstructural and compositional analyses of these long-term steady-state engine-tested HR-120 samples are used to illustrate the progression of alloy oxidation in the microturbine operating environment. [DOI: 10.1115/1.2966419]

Introduction

Unrecuperated microturbines achieve a thermal efficiency of ~15–20%. The addition of a heat exchanger or a recuperator to recover exhaust gas heat and to preheat combustion air can improve the thermal efficiency of the microturbine to ~30–40% [1]. Several different recuperator designs have been investigated over the years. The annular all-welded primary surface recuperator (PSR) utilized on the Capstone C30 and C65 MicroTurbines has been shown to be a robust design that has a significant impact on increasing the microturbine thermal efficiency [2]. The design is resistant to thermal fatigue and cracking. The original type 347 stainless steel (347SS) PSR core continues to perform exceptionally well on the C30 MicroTurbine, which has a lower recuperator inlet temperature than the C65 MicroTurbine.

Traditionally, 347SS foil was used for the PSR core as it offered a good combination of creep resistance, oxidation/corrosion resistance, and raw material costs. Significant research has shown that the rate of oxidation of chromia-forming austenitic stainless steels, such as 347SS, is accelerated by the presence of water vapor (a product of combustion) at operating temperatures greater than ~600°C (~1110°F) [3–8], which also leads to an increased rate of Cr consumption at the alloy surface and breakaway oxidation [9]. Breakaway oxidation (or chemical failure) is referred to as a mechanically induced chemical failure (MICF) at temperatures >600°C, and it occurs when Cr-depletion across the foil cross-section decreases below the critical concentration necessary for the reformation of a healing chromia scale [10]. Numerous studies have shown that accelerated attack may be prevented, or the rate reduced, by increasing the Cr and/or Ni content of the alloy [6–8,11]. Advanced alloys having higher Cr and Ni contents and alumina-forming austenitic alloys have been studied as possible alternatives for 347SS recuperators [12–19].

If the recuperator inlet temperatures remained relatively low (<600°C), the oxidation/corrosion resistance of 347SS was sufficient to ensure a recuperator life of >40,000 h of operation. This operating temperature is maintained in the Capstone C30 MicroTurbine. The Capstone C65 MicroTurbine exhaust has a standard water vapor content of ~3–4 vol % (similar to that of C30). However, the recuperator operates at an average inlet temperature of ~666°C (~1230°F) under normal operating conditions [9]. Based on observations of accelerated attack of 347SS following laboratory exposures at temperatures >600°C in water vapor [3–8] and the complementary analysis of field-operated recuperators at Capstone [9], alloy HR-120 has replaced 347SS in the C65 PSR core [16]. Steady-state elevated temperature microturbine testing of alloy HR-120 has been ongoing at Capstone for the past three years.

This paper will summarize the post-engine-exposure characterization results for HR-120 samples engine-exposed at an elevated turbine exit temperature (TET) set-point of ~55C° (~100F°) above the normal C65 MicroTurbine operating temperature, resulting in a recuperator average inlet temperature of ~720°C (1330°F). The sample exposure times in the microturbine ranged from 1800 h to 14,500 h. The progression of the surface oxidation and the Cr-depletion of the HR-120 foil will be compared with field-operated 347SS recuperators [9], and the superior oxidation resistance of the HR-120 will be demonstrated.

Experimental Procedure

PSR Core Production. The production of a PSR core is quite complex and involves several manufacturing steps. A commercially produced cold-rolled bright annealed foil, ~80 μm (3.2 mils) thick, is formed into a wavy corrugated pattern, known as the fin-fold [9,16,17]. Subsequent pressing and trimming operations produce individual aircell sheets containing both fin-folded and crushed regions. The sheets are formed with a slight offset in the fin-fold, resulting in an "A" sheet and a "B" sheet. The A and B primary sheets, along with various spacer bars and manifolds, are welded to make an individual aircell, as shown in Fig. 1. The

Contributed by the International Gas Turbine Institute of ASME for publication in the JOURNAL OF ENGINEERING FOR GAS TURBINES AND POWER. Manuscript received March 28, 2008; final manuscript received April 8, 2008; published online February 6, 2009. Review conducted by Dilip R. Ballal. Paper presented at the ASME Turbo Expo 2008: Land, Sea and Air (GT2008), Berlin, Germany, June 9–13, 2008.

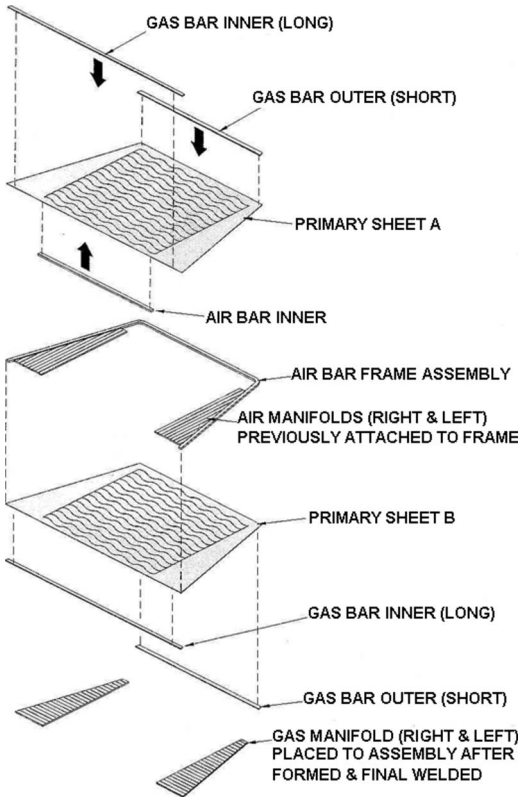

Fig. 1 Aircell assembly

aircells are then formed into a curved shape, and ~165–170 aircells are stacked together and welded into a PSR core, as shown in Fig. 2. After the fin-folding and crushing steps, the foil thickness is often reduced such that the foil thickness within the crushed region is as thin as 70 μm (~2.8 mils).

The PSR is used to preheat the combustor inlet air, resulting in a more complete combustion and improved efficiency [17]. The compressor discharge air flows inside the aircells and is heated prior to exiting to the combustor by the exhaust gas flowing between the aircells.

Both 347SS and HR-120 PSR cores are produced at Capstone, with alloy HR-120 replacing 347SS on the C65 MicroTurbine. The nominal chemical compositions of HR-120 and standard 347SS are given in Table 1.

Steady-State Elevated TET HR-120 Engine Testing. Steady-state elevated TET engine testing of HR-120 samples has been ongoing at Capstone during the past three years [17]. The engine used for testing has been assembled with a recuperator having an HR-120 PSR core and a removable aft dome, as shown in Fig. 3.

Samples were sectioned from the crushed region of actual HR-120 aircells and were subsequently tack welded to the inlet duct of the PSR core. When the aft dome is removed, the tack-welded HR-120 samples are visible around the hot inlet side of the PSR core, as shown in Fig. 4.

Fig. 2 PSR core

Table 1 Chemical compositions of HR-120 and 347SS (wt %)

Element	HR-120 (N08120) [20] Minimum	Maximum	347SS (S34700) [21] Minimum	Maximum
Ni	35.0	39.0	9.00	12.00
Cr	23.0	27.0	17.00	19.00
Mn	–	1.5	–	2.00
C	0.02	0.10	–	0.08
Cu	–	0.50	–	0.75
Si	–	1.00	–	1.00
S	–	0.030	–	0.030
Al	–	0.40	–	–
Ti	–	0.20	–	–
Nb	0.40	0.90	$10\times C$	1.10
Mo	–	2.50	–	0.75
P	–	0.040	–	0.040
W	–	2.50	–	–
Co	–	3.00	–	–
N	0.15	0.30	–	–
B	–	0.010	–	–
	Remainder (~33 wt %)		Remainder (~66 wt %)	

The engine operates at an elevated TET set-point of ~55C° (~100F°) above the normal operating temperature with minimal shutdowns to avoid cyclic effects on the oxidation behavior of the HR-120 samples. After approximately every 1500 h, the engine is shut down and allowed to cool to ambient temperature. The recuperator aft dome is removed, and the oxidized tack-welded HR-120 samples are removed for characterization. It should be noted that these samples are exposed to the hot exhaust gas of ~720°C (1330°F) on both the inside and the outside of the samples and do not experience the pressure differential of an actual PSR aircell.

For this study, samples were removed and characterized after 1800 h and 2500 h for comparison with results from cyclic-tested HR-120 for 1800 h and 2500 h, the results of which have been reported previously [17]. An additional eight samples were removed every ~1500 h, with the highest exposure time being ~14,500 h.

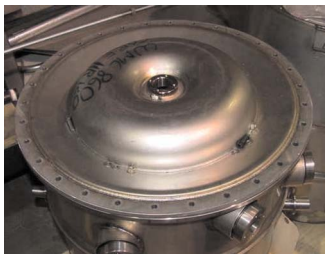

Fig. 3 Recuperator with a removable aft dome

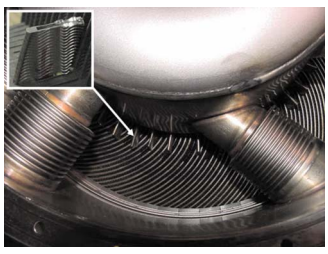

Fig. 4 Steady-state elevated TET engine testing of Haynes HR-120 alloy; tack-welded sample shown in the inset

Results

HR-120 samples taken from the removable-dome, elevated TET, steady-state engine test were examined using electron probe microanalysis (EPMA). Microstructural and compositional characterizations were conducted at ORNL using a JEOL JXA-8200 equipped with both wavelength and energy dispersive spectrometers (W/EDSs).

When referring to the samples removed (cut) from actual PSR aircells, the air-side refers to the inside of the aircell (exposed to compressor air) and the gas-side refers to the outside of the aircell (exposed to exhaust gas). The steady-state tack-welded HR-120 samples are exposed to exhaust gas on both the inside and the outside of the sample, although the gas flow rate on the inside of the sample is much lower than that on the outside. All figures shown herein will be labeled with the inside of the sample as the "air-side" and the outside of the sample as the "gas–side."

Qualitative Analysis. Elemental maps for each steady-state elevated TET HR-120 sample were acquired using W/EDS. These maps show the progression of the surface oxidation of the elevated TET HR-120 samples as a function of engine-exposure time in the microturbine recuperator.

Typically, the greatest amount of oxidation damage on the engine-exposed PSR foil samples accumulates on the gas-side of the foil, and a thin Cr-rich oxide layer is generally present on the air-side of the foil. Because the steady-state tack-welded HR-120 samples are exposed to exhaust gas on both the inside and the outside of the samples, the oxidation damage on the inside of the samples is expected to be greater than would be seen in normal PSR core operation due to the lack of internal "cooling" compressed air.

347SS samples removed after only ~1800 h field operation at ~666°C (~1230°F) exhibited an inward growing Cr-rich oxide layer and outward growing Fe-oxide nodules on the gas-side of the foil [9]. With increasing exposure time, the Fe-oxide nodules eventually link together to form a continuous Fe-oxide outer layer [9]. Elemental maps of the elevated temperature HR-120 samples exposed for similar times show that while these samples also exhibit the inward growing Cr-rich oxide layer, the outward growing oxide layer is quite different from that observed on 347SS specimens. The outward growing scale is an Fe–(Ni, Mn) oxide. Elemental maps of two steady-state elevated TET HR-120 samples after exposure for 5548 h and 14,501 h are presented in Figs. 5 and 6, respectively.

Both HR-120 samples shown in Figs. 5 and 6 exhibit similar scale thicknesses and Cr-depletion depths, even though the second sample (Fig. 6) accumulated almost three times the exposure time of the first sample. Cr-enrichment also occurs along grain boundaries within the center of the foil after ~14,500 h of exposure, as opposed to the Cr-depletion that has been observed in the 347SS PSR foil after a similar exposure time at lower TET [9]. Elemental analyses have shown that the Cr-enriched phase at the grain boundaries also contains Mo and Si, as observed previously in laboratory-tested foils [22].

The engine-exposed HR-120 samples exhibit a continuous Cr-depletion layer (see the gas-side surfaces in Figs. 5 and 6), with depletion occurring across the grains near the surface, while laboratory exposed samples exhibit Cr-depletion preferentially along the grain boundaries just below the oxidized surface [22]. There is a zone of Ni-enrichment and Mn-depletion that coincides with the Cr-depleted zone.

Quantitative Analysis. Elemental line profiles were acquired across the thickness of each steady-state elevated TET HR-120 sample and show the progression of the oxidation process for the HR-120. The compositional analyses include estimates of Cr-loss from the bulk (starting) Cr-reservoir and are based on a starting HR-120 composition of 25 wt % Cr (the nominal composition given in Table 1). A previous analysis of unexposed foil has confirmed that the Cr content of the HR-120 foil used in the PSR is typically 25 wt % [16]. The amount of Cr-depletion determined for the different regions of the steady-state elevated TET HR-120 samples is given in terms of %-depletion from a starting Cr content of 25 wt %. For the purposes of this analysis, an unaffected material is defined as material that retains a chemical composition that is within the compositional range defined for HR-120, as per Table 1. The unaffected material in these samples is not truly

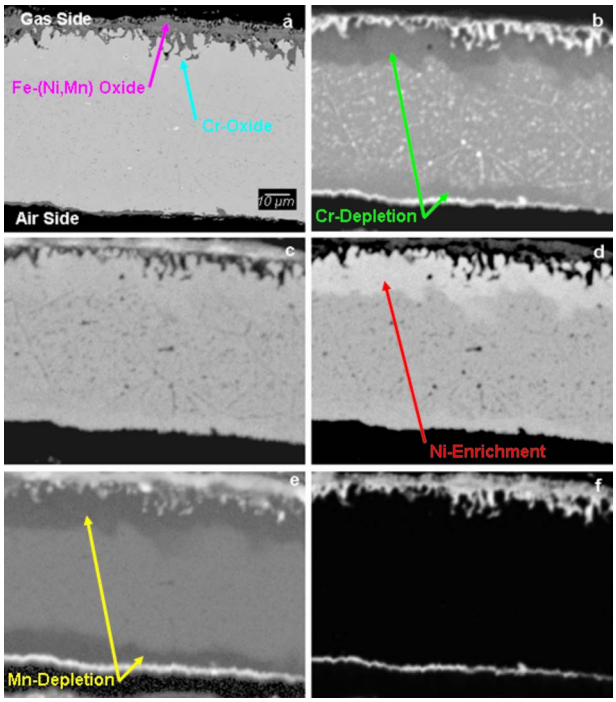

Fig. 5 HR-120 alloy exposed for 5548 h: (*a*) BSE image, (*b*) Cr map, (*c*) Fe map, (*d*) Ni map, (*e*) Mn map, and (*f*) O map

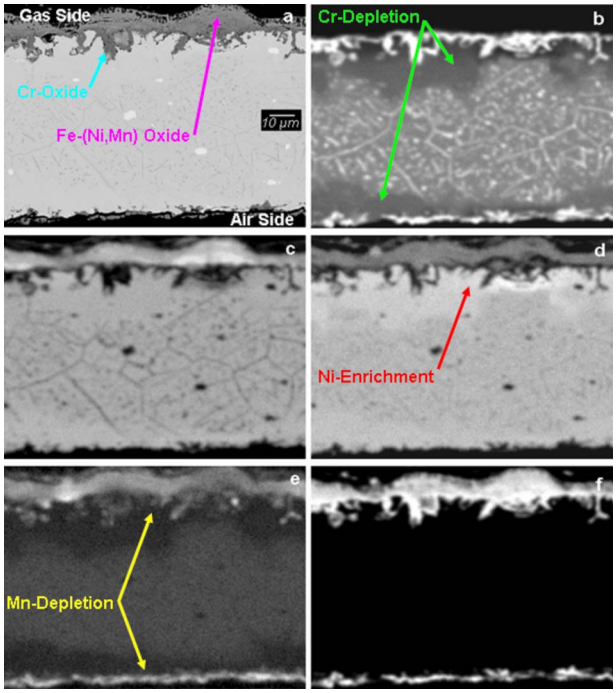

Fig. 6 HR-120 alloy exposed for 14,501 h: (*a*) BSE image, (*b*) Cr map, (*c*) Fe map, (*d*) Ni map, (*e*) Mn map, and (*f*) O map

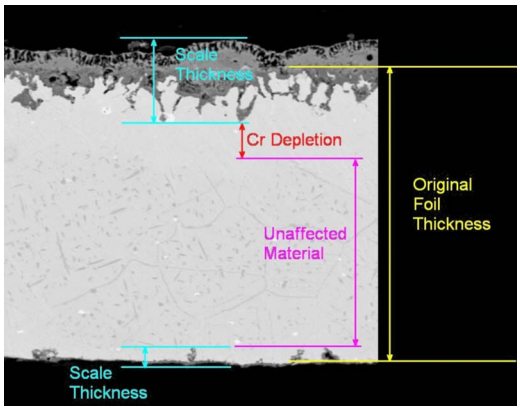

Fig. 7 Typical locations used for the measurement of the oxide scale, Cr-depleted zone, and unaffected alloy

unaffected because of the Cr-enrichment occurring at the grain boundaries. Figure 7 illustrates the locations for the measurement of the Cr-depletion zone and the unaffected material across the foil cross-section.

The total Cr-loss from the starting foil Cr-reservoir (25 wt %) was estimated for each of the steady-state elevated TET HR-120 samples. The method used for this analysis is the same as that reported previously for similarly analyzed 347SS samples, where the total Cr-loss is the sum of the Cr-loss due to the inward growing Cr-rich oxide scale (on both gas-side and air-side) and the Cr-loss due to Cr-depletion below the oxidized surface within the alloy (on both gas-side and air-side). The Cr-loss due to the inward growing Cr-rich oxide layer (Cr-loss due to surface oxidation and formation of a new phase, Cr_2O_3) is considered to be 100% Cr-depletion from the starting Cr content of 25 wt %. Thus, this Cr-loss is equivalent to the percentage of the original starting thickness of the foil that has been lost due to surface oxidation. The Cr-loss due to Cr-depletion within the bulk of the foil is the product of the percentage of the foil thickness subjected to Cr-depletion and the average wt % by which the Cr has been depleted in this region from the starting nominal content of 25 wt %. Thus, the total percentage of Cr-loss from the original starting reservoir of Cr is the sum of the Cr-loss from surface oxidation and the Cr-loss from Cr-depletion. In this way, an estimate of the percentage of Cr-loss from the bulk starting reservoir may be made for each steady-state elevated TET HR-120 sample, and these data are summarized in Table 2. Previously reported data for 347SS field-operated samples, exposed at ~666°C (~1230°F), is presented in Table 3 for reference.

Field operating conditions for the 347SS PSR core samples are given in terms of equivalent operating hours (EOHs). Capstone's extensive analysis of 347SS PSR core foil samples has shown that every stop/start cycle of the MicroTurbine is equivalent to 1.5 h of steady-state operation [9,23]. EOH is determined by taking the sum of the total number of cycles multiplied by a factor of 1.5 and the total steady-state hours of operation.

Table 2 HR-120 total Cr-loss from bulk starting reservoir (~720°C recuperator inlet)

Elevated TET operating hours	Total Cr-loss from starting reservoir (%)
1800	5.1
2500	10.6
4015	9.8
5548	15.9
7536	16.8
8497	17.6
10,157	22.7
11,500	24.1
13,025	25.1
14,501	26.2

Table 3 347SS total Cr-loss from bulk starting reservoir (~666°C recuperator inlet) [9]

Equivalent operating hours	Total Cr-loss from starting reservoir (%)
1800	2.2
5059	27.6
10,900	35.9
12,400	54.6
15,415	78.6

One field-operated HR-120 sample has been analyzed after ~7800 h of operation at ~666°C (~1230°F), and the Cr-loss for that sample (~1.5% from the bulk starting reservoir) is reported graphically, along with the data from Tables 2 and 3, in Fig. 8.

The 347SS Cr-loss data in Fig. 8 shows an accelerated rate of Cr-loss occurring near ~11,000 EOHs, corresponding to a Cr-loss from the bulk starting reservoir of ~35% at an exposure temperature of ~666°C (~1230°F). After an exposure of 347SS in the engine for this length of time, the amount of Cr remaining in the 347SS foil reservoir (in the unaffected material) has decreased to a level where breakaway oxidation occurs; i.e., when the Cr level in the 347SS has decreased to ~11–13 wt % (corresponding to a 30–40% Cr-loss), extremely rapid (breakaway) oxidation by MICF consumes the foil thickness [9].

The HR-120 samples exposed at ~720°C do not exhibit signs of breakaway oxidation, and the rate of oxidation appears to have taken on the characteristic parabolic oxidation of a protective oxide scale without any indication of accelerated attack, i.e., breakaway oxidation, even after ~14,500 h. The one data point for a field-operated HR-120 PSR core exposed at ~666°C (~1230°F) exhibits Cr-loss of only ~1.5 wt % after exposure for ~7800 h as compared with 2.2 wt % Cr-loss in the 347SS PSR core after only 1800 h of exposure.

Figures 9 and 10 are elemental line profiles across the entire foil thickness of the two HR-120 steady-state elevated TET samples that are shown in Figs. 5 and 6, respectively. The profiles show the O, Cr, Ni, and Fe contents for the engine-exposed PSR foils after 5548 h and 14,501 h, respectively. For each case, the elemental line profiles traverse from the gas-side to the air-side of the foil samples. These data were used to calculate the percentage of Cr-loss from the starting reservoir summarized in Table 2. The presence of Ni in the gas-side Fe-rich outer oxide layer can clearly

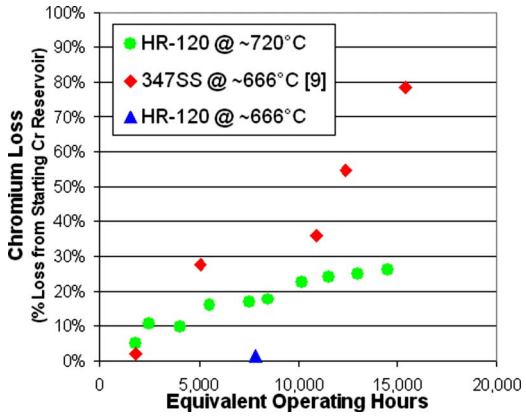

Fig. 8 Cr-loss from starting reservoir as a function of EOH: HR-120 at ~720°C and ~666°C, and 347SS at ~666°C

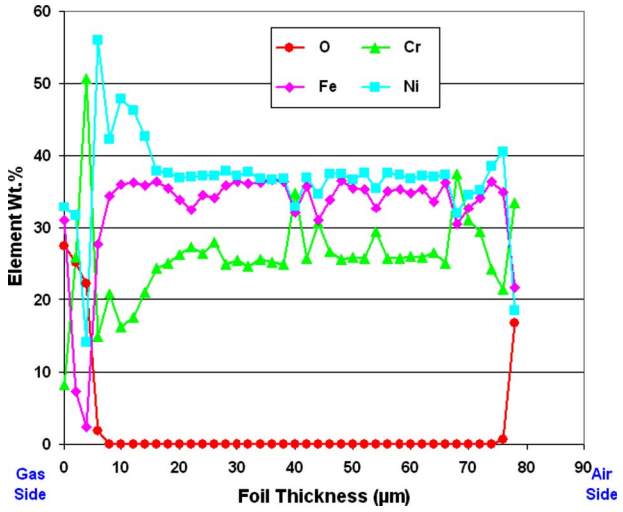

Fig. 9 5548 h: EPMA O, Cr, Fe, and Ni profiles

be seen in both of the elemental line profiles.

The depth of Cr-depletion below the gas-side surface oxide is consistently ~8–10 μm for both the 5548 h and 14,501 h samples. There is also some measurable Cr-depletion on the air-side to a depth of ~2–4 μm (evident in Cr maps in Figs. 5 and 6).

4 Summary

Engine-exposed 347SS foil has exhibited Cr-depletion along grain boundaries after only 1800 h at normal exposure temperatures of ~666°C (~1230°F) [9] and significant alloy oxidation after 1800 h of cyclic exposure at ~720°C (~1330°F) [17].

The formation of Fe-oxide nodules on 347SS is generally believed to signal the onset of accelerated attack, ultimately leading to breakaway oxidation [3,5,6,11]. The formation of Fe-oxide nodules appears to be associated with Cr-depleted grain boundaries exposed to the surface of the foil or to localized evaporation of Cr_2O_3 and/or rapid diffusion of Fe through the Cr-rich oxide [9,22]. Fe-oxide nodules have been observed on the gas-side surface of engine-exposed 3477SS foil after a relatively short exposure time of 1800 h [9].

Fe-oxide nodule formation has not been observed in the steady-state elevated TET HR-120 samples analyzed to date. The lack of nodule formation may be due to the higher Ni content of HR-120 compared with 347SS and the presence of both Ni and Mn in the Fe-rich outward growing oxide. The outward growing Fe-oxide observed on 347SS samples did not contain Ni or Mn. Since nodule formation on laboratory exposed HR-120 samples occurred at locations of grain boundary Cr-depletion [22], the nonselective Cr-depletion observed in the steady-state elevated TET HR-120 samples may also contribute to the lack of nodule formation.

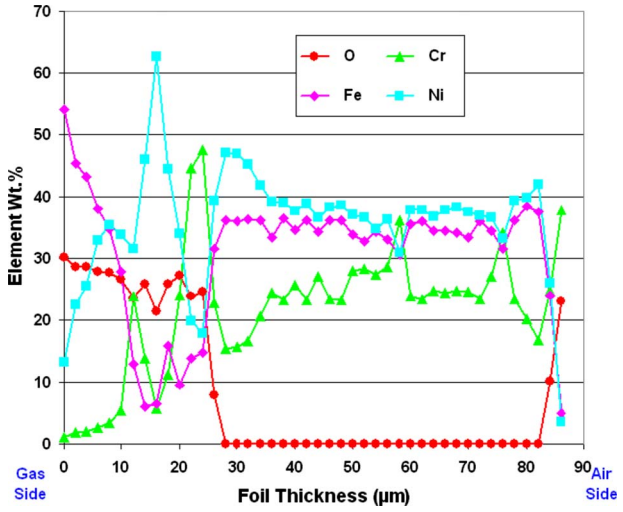

Fig. 10 14,501 h: EPMA O, Cr, Fe, and Ni profiles

The single field-operated data point for HR-120, exposed at ~666°C (~1230°F), illustrates the superior oxidation resistance of HR-120 over 347SS in the MicroTurbine operating environment. Additional field-operated HR-120 PSR cores will be characterized to gain a better understanding of the capabilities of HR-120 as a PSR core alloy.

Acknowledgment

Part of this research was sponsored by the Assistant Secretary for Energy Efficiency and Renewable Energy, Office of FreedomCAR and Vehicle Technologies as part of the High Temperature Materials Laboratory User Program, Oak Ridge National Laboratory, managed by UT-Battelle, LLC for the U.S. Department of Energy under Contract No. DE-AC05-00OR22725.

Nomenclature

BSE = backscatter electron
ORNL = Oak Ridge National Laboratory
347SS = type 347 stainless steel

References

[1] Kang, Y., and McKeirnan, R., 2003, "Annular Recuperator Development and Performance Testing for 200kW Microturbine," ASME Paper No. GT2003-38552.
[2] Treece, B., Vessa, P., and McKeirnan, R., 2002, "Microturbine Recuperator Manufacturing and Operating Experience," ASME Paper No. GT-2002-30404.
[3] Pint, B. A., and Peraldi, R., 2003, "Factors Affecting Corrosion Resistance of Recuperator Alloys," ASME Paper No. GT2003-38692.
[4] Rakowski, J. M., 2001, "The Oxidation of Austenitic Stainless Steel Foils in Humidified Air," ASME Paper No. 2001-GT-0360.
[5] Pint, B. A., Swindeman, R. W., More, K. L., and Tortorelli, P. F., 2001, "Materials Selection for High Temperature (750–1000°C) Metallic Recuperators for Improved Efficiency Microturbines," ASME Paper No. 2001-GT-0445.
[6] Pint, B. A., More, K. L., and Tortorelli, P. F., 2002, "The Effect of Water Vapor on Oxidation Performance of Alloys Used in Recuperators," ASME Paper No. GT-2002-30543.
[7] Rakowski, J. M., 2003, "The Oxidation of Metal Alloy Foils in the Presence of Water Vapor," ASME Paper No. GT2003-38059.
[8] Pint, B. A., and More, K. L., 2004, "Stainless Steels With Improved Oxidation Resistance for Recuperators," ASME Paper No. GT2004-53627.
[9] Matthews, W. J., More, K. L., and Walker, L. R., 2007, "Accelerated Oxidation of Type 347 Stainless Steel Primary Surface Recuperators Operating Above 600°C," ASME Paper No. GT2007-27190.
[10] Evans, H. E., Donaldson, A. T., and Gilmour, T. C., 1999, "Mechanisms of Breakaway Oxidation and Application to a Chromia-Forming Steel," Oxid. Met., **52**(5/6), pp. 379–401.
[11] Pint, B. A., and Rakowski, J. M., 2000, "Effect of Water Vapor on the Oxidation Resistance of Stainless Steels," presented at NACE Corrosion 2000, NACE Paper No. 00-259.
[12] Rakowski, J. M., Stinner, C. P., Lipschutz, M., and Montague, J. P., 2004, "The Use and Performance of Oxidation and Creep-Resistant Stainless Steels in an Exhaust Gas Primary Surface Recuperator Application," ASME Paper No. GT2004-53917.
[13] Maziasz, P. J., Pint, B. A., and Swindeman, R. W., 2003, "Selection, Development and Testing of Stainless Steels and Alloys for High-Temperature Recuperator Applications," ASME Paper No. GT2003-38762.
[14] Lara-Curzio, E., More, K. L., Maziasz, P. J., and Pint, B. A., 2004, "Screening and Evaluation of Materials for Microturbine Recuperators," ASME Paper No. GT2004-54254.
[15] Maziasz, P. J., Pint, B. A., Shingledecker, J. P., More, K. L., Evans, N. D., and Lara-Curzio, E., 2004, "Austenitic Stainless Steels and Alloys With Improved High-Temperature Performance for Advanced Microturbine Recuperators," ASME Paper No. GT2004-54239.
[16] Matthews, W. J., Bartel, T., Klarstrom, D. L., and Walker, L. R., 2005, "Engine Testing of an Advanced Alloy for Microturbine Primary Surface Recuperators," ASME Paper No. GT2005-68781.
[17] Matthews, W. J., 2006, "Additional Engine Testing of an Advanced Alloy for Microturbine Primary Surface Recuperators," ASME Paper No. GT2006-90068.
[18] Rakowski, J. M., Stinner, C. P., Lipschutz, M., and Montague, J. P., 2007,

"Environmental Degradation of Heat-Resistant Alloys During Exposure to Simulated and Actual Gas Turbine Recuperator Environments," ASME Paper No. GT2007-27949.
[19] Pint, B. A., Shingledecker, J. P., Brady, M. P., and Maziasz, P. J., 2007, "Alumina-Forming Austenitic Alloys for Advanced Recuperators," ASME Paper No. GT2007-27916.
[20] ASTM B 409, "Standard Specification for Nickel-Iron-Chromium Alloy Plate, Sheet, and Strip," ASTM International, West Conshohocken, PA, Paper No. UNS N08120.
[21] AMS 5512, "Steel, Corrosion and Heat Resistant, Sheet, Strip, and Plate 18Cr–0.5Ni–0.80Cb (SAE 30347) Solution Heat Treated," Aerospace Material Specification, SAE International, Warrendale, PA, Paper No. UNS S34700.
[22] Pint, B. A., 2005, "The Effect of Water Vapor on Cr Depletion in Advanced Recuperator Alloys," ASME Paper No. GT2005-68495.
[23] Confidential and proprietary internal correspondence, Capstone Turbine Corporation.

Robustness Analysis of Mistuned Bladed Disk Using the Upper Bound of Structured Singular Value

Jianyao Yao
e-mail: yaojianyao@sjp.buaa.edu.cn

Jianjun Wang
e-mail: wangjjb@263.net

Qihan Li

School of Jet Propulsion,
Beijing University of Aeronautics and Astronautics,
Beijing 100191, China

This paper presents a method for the robustness analysis of the bladed disk with bounded random mistuning. The robust stability and performance are evaluated by the upper bound of the structured singular value. The robust control model of the bladed disk is established in virtue of linear fractional transformation. The influences of intentional stiffness mistuning in harmonic patterns on the robustness of the mistuned bladed disk are investigated. The numerical results indicate that the robust performance of the mistuned bladed disk could be effectively enhanced by appropriate harmonic intentional mistuning. The proposed method can help us design a bladed disk, which is insensitive to dangerous random mistuning. [DOI: 10.1115/1.3018942]

1 Introduction

The bladed disk is a kind of cyclic symmetry structure whose dynamic characteristics have been deeply investigated. The research works are important to the vibration design, high cycle fatigue (HCF) analysis, and fault diagnosis of the aeroengine [1].

Theoretically the sectors of the bladed disk are identical, and there are many repeated values of natural frequencies due to the inherent symmetry in the structure. The mode shapes corresponding to these frequencies are periodic around the disk. However, blade mistuning is inevitable in practical bladed disks due to the small imperfections in manufacture, assembly process, and uneven wear. Stress levels and vibration amplitude distributions are highly sensitive to mistuning variations even in the small ranges restricted by manufacture tolerance [2]. These magnitudes could be anywhere from 10% to 50% or much greater than the tuned response. It is therefore of great interest to study the dynamic characteristics of mistuned bladed disks to predict the effects and to control the adverse influence of mistuning.

Generally, there are two kinds of methods for assessing the effects of mistuning—the statistical and deterministic approaches. The references lists on the dynamics of mistuned bladed disks before 2000 can be found in Refs. [1,3] Statistical methods are often used to model mistuning effects because of the stochastic nature of mistuning. They provide important information such as sensitivity and variability in forced response amplitude due to mistuning as well as approximations of the maximum or worst-case mistuning by sampling the random mistuning. The lumped-mass models [4,5] are used to capture the basic dynamics of the bladed disks in the early studies limited by the temporal level of computational hardware and software. Due to the inability to apply the symmetry relations, the detailed finite element analysis of mistuned bladed disks is extremely costly. Therefore, recently more efforts have been devoted to model realistic bladed disks using reduced-order methods (ROMs) based on the finite element models [6–11].

Although the statistical methods are the most direct and convenient in predicting the effects of mistuning, the stochastic nature of the sampling process could not guarantee to obtain the extreme situations, such as the worst-case mistuning patterns and the optimum arrangement of blades. The deterministic approaches are aimed to efficiently and precisely predict the worst mistuning pattern, which is most dangerous to the bladed disk, and to obtain the optimum arrangement of blades to increase the flutter margin and to decrease the maximal response amplitudes simultaneously. These kinds of problems are always solved as optimal design problems. The references introduced here mainly focus on the maximum response amplitudes and the worst-case mistuning. The optimization algorithms used for the mistuned bladed disks are gradient-based algorithm [12,13], genetic algorithm [14,15], simulated annealing algorithm [16], and other algorithms [17–19].

Nevertheless, the nature of the mistuning, could be considered as the structured uncertainties of the model in robust theory. Rotea and D'Amato [20] presented new tools for the calculation of the maximal response amplitude and the worst-case mistuning based on rigorous results from the robustness analysis of a dynamical system with uncertainty. The maximal response amplitude was obtained through the calculation of the upper bound for the maximal frequency response function (FRF) magnitude, and the worst-case mistuning was obtained by the lower bound of FRF magnitude. The effects of intentional mistuning were also considered, and the results indicated that the increased robustness was achieved at the expense of an increment in nominal response by mistuning.

Different from Rotea and D'Amato's work, in this paper, the upper bound of a more direct parameter—structured singular value (SSV)—is used to assess the robust stability and performance of the mistuned bladed disk. Early research [21,22] has indicated that the intentional mistuning could increase the robustness of the mistuned bladed disks, i.e., the structure becomes insensitive to unintentional or random mistuning. Here, intentional mistuning in harmonic patterns with different harmonic integers and amplitudes are introduced into the randomly mistuned bladed disk. The effects of the intentional mistuning on the robustness characteristics of the mistuned system are obtained by calculated the upper bounds of the SSVs at each point of a frequency gridding. The results could be reliable when the frequency step is small enough.

This paper has four more sections. The models of the bladed disk used for robustness analysis are established in Sec. 2. Section 3 describes the robust stability and performance using the upper bound of SSV. A robustness analysis example is presented in the Sec. 4, in which the effects of the intentional mistuning are demonstrated numerically. Conclusions and discussions are given in Sec. 5 of this paper.

Manuscript received June 18, 2007; final manuscript received September 16, 2008; published online January 29, 2009. Review conducted by David Walls.

2 Models of the Mistuned Bladed Disk

The descriptions of mistuning of the bladed disk are introduced in Sec. 2.1. The models and transfer functions for the mistuned system are presented in Sec. 2.2.

2.1 Mistuning Descriptions. The mistuning of the mistuned bladed disk is considered as the structured uncertainty of model. The mass, stiffness, and damping of the structure can be written as the sum of the nominal values and the perturbations and have the following forms:

$$M(\delta) = M_0 + \sum_{i=1}^{k} M_i \delta_i \tag{1a}$$

$$K(\delta) = K_0 + \sum_{i=1}^{k} K_i \delta_i \tag{1b}$$

$$C(\delta) = C_0 + \sum_{i=1}^{k} C_i \delta_i \tag{1c}$$

where δ is a vector of real parameters representing the perturbations or mistuning parameters. The entries of the vector δ are unknown but bounded. These uncertainties can be introduced into the system as feedback by using linear fractional transformation (LFT) [23]. The block structure of the uncertainties can be written as

$$\Delta(\delta) = \mathrm{diag}(\delta_1 I_{r_1}, \ldots, \delta_k I_{r_k}) \tag{2}$$

and

$$r_1 + \cdots + r_k = n \tag{3}$$

2.2 Transfer Functions of the Mistuned Bladed Disk. The models considered are of the form

$$M(\delta)\ddot{x} + C(\delta)\dot{x} + K(\delta)x = Gu \tag{4a}$$

$$y = Hx \tag{4b}$$

where x is the displacement vector, u is the excitation vector, y is the measured response, and G and H are the input and output matrices.

In the state space, the equations of motion can be written as

$$\begin{bmatrix} C & M \\ M & 0 \end{bmatrix} \begin{Bmatrix} \dot{x} \\ \ddot{x} \end{Bmatrix} + \begin{bmatrix} K & 0 \\ 0 & -M \end{bmatrix} \begin{Bmatrix} \dot{x} \\ \ddot{x} \end{Bmatrix} = \begin{bmatrix} G \\ 0 \end{bmatrix} \begin{Bmatrix} u \\ 0 \end{Bmatrix} \tag{5a}$$

$$y = \begin{bmatrix} H & 0 \end{bmatrix} \begin{Bmatrix} x \\ \dot{x} \end{Bmatrix} \tag{5b}$$

Let the state variable $z = \{x^T \ \dot{x}^T\}^T$ and the equations above be rewritten as

$$\dot{z} = Az + Gu \tag{6a}$$

$$y = Hz + Du \tag{6b}$$

where

$$A = \begin{bmatrix} 0 & I \\ -M^{-1}K & -M^{-1}C \end{bmatrix}, \quad D = 0, \quad G = \begin{bmatrix} 0 \\ M^{-1}G \end{bmatrix}, \text{ and } H = [H0]$$

Note that the matrices G and H are properly augmented.

If the structural parameters of the bladed disk, for example, the stiffness of the sectors are mistuned in the form of Eq. (2), the uncertainties of matrix A can be written as

$$A(\delta) = A_0 + \sum_{i=1}^{k} \delta_i A_i \tag{7}$$

where

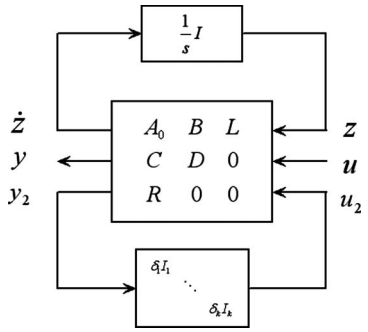

Fig. 1 LFT in state space

$$A_i = \begin{bmatrix} 0 & 0 \\ -M^{-1}K_i & 0 \end{bmatrix}$$

and A_0 is the nominal plant matrix. The singular value decomposition of $\delta_i A_i$ is

$$\delta_i A_i = L_i \delta_i I R_i \tag{8}$$

The transfer function of the mistuned bladed disk expressed using LFT is

$$G_\delta(\Delta) = F_u\left(F_l\left(\begin{bmatrix} A_0 & B & L \\ C & D & 0 \\ R & 0 & 0 \end{bmatrix}, \Delta(\delta)\right), \frac{1}{s}I\right) \tag{9}$$

where $s = j\omega$ is the Laplace variable, and

$$L = \begin{bmatrix} L_1 & \cdots & L_k \end{bmatrix} \tag{10a}$$

$$R = \begin{bmatrix} R_1^T & \cdots & R_k^T \end{bmatrix}^T \tag{10b}$$

F_u and F_l denote the upper and lower LFTs. It is noted that, when there is no mistuning in the system, that is, when $\Delta(\delta) = 0$, the transfer function becomes the nominal one.

$$G_\delta(\Delta) = F_u\left(\begin{bmatrix} A & B \\ C & D \end{bmatrix}, \frac{1}{s}I\right) \tag{11}$$

For the situation of damping mistuning, the equations of the same form can be obtained in the same way. The block diagram of the system is shown in Fig. 1.

For the model described in Eq. (4) and the mistuning in the form of Eq. (1), Eq. (4) can also be written as

$$(Z_0 + \Delta Z)x = Gu \tag{12a}$$

$$y = Hx \tag{12b}$$

in frequency domain, where Z_0 is the nominal impedance, and defined as

$$Z_0 = -\omega^2 M_0 + j\omega C_0 + K_0 \tag{13}$$

The uncertainty matrix ΔZ is defined by

$$\Delta Z = \sum_{i=1}^{k} \delta_i Z_i \tag{14a}$$

$$Z_i = -\omega^2 M_i + j\omega C_i + K_i \tag{14b}$$

The singular value decomposition of $\delta_i Z_i$ is

$$\delta_i Z_i = L_i \delta_i I R_i \tag{15}$$

Then the uncertainty matrix ΔZ can be written as

$$\Delta Z = \sum_{i=1}^{k} L_i \delta_i I R_i = L\Delta(\delta)R \tag{16}$$

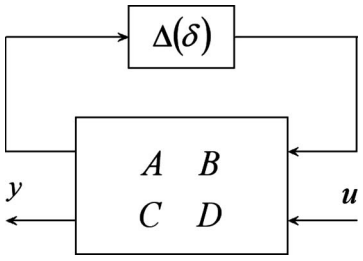

Fig. 2 LFT in frequency domain

where L and R have the same form in Eq. (10).

The transfer function of the mistuned bladed disk can also be obtained by LFT.

$$G_\delta(\Delta) = F_u\left(\begin{bmatrix} A & B \\ C & D \end{bmatrix}, \quad \Delta(\delta)\right) \tag{17}$$

where the matrices are defined by the following equation:

$$\begin{bmatrix} A & B \\ C & D \end{bmatrix} = \begin{bmatrix} R \\ H \end{bmatrix} Z_0^{-1} \begin{bmatrix} -L & G \end{bmatrix} \tag{18}$$

Equation (17) can be expanded as

$$G_\delta(\Delta) = H(K(\delta) + j\omega C(\delta) - \omega^2 M(\delta))^{-1} G = H(Z_0 + L\Delta(\delta)R)^{-1} G$$
$$= D + C\Delta(\delta)(I - A\Delta(\delta))^{-1} B \tag{19}$$

Also, for the nonmistuning situation, the transfer function becomes the nominal one.

$$G_\delta(\Delta) = D \tag{20}$$

The block diagram of the system in frequency domain is shown in Fig. 2.

Essentially, the two kinds of transfer functions expressions are the same for both the tuned and mistuned situations. When there is no mistuning in the models, that is when $\Delta(\delta)=0$, both the transfer functions in state space and frequency domain become the nominal one. The differences are that the plant matrices expressed in state space are frequency independent, and many algorithms for computing the bounds of the SSVs are designed for this kind of model [24,25], but there is the inverse of mass matrix M, which is inconvenient to consider the mass mistuning. By contraries, the plant matrices in the frequency domain are frequency dependent and no longer the constant matrices, but it is convenient to model all kinds of mistuning.

3 Robustness of Mistuned Bladed Disk

3.1 Structured Singular Value and Its Bounds. Let M now denote the value $M(j\omega)$ of the transfer matrix $M(s)$ at $s=j\omega$, while Δ is most generally a mixed perturbation containing real scalars (corresponding to parametric uncertainties in the physical coefficient of the model) as well as complex scalars and full complex blocks (which represent the neglected dynamics), i.e., Δ is a free complex matrix with an a priori fixed block diagonal structures. The structured singular value is defined as follows [23,24]:

$$\mu_\Delta(M) = \frac{1}{\min\{\bar{\sigma}(\Delta): \det(I - M(s)\Delta) = 0\}} \tag{21}$$

unless $\det(I-M(s)\Delta) \neq 0$ for all Δ, in which case $\mu_\Delta=0$.

It is known the general mixed (or real) μ problem is NP hard, which means it cannot be computed in polynomial time in the worst case. It is important to note that being NP hard is a property of the problem itself, not any particular algorithm. The computation of exact μ is prohibitively expensive for even moderately large examples. Therefore, there are many practical algorithms [24,25] for computing the bounds of the SSVs.

An upper bound of μ gives a sufficient condition of nonsingularity of the matrix $I-M\Delta$, which is thus guaranteed to be a nonsingularity for all possible uncertainties. An upper bound of the SSV thus gives a lower bound k_L of the robustness margin.

$$k_L = \min_{\omega \in [0,\infty)} \frac{1}{\mu(M(j\omega))} \tag{22}$$

Conversely, a lower bound of μ gives a sufficient condition of singularity of the matrix $I-M\Delta$. First, it gives a measure of the conservatism of the upper bound. Second, an associated worst-case model perturbation is usually provided with the lower bound by the computational algorithm.

3.2 Robust Stability and Robust Performance. The robustness of the mistuned bladed disk includes the robust stability and the robust performance, and reflects the sensitivity of the system dynamic characteristics to parameter mistuning. The robust stability is referred to as the maximum allowable variation in parameters, which keeps the system stable. Likewise, the robust performance is defined as the maximum allowable variation in parameters, which satisfies the performance requirements. For the mistuning problem, the variation in parameters is the bounded random mistuning, and the performance requirement is the forced response amplitude.

It can be known from Eq. (21) that the reciprocal of SSV is a measurement of the uncertain matrix Δ, which makes the closed loop lose stability. Hence, the upper bounds of SSVs are closely connected with the system robustness and a criterion of it.

3.3 $M-\Delta$ Model for Robustness Analysis of Mistuned Bladed Disk. The criteria of the robustness vary with the description of mistuning and the requirement of the system performance. Using LFT and SSV, all these problems can be solved in a uniform framework, shown in Fig. 3 [23]. In addition, the framework can also be helpful to resolve the robustness problem with multiple sources of uncertainties. Any interconnection system with

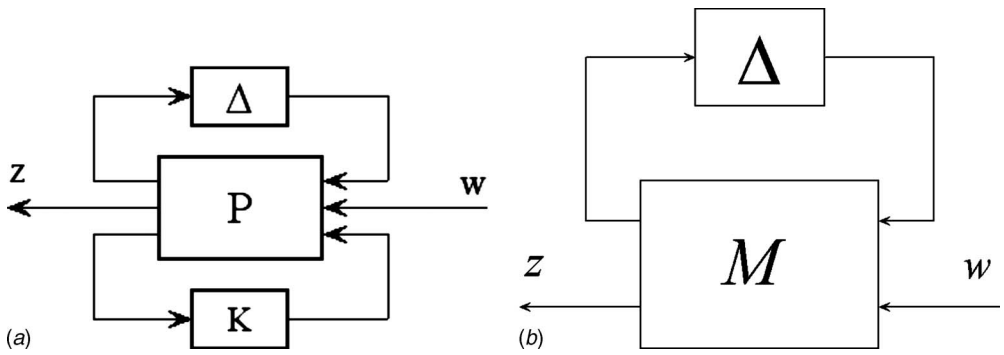

Fig. 3 Uniform framework

multiple uncertainties could be rearranged into the forms shown in Fig. 3. The difference between the two models is that the controller K in $P-K-\Delta$ is absorbed into the matrix M. Many algorithms for the computation of the bounds of SSVs are designed for the $M-\Delta$ model.

The matrices P and M in the uniform framework have the following form:

$$P(s) = \begin{bmatrix} P_{11}(s) & P_{12} & P_{13} \\ P_{21}(s) & P_{22} & P_{23} \\ P_{31}(s) & P_{32} & P_{33} \end{bmatrix} \tag{23}$$

$$M(s) = F_l(P(s), K(s)) = \begin{bmatrix} M_{11}(s) & M_{12}(s) \\ M_{21}(s) & M_{22}(s) \end{bmatrix} \tag{24}$$

The state space representation G of matrix P for mistuned bladed disk can be obtained in Sec. 2.2, and rearranged as

$$G = \begin{bmatrix} 0 & 0 & R \\ 0 & D & C \\ L & B & A \end{bmatrix} \tag{25}$$

The four portions of matrix $M(s)$, of which the SSVs would be calculated, can be written in terms of different blocks of G as

$$M_{11}(s) = 0 + R(sI - A)^{-1}L \tag{26a}$$

$$M_{12}(s) = 0 + R(sI - A)^{-1}B \tag{26b}$$

$$M_{21}(s) = 0 + C(sI - A)^{-1}L \tag{26c}$$

$$M_{22}(s) = D + C(sI - A)^{-1}B \tag{26d}$$

The closed-loop transfer matrix of the system can be written as

$$M_\Delta = M_{22} + M_{21}\Delta(I - M_{11}\Delta)^{-1}M_{12} \tag{27}$$

Robust stability and robust performance problems can be solved using different types of $M-\Delta$ models, $M_{11}-\Delta$ for the former and $M_\Delta-\Delta$ for the latter, and the corresponding blocks of G are $\left[\begin{smallmatrix} 0 & R \\ L & A \end{smallmatrix}\right]$ and

$$\begin{bmatrix} 0 & 0 & R \\ 0 & D & C \\ L & B & A \end{bmatrix}$$

In addition, the nominal performance problem can be analyzed by M_{22}, and the corresponding blocks are $\left[\begin{smallmatrix} D & C \\ B & A \end{smallmatrix}\right]$.

The robustness analysis can be processed in the $M-\Delta$ framework in virtue of the upper bounds of the SSVs of the mistuned structure. As mentioned above in Sec. 3.1, there are great difficulties in computing the bounds of SSVs. Here, the traditional frequency-grid-based algorithm is adopted, since the frequency interval methods [24,25] under high modal density circumstances would be not as effective as the ordinary ones. The results could be reliable when the frequency step is small enough.

4 Application Example

4.1 Model of the Example Bladed Disk. The bladed disk example is a mass-spring model with $N=56$ sectors, the same as in Ref. [20]. There are two degrees of freedom (DOFs) per sector, 1DOF represents the blade motion and the other the disk motion. The nondimensional model parameters are as follows: $k_1=1$, $k_2=1.1$, $k_c=493$, $m_1=1$, and $m_2=426$. The schematics of the example bladed disk is shown in Fig. 4.

The dynamic characteristics of the above model for both tuned and mistuned cases were deeply discussed in Refs. [20,26]. The results show that the modal density is considerably high close to the blade-alone frequency $\sqrt{k_1/m_1}=1$, and there are 56, half of the total number, natural frequencies between 0.98 and 1.01. Notice that the natural frequencies veer at the nodal diameters 8 and 9,

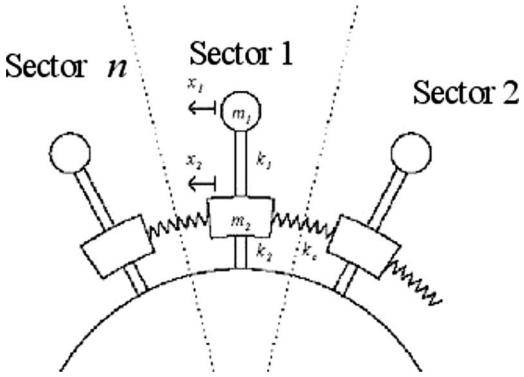

Fig. 4 Bladed disk model

where the vibration localization phenomenon is most prone to appear. Figure 5 shows the natural frequencies of the tuned bladed disk model.

The engine order excitations for the forced response have the following form:

$$f_E = \{1 \quad e^{jE\phi} \quad e^{j2E\phi} \quad \cdots \quad e^{j(N-1)E\phi}\}e^{j\omega t} \tag{28}$$

where E is the engine order, and $\phi=2\pi/N$ is the interblade phase angle. For the tuned cases, there are two distinct modes excited for each diameter E: a blade mode, with frequency close to the blade-alone natural frequency, and a disk mode. The robust performance under the excitation of engine order $E=9$ is to be analyzed for the free and forced vibration results indicate that the localization phenomena is most severe at these orders.

The mistuning of the bladed disk has the following forms: For the unintentional mistuning, bounded random mistuning of the blade stiffness k_1 is considered; for the intentional mistuning, the harmonic intentional mistuning, as shown in Eq. (29), is introduced to the structure.

$$ik_{1i} = a_k \sin\left(\frac{h(i-1)}{N}2\pi\right) \tag{29}$$

where ik_{1i} is the intentional stiffness change of the ith blade, a_k the amplitude and h the harmonic integer of intentional mistuning, respectively. When the harmonic integer is 28, the interblade phase angle is π and the intentional mistuning becomes an AB pattern.

4.2 Robust Stability of the Mistuned Bladed Disk. Based on the models established in Secs. 3.1–3.3, the robust stability of

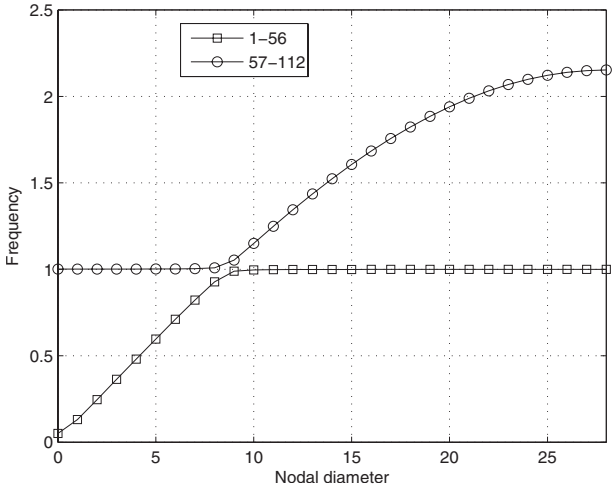

Fig. 5 Nodal diameter map

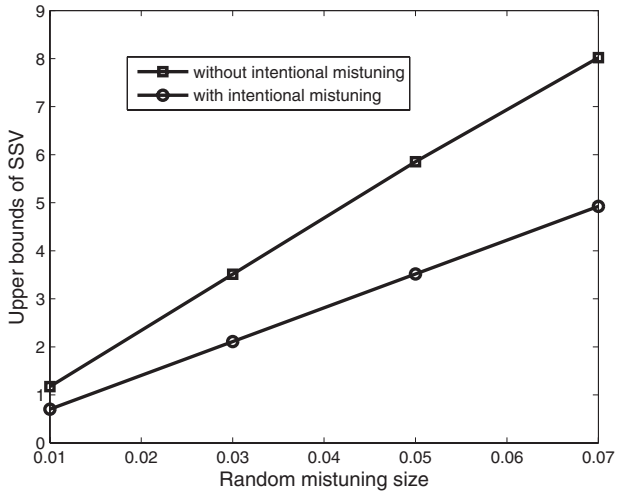

Fig. 6 Robust stability with different random mistuning sizes

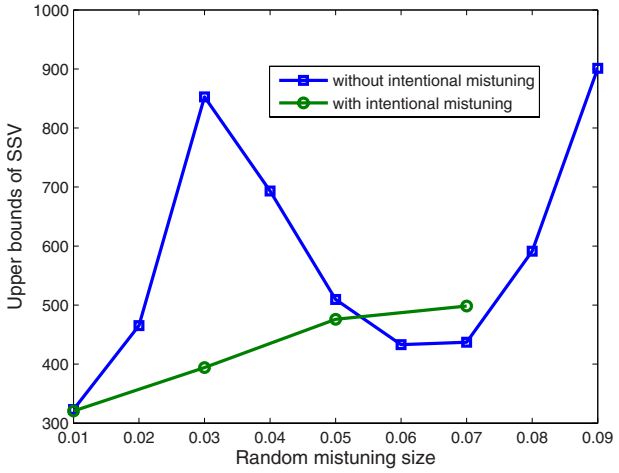

Fig. 8 Robust performance with different sizes of random mistuning, frequency range [0.85, 1.15] and frequency point number 1000

mistuned bladed disk can be estimated using the upper bound of the SSV of $M_{11}(s)$. The matrices A, L, and R in Sec. 2.2 are required to obtain $M_{11}(s)$. The influences of intentional mistuning with different harmonic integers and amplitudes on the robust stability of the bladed disk are discussed in this section.

The upper bounds of the SSVs on the frequency-grid Ω may be done by repeated evaluation at each frequency. Although the traditional grid-based algorithm is not absolutely reliable, the robust stability can still be effectively judged by the upper bounds of the obtained SSVs if the frequency-grid points are dense enough.

Figure 6 shows the upper bounds of SSVs versus different sizes of blade stiffness random mistuning. The intentional mistuning is harmonic 1 and the amplitude is 0.01. Note that the SSVs increase linearly with the random mistuning sizes, the bounds of δ_i. It can be easily derived by the definition of μ (Eq. (21)) and the expression of $M_{11}(s)$ (Eq. (26)). The conclusion is still tenable when intentional mistuning is introduced to the model. The results also indicate that the intentional mistuning makes the SSVs decrease, i.e., the introduced intentional mistuning could enhance the system robust stability.

Figure 7 shows the upper bounds of SSVs versus the intentional mistuning with different amplitudes and harmonic integers. The size of blade stiffness random mistuning is 0.03 in the figure. The results indicate that there are not distinct differences among the effects of these three kinds of introduced intentional mistuning,

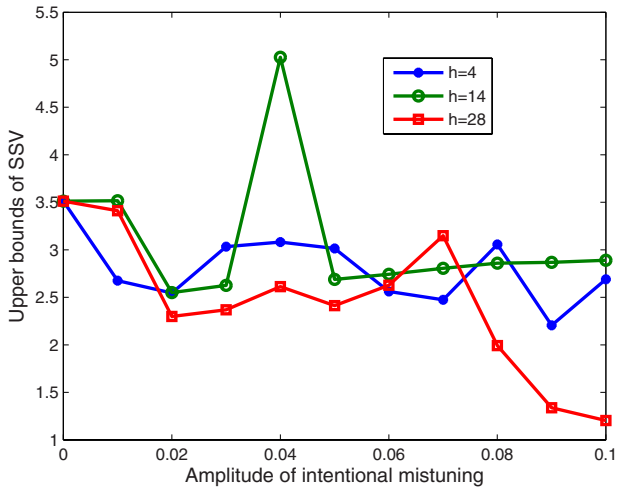

Fig. 7 Robust stability with different intentional mistunings

most of them are effective in reducing the SSVs. However, there is not a simple function of intentional mistuning and SSV to express the relation between them, we can only describe the trend qualitatively.

Generally, the obtained upper bounds of SSVs are small, and the intentional mistuning does not greatly change them. We could even conclude that the random mistuning and intentional mistuning have little effects on the robust stability of the mistuned bladed disk.

4.3 Robust Performance of the Mistuned Bladed Disk. The robust stability of the mistuned bladed disk is analyzed in Sec. 4.2. However, only robust stability analysis is not enough for the mistuned structure, since the performance may deteriorate to an unacceptable degree far before the system loses stability. Thus, it is necessary to carry out the robust performance analysis. In this subsection, we still consider the bounded random mistuning of blade stiffness and analyze the influence of different types of intentional mistuning on the upper bounds of SSVs.

The plant matrix for robust performance is

$$\begin{bmatrix} 0 & 0 & R \\ 0 & D & C \\ L & B & A \end{bmatrix}$$

and all these blocks can be obtained in Sec. 2.2. Thus, the closed-loop transfer matrix M_Δ is obtained with Eq. (27). Figure 8 shows the upper bounds of SSVs with and without intentional mistuning versus random mistuning sizes.

There are two obvious differences between the upper bounds of SSVs for the robust stability and performance analysis. First, compared with the results of robust stability, the upper bounds of SSVs of performance are much greater, that is the acceptable random mistuning ranges to keep the system performance are much smaller. Second, the relation of random mistuning sizes and the upper bounds of the SSVs is not linear anymore. The upper bounds of SSVs show a peak at the random mistuning size 0.03, and then decrease when the random mistuning size continues to increase, and increase again when random mistuning size is greater than 0.06. This trend is the same as the effect of random mistuning size on the amplitude magnification of this mistuned bladed disk, as shown in Fig. 9.

Both results of robust performance and amplitude magnification indicate that the random mistuning size of 0.03 is most dangerous, but its adverse influence could be effectively suppressed by intentional mistuning. The intentional mistuning in Fig. 8 is harmonic 28 with an amplitude of 0.01. It is most effective at the peak of the

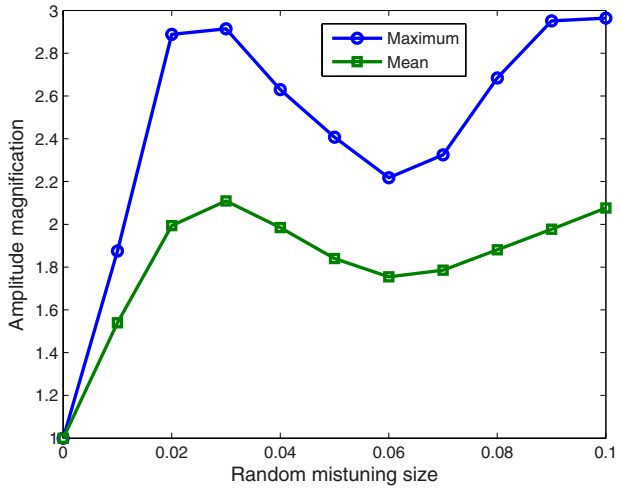

Fig. 9 Amplitude magnification with different sizes of random mistuning, sample number 1500, and frequency point number 112

curve for the upper bounds of SSVs, and is invalid when the random mistuning is comparatively small or large. The peak phenomenon of random mistuning size for both robust performance and amplitude magnification limits the range of adverse random mistuning size, and is helpful for us to find appropriate intentional mistuning patterns only aiming at suppressing the most dangerous random mistuning. Figure 10 shows the upper bounds of SSVs with the intentional mistuning of $h=4$, $h=14$, and $h=28$. According to the results, we can conclude the following.

(1) All three patterns of intentional mistuning with an amplitude of 0.01–0.04 are effective to reduce the SSVs, especially the amplitudes 0.02 and 0.03. As the intentional mistuning amplitudes in the studied range increase, the upper bounds of SSVs decrease rapidly at first, then increase, and decrease again.
(2) The relation between intentional mistuning amplitude and robust performance is generally the same as between it and forced response amplitude magnification, which is shown in Fig. 11. However, the latter varies much more smoothly.
(3) The best effects of all three kinds of intentional mistuning on the robust performance are almost the same. However, $h=28$ is preferred when the amplitude magnification is taken into account, and it only needs two kinds of blades (AB pattern) to realize the mistuning pattern.

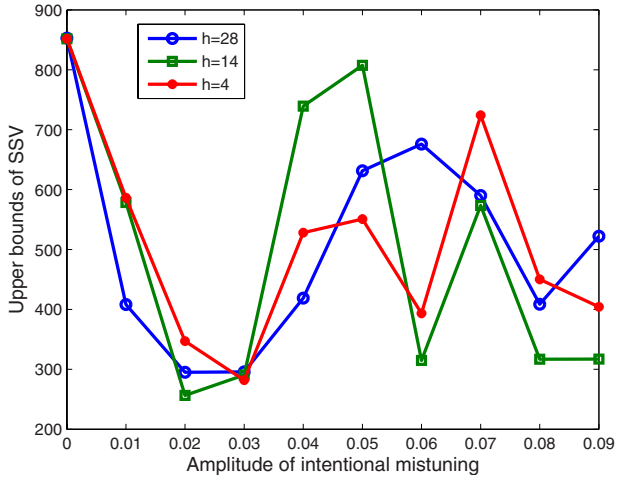

Fig. 10 Robust performance with different intentional mistunings, frequency range [0.85, 1.15], and frequency point number 1000

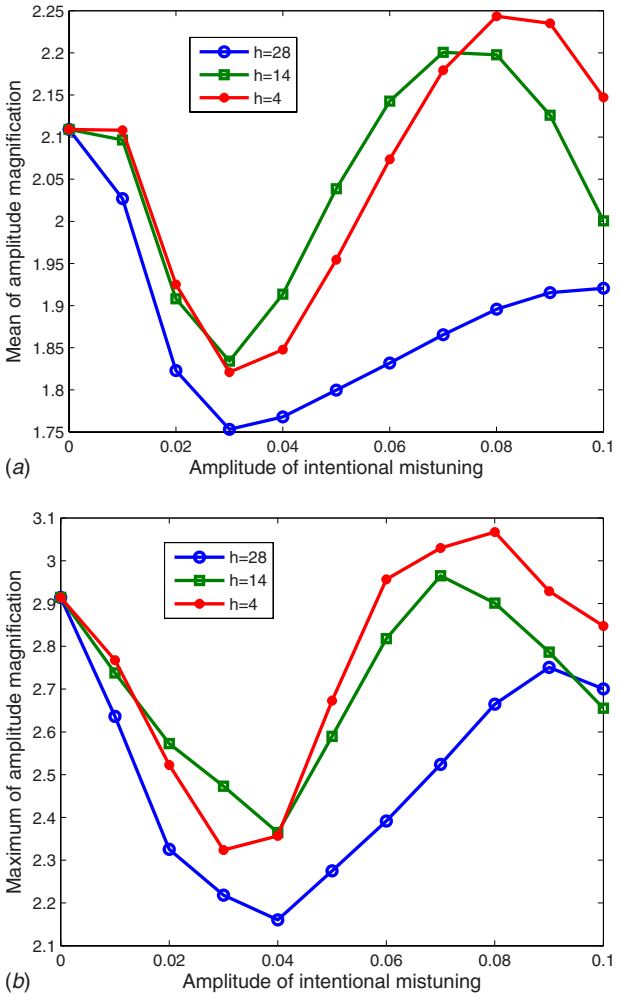

Fig. 11 Amplitude magnification with different intentional mistunings, sample number 1500, and frequency point number 112. (*a*) Mean of amplitude magnification and (*b*) maximum of amplitude magnification.

The computing time of the upper bounds of SSVs depends on the density of frequency grids and the tightness of the bounds and the real values (accuracy), and the time consuming of amplitude magnification depends on the density of frequency grids and the number of the samples. For the parameters selected in this paper, the computing time of the upper bounds of SSVs is about three or four times longer than that of the amplitude magnification. The agreement between the results of robust performance and forced response amplitude magnification for both random mistuning and intentional mistuning demonstrates that the upper bounds of SSVs could estimate the not only the robust performance but also the mistuning effects on the forced response levels.

Using the same model, the optimal size of AB pattern intentional mistuning for the worst-case perturbations of blade stiffness given by Rotea and D'Amato [20] was 0.06. However, it is not the optimal size for the robust performance according to the results in this paper. That is mainly because the optimization objectives are different. The worst-case performance is just one facet of the robust performance problem. The increased robustness is achieved at the expense of an incensement of the nominal response and even the maximum response of the blade at a specific range of

random mistuning.

For the most dangerous random mistuning size, the results of SSVs in this paper vary in the same way as the responses of the blades obtained by Castanier and Pierre [21]. They all exhibit a peak phenomenon versus the sizes of intentional mistuning.

5 Conclusions and Discussions

In this paper, we described the method to evaluate the robustness of the mistuned bladed disk with bounded random stiffness mistuning. From the viewpoint of robust control theory, the proposed method takes the upper bounds of SSVs as the robustness criterion for the structure, and a uniform framework, $M-\Delta$ model, for obtaining the SSVs is established using LFT. The method facilitates the robust stability and robust performance analysis of the mistuned bladed disk and can help us design the robust bladed disks that consistently perform their function despite manufacturing variations, wear, and other real-world imperfections.

The influences of intentional mistuning with harmonic types on the robustness and amplitude magnification of the example bladed disk are analyzed. The numerical results indicate that the AB pattern intentional mistuning can effectively enhance the robust performance of the bladed disk. Moreover, the optimal pattern of intentional mistuning can be obtained by the design of robust controller.

Acknowledgment

The research described in this paper was supported by the National Key Basic Research Program under Grant No. 6133601.

Nomenclature

$(\bullet)_0$ = subscript, denotes the tuned parameter
Δ = block structure of mistuning
δ = mistuned parameter vector
μ_Δ = structured singular value
A = system plant matrix
a_k = amplitude of intentional mistuning
C = damping matrix or system output matrix
E = engine order
f_E = traveling wave excitation
G, H = input and output matrices
G_δ = transfer matrix of the mistuned bladed disk
h = harmonic number of intentional mistuning
L, R = singular value decomposition matrix
M, K = mass and stiffness matrices
u = excitation vector
x = displacement vector
y = measured response vector
Z = impedance matrix

References

[1] Wang, J. J., Li, Q. H., and Zhu, Z. G., 2000, "Vibratory Localization of Mistuned Bladed Disk Assemblies—A Review," Adv. Mech., **30**(4), pp. 517–528.
[2] Petrov, E. P., and Ewins, D. J., 2003, "Analysis of the Worst Mistuning Patterns in Bladed Disk Assemblies," ASME J. Turbomach., **125**(4), pp. 623–631.
[3] Slater, J. C., Minkiewicz, G. R., and Blair, A. J., 1999, "Forced Response of Bladed Disk Assemblies—A Survey," Shock Vib. Dig., **31**(1), pp. 17–24.
[4] Griffen, J. H., and Hoosac, T. M., 1984, "Model Development and Statistical Investigation of Turbine Blade Mistuning," ASME J. Vib., Acoust., Stress, Reliab. Des., **106**(4), pp. 204–210.
[5] Wei, S. T., and Pierre, C., 1988, "Localization Phenomena in Mistuned Assemblies With Cyclic Symmetry, Part I: Free Vibration," ASME J. Vib., Acoust., Stress, Reliab. Des., **110**(4), pp. 429–438.
[6] Kruse M., and Pierre C., 1996, "Forced Response of Mistuned Bladed Disks Using Reduced-Order Modeling," Paper No. AIAA-96-1545-CP.
[7] Bladh, R., Ottarsson, G., and Pierre, C., 1999, "Reduced Order Modeling and Vibration Analysis of Mistuned Bladed Disk Assemblies With Shrouds," ASME J. Eng. Gas Turbines Power, **121**, pp. 515–522.
[8] Lim S.-H., Bladh R., Castanier M. P., Pierre C., 2003, "A Compact, Generalized Component Mode Mistuning Representation for Modeling Bladed Disk Vibration," Paper No. AIAA-2003–1545.
[9] Yang, M.-T., and Griffin, J. H., 2001, "A Reduced-Order Model of Mistuning Using a Subset of Nominal System Modes," ASME J. Eng. Gas Turbines Power, **123**(4), pp. 893–900.
[10] Feiner, D. M., and Griffin, J. H., 2002, "A Fundamental Model of Mistuning for a Single Family of Modes," ASME J. Turbomach., **124**(4), pp. 597–605.
[11] Ayers, J. P., Feiner, D. M., and Griffin, J. H., 2006, "A Reduced-Order Model for Transient Analysis of Bladed Disk Forced Response," ASME J. Turbomach., **128**(3), pp. 466–473.
[12] Petrov E. P., Vitali R., Haftka R. T., 2000, "Optimization of Mistuned Bladed Discs Using Gradient-Based Response Surface Approximations," Paper No. AIAA-2000–1522.
[13] Petrov, E. P., and Ewins, D. J., 2003, "Analysis of the Worst Mistuning Patterns in Bladed Disk Assemblies," ASME J. Turbomach., **125**(4), pp. 623–631.
[14] Choi, B.-K., and Lentz, J., 2003, "Optimization of Intentional Mistuning Patterns for the Reduction of the Forced Response Effects of Unintentional Mistuning: Formulation and Assessment," ASME J. Eng. Gas Turbines Power, **125**(1), pp. 131–140.
[15] Scarselli G., Lecce L., 2004, "Non Deterministic Approaches for the Evaluation of the Mistune Effects on the Rotor Dynamics," Paper No. AIAA-2004–1748.
[16] Thompson, E. A., and Bécus, G. A., 1993, "Optimization of Blade Arrangement in a Randomly Mistuned Cascade Using Simulated Annealing," Paper No. AIAA-93–2254.
[17] Rivas-Guerra, A. J., and Mignolet, M. P., 2003, "Maximum Amplification of Blade Response Due to Mistuning: Localization and Mode Shape Aspects of the Worst Disks," ASME J. Turbomach., **125**(3), pp. 442–454.
[18] Kenyon, J. A., Griffin, J. H., and Feiner, D. M., 2003, "Maximum Bladed Disk Forced Response From Distorsion of a Structural Mode," ASME J. Turbomach., **125**(2), pp. 352–363.
[19] Kenyon, J. A., 2004, "Maximum Mistuned Bladed Disk Forced Response With Frequency Veering," Paper No. AIAA-2004–3753.
[20] Rotea, M., and D'Amato, F., 2002, "New Tools for Analysis and Optimization of Mistuned Bladed Disks," Paper No. AIAA-2002–4081.
[21] Castanier, M. P., and Pierre, C., 1998, "Investigation of the Combined Effects of Intentional Mistuning and Random Mistuning on the Forced Response of Bladed Disks," Paper No. AIAA-98–3720.
[22] Kenyon, J. A., and Griffin, J. H., 2003, "Forced Response of Turbine Engine Bladed Disks and Sensitivity to Harmonic Mistuning," ASME J. Eng. Gas Turbines Power, **125**(1), pp. 113–120.
[23] Zhou, K. M., Doyle, J. C., and Glover, K., 1995, *Robust and Optimal Control*, Prentice-Hall, Englewood Cliffs, NJ.
[24] Ferreres, G., Magni, J.-F., and Biannic, J.-M., 2003, "Robustness Analysis of Flexible Structures: Practical Algorithms," Int. J. Robust Nonlinear Control, **13**, pp. 715–733.
[25] Lawrence, C. T., Tits, A. L., and Dooren, P. V., 2000, "A Fast Algorithm for the Computation of an Upper Bound of the μ-Norm," Automatica, **36**, pp. 449–456.
[26] Yao, J. Y., 2006, "Dynamic and Robust Characteristics Analysis of Mistuned Periodic Structures," MS thesis, Beihang University, Beijing.

On-Condition Maintenance for Nonmodular Jet Engines: An Experience

Mato F. Siladic

Bosko P. Rasuo
Professor

Department of Aeronautics,
Faculty of Mechanical Engineering,
University of Belgrade,
11120 Belgrade, Yugoslavia

Using updated knowledge and gained experience in engine control and maintenance, a specific on-condition maintenance concept of RD-33 engines installed on MiG-29s was developed. The engines had several built-in limitations: number of starts, number of hours at the maximum power and reheat, number of hours at the special regime of elevated temperatures, and time between overhauls (TBOs), that is, number of flight hours. During field data collection and analysis, it was found that engines worked with different working loads and different levels of life consumption. Hence, it was concluded that the limitation of TBO, expressed in terms of flight hours, do not represent actual engine health condition and that a new way of monitoring actual load needs to be introduced. An analysis of all flight profiles was carried out and a specific relation between flight hours and total accumulated cycles (TACs) was established. For this purpose, a distributed expert system in relation-operation unit—Air Force Technical Institute—overhaul depot was introduced. Each of the three participants has its own level of responsibility in the engine health monitoring, engine maintenance, and engine health condition decision-making process. Nondestructive inspection, remote visual inspection, spectral oil analysis, fault tolerant control techniques of hot engine parts, engine electronic control unit, airplane information-display system, engine performance trend monitoring, vibration monitoring, and postflight data analysis play key roles in the concept. It has been applied in practice since 1994; all faults were discovered right in time, and there were not any critical situations in flight. Detected faults were isolated and assessed for severity, so that the remaining useful life could be estimated. The original TBO was safely extended on the basis of TAC of up to more than 50% of the originally prescribed TBO hours, while maintaining the same safe margin. [DOI: 10.1115/1.3019104]

1 Introduction

In most air forces, which have aircrafts of the second and third generations within their arms, the predominant maintenance concept is the one in accordance with fixed prescribed service life (hard time between overhauls). Upon expiration of the time TBOs, the engine and/or aircraft is forwarded to the overhaul plant in order to be overhauled in accordance with prescribed technological operations. Such preventive maintenance procedure is the result of long-term estimation of nonfailure operation of components and systems that essentially affect the flight safety (with values of more than a hundred hours of running time or more years of operation), but without considering actual mechanical and thermal loads of individual engine/aircraft during operation. With certain safety margins, regardless of being necessary or not, aircraft and engines of the same type are overhauled after expiration of the prescribed TBO.

However, continuous price increase of new fighters and their engines, spare parts, maintenance and usage, and high prices of kerosene have generated modification of existing maintenance systems, as well as the development and the application of new maintenance concepts with the application of aircraft and engine diagnostic systems. As known, a major problem in designing, developing, establishing, or modifying maintenance systems for application on a high-speed jet fighter, and its power plant is the sudden change in operating conditions and operating environment, primarily temperature and vibrations levels, especially at low altitude flights. In order to establish an effective system of aircraft and engine maintenance, it is necessary to provide sufficient relevant information on their status through the application of an appropriate diagnostic system.

In the mid-1990s, the concept of specific on-condition maintenance of RD-33 jet engines for MiG-29 fighters was developed and applied in the Yugoslav Air Force due to expiration of the prescribed TBO, which included two components: on-condition maintenance with a discrete check of parameter condition and periodic partial engine disassembly in order to establish the mechanical condition of parts that had been effected by more serious problems in earlier operation. Thus, two benefits were realized: earlier maintenance system was changed and engine service life extension was performed.

2 Approach to Problem

After thorough theoretical consideration of fatigue, crack origination, and propagation, as well as the analysis of earlier experiences in aircraft engine maintenance [1], and in order to maximize the utilization of effective service life of RD-33 engine, the former concept of fixed service life maintenance started to be replaced by on-condition maintenance. The following key theoretical-experiential criteria were established to analyze possibilities and to define conditions for the continuous inspection and checking of the actual condition of engine systems, parts, and elements, which would supply accurate and reliable information on their technical condition, possible damage, fatigue indications, wear level and other factors, which might indicate probable failure in future period of operation before new inspection was due.

The aforementioned criteria imposed the performance of the following:

(1) analysis of foreign experiences in defining the overhaul life and the life of jet engines

Manuscript received November 22, 2007; final manuscript received September 10, 2008; published online January 29, 2009. Review conducted by David Walls.

(2) comparison of structural concept of modern western engines and the RD-33 engine
(3) analysis of own experiences in extending the life of jet engines (defining equivalent testing cycle and total accumulated cycle of engine in a combat assignment function type)
(4) analysis of all earlier failures and results of repairs before the expiration of the RD-33 engine operation life
(5) establishing the most critical parts and their effect on reliable engine operation and establishing the most critical automation elements
(6) forming engine total accumulated cycle based on annual running times and the type of assignments performed by aircraft
(7) establishing a relation between limitations imposed by the manufacturer and the TACs, i.e., hour operation life and number of TACs
(8) analysis of rationality of the RD-33 engine earlier utilization from the aspect of the consumption of set limitation
(9) defining the type and content of inspection and needed equipment
(10) determining the acceptable level of flow system element damage and deviations in engine operation parameters
(11) defining the program of engine operation check on test bed and test flight
(12) establishing the time interval of due inspection and the creation of appropriate technical documentation
(13) presenting the concept to competent level of decision-making and obtaining official approval of concept application
(14) presenting the concept to direct participants and operators
(15) continuous control of the applied concept on concrete engines and its refinement

3 Applied Methodology and Acquired Experiences

Comparison of structure and comparative analysis of existing diagnostic equipment and applied procedures of maintenance of RD-33, RB-199, PW1120, and F-404 engines were performed as initial element of estimation of possible application of the RD-33 engine on-condition maintenance. During the aforementioned analysis, it was established that the RD-33 engine, from technical-technological aspect, satisfied large-scale prerequisites for establishing on-condition maintenance concept [1].

The basic problem was the lack of information on the character and the number of allowed TACs during the life. Instead of them, the manufacturer introduced the following basic limitations in defining TBO:

(1) allowed hours of operation in air (Δ_1)
(2) allowed number of engines starting (Δ_2)
(3) allowed hours of operation on "maximal" and "reheat" ratings (Δ_3)
(4) allowed hours of operation on "special" rating with increased temperatures (Δ_4)
(5) approved service life of accessories (Δ_5)

By a thorough operational analysis of each individual engine, it was established that, in spite of the utilization of hour service life, prescribed limitations $\Delta_2-\Delta_4$ were utilized, 65% on average, which explicitly indicated the conclusion that engines had a certain reserve of usable service life.

Although the RD-33 engine is not entirely of modular structure, as the one applied on western engines, it was proved in practical applications that it could be conditionally divided into eight modules, which are interchangeable without additional testing. This enabled the introduction of differential life for engine modules and accessories, which is related to either hour service life or number of TACs.

When considering experiences in operation, the most complex problems regarding RD-33 engines were those of multiple jamming of the fourth bearing (Fig. 1), to which rests high pressure turbine and those of stator vanes burning (Fig. 2). Regardless of complexity and seriousness of jamming of the fourth bearing, it was decided to continue engine operation under the condition that reliable mechanism of monitoring its condition was provided. It was estimated that the way of failure creation was not critical for flight safety because it was of gradual character and could be controlled and was characterized with the following indications: color change and higher oil consumption, increase in iron and graphite concentration in oil, and shorter time of compressor rotor stoppage. The conclusion was reached that the above-mentioned characteristics could be timely discovered and filed by introducing a new maintenance concept, in which the bearing condition was monitored through the introduction of spectrochemical oil analysis, measuring vibrations and noise.

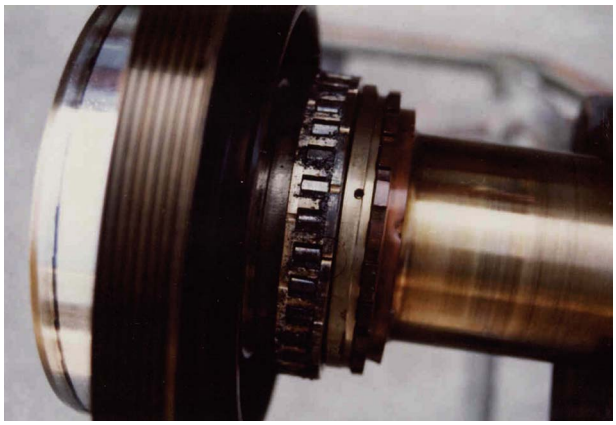

Fig. 1 An example of fourth bearing jamming

One of the main problems in turbine blades life prediction is a blade root crack initiation due to low-cycle fatigue. A formula that relates the low-cycle fatigue (LCF) damage to localized stress range is given in the following form:

$$\mathrm{Nf1}_L = \tfrac{1}{2}(\sigma_{\mathrm{L}}(\mathrm{true}) - \sigma(\mathrm{mean}))^{1/(n-c)} K^{1/(n-c)} \mathrm{Ef}^{(-1/c)} \qquad (1)$$

where $\mathrm{Nf1}_L$ is the low-cycle fatigue life for blade L, which is the mean number of cycles to the blade root crack initiation; $\sigma_{L(\mathrm{true})}$ is the localized true plastic stress amplitude at a blade root; n is the cyclic strain hardening exponent; c is the fatigue ductility exponent; K is the cyclic strength coefficient; and Ef is the fatigue ductility coefficient.

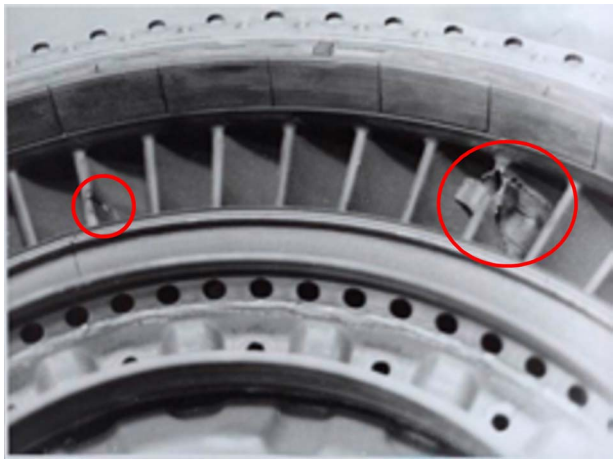

Fig. 2 Turbine stator vanes burn

The damage accumulated due to LCF may be given by a nonlinear damage accumulation rule suggested by Gary Halford at NASA Langley 1996. [2]

$$\text{Damage} = \left(\frac{n_1}{\text{Nf1}_L}\right)^{r_1} \tag{2}$$

where n_1 is the number of cycles experienced, r_1 is the nonlinear damage exponent, and Nf1 is the number of cycles to crack initiation.

The blade root crack initiation due to low-cycle fatigue is only one segment of the turbine blade prognostic. The complete turbine blade prognostic model must further account for the other failure modes at other critical locations on the blade, and the introduction of TACs could be a good experimental substitute for such model.

The rainflow method was used to count fatigue cycles. Allowable limits on the engine components crack size were prescribed based on data given in the Engine Overhaul Manual and were treated as critical flow size. The crack growth procedure starts with the generation of an initial crack and the calculation of the stress intensity factors. The life assessment criterion is that the allowable limits on engine components crack size are not to be exceeded.

In accordance with the main principles of TAC calculation and the limitations of RD-33 engine operation introduced by the manufacturer, the procedure for defining TAC for the RD-33 engine was started. Because data on exact TAC and realized profiles of aircraft flights were not available at this time, it was decided to perform, in cooperation with the pilots, a complete analysis of the annual training of MiG-29 aircraft pilots and to convert all training elements of the pilots into appropriate flight profiles into throttle lever shifting function. For this purpose, a complete training was divided into five groups of training elements, as follows:

(1) The first group included the assignments of interception and air-to-ground tasks.
(2) The second group included aerobatics.
(3) The third group included navigation flights, overflights, weather reconnaissance, and school circles.
(4) The fourth group included technical trials, accelerations, and ceiling.
(5) The fifth group included air combat.

The following elements were defined for each group of exercise elements: number of exercises, total number of flights per exercise, percentage share of concrete exercise[1] in the total number of flights, total flight duration time per concrete exercise, percentage share of total exercise duration time in total running time, average flight duration, average number of TACs per flight, total number of TACs per exercise, and average number of TACs per hour of flight. Based on these elements, a graphical presentation of the flight profile in the throttle lever shifting function was made for each exercise group. After the acquisition of all data related to the planned annual running time under defined groups of exercise elements, the most complex exercises were selected from each group of elements, and the analysis of five real flights for each of them was performed (using flight data recorder); the conclusion was reached that deviations between planned exercises and real flights were within the acceptable limit of 5%. In order to cover all possible deviations between planned and actually performed flights in each exercise, the calculation of TACs [3] was performed including elementary type IV cycle.

$$\text{TAC} = n \times \text{TAC type I} + n \times \frac{\text{TAC type III}}{4} + n \times \frac{\text{TAC type IV}}{40} \tag{3}$$

As a result, data were obtained for the following:

(1) average time of flight duration
(2) average number of TACs per flight
(3) average number of elementary type IV cycles per flight
(4) average number of TACs per group of exercise elements
(5) share of elementary type IV cycle in engine TAC
(6) average number of TACs per hour of flight, with and without elementary type IV cycles

Thus, the obtained TAC of the RD-33 engine clearly showed that the most intensive load of engine occurred in two training and flight stages: air combat (Fig. 3) and aerobatics. Regarding that at the moment of researching the possibility of expanding TBO, the procedure for mastering the overhaul of RD-33 engine in own overhaul works was initiated, valuable knowledge was reached about weak points of the engine flow system, as well as that of acceptable damage values, especially turbine stator vanes. It was concluded that engines on maximal operation rates are very loaded, and the result was the burning of turbine stator vanes, which additionally loaded operating blades and caused exfoliation of their coatings and initiation of cracks. For this reason, the decision was taken to reduce turbine temperature of all RD-33 engines by 20°C by adjusting the T4 temperature channel on the engine electronic control unit. This was one of the key factors that enabled turbine thermal unloading and further engine on-condition operation. Estimations and experimental confirmations on aircraft confirmed that the thrust was reduced by 3–4%, which created negligible (acceptable) effect on aircraft performances.

By integrating basic limitations prescribed by the manufacturer into TAC, the targeted engine service life was defined, expressed in number of running hours function and in possible TAC number function, which was corrected against the actual TAC of each engine separately. Such definition of targeted service life is necessary for planning the annual running time of the aircraft, load calculation of aircraft workshop capacity, and calculation of effective service life residue. The correction of targeted service life is performed in accordance with the following criteria: for each hour of saving prescribed operation on "maximal+reheat" ratings, the targeted service life is extended by additional n hours, and for each hour of saving increased temperature ratings, the targeted service life is extended by additional m hours [4–6]:

$$T_N[h] = T_P + \Delta T = T_P + [\Delta T(n) + \Delta T(m)] = T_P + [\Delta_{3\text{rez}}\delta_1 + \Delta_{4\text{rez}}\delta_2] \tag{4}$$

where T_N is the target TBO, T_P is the prescribed TBO by the manufacturer, ΔT is the increased life, $\Delta_{3\text{rez}}$ is the part of unused prescribed work at the maximal+reheat regimes, $\Delta_{4\text{rez}}$ is the part of unused prescribed work at the "elevated temperature" regime, and δ_1 and δ_2 are weight factors.

It should be noted that the engine service lives are not fixed anymore, but a check of condition and an evaluation of technical condition and parameters of engine operation are performed after utilization of 60 TAC (equivalent to 20–30 h of engine operation), and based on the performed analysis, further effective service life of 60 TAC is approved. At this, information on the maximum possible effective service life residue of engine is always available to the user.

3.1 Importance of Spectrochemical Oil Analysis. Spectrochemical oil analysis has a very important role in diagnostics of engine condition [7]. Regarding that rotation of the compressor rotor is running on oil film in thickness of 10 μm, oil should be of adequate quality, pure, and free of humidity. Experiences have

[1]Each group of training elements consists of a set of typical exercises that are coded in pilot language and defined by flight profile, duration, number of planes and pilots involved, types of maneuvers, and so on. For example, some details of the Exercise 101 are defined by the following: purpose—target interception; duration—45 min; type and number of involved airplanes—a single-seat airplane; way of interception—free target hunting; way of target identification—IR and visual target contact, etc.

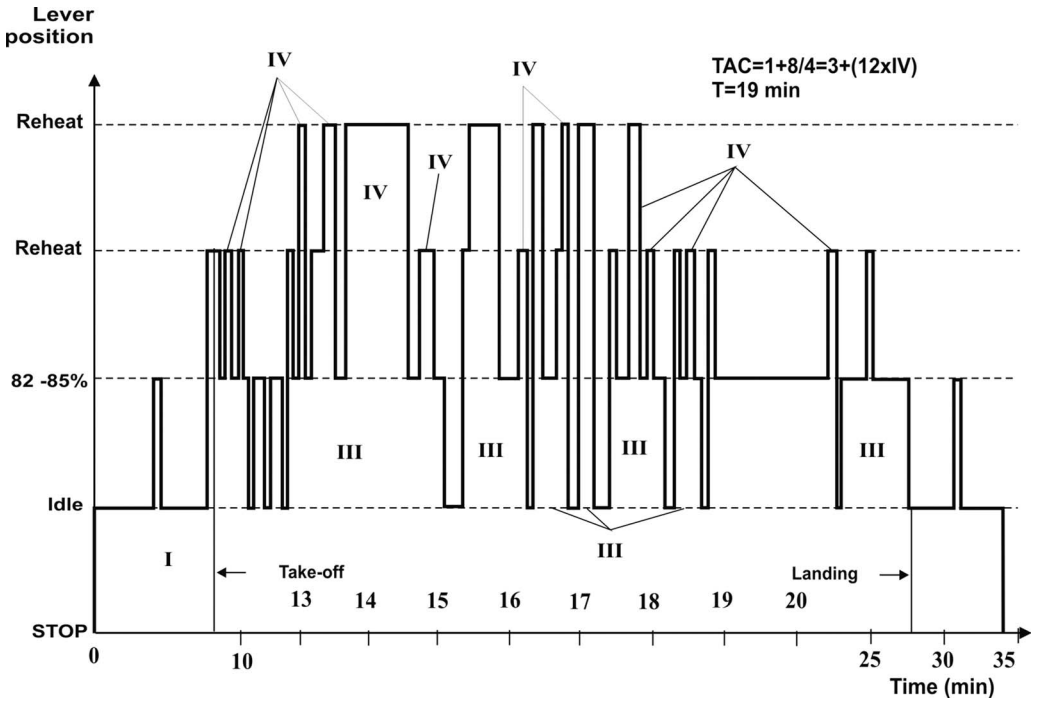

Fig. 3 An example of TAC representation for air-combat exercise

proved that engine oil indicates engine appropriateness and that spectrochemical oil analysis converts the indications into valuable information, which help in making correct decisions on engine operation and maintenance procedures. An insight into the wear intensity of bearings, gears, filters, and accessory box in engine oil system may be gained, i.e., abnormal operation of some parts may be preventively discovered. During the on-condition maintenance concept implementation of spectrochemical oil analysis contributed to the saving of five engines. Namely, the observable peaks of iron content, followed by increased zinc and nickel content and dirt undoubtedly indicated that the bearings of these engines approached the limit of safe use and that their jamming was unequivocal if operation continued. The engines were removed from the aircraft, whereby more serious transmission damage was prevented and thus the costs of repair were considerably reduced. Experiences proved that the standard form of spectrochemical oil analysis in laboratories distant from aviation base location, in some cases, do not provide satisfactory results. Namely, in practice, more problems occur in relation to inappropriate and nontimely oil sampling, and in more cases spectrochemical oil analysis had to be repeated, or the sampling interval had to be shortened.

In general, allowable limits of six key element content in oil were established: iron, copper, nickel, zinc, chromium, and magnesium. Spectrochemical analysis has been proven as a very effective method in engine condition monitoring because its results indicate timely when the operating performance of components in the lubricating system is degraded, and that appropriate procedures or maintenance procedures should be applied at certain levels of metallic debris content.

3.2 The Role of Remote Visual Inspection. When elaborating the concept and considering the possibilities of monitoring the RD-33 engine condition, the most serious problem was how to provide a reliable inspection of flow system-compressor, main combustion chamber, fuel injectors, and turbine, i.e., how to detect cracks, damage, exfoliation of protective coatings, vanes and blades burns, or corrosion traces, their actual sizes, and the speed of their propagation on inaccessible components of engine flow system. In order to solve this problem, new modern remote visual inspection (RVI) equipment was purchased (video image scopes with a CCD image sensor mounted at the end of the flexible probe and computerized video analyzer with inspection manager software). From the CCD image sensor, a picture is transferred to a special liquid crystal display or to a special display mounted on the head of an inspector (head mount LCD), or to a PC monitor, and at this, the picture may be zoomed, frozen, and kept for subsequent analyses. It is also possible to enter numerical grid of stator vanes and rotor blades, which may be integrated with the picture from the CCD "camera" and so measure the actual length of detected cracks or damage. In this way, it is possible to establish the condition of engine flow system with high precision and reliability, detect cracks or damage at the bottom limit of detectability, monitor crack propagation speed, forecast service life residue, and undertake timely optimal maintenance procedures. The modern RVI equipment with CCD cameras provided an objective inspection of the engine flow system condition because it enabled the following: a few experts simultaneously watched inspected surfaces on the monitor, the condition of inspected surfaces was documented in a computer video-record format, a subsequent thorough analysis of the condition of suspicious cracks or damage was performed, and crack lengths or other types of detected damage were measured. There are 13 bores that are used for the inspection of the engine interior: 5 on low pressure compressor casing, 4 on high pressure compressor casing, 2 on combustion chamber, and 2 on the turbine. For all parts of the engine flow system, allowable limits are defined for crack size based on which further schedule of engine utilization is approved.

3.3 Integration of Applied Methodology. In order to monitor engine condition more reliably, a distributed expert system consisting of three participants was introduced: Flight Unit, Air Depot, and Air Force Technical Institute (Figs. 4 and 5). Each of the above-mentioned participants has precisely defined assignments and decision-making competence. Flight unit performs continuous monitoring of engine condition parameters, additional RVI of main combustion chamber, and high pressure turbine and updating of TAC. Air Depot performs inspection of engine condition with partial disassembling (RVI and other types of nondestructive testing) and evaluation of residual service life. Military

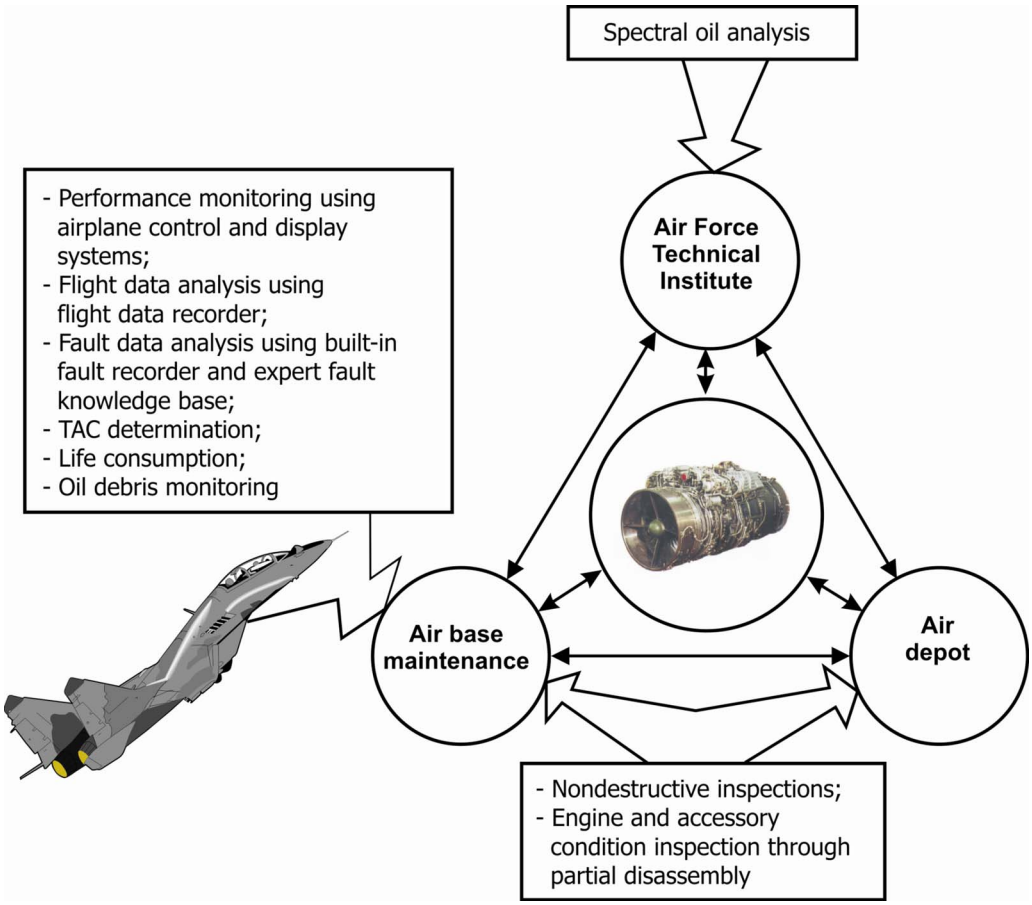

Fig. 4 Established distributed expert system for engine condition monitoring

Technical Institute performs spectrochemical oil analysis. On-line information exchange between members of distributed expert system is realized.

Key role in decision-making on further engine serviceability has the expert knowledge base of typical failures, their symptoms and consequences, as well as the database of allowed length of cracks in turbine and compressor blades.

3.4 Preparation and Training of Personnel. Before initial application of on-condition maintenance concept of RD-33 engines, it was necessary to have professional discussion with pilots and aviation-technical staff, during which the concept postulation, possible risks, and responsibility of all participants in consistent implementation of all inspections, checks, and monitoring of engine operation parameters were presented. At the same time, it was necessary to carry out the training of direct participants in the maintenance of the RD-33 engine, to establish precise coordination of the joint work of personnels from the first level of maintenance and Air Depot in performing an inspection of the engine condition, and to provide conditions for comprehensive and undisturbed work of experts for flight data analysis and planned performance of spectrochemical oil analysis. It was decided that the leader of spectrochemical oil analysis was the laboratory of Air Force Technical Institute, which had available necessary equipment, experts for spectrochemical oil analysis, and methods needed for evaluation of analyzed oil samples and for adjusting oil sampling schedule. The coordination of implementation of the whole project was carried out at the highest level of aviation-technical service.

The analysis of flight parameters from aircraft flight parameter register is performed in two steps. The first step or the so-called express analysis of parameters is performed by a laptop computer immediately after aircraft landing, between two flights, in order to check possible exceeding values of engine running key parameters. The second step or the detailed analysis of flight parameters is performed after the completion of flight day, and the filing of necessary data and needed correction of TAC is performed during this.

Regarding unknown risk level in forecasting the condition of parts and the reliability of correct choice of time intervals for the inspection of engine hot parts, which existed when implementing on-condition maintenance concept of RD-33, it was decided to introduce additional safety reserve until final approval of the concept. It included fitting in the redistribution of the engine, i.e., the principle of combining one engine with an extended service life and one with the originally prescribed service life, on the aircraft was introduced.

4 Conclusion

Established on-condition maintenance concept of RD-33 engines with its diagnostic system satisfied its original purpose—it prevented disastrous failures and provided extension of engine service life. This concept has clearly demonstrated the following advantages of the on-condition maintenance approach: controlled usage of engine life, introduction of life algorithm based on total accumulated cycles instead of hours, extension of earlier prescribed engine life by 50–60%, and considerable savings. Key role in its application had distributed expert system established in relation fighter regiment—Air Depot—Air Force Technical Institute. Introduction of the algorithm of the RD-33 engine service life, based on actual TAC instead of hour operation life, enabled the extension of service life maintaining the same safety margin, valid evaluation of effective service life residue, and considerable maintenance cost reduction. One of the significant deficiencies of the aforementioned diagnostic system is limited the forecasting

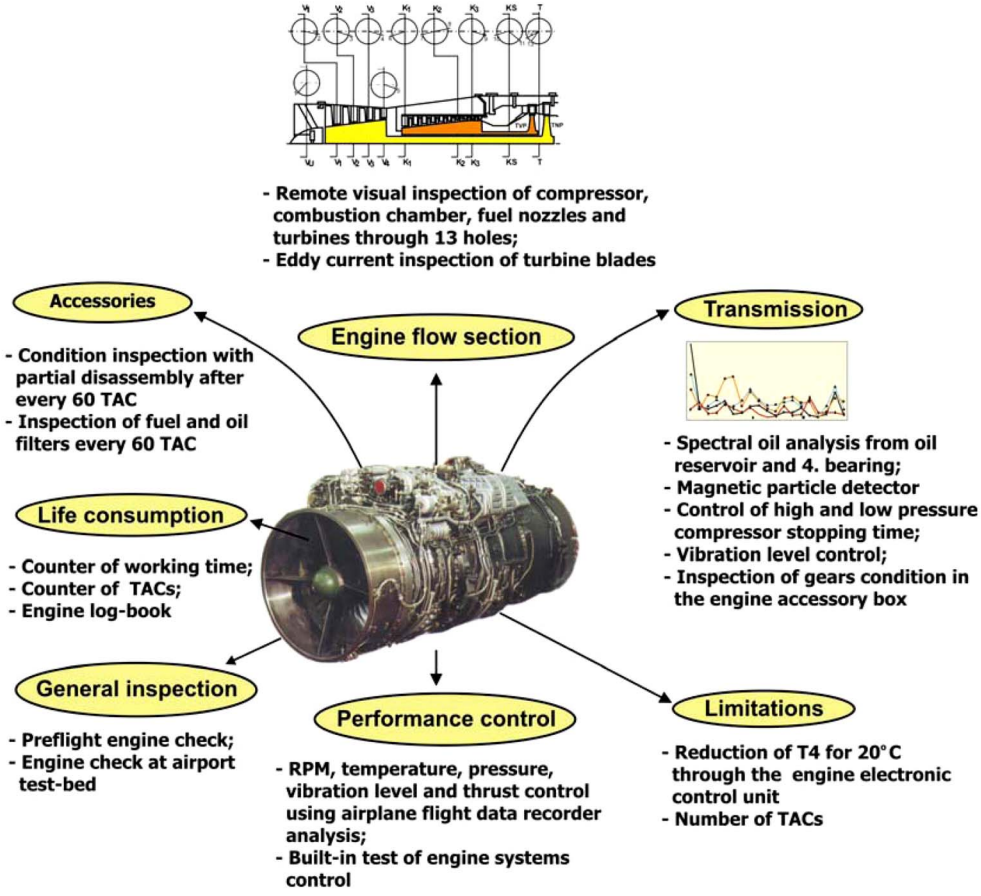

Fig. 5 Content of the engine on-condition maintenance procedure

capability of the future condition of engine components, which is presently implemented based on experience rates. For this reason, it is necessary to upgrade the existing diagnostic system by an intelligent algorithm [8–11], which would be capable of recognizing failure modes automatically.

Nomenclature

c = fatigue ductility exponent
Ef = fatigue ductility coefficient
K = cyclic strength coefficient
n = cyclic strain hardening exponent
n_1 = number of cycles experienced
Nf1 = number of cycles to crack initiation
$\mathrm{Nf1}_L$ = low-cycle fatigue life for blade (L), which is the mean number of cycles to blade root crack initiation
r_1 = nonlinear damage exponent
T_N = target TBO
T_P = prescribed TBO by the manufacturer
ΔT = increased life
Δ_1 = allowed hours of operation in the air
Δ_2 = allowed number of engines starting
Δ_3 = allowed hours of operation on maximal and reheat ratings
Δ_4 = allowed hours of operation on special rating with increased temperatures
Δ_5 = approved service life of accessories
$\Delta_{3\mathrm{rez}}$ = part of unused prescribed work at maximal +reheat regimes
$\Delta_{4\mathrm{rez}}$ = part of unused prescribed work at the elevated temperature regime
δ_1 = weight factor
δ_2 = weight factor
$\sigma_{L(\mathrm{true})}$ = localized true plastic stress amplitude at a blade root

References

[1] Siladic, M., Komljenovic, D., and Milosavljevic, D., 1995, "Introduction of On-Condition Maintenance Concept for Turbofan Engine of Combat Airplane," International Aerospace Congress, Belgrade, pp. 22–27.
[2] Halford, G., 1996, "Cumulative Fatigue Damage Modeling—Crack Nucleation and Early Growth," First International Conference on Fatigue Damage, pp. 342–354.
[3] 1984, "Proposal for PW1120Y for Yugoslavia's Supersonic, Multipurpose, High Performance Combat Aircraft Program," U.T. Pratt & Whitney Aircraft, Report No. FP 84-614.
[4] Chupp, R. E., Hendricks, R. C., Lattime, S. B., and Steinetz, B. M., 2006, "Sealing in Turbomachinery," J. Propul. Power, **22**(2), pp. 313–349.
[5] Hamed, A., Tabakoff, W. C., and Wenglarz, R. V., 2006, "Erosion and Deposition in Turbomachinery," J. Propul. Power, **22**(2), pp. 350–360.
[6] Siladic, M., 2007, *Life Management of Aircraft and Engines*, 1st ed., BB-Soft, Belgrade.
[7] Mishra, C., and Muncherji, S., 1996, "Expert System for Wear Debris Analysis—A Powerful Tool for Condition Monitoring," Trends in NDE Science & Technology, *Proceedings of the 14th World Conference on Non-Destructive Testing*, New Delhi, pp. 103–115.
[8] Tumer, Y. I., and Bajwa, A., 1999, "A Survey of Aircraft Engine Health Monitoring Systems," American Institute of Aeronautics and Astronautics, Inc., Report No. AIAA-99–2528.
[9] Siladic, M., Pokorni, S., and Rasuo, B., 2003, "Possibilities of Jet Engine Diagnostic Improvement by Using Neural Networks," 47th Conference of ET-

RAN, Herceg Novi.
[10] Roemer, J. M., and Kacprzynski, J. G., 2000, "Advanced Diagnostic and Prognostic for Gas Turbine Engine. Risk Assessment," IGTI/ASME Turbo Expo, Munich, Germany.
[11] Zhernakov, V. S., 2000, "Diagnostics and Checking of Gas-Turbine Engines Parameters With Hybrid Expert Systems," *Proceedings of the Workshop on Computer Science and Information Technologies CSIT 2000*, Ufa, Russia, pp. 227–234.

Impact of Manufacturing Variability on Combustor Liner Durability

Sean Bradshaw
e-mail: sdbrad@alum.mit.edu

Ian Waitz
e-mail: iaw@mit.edu

Department of Aeronautics and Astronautics,
Massachusetts Institute of Technology,
77 Massachusetts Avenue,
Cambridge, MA 02139

This paper presents a probability-based systems-level approach for assessing the impact of manufacturing variability on combustor liner durability. Simplified models are used to link combustor life, liner temperature variability, and the effects of manufacturing variability. A probabilistic analysis is then applied to the simplified models to estimate the combustor life distribution. The typical combustor life was found to be approximately 20% less than the estimate life using deterministic methods for these combustors, and the probability that a randomly selected combustor will fail earlier than expected using deterministic methods is approximately 80%. The application of a sensitivity analysis to a surrogate model for the life identified the leading drivers of the minimum combustor life and the typical combustor life as the material property variability and the circumferential variability of turbulent mixing rates, respectively. [DOI: 10.1115/1.2980016]

Keywords: combustor, heat transfer, durability, variability

1 Introduction

1.1 Background. The lifetime of a gas turbine combustor is typically limited by the durability of its liner, the structure that encloses the high-temperature combustion products. The primary objective of the combustor thermal design process is to ensure that the liner temperatures do not exceed a maximum value set by metallurgical limits while minimizing the amount of film cooling air used in the process. Liner temperatures exceeding this limit hasten the onset of cracking and buckling [1], such as is shown in Fig. 1. These forms of distress increase the frequency of unscheduled engine removals, which causes the maintenance and repair costs of the engine to increase.

A combination of analytical tools and rig tests is necessary to ensure that a combustor design satisfies durability and other requirements. However, variability arising from imperfect manufacturing processes introduces uncertainty into the deterministic quantification of combustor liner life. The computational expense of high fidelity numerical tools typically used in combustor design prohibits the use of probabilistic methods with these tools. Moreover, the connections between structural reliability, aerothermal variability, and manufacturing variability are seldom made due to the complexity of the task. In particular, causal relationships are not typically established among the sources of manufacturing variability, liner temperature, and liner life. The absence of these relationships prohibits an understanding of the extent to which the effects of manufacturing variability impact the combustor liner life. As a result, the impact of manufacturing variability is accounted for by making conservative assumptions and adopting design margins based on experience with similar products. These approaches may yield combustors that are overdesigned in order to meet one requirement while yielding combustors that are suboptimal with respect to other aspects of the design.

Probability-based design and analysis methods have been used to assess the reliability of aerospace products for over three decades [2]. These techniques replace the conservatism of margin-based risk assessment methods by directly estimating part failure rates. However, there are few papers on gas turbine aerothermal design and analysis with variability. Garzon and Darmofal [3] proposed a probabilistic methodology for quantifying the impact of manufacturing variability on compressor aerodynamic performance. The authors showed that the effect of geometric variability reduced overall compressor efficiency by 1%. Sidwell and Darmofal [4] quantified the impact of manufacturing variability on turbine blade cooling flow and oxidation life. The application of a sensitivity analysis revealed the leading driver to be the blade flow passage area. The authors proposed a selective assembly method to mitigate the impact of variability on turbine blade oxidation life. Mavris and Roth [5] introduced a general robust design methodology for the high speed civil transport (HSCT) impingement-cooled combustor liner. They used a finite element model to estimate the liner thermal loads deterministically. Using design of experiments (DoE) techniques, they assembled a response surface equation (RSE) for liner temperature as a function of several design parameters. The flame temperature, the film cooling air temperature, and the hot-side convection coefficient were classified as noise parameters. Mavris and Roth showed that the impingement hole spacing and the thermal barrier coating (TBC) thickness were the key drivers of liner temperature variance. The authors modeled the variability of the hot-side convection coefficient, the compressor discharge temperature, and the adiabatic flame temperature using triangular probability density functions, where the first and second moment characteristics were based on design experience. A triangular distribution was chosen because the true natures of the probability distributions for these parameters were not known.

1.2 Scope of Paper. This paper presents a probabilistic framework for quantifying the impact of manufacturing variability on combustor liner life. This approach extends prior work because it goes beyond liner temperature variability to include directly an assessment of liner life. Further, the model is directly assessed using data available from a combustor development program as well as data obtained from in-service maintenance records. Section 2 (Probabilistic Modeling Framework) introduces the probabilistic model. Section 3 (Probabilistic Model Assessment) briefly summarizes the main results of the probabilistic analysis. Section 4 (Sensitivity Analysis) presents a methodology for identifying the leading drivers of the combustor liner life.

Contributed by the International Gas Turbine Institute of ASME for publication in the JOURNAL OF ENGINEERING FOR GAS TURBINES AND POWER. Manuscript received December 22, 2007; final manuscript received May 21, 2008; published online January 29, 2009. Review conducted by Dilip R. Ballal. Paper presented at the ASME Turbo Expo 2006: Land, Sea and Air (GT2006), Barcelona, Spain, May 8–11, 2006.

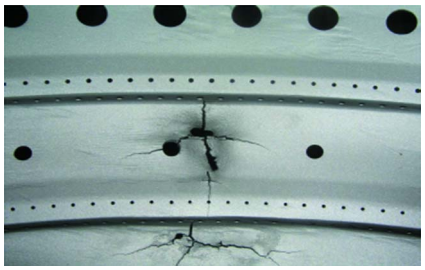

Fig. 1 Combustor liner distress (courtesy of Delta Airlines)

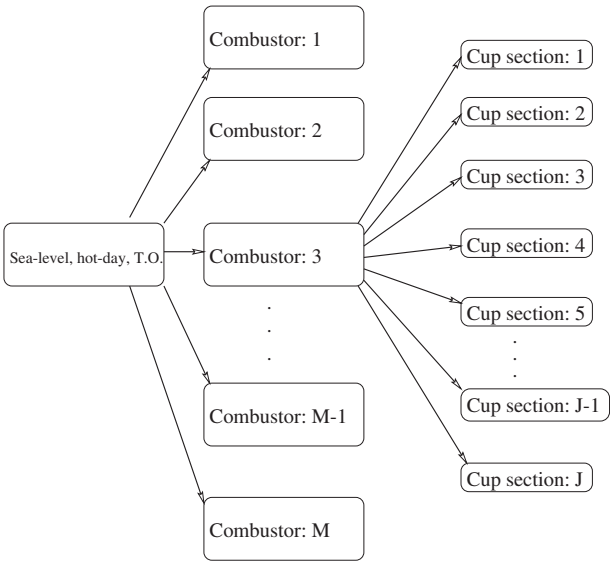

Fig. 2 Heirarchical analysis for *M* combustors and *J* cup sections at sea-level, hot-day, take-off operating condition

2 Probabilistic Modeling Framework

2.1 Hierarchical Analysis. The combustor fabrication process produces variability in the part dimensions, material properties, and radial gradients of combustion gas temperature. These effects are separated into two classes: cup-to-cup variations (I) and combustor-to-combustor variations (II). A hierarchical analysis is used to account for these nested classes of variability for M combustors with J cup sections, as shown in Fig. 2. First, each simulated combustor is assigned J fuel injectors and J air admission ports at the front end. Second, each combustor-to-combustor parameter has a value that is randomly sampled from its probability distribution. Third, these parameters are used to estimate the combustor liner temperature and life using a combustor model. Finally, the process is repeated for the next $M-1$ combustors to yield a liner life distribution for M combustors. These steps are integrated with a Monte Carlo analysis.

2.2 Random Variables. The effects of manufacturing variability are represented by independent, normally distributed random variables, as shown in Fig. 3. These parameters are the cooling slot metering hole diameter (MHD) multiplier (δ_d), the slot height (s), the TBC surface emissivity ($\varepsilon_{\mathrm{TBC}}$), the TBC thickness ($t_{\mathrm{TBC}}$), the liner thickness ($t_m$), the bond coat thickness (t_{bnd}), the TBC thermal conductivity (k_{TBC}), the liner thermal conductivity (k_m), the bond coat thermal conductivity (k_{bnd}), the dome air flow rate (G_{air}), the fuel injector flow rate ($\dot{m}_{\mathrm{fuel}}$), the combustor mixedness parameter (ζ), and the life curve multiplier (LCM) (Ψ). The MHD and LCM parameters account for the combustor hole size and material property variabilities, respectively. The combustor mixedness parameter quantifies the near-wall gas temperature variability. Parameters 1–9 and 13 are classified as cup-to-cup variables, while Parameters 10, 11, and 12 are assumed to vary from combustor to combustor.

2.3 Combustor Model. A simplified combustor model was used to establish causal relationships among geometric design parameters, material properties, liner temperature, and liner life, as

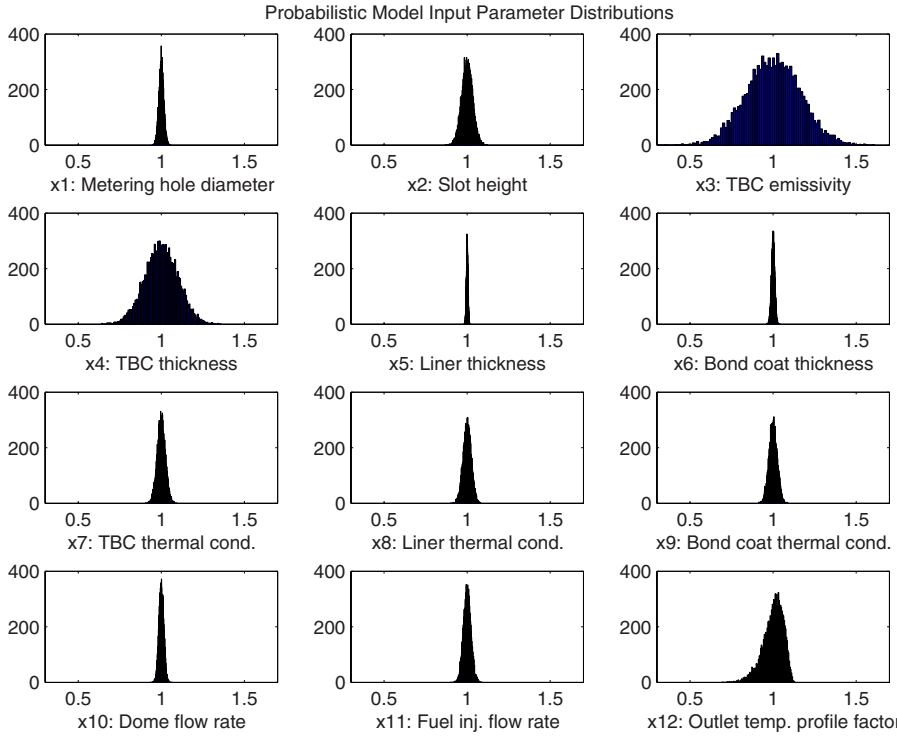

Fig. 3 Random variables

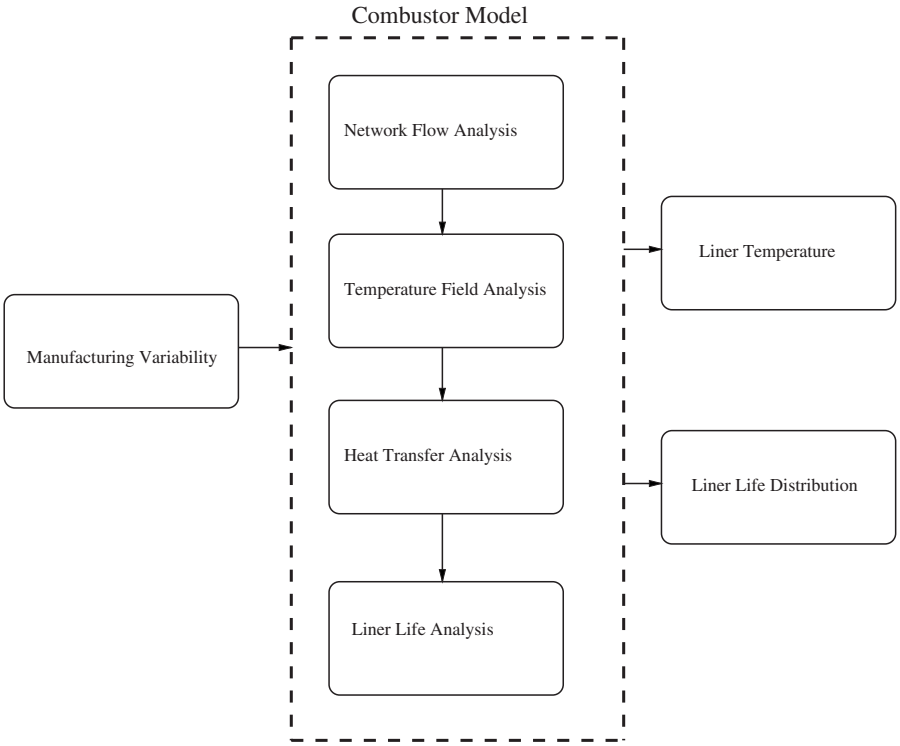

Fig. 4 Probabilistic modeling framework for assessing the impact of manufacturing variability on combustor liner temperature and liner life

shown in Fig. 4. The model consists of several elements: a network flow analysis, a combustor temperature field analysis, a liner heat transfer analysis, and a low-cycle fatigue life analysis. The model outputs are the liner temperature distribution and the liner life distribution.

2.3.1 Network Flow Analysis. A network flow analysis of a gas turbine combustor links the mass-flows across the liner and the bulk mass-flows inside the liner, as shown in Fig. 5. Each flow path is modeled as a circuit branch with a mass-flow conductance, as shown in Fig. 6. The bulk gas mass-flows are related by

$$\dot{m}_{\text{bulk},i,j} = \dot{m}_{\text{bulk},i-1,j} + \dot{m}_{\text{film},i-1,j} + \dot{m}_{\text{dilution},i,j} \tag{1}$$

where $\dot{m}_{\text{bulk},i,j}$, $\dot{m}_{\text{film},i,j}$, and $\dot{m}_{\text{dilution},i,j}$ are the bulk gas mass-flow, the film cooling mass-flow, and the dilution air mass-flow, respectively, for the ith panel and jth cup section, as shown in Fig. 5. The bulk mass-flow that crosses the ith face of cell i ($\dot{m}_{\text{bulk},i,j}$) is equal to the sum of the bulk mass-flow that crosses the $i-1$ face of the ith cell ($\dot{m}_{\text{bulk},i-1,j}$), the dilution air that enters the ith cell ($\dot{m}_{\text{dilution},i,j}$), and the film cooling air that enters the $i-1$ cell ($\dot{m}_{\text{film},i-1,j}$). The total combustor mass-flow and the mass-flows crossing the liner are related by the following equation to satisfy the conservation of mass:

$$\dot{m}_c = \sum_{j=1}^{J} \dot{m}_{\text{air},j} + \sum_{i=1}^{I-1} \sum_{j=1}^{J} \dot{m}_{\text{film},i,j} + \sum_{i=1}^{I-1} \sum_{j=1}^{J} \dot{m}_{\text{dilution},i,j} \tag{2}$$

In the probabilistic analysis, the mass-flow conductances and the combustor discharge pressures vary and the total combustor mass-flow $\dot{m}_c$ remains the same from combustor to combustor. Furthermore, it is assumed that the pressure inside each combustor is uniform. For a given set of mass-flow conductances and P_3, the local film, dilution, and bulk mass-flows can be found by solving Eqs. (3)–(5). This solution is found using a standard circuit analogy since the combustor flow network is equivalent to a parallel resistance network.

$$\dot{m}_{\text{air},j} = G_{\text{air},j}\sqrt{2\rho_3(P_3 - P_4)} \tag{3}$$

$$\dot{m}_{\text{film},i,j} = G_{\text{film},i,j}\sqrt{2\rho_3(P_3 - P_4)} \tag{4}$$

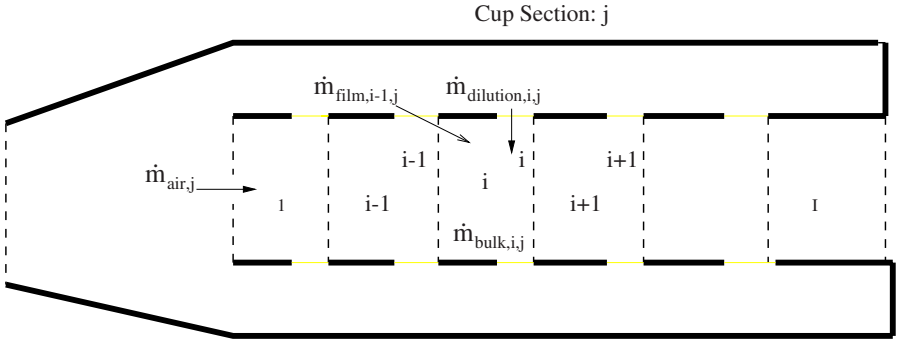

Fig. 5 Sketch of the mass-flows crossing the combustor liner

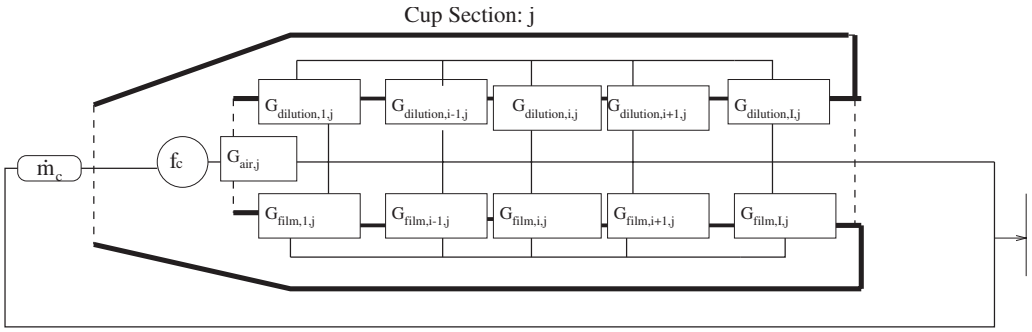

Fig. 6 Sketch of the combustor mass-flow circuit. $\dot{m}_c$ is the total combustor mass-flow, $G_{film,i,j}$ is the flow conductance for the film flow, $G_{dilution,i,j}$ is the flow conductance for the dilution mass-flow, $G_{air,j}$ is the conductance for the dome flow, and f_c is the mass flow-pressure drop function

$$\dot{m}_{dilution,i,j} = G_{dilution,i,j}\sqrt{2\rho_3(P_3 - P_4)} \tag{5}$$

2.3.2 Temperature Field Analysis. A lumped-parameter analysis is used to determine the combustion gas temperatures and the film temperature. The combustor temperature field adjacent to each panel is divided into three elements: the bulk gas temperature, the near-wall gas temperature, and the cooling film temperature. An illustration of these elements is shown in Fig. 7.

The bulk gas temperature ($T_{bulk,i,j}$), the temperature of the mainstream flow near ith panel and jth cup section, is computed using a response surface equation relating the bulk gas temperature to the compressor discharge temperature (T_3) and the bulk gas equivalence ratio ($\phi_{i,j}$).

$$T_{bulk,i,j} = g_1(T_3, \phi_{i,j}) \tag{6}$$

The response surface equation was created by performing a well-stirred reactor analysis at the combustor pressure and average residence time over a range of T_3 and ϕ and, then, applying a regression analysis to these data.

The near-wall gas temperature ($T_{gas,i,j}$) is the temperature of the flow near the liner wall and above the cooling film for the ith panel and jth cup section. The difference between the bulk gas temperature and the near-wall gas temperature is an indication of the radial inhomogeneity of the combustor temperature field. Fast mixing promoted by elevated turbulence levels in the combustion chamber increases the homogeneity of the temperature field. A first-principles approach that links the effects of manufacturing variability to the radial temperature gradients could not be obtained due to the complexity of the combustor aerodynamics and chemistry. As a result, an empirical model was applied in the probabilistic analysis to account for the magnitude and the variability of these radial gas temperature gradients. The empirical model is

$$\frac{T_{gas,i,j} - T_3}{T_{bulk,i,j} - T_3} = g_2\left(\zeta_{i,j}, \frac{x_c}{L_c}\right) = 1 - e^{(-\zeta_{i,j}x_c/L_c)} \tag{7}$$

where x_c is the longitudinal distance from the fuel injector, L_c is the combustor length, and g_2 is a function for the radial gas temperature gradient. $\zeta_{i,j}$, an empirically determined parameter, quantifies the impact of the complex turbulent mixing processes inside the combustor on the radial gas temperature profiles near each liner panel. Higher values of $\zeta_{i,j}$ result in flatter temperature profiles. In particular, the difference between the near-wall gas temperatures and the bulk gas temperatures decreases exponentially as the combustor mixedness level and the distance from the front of the combustor increase. g_2, which is equal to zero at the front of the combustor, signifies that the near-wall gas temperature is equal to the film cooling air temperature. The nominal value of g_2 was determined using rig data for the outlet temperature field, where the bulk temperature is defined as the average of the outlet temperature measurements in each cup section, and the outlet near-wall gas temperature is defined as the average of the thermocouple measurements adjacent to the liner wall in each cup section.

The film cooling flow impacts the liner convection heat transfer load by altering the near-wall film temperature and velocity profiles [1]. The film effectiveness η models the effects of the former. This parameter is used to calculate the cooling film temperature T_{film} along the combustor liner (see Fig. 8). The film effectiveness

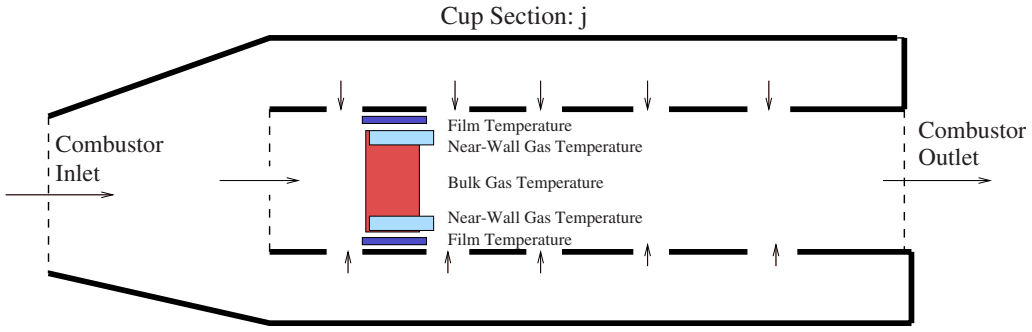

Fig. 7 Sketch of a lumped-parameter model for the combustor temperature field. The temperature field is separated into three driving temperatures and applied in a one-dimensional heat transfer analysis. These temperatures are the bulk gas temperature, the near-wall gas temperature, and the cooling film temperature.

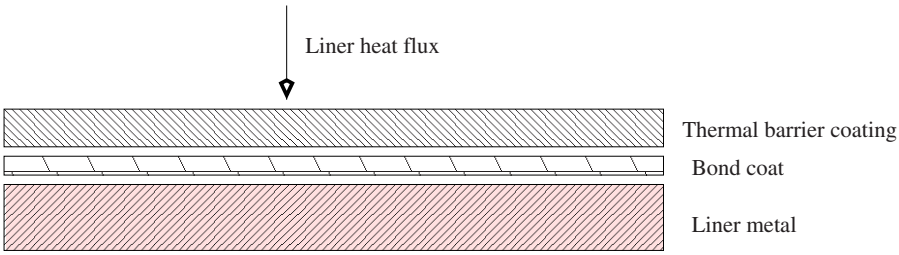

Fig. 8 Sketch of a combustor liner wall

is related to the film temperature, the near-wall gas temperature, and the compressor discharge air temperature for the ith panel and jth cup section by

$$\eta_{i,j} = \frac{T_{\text{gas},i,j} - T_{\text{film},i,j}}{T_{\text{gas},i,j} - T_3} \tag{8}$$

The film effectiveness parameter correlation is a function of the distance from the cooling slot, the cooling slot height (s), and the blowing parameter, which is the ratio of the cooling film mass flux to the mass flux of the near-wall gas flow (B) [1]. The film effectiveness is applied to the degraded cooling film for one panel length. Further mathematical analysis yields a functional relationship among the film effectiveness and three randomly varying parameters, as shown in

$$\frac{T_{\text{gas},i,j} - T_{\text{film},i,j}}{T_{\text{gas},i,j} - T_3} = g_3(\delta_{d,i,j}, s_{i,j}\dot{m}_{\text{air},i,j}) \tag{9}$$

2.3.3 1D Heat Transfer Analysis. A steady one-dimensional heat transfer analysis is performed to estimate the hot-side metal temperature on the inner and outer liners in the ith panel and jth cup section. The model incorporates the effects of radiation, convection, and conduction:

$$\dot{q}_{i,j} = h_{f,i,j}(T_{\text{film},i,j} - T_{\text{TBC},i,j}) + \dot{q}_{\text{rad},i,j} \tag{10}$$

$$\dot{q}_{\text{rad},i,j} = \frac{1}{2}(1 + \epsilon_{\text{TBC}})\bar{\sigma}(\epsilon_{\text{rad},i,j}T_{\text{rad},i,j}{}^4 - \alpha_{\text{rad},i,j}T_{\text{TBC},i,j}{}^4) \tag{11}$$

$$\dot{q}_{i,j} = \frac{k_{\text{TBC}}}{t_{\text{TBC}}}(T_{\text{TBC},i,j} - T_{\text{bnd},i,j}) \tag{12}$$

$$\dot{q}_{i,j} = \frac{k_{\text{bnd}}}{t_{\text{bnd}}}(T_{\text{bnd},i,j} - T_{\text{mh},i,j}) \tag{13}$$

$$\dot{q}_{i,j} = \frac{k_m}{t_m}(T_{\text{mh},i,j} - T_{\text{mc},i,j}) \tag{14}$$

$$\dot{q}_{i,j} = h_{b,i,j}(T_{\text{mc},i,j} - T_3) \tag{15}$$

$$\frac{\alpha_{\text{rad},i,j}}{\varepsilon_{\text{rad},i,j}} = \left(\frac{T_{\text{rad},i,j}}{T_{\text{TBC},i,j}}\right)^{1.5} \tag{16}$$

$$\varepsilon_{\text{rad},i,j} = 1 - \exp(-28\,600P_4\hat{L}(f_{st}\phi_{i,j}l_b)^{0.5}(T_{\text{rad},i,j})^{-1.5}) \tag{17}$$

The random inputs are the thermal conductivities and thicknesses of the TBC, bond coat, and liner (k_{TBC}, k_{bnd}, k_m, t_{TBC}, t_{bnd}, and t_m) and the TBC surface emissivity (ϵ_{TBC}). The random output is the hot-side metal temperature (T_{mh}). The effective radiation temperature ($T_{\text{rad},i,j}$) is set equal to the bulk gas temperature ($T_{\text{bulk},i,j}$). The total liner heat flux ($\dot{q}$), the radiative heat flux ($\dot{q}_{\text{rad}}$), and the TBC, bond coat, and liner temperatures (T_{TBC}, T_{bnd}, T_{mh}, and T_{mc}) are estimated by solving the model equations with a Newton–Raphson method.

2.3.4 Liner Life Analysis. The primary failure mode for the combustor liners studied is low-cycle fatigue (LCF) [6–8]. The cracks that form and propagate along the liner are caused by elevated liner temperatures, temperature gradients, and thermal stresses. Combustor liners with crack lengths exceeding specified limits are classified as failed parts. The model output is the low-cycle fatigue life. The random input to the life model is the hot-side liner temperature, and the deterministic inputs are the compressor discharge temperature, the baseline liner stress, the baseline liner temperature, and a parameter that accounts for the material property variability. The baseline liner temperature and stress for each combustor panel were determined from three-dimensional thermal analyses conducted by an engine company during the combustor development process [8].

An LCF life analysis was applied to each section of the combustor liner in order to account for these effects. For a combustor with J cup sections, I panels, an inner liner, and an outer liner, the number of liner life calculations equals $2IJ$. The overall liner life for each combustor is defined as the minimum life in a set consisting of $2IJ$ points. The failure of one part of the liner constitutes an overall failure of the combustor.

The total low-cycle fatigue life of the ith panel and jth cup section is determined from

$$N_{f,i,j} = (N_{f,i,j}^{\text{init}} + N_{f,i,j}^{p})(1 + \Psi) \tag{18}$$

where $N_{f,i,j}$ is the low-cycle fatigue life, $N_{f,i,j}^{\text{init}}$ is the crack initiation life, $N_{f,i,j}^{p}$ is the crack propagation life, and Ψ, the LCM, accounts for the effects of the material property variability. Ψ is set to zero during a deterministic analysis. For a probabilistic analysis, Ψ is represented by a normally distributed random variable. Its standard deviation is determined from the data scatter about the average crack initiation life curve.

The crack initiation life analysis was based on a low-fidelity model used by an engine company [6]. The model consists of two curves: an average life curve and a minimum life curve. The average life curve is a response surface equation that relates the alternating strain to the number of cycles-to-crack initiation. The minimum life curve, which is three standard deviations below the average life curve, accounts for the data scatter caused by the effects of material property variability. Using these curves in combination at a specified metal temperature yields the average crack initiation life and its variability.

The crack propagation life analysis was conducted using response surface equation derived from data for crack growth rates for Hastelloy X [9]. The variability of the crack propagation life due to material property variability could not be quantified due to the absence of data. As a result, the material property variability effects applied to the crack initiation life model were also applied to the crack propagation life model for the analysis presented in this paper.

3 Probabilistic Model Assessment

A Monte Carlo analysis was applied to the simplified models of two aircraft gas turbine combustor designs from two different en-

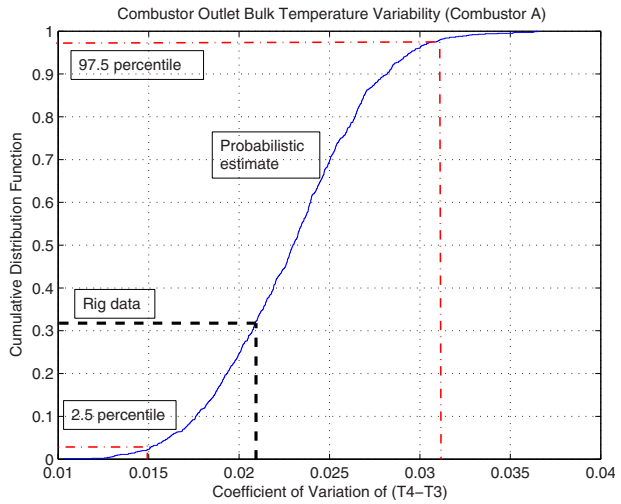

Fig. 9 Combustor A outlet bulk temperature variability

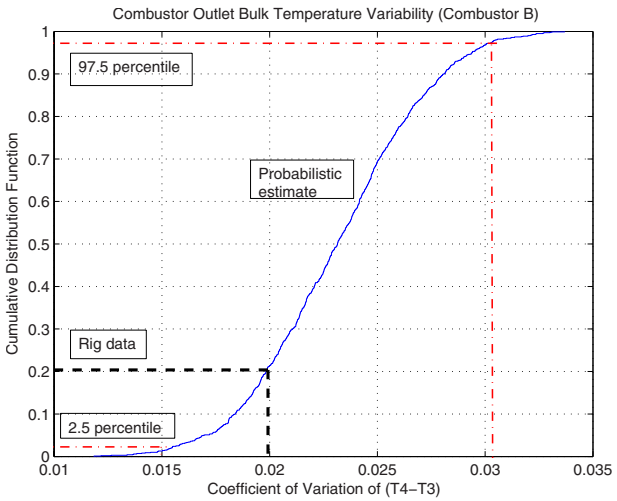

Fig. 10 Combustor B outlet bulk temperature variability

gine families that are currently in use in the commercial fleet. We label them Combustors A and B. The results were compared with a statistical analysis of the bulk gas temperature distribution at the combustor outlet, the liner wall temperature measurements, and the field failure data provided by an engine company [6].

3.1 Combustor Outlet Temperature. A comparative analysis of the bulk temperature variability at the combustor outlet was performed to assess the network flow model. The combustor data were acquired from a five thermocouple-rake that traversed the outlet plane in 3.6 deg increments, yielding 500 data points. The combustor annulus was divided into J regions corresponding with the J cup sections. The data points in each cup section were averaged to compute the outlet bulk gas temperature for each cup section, and this analysis yielded J outlet bulk temperatures. Then, the coefficient of variation of the J bulk temperatures at the outlet were calculated.

The probabilistic model estimates of the coefficient of variation of the temperature rise $(T_4 - T_3)$ across Combustors A and B were compared with statistical estimates of the bulk temperature variability obtained from the combustor rig data. The probabilistic model estimate of the coefficient of variation was calculated from a 1000-trial Monte Carlo simulation, where the coefficient of variation of the combustor temperature rise was determined for each trial.

The outlet bulk temperature variabilities determined from the rig data are within the 2.5- and 97.5-percentile values of the probabilistic estimates for Combustors A and B, as shown in Figs. 9 and 10. The probabilistic estimates of the bulk temperature variability of the outlet are consistent with the statistical estimates from the combustor rig data, which validates the application of the network flow model for determining the cup-to-cup bulk gas temperature variability.

3.2 Combustor Liner Temperature. The probabilistic model estimates of the combustor liner temperatures determined from 1000-trial Monte Carlo simulations were compared with wall temperature measurements acquired from combustor rig tests performed by an engine company. However, these combustor rig data do not present an ideal data set. These liner data were not collected for the purpose of assessing this model but rather were data that were available from prior testing of the combustor. For a statistical analysis, the thermocouples in each combustor cup section should have been assigned to coordinates that were fixed relative to each fuel injector to mitigate the influence of circumferential and longitudinal metal temperature gradients on the wall temperature measurements. The paucity of data resulted in the inner and outer liner temperature measurements being lumped into the same data set prior to the statistical analysis of Combustor A. In addition, the thermocouples were placed in a single cup section over four panels for Combustor B. As a result, a comparison of the probabilistic estimate of the cup-to-cup wall temperature variability to a statistical analysis of the data was not performed.

Liner wall temperature measurements for Combustor A were acquired from a rig test. The thermocouples were placed on hot spots, or elevated-temperature areas, that were previously identified using thermal paint [10]. In particular, the hot spots were located in four to eight separate cup sections for Panels 1–4. The inner and outer liner wall temperature measurements for each panel were lumped together prior to the statistical analysis due to the small amount of available data. These measurements were averaged within each cup section to yield a single temperature. The mean and standard deviation of the temperature difference between the thermocouple measurements and a reference temperature (T^o_{mh}) for each Combustor A panel were computed and then compared to the probabilistic model estimates, as shown in Figs. 11 and 12. The probabilistic estimates of the mean and standard deviation of the liner temperatures for Panels 1, 2, and 4 fall outside of the 95% confidence bounds of the thermocouple data. The mean liner temperature estimate falls within these confidence bounds for Panel 3. The estimate of the liner temperature standard deviation is approximately 1–2 K less than the lower confidence bound on the standard deviation of the thermocouple data for Panels 1 and 2. For Panel 3, the model estimate of the standard deviation is approximately 12 K less than the lower confidence bound on the estimate from the thermocouple data. For Panel 4, the probabilistic model estimate of the standard deviation falls within the confidence bounds of the thermocouple data measurements. Overall, the probabilistic model underestimates the cup-to-cup liner temperature variability compared to the variability estimated from the thermocouple data. However, given the incomplete nature of the rig data that were available, this comparison only provides a limited assessment of the model.

3.3 Combustor Liner Life. Monte Carlo analyses of two gas turbine combustors A and B from different engine families were performed. Each Monte Carlo analysis consisted of 10 000 trials and required approximately 12 h of computation time. The liner life distributions of these combustors are shown in Fig. 13 and Fig. 14, where the difference between the probabilistically determined liner life (N_f) and the deterministically determined liner life (N^o_f) is normalized by the latter parameter. This derived parameter quantifies the shift of the life distribution away from the nominal life. For each combustor, the typical, or median, life is 20% less

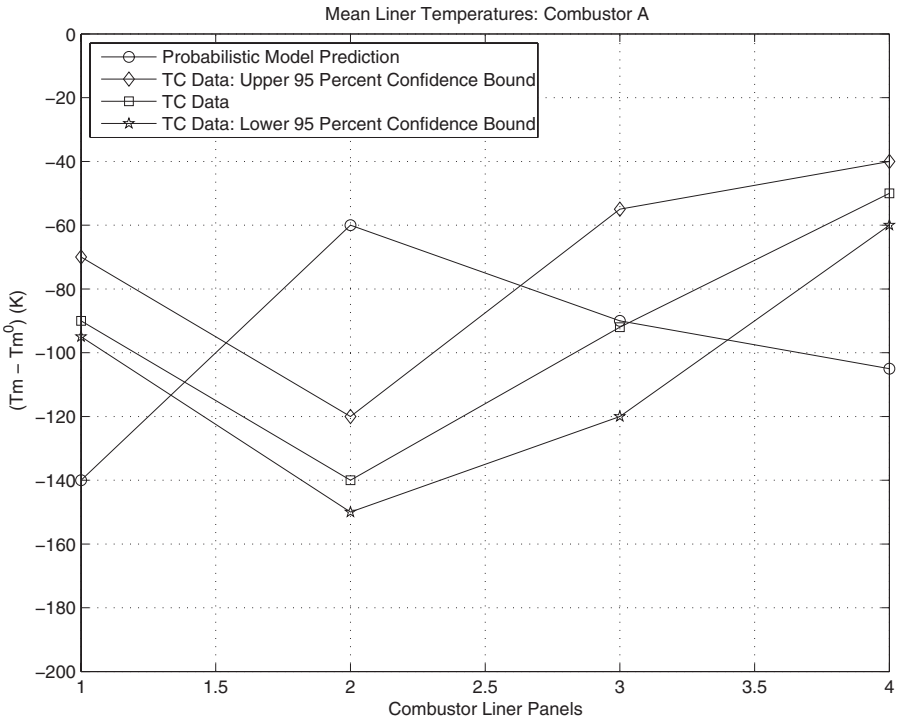

Fig. 11 Mean liner temperatures: Combustor A

than the nominal life, and the probability that a particular combustor will fail earlier than predicted using a deterministic calculation is 80%.

A Weibull analysis of the Combustor B field data and the results of the probabilistic analysis (Fig. 15) were compared. The parameters used in the comparison were the coefficient of variation of the life distribution and the Weibull distribution shape parameter. The probabilistic analysis yields a coefficient of variation that is 100% of the field data value. Furthermore the shape parameter—another measure of the variability of a Weibull distribution—is 96% of the field data value. Thus, incorporating the effects of the material property variability into the lifing analysis yields an accurate estimate of the variability in the Combustor B field failure data.

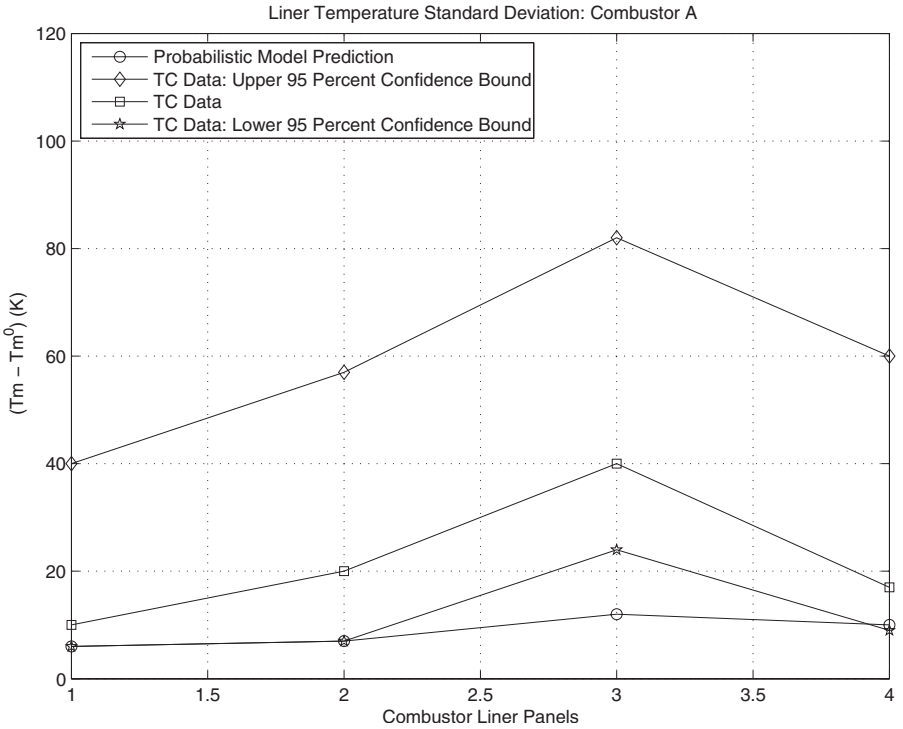

Fig. 12 Liner temperature standard deviation: Combustor A

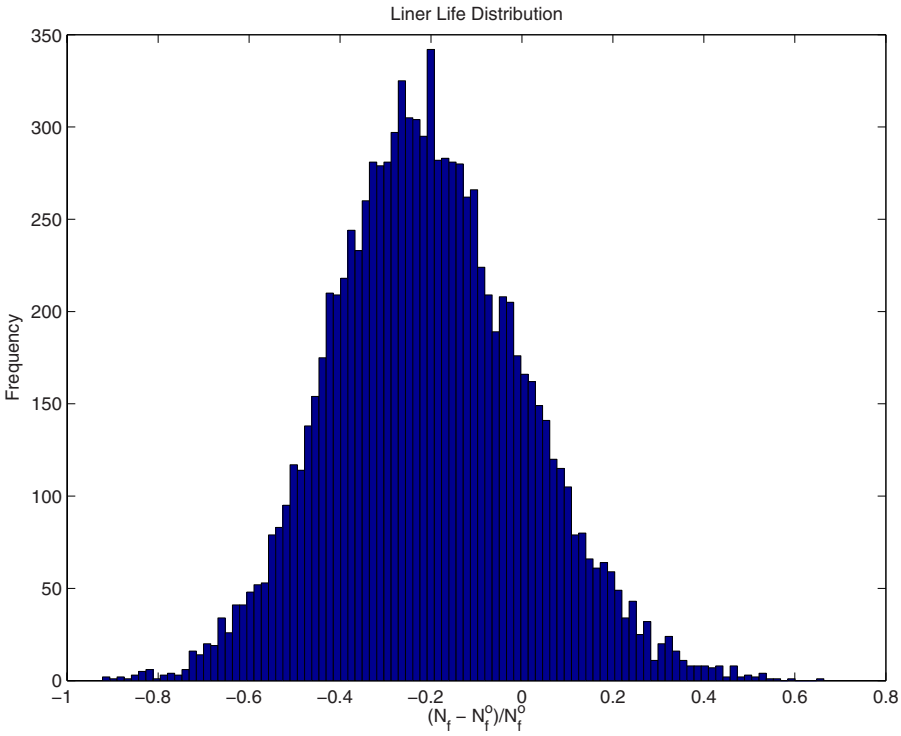

Fig. 13 Combustor A liner life distribution

4 Sensitivity Analysis

4.1 Methodology. This section presents a methodology for determining the leading drivers of the combustor liner life. A regression analysis is applied to the Monte Carlo data in order to establish a simplified representation of the relationship between the combustor liner life in each cup section and the random variables introduced in Sec. 2.2. This surrogate model is subsequently used to identify the leading drivers of the liner life (see Fig. 15). Specifically, the impact of increasing and decreasing the manufacturing tolerances on the combustor liner life distribution is quantified. Applying a surrogate model for the life enables an execution of several sensitivity studies at a lower computational expense than directly applying the combustor model.

The response surface analysis is applied to the Monte Carlo

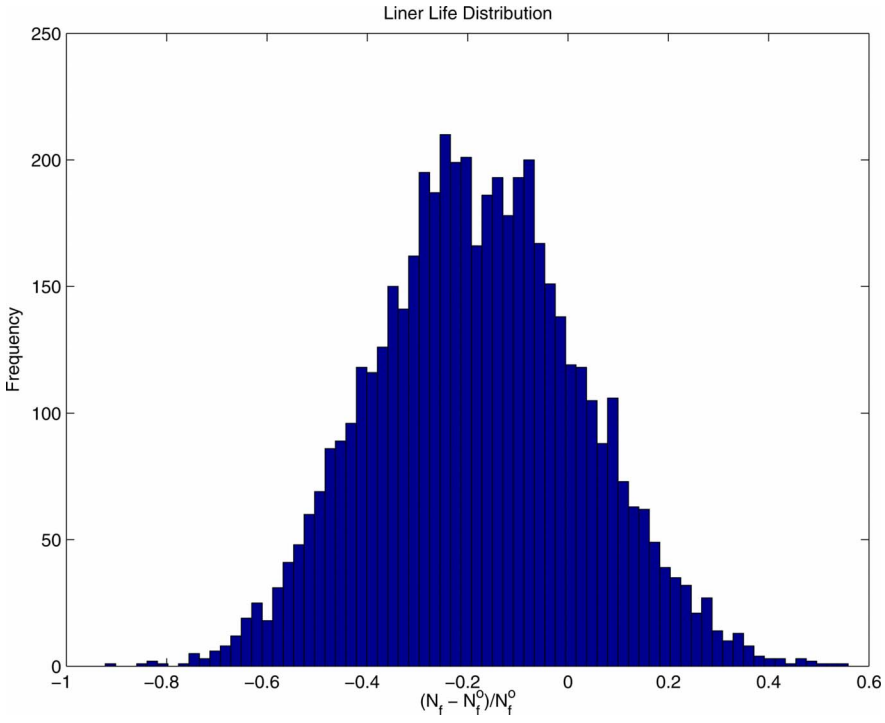

Fig. 14 Combustor B liner life distribution

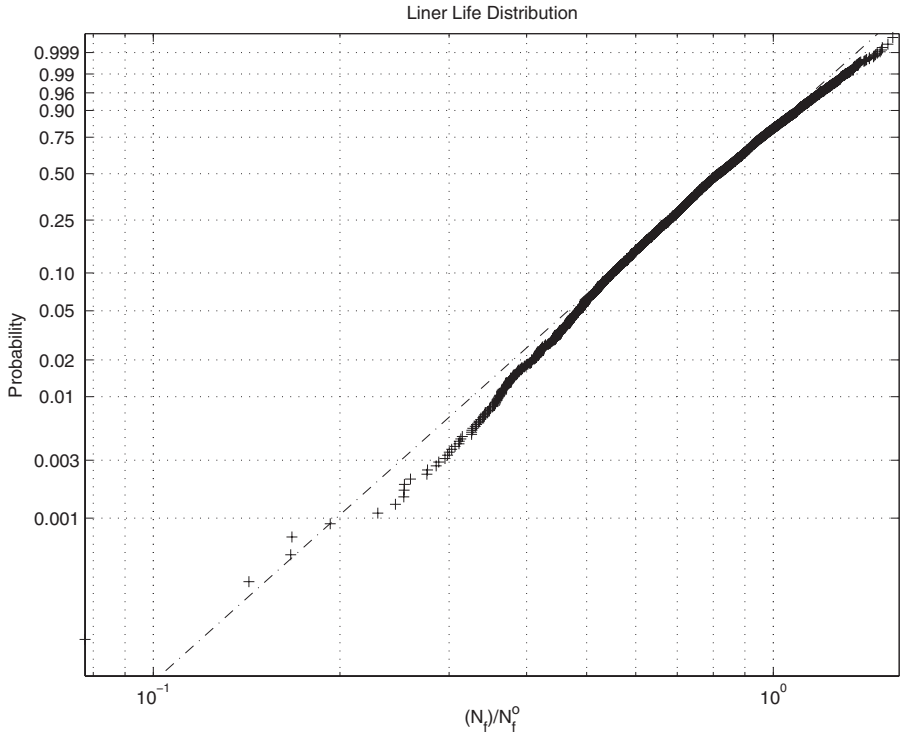

Fig. 15 Combustor B life CDF on a Weibull scale

data in the following manner. First, the liner life data are separated by cup sections. Second, a regression analysis is applied to the life distribution and input Parameters 1–12 for the jth cup section. These data are fitted to a quadratic multivariate response surface equation

$$Y_j = a_{0,j} + \sum_{n=1}^{12} b_{n,j}\hat{x}_{n,j} + \sum_{n=1}^{12} c_{n,j}\hat{x}_{n,j}^2 \tag{19}$$

where Y_j, the standardized random variate for the natural logarithm of liner life for the jth cup section, is determined from

$$Y_j = \ln(N_{f_j}) \tag{20}$$

and $\hat{x}_{n,j}$, the nth standardized random input in the jth cup section, is determined from

$$\hat{x}_{n,j} = \frac{x_{n,j} - \mu_n}{\sigma_n} \tag{21}$$

Third, the adequacy of the response surface fit is checked. These response surface equations capture most of the variability exhibited in the Monte Carlo data. The coefficient of multiple determination quantifies the proportion of variability explained by the response surface equation. It is approximately 97% and 93% for the Combustors A and B response surfaces, respectively. Furthermore, the percent errors of the standard deviation estimated by the response surfaces are 2% and 4% for Combustors A and B, respectively.

Each regression coefficient exhibits a cup-to-cup variability. The source of this variability is sampling error. The variability of the coefficients implies that the cup sections will yield different nominal values of liner life for the same inputs. Ideally, the nominal cup section lives would be identical for the same inputs.

There are two ways to mitigate the effects of sampling error. The first approach consists of increasing the number of trials run in the Monte Carlo analysis. However, the slow convergence of the Monte Carlo simulation increases the computational expense of this option. An alternative approach is to define the response surface based on cup-average regressors. In other words, each regression coefficient was averaged over J cups. The averaged coefficients are determined from

$$\bar{a}_0 = \frac{1}{J}\sum_{j=1}^{J} a_{0,j} \tag{22}$$

$$\bar{b}_n = \frac{1}{J}\sum_{j=1}^{J} b_{n,j} \tag{23}$$

$$\bar{c}_n = \frac{1}{J}\sum_{j=1}^{J} c_{n,j} \tag{24}$$

The averaging procedure yields

$$\ln(N_{f,j}) = \bar{a}_0 + \sum_{n=1}^{12} \bar{b}_n\hat{x}_{n,j} + \sum_{n=1}^{12} \bar{c}_n\hat{x}_{n,j}^2 \tag{25}$$

a response surface for the life that uniformly responds to perturbations of the inputs. The liner life of the jth cup section is estimated using

$$N_{f,j} = \exp\left(\bar{a}_0 + \sum_{n=1}^{12} \bar{b}_n\hat{x}_{n,j} + \sum_{n=1}^{12} \bar{c}_n\hat{x}_{n,j}^2\right)(1+\Psi) \tag{26}$$

where Ψ incorporates the effects of the material property variability. Equation (26), which determines the life distribution of the jth cup section for M combustors, is then postprocessed to yield the total combustor life distribution.

A one-at-a-time (OAT) sensitivity analysis was applied to the response surfaces to quantify the impact of changing the input variations on the life distribution. The standard deviation of each random variable was reduced by 90% while holding the remaining parameter standard deviations constant. Next, a Monte Carlo analysis consisting of 50 000 trials was performed with the updated standard deviations of these parameters. Then, the combus-

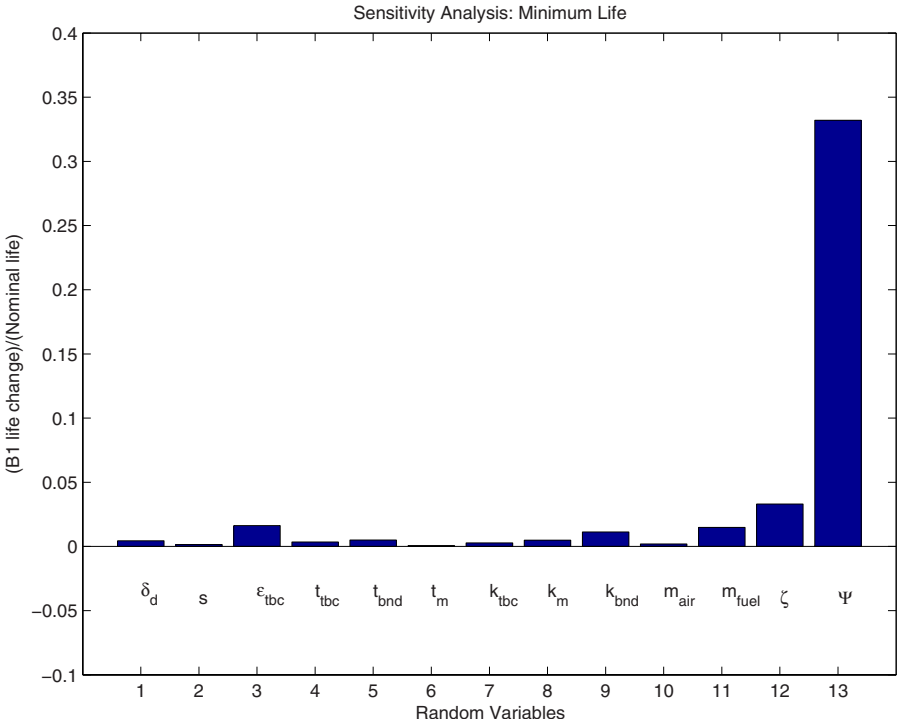

Fig. 16 Combustor A: B_1 life change for a 90% tolerance decrease

tor life was computed by taking the minimum value of the response surfaces over J cups for each combustor. The minimum combustor lives B_1 and the typical combustor lives B_{50} of M combustors were estimated for each case. These estimates were compared with the Monte Carlo results presented earlier in the paper. The B_1 and the B_{50} were normalized by the nominal life and presented on bar graphs.

4.2 Results. Decreasing the input standard deviations in a one-at-a-time fashion by 90% increases the B_1 and the B_{50} lives, as shown in Figs. 16 and 17. Specifically, the Combustor A B_1 life increases by approximately 33% of the nominal life when the standard deviation of the life curve multiplier Ψ is reduced by 90%. The B_1 life increases by less than 3% of the nominal life

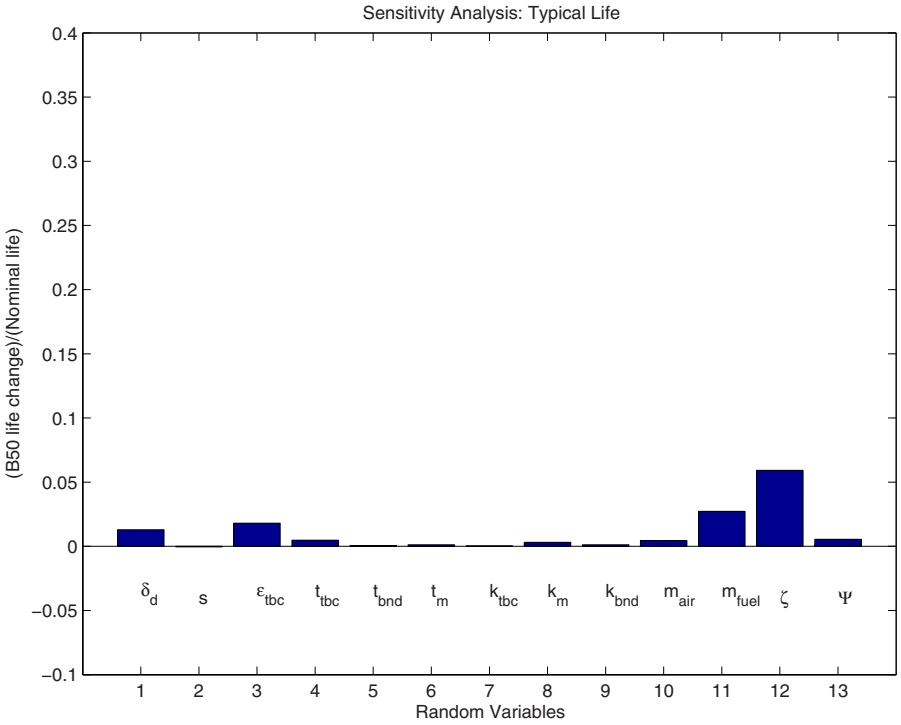

Fig. 17 Combustor A: B_{50} life change for a 90% tolerance decrease

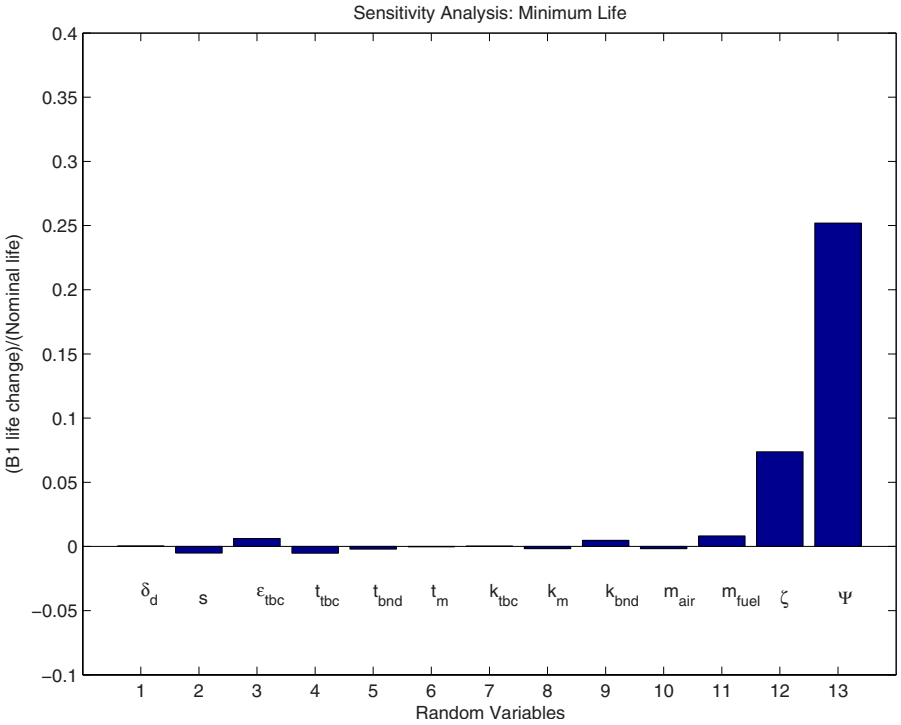

Fig. 18 Combustor B: B_1 life change for a 90% tolerance decrease

when the standard deviations of Parameters 1–12 are reduced by 90%. Futhermore, the Combustor A B_{50} life increases by approximately 6% of the nominal life when the standard deviation of ζ is reduced by 90%. Reducing the variability of Ψ by 90% changes the B_{50} life by less than 1% of the nominal life. The results show that Ψ and ζ are the leading drivers of the B_1 life and B_{50} life, respectively, for Combustor A.

Figures 18 and 19 show decreasing the variability of Ψ by 90% yields a B_1 life increase of approximately 25% of the nominal life and a B_{50} life increase of approximately 1% of the nominal life for Combustor B. Also, decreasing the variability of the mixedness parameter ζ by 90% increases the combustor B B_1 life and B_{50} life by approximately 7% and 17% of the nominal life, respectively. The results show that the life curve multiplier Ψ and the mixedness parameter ζ, are the leading drivers of the B_1 life and B_{50} life, respectively, for Combustor B.

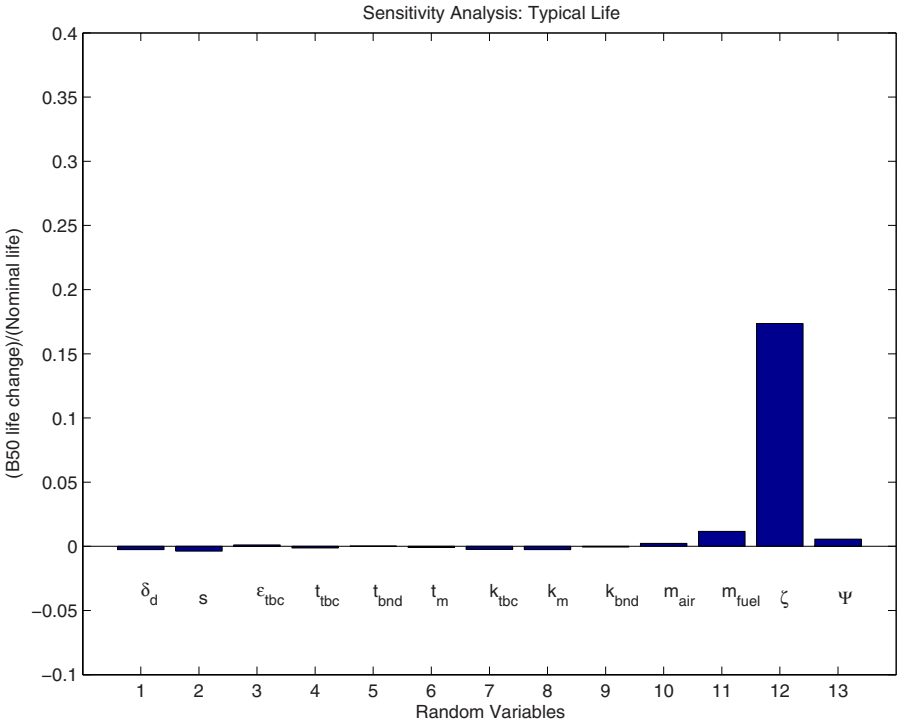

Fig. 19 Combustor B: B_{50} life change for a 90% tolerance decrease

5 Summary

This paper has presented probabilistic and statistical techniques used to assess the impact of manufacturing variability on combustor liner durability. A probabilistic modeling framework that links the manufacturing variability of the liner, the fuel flow variability, and the dome air flow variability to the combustor liner temperature and combustor liner low-cycle fatigue life was presented. A probabilistic analysis showed that a randomly selected combustor designed to the life predicted using deterministic methods may fail earlier than expected, and that the typical combustor life is 20% less than the nominal life. Futhermore, the probabilistic estimate of the life distribution variability for Combustor B was consistent with the variability in the field failure data. A sensitivity analysis showed that the material property variability and the combustor mixedness parameter were the leading drivers of the minimum combustor life and the typical combustor life, respectively. The selection of materials with lower material property variability will reduce the liner life variability, and by extension, increase the minimum combustor life. Furthermore, combustor configurations yielding lower circumferential variability of turbulent mixing rates will increase the typical combustor life.

Acknowledgment

The authors would like to acknowledge the funding provided by the Ford Foundation. We would also like to thank Harris Abramson and Aureen Currin of GE Aircraft Engines for providing us with the experimental and numerical data that were used to assess our model. Finally, we would like to thank David Darmofal and Edward Greitzer of MIT for their insightful critiques of this research.

Nomenclature

α = absorptivity
L_c = combustor length
ρ = density
x_c = distance from combustor front end
ε = emissivity
ϕ = equivalence ratio
η = adiabatic film effectivness
$\hat{L}$ = flame luminosity factor
h = heat transfer coefficient
$\dot{q}$ = liner heat flux
N_f = low-cycle fatigue life
$\dot{m}$ = mass-flow rate
f_c = mass flow-pressure drop function
G = mass-flow conductance
l_b = mean beam length
μ = mean value
δ_d = metering hole diameter multiplier
P = pressure
χ = random variable
Y = response surface equation output
s = slot height
σ = standard deviation
$\bar{\sigma}$ = Stefan–Boltzmann constant
fst = stoichiometric fuel-air ratio
$\hat{\sigma}$ = stress
T = temperature
k = thermal conductivity
t = thickness
ζ = turbulent mixing parameter

References

[1] Lefebvre, A., 1999, *Gas Turbine Combustion*, Taylor and Francis, London.
[2] Lykins, C., Thompson, D., and Pomfret, C., 1994, "The Air Force's Application of Probabilistics to Gas Turbine Engines," AIAA Paper No. 94-1440-CP.
[3] Garzon, V. E., and Darmofal, D. L., 2003, "Impact of Geometric Variability in Axial Compressor Performance," ASME J. Turbomach., **125**(4), pp. 692–703.
[4] Sidwell, V., and Darmofal, D. L., 2004, "A Selective Assembly Method to Reduce The Impact of Blade Flow Variability on Turbine Life," ASME Paper No. GT2004-53581.
[5] Mavris, D., and Roth, B., 1997, "A Methodology For Robust Design of Impingement Cooled HSCT Combustor Liners," AIAA.
[6] Stephens, S., and Shaw, M., 2004, personal communication, GE Aircraft Engines.
[7] Mascarenas, A., 2004, personal communication, Delta Airlines.
[8] Currin, A., 2004, personal communication, GE Aircraft Engines
[9] Jablonski, D. A., 1978, "Fatigue Behavior of Hastelloy-X at Elevated Temperatures in Air, Vacuum, and Oxygen Environments," Ph.D thesis, MIT, Cambridge, MA.
[10] Monty, J., 2003, personal communication, GE Aircraft Engines.

Modeling Soot Formation Using Reduced Polycyclic Aromatic Hydrocarbon Chemistry in *n*-Heptane Lifted Flames With Application to Low Temperature Combustion

Gokul Vishwanathan
Research Assistant
e-mail: gvishwanatha@wisc.edu

Rolf D. Reitz
Wisconsin Distinguished Professor
e-mail: reitz@engr.wisc.edu

Engine Research Center,
Department of Mechanical Engineering,
University of Wisconsin-Madison,
Madison, WI 53706

A numerical study of in-cylinder soot formation and oxidation processes in n-heptane lifted flames using various soot inception species has been conducted. In a recent study by the authors, it was found that the soot formation and growth regions in lifted flames were not adequately represented by using acetylene alone as the soot inception species. Comparisons with a conceptual model and available experimental data suggested that the location of soot formation regions could be better represented if polycyclic aromatic hydrocarbon (PAH) species were considered as alternatives to acetylene for soot formation processes. Since the local temperatures are much lower under low temperature combustion conditions, it is believed that significant soot mass contribution can be attributed to PAH rather than to acetylene. To quantify and validate the above observations, a reduced n-heptane chemistry mechanism has been extended to include PAH species up to four fused aromatic rings (pyrene). The resulting chemistry mechanism was integrated into the multidimensional computational fluid dynamics code KIVA-CHEMKIN for modeling soot formation in lifted flames in a constant volume chamber. The investigation revealed that a simpler model that only considers up to phenanthrene (three fused rings) as the soot inception species has good possibilities for better soot location predictions. The present work highlights and illustrates the various research challenges toward accurate qualitative and quantitative predictions of the soot for new low emission combustion strategies for internal combustion engines. [DOI: 10.1115/1.3043806]

Keywords: soot modeling, low temperature combustion, polycyclic aromatic hydrocarbons, lift-off length, reduced chemistry

1 Introduction

Modeling soot formation under internal combustion (IC) engine operating conditions has been a long-standing challenge for researchers. As Kennedy [1] summarized, the complexity of modeling soot has motivated three approaches in soot modeling, viz., empirical modeling, semi-empirical modeling, and detailed soot modeling. Empirical correlations may use a single rate equation based on curve fits of experimental data. Semi-empirical models may use one or more rate equations for soot formation and oxidation, while detailed models incorporate comprehensive chemical kinetics, including polycyclic aromatic hydrocarbons (PAHs). The complexity of soot modeling is further aggravated by the many physical processes that soot particles undergo at these conditions, viz., coagulation, surface growth, condensation, etc. Nevertheless, detailed models are computationally prohibitively expensive, particularly for 3D engine computational fluid dynamics (CFD) calculations and hence simpler, yet reasonably accurate models are currently being used for engine calculations.

The type of precursors responsible for soot formation is still under debate. For example, it has been found in ethylene flames that acetylene (C_2H_2) provides the major contribution to the total soot mass [2]. Also, C_2H_2 has been widely used as the soot precursor in engine calculations. However, in a recent study by the authors [3], it was found that C_2H_2 was not satisfactory for soot predictions in *n*-heptane lifted flames, particularly under low temperature combustion (LTC) conditions. It was found that although present generation soot models applicable to IC engines could be tuned to yield the total in-cylinder soot, the regimes of soot formation/oxidation could not be accurately captured using only C_2H_2 as the precursor for soot. The experimental observations of Idicheria and Pickett [4] against which the soot models [3] were compared showed PAH formation occurring far downstream in the lifted flame and hence the soot formation/oxidation region was far downstream when compared with the predictions of the model. This led to the conclusion that PAH chemistry might play an important role not only for accurate soot mass predictions but also for accurate predictions of soot location within the flame.

Accordingly, the present study focuses on incorporating PAH chemistry up to four fused aromatic rings (pyrene or A_4) into the present reduced *n*-heptane chemistry mechanism. 2D axisymmetric spray simulations were run for *n*-heptane lifted flames in a constant volume combustion chamber using the CFD code KIVA-CHEMKIN. Four precursor candidates, viz., benzene (A_1), naphthalene (A_2), phenanthrene (A_3), and pyrene (A_4), were considered for soot inception. It was found that A_3 is promising for use as a

Manuscript received May 28, 2008; final manuscript received May 31, 2008; published online February 11, 2009. Review conducted by Dilip R. Ballal. Paper presented at the 2008 Spring Conference of the ASME Internal Combustion Engine Division (ICES2008), Chicago, IL, April 27–30, 2008.

Table 1 Original and present ERC reaction mechanisms; note that units are mol, cm, K, and cal

Reaction	Baseline mechanism rates [8]	Updated ERC mechanism rates
$nC_7H_{16}+OH=C_7H_{15}-2+H_2O$	9.7×10^9, 1.3, 1690	4.8×10^9, 1.3, 690.5 [9]
$nC_7H_{16}+O_2=C_7H_{15}-2+HO_2$	2×10^{15}, 0, 47,380	2.8×10^{14}, 0, 47,180 [9]
$C_7H_{15}-2+O_2=C_7H_{15}O_2$	2×10^{12},0,0	1.56×10^{12},0,0 [9]
$C_7H_{15}O_2=C_7H_{14}O_2H$	-	6.00×10^{11}, 0, 20,380 [9]
$C_7H_{14}O_2H+O_2=C_7H_{14}O_2HO_2$	-	2.34×10^{11},0,0 [9]
$C_7H_{14}O_2HO_2=nC_7KET_{21}+OH$	-	2.96×10^{13}, 0, 26,700 [9]
$CH_3O(+M)=CH_2O+H(+M)$	-	$K_\infty=2\times10^{13}$, 0, 27,420 $K_0=2.34\times10^{25}$, −2.7, 30,600 [9]
$OH+OH(+M)=H_2O_2(+M)$ [a] (present study)		$K_\infty=2.5\times10^{13}$, −0.37, 0 $K_0=3.0\times10^{30}$, −4.6, 2049 [12]
$H_2O_2+M=OH+OH+M$ [8]	1×10^{16}, 0, 45,500	
$CH_3+CH_3(+M)=C_2H_6(+M)$ [b]	-	$K_\infty=1.81\times10^{13}$,0,0 $K_0=1.27\times10^{41}$, −7, 2762.91 [10]
$C_2H_6+H=C_2H_5+H_2$	-	540, 3.5, 5210.33 [10]
$C_2H_6+O=C_2H_5+OH$	-	1.4, 4.3, 2772.47 [10]
$C_2H_6+OH=C_2H_5+H_2O$	-	2.2×10^7, 1.9, 1123.33 [10]
$C_2H_6+CH_3=C_2H_5+CH_4$	-	0.55, 4, 8293.50 [10]
$C_2H_6(+M)=C_2H_5+H(+M)$ [c]	-	8.85×10^{20}, −1.23, 102,222.7 [10]
$C_2H_6+HO_2=C_2H_5+H_2O_2$	-	1.32×10^{13}, 0, 20,470 [10]

[a]The pre-exponential factor of the high pressure rate is 1×10^{14} but has been tuned to 2.5×10^{13}.
[b]Troe parameters are 0.62, 73, and 1180 and $\eta_{H_2}=2$, $\eta_{H_2O}=6$, $\eta_{CH_4}=2$, $\eta_{CO}=1.5$, $\eta_{CO_2}=2$, and $\eta_{C_2H_6}=3$.
[c]Troe parameters are 0.84, 125, 2219, and 6882 and $\eta_{H_2}=2$, $\eta_{H_2O}=6$, $\eta_{CH_4}=2$, $\eta_{CO}=1.5$, $\eta_{CO_2}=2$, and $\eta_{C_2H_6}=3$.

soot inception species for better resolution of soot formation and oxidation regimes.

2 Models

Combustion model. The combustion model used in the present study is incorporated in the KIVA-CHEMKIN code [5]. CHEMKIN [6] is the chemistry solver that is coupled to the multidimensional CFD code KIVA [7] for solving detailed gas phase chemistry. The CFD solver KIVA provides local thermodynamic and species information to the CHEMKIN solver, which, in turn, calculates the formation/consumption of species based on the local conditions. In this study the chemistry is directly integrated with the species and energy conservation equations and subgrid scale turbulence-chemistry interaction is not considered. Detailed information about the combustion model is given by Kong et al. [5].

Chemistry mechanism. An *n*-heptane reduced chemistry mechanism developed by Patel et al. [8] was modified for the present study. Modifications were made to better predict lift-off lengths in flames. The reactions suggested by Maroteaux and Noel [9] were added to the mechanism. In addition, ethane (C_2H_6) chemistry [10] was also added. The addition of C_2H_6 chemistry was found not to change the ignition delay time but the dissociation of C_2H_6 to the ethyl radical (C_2H_5), which then leads to the formation of ethylene (C_2H_4) and subsequently to C_2H_2, provides an additional pathway for PAH and soot formation. Warnatz [11] showed that for rich methane-air flames, the methyl radical (CH_3) reacts with itself to form C_2H_6, which, in turn, forms a major pathway for C_2H_2 and hence PAH formation as the higher PAH molecules are formed from C_2H_2 by the hydrogen abstraction carbon addition (HACA) mechanism. Table 1 shows the major modifications done to the baseline engine research center (ERC) mechanism.

The reduced PAH mechanism used in the present study was that of Xi and Zhong [13]. This reduced mechanism has 30 additional reaction steps, which lead to the formation of ring aromatic species (up to four rings) from linear hydrocarbons. The important steps for the ring formation are as follows:

$$C_3H_3 + C_3H_3 \rightarrow A_1$$

$$A_{1^-} + C_4H_4 \leftrightarrow A_2 + H$$

$$A_1 + A_{1^-} \leftrightarrow P_2 + H$$

$$A_2\text{-}1 + C_4H_4 \leftrightarrow A_3 + H$$

$$A_1C_2H^* + A_1 \leftrightarrow A_3 + H$$

$$A_3\text{-}4 + C_2H_2 \leftrightarrow A_4 + H$$

The final *n*-heptane/PAH reduced reaction mechanism consisted of 56 species and 108 reactions.

Soot model. The soot model used in the present study is the two-step soot model consisting of competing formation and oxidation steps. The Hiroyasu soot formation [14] and Nagle and Strickland-Constable oxidation [15] models were used. The governing equations for the soot model are as follows:

$$\frac{dM_s}{dt} = \frac{dM_{sf}}{dt} - \frac{dM_{so}}{dt} \tag{1}$$

$$\frac{dM_{sf}}{dt} = K_f M_{pre} \tag{2}$$

$$K_f = A_{sf} P^n \exp(-E_f/RT) \tag{3}$$

$$\frac{dM_{so}}{dt} = \frac{6M_{w_C}}{\rho_s D_s} M_s R_{total} \tag{4}$$

In the present study, $n=0.5$, $E_f=12{,}500$ cal/mol, $\rho_s=2$ g/cm^3, and $D_s=25$ nm. More details about the soot model are given by Vishwanathan and Reitz [3]. Similar to the previous study [3], the re-normalized group (RNG) k-ε model was used for turbulence modeling and the spray droplet breakup was modeled using the Kelvin–Helmholtz and Rayleigh–Taylor (KH-RT) hybrid model.

3 Numerical Considerations

The SANDIA constant volume chamber is a cube, 108 mm on each side. The chamber is equipped with sapphire windows for line of sight and orthogonal optical access [16]. Laser extinction measurements and planar laser induced incandescence (PLII) images were taken to estimate the soot mass in the *n*-heptane fuel jet. Integrated in-cylinder soot mass across the jet (i.e., in the radial direction) was estimated in the experiments. The integrated soot mass along each 1 mm radial slice probed by the laser was calculated during the quasisteady stage of combustion based on the experimental extinction signal and PLII images. More details can be found in Ref. [16].

In the present study, 2D axisymmetric spray computations were performed using a cylindrical mesh (bore of 12.6 cm and height of 10 cm) with volume similar to the experimental chamber. The

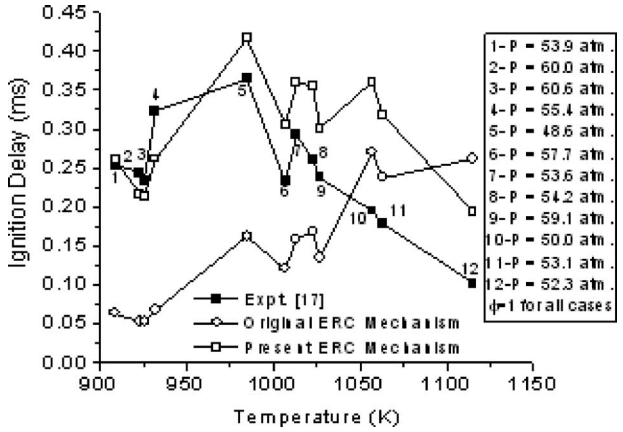

Fig. 1 Ignition delay predictions with original and present ERC mechanisms compared with experiments [17]

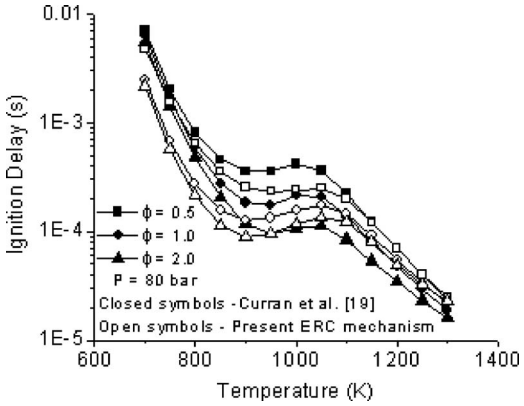

Fig. 3 Ignition delay predictions of the present ERC and the mechanisms of Curran et al. [19] at 80 bar

computational grid had cell sizes expanding from 0.5×0.5 mm^2 near the nozzle to 1.5×1.5 mm^2 far away from the nozzle. This mesh resolution has been found to give adequate mesh-free results [3]. Integrated soot and precursor mass along the radial direction for 1 mm radial slices at the end of injection (6.8 ms) was estimated and compared with the experiments. The injector nozzle diameter was 100 μm and a top hat injection profile was used, as described in Ref. [3].

4 Results and Discussion

Ignition delay validation. The modified mechanism incorporating the revised reactions of Table 1 and the PAH chemistry was also tested with the experimental shock tube ignition delay data of Gauthier et al. [17]. Figure 1 shows predictions of ignition delay with the modified and the original ERC mechanisms as compared with the experimental data points (the lines in the plot are for the sake of clarity). The predicted ignition delays were obtained with the 0D constant volume SENKIN code [18]. It is seen that the modified mechanism agrees fairly well with the experimental ignition delay data, particularly in the temperature range of 900–1025 K. Since there is a dearth of experimental ignition delay data for pressures higher than 60 atm., the ignition delay predictions of the present modified mechanism were also compared with the predictions of the comprehensive primary reference fuel (PRF) mechanism (910 species and 4236 reactions) of Curran et al. [19]. Ignition delay times at various conditions (P=40 bar and 80 bar, temperature of 700–1300 K, and Φ=0.5, 1, and 2) were tested for constant volume combustion chamber using SENKIN, as shown in Figs. 2 and 3. It is seen that the modified mechanism predicts the trends reasonably well. Further model constant adjustments were found to deteriorate the ignition delay predictions of Fig. 1.

Aromatic/PAH predictions of reduced mechanism. The reduced mechanism was further validated to test its capability to predict mole fractions of five aromatic species, viz., A_1, A_2, P_2, A_3, and A_4. The predictions of the reduced mechanism were compared with the predictions of the PAH mechanism of Wang and Frenklach [20] (99 species and 533 reactions) using the 0D SENKIN code [18]. Since this PAH mechanism did not consider *n*-heptane (C_7H_{16}) species and the associated reactions, relevant reactions from the modified ERC mechanism were added. However, since the comprehensive PAH mechanism is well established for lower carbon number (C4 and below) and hydrogen species, those reactions were unchanged. Finally, the comprehensive mechanism consisted of 110 species and 552 reactions. The ignition delays predicted by both the mechanisms for these calculations were very similar. Constant pressure simulations were also run in SENKIN at two different pressures (40 bar and 80 bar) with an initial temperature of 1000 K and for four rich equivalence ratios (Φ=2.5, 3.0, 3.5, and 4.0). Figures 4 and 5 show representative results where it is seen that the PAH species are underpredicted by the reduced mechanism, but the trends are well reproduced.

The discrepancies in the predictions may also be due to differences in the local peak temperatures predicted by the mechanisms. It was seen that the reduced mechanism overpredicted peak temperatures by about 70 K. Obviously, it is very difficult to get

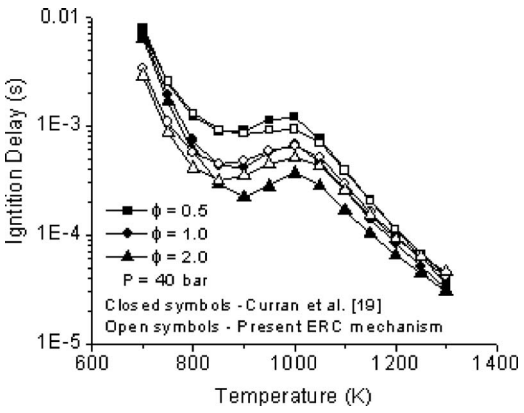

Fig. 2 Ignition delay predictions of the present ERC and the mechanisms of Curran et al. [19] at 40 bar

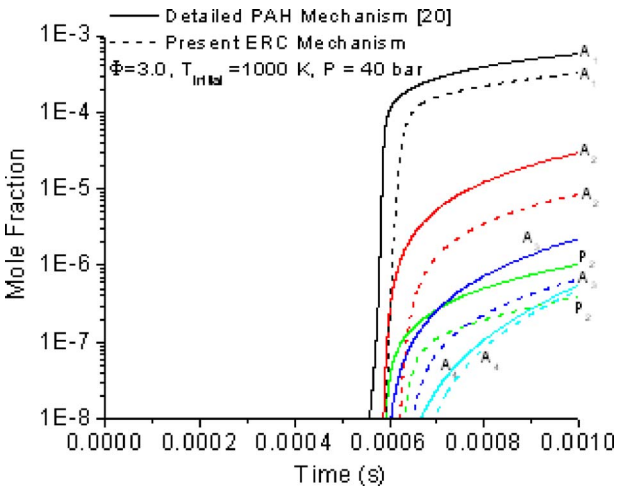

Fig. 4 Mole fraction predicted by the comprehensive [20] and present reduced PAH mechanisms: P=40 bar, initial temperature=1000 K, and Φ=3.0

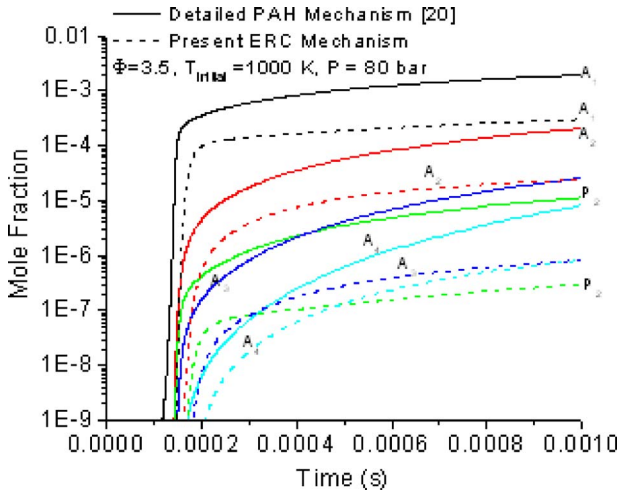

Fig. 5 Mole fraction predicted by the comprehensive [20] and present reduced PAH mechanisms: *P*=80 bar, initial temperature=1000 K, and Φ=3.5

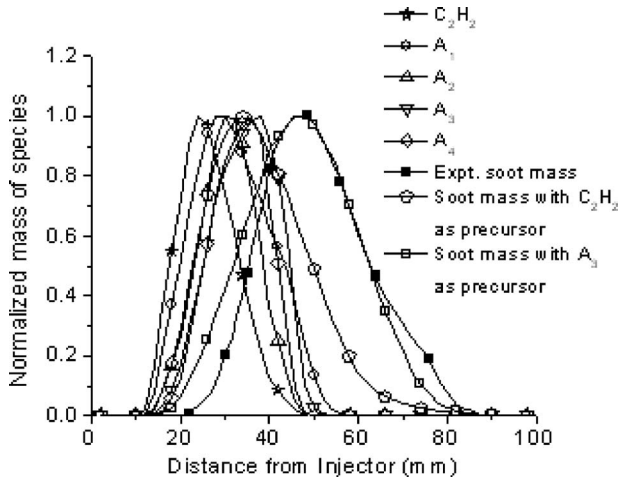

Fig. 7 Predicted formation/oxidation regimes of soot precursors and soot for 15% O_2 ambient oxygen compared with experimental soot formation/oxidation regime

accurate matches for all the species over a wide range of conditions. Nevertheless, the above reduced mechanism was considered adequate for the present study.

Spray/lift-off simulations. The five cases shown in Table 2 were considered for the spray lift-off simulations. Figure 6 shows the lift-off length predictions of the model as compared with the experiments [16]. It is seen that the model performs reasonably well in terms of lift-off lengths.

In the experiments [16], the lift-off length was obtained using OH chemiluminescence and the model predicted lift-off lengths were likewise taken as the distance from the injector to the location of significant OH production. Also, a lift-off length based on the distance from the injector to the point of peak temperature correlated well with the OH definition of the lift-off length.

Accurate prediction of the lift-off length was considered to be high priority for obtaining accurate soot predictions since the lift-off length indicates the entrainment rate and hence the local equivalence ratios, and thus the sooting tendency [21]. Figures 7 and 8 show the normalized integrated mass in 1 mm radial slices for the various soot precursors and soot at the end of injection (6.8 ms) as a function of axial distance from the injector at two operating conditions (15% and 8% O_2).

It is seen that for the 15% O_2 case, the profiles of soot mass with A_3 as the precursor match very well with the experiments as compared with the soot mass obtained using C_2H_2 as the precursor. However, the soot inception process in the experiment occurs about 6 mm further downstream. But for the 8% O_2 case, the location of C_2H_2 and the soot formed from C_2H_2 is far behind the experimental development of the soot. The mole fractions of A_3 and A_4 peak at about 22 mm downstream of the peak of C_2H_2. Use of A_3 as the precursor species improves the soot inception and peak location but there are still discrepancies with the experiments. For the 8% case, the soot reached the end wall of the

Table 2 Summary of experimental conditions [16]

Initial temperature (K)	Ambient density (kg/m^3)	O_2 (vol %)	N_2 (vol %)	CO_2 (vol %)	H_2O (vol %)
1000	30	15	75.15	6.22	3.63
1000	30	12	78.07	6.28	3.65
1000	30	10	80.00	6.33	3.67
1000	30	8	81.95	6.36	3.69

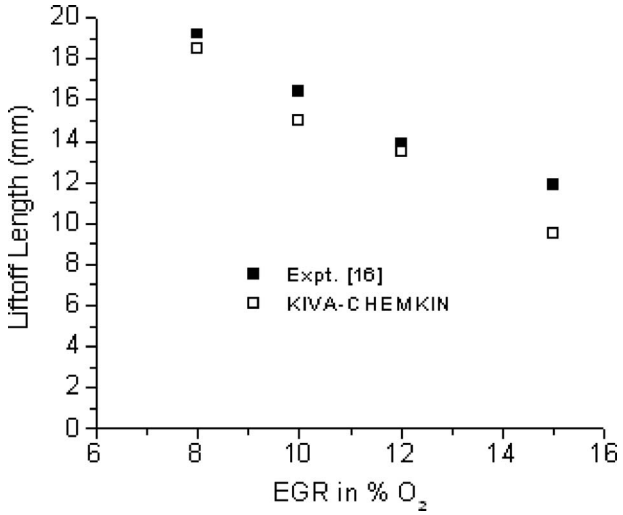

Fig. 6 Lift-off length predictions as compared with the experiments [16] for the conditions of Table 2

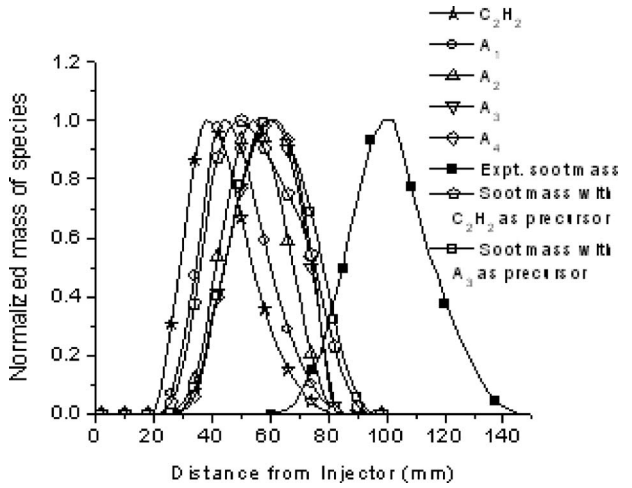

Fig. 8 Predicted formation/oxidation regimes of soot precursors and soot for 8% O_2 ambient oxygen compared with experimental soot formation/oxidation regime

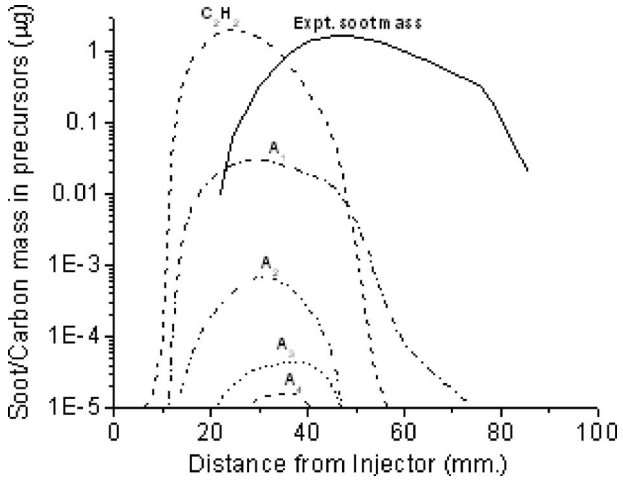

Fig. 9 Soot mass from experiments and estimated carbon mass in precursor species for 15% O_2 case

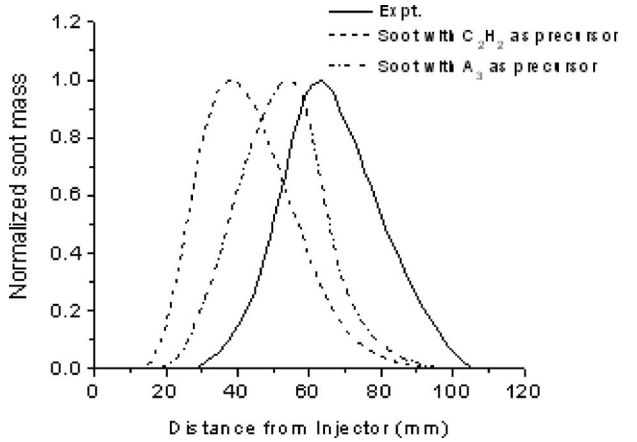

Fig. 11 Normalized soot mass with C_2H_2 and A_3 as precursors for 12% O_2

combustion chamber located at 108 mm in the experiments but no significant soot reached the end wall in the model.

Figure 9 shows the carbon mass contribution of each of the precursor species for 15% O_2 ambient condition along with the soot mass obtained from the experiments. Similar profiles were seen for other ambient conditions. Since the soot model only features dry carbon, it is seen from the figure that most of the carbon mass for soot passes through C_2H_2. Also, there were discrepancies in predicting the absolute mass of aromatic precursors, as seen in Fig. 5. Hence improved predictions of the aromatic species mass need to be captured for accurate positional and quantitative soot mass results. Accordingly, the following results are based on normalized soot mass.

Figures 10–12 show experimental and model predicted normalized soot mass at the end of injection (6.8 ms) using C_2H_2 and A_3 as precursors for three conditions, viz., 15% O_2, 12% O_2, and 10% O_2 normalized by their respective peaks at the 12% O_2 condition. It is seen from the figures that while using C_2H_2 as the precursor for the soot, the maximum soot peak occurs at 12% O_2 conditions, similar to the experiments. However, when using A_3 as the precursor species, improved positional shifts are obtained but the maximum soot peak occurs at the 15% O_2 condition. This is contradictory to the observations of Pickett and Idicheria [16] who argued that the increased soot at the 12% O_2 condition is due to a tradeoff between the increased residence time (due to the longer lift-off length) due to the lower air entrainment rate and reduced rates of soot formation and oxidation due to the lower local temperatures at higher exhaust gas recirculation (EGR) rates. The two-stage Lagrangian (TSL) model of Pickett and Idicheria [16] also predicts the peak of A_4 for the 12% O_2.

The present reduced chemistry mechanism is unable to predict this trend for all the precursors and hence it is unable to predict the soot peak at 12% O_2. For all the cases, the model also predicts the soot inception closer to the lift-off length. The use of an aromatic precursor such as A_3 alleviates this problem to a certain extent, as seen in Figs. 11 and 12, but the experimental soot formation and oxidation regimes are still located further downstream. Soot mass fraction contours from the model predictions and the experimental soot volume fraction contours are compared in Fig. 13 for two cases (15% O_2 and 8% O_2).

It is seen from Fig. 13(*a*) that for the 15% O_2 case, the soot formation and oxidation zones are closer to the lift-off length location and the model performs very well for this case. However, for the 8% O_2 case, the soot formation and oxidation zones are located far downstream of the lift-off length location and the model is unable to capture the lag between the lift-off length position and the soot formation regions, as seen in Fig. 13(*b*). The model consistently predicts the species formation regions to be closer to the lift-off length position than experiments [16,22]. However, in both of the above cases, C_2H_2 was seen to be formed at the lift-off location (not shown) and hence better positional shifts in the soot are seen while using A_3 as the precursor species for soot formation (also refer to Figs. 11 and 12).

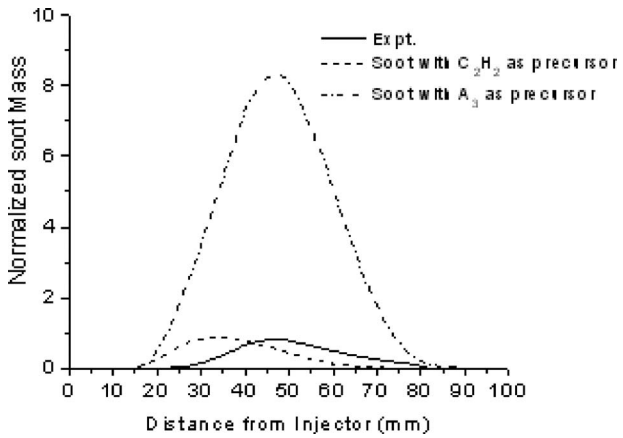

Fig. 10 Normalized soot mass with C_2H_2 and A_3 as precursors for 15% O_2 (normalized with peak soot mass at 12% O_2)

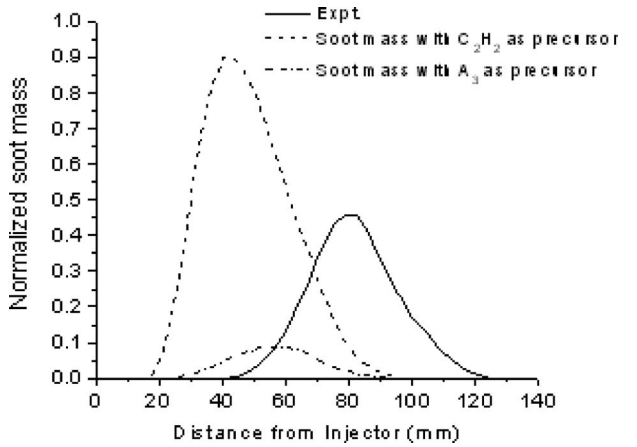

Fig. 12 Normalized soot mass with C_2H_2 and A_3 as precursors for 10% O_2 (normalized with peak soot mass at 12% O_2)

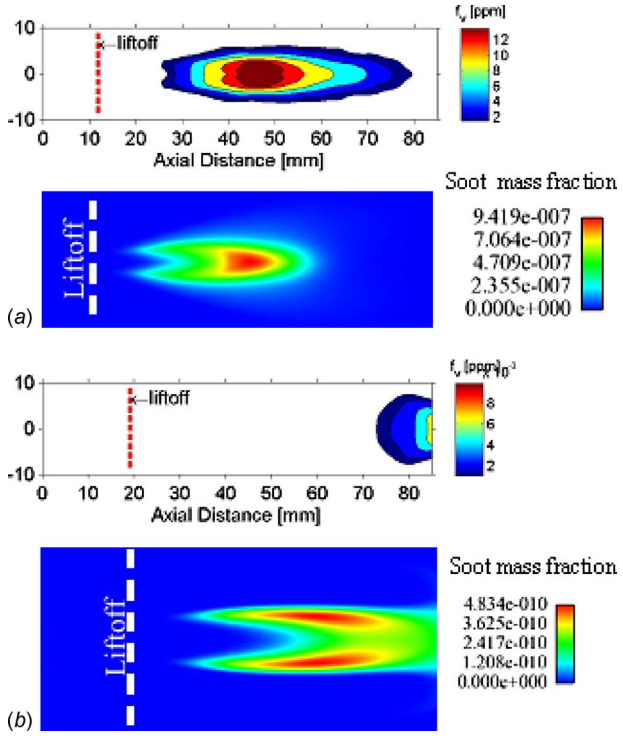

Fig. 13 Soot volume fraction contours from experiment [16,22] (top) and soot mass fraction contours (bottom): (*a*) at 15% O_2 conditions at the end of injection and (*b*) 8% O_2 conditions at the end of injection

Table 3 shows order of magnitude estimates of the peak yield of various precursors for 15% O_2 case and the peak A_4 yield as obtained from the TSL model of Pickett and Idicheria [16]. The pyrene yield is approximately considered as the soot yield in the TSL model. The precursor yield was defined as the ratio of the mass of the precursor to the initial fuel mass, i.e., initial mass of *n*-heptane. For the present modeling study, the peak mass of the precursor at the end of injection (6.8 ms) was used for comparisons. It is seen that the precursor yield on the whole, possibly except for C_2H_2, is severely underpredicted and C_2H_2 shows the best potential for quantitative soot predictions among the different precursors considered in this study. The reduced PAH chemistry, which was seen to perform well for the present SENKIN calculations, evidently does not perform well for spray simulations. This emphasizes the inherent complexities in modeling soot with reduced PAH chemistry for IC engine operating conditions.

5 Conclusions and Future Work

The present study focuses on soot models for practical multidimensional CFD predictions of LTC. The present reduced PAH chemistry mechanism works well for SENKIN calculations but underpredicts precursor species concentrations in spray flames, especially under LTC conditions. However, improved axial position predictions of the precursor species were seen as compared with a previous study, which used only C_2H_2 as the precursor species. The discrepancies in the predictions of soot profiles at LTC conditions indicate that improved PAH chemistry mechanisms are needed. The inception point prediction of the soot for all the conditions was seen to be closer to the lift-off length location. The soot forming regions tend to shift downstream of the lift-off location for LTC conditions. The inclusion of the PAH mechanism alleviates this problem to a certain extent. However, the role of detailed C_2H_2 chemistry and the pathways to the formation of C_2H_2 via C_2H_6, C_2H_5, C_2H_4, and C_2H_3 need to be reassessed. Accurate predictions of C_2H_2 locations are a prerequisite for accurate PAH predictions. Lastly, the effect of thermophoretic diffusion on the soot under LTC conditions needs to be evaluated as the present model does not consider thermophoresis [23].

Table 3 Peak precursor yield as percentage of initial *n*-heptane fuel amount

Precursor	Peak yield (%)	Peak A_4 yield (%) [16]
C_2H_2	9.062	-
A_1	0.1380	-
A_2	3.7e-03	-
A_3	3.5e-04	-
A_4	1.3e-04	0.34

Acknowledgment

The authors would like to acknowledge the financial support of DOE (Office of FreedomCAR and Vehicle Technologies). Thanks are also due to Jessica Brakora and Dr. Youngchul Ra of the Engine Research Center for their suggestions in improving the *n*-heptane mechanism.

Nomenclature

M_s = net soot mass
M_{sf} = mass of the soot formed
M_{so} = mass of the soot oxidized
K_f = soot formation rate
M_{pre} = mass of the precursor (either C_2H_2 or A_3 in this study)
A_{sf} = pre-exponential factor in the soot formation rate
P = pressure (bar)
E_f = activation energy for soot formation
R = universal gas constant
M_{W_C} = molecular weight of carbon
D_s = soot particle diameter
R_{total} = Nagle and Strickland-Constable oxidation rate
η = collision efficiency
Φ = equivalence ratio
ρ_s = soot density
A_1 = benzene
A_2 = naphthalene (two fused rings)
P_2 = biphenyl
A_3 = phenanthrene (three fused rings)
A_4 = pyrene (four fused rings)

References

[1] Kennedy, I. M., 1997, "Models of Soot Formation and Oxidation," Prog. Energy Combust. Sci., **23**, pp. 95–132.
[2] Leung, K. M., Linstedt, R. P., and Jones, W. P., 1991, "A Simplified Reaction Mechanism for Soot Formation in Nonpremixed Flames," Combust. Flame, **87**, pp. 289–305.
[3] Vishwanathan, G., and Reitz, R. D., 2008, "Numerical Predictions of Diesel Flame Lift-Off Length and Soot Distributions Under Low Temperature Combustion Conditions," SAE Paper No. 2008-01-1331.
[4] Idicheria, C. A., and Pickett, L. M., 2006, "Formaldehyde Visualization Near Lift-Off Location in a Diesel Jet," SAE Paper No. 2006-01-3434.
[5] Kong, S. C., Sun, Y., and Reitz, R. D., 2007, "Modeling Diesel Spray Flame Liftoff, Sooting Tendency, and NOx Emissions Using Detailed Chemistry With Phenomenological Soot Model," ASME J. Eng. Gas Turbines Power, **129**, pp. 245–251.
[6] Kee, R. J., Rupley, F. M., and Miller, J. A., 1989, "CHEMKIN-II: A FORTRAN Chemical Kinetics Package for the Analysis of Gas Phase Chemical Kinetics," Sandia Report No. SAND-89-8009.
[7] Amsden, A. A., 1997, "KIVA-3V: A Block Structured KIVA Program for Engines With Vertical or Canted Valves," Los Alamos National Laboratory Report No. LA-13313-MS.
[8] Patel, A., Kong, S. C., and Reitz, R. D., 2004, "Development and Validation of a Reduced Reaction Mechanism for HCCI Engine Simulations," SAE Paper No. 2004-01-0558.

[9] Maroteaux, F., and Noel, L., 2006, "Development of a Reduced n-Heptane Oxidation Mechanism for HCCI Combustion Modeling," Combust. Flame, **146**, pp. 246–267.
[10] Petrova, M. V., and Williams, F. A., 2006, "A Small Detailed Chemical-Kinetic Mechanism for Hydrocarbon Combustion," Combust. Flame, **144**, pp. 526–544.
[11] Warnatz, J., 1984, "Critical Survey of Elementary Reaction Rate Coefficients in the C/H/O System," *Combustion Chemistry*, Springer-Verlag, New York.
[12] http://www-cmls.llnl.gov/?url=science_and_technology-chemistry-combustion-mbutanoate.
[13] Xi, J., and Zhong, B., 2006, "Reduced Kinetic Mechanism of n-Heptane Oxidation in Modeling Polycyclic Aromatic Hydrocarbon Formation in Diesel Combustion," Chem. Eng. Technol., **29**, pp. 1461–1468.
[14] Hiroyasu, H., and Kadota, T., 1976, "Models for Combustion and Formation of Nitric Oxide and Soot in DI Diesel Engines," SAE Paper No. 760129.
[15] Nagle, J., and Strickland-Constable, R. F., 1962, "Oxidation of Carbon Between 1000–2000 °C," *Proceedings of the Fifth Carbon Conference*, Vol. 1, Pergamon, New York, pp. 154–164.
[16] Pickett, L. M., and Idicheria, C. A., 2006, "Effects of Ambient Temperature and Density on Soot Formation Under High-EGR Conditions," THIESEL 2006 Conference on Thermo- and Fluid Dynamic Processes in Diesel Engines.
[17] Gauthier, B. M., Davidson, D. F., and Hanson, R. K., 2004, "Shock Tube Determination of Ignition Delay Times in Full-Blend and Surrogate Fuel Mixtures," Combust. Flame, **139**, pp. 300–311.
[18] Lutz, A. E., Kee, R. J., and Miller, J. A., 1988, "SENKIN: A FORTRAN Program for Predicting Homogeneous Gas Phase Chemical Kinetics With Sensitivity Analysis," Sandia Report No. SAND-87-8248.
[19] Curran, H. J., Gaffuri, P., Pitz, W. J., and Westbrook, C. K., 2002, "A Comprehensive Modeling Study of Iso-Octane Oxidation," Combust. Flame, **129**, pp. 253–280.
[20] Wang, H., and Frenklach, M., 1997, "Detailed Kinetic Modeling Study of Aromatics Formation in Laminar Premixed Acetylene and Ethylene Flames," Combust. Flame, **110**, pp. 173–221.
[21] Siebers, D., and Higgins, B., 2001, "Flame Liftoff on Direct-Injection Diesel Sprays Under Quiescent Conditions," SAE Paper No. 2001-01-0530.
[22] http://www.ca.sandia.gov/ecn/cvdata/frameset.html.
[23] Santoro, R. J., Yeh, T. T., Horvath, J. J., and Semerjian, H. G., 1987, "The Transport and Growth of Soot Particles in Laminar Diffusion Flames," Combust. Sci. Technol., **53**, pp. 89–115.

A Comparison of Ethanol and Butanol as Oxygenates Using a Direct-Injection, Spark-Ignition Engine

Thomas Wallner
Scott A. Miers
Steve McConnell

Argonne National Laboratory,
Argonne, IL 60439

This study was designed to evaluate a "what if" scenario in terms of using butanol as an oxygenate in place of ethanol in an engine calibrated for gasoline operation. No changes to the stock engine calibration were performed for this study. Combustion analysis, efficiency, and emissions of pure gasoline, 10% ethanol, and 10% butanol blends in a modern direct-injection four-cylinder spark-ignition engine were analyzed. Data were taken at engine speeds of 1000 rpm up to 4000 rpm with load varying from 0 N m (idle) to 150 N m. Relatively minor differences existed between the three fuels for the combustion characteristics such as heat release rate, 50% mass fraction burned, and coefficient of variation in indicated mean effective pressure at low and medium engine loads. However at high engine loads the reduced knock resistance of the butanol blend forced the engine control unit to retard the ignition timing substantially, compared with the gasoline baseline and, even more pronounced, compared with the ethanol blend. Brake specific volumetric fuel consumption, which represented a normalized volumetric fuel flow rate, was lowest for the gasoline baseline fuel due to the higher energy density. The 10% butanol blend had a lower volumetric fuel consumption compared with the ethanol blend, as expected, based on energy density differences. The results showed little difference in regulated emissions between 10% ethanol and 10% butanol. The ethanol blend produced the highest peak specific NO_x due to the high octane rating of ethanol and effective antiknock characteristics. Overall, the ability of butanol to perform equally as well as ethanol from an emissions and combustion standpoint, with a decrease in fuel consumption, initially appears promising. Further experiments are planned to explore the full operating range of the engine and the potential benefits of higher blend ratios of butanol.
[DOI: 10.1115/1.3043810]

1 Introduction

In an effort to decrease vehicle emissions and increase the octane rating of gasoline after the mandated removal of lead, oxygenates such as methyl tertiary butyl ether (MTBE) were added to gasoline. However, when it was discovered that MTBE was leaking from gas stations and polluting ground water, ethanol was proposed as a replacement. Ethanol is biodegradable and less detrimental to ground water with the positive impact of emissions reduction and octane improvement. Unfortunately, ethanol is classified as a solvent and is fully miscible in water [1], preventing it from being transported via pipeline [2] like pure gasoline. In addition, ethanol has 30% less energy per unit volume compared with gasoline, which has been shown to negatively impact vehicle fuel economy, especially at higher blend ratios. 1-butanol, on the other hand, has an energy density only 15% less than that of gasoline, an octane rating of 87, and is much less soluble in water. This permits the transportation of gasoline/butanol blends in existing pipelines [3]. Butanol combines the advantages of gasoline in terms of energy density with the oxygen content and renewability of ethanol without being hydrophilic.

2 Properties of Butanol

Butanol (C_4H_9OH) is a higher-chain alcohol with a four-carbon structure. It exists as different isomers based on the location of the hydroxyl (OH) group and carbon chain structure. 1-butanol, also known as *n*-butanol, has a straight-chain structure with the alcohol at the terminal carbon. 2-butanol, also known as *sec*-butanol, is also a straight-chain alcohol but with the OH group at an internal carbon. Isobutanol is a branched isomer with the OH group at the terminal carbon and *tert*-butanol refers to the branched isomer with the OH group at an internal carbon. The different structures of butanol isomers have a direct impact on the physical properties, which are summarized in Table 1.

1-butanol has physical properties similar to gasoline and is therefore considered a potential candidate for replacing ethanol as an oxygenate or gasoline entirely. *sec*-butanol is not considered a potential alternative engine fuel due to its low motor octane number. *tert*-butanol at low volumetric fractions is used as a denaturant for ethanol or to improve the knock behavior of gasoline. It is not considered to be used as an alternative fuel at higher volumetric concentrations, due to its high melting point.

3 Comparison of Fuels

Standard gasoline contains a variety of hydrocarbons with different chain lengths; therefore the fuel properties for standard gasoline are represented within a range of values rather than one specific number. Ethanol is a straight-chain alcohol and has a strictly defined fuel properties. As mentioned earlier, butanol as a higher-chain alcohol exists as different isomers but for this study 1-butanol, from here on simply called butanol, was used exclusively. The fuel properties of the base fuels are summarized in Table 2.

Both ethanol and butanol differ from gasoline due to the addition of the hydroxyl group (OH). Pure ethanol contains

Manuscript received June 6, 2008; final manuscript received June 9, 2008; published online February 11, 2009. Review conducted by Dilip R. Ballal. Paper presented at the 2008 Spring Conference of the ASME Internal Combustion Engine Division (ICES2008), Chicago, IL, April 27–30, 2008.

Table 1 Comparison of butanol isomers

	1- butanol	*sec*-butanol	*tert-butanol*	Isobutanol
Density (kg/m^3) [4]	809.8	806.3	788.7	801.8
Research octane number (RON) [5,6]	96	101	105	113
Motor octane number (MON) [5,6]	78	32	89	94
Melting temperature (°C) [7–10]	−89.5	−114.7	25.7	−108
Boiling temperature (°C) [7–10]	117.7	99.5	82.4	108
Enthalpy of vaporization at T_{boil} (kJ/kg) [11]	582	551	527	566
Self-ignition temperature (°C) [4]	343	406.1	477.8	415.6
Flammable limits [7–10]	1.4	1.7	2.4	1.2
Lower limit (vol %)				
Upper limit (vol %)	11.2	9.8	8	10.9
Viscosity (MPa s) at 25°C [4]	2.544	3.096	-	4.312

35 mass % oxygen and pure butanol contains 21.5 mass % oxygen. Oxygenates have been shown to lower emissions, raise the octane number [13], and effectively displace petroleum fuel with the possibility of being renewable, unlike previous additives such as lead or MTBE. The lower heating values of pure ethanol and pure butanol are 37% less and 22.5% less than gasoline, respectively. Lower blend ratios experience a minor reduction in the lower heating value, however the reduction becomes more significant as the blend ratio increases. Both pure ethanol and pure butanol have densities greater than gasoline, partially a result of the hydroxyl group. The increased density of ethanol and butanol improves the energy density values for the two alcohols. The distillation temperatures vary widely between the three base fuels. Because of the various hydrocarbon molecules that make up a typical gasoline, boiling begins with the lightest hydrocarbons and continues until the heaviest hydrocarbons are boiled off. With ethanol and butanol, both single component fuels, there is a single-value distillation temperature. This, combined with the higher latent heat of vaporization, reduces the ease of cold-starting for these alcohol fuels [14]. The stoichiometric air/fuel ratios for the base alcohols are lower than gasoline, due to the oxygen content in the fuel. Laminar flame speed is seen to increase for ethanol compared with gasoline. The actual laminar flame speed could not be located in the literature for butanol; however the combustion data display a trend that is in agreement with the literature statements concerning higher alcohol blends [15]. The increase in flame speed will reduce combustion duration but increase combustion temperatures. Of particular interest are the mixture calorific values for the three base fuels. Ethanol has been associated with reduced fuel mileage, but from the fuel property data, it is clear this is not a result of reduced mixture calorific value, but rather a lower energy density and correspondingly higher volumetric fuel flow rate.

The fuels tested in this study were neat gasoline as a baseline and blends of 10 vol % of ethanol in gasoline (E10) and

Table 2 Typical properties of base fuels

	Gasoline	Ethanol	1-butanol
Chemical formula	C_4–C_{12}	C_2H_5OH	C_4H_9OH
Composition (C, H, O) (mass %)	86, 14,0	52, 13, 35	65, 13.5, 21.5
Lower heating value (MJ/kg)	42.7	26.8	33.1
Density (kg/m^3)	715–765	790	810
Octane number ($(R+M)/2$)	90	100	87
Boiling temperature (°C)	25–215	78	118
Latent heat of vaporization (25°C) (kJ/kg)	380–500	904	716
Self-ignition temperature (°C)	~300	420	343
Stoichiometric air/fuel ratio	14.7	9.0	11.2
Laminar flame speed (cm/s)[a,b] [12]	~33	~39	
Mixture calorific value (MJ/m^3) [b]	3.75	3.85	3.82
Ignition limits in air (vol %)	0.6	3.5	1.4
Lower limit	8	15	11.2
Upper limit			
Solubility in water at 20°C (ml/100 ml H_20)	<0.1	Fully miscible	7.7

[a]$T=325$ K and $p=100$ kPa.
[b]Stoichiometric mixture, standard temperature and pressure (STP).

Table 3 Specific properties of test fuels (calculated)

	Gasoline	E10	Bu10
Composition (C, H, O) (mass %)	86, 14, 0	82, 13.5, 4.5	83.3, 13.5, 3.2
Lower heating value (MJ/kg)	42.7	41.2	41.8
Octane number (calculated)	90	91	89.7
Density (kg/m^3)	742	747	749
Energy Density (MJ/l)	31.8	30.7	31.3
Stoichiometric air/fuel ratio	14.7	14.1	14.3
Mixture calorific value (MJ/m^3) [a]	3.75	3.78	3.78

[a]Stoichiometric mixture, STP.

Table 4 Major specifications of the test engine

Engine type	2.2 l Ecotec Direct
Cylinders	4
Displacement	2.198 l
Bore	86 mm
Stroke	94.6 mm
Connecting rod length	145.5 mm
Compression ratio	12:1
Maximum power	114 kW at 5600 rpm
Maximum torque	220 N m at 3800 rpm

10 vol % of butanol in gasoline (Bu10). The relevant properties of the test fuels have been calculated and are summarized in Table 3. Although the volumetric content of the alcoholic component is only 10 vol %, the oxygen content increases to 4.5% for the E10 blend and 3.2% for the Bu10 blend. The lower heating value of the blends is reduced by approximately 3.5% for E10 and approximately 2.1% for Bu10, compared with gasoline, due to the lower specific energy content of the alcohol components. The energy density is only reduced by 3.5% for E10 and 1.6% for Bu10, compared with gasoline, due to the higher densities of the alcohol blends. However, the mixture calorific values of the blends are slightly higher than that of the base fuel. This is a result of the lower stoichiometric air demand of the alcohol blends compared with neat gasoline.

4 Test Setup and Test Plan

An Opel 2.2 l Ecotec direct engine (GM L850) was used as the platform to perform the experimental investigations (for details see Ref. [16]). The modern dual-overhead camshaft (DOHC) four-cylinder engine is equipped with direct fuel injection and exhaust gas recirculation (EGR). The manufacturer recommends 90–93 octane fuel for proper engine operation. The cylinder head was modified to accommodate an uncooled cylinder pressure transducer in each combustion chamber. Major specifications of the test engine are summarized in Table 4. More details on the engine setup and the fuel system can be found in Ref. [17].

The stock engine control unit (ECU) was utilized for all the tests. Specific modifications to the ECU were made in order to enable the engine controller to be used for operation in a test cell environment; however the features of a modern gasoline engine controller were still active. These features include the adjustments of the following parameters based on lookup tables within the ECU and sensor inputs from the engine:

- EGR ratio
- spark timing
- injection timing
- injection duration
- fuel rail pressure
- swirl plate position

The engine controller relies on feedback from the following sensors to properly adjust the abovementioned parameters:

- crank shaft position
- cam shaft position
- fuel rail pressure
- engine coolant temperature
- knock
- throttle position feedback
- exhaust oxygen content precatalyst
- exhaust oxygen content postcatalyst
- EGR valve position
- swirl valve position
- intake mass air flow

The test plan consisted of speed and load sweeps for gasoline as a baseline and the two 10 vol % alcohol blends. The engine was operated at speeds of 1000 rpm, 2000 rpm, 3000 rpm, and 4000 rpm with loads starting from 0 N m (idle) up to 100 N m at 1000 rpm and 4000 rpm and 150 N m at 2000 and 3000 rpm with a step change in load of 25 N m. At high loads, the engine cycles between stoichiometric operation and fuel enrichment mode to internally cool the cylinders. Reproducible efficiency and emissions data could not be generated at these load points and therefore they were not included in the analysis.

The data for each operating point were recorded twice for a time period of 30 s each, at a sample rate of 10 Hz, in order to confirm stable engine operation and to allow for an estimation of measurement uncertainty. The data displayed in the resulting plots show the time-averaged results for both data sets at each operating point.

5 Efficiency Results

The brake thermal efficiency maps as a function of engine speed and load for gasoline as well as E10 and Bu10 are plotted in Fig. 1. The overall shapes of the plots are characteristic for spark ignition (SI) engines with throttled stoichiometric operation. The efficiencies generally increase with increasing load due to the reduction in pumping losses when opening the throttle. This trend is maintained up to medium high loads (<100 N m) until the increasing wall heat losses overcome the reduction in the gas exchange losses. The speed dependence of brake thermal efficiency is dominated by the frictional behavior of the engine and the decreasing wall heat losses with increasing engine speed [18].

For all three fuels, a peak brake thermal efficiency of about 36% was measured (36.4% for gasoline, 36.1% for E10, and 35.8% for Bu10). As expected the overall shape of the efficiency isolines are very similar; however there are visible differences in the absolute efficiency values for the different blends, in particular, at high engine loads. Below a threshold of approximately 75 N m, the engine efficiencies for the different blends are almost identical.

To further investigate the efficiency trends at low to medium loads, cylinder pressure and rate of heat release for the three fuels were compared. Figure 2 shows the traces for a medium engine load (50 N m) at a speed of 2000 rpm.

As can be seen, the peak pressure for the butanol blend (26.2 bar) was slightly higher than the ethanol blend (25.2 bar) and the gasoline baseline (24.3 bar). However, the location of peak pressure (11 deg CA ATDC) was the same for all three blends. The spark timing for the three blends (31 deg CA BTDC) and the onset of combustion (first increase in heat release rate) were identical. The maximum rate of heat release for Bu10 (38.8 kJ/m^3 deg CA) was the highest, followed by E10 (37.2 kJ/m^3 deg CA) and the lowest was gasoline (35.9 kJ/m^3 deg CA). The location of 50% mass fraction burned (MFB) occurred at about 1.5 deg CA earlier for Bu10 compared with gasoline and 1 deg CA earlier for E10 compared with gasoline. From Table 2 it can be observed that the laminar flame speed for ethanol is higher than gasoline, which explains the observed trends in maximum rate of heat release and 50% MFB location. The actual laminar flame speed of butanol could not be located in the literature. However, it was suggested that larger chain alcohol fuels have higher burning velocities [15]. The medium load data are consistent with this statement as the early peak rate of heat release suggests that the laminar flame speed for butanol is measurably higher than both ethanol and gasoline.

As load was increased beyond 75 N m slight advantages in brake thermal efficiencies for the gasoline and E10 blend compared with the Bu10 blend were realized. Analyzing the pressure traces and heat release rates for a high load point (150 N m) at 3000 rpm (Fig. 3) reveals that the combustion phasing for the different fuels changed significantly.

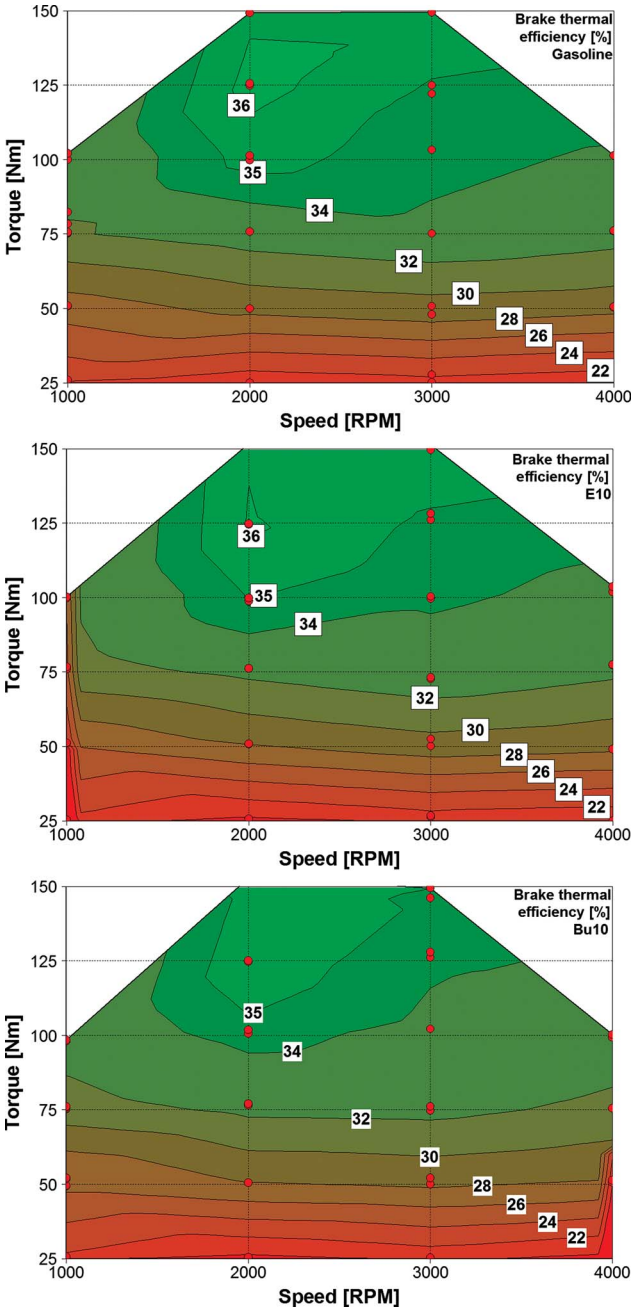

Fig. 1 Efficiency maps for gasoline (top), E10 (middle), and Bu10 (bottom)

Comparing the spark timings for this load point shows that the gasoline baseline spark timing (~10.5 deg CA BTDC) was retarded compared with the ethanol blend (~15.5 deg CA BTDC) but was earlier than the Bu10 blend (~9.0 deg CA BTDC). This advanced spark timing for the E10 blend results in a higher peak cylinder pressure and an earlier location of peak pressure (54.1 bar at 14 deg CA ATDC) compared with gasoline (51.3 bar at 16 deg CA ATDC) as well as the Bu10 blend (49 bar at 18 deg CA ATDC). It is estimated that E30 would have an octane rating of 93 and result in zero ignition retard from the baseline ignition map. The peak heat release rates for the three test fuels showed similar values (~115 kJ/m^3 deg CA); however due to the changes in spark timing, the combustion phasing was significantly different. The ethanol/gasoline blend permits the most ideal combustion phasing with a 50% MFB timing of approximately 10 deg CA

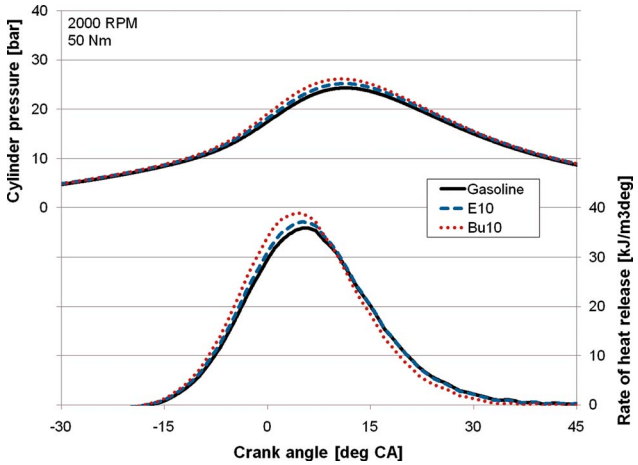

Fig. 2 Pressure traces and rates of heat release for gasoline, E10, and Bu10 at medium engine

ATDC [18]. The 50% MFB timing for gasoline and for Bu10 were about 11 deg CA ATDC and 13 deg CA ATDC, respectively.

The reason for the differences in combustion phasing at high engine loads can be found in the fuel properties of the tested blends and their impact on combustion. The engine is calibrated for gasoline operation and is equipped with a knock sensor. Without engine knock, the spark timing is set based on look-up tables and corrected for operating parameters, such as EGR ratio. If knocking is detected, the ECU retards the ignition timing until knock-free operation can be sustained.

Ethanol has a significantly higher octane rating (100) than gasoline (86–90) or butanol (87) (see Table 2). The impact of octane rating on the knock resistance is very pronounced and can be clearly seen even with the rather low volumetric alcohol content in the tested blends. As an indicator for knock resistance, the spark advance of E10 and Bu10 relative to the gasoline baseline are plotted in Fig. 4. The ethanol blend permitted a 5 deg CA advance in spark timing at high engine loads and speeds due to the higher octane rating of ethanol compared with gasoline. On the other hand the reduced knock resistance of the butanol blend compared with gasoline required a more delayed spark timing for the Bu10 blend compared with gasoline.

The brake thermal efficiency maps in Fig. 1 represented the fuel conversion efficiency as a ratio of engine power output versus fuel energy input. However, the fuel energy input changes with the

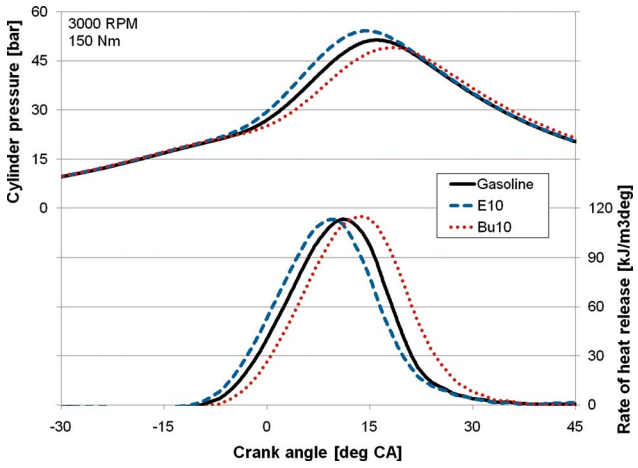

Fig. 3 Pressure traces and rates of heat release for gasoline, E10, and Bu10 at high engine load

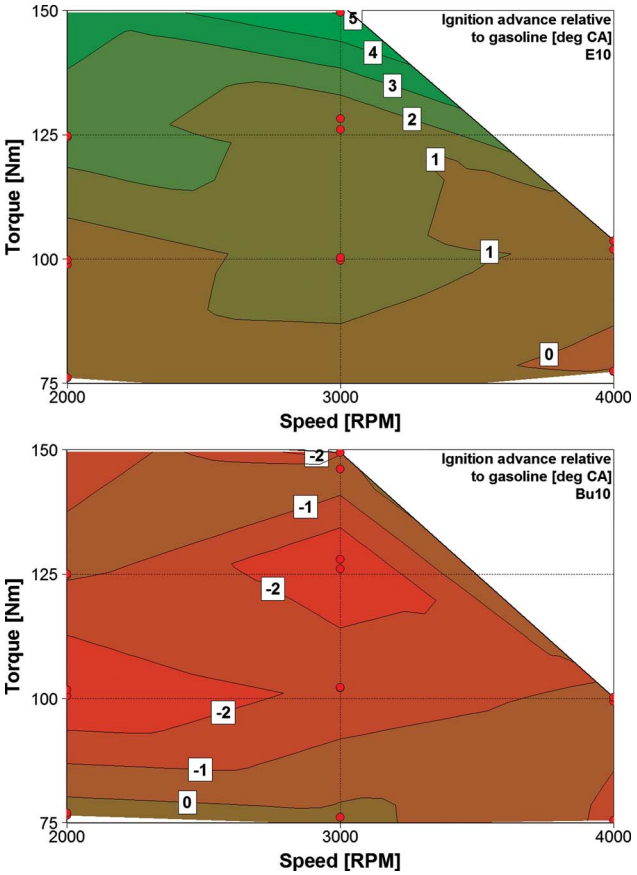

Fig. 4 Ignition advance relative to gasoline for E10 (top) and Bu10 (bottom)

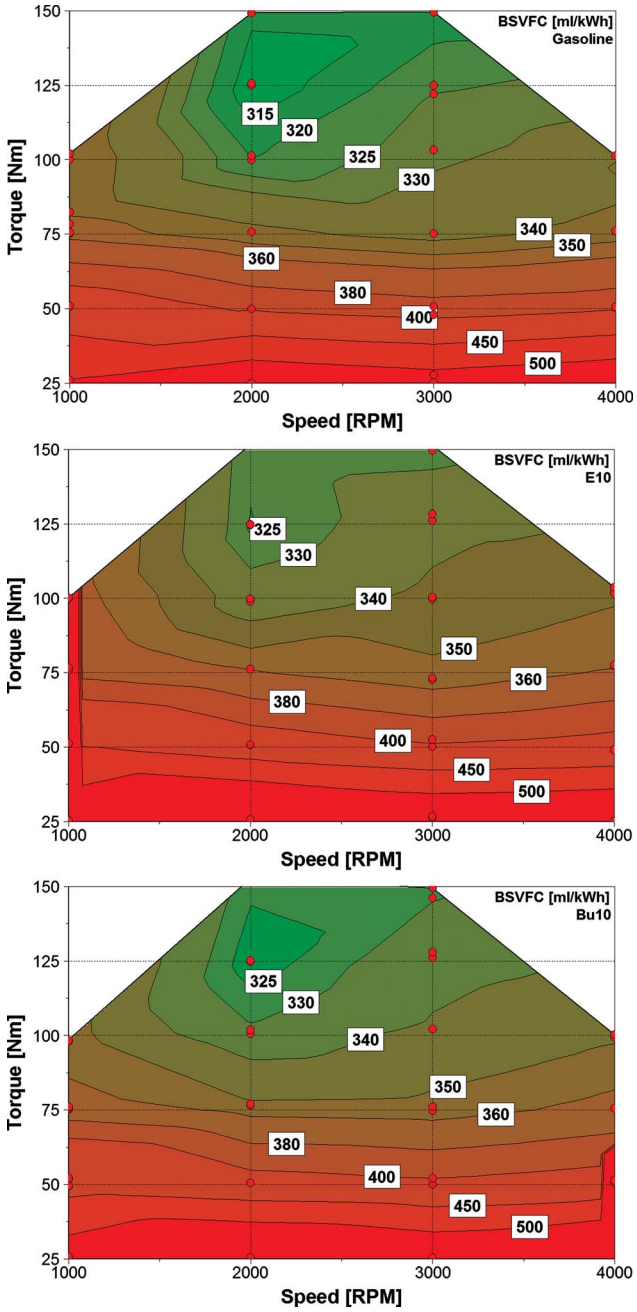

Fig. 5 Brake specific volumetric fuel consumption for gasoline (top), E10 (middle), and Bu10 (bottom)

fuel properties, mainly based on the ratio of lower heating value to stoichiometric air demand. For the actual vehicle application and driver perception, the volumetric fuel consumption is an important parameter to track because it directly relates to the widely used miles-per-gallon (mpg) metric and also determines the total vehicle range per tank of fuel. To ensure an unbiased comparison in volumetric fuel consumption, the brake specific volumetric fuel consumption (BSVFC) was calculated, which represents the volumetric fuel consumption (Q_{fuel}) as a function of engine power output (P). The results are shown in Fig. 5,

$$\text{BSVFC} = \frac{Q_{\text{fuel}}}{P} \tag{1}$$

It is apparent from Fig. 5 that the minimum brake specific volumetric fuel consumption was lowest for gasoline (311 ml/kWh) versus 321.5 ml/kWh for Bu10 and 324 ml/kWh for E10. The increase in BSVFC was approximately 3.4% for Bu10 and 4.2% for E10 compared with gasoline. The differences result from a combination of lower volumetric energy density (see Table 3) as well as a reduction in the fuel conversion efficiency due to the spark timing differences shown earlier.

At low and medium loads (<100 N m) where brake thermal efficiency is very similar among the fuels, the differences in BSVFC correspond with the differences in energy density between the three fuels. The butanol blend would theoretically achieve slightly higher fuel economy and an increased vehicle range compared with the ethanol blend.

At high loads, the BSVFC is not only a function of energy density but is also a function of other fuel properties such as octane number. Knock resistance has a direct affect on brake thermal efficiency, as shown earlier in Fig. 1 and ultimately the BSVFC.

The cyclic variability of combustion is an important parameter to compare the quality and stability of consecutive combustion events. The coefficient of variation (COV) of indicated mean effective pressure (IMEP) is generally used to compare the combustion stability and is defined as the standard deviation of IMEP (σ_{IMEP}) divided by the mean IMEP, as follows:

$$\text{COV}_{\text{IMEP}} = \frac{\sigma_{\text{IMEP}}}{\text{IMEP}} \times 100 \tag{2}$$

It has been found that vehicle drivability problems can occur when COV_{IMEP} exceeds about 10 [19].

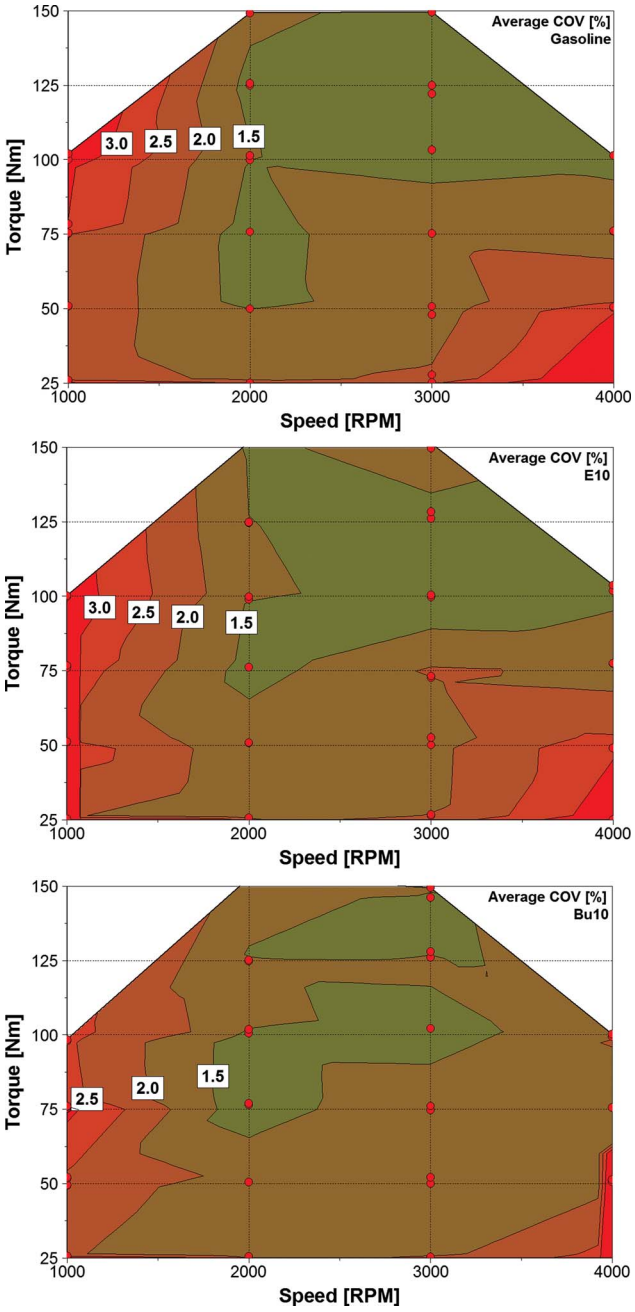

Fig. 6 Coefficient of variation (COV) of indicated mean effective pressure (IMEP) for gasoline (top), E10 (middle), and Bu10 (bottom)

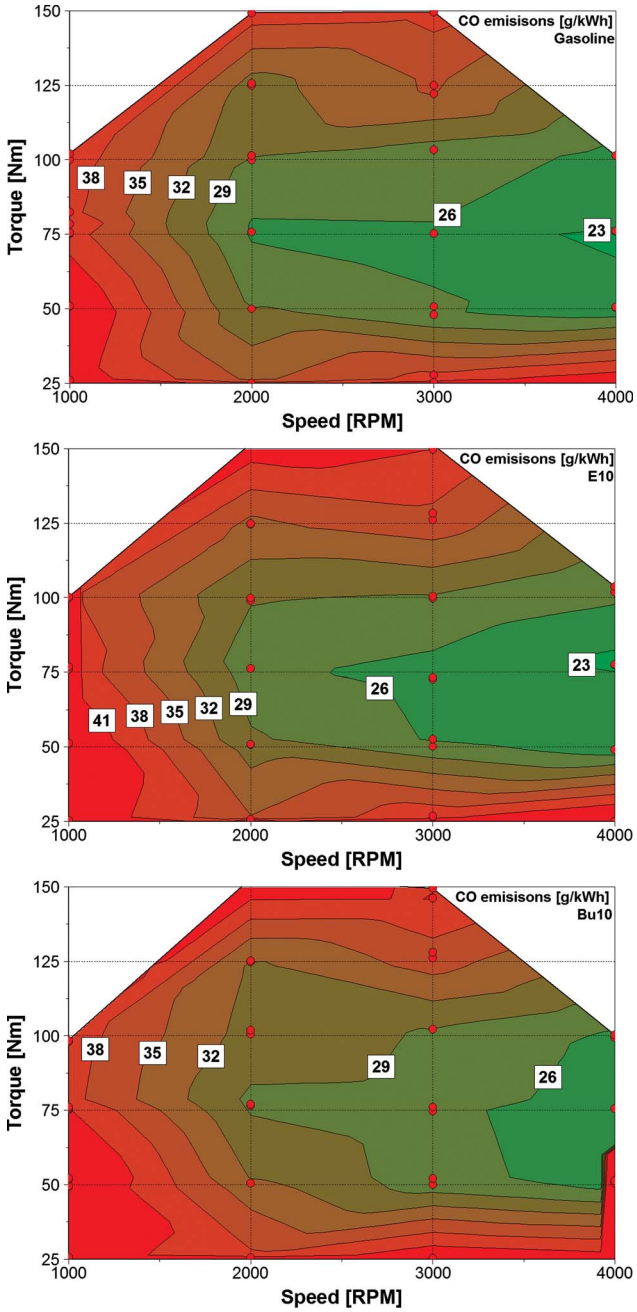

Fig. 7 CO emissions for gasoline (top), E10 (middle), and Bu10 (bottom)

Figure 6 compares the coefficients of variation for the gasoline baseline and the two alcohol blends. An overall trend of improved combustion stability with increasing engine speed can be observed, which is likely attributable to the higher in-cylinder turbulence and improved mixing. Low engine loads generally result in higher COV values, which is mainly due to the reduced in-cylinder turbulence and the fact that the denominator (mean IMEP) in Eq. (2) is small. A comparison of the combustion stability for the test fuels clearly shows that no significant combustion stability issues exist for either alcohol blend compared with the gasoline baseline. Overall, maximum COV values were less than 3 and over a wide operating range were less than 1.5.

6 Emission Behavior

All reported emissions are raw emissions without the use of a catalytic converter. Engine-out, specific carbon monoxide emissions for gasoline and the two fuel blends are shown in Fig. 7. Carbon monoxide (CO) production is primarily controlled by the air/fuel ratio in the cylinder [19]. Mixtures richer than stoichiometric produce high levels of CO and are sensitive to small changes in air/fuel ratio. Mixtures at stoichiometric and leaner produce little CO emissions and are relatively insensitive to air/fuel ratio changes. The Opel Ecotec engine utilizes a closed-loop wide-band oxygen sensor to maintain a global equivalence ratio very close to 1.0. Therefore no significant differences in CO emissions were expected between the three fuels, which are quite evident from Fig. 7.

The high specific CO level at low engine speed (<2000 rpm)

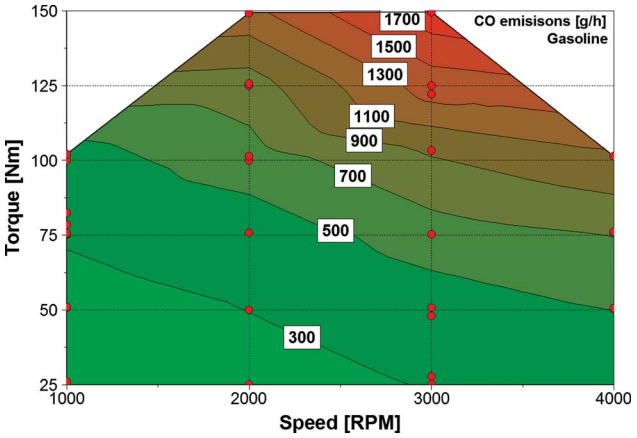

Fig. 8 Mass rate of CO emissions in gasoline operation

results primarily from the increase in COV of IMEP, as shown earlier in Fig. 6. Between 2000–4000 rpm, specific CO emissions at low load are higher due to the low power output of the engine but decrease as load is increased up to 75 N m. As load increases above 75 N m, the mass flow rate (g/h) of CO emissions substantially increases, as shown for gasoline in Fig. 8. The increase in mass flow rate of CO is greater than the increase in power, and thus the specific CO emissions increase and show a peak at the highest load condition.

Specific total hydrocarbon (THC) emissions are shown in Fig. 9 for the baseline gasoline and two fuel blends. Engine-out THC emissions are primarily a result of engine configuration, fuel structure, oxygen availability, and residence time. It might be hypothesized that the addition of an alcohol such as ethanol or butanol to gasoline would improve THC oxidation due to the higher oxygen content in the cylinder and exhaust. However, the engine is operated at the stoichiometric air fuel ratio for each specific fuel blend, and thus excess oxygen is not available. The fact that the oxygen is attached to the fuel is unique compared with gasoline, and it will be interesting to observe hydrocarbon (HC) emissions trends with higher blend ratios in the near future. For the blends tested, there was no noticeable difference between gasoline, E10, and Bu10 for THC emissions, as shown in Fig. 9.

In general, the THC emissions were more heavily influenced by changes in load than speed. An increase in load does not significantly impact the formation of THC but does produce a higher in-cylinder and exhaust manifold temperatures. Figure 10 shows the exhaust manifold temperature map for gasoline operation. Higher temperatures also increase gas flow velocities, which reduce the residence time of the THC emissions in the cylinder and hot exhaust port. The net effect with increasing load is an improvement in the oxidation mechanism of THC emissions. As speed increases at constant load, in-cylinder turbulence increases, improving in-cylinder mixing. Power also increases and the net effect on specific THC emissions is a slight reduction with increasing speed.

Specific NO_x emissions for gasoline and the two fuel blends are shown in Fig. 11. For the most common operating conditions of the engine (1000–3000 rpm, 50–100 N m), medium to high levels of EGR are used to maintain low NO_x emissions. In order to produce sufficient peak power, the EGR rate is significantly reduced as speed increases above 3000 rpm and load increases above 100 N m. As might be expected, the peak NO_x values were found at the highest load and speed conditions. The E10 blend produced a larger peak NO_x island compared with pure gasoline. The improved antiknock behavior of the ethanol blend did not require the ignition timing to be retarded at higher speeds and loads. Advanced ignition timing produces higher in-cylinder temperatures and NO_x. This same trend is very clear for the Bu10 blend, which has the lowest octane rating of the three fuels. The ignition timing was significantly retarded for the Bu10 blend to prevent knock and thus in-cylinder temperatures were substantially reduced, lowering the production of NO_x.

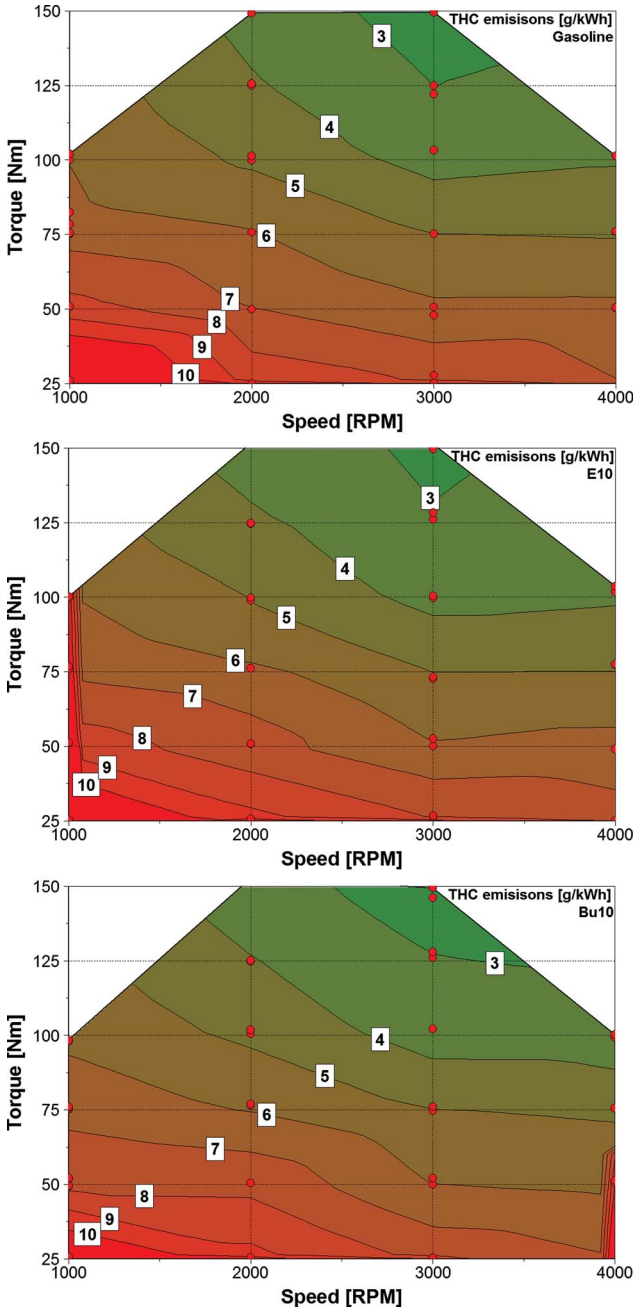

Fig. 9 THC emissions for gasoline (top), E10 (middle), and Bu10 (bottom)

7 Conclusions

This study was designed to evaluate a "what if" scenario in terms of using butanol as an oxygenate, in place of ethanol in an engine calibrated for gasoline operation. Combustion analysis, performance, and emissions of pure gasoline, 10% ethanol and 10% butanol blends in a modern direct-injection four-cylinder spark ignition engine were analyzed. The major results are as follows.

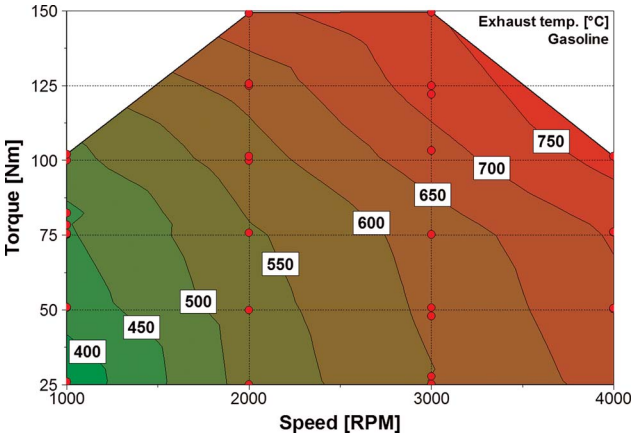

Fig. 10 Exhaust manifold temperature in gasoline operation

- The brake thermal efficiency was very similar between the three fuels, and the peak values differed by less than 2% relative.
- Combustion analysis showed that before the onset of knock (load less than 75 N m), the locations of start-of-combustion and peak pressure were identical for the three fuels. The magnitude of peak pressure was the highest for the Bu10 blend, the 50% MFB point was the most advanced, and the maximum rate of pressure increase was highest for the Bu10 blend. This suggests that the burning velocity of the Bu10 blend was higher than those of both the E10 blend and gasoline.
- The E10 blend had the highest octane rating, which allowed the spark timing to be advanced up to 5 deg compared with gasoline at the highest load of 150 N m. At high loads, the ECU retarded the ignition timing to prevent knock with pure gasoline and the Bu10 blend, due to the lower octane rating compared with ethanol. Once knock occurs, the magnitude of peak pressure drops measurably for the Bu10 blend and the peak occurs several degrees later than gasoline or E10.
- Brake specific volumetric fuel consumption, a normalized measure of engine fuel consumption, showed an increase of approximately 3.4% for Bu10 and 4.2% for E10 compared with gasoline. Gasoline had the lowest BSVFC of the three fuels (311 ml/kW h) due to the high energy density.
- Combustion stability did not vary significantly between the three fuels, over the tested speed and load range. COV of IMEP was less than 3% for the entire operating range.
- Specific carbon monoxide emissions did not show a significant difference between gasoline and the two fuel blends. This was not an unexpected result due to the closed-loop feedback on the engine to maintain stoichiometric operation.
- Specific THC emissions did not show significant differences between the three fuels, due to the formation and oxidation mechanisms not being dramatically altered for the three fuels. It is expected that as alcohol blend ratio increases, the impact on THC emissions should be positive due to the reduction in aromatic content in the blended fuel.
- Specific NO_x emissions reflected the ignition timing changes due to knock. The E10 blend produced the highest specific NO_x emissions and the largest peak NO_x island, due to the advanced ignition timing. The lowest specific NO_x emissions were for Bu10, which had the largest ignition delay at the high load conditions due to the low octane rating of pure butanol.

The data suggest that 10 vol % butanol can be substituted for ethanol as an effective oxygenate, with an improvement in fuel economy and no degradation in emission or combustion stability.

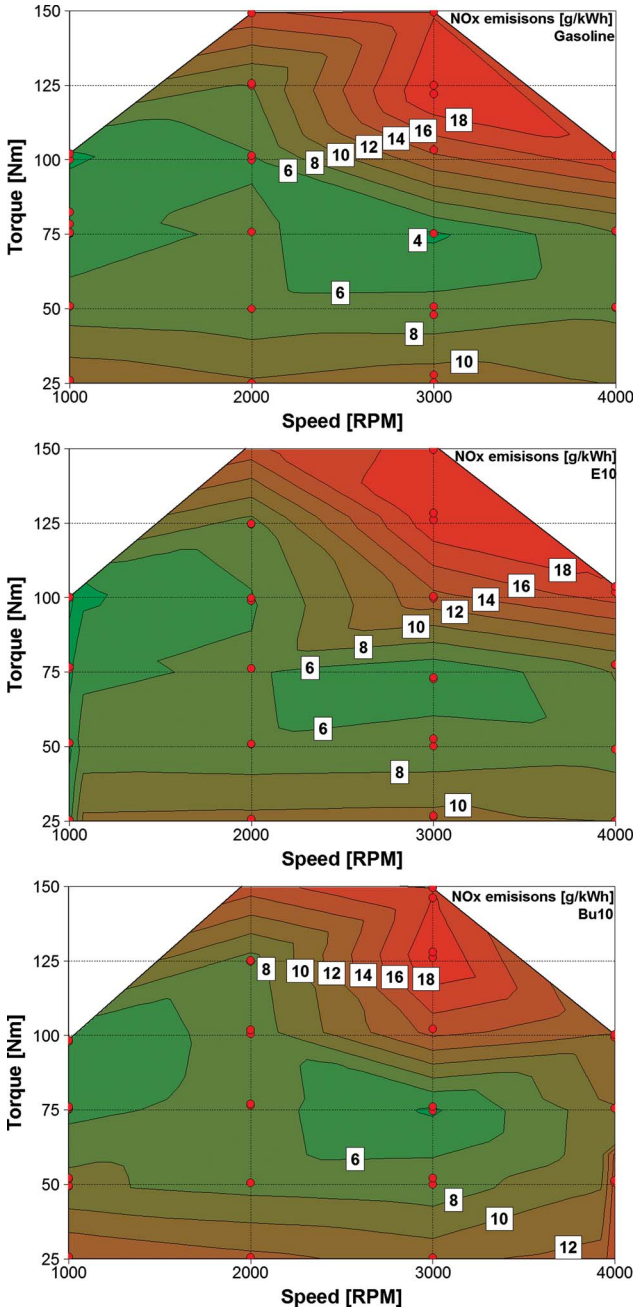

Fig. 11 NO_x emissions for gasoline (top), E10 (middle), and Bu10 (bottom)

Cold-start and long-term durability and higher butanol blends are areas of research that should be explored in the future to further understand the potential of butanol as an alternative fuel.

Acknowledgment

The submitted manuscript has been created by UChicago Argonne, LLC, Operator of Argonne National Laboratory ("Argonne"). Argonne, a U.S. Department of Energy Office of Science laboratory, is operated under Contract No. DE-AC02-06CH11357. The U.S. Government retains for itself, and others acting on its behalf, a paid-up nonexclusive, irrevocable worldwide license in said article to reproduce, prepare derivative works, distribute copies to the public, and perform publicly and display publicly, by or on behalf of the Government.

Nomenclature

ATDC = after top dead center
BTDC = before top dead center
Bu10 = 10 vol % 1-butanol, 90 vol % gasoline
CA = crank angle
CO = carbon monoxide (emissions)
COV = coefficient of variation
ECU = engine control unit
E10 = 10 vol % denatured ethanol, 90 vol % gasoline
HC = hydrocarbon (emissions)
mpg = miles per gallon
MSDS = material safety data sheet
MTBE = methyl tertiary butyl ether
Nm = Newton meter
NO_x = oxides of nitrogen (emissions)
OH = hydroxyl group
P = engine power output
Q_{fuel} = volumetric fuel consumption
σ_{IMEP} = standard deviation of IMEP
T_{boil} = boiling temperature

References

[1] MSDS ethanol, CAS No. 64-17-5.
[2] Whims, S., 2002, *Pipeline Considerations for Ethanol*, Iowa State University, Ames, IA.
[3] Wolf, L., 2007, "1-Butanol as a Gasoline Blending Bio-Component," Presentation at the Mobile Sources Technical Review Subcommittee Meeting.
[4] Lide, D., 1995, *Handbook of Chemistry and Physics*, 76th ed., CRC Press, Boca Raton, FL.
[5] Graboski, M., 2003, "An Analysis of Alternatives for Unleaded Petrol Additives for South Africa," United Nations Environment Programme.
[6] Rice, R., Sanyal, A., Elrod, A., and Bata, R., 1991, "Exhaust Gas Emissions of Butanol, Ethanol, and Methanol-Gasoline Blends," ASME J. Eng. Gas Turbines Power, **113**, pp. 377–381.
[7] MSDS 1-butanol, CAS No. 71-36-3.
[8] MSDS sec-butyl alcohol, CAS No. 78-92-2.
[9] MSDS tert-butyl alcohol, CAS No. 75-65-0.
[10] MSDS isobutyl alcohol, CAS No. 78-83-1.
[11] Chickos, J., and Acree, W., 2003, "Enthalpies of Vaporization of Organic and Organometallic Compounds, 1880–2002," J. Phys. Chem. Ref. Data, **32**(2), pp. 519–878.
[12] Hara, T., and Tanoue, K., 2006, "Laminar Flame Speed of Ethanol, n-Heptane, Iso-Octane Air Mixtures," JSAE Paper No. 20068518.
[13] Gautam, M., and Martin, D., 2000, "Combustion Characteristics of Higher Alcohol/Gasoline Blends," Proc. Inst. Mech. Eng., Part A, **214**(5), pp. 377–409.
[14] Davis, G., Heil, E., and Rust, R., 2002, "Ethanol Vehicle Cold Start Improvement When Using a Hydrogen Supplemented E85 Fuel," American Institute of Aeronautics and Astronautics, Paper No. AIAA-2000-2849.
[15] Farrell, J. T., Johnston, R. J., and Androulakis, I. P., 2004, "Molecular Structure Effects on Laminar Burning Velocities at Elevated Temperature and Pressure," SAE Paper No. 2004-01-2936.
[16] Voss, E., Schnittger, W., Königstein, A., Scholten, I., Pöpperl, M., Pritze, S., Rothenberger, P., and Samstag, M., 2003, "2.2 l ECOTEC DIRECT—The New All-Aluminium Engine With Gasoline Direct Injection for the Opel Signum," 24th International Vienna Engine Symposium.
[17] Wallner, T., and Miers, S. A., 2008, "Combustion Behavior of Gasoline and Gasoline/Ethanol Blends in a Modern Direct-Injection 4-Cylinder Engine," SAE Paper No. 2008-01-0077.
[18] Pischinger, R., Klell, M., and Sams, T., 2002, *Thermodynamics of Internal Combustion Engines*, Springer-Verlag, Berlin.
[19] Heywood, J., 1988, *Internal Combustion Engine Fundamentals*, McGraw-Hill, New York.

Extending the Lean Limit of Natural-Gas Engines

R. L. Evans
Department of Mechanical Engineering,
The University of British Columbia,
Vancouver, BC, V6T 1Z4, Canada

Two different methods to improve the thermal efficiency and reduce the emissions from lean-burn natural-gas fueled engines have been developed and are described in this paper. One method used a "squish-jet" combustion chamber designed specifically to enhance turbulence generation, while the second method provided a partially stratified-charge mixture near the spark plug in order to enhance the ignition of lean mixtures of natural gas and air. The squish-jet combustion chamber was found to reduce brake specific fuel consumption by up to 4.8% in a Ricardo Hydra engine, while the NO_x efficiency trade-off was greatly improved in a Cummins L-10 engine. The partially stratified-charge combustion system extended the lean limit of operation in the Ricardo Hydra by some 10%, resulting in a 64% reduction in NO_x emissions at the lean limit of operation. Both techniques were also shown to be effective in increasing the stability of combustion, thereby reducing cyclic variations in cylinder pressure.
[DOI: 10.1115/1.3043814]

1 Introduction

Several techniques may be used to reduce emissions from natural-gas engines, including the use of a three-way catalytic converter for engines running with a stoichiometric air-fuel ratio and a prechamber to improve the performance of lean-burn engines. Both techniques add considerable cost to the engine, however, and so simpler techniques to reduce emissions have been sought. It is well known [1] that lean operation of homogeneous-charge engines is effective in increasing thermal efficiency and reducing exhaust emissions.

The principal benefits of this operating strategy are a reduction in greenhouse gas emissions and NO_x emissions. Lean operation is normally restricted, however, by the "lean-limit" of combustion, as measured by the air-fuel ratio above which ignition is impossible, or combustion is incomplete. Since very lean mixtures have a much slower burning rate than do stoichiometric mixtures and are difficult to ignite, any technique that increases the burning rate or provides a stronger initial flame kernel is likely to be beneficial in extending the lean limit. Two different methods to improve the thermal efficiency and reduce the emissions from natural-gas fueled engines have been developed. Turbulence is one of the most important parameters in determining the burning rate in homogeneous-charge mixtures so that combustion chamber designs, which enhance turbulence levels in the mixture during the combustion event, should be beneficial. A combustion chamber design aimed at increasing turbulence generation in the mixture just before ignition and during the early combustion phase was designed and used to increase the burning rate during lean operation. The increased burning rate was then used to significantly improve the NO_x efficiency trade-off in the lean-burn natural-gas engine.

The second technique was designed to extend the lean limit of operation by relying on the fact that a stronger initial flame kernel produced following the spark event should also be effective in igniting a very lean mixture, which may not otherwise ignite or which may result in incomplete combustion. This technique used a "partially stratified-charge" (PSC) concept to produce a small pocket of relatively rich mixture near the spark plug so that it could more readily ignite the main, very lean, combustion charge. This technique was also used to extend the lean-limit of operation of natural-gas fueled spark-ignition engines, resulting in reduced brake specific fuel consumption (BSFC) and lower levels of NO_x emissions. This paper provides a review of several studies, which have demonstrated the ability of these two approaches to increase efficiency and reduce emissions.

Manuscript received June 12, 2008; final manuscript received June 19, 2008; published online February 12, 2009. Review conducted by Dilip R. Ballal. Paper presented at the ICES 2008.

2 The Squish-Jet Combustion Chamber

The combustion chamber of a spark-ignited engine is normally designed to generate some mixture motion, or turbulence, during the intake and compression strokes in order to increase the mixture burning velocity. The shape of the intake port is often designed to provide a tangential component to the velocity of the fresh mixture entering the chamber, thereby producing a swirl motion that will degenerate into small-scale turbulence during the compression stroke. The generation of this swirl usually also requires some increase in the pumping work, however, resulting in reduced thermal efficiency. Turbulence can also be generated during the compression stroke by implementing some "squish motion," which results when the piston is designed in a bowl shape. With this geometry, as the piston nears top-dead-center, the outer edge of the "bowl" comes to within a few millimeters of the cylinder head, thereby forcing mixture to move into the center of the piston bowl. Most modern engines use some combination of "swirl" and "squish" motion to enhance mixture turbulence near top-dead-center just before the ignition takes place. Much of the fluid motion generated by these two processes tends to be large-scale motion, however, rather than the smaller scale turbulence, which is more effective in increasing the burning rate. To implement a successful lean-burn strategy, the combustion chamber design needs to provide a fast combustion rate under all operating conditions. In practice, this means using the chamber geometry to generate high levels of small-scale turbulence just prior to ignition and during the early combustion phase.

The combustion chamber design investigated here was based on the principle of using squish motion to generate a series of jets directed toward the center of the chamber just prior to ignition. Evans [2] proposed a variation in the standard bowl-in-piston chamber, described as a "squish-jet" chamber, which enhances the squish effect by using channels in the top of the piston to trap fluid and generate a series of jets. One variation of this concept, referred to in the experimental results as "UBC 1C," is shown in the piston inset drawing of Fig. 1.

The cut-out areas, machined into the piston crown to a depth of 3.0 mm, trap some of the mixture, which is then ejected through the narrow exit passages as the piston nears top-dead-center. In

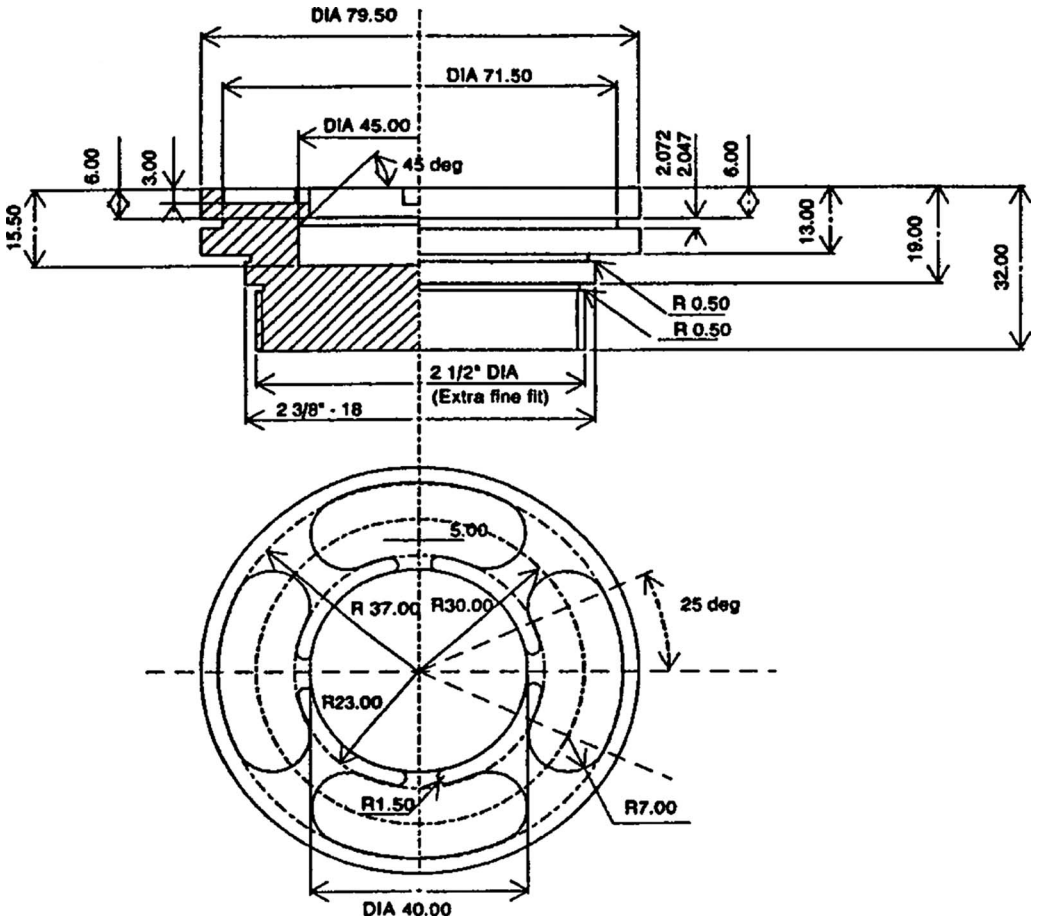

Fig. 1 UBC 1C squish-jet combustion chamber

this way, a series of jets is generated, and these jets, colliding near the center of the chamber, break down into small-scale turbulence. By carefully choosing the dimensions of both the pocket in the piston crown and the outlet passages, the scale of turbulence, as well as the intensity, can be controlled. Evans and Cameron [3] evaluated this concept experimentally with hot-wire anemometer velocity measurements and combustion pressure measurements in a Cooperative Fuel Research (CFR) experimental engine. Initial results showed increased peak pressure and reduced combustion duration compared with a standard bowl-in-piston geometry. Subsequent investigations carried out by Dymala-Dolesky [4], Mawle [5], and Evans [6] further illustrated the influence of combustion chamber design on turbulence enhancement in a lean-burn engine. The squish-jet action was found to improve engine efficiency and increase the knock limit. The performance of the squish-jet combustion chamber configuration was compared with more conventional diesel engine combustion chamber configurations, both in a single-cylinder Ricardo Hydra research engine and in a single-cylinder version of the Cummins L-10 engine. An open combustion chamber, typical of that used in a Detroit Diesel (DD) two-stroke diesel engine, labeled as "DD" in the figures, was used for comparison with the squish-jet configurations.

Most of the experimental work was conducted in a naturally aspirated spark-ignited Ricardo Hydra single-cylinder research engine using natural-gas fuel. The engine specifications are shown in Table 1. All test procedures conformed to SAE standard J1829. The engine configuration had a flat cylinder-head fire-deck and used piston inserts with combustion chambers machined into them. This configuration was chosen to be representative of most medium-duty direct-injection diesel engines, which are commonly used for conversion to spark-ignited natural-gas operation in trucks and buses. Since several different piston-top geometries were required for testing, a single piston "body" was used, with separate removable piston crown inserts, which were threaded for attachment to the main piston body. This permitted rapid changes in piston crown geometry to be made by simply unscrewing one insert and replacing it with another, leaving the same piston body in place in the cylinder. The piston bowl depth was adjusted in each case in order to maintain a constant clearance volume and compression ratio of 10.2:1 for all cases. This procedure also ensured exactly the same piston skirt frictional characteristics for each different piston geometry tested.

Figures 2–4 compare the performance of the Ricardo Hydra engine with the UBC 1C combustion chamber, and the DD chamber. All results are shown for the standard test conditions of wide-

Table 1 Ricardo Hydra Engine specifications

Number of cylinders	1	
Bore	80.26 mm	
Stroke	88.90 mm	
Connecting rod length	158.0 mm	
Swept volume	450 cc	
Clearance volume	49.0 cc	
Compression ratio	10.2:1	
Maximum speed	90 rev/s	
Maximum power	15 kW	
Valve timing	Inlet opens	12° BTDC
	Inlet closes	56° ABDC
	Exhaust opens	56° BBDC
	Exhaust closes	12° ATDC

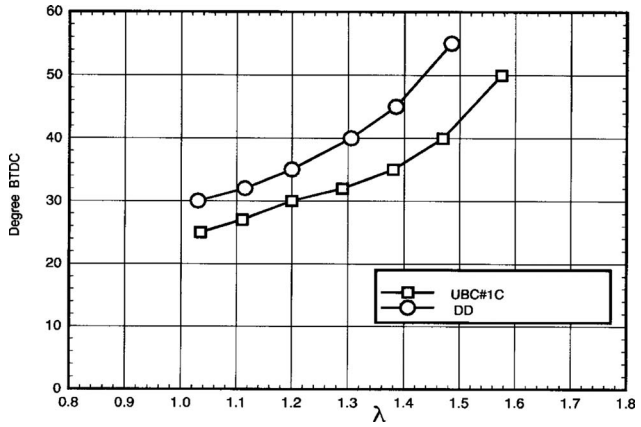

Fig. 2 MBT ignition advance

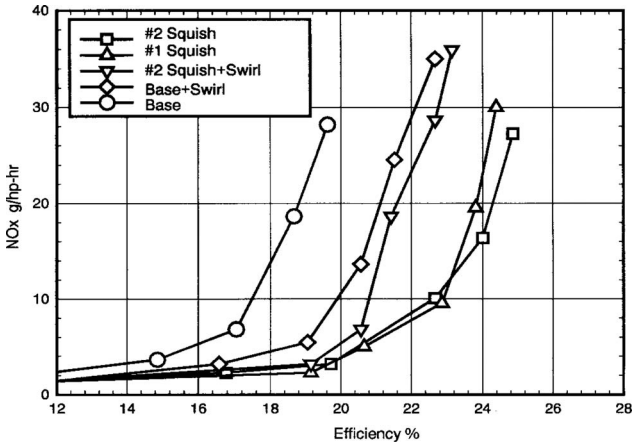

Fig. 5 NO_x versus efficiency trade-off

open-throttle (WOT) at 2000 rpm as a function of the relative air-fuel ratio, λ, from stoichiometric (λ=1.0) to near the lean limit of combustion. The relationship between minimum advance for best torque (MBT) ignition timing and λ for both combustion chambers is shown in Fig. 2. The MBT spark advance provides a direct measure of the burning rate of the air-fuel mixture, since a slower burning rate requires a greater spark advance so that the combustion process starts earlier in the cycle. The MBT ignition timing therefore increases with increasing λ, due to the decreasing burning velocity of lean mixtures. The optimum ignition timing with the UBC 1C chamber can be seen in Fig. 2 to be from 5 deg to 10 deg less advanced than for the DD chamber over a wide range of air-fuel ratios, with the greatest difference occurring at the leanest operating point. This reduction in MBT spark advance provides clear evidence of the faster burning rate achieved by the squish-jet combustion chamber design.

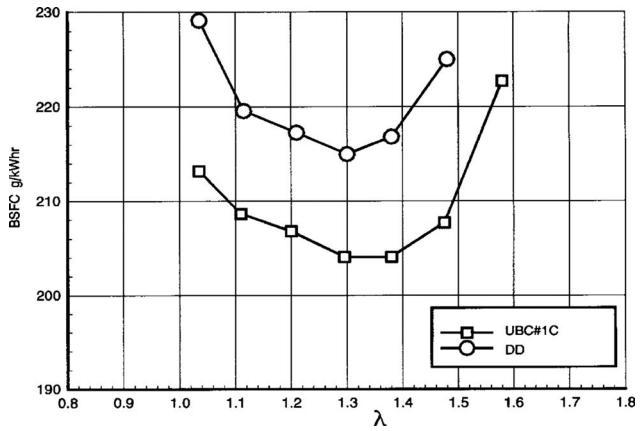

Fig. 3 Brake specific fuel consumption

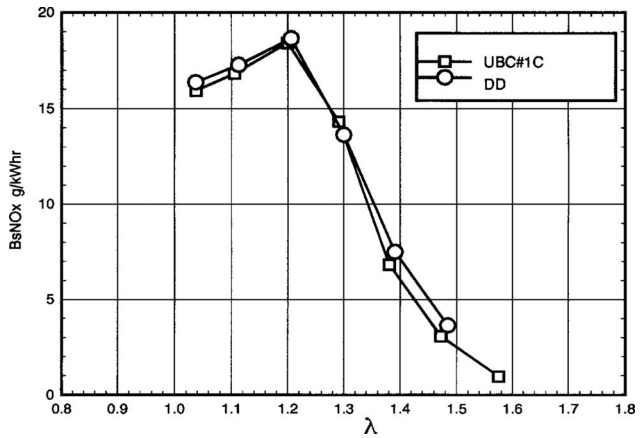

Fig. 4 Brake specific NO_x emissions

The BSFC is shown in Fig. 3 as a function of λ. The faster combustion provided by the squish-jet configuration resulted in much better fuel utilization with the UBC 1C chamber compared with the DD chamber. On a mass basis, there is an indicated 4.8 % reduction in natural-gas consumption per kW h with the UBC chamber compared with the DD chamber at the minimum specific fuel consumption point of λ=1.3.

The relationship between brake specific nitrogen oxides ($BsNO_x$) and λ for both combustion chamber designs is shown in Fig. 4. The NO_x emission at all values of λ are very similar for both cases, showing the highest levels near the maximum efficiency point, as expected. The reduction in the required MBT spark advance evidently results in a moderation of the peak combustion temperature, thereby reducing NO_x emissions compared with what might otherwise be expected with a faster burning rate. Also, the extension to the lean limit of operation provides a significant reduction in NO_x emissions at the leanest operating point.

Additional experiments were conducted at Ortech International by Goetz et al. [7] using a single-cylinder version of the Cummins L-10 engine, and the results are summarized in Fig. 5. The experiments were designed to compare the effectiveness of the UBC squish-jet design to a high-swirl design during lean operation of a spark-ignited engine. In total there were five different experimental configurations tested. The base-case consisted of the standard Cummins L-10 engine configuration, with a relatively quiescent combustion chamber design.

The base-case was compared with two variations of the UBC squish-jet design, shown in Fig. 5 as "No. 1 Squish" and "No. 2 Squish." The No. 1 Squish combustion chamber was similar to that shown in Fig. 1, while theNo. 2 Squish case utilized a tangential squish-jet outlet to provide a swirl component to the squish motion. In addition, a swirl deflection plate was used in the intake port to increase the swirl ratio for both the "base+swirl" configuration and the "No. 2 squish+swirl" configuration. The important trade-off between brake-specific NO_x emissions is illustrated for the five combustion chamber configurations in Fig. 5. The base-case combustion chamber for the L-10 engine configuration provided the poorest performance, while the two squish-jet cases exhibited the best performance over the complete range of air-fuel ratios. It is very interesting to see that a combination of both the squish-jet combustion chamber and enhanced swirl, as shown by the case labeled No. 2 squish+swirl is less effective than using the squish-jet combustion chamber alone. The mixture motion generated near the center of the chamber by the squish-jet cases is

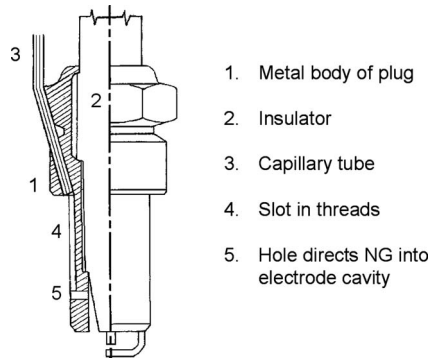

Fig. 6 The partially stratified charge sparkplug

evidently much more effective than that generated near the cylinder walls by the swirl cases, which tend to increase heat transfer losses.

3 The Partially Stratified-Charge Combustion System

A partially stratified-charge combustion system was developed by Evans [8] in order to extend further the lean limit of operation of spark-ignited lean-burn natural-gas engines. In this configuration, a standard spark plug was modified so that a small quantity of natural gas (less than 5% of the overall fuel mass) could be injected in the region of the electrodes, as shown in Fig. 6. The objective of this design was to improve the reliability of combustion initiation by providing a relatively rich fuel-air charge near the spark-plug electrodes, surrounded by the otherwise ultralean homogeneous bulk charge.

The concept is referred to as PSC combustion, and Reynolds and Evans [9,10] showed this technique to be effective in improving the reliability of combustion initiation in ultralean mixtures. The engine used for this experimental work was again the Ricardo Hydra single-cylinder research engine, as described in Table 1. It was configured with a flat cylinder-head fire-deck and a bowl-in-piston combustion chamber. The test engine was instrumented with a water-cooled piezoelectric cylinder pressure transducer to provide data for combustion heat-release analysis. Homogeneous fueling was achieved by metering natural gas into the intake air upstream of the throttle body. An exhaust emissions bench enabled measurement of nitrogen oxides, carbon monoxide, total hydrocarbons, methane, oxygen, and carbon dioxide.

The PSC system uses high-pressure natural gas (200 bar), which is regulated to lower pressures (around 20–50 bar) to supply the spark-plug injector mounted in the research engine. The PSC injection flow-rate is measured using a low-range thermal mass flow meter. A fast-response solenoid valve is used to control the injection timing and quantity. After the solenoid, a capillary tube with 0.53 mm internal diameter channels the PSC fuel to the plug-injector, and a check-valve installed close to the plug prevents backflow of combustion gases. Software control of both the spark timing and the PSC injector settings are accomplished using a LABVIEW interface. The spark-plug/injector design is critical to the operation of the partially stratified-charge engine. It must provide a means of precisely directing fuel into the region of the spark-plug electrodes, without compromising the quality or reliability of the spark. Natural gas is delivered to the electrodes via the capillary tube, which connects to a fine slot in the threads, and the fuel is then delivered through a very small hole into the space between the insulator and the metal body of the spark plug.

For all test results reported here, the spark timing was set to minimum spark advance for best torque, MBT. A test speed of 2000 rpm was chosen as a useful representative speed for medium-duty engines. The lean limit has been defined for this research as the point at which the coefficient of variation of gross indicated mean effective pressure (COV_{IMEP} becomes greater than

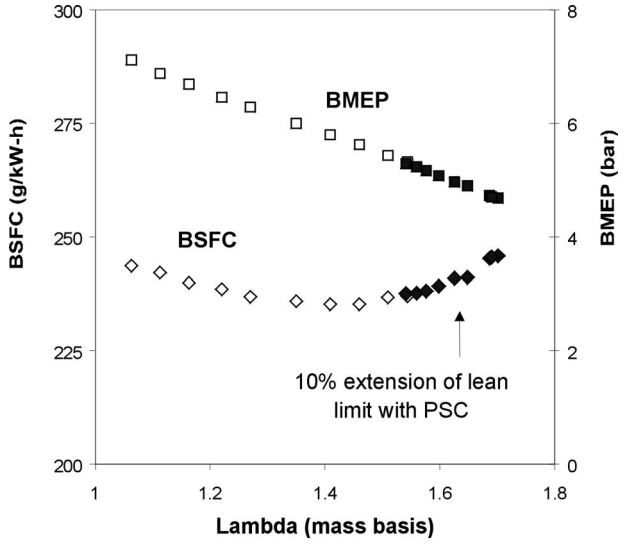

Fig. 7 Extension of the lean limit

5%. The relative air-fuel ratio, λ, is calculated using the total fuel mass flow-rate, including the small quantity of gas injected through the spark plug. A 10% extension of the lean limit was achieved using optimized PSC injection characteristics determined from previous studies: 40 g/h flow-rate, a BOI timing of 10 deg before the spark, and an injection pressure of 25 bar. Figure 7 shows both brake mean effective pressure (BMEP) and BSFC during WOT operation as a function of λ and clearly shows an extension of the lean limit of operation made possible by incorporating the PSC combustion system.

The "low-NO_x" potential of ultralean engine operation was the driving force behind the experimental investigation of the PSC combustion system. Figure 8, which includes data ranging from WOT conditions down to 35% throttle opening, demonstrates that ultralean air-fuel mixtures, achievable by using the PSC system, can provide load control with reduced throttling, while maintaining NO_x emissions at extremely low levels. The reason PSC results in lower NO_x is that, for a given BMEP, the PSC engine runs leaner than the homogeneous- charge engine, which means lower in-cylinder temperatures. The long-term goal of this project is to develop a throttleless load control system, but this may require an even more sophisticated combination of engine technologies. Ultimately, the mode of engine operation may depend on the particular speed and load conditions encountered and on the pertinent emissions regulations.

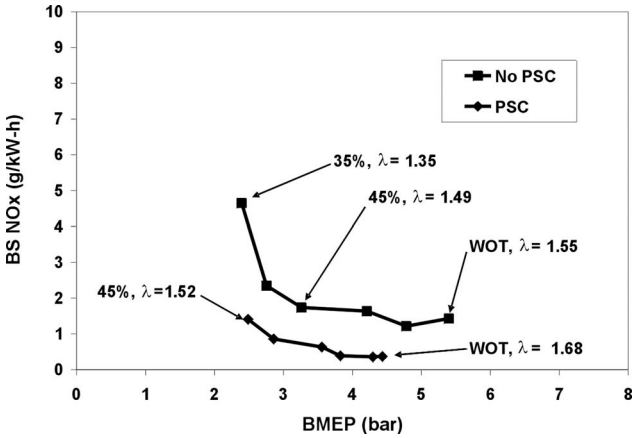

Fig. 8 NO_x reduction with PSC operation

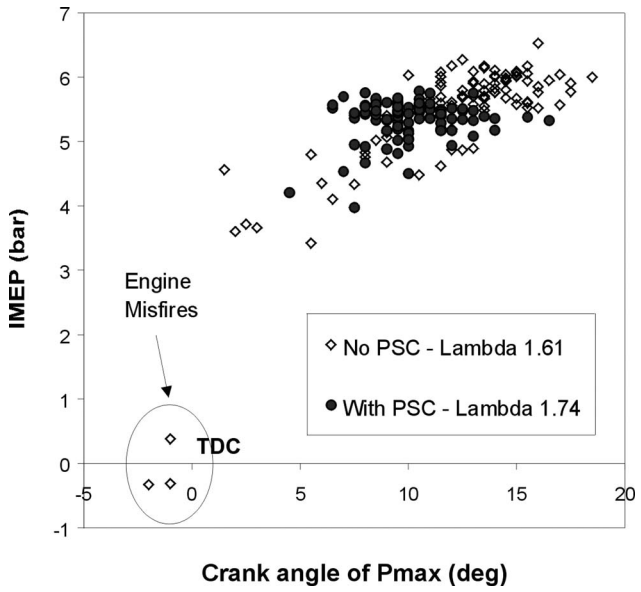

Fig. 9 IMEP distribution with respect to crank-angle

Only data that have a COV_{IMEP} of below 5% are presented in Figs. 7 and 8. With PSC, the engine operates well within this limit at higher values of λ. In order to further investigate the effect of PSC on combustion stability, the in-cylinder pressure data for 100 consecutive combustion cycles were analyzed in detail for two points producing similar indicated mean effective pressure (IMEP): (a) with PSC, at $\lambda=1.75$, and (b) without PSC, at $\lambda=1.61$. At $\lambda=1.75$, the PSC combustion system had a COV_{IMEP} that was just beyond the 5% "lean limit" of stable operation, but PSC continues to ensure reliable ignition. This is demonstrated in the lack of misfires evident with PSC, as shown in Fig. 9, which plots IMEP against the crank-angle position of maximum cylinder pressure. Misfires are readily observed, however, in pressure data for the homogeneous-charge case at a reduced $\lambda=1.61$. The purely homogeneous mixture also has a much higher COV_{IMEP} even though it is less lean than the PSC operation. In the PSC case, any instability in combustion is probably due to poor flame propagation through the ultralean homogeneous charge. The plots of IMEP data in Fig. 9 makes it clear that reliability of flame initiation is considerably improved during PSC operation. This enables a PSC "lean-burn" engine to run much leaner than is possible in a purely homogeneous-charge engine using a conventional spark plug.

4 Conclusions

Two quite different techniques aimed at extending the lean limit of operation and improving the performance of lean-burn natural-gas engines were investigated in the various studies reviewed in this paper. Both techniques were aimed at increasing the combustion rate of lean mixtures, the first by increasing the turbulence level during the early phase of combustion and the second by providing a more readily ignitable mixture of fuel and air at the spark-plug electrodes. For different reasons, the two techniques were shown to be effective in reducing the brake specific fuel consumption and increasing the stability of engine operation. The squish-jet combustion chamber was found to reduce BSFC by up to 4.8% in a Ricardo Hydra engine, while NO_x efficiency trade-off was greatly improved in a Cummins L-10 engine. The partially stratified-charge combustion system extended the lean limit of operation in the Ricardo Hydra by some 10%, resulting in a 64% reduction in NO_x emissions, from 1.1 g/kW h to 0.4 g/kW h at the lean limit of operation.

Nomenclature

COV_{IMEP} = coefficient of variation of IMEP
λ = relative air-fuel ratio

References

[1] Evans, R. L., 2007, "Lean-Burn Spark-Ignited Internal Combustion Engines," *Lean Combustion Technology and Control*, D. Dunn-Rankin, ed., Academic, New York, pp. 95–120.
[2] Evans, R. L., 1986, "Internal Combustion Engine Squish Jet Combustion Chamber," U.S. Patent No. 4,572,123.
[3] Evans, R. L. and Cameron, C., 1986, "A New Combustion Chamber for Fast Burn Applications," SAE Paper No. 860319.
[4] Dymala-Dolesky, R., 1986, "The Effects of Turbulence Enhancements on the Performance of a Spark-Ignition Engine," M.A.Sc. thesis, University of British Columbia, Vancouver.
[5] Mawle, C. D., 1989, "The Effects of Turbulence and Combustion Chamber Geometry on Combustion in a Spark Ignition Engine," UBC Alternative Fuels Laboratory, Report No. AFL-89–02.
[6] Evans, R. L., "Combustion Chamber Design for a Lean-Burn SI Engine," SAE Paper No. 921545, 1992.
[7] Goetz, W., Evans, R. L., and Duggal, V., 1993, "Fast Burn Combustion Chamber Development for Natural Gas Engines," Proceedings of the Windsor Workshop on Alternative Fuels, pp. 577–601.
[8] Evans, R. L., 2000, "A Control Method for Spark Ignition Engines," U.S. Patent No. 6,032,640.
[9] Reynolds, C., and Evans, R. L., 2004, "The Low Nox Potential of Partially Stratified-Charge Combustion in a Natural Gas Engine," Proceedings of the Combustion Institute/Canadian Section, Spring Technical Meeting, Kingston, ON, Canada, May 9–12.
[10] Reynolds, C., and Evans, R. L., 2004, "Improving Emissions and Performance Characteristics of Lean Burn Natural Gas Engines Through Partial-Stratification," Int. J. Engine Res., **5**(1), pp. 105–114.

Addressing Cam Wear and Follower Jump in Single-Dwell Cam-Follower Systems With an Adjustable Modified Trapezoidal Acceleration Cam Profile

Forrest W. Flocker
Wade Department of Mechanical and Aerospace Engineering,
Trine University,
One University Boulevard,
Angola, IN 46703
e-mail: flockerf@trine.edu

Presented is a modified trapezoidal cam profile with an adjustable forward and backward acceleration. The profile is suitable for single-dwell cam and follower applications. The main benefit of the profile is that it allows cam designers to choose easily a value for the maximum forward or maximum backward acceleration to achieve design objectives. An additional benefit of the profile is that it has a continuous jerk curve. Follower acceleration is one of the primary factors affecting cam wear and follower jump, two main concerns of cam designers. Large forward acceleration against a load creates cam-follower interface forces that can cause excessive wear. Backward acceleration tends to reduce the cam-follower interface force, and if the backward acceleration is sufficiently large, separation between the cam and follower ("follower jump") can occur. The cam profile presented in this paper gives cam designers an easy way to adjust the maximum forward or backward acceleration to prevent these problems. [DOI: 10.1115/1.3030874]

Keywords: cam acceleration, cams, cam wear, cam profile, follower jump

1 Introduction

Figure 1 illustrates a typical plate cam driving an axial follower. The cam turns at rate $\omega = d\theta/dt$, where t denotes time and θ is the cam angle relative to a fixed axis. The axial position of the follower is given by $s(\theta)$. In this paper, derivatives of follower motion with respect to cam angle will be called pseudoquantities. For example, $v(\theta) = ds/d\theta$ is called pseudo velocity, $a(\theta) = d^2s/d\theta^2$ is called pseudo acceleration, $j(\theta) = d^3s/d\theta^3$ is called pseudojerk and so forth. Derivatives of follower motion with respect to time give the true follower velocity, acceleration, jerk, etc., and will be denoted by $\bar{v}$, $\bar{a}$, etc., respectively. In this paper, the terms, velocity, acceleration, jerk, etc., are used interchangeably to indicate both pseudo- and true quantities. The actual meaning is usually clear from the context; otherwise the full name is used. For cams operating at constant angular velocity, the relationship between the true and pseudoquantities is [1]

$$\frac{d^n s}{dt^n} = \omega^n \frac{d^n s}{d\theta^n} \tag{1}$$

where $n = 0, 1, 2, \ldots$ is the order of the derivative. For nearly all practical applications, changes in angular velocity are relatively gradual and the above equation is entirely valid even if the angular velocity is not constant. Therefore, in this paper, we assume that Eq. (1) is valid for all practical design applications, that is, that $\bar{v} = \omega v$, $\bar{a} = \omega^2 a$, $\bar{j} = \omega^3 j$, etc.

The two most important parameters to the single-dwell cam designer are the amount of cam lift, h, and the cam angle of the rise/fall interval, 2β. Both of these are illustrated in Fig. 2. After that, the cam profile is chosen to satisfy other design requirements. For example, for single-dwell cams, we must have $s = v = a = 0$ at $\theta = 0$ and 2β to satisfy what is commonly known as the fundamental law of cam design [2]. This paper focuses on the ability of the designer to choose maximum values for the forward or backward acceleration of the follower. Follower acceleration is important to the cam designer because it is directly related to the cam/follower interface force through Newton's second law of motion. The cam/follower interface force is largest during the rise portion of the cycle; therefore, the maximum forward acceleration is an important parameter with regard to cam/follower wear. During the fall portion of the cycle, the interface force is at a minimum and if this force reaches zero, a highly undesirable phenomenon know as "follower jump" can occur. The purpose of the acceleration profile presented in this paper is to offer flexibility to the single-dwell cam designer in setting maximum follower acceleration values.

2 The Acceleration Profile

Figure 3 illustrates the follower acceleration profile introduced in this paper. The profile is suitable for single-dwell applications, which are characterized by a rise/fall interval followed by single dwell period, as illustrated in Fig. 2. The follower rise occurs during $0 \leq \theta \leq \beta$, followed immediately by the fall during $\beta \leq \theta \leq 2\beta$. Dwell is defined by $s(\theta) = 0$ and this occurs for $2\beta \leq \theta \leq 360$ deg. As seen in Fig. 3, the acceleration profile is symmetric about $\theta = \beta$ and, characteristic of single-dwell trapezoidal acceleration profiles, there are three regions where the acceleration is constant. The pure trapezoids are modified by placing quarter or half cosine functions between the regions of constant acceleration. The cosine functions provide a continuous follower jerk function throughout the cam cycle. In Fig. 3, A and B denote the amplitude parameters (both positive numbers) for forward and backward accelerations, respectively, p and q are the cam angles where acceleration is constant, and m and n are the parameters that control how quickly the acceleration transitions from forward to backward and vice versa.

Manuscript received June 18, 2008; final manuscript received June 30, 2008; published online February 12, 2009. Review conducted by Dilip R. Ballal. Paper presented at the 2008 Spring Conference of the ASME Internal Combustion Engine Division (ICE2008), April 27–30, 2008, Chicago, IL.

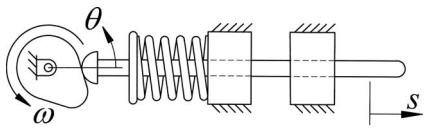

Fig. 1 A plate cam driving an axial follower

To simplify the design process, the acceleration profile should be defined in terms of the smallest number of parameters as possible. The following set of parameters is proposed: (1) h, the cam lift; (2) 2β, the cam angle interval for rise/fall; (3) R, the ratio of the forward to backward acceleration, $R=A/B$; and (4) n, a parameter that controls the maximum follower jerk during the cycle. All other parameters of Fig. 3 will be related to these four.

We begin by noting that the requirement of zero velocity at $\theta=0$ and 2β requires that

$$\int_0^{2\beta} a(\theta)d\theta = 0 \tag{2}$$

In other words, this says that the area of the two positive areas must equal that of the one negative area in Fig. 3. The functions chosen for the rise portion of the cycle are, for $0 \le \theta \le \beta/n$,

$$a_n(\theta) = \frac{Ah}{2\beta^2}\left[1 - \cos\left(\frac{n\pi\theta}{\beta}\right)\right] \tag{3}$$

and for $(\beta/n+p) \le \theta \le (\beta/n+p+\beta/m)$,

$$a_m(\theta) = \frac{h}{2\beta^2}\left\{(A+B)\cos\left[\frac{m\pi}{\beta}\left(\theta - \frac{\beta}{n} - p\right)\right] + A - B\right\} \tag{4}$$

The functions for the fall portion of the cycle are the mirror images of the above appropriately indexed for the correct cam angle. Therefore, Eq. (2) requires

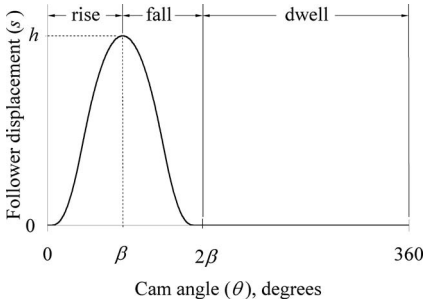

Fig. 2 Follower displacement for a typical single-dwell cam-follower system

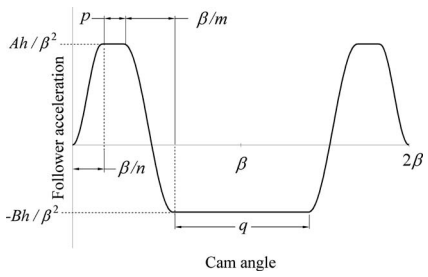

Fig. 3 Follower acceleration during the rise and fall interval

$$2\left(\int_0^{\beta/n} a_n(\theta)d\theta + \int_{\beta/n+p}^{\beta/n+p+\beta/m} a_m(\theta)d\theta\right) + \frac{2Ahp}{\beta^2} - \frac{Bhq}{\beta^2} = 0 \tag{5}$$

Using Eqs. (3) and (4) in Eq. (5) and simplifying provide

$$A\left(\frac{1}{n} + \frac{1}{m} + \frac{2p}{\beta}\right) - B\left(\frac{1}{m} + \frac{q}{\beta}\right) = 0 \tag{6}$$

In addition, the total rise/fall interval requires

$$\frac{2\beta}{n} + \frac{2\beta}{m} + 2p + q = 2\beta \tag{7}$$

The parameters m and n control the maximum magnitude of jerk (the slope of the acceleration function) in their respective regions. A reasonable approach is to choose m such that the maximum magnitude of positive jerk equals the maximum magnitude of negative jerk. This requires that

$$\left|\frac{da_n}{d\theta}\right|_{\theta=\beta/2n} = \left|\frac{da_m}{d\theta}\right|_{\theta=(\beta/n)+p+(\beta/2m)} \tag{8}$$

resulting in

$$m = \left(\frac{A}{A+B}\right)n = \left(\frac{R}{1+R}\right)n \tag{9}$$

where the reader may recall that R is the acceleration amplitude ratio defined by $R=A/B$. Substituting Eq. (9) in Eqs. (6) and (7) and using $R=A/B$ give

$$R\left[\frac{1}{n}\left(2 + \frac{1}{R}\right) + \frac{2p}{\beta}\right] - \left[\left(1 + \frac{1}{R}\right)\frac{1}{n} + \frac{q}{\beta}\right] = 0 \tag{10}$$

$$\frac{2\beta}{n}\left(2 + \frac{1}{R}\right) + 2p + q = 2\beta \tag{11}$$

Solving Eqs. (10) and (11) simultaneously for p and q gives

$$p = \frac{-\beta}{2}\left(\frac{2R^2 + 2R(2-n) + 1}{nR(1+R)}\right) \tag{12}$$

$$q = \beta\left(\frac{2R^2(n-1) - 2R - 1}{nR(1+R)}\right) \tag{13}$$

Of course, the values for p and q cannot be negative. To ensure that both are non-negative requires that the parameter n be at least some minimum value. From Eqs. (12) and (13), it is not hard to show that this minimum value is given by

$$n_{\min} = \max\left[2 + R + \frac{1}{2R}, \quad \frac{2R+1}{2R^2} + 1\right] \tag{14}$$

All that is left is to define our acceleration amplitude parameters, A and B, in terms of our desired parameter set. We choose to determine first A then get B with the relation $B=A/R$. The process starts by requiring that a set of kinematic constraints in the form of function boundary conditions be met when determining velocity and displacement functions. The following set, appropriate for single-dwell applications, is chosen:

$$1 \cdot s(0) = 0$$

$$2 \cdot v(0) = 0$$

$$3 \cdot a(0) = 0$$

$$4 \cdot j(0) = 0$$

$$5 \cdot s(2\beta) = 0$$

$$6 \cdot v(2\beta) = 0$$

$$7 \cdot a(2\beta) = 0$$

$$8 \cdot j(2\beta) = 0$$

$$9 \cdot s(\beta) = h \tag{15}$$

The parameter A is determined by enforcing boundary condition (9), which requires that the acceleration function be successively integrated twice, first to get the velocity and then the displacement. In doing this, the other two boundary conditions (1) and (5) are used to enforce continuity between dwell segments. The interested reader can find details of the procedure in Ref. [2]. The result is

$$A = \frac{8\pi^2(1+R)n^2R^3}{2R^3\pi^2(2n^2-2n-1)+(8-\pi^2)(6R^2+4R+1)+24R^3} \tag{16}$$

To make computer implementation easier, the following shorthand notation is introduced:

$$\phi_1 = \frac{\beta}{n}, \quad \phi_2 = \phi_1 + p, \quad \phi_3 = \phi_2 + \frac{\beta}{m}, \quad \phi_4 = \phi_3 + q,$$

$$\phi_5 = \phi_4 + \frac{\beta}{m}, \quad \phi_6 = \phi_5 + p, \quad \phi_7 = \phi_2 + q \tag{17}$$

$$C_1 = \frac{1}{2n^2} - \frac{2}{n^2\pi^2}, \quad C_2 = 1 - \frac{n}{2m}, \quad C_3 = \frac{n}{m} - \frac{1}{2n} - \frac{n}{2m^2} - 1,$$

$$C_4 = C_1 + \frac{n}{m^3\pi^2} - \frac{n}{2m}\left(\frac{\phi_2}{\beta}\right)^2, \quad C_5 = \frac{m-n}{m},$$

$$C_6 = 1 + C_1 + C_5 - \frac{1}{n} - \frac{m}{n} + \frac{m}{n^2} - \frac{m}{4n^3} + \frac{n(8-\pi^2)}{4\pi^2m^3},$$

$$C_7 = \frac{2n}{m} - C_3 - 4, \quad C_8 = 2 - \frac{1}{n} - \frac{n}{m^2} + C_4, \quad C_9 = \frac{1}{n} - 4,$$

$$C_{10} = C_1 + 4 - \frac{2}{n}, \quad C_{11} = 2 - \frac{1}{n^2\pi^2} \tag{18}$$

With all of theses definitions in place, we have the following for the acceleration function:

$$a(\theta) = \begin{cases} \dfrac{Ah}{2\beta^2}\left[1 - \cos\left(\dfrac{n\pi\theta}{\beta}\right)\right], & 0 \le \theta \le \phi_1 \\ \dfrac{Ah}{\beta^2}, & \phi_1 < \theta \le \phi_2 \\ \dfrac{Ah}{2\beta^2}\left\{\dfrac{n}{m}\cos\left[m\pi\left(\dfrac{\theta-\phi_2}{\beta}\right)\right] + 2C_2\right\}, & \phi_2 < \theta \le \phi_3 \\ \dfrac{-Bh}{\beta^2}, & \phi_3 < \theta \le \phi_4 \\ \dfrac{Ah}{2\beta^2}\dfrac{n}{m}\left\{\cos\left[m\pi\left(\dfrac{\theta-\phi_7}{\beta}\right)\right] + \dfrac{2m}{n} - 1\right\}, & \phi_4 < \theta \le \phi_5 \\ \dfrac{Ah}{\beta^2}, & \phi_5 < \theta \le \phi_6 \\ \dfrac{Ah}{2\beta^2}\left\{1 - \cos\left[n\pi\left(\dfrac{\theta-2\beta}{\beta}\right)\right]\right\}, & \phi_6 < \theta \le 2\beta \\ 0, & 2\beta < \theta \le 2\pi \end{cases} \tag{19}$$

3 The Displacement, Velocity, and Jerk Profiles

Figure 2 illustrates the follower displacement that was obtained by integrating the acceleration function twice. The equation describing the displacement is

$$s(\theta) = \begin{cases} \dfrac{Ah}{2}\left\{\dfrac{1}{n^2\pi^2}\left[\cos\left(\dfrac{n\pi\theta}{\beta}\right) - 1\right] + \dfrac{1}{2}\left(\dfrac{\theta}{\beta}\right)^2\right\}, & 0 \le \theta \le \phi_1 \\ \dfrac{Ah}{\beta}\left[\left(\dfrac{\theta}{\beta}\right)^2 - \dfrac{1}{n}\left(\dfrac{\theta}{\beta}\right) + C_1\right], & \phi_1 < \theta \le \phi_2 \\ \dfrac{Ah}{2}\left\{\dfrac{-n}{m^3\pi^2}\cos\left[m\pi\left(\dfrac{\theta-\phi_2}{\beta}\right)\right] + C_2\left(\dfrac{\theta}{\beta}\right)^2 + C_3\left(\dfrac{\theta}{\beta}\right) + C_4\right\}, & \phi_2 < \theta \le \phi_3 \\ \dfrac{Ah}{2}\left[C_5\left(\dfrac{\theta}{\beta}\right)^2 - 2C_5\left(\dfrac{\theta}{\beta}\right) + C_6\right], & \phi_3 < \theta \le \phi_4 \\ \dfrac{Ah}{2}\left\{\dfrac{-n}{m^3\pi^2}\cos\left[m\pi\left(\dfrac{\theta-\phi_7}{\beta}\right)\right] + C_2\left(\dfrac{\theta}{\beta}\right)^2 + C_7\left(\dfrac{\theta}{\beta}\right) + C_8\right\}, & \phi_4 < \theta \le \phi_5 \\ \dfrac{Ah}{2}\left[\left(\dfrac{\theta}{\beta}\right)^2 + C_9\left(\dfrac{\theta}{\beta}\right) + C_{10}\right], & \phi_5 < \theta \le \phi_6 \\ \dfrac{Ah}{2}\left\{\dfrac{1}{n^2\pi^2}\cos\left[n\pi\left(\dfrac{\theta-2\beta}{\beta}\right) + \dfrac{1}{2}\left(\dfrac{\theta}{\beta}\right)^2\right] - 2\left(\dfrac{\theta}{\beta}\right) + C_{11}\right\}, & \phi_6 < \theta \le 2\beta \\ 0, & 2\beta < \theta \le 2\pi \end{cases} \tag{20}$$

Figure 4 illustrates the follower velocity profile that was obtained by integrating the acceleration function. The reader will notice that the profile is antisymmetric about $\theta=\beta$, providing equal magnitudes of forward and backward velocities.

The equation describing the velocity function is

$$v(\theta)=\begin{cases}\dfrac{Ah}{2\beta}\left[\dfrac{-1}{n\pi}\sin\left(\dfrac{n\pi\theta}{\beta}\right)+\dfrac{\theta}{\beta}\right], & 0\le\theta\le\phi_1\\ \dfrac{Ah}{\beta}\left(\dfrac{\theta}{\beta}-\dfrac{1}{2n}\right), & \phi_1<\theta\le\phi_2\\ \dfrac{Ah}{2\beta}\left\{\dfrac{n}{m^2\pi}\sin\left[m\pi\left(\dfrac{\theta-\phi_2}{\beta}\right)\right]+2C_2\left(\dfrac{\theta}{\beta}\right)+C_3\right\}, & \phi_2<\theta\le\phi_3\\ \dfrac{Ah}{\beta}C_5\left(\dfrac{\theta}{\beta}-1\right), & \phi_3<\theta\le\phi_4\\ \dfrac{Ah}{2\beta}\left\{\dfrac{n}{m^2\pi}\sin\left[m\pi\left(\dfrac{\theta-\phi_7}{\beta}\right)\right]+2C_2\left(\dfrac{\theta}{\beta}\right)+C_7\right\}, & \phi_4<\theta\le\phi_5\\ \dfrac{Ah}{2\beta}\left(\dfrac{2\theta}{\beta}+C_9\right), & \phi_5<\theta\le\phi_6\\ \dfrac{Ah}{2\beta}\left\{\dfrac{-1}{n\pi}\sin\left[n\pi\left(\dfrac{\theta-2\beta}{\beta}\right)\right]+\dfrac{\theta}{\beta}-2\right\}, & \phi_6<\theta\le 2\beta\\ 0, & 2\beta<\theta\le 2\pi\end{cases} \tag{21}$$

The maximum velocity occurs when the acceleration is zero. Finding the cam angle at zero acceleration from Eq. (19) and substituting into Eq. (20) give the maximum velocity:

$$v_{\max}=\frac{Ah}{2\beta}\left\{\frac{2}{m\pi}\left[\sqrt{\frac{n}{m}-1}+C_2\cos^{-1}\left(1-\frac{2m}{n}\right)\right]+\frac{2C_2\phi_2}{\beta}+C_3\right\} \tag{22}$$

Figure 5 shows the follower jerk. This curve is continuous across the full cam cycle. And, like the velocity profile, the jerk curve is balanced in that all of the peak values have the same magnitude.

The equation describing the jerk is obtained by differentiating Eq. (19) with respect to cam angle and is given by

$$j(\theta)=\begin{cases}\dfrac{Ahn\pi}{2\beta^3}\sin\left(\dfrac{n\pi\theta}{\beta}\right), & 0\le\theta\le\phi_1\\ 0, & \phi_1<\theta\le\phi_2\\ \dfrac{-Ahn\pi}{2\beta^3}\sin\left[m\pi\left(\dfrac{\theta-\phi_2}{\beta}\right)\right], & \phi_2<\theta\le\phi_3\\ 0, & \phi_3<\theta\le\phi_4\\ \dfrac{-Ahn\pi}{2\beta^3}\sin\left[m\pi\left(\dfrac{\theta-\phi_7}{\beta}\right)\right], & \phi_4<\theta\le\phi_5\\ 0, & \phi_5<\theta\le\phi_6\\ \dfrac{Ahn\pi}{2\beta^3}\sin\left[n\pi\left(\dfrac{\theta-2\beta}{\beta}\right)\right], & \phi_6<\theta\le 2\beta\\ 0, & 2\beta<\theta\le 2\pi\end{cases} \tag{23}$$

The maximum jerk can be obtained by noting that the first peak occurs at $\theta=\beta/2n$. Substituting this into Eq. (23) gives

$$j_{\max}=\frac{Ahn\pi}{2\beta^3} \tag{24}$$

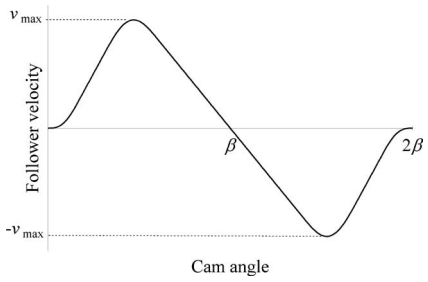

Fig. 4 Follower velocity during the rise and fall interval

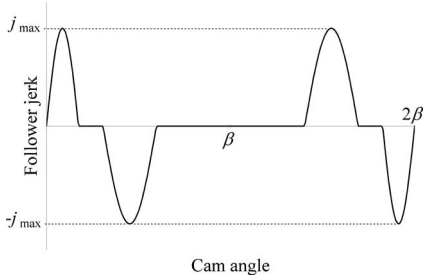

Fig. 5 Follower jerk during the rise and fall interval

4 Computational Algorithm

Because the kinematic functions contain eight separate regions that are pasted together, their calculation is best suited for an equation solver program. The algorithm for doing the calculations is given below.

1. Input the cam lift (h), the rise/fall interval (2β), the ratio of forward to backward acceleration (R), and the jerk control parameter (n). Note that n must be greater than or equal to the minimum value given by Eq. (14).
2. Calculate m using Eq. (9).
3. Calculate p and q using Eqs. (12) and (13).
4. Calculate A using Eq. (16), and then B using $B=A/R$.
5. Calculate $\phi_1,\phi_2,\ldots,\phi_7$ using Eq. (17).
6. Calculate $C_1,C_2,\ldots,C_{11}$ using Eq. (18).
7. Calculate s, v, a, and j using Eqs. (20), (21), (19), and (23), respectively.

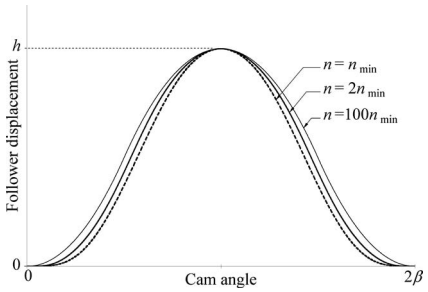

Fig. 6 Effect of the jerk control parameter on follower displacement for $R=1$

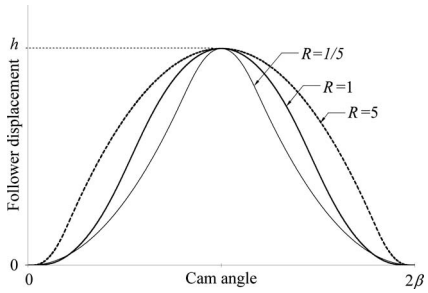

Fig. 10 Effect of the acceleration ratio parameter on follower displacement for $n=2n_{min}$

5 Results and Discussion

5.1 Effect of R and n on Follower Displacement, Velocity, Acceleration, and Jerk. Figures 6–9 show the effect of the jerk control parameter (n) on the various kinematic quantities. For these four figures, the amplitude ratio was fixed at $R=1$. Figures 6 and 7 show that n has little effect on follower displacement and velocity. However, Fig. 8 shows that the effect of increasing n is to change the acceleration profile from a modified (rounded) trapezoidal form to one with discontinuous constant acceleration regions, violating the fundamental law of cam design [2]. In general, Figs. 8 and 9 show that increasing n reduces peak acceleration while increasing peak jerk with $j_{max} \to \infty$ as $n \to \infty$. Thus, there is a trade–off between reducing peak acceleration and increasing peak jerk. And, Norton et al. [3] reported that smoother jerk profiles give reduced residual vibrations in cam systems. Therefore, there is evidence that designers should try to avoid cam systems with excessive jerk.

Figures 10–13 show the effect of the acceleration ratio parameter (R) on the various kinematic quantities. For these four figures, the jerk control parameter was fixed at $n=2n_{min}$. Figure 11 shows that R has the effect of moving the cam angle location where peak velocity occurs but has little effect on the more important peak velocity. Figure 12 illustrates the primary motivation for this paper: It shows how forward and backward peak accelerations can be chosen by the designer through the proper selection of the parameter R. Figure 13 illustrates that peak jerk is minimized for the balanced acceleration profile, the case where $R=1$. Of course, if the designer must use an R value different from 1, peak jerk can be reduced by reducing the parameter n.

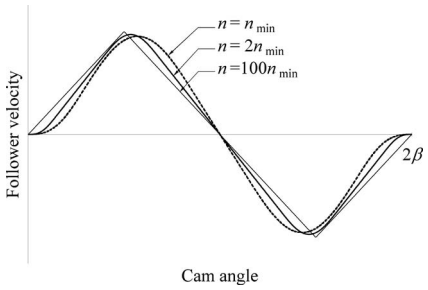

Fig. 7 Effect of the jerk control parameter on follower velocity for $R=1$

5.2 Controlling Follower Jump. Figure 14 is a schematic of a typical automotive overhead valve train showing the cam/follower interface. The interface joint is maintained during the fall

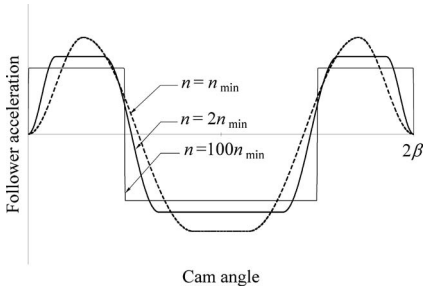

Fig. 8 Effect of the jerk control parameter on follower acceleration for $R=1$

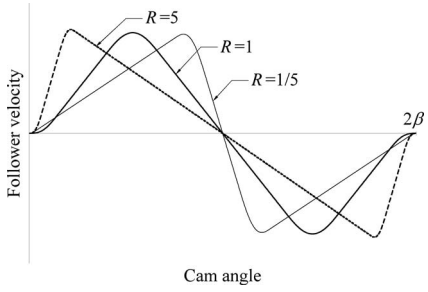

Fig. 11 Effect of the acceleration ratio parameter on follower velocity for $n=2n_{min}$

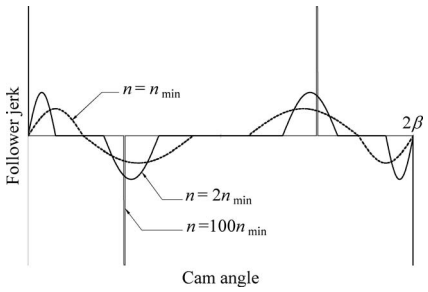

Fig. 9 Effect of the jerk control parameter on follower jerk for $R=1$

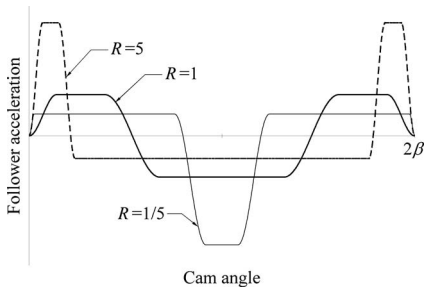

Fig. 12 Effect of the acceleration ratio parameter on follower acceleration for $n=2n_{min}$

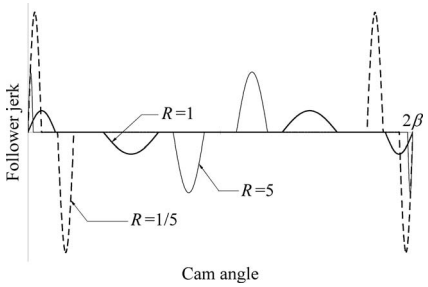

Fig. 13 Effect of the acceleration ratio parameter on follower jerk for $n=2n_{min}$

portion of the cycle by the return spring. However, if the backward acceleration is too high, the joint separates, resulting in the undesirable phenomenon known as "follower jump" or, in the case of automotive valve trains, "valve float." A common way to analyze a valve train for follower jump is to create the single-degree-of-freedom model shown in Fig. 15. In this type of model, $F_i(t)$ is the cam/follower interface force, k_{eq} represents a linear spring with stiffness equivalent to that of the system, c_{eq} represents a linear viscous damper that models frictional losses in the system, and m_{eq} represents an equivalent system mass. Details of process of model creation can be found in Ref. [4].

Applying Newton's second law of motion to the system results in

$$F_i(t) = m_{eq}\ddot{x} + c_{eq}\dot{x} + k_{eq}(x + x_0) \tag{25}$$

where x_0 is the initial spring deflection that creates the spring preload force $F_0 = k_{eq}x_0$. The superimposed dots in Eq. (25) represent time derivatives. Also, in the simplified model, we assume that $x(t) = s(t)$. Therefore, recalling the relationships between pseudo- and true quantities, Eq. (25) can be written as

$$F_i(\theta) = m_{eq}\omega^2 a(\theta) + c_{eq}\omega v(\theta) + k_{eq}(s + s_0) \tag{26}$$

To maintain the interface joint requires that $F_i(\theta)$ be greater than zero. Impending follower jump is predicted when the interface force goes to zero. During portions of the fall, both a and v are

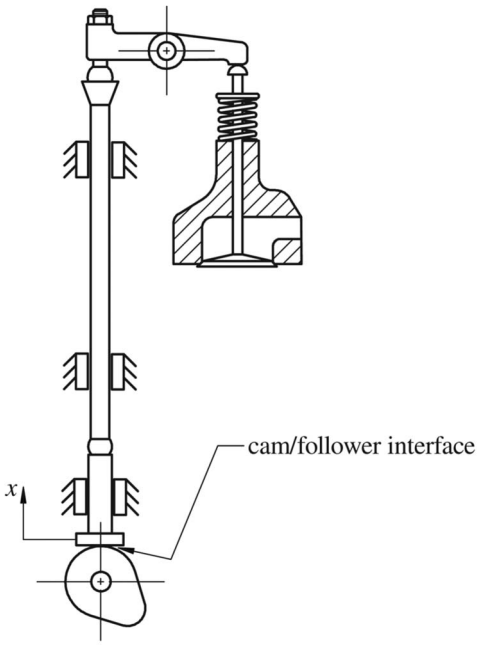

Fig. 14 Schematic of an overhead valve train

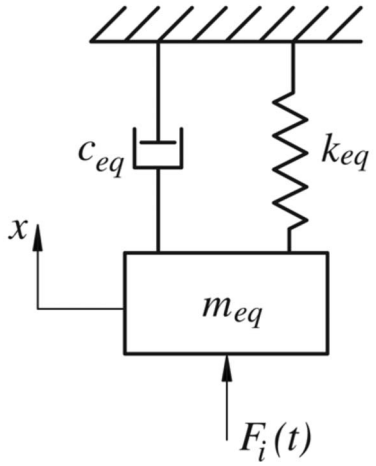

Fig. 15 Single-degree-of-freedom model of a cam/follower system

negative, and both tend to subtract from the spring preload force that maintains the joint. Furthermore, because of the ω^2 factor, the acceleration is especially important in reducing the interface force during the fall portion of the cycle. Shown in Fig. 16 is the interface force for a typical automotive valve train. The system parameters used in this illustration were $h=8$ mm, $2\beta=128$ deg, $n=1.5n_{min}$, $m_{eq}=0.13$ kg, $c_{eq}=8.1$ kg/s (6% of critical), $k_{eq}=35$ N/mm, and $x_0=15$ mm. The acceleration profile was balanced with $R=1$ for this analysis. As the cam speed increases, the inertia and damping forces drive the interface force higher during periods of positive acceleration; during periods of negative acceleration and velocity, the force is driven lower. Eventually the cam speed becomes sufficient to make the interface force zero, at which point we have impending follower jump.

Figure 17 shows the results of an analysis with $R=5$ and all other parameters the same as before. Of course, the interface force during rise is much greater than before, the acceleration being adjusted to have larger forward values. However, the reduction in backward acceleration, delays the point where follower jump occurs. In this example, follower jump occurs at 4750 rpm, a 20% improvement over the previous case. Figure 18 shows the results of an analysis with $R=1/5$ and all other parameters the same as before. Here the increased backward acceleration is seen to cause follower jump at a much lower cam speed, 2610 rpm.

Traditional ways of handling the follower jump problem are as follows: (1) increase the spring force through stiffness and/or preload and/or (2) reduce the system equivalent mass. Both of these have the effect of increasing the maximum operating speed of a cam/follower system before follower jump occurs. Now, with the

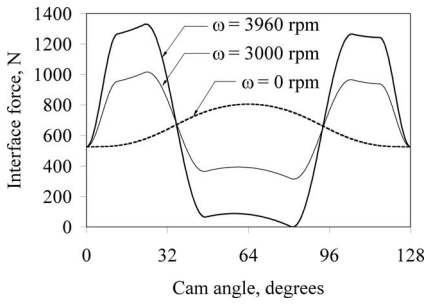

Fig. 16 Cam interface force for a typical automotive valve train with $R=1$

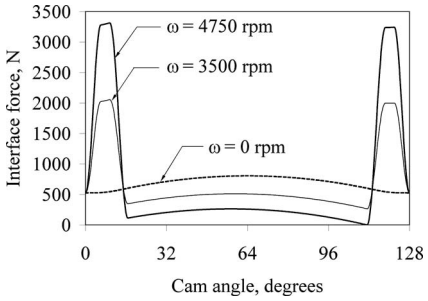

Fig. 17 Cam interface force for a typical automotive valve train with *R*=5

acceleration profile introduced in this paper, designers have the added option of reducing the backward acceleration by changing the value of R, the acceleration ratio parameter.

5.3 Wear Control. With all other factors held constant (surface hardness, for example), wear at the cam/follower interface is largely governed by the interface force [4–7]. In some modes (e.g., abrasion and sliding), wear is proportional to the interface force [5,6]. In other modes (e.g., fatigue induced by rolling contact), wear is proportional to $(F_i)^p$, where p can be 3 or higher [7]. Therefore, wear problems at the cam/follower interface can be improved by reducing the maximum interface force. As shown in Figs. 16–18, this force is maximal during the early portion of the rise where both acceleration and velocity are positive. Figure 19 shows the maximum values of interface force for the cases of $R=1$ and $R=5$, for cam speeds from zero to 3500 rpm. As can be seen, reduction in interface force is most pronounced at higher cam speeds where the inertia forces dominate. At lower cam speeds, the spring force dominates, and this is not affected by follower acceleration. Therefore, the technique presented here works best for high-speed cams.

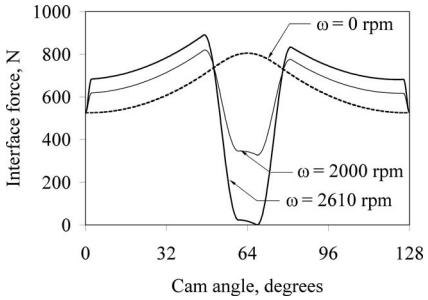

Fig. 18 Cam interface force for a typical automotive valve train with *R*=1/5

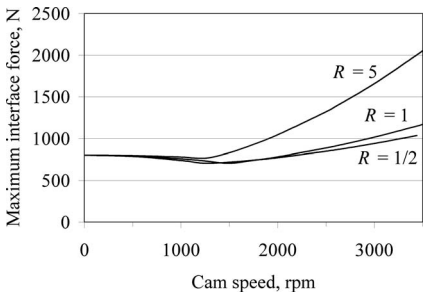

Fig. 19 Maximum interface force for a typical automotive valve train with three different acceleration profiles

6 Concluding Remarks and Future Work

Presented in this paper is a versatile cam profile that offers the single-dwell cam designer the following benefits.

1. A method to bias peak forward and backward acceleration in the three pulses (two positive and one negative) shown in Fig. 3. These acceleration pulses are typically the ones that are adjusted to get desirable automotive valve motion [8]. This allows designers better control over the design objectives of preventing follower jump and reducing cam wear.
2. Balanced velocity and jerk functions that give equal magnitude for both the forward and backward velocities and jerk.
3. Well-rounded interfaces between the constant acceleration regions that have the beneficial effect of providing a continuous jerk function.
4. Control over the amount of peak jerk in the cycle through the jerk control parameter n.

The acceleration profile presented here provides a general approach to biasing acceleration pulses. However, in some instances, particularly in automotive applications, it is desirable to provide a "hard stop" to seat the valve firmly, providing good gas sealing and heat transfer coupling [2,8]. In these cases, the addition of opening and closing "ramps" are added to the profile of Fig. 3. These ramps add small well-defined regions of positive area to the beginning and ending of the acceleration profile that must be balanced in the negative area. The author plans to address the opening and closing ramps in a future work.

Nomenclature

a = pseudoacceleration of the follower
$\bar{a}$ = true acceleration of the follower
A = amplitude parameter for forward acceleration
B = amplitude parameter for backward acceleration
c_{eq} = equivalent damping constant of the single-degree-of-freedom model
$C_1, C_2, \ldots, C_{11}$ = numeric constants (see Eq. (18))
$F_i(t)$ = cam/follower interface force
h = follower lift
k_{eq} = equivalent system stiffness in the single-degree-of-freedom model
j = pseudojerk of the follower
$\bar{j}$ = true jerk of the follower
m, n = parameters that control the amount of cam angle needed to transition between constant acceleration regions
m_{eq} = equivalent mass in the single-degree-of-freedom model
p, q = cam angle durations where acceleration is constant
R = A/B is the acceleration amplitude ratio
s = follower position
s_0 = x_0
t = time
v = pseudovelocity of the follower
$\bar{v}$ = true velocity of the follower
x = displacement of equivalent mass in single-degree-of-freedom model
x_0 = initial return spring deflection in single-degree-of-freedom model
β = cam angle during which rise or fall occurs
$\phi_1, \phi_2, \ldots, \phi_7$ = angle constants (see Eq. (17))
θ = cam angle
ω = cam angular velocity

References

[1] Shigley, J. E., and Uicker, J. J., Jr., 1980, *Theory of Machines and Mechanisms*, McGraw-Hill, New York, Chap. 6, pp. 204–207.

[2] Norton, R. L., 2002, *Cam Design and Manufacturing Handbook*, Industrial, New York, Chaps. 2, 3, 4, 9, and 10.
[3] Norton, R. L., Levasseur, D., Pettit, A., and Alamsyah, C., 1988, "Analysis of the Effect of Manufacturing Methods and Heat Treatment on the Performance of Double Dwell Cams," Mech. Mach. Theory, **23**(6), pp. 461–473.
[4] Chen, F. Y., 1982, *Mechanics and Design of Cam Mechanisms*, Pergamon, New York, Chaps. 12 and 14.
[5] Tylczak, J. H., 1992, "Abrasive Wear," *Friction, Lubrication and Wear Technology* (ASM Handbook), Vol. 18, ASM International, Materials Park, OH.
[6] Ludema, K. C., 1992, "Sliding and Adhesive Wear," *Friction, Lubrication and Wear Technology* (ASM Handbook), Vol. 18, ASM International, Materials Park, OH.
[7] Blau, P. J., 1992, "Rolling Contact Wear," *Friction, Lubrication and Wear Technology* (ASM Handbook), Vol. 18, ASM International, Materials Park, OH.
[8] Mosier, R. G., Geist, B., and Resh, W. F., 2006, "Method for Producing a Constraint-Satisfied Cam Acceleration Profile," U.S. Patent No. 7,136,789.

Pressure Load Estimation During Ex-Vessel Steam Explosion

Matjaž Leskovar
Reactor Engineering Division,
Jožef Stefan Institute,
Jamova cesta 39,
SI-1000 Ljubljana, Slovenia
e-mail: matjaz.leskovar@ijs.si

An ex-vessel steam explosion may occur when, during a severe reactor accident, the reactor pressure vessel fails and the molten core pours into the water in the reactor cavity. A steam explosion is a fuel-coolant interaction process where the heat transfer from the melt to water is so intense and rapid that the timescale for heat transfer is shorter than the timescale for pressure relief. This can lead to the formation of shock waves and production of missiles that may endanger surrounding structures. A strong enough steam explosion in a nuclear power plant could jeopardize the containment integrity and so lead to a direct release of radioactive material to the environment. In the article, different scenarios of ex-vessel steam explosions in a typical pressurized water reactor cavity are analyzed with the code MC3D, which is being developed for the simulation of fuel-coolant interactions. A comprehensive parametric study was performed by varying the location of the melt release (central and side melt pours), the cavity water subcooling, the primary system overpressure at vessel failure, and the triggering time for explosion calculations. The main purpose of the study was to determine the most challenging ex-vessel steam explosion cases in a typical pressurized water reactor and to estimate the expected pressure loadings on the cavity walls. Special attention was given to melt droplet freezing, which may significantly influence the outcome of the fuel-coolant interaction process. The performed analysis shows that for some ex-vessel steam explosion scenarios much higher pressure loads are predicted than obtained in the OECD program SERENA Phase 1. [DOI: 10.1115/1.3078789]

Keywords: steam explosion, ex-vessel, reactor cavity, pressure load, severe accident

1 Introduction

What is generally called a steam explosion in the frame of reactor safety is a process occurring during the interaction of the core melt with water when the energy transfer from the melt to the coolant is so rapid that very high pressure regions are created, which, when expanding, induce dynamic loading of the surrounding structures [1]. The steam explosion is also called an energetic fuel-coolant interaction. The dynamic loads generated on the reactor pressure vessel walls by an in-vessel steam explosion can potentially lead to the early failure of the vessel and challenge the in-vessel retention strategies. The dynamic loads generated on the cavity walls and the reactor pressure vessel by an ex-vessel steam explosion can potentially lead to cavity damage or failure and/or to primary system piping severe loads that could challenge the containment integrity.

Details of processes taking place prior and during a steam explosion have been experimentally studied for a number of years with adjunct efforts in modeling these processes to address the scaling of experimental results to reactor conditions. Despite great efforts in steam explosion research, the confidence in prediction of reactor situations is not such that an unambiguous position could be taken whether the early failure of the containment due to a steam explosion would be possible or not. Therefore, in the year 2002, the first phase of the Organization for Economic Cooperation and Development (OECD) program steam explosion resolution for nuclear applications (SERENA) was launched, bringing together most international experts in the area of fuel-coolant interaction (FCI) with the objective of evaluating the capabilities of the current generation of FCI computer codes in predicting steam explosion induced loads, reaching consensus on the understanding of important FCI phenomena relevant to the reactor simulations, and to propose confirmatory research to bring the predictability of FCI energetics to required levels for risk management [2]. One of the outcomes of the OECD/SERENA Phase 1 program is that for in-vessel steam explosions the calculated loads are far below the capacity of typical reactor vessels, which allows thinking that the safety margin for in-vessel FCI might be sufficient. But for ex-vessel steam explosions the calculated loads are above the capacity of typical reactor cavity walls. Due to the large scatter of simulation results, reflecting the uncertainties in steam explosion understanding, modeling, and scaling, the safety margin for ex-vessel FCI cannot be quantified reliably.

To get a better insight in the ex-vessel steam explosion phenomenon and the resulting pressure loads, a comprehensive analysis has been performed simulating different scenarios of ex-vessel steam explosions in a typical pressurized water reactor cavity with the FCI code MC3D [3]. In this article the performed study is described and the main results are presented.

2 Modeling

The simulations were performed with the MC3D computer code, which is being developed by IRSN, France [3]. MC3D is a code for the calculation of different types of multiphase multicomponent flows. It has been built with the fuel-coolant interaction calculations in mind. It is, however, able to calculate very different situations and has a rather wide field of potential applications. MC3D is a set of two fuel-coolant interaction codes with a common numeric solver, one for the premixing phase and one for the explosion phase. In general, the steam explosion simulation with MC3D is being carried out in two steps. In the first step, the distributions of the melt, water, and vapor phases at steam explosion triggering are being calculated with the premixing module. These premixing simulation results present the input for the second step when the escalation and propagation of the steam explosion through the premixture are being calculated with the explosion module.

The MC3D premixing model [4] is a six-field application in which the melt is described by three fields. The first one is called "continuous" and can describe many situations as, e.g., a jet or the

Manuscript received August 19, 2008; final manuscript received August 21, 2008; published online February 13, 2009. Review conducted by Dilip R. Ballal.

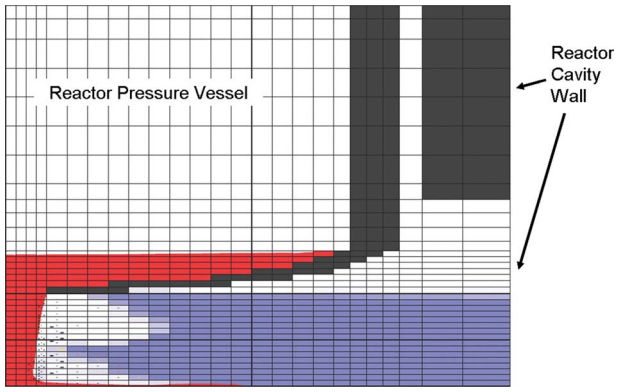

Fig. 1 Geometry and mesh of 2D axial symmetric model of reactor cavity for central melt pour. The scales in horizontal and vertical directions are different.

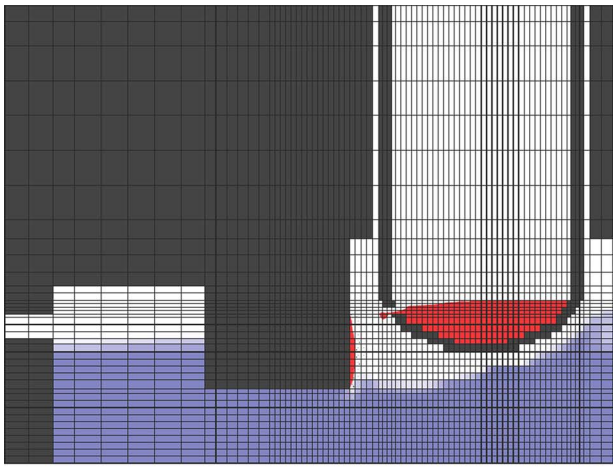

(*a*)

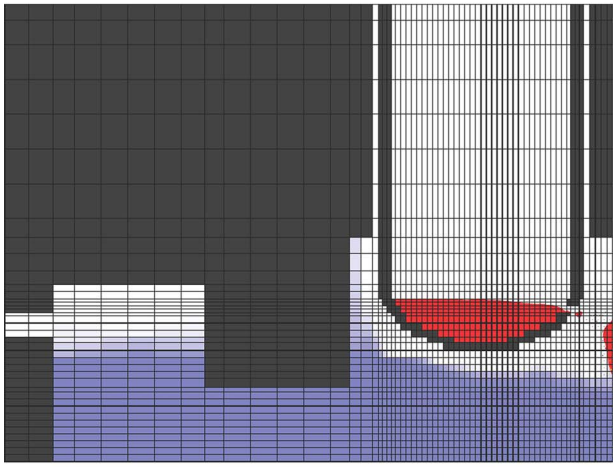

(*b*)

Fig. 2 Geometry and mesh of 2D slice model of reactor cavity for left (top) and right (bottom) side melt pours. The scales in horizontal and vertical directions are different.

melt lying on the bottom of a vessel. The second field corresponds to the droplets issued from the jet fragmentation. This field describes the discontinuous state of the fuel. The third field is optional and describes the fuel fragments issuing from drop fine fragmentation. The remaining three fields are the water, the vapor, and a noncondensable gas. The drop surface area is modeled with a standard interfacial area transport equation. In the explosion model [4], the continuous phase is not present and only the two fields related to the dispersed fuel are considered. There is also another difference between the two applications: In the premixing model, the fuel fragments are in equilibrium with the water, whereas in the explosion model, the fragments have their own dynamical and thermal fields. They interact with the coolant in a similar way to the drops; in particular, the coolant mass transfer that they impose is calculated by applying a disequilibrium approach.

To be able to perform a series of simulations of different ex-vessel steam explosion scenarios, the reactor cavity was modeled in a simplified 2D geometry since the central processing unit (CPU) times of 3D simulations would be too long. To assure that the 2D simulation results reflect qualitatively and quantitatively as closely as possible the conditions in a real 3D reactor cavity, the 2D geometry has to be appropriately defined. Therefore, the simulations were performed with two different 2D representations of a typical 3D pressurized water reactor cavity: the 2D axial symmetric model (Fig. 1) and the 2D slice model (Fig. 2). The 2D axial symmetric model is, due to its axial symmetry, limited on the treatment of axial symmetric phenomena with axial symmetric initial conditions in the axial symmetric part of the reactor cavity directly below the reactor pressure vessel and around it. Consequently, the venting through the instrument tunnel cannot be directly considered in the axial symmetric model, and therefore the venting through the instrument tunnel was not considered in the model, which is conservative. Contrary to the axial symmetric model, which treats only part of the reactor cavity, the 2D slice model treats the whole reactor cavity. However, it does not take into account the 3D geometry and the 3D nature of the phenomena. So the cylindrical part of the reactor cavity and the cylindrical reactor pressure vessel are not treated as cylinders but as plan-parallel infinite plates. In the 2D slice model the opening on the left side was determined so that the opening area per reactor cavity width corresponds to the real 3D reactor cavity geometry.

The cavity geometry and dimensions were set in accordance with a typical pressurized water reactor cavity [5,6]. In the models the dimensions of the cavity are length $x \approx 10.5$ m, radius of cylindrical part $r \approx 2.5$ m, and height $z \approx 13$ m, and the mesh sizes are 2D axial symmetric model—25×35 cells (Fig. 1) and 2D slice model: left melt pour—77×39 cells and right melt pour—62×39 cells (Fig. 2). In regions, which are more important for the modeling of the FCI phenomena, the numerical mesh was adequately refined; therefore the meshes for the left and right side melt pours are not identical (Fig. 2). The initial pressure in the domain was set to the assumed containment pressure, and a constant pressure boundary condition at the cavity openings was applied.

3 Simulation

3.1 Simulated Cases. In the performed ex-vessel steam explosion study, a wide spectrum of different relevant scenarios has been analyzed to capture the most severe steam explosions and to establish the influence and importance of different accident conditions on the FCI outcome. The simulations have been performed in two steps. In the first step, the premixing phase of the FCI process has been simulated for selected scenarios and then, in the succeeding second step, the explosion phase simulations have been performed by triggering the so established premixtures at different times. The premixing phase simulations have been performed for the cases presented in Table 1, varying the following parameters: melt pour location, primary system overpressure, and cavity water subcooling. In the premixing simulations, the initial conditions were set reasonably according to expected conditions at the vessel failure during a severe accident in a typical pressurized water reactor. They are similar to the conditions used in the ex-vessel reactor simulations in the OECD program SERENA Phase

Table 1 Initial conditions for simulated premixing cases

Parameter	Value	Designator
Melt temperature	3000 K	/
Melt level	1.25 m	/
Melt mass	50 t	/
Reactor vessel	Central pour: r=0.2 m	/
Opening size	Side pours: h=0.2 m	
Water level	3 m	/
Containment pressure	1.5 bars	/
Melt pour location	Central (Fig. 1)	C
	Left (Fig. 2)	L
	Right (Fig. 2)	R
Primary system	0 bar	0
Overpressure	2 bars	2
Water temperature	100°C	100
	80°C	80
	60°C	60

1 [2]. Central and side melt pours were considered, and a parametric analysis was performed by varying the primary system overpressure (0 bar and 2 bars) and the water temperature (100–60°C). The water saturation temperature at the assumed 1.5 bar containment pressure is 111.4°C; so the cavity water subcooling was in the range of 11.4–51.4°C. The simulated cases were denoted with three designators defined in Table 1 (e.g., case C2-60 is a central melt pour at 2 bar primary system overpressure into cavity water with a temperature of 60°C).

The premixing phase was simulated for 10 s after the start of the melt release. For each premixing simulation, a number of explosion simulations were performed triggering the premixture at different times. The explosion triggering times (Table 2) were selected depending on the melt pour location and the primary system pressure so that the most important stages of the case specific melt releases were captured. In the central melt pour cases at 2 bar primary system overpressure (C2), after 5 s most melt was released from the reactor vessel and gas started to flow out of the vessel opening and dispersing the melt jet; so the premixture was triggered also at a somewhat later time to capture this phenomenon. The side melt pour cases at a depressurized primary system (L0, R0) were not triggered before 1.5 s since about 1 s was needed for the melt to reach the water surface.

In addition to the triggering times listed in Table 2, for each simulated premixing case the explosions were triggered also at one to three additional times when the explosivity criteria crit1 and crit2, which are based on the volume of liquid melt drops in contact with water as

$$\text{crit1:}\quad V_1 = \sum_{\text{cells}} \alpha_d \frac{\alpha_l}{\alpha_d + \alpha_l} C_m V_c$$

$$\text{crit2:}\quad V_2 = \sum_{\text{cells with } \alpha_{lr} > 0.3} \alpha_d V_c$$

$$C_m = \min\left(1, \max\left(0, \frac{\alpha_{lr} - 0.3}{0.4}\right)\right), \quad \alpha_{lr} = \frac{\alpha_l}{\alpha_l + \alpha_g} \tag{1}$$

were the highest. The symbols α_l, α_g, and α_d denote the liquid water, void, and liquid melt droplet volume fractions, and V_c is the mesh cell volume. In this way, we tried to capture also the strongest steam explosions. For the most explosive central melt pour case, that is, case C2-60 as presented in Sec. 3.2, a series of explosion simulations was performed triggering the premixture every 0.2 s during the whole simulated premixing duration of 10 s to get a better insight in the influence of the triggering time on the steam explosion outcome. The explosion phase was simulated for 0.1 s after triggering. The premixture was triggered in the cell, where the local cell explosivity criteria crit2 was the highest (Eq. (1)).

3.2 Simulation Results. The premixing and explosion simulations were performed with the code MC3D Version 3.5 with patch 1 on a network of personal computers with Windows operating system, having altogether about 30 processors, using the Condor distributed computing system. So a number of simulations could be performed simultaneously, each simulation running on its own processor. To establish the best model parameters enabling stable calculations, first a number of testing simulations were performed. During the study, some minor code bugs were identified and corrected, and some code improvements were done.

In Fig. 3, the maximum calculated pressures in the cavity and the maximum calculated pressure impulses (integral of pressure over time) at the cavity walls (cavity bottom and lateral wall) are presented for the simulated cases. In the calculation of the pressure impulses, the initial containment pressure was subtracted from the calculated absolute pressure since the dynamical pressure loads on the cavity walls are caused by the pressure difference. The points on the graphs are connected with lines to make the figures clearer, but since the triggering times are too rare for interpolation (except for case C2-60), these lines mostly do not correctly represent the expected pressures and pressure impulses between two calculated points. On some graphs for the same simulated case more points are plotted at the same triggering time (e.g., the white (yellow) curves on all figures). This means that, in these cases, more premixing simulations were performed for the same conditions, using different minimum bubble diameters in the calculations, most probably due to convergence problems during premixing or later during the explosion simulation, and so on the graphs the available explosion simulation results based on different premixing simulations are presented. Some explosion simulations did not converge, and the results for these cases are consequently not presented in the graphs.

The results for the central melt pour cases show that, in the initial stage of the melt pour, stronger explosions occur for higher cavity water subcooling and higher melt pour driving pressure. The reason for this could be that higher water subcooling results in less void buildup and higher driving pressure in increased melt fragmentation. On the contrary, at the later stage of the simulations, stronger explosions occur for lower water subcooling and the driving pressure has no significant influence anymore (until in the pressurized case most of the melt is released after 5 s and gas starts to flow through the vessel opening). This difference could

Table 2 Basic triggering times for explosion simulations

Cases	Triggering times (s)							
C0	0.5	1	/	2	/	5	/	10
C2	0.5	1	/	2	/	5	6.5	10
L0, R0	/	/	1.5	2	3	5	/	10
L2, R2	0.5	1	/	2	3	5	/	10

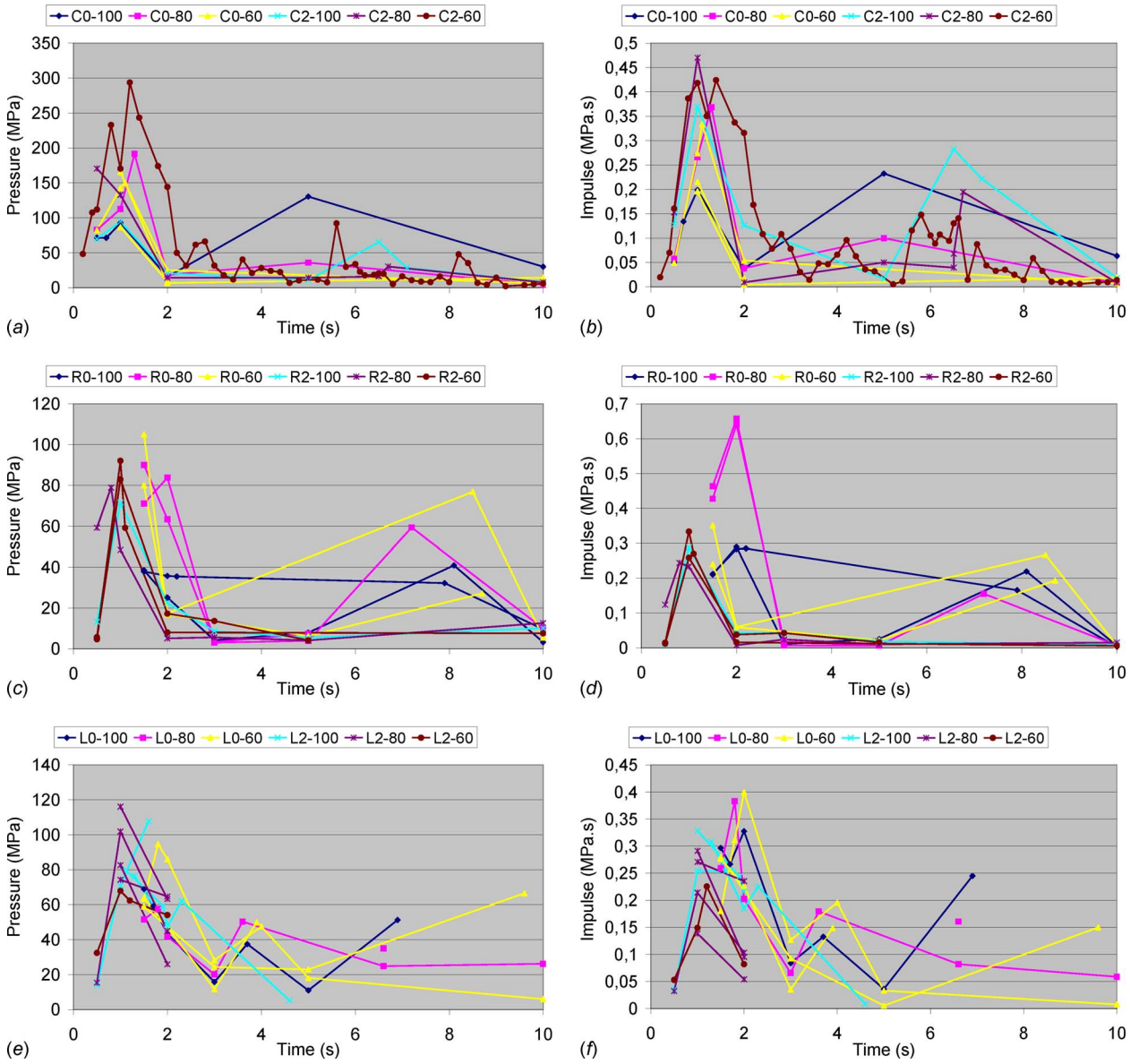

Fig. 3 Maximum calculated pressure in cavity (left) and maximum calculated pressure impulse at cavity walls (right) for simulated cases

be due to less droplet solidification with lower water subcooling. The results of the side melt pour cases reveal that stronger explosions may be expected with a depressurized primary system. The reason for this could be that with a pressurized primary system the melt is ejected sideward on the cavity wall, sliding then into water at the wall, which hinders the formation of an extensive premixture. In addition, with a pressurized system, gas flows through the vessel opening into the cavity and pushes the cavity water through the instrument tunnel out of the cavity, creating a highly voided region below the reactor pressure vessel.

In general, the highest maximum pressures and maximum pressure impulses were reached with higher cavity water subcooling (Table 3). The highest maximum pressure was reached in case C2-60 (nearly 300 MPa) and the highest pressure impulse in case R-80 (nearly 700 kPa s). These values significantly overpredict the results obtained in the frame of the OECD program SERENA Phase 1 [2], where the calculated maximum pressure loads at the lateral cavity wall for a central melt pour varied from a few megapascals to ~40 MPa and the pressure impulses from a few kPa s to ~100 kPa s. But it should be stressed that the presented pressure loads are not directly comparable to SERENA results since the pressure loads in SERENA are given for the lateral cavity wall, whereas the pressure loads in our analysis consider all cavity walls, i.e., beside the lateral cavity wall also the bottom of the cavity, where the highest pressure loads were obtained.

Table 3 Maximum pressures and pressure impulses for different melt pour locations

	Maximum pressure		Maximum impulse	
Pour location	p (MPa)	Case	I (kPa s)	Case
C	292.9	C2-60	470.4	C2-80
R	105.1	R0-60	657.6	R0-80
L	116.1	L2-80	399.9	L0-60
SERENA lateral wall	A few to ~40 MPa		A few to ~100 kPa s	

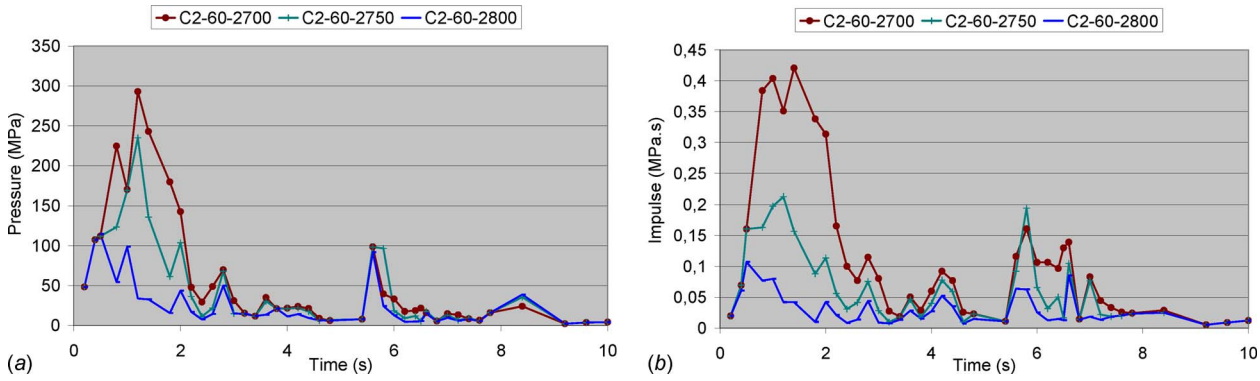

Fig. 4 Maximum calculated pressure in cavity (left) and maximum calculated pressure impulse at cavity walls (right) for most explosive case C2-60, considering different corium droplet bulk temperatures, below which the fine fragmentation process is suppressed

The high calculated pressure loads in the side melt pour cases could be attributed to the used 2D slice modeling of the reactor cavity, where the melt is released in the form of an infinite wide curtain and the explosion is triggered through the whole width of that curtain (Fig. 2). This is quite conservative since, due to the 2D treatment, venting and pressure relief is underpredicted and the explosion development is overpredicted. In addition the appropriateness of the applied premixing and explosion models in such a 2D geometry is questionable. So the side melt pour simulations (L, R) should be regarded more as providing only some basic qualitative insight in the FCI behavior for side melt pour scenarios.

The central melt pour cases are closer to the reality since, for a central melt pour, the 2D axial symmetric representation is quite suitable and the applied FCI models are adjusted to such a geometry (Fig. 1). If the explosion is not triggered at the symmetry axis, venting is again underpredicted and the explosion development overpredicted, but less than in the side melt pour cases. So the reliability of central melt pour simulation results is higher than the reliability of side melt pour simulation results. As we see in Table 3, also in the central pour simulations the maximum pressure loads (impulse nearly 500 kPa s) significantly overpredict the pressure loads obtained in SERENA Phase 1 and significantly exceed the pressure impulses, which could be consequential to the integrity of the cavity and are estimated to be of the order of some tens of kPa s [2].

3.3 Influence of Droplet Freezing. In the explosion simulations it was assumed that the corium droplets in the premixture can potentially fine fragment, and so contribute to the explosion escalation, if the droplet bulk temperature is higher than the corium solidus temperature. This overpredicts the ability of corium droplets to efficiently participate in the explosion, since in reality, during premixing, a crust is formed on the corium droplets much earlier than the droplet bulk temperature drops below the solidus temperature [7]. This crust inhibits the fine fragmentation process and if the crust is thick enough it completely prevents it. To find out the impact of the crust formation on the explosion results, for the most explosive case C2-60 (Fig. 3) additional explosion simulations were performed, considering different corium droplet bulk temperatures, below which the fine fragmentation process is suppressed. In this parametric study for the minimum fine fragmentation temperatures the corium solidus temperature of 2700 K (default), the liquidus temperature of 2800 K, and the temperature of 2750 K in-between were taken. The simulation results are presented in Fig. 4.

We see that the minimum fine fragmentation temperature has a significant influence on the strength of the steam explosion. As is summarized in Table 4, both the maximum pressure in the cavity and the maximum pressure impulse at the cavity walls decrease with increasing minimum fine fragmentation temperature. This was expected since with a higher minimum fine fragmentation temperature a smaller fraction of the corium in the premixture is hot enough to fulfill the strained temperature criterion for fine fragmentation, and consequently a smaller fraction of the corium in the premixture can potentially participate in the explosion.

In Fig. 5 the time evolution of the mass of hot corium droplets, with the bulk temperature higher than the minimum fine fragmentation temperature, in regions with different void fractions is presented during premixing. During premixing nearly 8000 kg corium droplets are formed (curve: total). The mass of hot corium droplets, which are potentially available to participate in the explosion (curves: $<100\%$), depends on the selected minimum fine fragmentation temperature and is up to ~3000 kg for the minimum fine fragmentation temperature $T_{mff}=2700$ K, up to ~2500 kg for $T_{mff}=2750$ K, and up to ~2000 kg for $T_{mff}=2800$ K. The hot corium droplets can efficiently participate in the explosion only in regions with enough water available for vaporization and for enabling the fine fragmentation process, which is essential for the steam explosion development. Therefore a better indicator for the expected strength of the resulting explosion is the available mass of hot droplets in regions, where the void fraction is not too large, that is, in regions, where the vapor fraction is below at least 70%. The so established corium droplet masses are much lower, up to ~900 kg for $T_{mff}=2700$ K, up to ~600 kg for $T_{mff}=2750$ K, and up to ~300 kg for $T_{mff}=2800$ K, and these mass differences are reasonably reflected in the calculated pressure loads presented in Table 4. We see that also for the highest selected minimum fine fragmentation temperature of 2800 K, which assumes that the fine fragmentation process can take place only for melt droplets with the bulk temperature higher than the liquidus temperature, the calculated pressure loads exceed the values obtained in the OECD program SERENA Phase 1.

Table 4 Maximum pressures and pressure impulses for different minimum fine fragmentation temperatures for most explosive case C2-60

Fine frag. temperat. (K)	Maximum pressure (MPa)	Maximum impulse (kPa s)
2700	292.9	420.8
2750	235.0	212.7
2800	114.7	107.2
SERENA lateral wall	A few to ~40 MPa	A few to ~100 kPa s

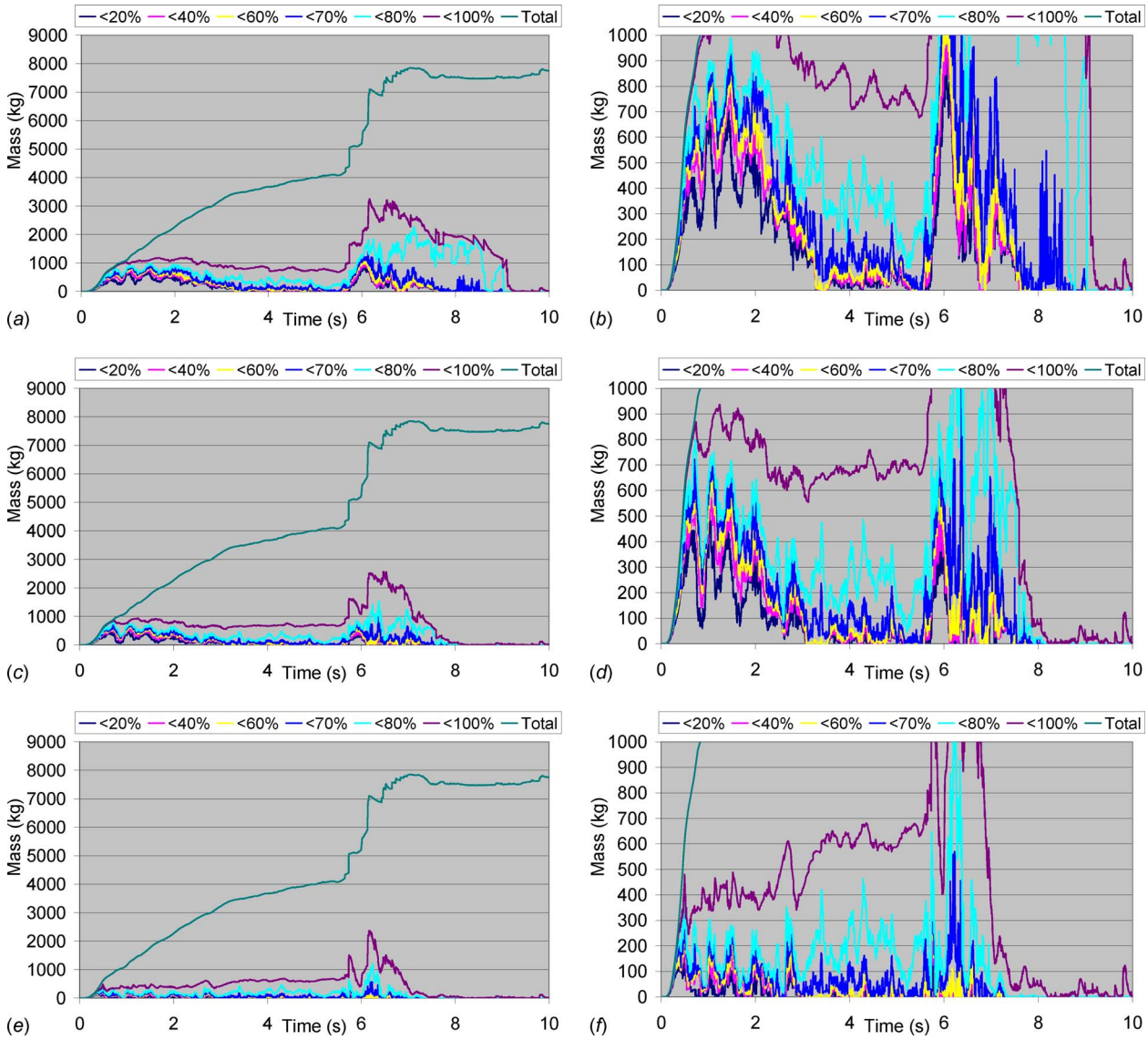

Fig. 5 Mass of hot corium droplets with the bulk temperature above the selected minimum fine fragmentation temperatures (2700 K - top, 2750 K - middle, 2800 K - bottom) in regions with the vapor fraction less than the specified values (<20–<100%) during premixing (left side large scale, right side small scale). In addition also the total (hot and cold) corium droplet mass is presented (total).

4 Conclusions

A comprehensive analysis of the ex-vessel steam explosion phenomenon in a typical pressurized water reactor cavity was performed with the FCI code MC3D. The main purpose of the study was to establish the most challenging ex-vessel steam explosion scenarios and to estimate the expected pressure loadings on the cavity walls.

The simulation results revealed that the strongest steam explosions may be expected in the initial stage of the melt release when the void buildup is not so extensive yet, and at higher water subcooling, where condensation efficiently hinders the void buildup. The results for the central melt pour cases show that, in the initial stage of the melt pour, stronger explosions occur for higher water subcooling and higher primary system overpressure, whereas later stronger explosions occur for lower water subcooling and the driving pressure has no significant influence anymore. An explanation for this could be that, in the initial stage, higher water subcooling results in less void buildup and the higher driving pressure in increased melt fragmentation, whereas at later times mainly droplet freezing, which is more expressive at higher water subcooling, accounts for the observed differences. The results of the side melt pour cases reveal that stronger explosions may be expected with a depressurized primary system. With a pressurized primary system melt is ejected sideward on the cavity wall, hindering the formation of an extensive premixture, and in addition since gas flows through the vessel opening into the cavity a highly voided region below the reactor pressure vessel is formed.

For some side melt pour scenarios as well as for some central melt pour scenarios, the maximum calculated pressures and pressure impulses significantly overpredict the pressure loads obtained in the OECD program SERENA Phase 1. The high calculated pressure loads in the side melt pour cases could be attributed to the 2D modeling of the reactor cavity, where, due to the 2D treatment, venting and pressure relief are underpredicted and the explosion development is overpredicted. Besides, the appropriateness of the applied premixing and explosion models in such a 2D geometry is questionable. But the central melt cases are closer to reality and they have been performed in similar conditions as selected for the SERENA ex-vessel reactor case; so it has to be explored if the

pressure loads during an ex-vessel steam explosion could possibly be higher than expected.

The analysis of the influence of droplet freezing on the explosion results revealed that droplet freezing has a significant impact on the calculated pressure loads. By increasing the minimum fine fragmentation temperature, below which fine fragmentation is suppressed, from the solidus temperature to the liquidus temperature, the calculated maximum pressure impulse at the cavity walls was significantly reduced by a factor of 4. This suggests that appropriate modeling of droplet freezing during premixing and appropriate modeling of the influence of the crust formation on the fine fragmentation process during the explosion phase are essential to be able to perform reliable steam explosion simulations in reactor conditions.

Acknowledgment

The author acknowledges the support of the Ministry of Higher Education, Science and Technology of the Republic of Slovenia within the cooperative CEA-JSI research project (Contract No. 1000-07-380044) and the research program P2-0026. The Jožef Stefan Institute is a member of the Severe Accident Research Network of Excellence (SARNET) within the Sixth EU Framework Program.

Nomenclature

List of Abbreviations

CEA = Commissariat à l'Énergie Atomique
IRSN = Institut de Radioprotection et de Sûreté Nucléaire
JSI = Jožef Stefan Institute

List of Symbols

C_m = melt coefficient in explosivity criterion 1
h = opening height for side pours
r = radius of cylindrical part of cavity, opening radius for central pours
T_{mff} = minimum fine fragmentation temperature
V_c = mesh cell volume
V_1 = volume of liquid melt in contact with water according to explosivity criterion 1
V_2 = volume of liquid melt in contact with water according to explosivity criterion 2
x = cavity length
z = cavity height
α_d = liquid melt droplet volume fraction
α_g = void volume fraction
α_l = liquid water volume fraction
α_{lr} = relative liquid water volume fraction (without considering the melt)

References

[1] Berthoud, G., 2000, "Vapour Explosions," Annu. Rev. Fluid Mech., **32**, pp. 573–611.
[2] Magallon, D., Bang, K. H., Basu, S., Berthoud, G., Bürger, M., Corradini, M. L., Jacobs, H., Meignen, R., Melikhov, O., Moriyama, K., Naitoh, M., Song, J. H., Suh, N., and Theofanous, T. H., 2005, "Results of Phase 1 of OECD Programme SERENA on Fuel-Coolant Interaction," ERMSAR-2005, Aix-en-Provence, France, pp. 1–12.
[3] Meignen, R., and Picchi, S., 2005, "MC3D Version 3.5: User's Guide," IRSN Report No. NT/DSR/SAGR/05-84.
[4] Meignen, R., 2005, "Status of the Qualification Program of the Multiphase Flow Code MC3D," *Proceedings of ICAPP '05*, Seoul, Korea, pp. 1–12.
[5] Leskovar, M., Cizelj, L., Končar, B., Parzer, I., and Mavko, B., 2005, "Analysis of Influence of Steam Explosion in Flooded Reactor Cavity on Cavity Structures," Jožef Stefan Institute, Report No. IJS-DP-9103.
[6] Cizelj, L., Leskovar, M., and Končar, B., 2006, "Vulnerability of a Partially Flooded PWR Reactor Cavity to a Steam Explosion," Nucl. Eng. Des., **236**, pp. 1617–1627.
[7] Leskovar, M., Meignen, R., Brayer, C., Bürger, M., and Buck, M., 2007, "Material Influence on Steam Explosion Efficiency: State of Understanding and Modelling Capabilities," ERMSAR-2007, Karlsruhe, Germany, pp. 1–16.

Experimental Study on Natural Circulation and Air-Injection Enhanced Circulation With Different Fluids

W. Ambrosini
e-mail: walter.ambrosini@ing.unipi.it

N. Forgione

F. Oriolo

E. Semeraro

M. Tarantino

Dipartimento di Ingegneria Meccanica Nucleare
e della Produzione,
Università di Pisa,
Via Diotisalvi 2,
56126 Pisa, Italy

This paper reports on an experimental investigation on natural circulation and air-injection enhanced circulation performed adopting different fluids. This work is aimed at providing information on the basic mechanisms proposed in the design of future reactors relying on such circulation mechanisms for core cooling. Though the final objective of the research is the study of heavy metal cooling, the work is here limited to nonmetallic fluids. The working fluid adopted in past analyses was water. Further experimental campaigns were recently performed using the Novec™ HFE-7100 fluid, providing additional information on basic phenomena and the related scaling laws. The new fluid has a greater density and a greater thermal expansion coefficient with respect to water. Air was adopted for gas injection. Both natural circulation and gas-injection enhanced circulation are addressed in this work, drawing quantitative conclusions about the observed parametric trends. A systematic comparison is performed with the results obtained in previous experimental activities using water. [DOI: 10.1115/1.3043819]

1 Introduction

Natural circulation plays a well-known role in many design concepts proposed for future nuclear reactors (see, e.g., Ref. [1]). This is the consequence of its suitability as a passive mechanism of core cooling during normal operation or abnormal transients involving loss of forced flow. Though passivity represents an obvious attractive feature in view of increasing plant safety, the intrinsic weakness of forces driving natural circulation must be regarded with due caution. In fact, it is not so obvious that greater passivity means greater safety, unless it is demonstrated that passive phenomena relied on come into play with the desired efficiency when necessary.

Concerning future molten metal cooled reactors, both natural circulation and gas-injection enhanced circulation are considered as possible candidates for granting core cooling in cases in which pumps are not considered strictly necessary. In particular, an example of use of gas-injection enhanced circulation in experiments devoted to studying the cooling of accelerator driven systems (ADS) and other molten metal cooled reactors can be found in the activities performed at the ENEA Brasimone Centre in Italy [2]. A proposal for adopting the air-lift mechanism for target cooling can be also found in Ref. [3].

In past work, the University of Pisa contributed to the experimental and computational analysis of these phenomena by cooperating with ENEA, by supporting experimental activities [4–6], and with specific experiments of its own [7–10]. These experiments were carried out in a facility conceived to adopt different working fluids, starting with water and possibly including low melting point metal alloys. Water was used in past experiments (see, e.g., Ref. [10]) and only recently a different fluid was adopted to acquire greater confidence in the scaling laws representing natural circulation and gas-injection enhanced circulation in loops. Though this fluid, being the Novec™ HFE-7100, has properties that can be hardly compared with those of molten metals, the future cooperation in a similar activity to be performed by lead bismuth eutectic (LBE) at ENEA Brasimone will make available meaningful experimental data for comparison.

The results discussed in the present work concern the experiments performed using the new fluid. In this paper, the data of natural circulation and gas-injection enhanced circulation for the new experimental campaign are discussed, drawing conclusions about the observed phenomena. In addition, a comparison is performed with the results obtained in the previous experimental activities using water.

2 Experimental Apparatus

A sketch of the analysis of natural and gas-injection enhanced circulation (ANGIE) experimental facility, adopted in the present work, is shown in Fig. 1. The piping is made by 1.5 in. i.d. tubes welded or connected through flanges to each other.

The 1 m long heated section consists of four 250 mm long band heaters capable of 1.25 kW each, supplied with a voltage limited to 42 V for operational safety reasons. The riser has a height of 3 m and at its bottom air injection is available through a nozzle, as required for studying gas-injection enhanced circulation. An expansion tank is located at the top of the riser and has the twofold purpose to allow for thermal expansion of the fluid during transient operation and to separate the injected gas from the liquid. The 2 m long heat exchanger located in the descending leg consists of two coaxial tubes, with secondary water flowing through the gap; a helical stainless steel sheet is wound on the outer surface of the internal pipe to enhance heat transfer by swirling flow. A spherical valve is also introduced to allow for varying the loop friction characteristics; a similar spherical valve, normally kept closed, is included in a fluid dump line.

The secondary cooling loop includes a stainless steel circulation pump, a throttling valve placed on its downstream line for flow rate regulation, and a large reservoir for storage of the circulating water. Water enters the heat exchanger at ambient temperature and is discharged back into the reservoir after removing heat from the primary circuit.

The measuring instrumentation includes the following:

Contributed by the International Gas Turbine Institute of ASME for publication in the JOURNAL OF ENGINEERING FOR GAS TURBINES AND POWER. Manuscript received August 8, 2008; final manuscript received August 11, 2008; published online February 13, 2009. Review conducted by Dilip R. Ballal. Paper presented at the 16th International Conference on Nuclear Engineering (ICONE16), Orlando, FL, May 12–15, 2008.

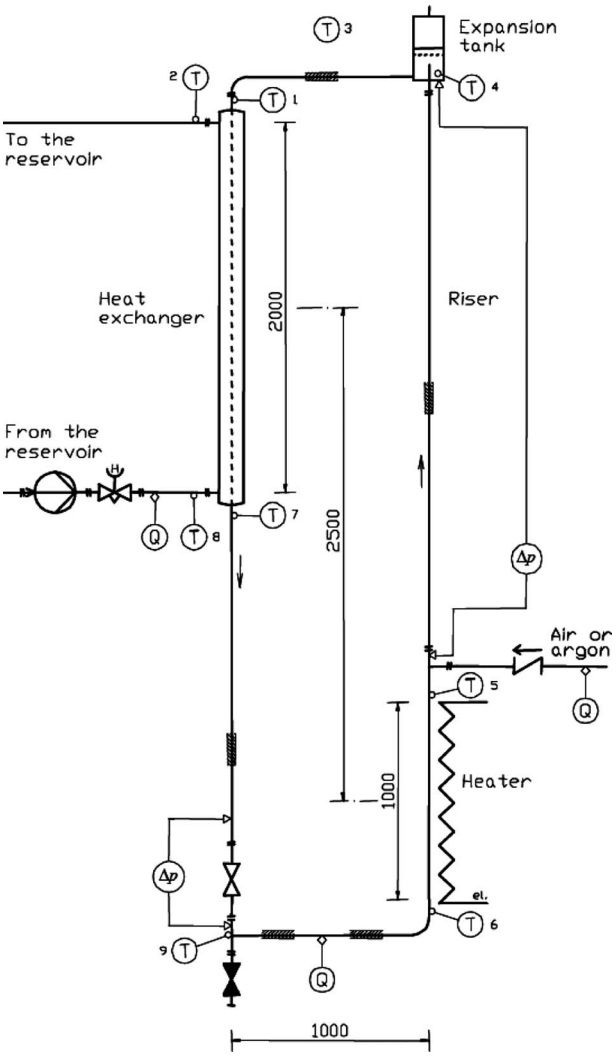

Fig. 1 Sketch of the ANGIE experimental facility

- K-type thermocouples, periodically recalibrated, for measuring the primary fluid temperatures at different locations and the inlet and outlet secondary fluid temperatures
- an ultrasonic flow meter, measuring loop flow rate without perturbing the flow
- an electromagnetic flow meter, placed in the secondary cooling loop
- a rotameter, for measuring the air flow injected into the bottom of the riser
- a current transducer needed to evaluate the electrical heating power
- differential pressure transducers, across the spherical valve and the riser; the pressure drop across the riser is used in estimating the average void fraction during tests with air injection

The electrical power supplied to the heaters is evaluated by signals proportional to the instantaneous values of current and voltage. All the measuring instruments have been calibrated by the manufacturer (as the rotameter and the electromagnetic flowmeter) or directly in the laboratory (as the ultrasonic flowmeter and thermocouples) to assess the uncertainty affecting experimental data.

The building, in which the loop is located, and the control room are separated to avoid any possible hazard to the operating personnel coming from the use of any toxic substance. Actually, this caution is not needed in the case of the fluids used up to now, since also HFE-7100 has benign characteristics from the safety and environmental points of view. The control room equipment includes the data acquisition system and panels for the manual control of the heating power, mass flow in the secondary cooling circuit, and flow rate of the injected air.

Table 1 Matrix of natural circulation tests

Valve closure angle (deg)	Nominal heating power (W)
0	500, 750, 1000, 1250, 1500, 1750, 2000
45	500, 750, 1000, 1250, 1500

3 Experimental Tests

The experimental activity reported herein involved two different test campaigns concerning natural circulation and gas-injection enhanced circulation, respectively.

In natural circulation tests, the main parameters were the heating power and the throttling of the spherical valve available to vary friction along the loop. Tests at different power levels were performed according to valve throttling: from 500 W to 2000 W with a full open valve and from 500 W to 1500 W for 45 deg valve throttling. The lower value of power in the latter case was chosen in order to avoid boiling of the HFE-7100 fluid as a consequence to the lower flow rate. In fact, HFE-7100 has a boiling point of around 61 °C at atmospheric pressure; such a low value may cause subcooled boiling to take place on the heater surface, unless a sufficiently low power is maintained.

In gas-injection enhanced tests, air flow was varied from 0.2 nl/min to 43 nl/min with a fully opened valve or 45 deg throttling. Tables 1 and 2 summarize the main boundary conditions adopted in the tests.

At 50 °C, HFE-7100 has a density of about 1425 kg/m^3, a viscosity of 4.1×10^{-4} kg/(m s), a specific heat of 1233 J/kg K, a thermal conductivity of 0.06 W/m K, and a thermal expansion coefficient of 1.6×10^{-3} K^{-1}. These properties are sufficiently different from those of water to make the use of this fluid interesting to obtain additional data for scaling analyses.

4 Results

4.1 Natural Circulation. While performing the tests, in addition to making use of the ultrasonic flowmeter, it was considered advisable to get an additional estimate of the fluid flow by an energy balance. This was suggested by observing a somehow abnormal behavior of the adopted measuring device in a limited number of operating conditions, possibly due to the high operating temperature. The comparison of the two values of flow rate in a case in which both estimates are available is presented in Fig. 2; as it can be noted, a reliable evaluation of flow rate by the energy balance requires a sufficient waiting time, mainly because of unsteadiness in temperature distribution along the loop. This aspect

Table 2 Matrix of gas-injection enhanced circulation tests

Valve closure angle (deg)	Injected air flow (nl/min)
45	8.2, 17.6, 24.2, 34.0, 45.1, 4.8, 14.3, 21.8, 28.5, 36.7
45	2.0, 5.0, 10.0, 15.0, 17.5, 20.0, 22.0
45	7.1, 16.8, 24.4, 33.0, 39.8, 7.4, 11.5, 20.9, 29.8
45	2.0, 5.0, 10.0, 15.5, 20.0, 7.5, 12.5, 17.5, 22.0
45	0.2, 0.5, 1.0, 2.0, 3.0, 4.0, 1.5, 2.5, 3.5, 4.5
0	7.9, 17.3, 24.9, 33.1, 43.2
0	1.0, 2.0, 3.0, 4.5, 5.0, 10.0, 15.0, 20.0

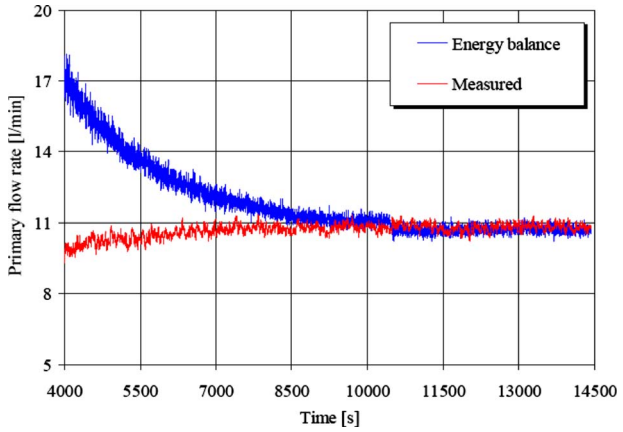

Fig. 2 Typical evolution of flow rate measured by two different techniques for natural circulation tests (500 W, full open valve)

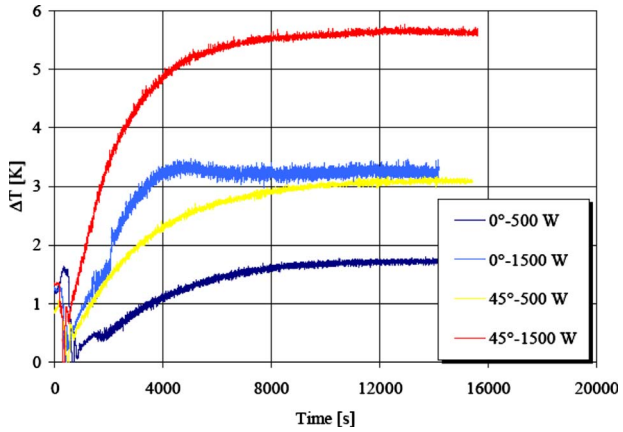

Fig. 4 Time evolution of temperature difference between primary hot and cold leg fluid at different powers and valve closure angles

was duly taken into account in the limited number of cases in which it was necessary to rely on energy balance to estimate the flow rate, checking for actual steadiness of the process.

Figure 3 reports the time evolution of flow rate, as measured during selected tests performed with different heating powers and various degrees of valve closure. As it can be noted, the time required to achieve steady-state conditions tends to decrease with increasing heating power, thus simplifying the test procedure. In one of the cases it was therefore possible to assume the attained value of flow rate as a sufficiently asymptotic one, then shifting to a higher power (from 750 W to 1250 W) for analyzing a further test condition. On the other hand, the time evolution of the temperature differences between the hot leg and the cold leg in the facility shows a remarkable thermal inertia of the apparatus (Fig. 4).

Figure 5 describes the dependence of the volumetric flow rate on the heating power at different degrees of valve closure, making use of the experimental data collected in the present work with HFE-7100 and of previous data obtained with water [11,12]. As it can be noted, a greater flow rate is always observed for HFE-7100 with respect to water, even if in the case of water a greater heating power could be adopted owing to the higher boiling temperature.

Figure 6 presents a more comprehensive overview of data, also including predictions obtained by the RELAP5/MOD3.2 system code [13] and the FLUENT computational fluid dynamics (CFD) code [14]. Moreover, simplified theoretical predictions are reported based on an analysis of the loop steady-state performance, leading to the formulation

$$W = \sqrt[3]{\frac{2\rho_{f,0}^2 g \beta_f A^2 QH}{c_{p,f}\left(\sum_k K_k + \frac{f(\mathrm{Re})L}{D}\right)}} \tag{1}$$

where appropriate values were used for the singular pressure drop coefficients. The figure clearly shows a reasonable agreement be-

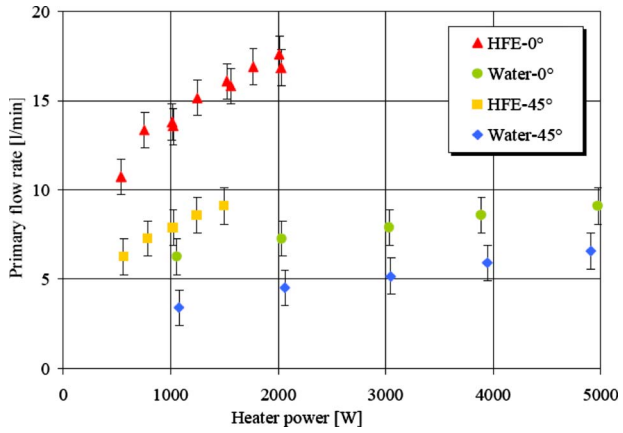

Fig. 5 Fluid flow rate as a function of heating power for present tests with HFE-7100 and previous tests with water

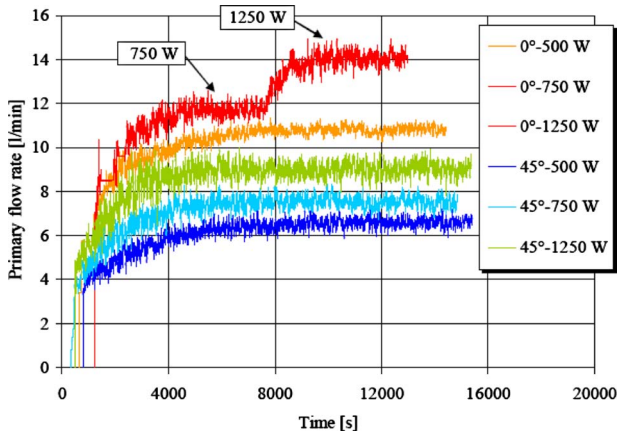

Fig. 3 Time evolution of flow rate at different powers and valve closure angles

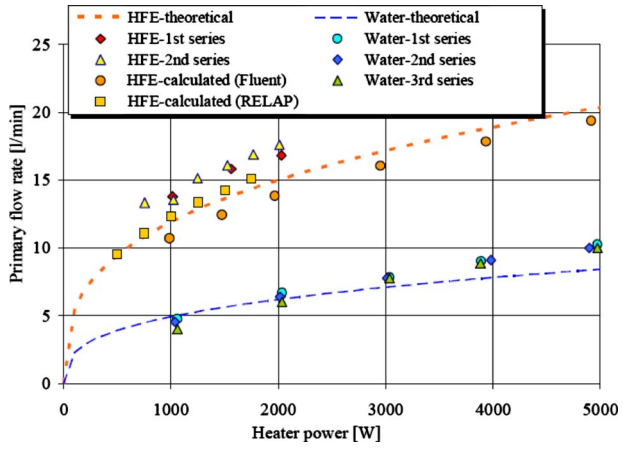

Fig. 6 Comparison between the values of natural circulation flow rate at different operating conditions for the two fluids

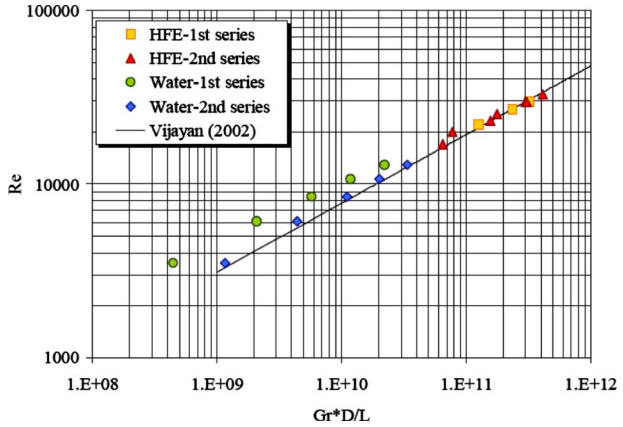

Fig. 7 Dimensionless representation of obtained results for natural circulation with full open valve

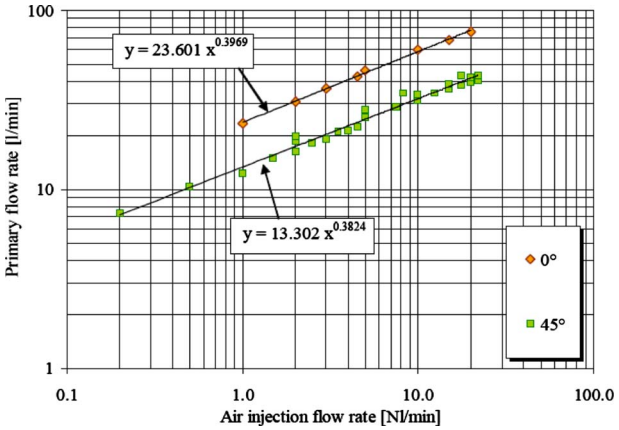

Fig. 9 HFE-7100 flow rate as a function of injected air flow for the tests performed in this work at relatively low air-injection flow

tween theoretical and computational predictions, on one side, and experimental data, on the other, in the limits in which these models can be considered reliable to confirm the overall adequacy of obtained data.

A comparison between experimental data and a correlation is proposed in Figs. 7 and 8, making use of the dimensionless formulations introduced by Vijayan [15]. The following definition of the modified Grashof number is used

$$\mathrm{Gr} = \frac{\rho_f^2 \beta_f g Q H D^3}{\mu_f^3 A c_{p,f}} \tag{2}$$

A very good agreement is observed for data with both water and HFE-7100 and a full open valve. Obviously, since the correlation proposed by Vijayan holds for loops having a rectangular layout, where the main singular pressure drops are due to the bends and the presence of a few tee junctions, increasing the loop friction by throttling the valve results in a lower correlating line.

4.2 Gas-Injection Enhanced Circulation. Figures 9 and 10 describe the power law trends observed for primary flow with respect to air-injection flow in the case of gas-injection enhanced circulation tests performed in the present work. The two figures refer to different ranges of air injection, resulting in different exponents in the power laws.

Figure 11 reports a flow pattern map obtained by classical flow regime transition criteria from the work of Taitel et al. [16], reporting the working points obtained in the riser of the facility during the tests. As it can be noted, most of the considered experimental conditions can be assumed to belong to the bubbly flow regime, while a smaller fraction may be close to the transition between the bubbly and slug regimes.

Figure 12 compares the power law relationships between the liquid flow and injected flow obtained for HFE-7100 with those of

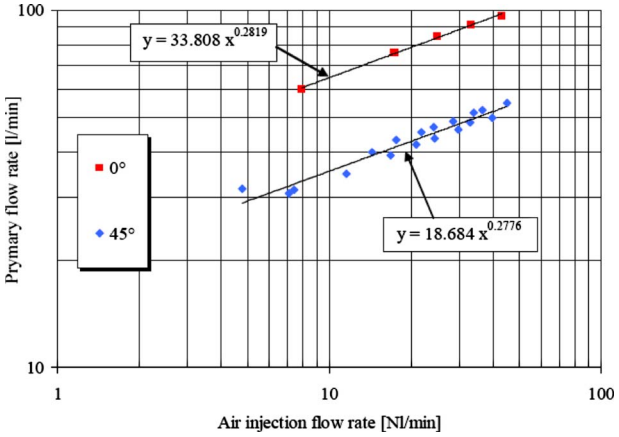

Fig. 10 HFE-7100 flow rate as a function of injected air flow for the tests performed in this work at relatively high air-injection flow

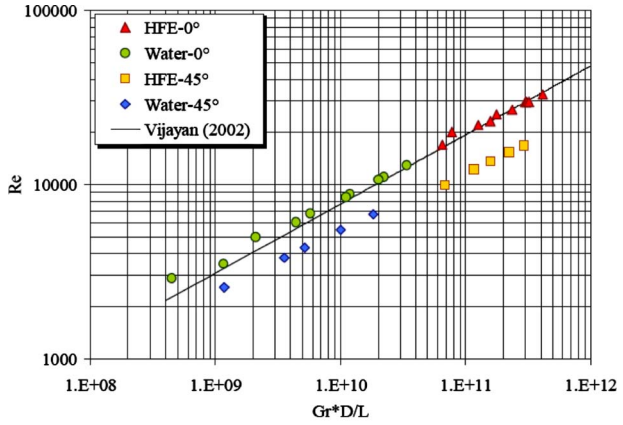

Fig. 8 Dimensionless representation of obtained results for natural circulation with different valve closure angles

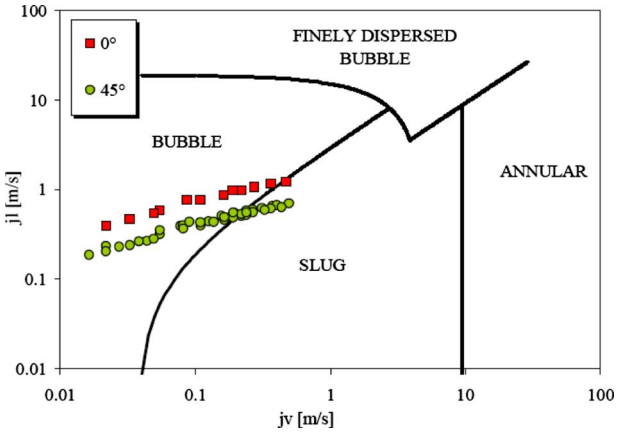

Fig. 11 Flow pattern map and working points for the gas-injection enhanced circulation experiments performed in this work

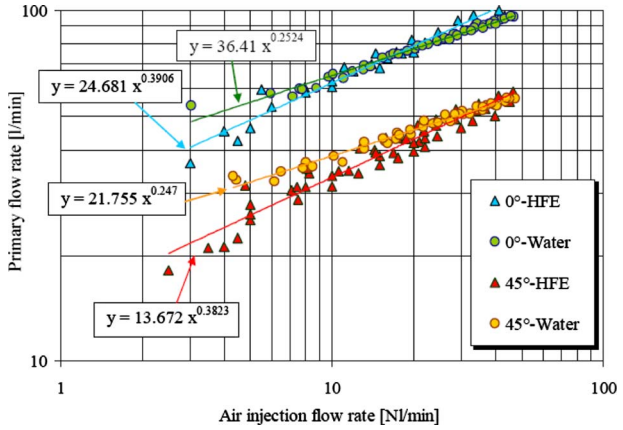

Fig. 12 Comparison of flow rates of water and HFE-7100 from this work and previous experimental campaigns

water data from previous works for different throttling of the valve. Though the obtained exponents are slightly different, Fig. 13 shows that both water and HFE-7100 trends in terms of superficial velocities for full open valve are in good agreement anyway with a correlation proposed by Bello et al. [17] for similar loops. Again, as expected, throttling the valve has the result of decreasing the flow rate with respect to the predicted trend, though the exponent in the power law changes only slightly.

5 Dimensionless Analysis of Data

In a previous work (see, e.g., Ref. [8]), a scaling analysis of natural and gas-injection enhanced circulation was carried out, devising relevant dimensionless groups applicable to both cases.

In particular, for the case in which buoyancy is mainly due to temperature differences, the following dimensionless momentum equation was reached:

$$\Pi_{\text{in,GT}}\frac{dW^*}{dt^*} = G_T^* + \Pi_{G\alpha,\text{GT}}G_\alpha^* - \Pi_{\text{RS,GT}}|W^*|W^* \tag{3}$$

where the appearing dimensionless numbers are

$$\Pi_{\text{in,GT}} = \frac{\sum_i \left[\frac{L}{A(1-\alpha)}\right]_i c_{p,f}W_{\text{ref}}^3}{\rho_{f,0}^2 g H \beta_f Q_{\text{ref}} V_{f,\text{loop}}} = \frac{\text{flow inertia}}{\text{thermal buoyancy}} \tag{4}$$

$$\Pi_{G\alpha,\text{GT}} = \frac{c_{p,f}W_{\text{ref}}H_{\text{ris}}\alpha_{\text{ref}}}{H\beta_f Q_{\text{ref}}} = \frac{\text{void buoyancy}}{\text{thermal buoyancy}} \tag{5}$$

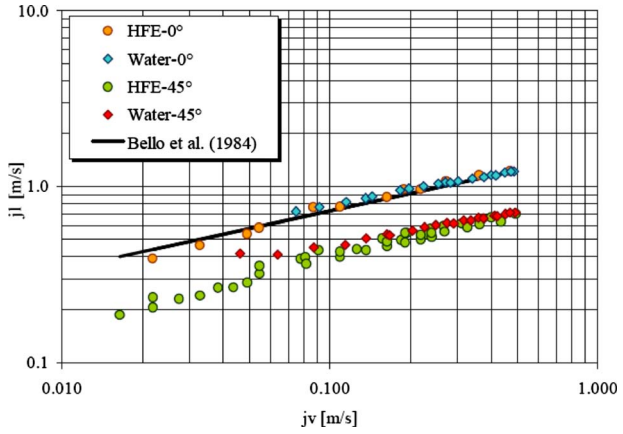

Fig. 13 Comparison of superficial velocities for water and HFE-7100 from this work and previous experimental campaigns

$$\Pi_{\text{RS,GT}} = \frac{c_{p,f}W_{\text{ref}}^3}{\rho_{f,0}gH\beta_f Q_{\text{ref}}}\sum_i R_i = \frac{\text{friction}}{\text{thermal buoyancy}} \tag{6}$$

Conversely, in the case of void-dominated buoyancy effects, the momentum balance along the loop can be more conveniently rewritten as

$$\Pi_{\text{in},G\alpha}\frac{dW^*}{dt^*} = \Pi_{\text{GT},G\alpha}G_T^* + G_\alpha^* - \Pi_{\text{RS},G\alpha}|W^*|W^* \tag{7}$$

where it is

$$\Pi_{\text{in},G\alpha} = \frac{\Pi_{\text{in,GT}}}{\Pi_{G\alpha,\text{GT}}} = \frac{\text{flow inertia}}{\text{void buoyancy}} \tag{8}$$

$$\Pi_{\text{GT},G\alpha} = \frac{1}{\Pi_{G\alpha,\text{GT}}} = \frac{\text{thermal buoyancy}}{\text{void buoyancy}} \tag{9}$$

$$\Pi_{\text{RS},G\alpha} = \frac{\Pi_{\text{RS,GT}}}{\Pi_{G\alpha,\text{GT}}} = \frac{\text{friction}}{\text{void buoyancy}} \tag{10}$$

The other dimensionless quantities appearing in the momentum equations are defined as

$$W^* = \frac{W}{W_{\text{ref}}}, \quad t^* = t/\tau, \quad \tau = \rho_{f,0}V_{f,\text{loop}}/W_{\text{ref}} \tag{11}$$

$$T^* = \frac{T - T_0}{\Delta T_{\text{ref}}}, \quad \Delta T_{\text{ref}} = \frac{Q_{\text{ref}}}{c_{p,f}W_{\text{ref}}} \tag{12}$$

$$\alpha^* = \frac{\alpha}{\alpha_{\text{ref}}}\frac{H}{H_{\text{ris}}}, \quad s^* = \frac{s}{H}, \quad z^* = \frac{z}{H} \tag{13}$$

$$G_T^* \equiv \oint T_f^* dz^*, \quad G_\alpha^* \equiv \int_{\text{ris}} \alpha^* dz^* \tag{14}$$

and the flow resistance of each loop branch is defined as

$$R_i = \frac{1}{2\rho_{f,0}}\left(\frac{\rho_{f,0}}{\rho_{f,i}}\right)\sum_k \frac{K_k + \frac{f_k L_k}{D_{\text{hyd},k}}}{A_k^2} \tag{15}$$

(see, e.g., Ref. [8] for a more detailed discussion).

In the two cases of natural circulation and gas-injection enhanced circulation, momentum equations (3) and (7) predict that in steady-state conditions the dimensionless flow rate should be roughly equal to the square root of $G_T^*/\Pi_{\text{RS,GT}}$ and $G_\alpha^*/\Pi_{\text{RS},G\alpha}$, respectively. This result holds if the flow resistance in each branch of the loop is reasonably constant with respect to flow rate. Figures 14 and 15 show how much this assumption can be considered acceptable on the basis of the present data for the purpose of the application of scaling laws. As it can be noted, though a general agreement is observed, slight discrepancies do appear in excess for natural circulation and in defect for gas-injection enhanced circulation.

6 Conclusions

The experimental data reported in this paper extend the information about natural circulation and gas-injection enhanced circulation available from previous experimental campaigns conducted with the same facility. The use of a fluid other than water, allowed us to explore additional operating conditions with respect to previously addressed ones.

Relevant indications provided by the experiments are as follows:

- the good match of natural circulation data for both fluids in the case of full open valve with the correlation by Vijayan [15]

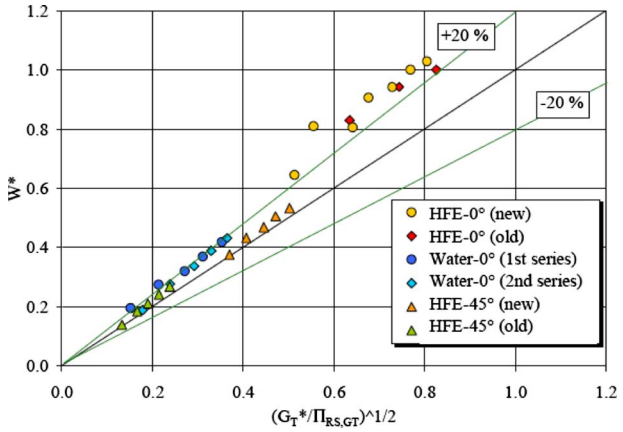

Fig. 14 Representation of water and HFE-7100 data from natural circulation tests in dimensionless form

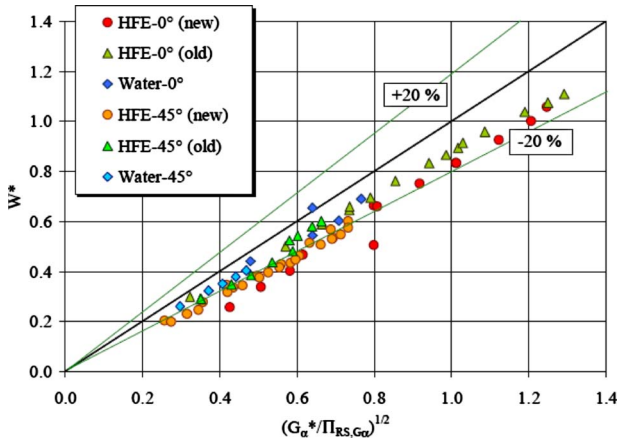

Fig. 15 Representation of water and HFE-7100 data from gas-injection enhanced circulation tests in dimensionless form

- the good match of gas-injection enhanced circulation data for both fluids in the case of full open valve with the correlation by Bello et al. [17]
- the close similarity between the data for gas-injection enhanced circulation in terms of superficial velocities for both fluids

As a result of this new information, the level of confidence that can be expected in predictions based on scaling laws could be better assessed.

Acknowledgment

The Italian Ministry of Education, University and Research (MIUR) is acknowledged for supporting the activity related to the construction of the facility through the Contract COFIN 2002 No. 30.

Nomenclature

Latin Letters

A = area (m^2)
c_p = specific heat at constant pressure (J/kg K)
D = diameter (m)
f = Darcy–Weisbach friction factor
g = gravity (m/s^2)
G_T^* = dimensionless temperature integral along the loop
G_α^* = dimensionless void fraction integral in the riser
H = elevation change between heating and cooling centers (m)
H_{ris} = height of the riser (m)
L = length (m)
K = singular pressure drop coefficient
M = mass (kg)
p = pressure (Pa)
Q = thermal power (W)
R = flow resistance (kg^{-1} m^{-1})
s = axial coordinate along the loop (m)
t = time (s)
T = temperature (K)
V = volume (m^3)
W = loop flow rate (kg/s)
z = elevation (m)

Greek Letters

α = void fraction
β = fluid isobaric thermal expansion coefficient (K^{-1})
μ = dynamic viscosity (kg/m s)
Π = dimensionless group
ρ = density (kg/m^3)
τ = time scale (s)

Subscripts

f = fluid
g = injected gas (air)
GT = identifying the thermal buoyancy term
$G\alpha$ = identifying the void buoyancy term
i = refers to the ith loop branch
in = inertia
loop = refers to the entire loop
ref = reference value
ris = riser
RS = flow resistance
0 = reference value

Superscripts

* = dimensionless variable

References

[1] Natural Circulation in Water Cooled Nuclear Power Plants, 2005, Paper No. IAEA-TECDOC-1474.
[2] Benamati, G., Foletti, C., Forgione, N., Oriolo, F., Scaddozzo, G., and Tarantino, M., 2007, "Experimental Study on Gas-Injection Enhanced Circulation Performed With the CIRCE Facility," Nucl. Eng. Des., **237**(7), pp. 768–777.
[3] Mantha, V., Chaudhary, R., Pal, S., Gourai, S., Murthy, P. S. S., Sahasrabudhe, S. N., Biswas, G., Das, A. K., and Satyamurthy, P., 2006, "Intense Heat Simulation Studies on Window of High Density Liquid Metal Spallation Target Module for Accelerator Driven Systems," Int. J. Heat Mass Transfer, **49**, pp. 3728–3745.
[4] Ambrosini, W., Forgione, N., Oriolo, F., Agostini, P., Bertacci, G., Gherardi, G., Bianchi, F., Meloni, P., Nicolini, D., and Fruttuoso, G., 2002, "Natural Circulation of Lead-Bismuth in a One-Dimensional Loop: Experiments and Code Predictions," Tenth International Conference on Nuclear Energy, Nuclear Energy—Engineering Today the Power for Tomorrow (ICONE-10), Arlington, VA, Apr. 14–18.
[5] Ambrosini, W., Azzati, M., Benamati, G., Bertacci, G., Cinotti, L., Forgione, N., Oriolo, F., Scaddozzo, G., and Tarantino, M., 2004, "Testing and Qualification of CIRCE Instrumentation Based on Bubble Tubes," J. Nucl. Mater., **335**(2), pp. 293–298.
[6] Agostini, P., Alemberti, A., Ambrosini, W., Benamati, G., Bertacci, G., Cinotti, L., Elmi, N., Forgione, N., Oriolo, F., Scaddozzo, G., and Tarantino, M., 2005, "Testing and Qualification of CIRCE Venturi-Nozzle Flow Meter for Large Scale Experiments," 13th International Conference on Nuclear Engineering (ICONE 13), Beijing, China, May 16–20.
[7] Ambrosini, W., Forasassi, G., Forgione, N., Oriolo, F., and Müller, C., 2003, "Experimental Investigation on Natural and Gas-Injection Enhanced Circulation," International Congress on Advances in Nuclear Power Plants, ICAPP '03, Congress Palais, Córdoba, Spain, May 4–7.
[8] Ambrosini, W., Forasassi, G., Forgione, N., Oriolo, F., and Tarantino, M., 2003, "Natural and Gas-Injection Enhanced Circulation in a Loop With Variable Friction," International Conference on Global Environment and Advanced

Nuclear Power Plants, GENES4/ANP2003, Kyoto Research Park, Kyoto, Japan, Sept. 15–19.
[9] Ambrosini, W., Forasassi, G., Forgione, N., Oriolo, F., and Tarantino, M., 2004, "Experimental Study on Combined Natural and Gas-Injection Enhanced Circulation," Third International Symposium on Two-Phase Flow Modelling and Experimentation, Pisa, Italy, Sept. 22–25, pp. 1–7.
[10] Ambrosini, W., Forasassi, G., Forgione, N., Oriolo, F., and Tarantino, M., 2005, "Experimental Study on Combined Natural and Gas-Injection Enhanced Circulation," Nucl. Eng. Des., **235**(10–12), pp. 1179–1188.
[11] Ambrosini, W., Forgione, N., Oriolo, F., Pellacani, F., Tarantino, M., and Struckmann, C., 2005, "Experimental Investigation on Natural Circulation and Air-Injection Enhanced Circulation in a Simple Loop," 23rd UIT National Heat Transfer Conference, Parma, 20–22 Giugno.
[12] Ambrosini, W., Forgione, N., Oriolo, F., and Catarci, V., 2007, "Natural Circulation and Air-Injection Enhanced Circulation of HFE-7100 in a Simple Loop," 25th UIT National Heat Transfer Conference, Trieste, Italy, June 18–20.
[13] 1999, RELAP5/MOD3.3 Code Manual, SCIENTECH Inc.
[14] 2004, FLUENT User Guide, Fluent Inc.
[15] Vijayan, P. K., 2002, ""Experimental Observations on the General Trends of the Steady State and Stability Behaviour of Single-Phase Natural Circulation Loops," Nucl. Eng. Des., **215**, pp. 139–152.
[16] Taitel, Y., Bornea, D., and Dukler, A. E., 1980, "Modelling Flow Pattern Transitions for Steady Upward Gas-Liquid Flow in Vertical Tubes," AIChE J., **26**, pp. 345–354.
[17] Bello, R. A., Robinson, C. W., and Moo-Young, M., 1984, "Liquid Circulation and Mixing Characteristics of Airlift Contactors," Can. J. Chem. Eng., **62**(5), pp. 573-577.

Simulations of Metal Oxidation in Lead Bismuth Eutectic at a Mesoscopic Level

Taide Tan

Yitung Chen[1]
e-mail: uuchen@nscee.edu

Department of Mechanical Engineering,
University of Nevada,
Las Vegas, NV 89154-4027

The corrosiveness of lead bismuth eutectic (LBE), as an ideal coolant candidate in reactors and accelerator driven systems (ADSs), presents a critical challenge for safe applications. One of the effective ways to protect the materials is to form and maintain a protective oxide film along the structural material surfaces by active oxygen control technology. The oxidation of metals in LBE environment has been investigated numerically at a mesoscopic scale. A novel stochastic cellular automaton (CA) model has been proposed considering the transport of oxygen along the grain boundaries. The proposed mesoscopic CA model has been mapped with the experimental data. A parametric study was conducted in order to check the importance of the main explicit parameters of the mesoscopic model. The boundary condition at the far end of the specimen has been investigated for the CA model. The model has benchmarked with the analytical solution and with the previous work of a pure diffusion process, and significant agreement has been reached. The developed CA model can be used to solve diffusion problem.
[DOI: 10.1115/1.3078702]

Keywords: mesoscopic, oxidation, model, lead bismuth eutectic, cellular automaton

1 Introduction

The corrosiveness of LBE, as an ideal coolant candidate in reactors and ADS, presents a critical challenge for safe applications [1–3]. The active oxygen control technology has been proposed and developed in order to protect the structural materials by forming and maintaining a protective oxide film along the structural material surfaces [4–12]. The mechanism of the oxide layer growth of stainless steel in liquid lead and lead alloys has been analyzed [8,12]. To study such a problem at a microscopic level, such as from an atomic or molecular point of view, has always been a great challenge for the scientists and researchers in the field of fluid mechanics, heat transfer, computational fluid dynamics (CFD), etc. It is difficult and time consuming to study so complex a macroscopic phenomenon at a microscopic level [8]. To build a mesoscopic model for the oxidation of metals in lead or LBE environment will be significant and beneficial for the future study of oxidation problems at a mesoscopic scale. To the best of our knowledge, there has been no such mesoscopic work yet done, with consideration of the diffusion of metal and transport of oxygen separately.

The Eden model [13] and the diffusion-limited aggregation (DLA or LDA) [14,15] model represent two basic starting points from which a theoretical description of the interface growth processes can be elaborated. The Eden model was extended by Saunier et al. [16] by introducing a feedback effect of the layer formed on the corrosion rate, based on the concept of cellular automaton (CA), which has been proposed to study the effect of kinetic parameters involved in the corrosion mechanisms on the corroded surface roughness [16–18]. No matter how the Eden model and the DLA model were explored, they were a simple way in which only the lattices were considered as the reaction sites and diffusion pathway. Thus, the Eden model and the DLA model are in the range of "simple models." For example, even in the extended model of Saunier et al. [16], only the diffusion of iron was considered. The role of oxygen was neglected and no inner reaction by iron and the inward transported oxygen was considered. However, as discussed in Ref. [8], the transport of oxygen plays an important role in the oxidation of stainless steel in molten lead or LBE. The reactions take place on the oxide/liquid interface, on the steel/oxide interface, and even inside the oxide films as well. Moreover, the transport of oxygen is different from iron and other added alloying elements. The oxygen should be transported along the grain boundaries, or some other pores and vacancies by some unclear mechanisms [19]. Therefore, it is necessary to build a suitable mesoscopic model for estimating the long term behaviors of stainless steels in the nuclear coolant systems. The proposed improved mesoscopic oxidation model is trying to lay a new base for the future mesoscopic study of corrosion and oxidation of stainless steel in nonisothermal molten lead or LBE environments.

2 Oxidation of Steels in LBE

LBE is the eutectic of lead and bismuth and its melting temperature is 123.5°C. The operating temperature of LBE coolant system is at around 500°C or higher [9]. The oxidation of stainless steel in LBE is a complex problem involving high temperature chemical reactions. In the oxidation process for pure iron, the dissolution of oxygen into the alloys is involved, together with the ionization of iron, migration of iron ions, and electrons through the formed oxide film. The chemical reactions between metal atoms and atomic oxygen take place on the oxide/metal interface, on the oxide/liquid interface, and inside the oxide simultaneously, in LBE environments.

It is reported in Refs. [8,20] that the oxygen in high temperature metal flow is in atomic phase instead of molecular phase through a dissolution process. The chemical reactions are much faster than mass transfer during the oxidation process. Therefore, it is reasonable to assume that all the chemical reactions are at their local equilibrium states [19]. In a practical LBE coolant system or a LBE test facility, the flow is fully turbulent and it can mix the corrosion product quickly. As a result, the mass transfer rate in the

[1]Corresponding author.

Manuscript received August 19, 2008; final manuscript received August 25, 2008; published online February 18, 2009. Review conducted by Dillip R. Ballal. Paper presented at the 16th International Conference on Nuclear Engineering (ICONE16) Orlando, FL, May 12–15, 2008.

boundary layer dominates the transport in the liquid. It was commonly accepted that the mass transport in the oxide layer dominates the whole oxide process [19].

The oxidation reaction can be divided into three parts: inner interface action, outer interface reaction, and reaction in the oxide layer. At the inner interface reaction (oxide/metal interface), the oxygen atoms, which were transported to the inner interface, react with the iron atoms at the inner interface. At a high temperature, this reaction induces the growth of an inner oxide layer easily. Also, at the inner interface between oxide layer and iron, atomic iron ionizes. The iron ions and electrons are transported outward through the oxide layer. At a high temperature, iron ions can form new iron atoms any time by reacting with the electrons. The reactants, atomic iron, react with the oxygen, which was transported in the oxide. This part of reactions occur whenever iron atoms meet enough oxygen atoms during the transport and cause the redistribution of oxide layer and the volume expansion of the oxide layer. At the outer interface (oxide/liquid interface), surface reactions take place. This part of oxidations account for the outward growth of the oxide layer. The migration processes of oxygen and iron ions and the oxide layer growth, in both sides of inward and outward, were analyzed in Ref. [21]. In summary, the overall equation for the chemical reactions during oxidation can be expressed in a general form:

$$\alpha M + \frac{\beta}{2}O_2 = M_\alpha O_\beta \tag{1}$$

The driving force for this reaction is, of course, the free energy change associated with the formation of oxide from the reactants and can be calculated if the pertinent thermochemical data are available [22]. The mass transport of steel components in the oxide layer is mainly by diffusion [5,7,8]. The mass transport of oxygen in the oxide layer is very complex and not well understood. The oxygen self-diffusion coefficient is very small. However, oxygen was observed in the inner layer in experiments. The oxygen was assumed to be transported along the grain boundaries or some other pores and vacancies by some unclear mechanisms [19]. The mass transport of oxygen can be treated as effective diffusion, which will follow the diffusion equation but with a much higher diffusivity [23]. The diffusion of iron in oxide layer can be explained by point defect theory. The diffusion rate of iron is influenced by the oxygen pressure, temperature, and point defects (such as vacancies and interstitials) [24]. The oxygen is assumed to migrate through the oxide film by some unclear mechanisms [8,19]. It is reasonable to assume that the transport rates of iron (diffusion) and oxygen (effective diffusion) are of the same order, and both the transport rates of iron and oxygen control the oxidation rates. The transport of electrons is comparatively fast [8,19]. The oxidation of stainless steel becomes more complex because of the added alloying components, impurities, and other defects. With various temperature and flow conditions, the oxide film for a particular material may be different.

3 An Improved CA Oxidation Model

An improved stochastic CA model is built to simulate the oxidation process. Four main processes will be studied at a mesoscopic scale: the outward diffusion of iron species across the oxide layer, the inward transport (effective diffusion) of oxygen along the grain boundaries, the ionization, and the oxidation reaction between oxygen and iron. The diffusion and transport process is simulated by a random walk model. The CA model starts from a pure metal material. It is assumed that the concentration of oxygen in the turbulent flow is well mixed since LBE or molten lead was reported to be turbulent flow. The oxygen atoms are assigned randomly at the interstitial sites in the fluid domain at each step of calculation. A synchronous dynamics scheme [25] is applied in the simulation of random walk model in order to satisfy the physical phenomena. To make the model work randomly, a number of random selections will be conducted at each calculating step for the random walk model. In the present proposed model, the simple mathematical model was used to investigate self-organization of oxide and metal in statistical mechanics. A global random walk method is included to characterize the diffusion process of iron and transport of oxygen. With this improved CA oxidation model, a continuous oxide layer growth model is simulated to explain the oxidation mechanism of steels in a high temperature corrosive liquid metal environment.

The basic idea of CA model is to treat a cluster of molecules/atoms as a mesoscopic unit, which is simplified to a square site and moves and reacts as a whole [16]. The lattice sites are considered isotropic and they move and react as a unit randomly or with some probability in discrete time steps. The transport of iron or oxygen and the reactions of cells are governed by special rules. These local rules for many CA models in materials science can be derived through finite difference formulations of the underlying differential equations that govern the system dynamics at a mesoscopic level [25]. The grain boundary is simplified to be the edge of the lattice site, which serves as the pathway of the oxygen in the present model. The interstitial site stands for the possible congregating location of clusters of oxygen atoms since oxygen exists in atomic phase [19]. The clusters of oxygen keep transporting along these pathways in the domain until they are consumed in chemical reaction. The self-diffusion of atomic oxygen through the metallic lattice and the influence of atomic oxygen on the metallic atoms in the lattice are neglected unless chemical reaction takes place between the cluster of oxygen and metallic atoms in the neighboring lattice. By this treatment, the atomic oxygen clusters can transfer much faster than the self-diffusion of oxygen atoms in metals or steels, which was observed in the experiments [19]. The state of a lattice or an interstitial site is a function of its previous state and the state of its neighboring sites. The status variables of each lattice or interstitial site will be updated synchronously after each calculating time step. The basic assumptions of the model are made as follows in the present model.

(a) The LBE flow is fully turbulent so that the concentration of oxygen is uniform.
(b) The direct dissolution of metal in a liquid lead alloy system for the initial stage is neglected. The formed oxide layer is insoluble.
(c) There are micropores or other routes along the grain boundary inside the oxide layer for the transport of oxygen.
(d) The diffusion of iron is in ionic form only, i. e., the atomic iron movement is neglected.
(e) The reaction rate is much faster than the transport rate of oxygen and metal.

In the present stochastic mesoscopic CA model, the intrinsic rules are defined as follows.

(a) A square lattice with a width, a (meters), represents a site, which will be occupied by metal or oxide in solid phase or be occupied by LBE in liquid phase. The interstitial sites are routes for oxygen to occupy and transport (as shown in Fig. 1).
(b) The state of each interstitial site can be represented by the site state variable $\mathrm{Inte}_{ij}(t)$ at the site (i,j) and at time t. Inte_0 denotes an unoccupied site by oxygen (a "vacancy" site), while Inte_1 denotes an occupied site by oxygen (an "occupied" site). Therefore,

$$\mathrm{Inte}_{i,j}(t) \in \{\mathrm{Inte}_0, \mathrm{Inte}_1\} \tag{2}$$

(c) The state of each lattice can be represented by the site state variable $\mathrm{Lat}_{ij}(t)$, which denotes a different component at the site (i,j) and at time t.

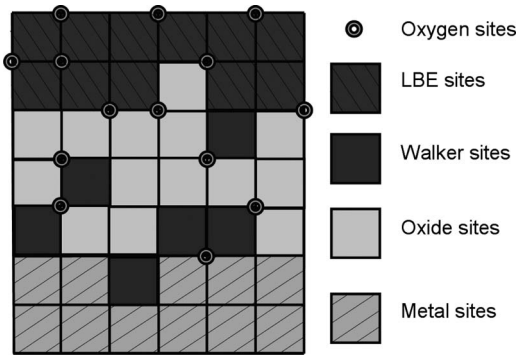

Fig. 1 Schematic of CA model of corrosion/oxidation of metal in LBE

$$\mathrm{Lat}_{i,j}(t) \in \{\mathrm{Lat}_2, \mathrm{Lat}_3, \mathrm{Lat}_4, \mathrm{Lat}_5\} \tag{3}$$

where Lat_2 represents the atomic metal site (solid phase); Lat_3 denotes the LBE site (liquid phase); Lat_4 denotes the oxide site (solid phase); and Lat_5 denotes the site of oxide with overlapping with ironic metal (solid phase).

(d) Generally, the state of a given site in the next time step will be determined by the state of itself and its neighbors in the previous time step. The control variables can be formulated as follows:

$$\mathrm{Inte}_{i,j}(t+\delta t) = \Phi_{\mathrm{Inte}}(\mathrm{Inte}_{i,j}(t), \{\mathrm{Inte}_{i,j}^{\mathrm{Nb}}(t)\}, \{\mathrm{Lat}_{i,j}^{\mathrm{Nb}}(t)\}, \varphi_{\mathrm{Inte}}) \tag{4}$$

$$\mathrm{Lat}_{i,j}(t+\delta t) = \Phi_{\mathrm{Lat}}(\mathrm{Lat}_{i,j}(t), \{\mathrm{Lat}_{i,j}^{\mathrm{Nb}}b(t)\}, \{\mathrm{Inte}_{i,j}^{\mathrm{Nb}}(t)\}, \varphi_{\mathrm{Lat}}) \tag{5}$$

where Φ_{Lat} and Φ_{Inte} are the local evolution rules of CA for lattice sites and interstitial sites, respectively. φ_{Lat} and φ_{Inte} are the control variables for lattice sites and interstitial sites, respectively, and $\{\mathrm{Lat}_{i,j}^{\mathrm{Nb}}(t)\}$ are the neighbor lattices and $\{\mathrm{Inte}_{i,j}^{\mathrm{Nb}}(t)\}$ are the neighbor interstitial sites of $\mathrm{Inte}_{i,j}(t)$ or $\mathrm{Lat}_{i,j}(t)$.

An improved neighborhood system based on Moore neighborhood system [26] is employed for lattice sites, coupling with four closest interstitial sites in this improved 2D oxidation CA model. For each lattice $\mathrm{Lat}_{i,j}(t)$, the status of eight neighbor lattices $\{\mathrm{Lat}_{i,j}^{\mathrm{Nb}}(t)\}$ (northern, southern, eastern, western, northwestern, southwestern, northeastern, and southeastern) and four interstitial sites $\{\mathrm{Inte}_{i,j}^{\mathrm{Nb}}(t)\}$ (northwestern, southwestern, northeastern, and southeastern) will influence its evolution for the next time step (as shown in Fig. 2). With this neighborhood system, both the impact of the neighbor element and the close oxygen transported along the boundaries will be considered. For each interstitial site $\mathrm{Inte}_{i,j}(t)$, the status of four neighbor lattices $\{\mathrm{Lat}_{i,j}^{\mathrm{Nb}}(t)\}$ (northwestern, southwestern, northeastern, and southeastern) and four interstitial sites $\{\mathrm{Inte}_{i,j}^{\mathrm{Nb}}(t)\}$ (northern, southern, eastern, and western) will influence its evolution for the next time step (as shown in Fig. 2).

It is assumed that each metal lattice contains $\varepsilon+1$ of metal atoms (M) and each occupied interstitial site contains ω atoms of oxygen. When the metal lattice is involved in a reaction, one of the $(\varepsilon+1)$ metal atoms in the lattice site is consumed and a lattice site of oxide is formed. During the same time, ε metal atoms ionize and begin to diffuse outward. The ε ionic metal, as a whole lattice overlapping with any oxide lattice site, diffuses through the oxide and reacts with oxygen when they meet at the oxide/LBE interface. The value ε relates to the Pilling–Bedworth ratio that

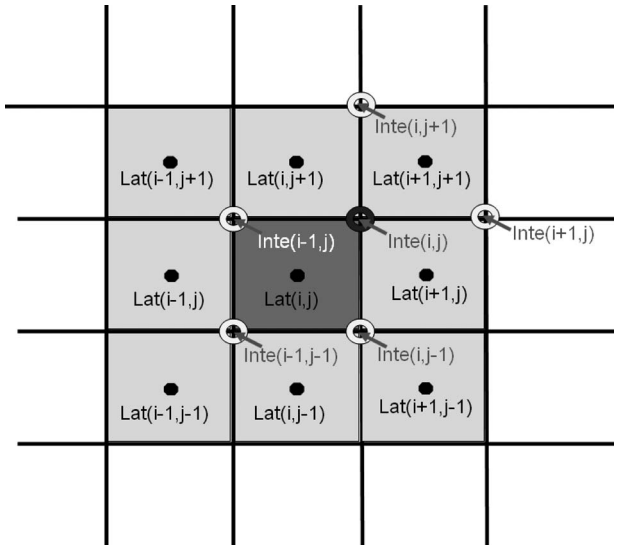

Fig. 2 The neighborhoods for lattice $\mathrm{Lat}_{i,j}(t)$ and interstitial site $\mathrm{Inte}_{i,j}(t)$

corresponds to the molar oxide volume/molar metal volume ratio. The basic rules for this improved oxidation CA model are listed below.

(a) In LBE, the oxygen concentration is kept constant and the oxygen distribution is uniform (randomly distributed for each step).

(b) For a metal site, if none of the four nearest interstitial sites (southwest, southeast, northwest, and northeast as shown in Fig. 2) is occupied by oxygen, no oxidation occurs.

(c) For a metal site, a reaction occurs possibly if there is one or more of the nearest interstitial sites occupied by oxygen.

(1) If none of the eight neighbor sites (southwest, south, southeast, east, northeast, north, northwest, and west as shown in Fig. 2) is oxide, no reaction occurs.

(2) If one or more of the eight neighbor sites are oxide, the oxidation reaction occurs immediately with a probability, P_{act}. As mentioned previously, the reaction speed is assumed to be much faster than the transport speed of oxygen. One of the oxygen sites is chosen randomly from the nearest interstitial sites for reaction and disappears. The site of metal disappears and an overlapping site of oxide and ionic metal substitutes. The ionic metal site always overlaps with an oxide site and the ionic metal site can diffuse in the oxide layer in any random direction and is called a "walker." The higher is the value of P_{act}, the stronger the reactivity of the substrate in contact with oxygen.

(d) In each oxygen transport step, the atomic oxygen transports randomly in four possible directions along the interstitial edge of the lattices in the oxide layer or the metal zone. After each step of transport of all oxygen sites, the metal sites and their neighbors' status are checked again, and the calculation code takes actions following procedure (c).

(e) After finite steps of transport of oxygen, for example, N_{OT}, the walkers' diffuse N_{WD} steps in the oxide layer. The ratio of transport steps $K_d = N_{\mathrm{OT}}/N_{\mathrm{WD}}$ depends on the mass transport rate of oxygen and ionic metal in the oxide layer. Usually the transport rate of oxygen is faster than the diffusion of ionic metal even though the self-mass diffusivity of oxygen may be slower. In each calcu-

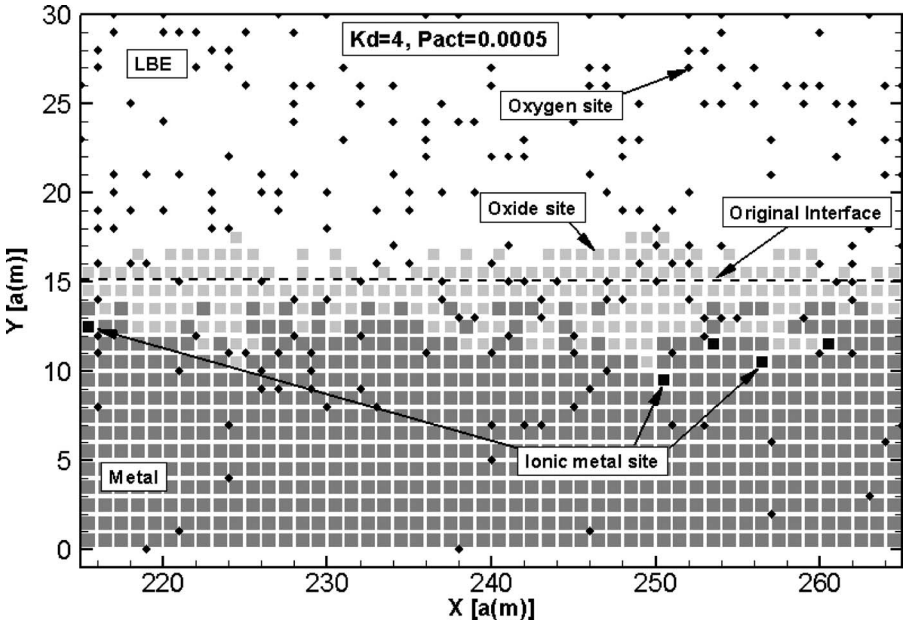

Fig. 3 Snapshot of the mesoscopic structure with K_d=4, C_{oxy}=0.2, and P_{act}=0.0005 at N_t=1000

lating step, the N_{WD} steps of walkers' diffusion, the N_{WD} steps of reaction between a walker site with oxygen on LBE/oxide interface, the N_{OT} steps of transport oxygen, and the N_{OT} steps of inner reaction of oxygen with metal will be involved.

(f) When a walker meets LBE, oxidation occurs immediately, since it is assumed the oxygen diffuses very fast in LBE. By controlling the number of the newly formed oxide by an ionic metal lattice (walker), the volume expansion effect can be realized.

(g) The transported oxygen in the metal will walk randomly in the metal domain and cause "noise" in the simulation. They will be eliminated whenever the oxygen site reaches the far end of the calculating domain. Physically, it can be explained by the deposition of oxygen in some pores and vacancies during transport. Furthermore, it makes the far boundary satisfies the Dirichlet boundary conditions.

Therefore, the simulated oxidation reactions are

$$(\varepsilon+1)M+\omega\mathrm{O}\rightarrow MO_{\omega}+\varepsilon W$$
$$[1\ \text{lattice}][1\ \text{interstitial site}][1\ \text{lattice}][1\ \text{overlapping lattice}] \tag{6}$$

and

$$\varepsilon W[1\ \text{overlapping lattice}]\rightarrow \varepsilon MO_{\omega}[\varepsilon\ \text{lattices}] + \varepsilon\omega\mathrm{O}[\text{from LBE}] \tag{7}$$

Equation (6) accounts for the oxidation and ionization at the inner interface of oxide/metal. Equation (7) denotes the process of the outer surface reaction. The $\varepsilon\omega$ product of oxygen is of no concern in the LBE domain, since it is assumed that the concentration of oxygen in LBE is constant and enough oxygen can be acquired from the LBE domain. The products εW are in a lattice and overlap with any oxide lattice. If ε is assigned a value of 2, for example, the ideal volume is expanded by about three times, since a molecular MO_{ω} is assigned in one lattice. From the proposed rules, a continuous oxide layer will be formed. The ionization of metal will take place in the oxide/metal interface and oxidation occurs on both the liquid/oxide and oxide/metal interfaces, which accounts for outer oxidation and inner oxidation in the formation of a duplex oxide layer. The volume expansion effect can be realized by control the parameter of ε. The ideal volume expansion rate (the oxide layer volume by the consumed metal volume) is $(\varepsilon+1)$.

In summary, the present model contains three explicit parameters: ε, P_{act}, and K_d. The volume control parameter ε is set to be unity in the present model, as an initial work of the mesoscopic model. The diffusion step number of walkers, N_{WD}, is set to be unity as well. Therefore, in each calculating step, only one step of diffusion of walkers and K_d steps of transport of oxygen are involved.

4 Results and Discussions

4.1 Examination of the Boundary Conditions. Two different kinds of boundary condition of oxygen concentration have been studied at the far end of the specimen (at y=0). At the beginning, the oxygen sites were eliminated whenever an oxygen site reaches the far end of the specimen. By doing this, the boundary condition of the oxygen concentration was forced to satisfy the Dirichlet boundary condition

$$C_{\mathrm{O}}=0 \quad \text{at } y=0 \tag{8}$$

The Dirichlet boundary condition can be employed when the chemical reaction rate is much faster than transport rate of oxygen. In this case, the oxygen atoms are consumed before any of them reaches the far boundary of the specimen. However, a Neumann boundary condition of the oxygen concentration is more realistic physically, i.e.,

$$\left.\frac{\partial C_{\mathrm{O}}}{\partial y}\right|_{y=0}=0 \tag{9}$$

For cases with a lower reaction probability and a higher diffusivity of oxygen in oxide and metal, the correct setting of this boundary condition is more important. To verify the modified code, a 2D case with $500(x)\times 30(y)$ nodes and mesh size of a (meters) has been studied with K_d=4, C_{oxy}=0.2, and P_{act} =0.0005 at N_t=1000. The snapshot of the mesoscopic structure is shown in Fig. 3. As can be seen, the Neumann boundary condition has been successfully utilized. The oxygen sites have been dif-

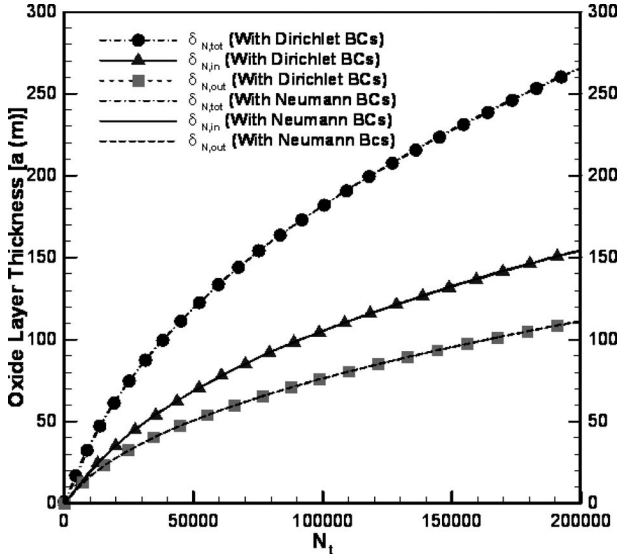

Fig. 4 Growth of the oxide layer for K_d=4, C_{oxy}=0.2, and P_{act}=0.0005 at N_t=200,000 with Neumann and Dirichlet boundary conditions at y=0

fused to the far boundary successfully without the forced elimination. A larger domain with $500(x)\times500(y)$ nodes has been studied with K_d=4, C_{oxy}=0.2, and P_{act}=0.0005 for a longer time N_t=200,000. The growth of the oxide layer (inner layer, outer layer, and total layer thickness) with Neumann boundary conditions at y=0 is shown in Fig. 4 together with the results with the Dirichlet boundary conditions at y=0. As can be seen, there is no obvious difference between the results. This means the boundary condition in the far end as a Neumann boundary condition or a Dirichlet boundary condition does not affect the result too much if the oxygen diffusion rate is low. The reason for this phenomenon can be explained by the fact that a relatively low diffusion rate will cause almost all of the oxygen to be consumed before they reach the far end. The percentage of the oxygen occupied sites is shown in Fig. 5. There is no big difference between the results from the two boundary conditions. Therefore, the oxygen concentration in the far end of the specimen (at y=0) satisfies both of the two boundary conditions, i.e., the Dirichlet boundary condition and the Neumann boundary condition, since the oxygen diffusion rates in

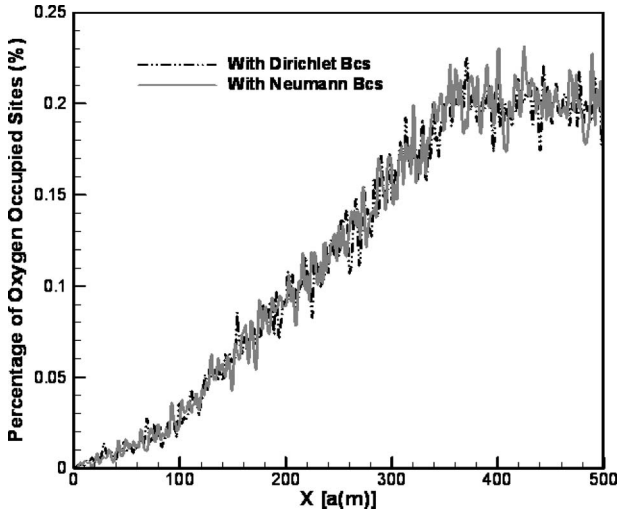

Fig. 5 The percentage of the oxygen occupied sites for K_d=4, C_{oxy}=0.2, and P_{act}=0.0005 at N_t=200,000 with Neumann and Dirichlet boundary conditions at y=0.

Table 1 The parameters and results for the reaction probability study

P_{act}	δ_{in} (a) (m)	δ_{out} (a) (m)	δ_{tot} (a) (m)	Parameters
0.0005	68	62	130	
0.3	102	88	190	
0.5	102	88	190	All with K_d=1, C_{oxy}=0.2,
0.8	102	88	190	and N_t=200,000

the oxide layer and the metal are relatively small in most of the real cases and the specimen is usually relatively large comparing to the oxide layer.

4.2 Influence of the Reaction Probability. The influence of the reaction probability P_{act} has been studied in a two-dimensional domain of 500×500 grids, with mesh size of a (meters). The simulating parameters are listed in Table 1. The snapshots of the simulated mesoscopic structures of cases with P_{act}=0.0005, P_{act}=0.3, P_{act}=0.5, and P_{act}=0.8 after 200,000 calculating steps are shown in Fig. 6. From the snapshots, there is no obvious difference among the cases with P_{act}=0.3, P_{act}=0.5, and P_{act}=0.8. The case with P_{act}=0.0005 shows a slower growth of the oxide layer in both directions and the oxide/metal interface is much rougher. The increases in thickness of the inner oxide layer, outer oxide layer, and the total oxide layer with calculating steps are compared in Figs. 7–9. From the comparisons, a small change in the reaction probability (in the same order) does not impact the thicknesses of oxide layer too much on a long time scale. The oxide layer thicknesses are listed in Table 1. For example, the thicknesses of the inner oxide layers are estimated at about 102 m (a) for P_{act}=0.3, P_{act}=0.5, and P_{act}=0.8, and at about 68 m (a) for P_{act}=0.0005 at N_t=200,000. The outer layer thicknesses are about 88 m (a) for P_{act}=0.3, P_{act}=0.5, and P_{act}=0.8, and 62 m (a) for P_{act}=0.0005 at N_t=200,000. The total thicknesses are about 190 m (a) for P_{act}=0.3, P_{act}=0.5, and P_{act}=0.8, and 130 m (a) for P_{act}=0.0005 at N_t=200,000. Between the cases of reaction probability in the same order (for example, P_{act}=0.3 and P_{act}=0.8 in Fig. 8), the difference of the thicknesses is very small. Only a very small difference can be observed at the initial stage (see Fig. 9). The reason is that such a high reaction probability will ensure that most of the transported-in oxygen is consumed, sooner or later, in a long time. The oxygen keeps transporting randomly in four directions (some may go to and fro and react when they meet oxygen), and only a few of them will be transported to the far end of the specimen, to cause "noises" of the simulation.

The metal ion (walkers) concentration distributions for the cases with P_{act}=0.0005, P_{act}=0.3, P_{act}=0.5, and P_{act}=0.8 after 200,000 calculating steps are shown in Figs. 10–13. The oxygen concentration distributions for the cases with P_{act}=0.0005, P_{act}=0.3, P_{act}=0.5, and P_{act}=0.8 after 200,000 calculating steps are shown in Figs. 14–17. From the comparisons, a small change in the reaction probability does not much affect the results of the concentration distributions of oxygen and walkers in a long time scale either. A much lower concentration distribution of metal ions can be observed in the case of P_{act}=0.0005 (shown in Fig. 10) than the cases with P_{act}=0.3, P_{act}=0.5, and P_{act}=0.8 (shown in Figs. 11–13). The concentration distributions of oxygen and walkers look similar for cases with P_{act}=0.3, P_{act}=0.5, and P_{act}=0.8, as shown in Figs. 15–17. A larger amount of oxygen can be observed in the metal domain in the case with P_{act}=0.0005 (in Fig. 14) than other cases with a higher reaction probability, as shown in Figs. 15–17. The difference is mostly because that the model is a stochastic and the random walk and the random selection for each lattice or interstitial site. The observation illustrates that a slower ionization process accompanies a slower oxidation reaction. One reason is that the reaction rate is relatively lower and

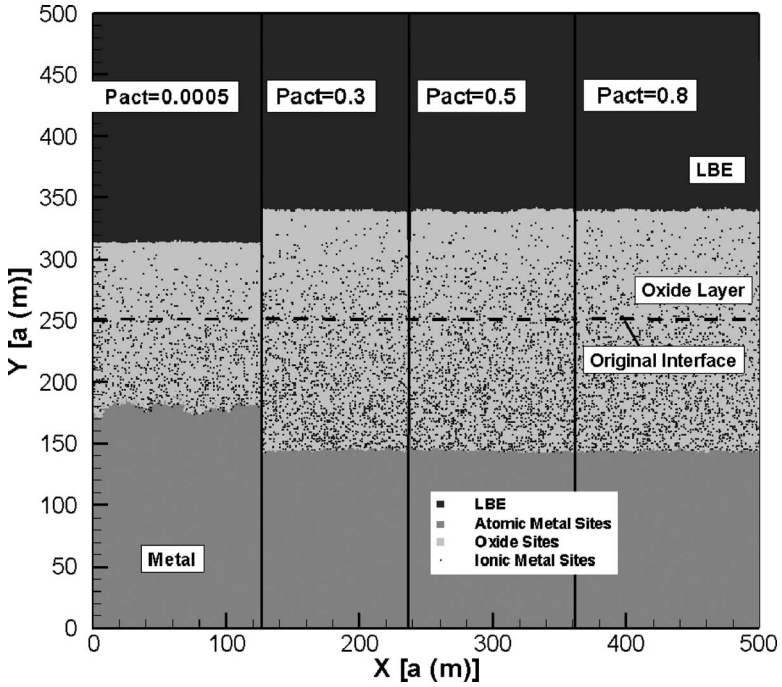

Fig. 6 The snapshot of the mesoscopic structure for N_t=200,000, with K_d=1, C_{oxy}=0.2, and P_{act}=0.0005, P_{act}=0.3, P_{act}=0.5, and P_{act}=0.8

another is that the extra oxygen is transported into the metal domain, as shown in Fig. 14. The comparison above shows that the reaction probability does not impact the results markedly. The study will be conducted on cases of P_{act}=0.0005 and P_{act}=0.5 only with different values of K_d.

4.3 Influence of the Transport Ratio. The comparison of thickness for different values of K_d and with same values of C_{oxy}=0.2 at calculating N_t=200,000 time steps is shown in Fig. 18, for P_{act}=0.0005 and P_{act}=0.5. The total thicknesses are about 190 m (a) for P_{act}=0.5 and 130 m (a) for P_{act}=0.0005 at N_t=200,000. From the comparisons, the transport ratio K_d in the model has great impact on the thickness of the oxide layer. Increasing the value of the transport ratio K_d will increase the oxide film growth greatly for the same calculating steps. The first reason is that the transport steps for oxygen sites are K_d times that of the metal ions for a particular calculating step number. The second reason is that a relatively fast transport will lead to more extra oxygen penetration into the metal, especially for a low reaction probability case. Obviously, a higher reaction probability leads to a faster growth of the oxide layer in two directions.

4.4 Mapping Between the Mesoscopic Model and the Experimental Data. The growth of the total thickness, inner layer thickness, and outer layer thickness all follows the parabolic law. Therefore, the growth of the total thickness can be fitted in the following parabolic relation:

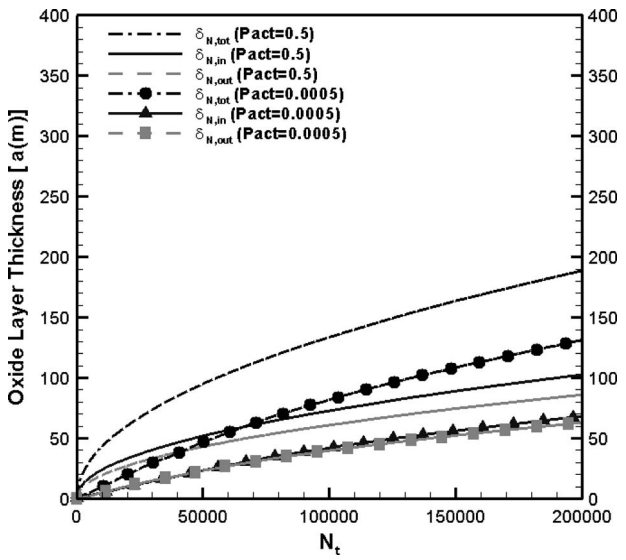

Fig. 7 The comparison of the oxide layer thickness of cases with P_{act}=0.0005 and P_{act}=0.5 at N_t=200,000, with K_d=1 and C_{oxy}=0.2

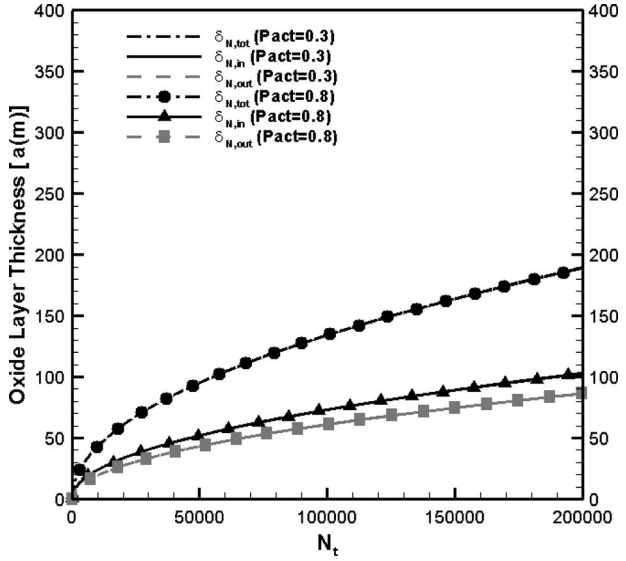

Fig. 8 The comparison of the oxide layer thickness of cases with P_{act}=0.3 and P_{act}=0.8 at N_t=200,000, with K_d=1 and C_{oxy}=0.2

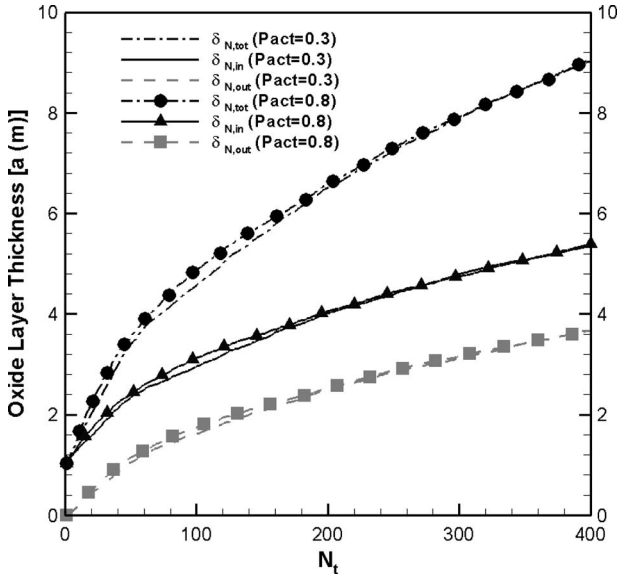

Fig. 9 The comparison of the oxide layer thickness of cases with P_{act}=0.3 and P_{act}=0.8 at the initial stage, with K_d=1 and C_{oxy}=0.2.

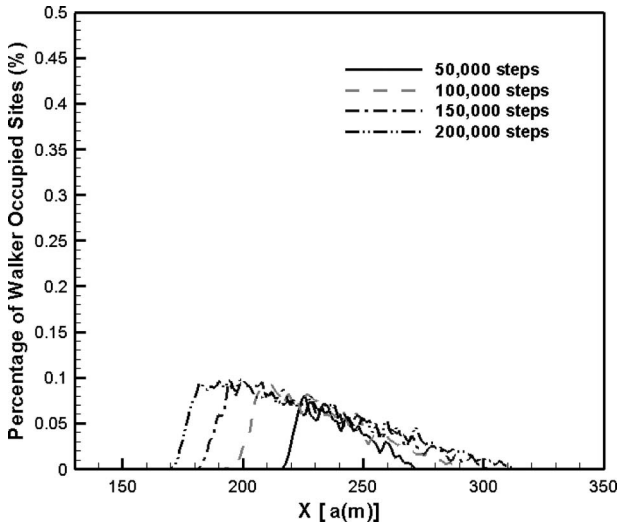

Fig. 10 The walker distributions for N_t=200,000, with K_d=1, C_{oxy}=0.2, and P_{act}=0.0005

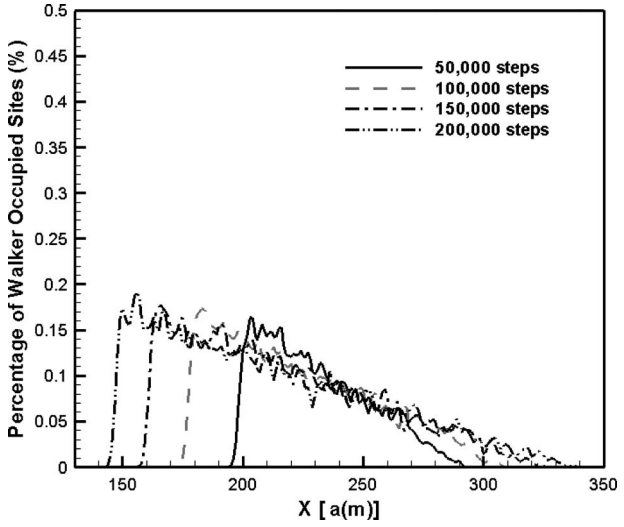

Fig. 11 The walker distributions for N_t=200,000, with K_d=1, C_{oxy}=0.2, and P_{act}=0.3

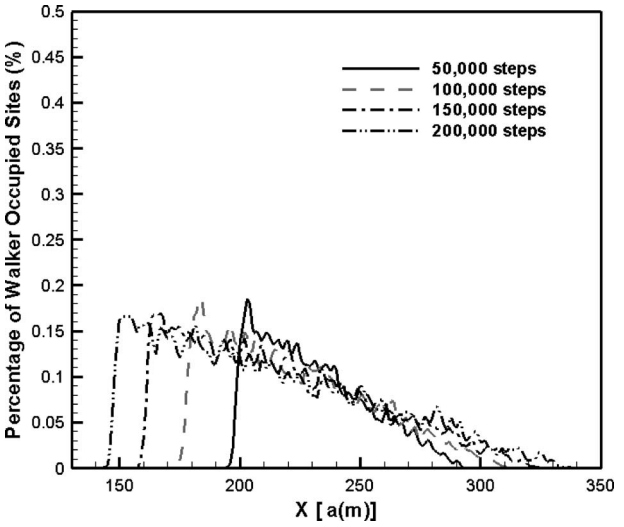

Fig. 12 The walker distributions for N_t=200,000, with K_d=1, C_{oxy}=0.2, and P_{act}=0.5

$$\delta_{N,\text{tot}}^2 = k_{N,p} N_t \tag{10}$$

where $k_{N,p}$ is the calculated parabolic rate coefficient for the CA model with distance based on the lattice number. For the case of P=0.5, ε=1, and K_d=2, $k_{N,p}$ can be fitted to 0.3434 from Fig. 19. According to the Wagner's theory [28], the real thickness of the oxide layer follows the relationship

$$\delta_{\text{tot}}^2 = k_p t \tag{11}$$

where k_p is the parabolic rate coefficient for real oxide layer growth, which can be obtained from experiments. The thickness, δ_{tot}, can be measured in experiments, while $\delta_{N,\text{tot}}$ is the calculated thickness from the developed CA model. The time for forming thickness a (meters) of oxide layer is assumed to be Δt(s). Then,

$$\delta_{\text{tot}} = \delta_{N,\text{tot}} a \tag{12}$$

$$t = N_t \Delta t \tag{13}$$

Substituting Eqs. (12) and (13) into Eq. (11),

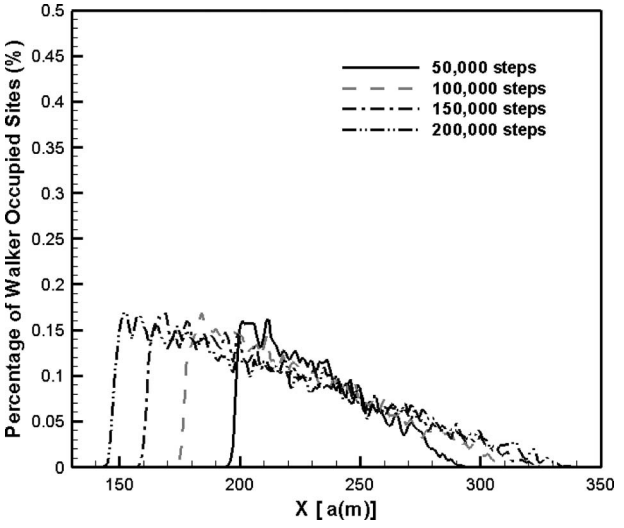

Fig. 13 The walker distributions for N_t=200,000, with K_d=1, C_{oxy}=0.2, and P_{act}=0.8

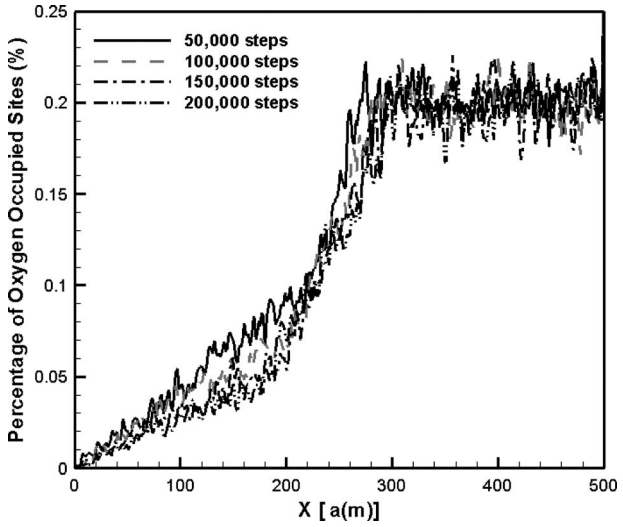

Fig. 14 The oxygen distributions for N_t=200,000, with K_d=1, C_{oxy}=0.2, and P_{act}=0.0005

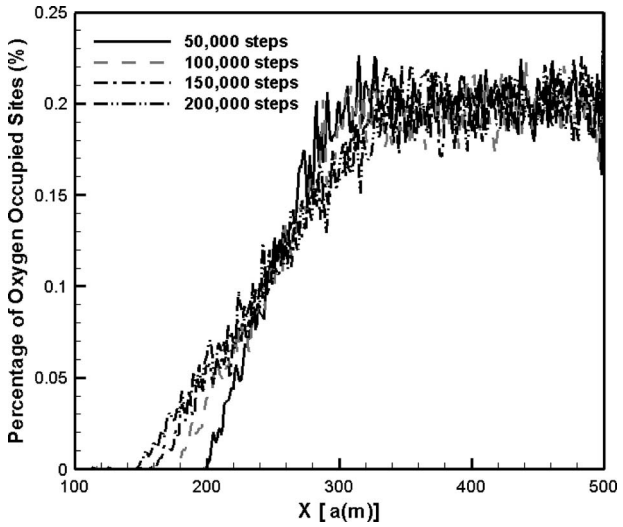

Fig. 15 The oxygen distributions for N_t=200,000, with K_d=1, C_{oxy}=0.2, and P_{act}=0.3

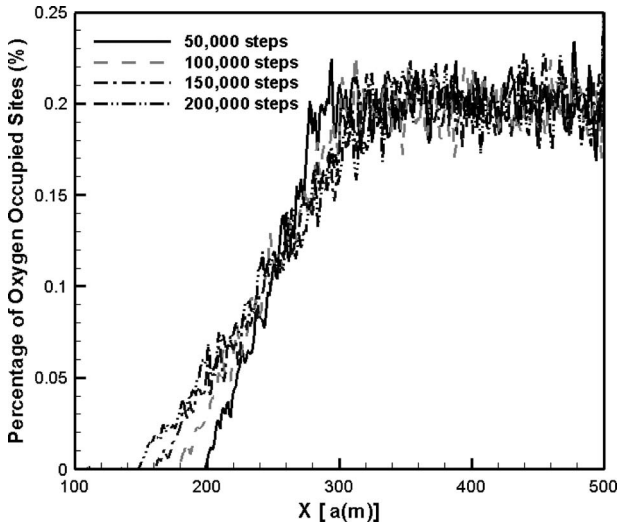

Fig. 16 The oxygen distributions for N_t=200,000, with K_d=1, C_{oxy}=0.2, and P_{act}=0.5

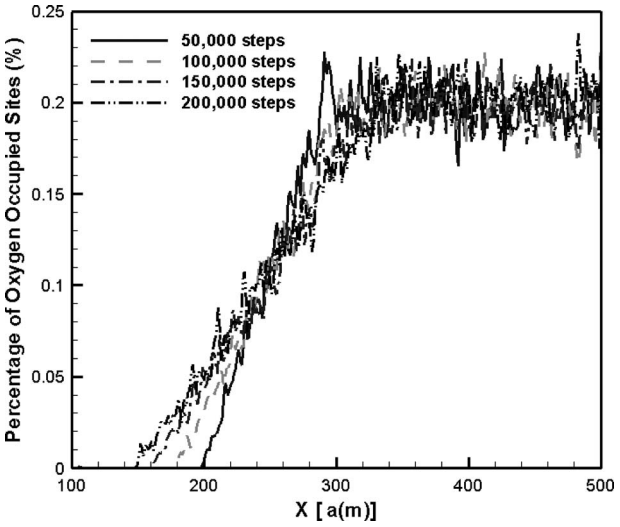

Fig. 17 The oxygen distributions for N_t=200,000, with K_d=1, C_{oxy}=0.2, and P_{act}=0.8

$$(\delta_{N,\mathrm{tot}}a)^2 = k_p N_t \Delta t \tag{14}$$

Comparing Eqs. (10) and (14),

$$\Delta t = k_{N,p} a^2 / k_p \tag{15}$$

From Ref. [27], the fitted values of k_p from the experimental data for a LBE loop at temperature 550°C with oxygen concentration controlled at 0.03 ppm are estimated to be 2.29×10^{-17} m^2/s for 316, 2.35×10^{-17} m^2/s for D-9, and 2.82×10^{-17} m^2/s for HT-9, respectively. Therefore, the time step spans equal to 0.3749 s, 0.3653 s, and 0.3044 s for 316, D-9, and HT-9 with the above conditions, respectively, for a length a =5 nm in the developed mesoscopic model.

4.5 Benchmark of the Pure Diffusion Process Without Reaction. The developed mesoscopic model can be used to study the pure diffusion process, in which no chemical reaction is involved. The CA model is benchmarked with a diffusion process of oxygen:

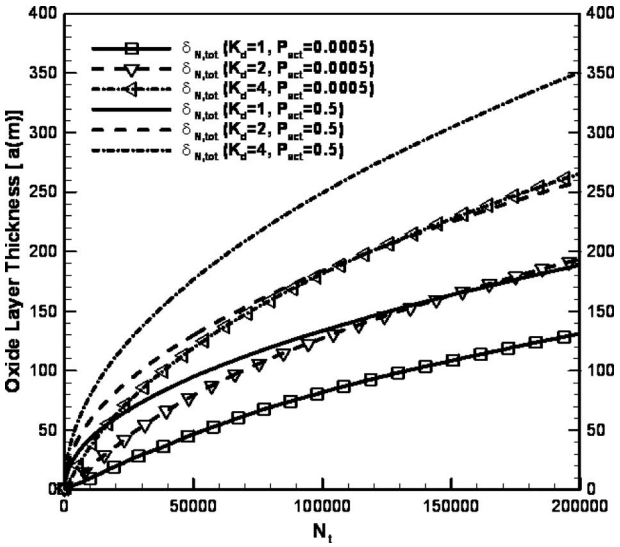

Fig. 18 Comparison of thickness for different value of K_d, with C_{oxy}=0.2, P_{act}=0.0005, and P_{act}=0.5

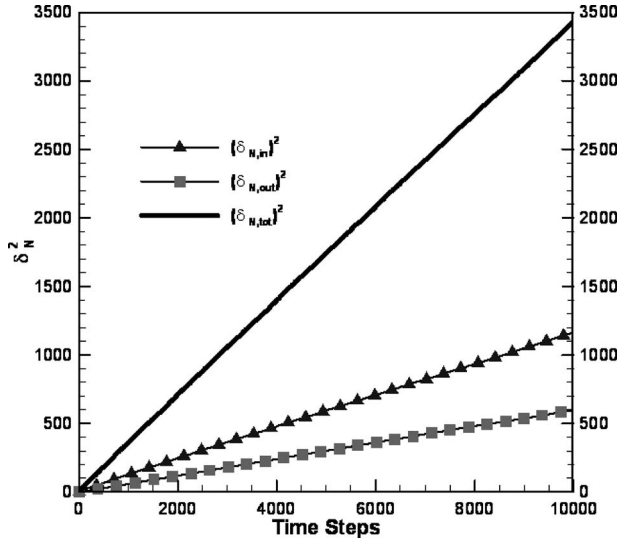

Fig. 19 Values of $(\delta_{N,\text{in}})^2$, $(\delta_{N,\text{out}})^2$, and $(\delta_{N,\text{tot}})^2$ versus time steps

$$\frac{\partial u}{\partial t} = \frac{1}{2}\frac{\partial^2 u}{\partial x^2} \quad \text{with} \begin{cases} u(0,t) = 0 \\ u(1,t) = 1 \\ u(x,t) = 0 \quad (\text{when } x \neq 1) \end{cases} \tag{16}$$

This diffusion problem has an analytical solution and the steady-state solution for Eq. (16) can be expressed as

$$u(x,t) = x \tag{17}$$

To benchmark this diffusion problem, the partial difference equation (16) was simulated in a square domain of 1000×1000 grids where the mesh is uniform. Since neither the diffusion of metal nor the chemical reaction is involved in this simple problem, K_d is set to 1 to make the diffusion steps equal to the calculating steps (N_t). As proved in Ref. [9], the concentration distribution approaches to a steady solution with time steps exceeding 15,000 steps. For benchmark, the calculated concentration of oxygen sites at 20,000 steps from the present model is compared with the steady-state solution and Brieger and Bonomi's result [25]. From Fig. 20, the diffusion from the interface into the structural material is simulated. It can be seen from Fig. 21 that the result from the proposed model is in good agreement with the steady-state solution and Brieger and Bonomi's solution. The benchmark shows that the proposed CA model satisfies the anticipated estimation of the transport of oxygen at a mesoscopic level.

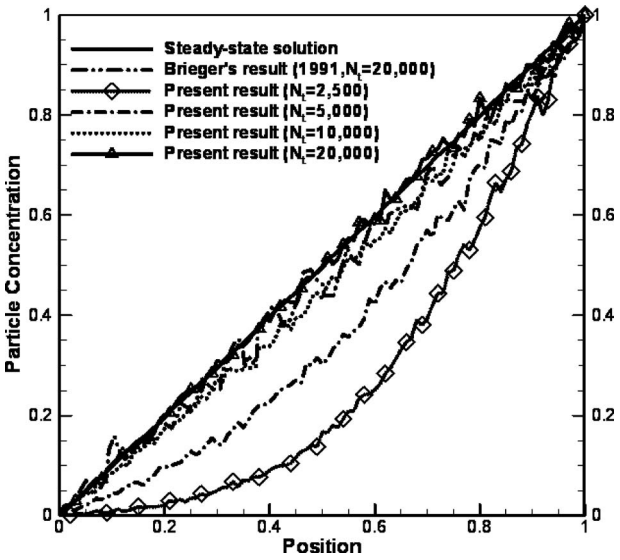

Fig. 21 Benchmark of the results form the present model with the analytical solution and Brieger and Bonomi's result [25]

5 Conclusions

In this paper, an improved stochastic mesoscopic CA model has been developed to investigate the development of a continuous oxide layer of metals. The metal oxidation process has been studied at a mesoscopic level with the developed CA model.

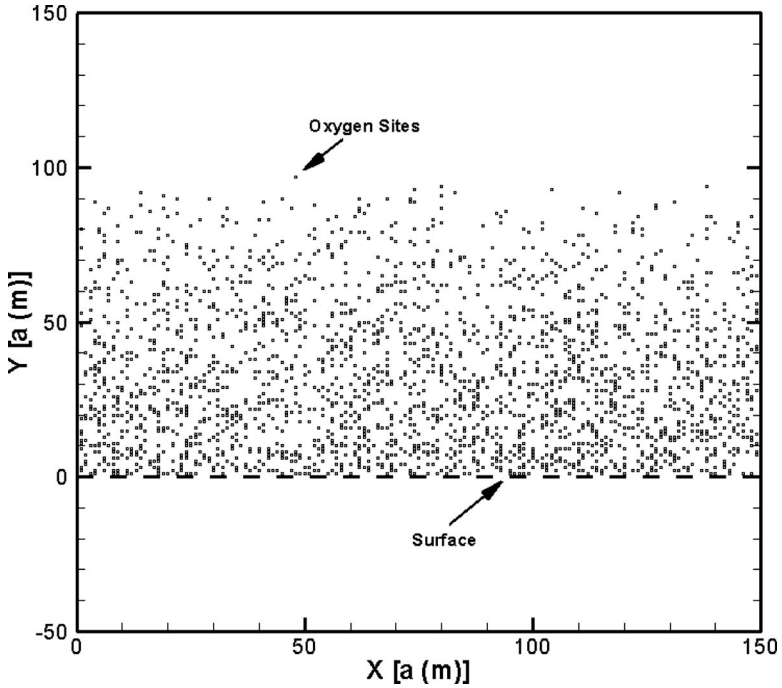

Fig. 20 The diffusion process of oxygen without chemical reaction

In this CA model, a new scheme of the mesoscopic transport of oxygen has been proposed, in which along the oxygen diffuses along the grain boundaries. The oxide layer growth in the mesoscopic CA model is controlled by three main explicit parameters, the volume control parameter (ε), the reaction probability (P_{act}), and the transport step ratio of oxygen and metallic ions (K_d). A parametric study was conducted in order to check the importance of the main explicit parameters of the mesoscopic model.

Two different kinds of boundary condition of oxygen concentration have been studied at the far end of the specimen (at $y=0$). The oxygen concentration in the far end of the specimen (at $y=0$) satisfies both of the Dirichlet boundary condition and the Neumann boundary condition since the oxygen diffusion rates in the oxide layer and the metal are relatively small in most of the real cases and the specimen is usually relatively large compared to the oxide layer.

The developed mesoscopic model can be extended to study the pure diffusion process, in which no chemical reaction is involved. The CA model was benchmarked with a pure diffusion process, both with the analytical solution and with the previous work in Ref. [25]. Significant agreement was reached between the data, which shows the basic abilities of the present model for mesoscopic studies. From the present model, the thicknesses of inner oxide layer, outer oxide layer, and the total oxide layer grow parabolically, which accords with Wagner's oxide layer growth theory [28]. The model is also mapped with the experimental data from a LBE loop [26] to show the development of the oxide layer quantificationally in a nanometer scale.

Acknowledgment

This research is supported by U.S. Department of Energy (Grant No. DE-FG04-2001AL67358) through the Transmutation Research Program (TRP) at the University of Nevada, Las Vegas.

Nomenclature

a = width of a square lattice in CA model, m
B = Pilling–Bedworth ratio
C = concentration of oxygen
i = node number of the calculating domain
$\mathrm{Inte}_{ij}(t)$ = state variable of the interstitial sites
$\mathrm{Inte}_{i,j}^{\mathrm{Nb}}(t)$ = state variable of the neighbor interstitial sites of the lattice (i,j)
Inte_0 = a "vacancy" interstitial site
Inte_1 = an "occupied" interstitial site by oxygen
k = iteration step number
$k_{N,p}$ = parabolic rate coefficient based on CA model
k_p = parabolic rate coefficient for real oxide layer growth
K_d = ratio of transport steps of an oxygen site and diffusion steps of a walker
$\mathrm{Lat}_{ij}(t)$ = state variable of the lattice site
$\mathrm{Lat}_{i,j}^{\mathrm{Nb}}(t)$ = state variable of the neighbor lattice sites of the lattice (i,j)
Lat_2 = an atomic metal lattice site (solid phase)
Lat_3 = a LBE lattice site (liquid phase)
Lat_4 = an oxide lattice site (solid phase)
Lat_5 = a lattice site of oxide with overlapping with ironic metal (solid phase)
N_{OT} = transport steps of oxygen in a calculating step
N_{WD} = diffusion steps of walker in a calculating step
N_t = calculating steps
N = lattice number in x direction
P_{act} = reaction probability of oxygen sites and metal sites
t = time
Δt = a short time difference
x = coordinate in longitude direction
α = number of metallic ions in an oxide molecular
β = number of oxygen ions in an oxide molecular
δ = thickness of laminar sublayer
$\delta_{N,\mathrm{in}}$ = mean inner layer thickness
$\delta_{N,\mathrm{out}}$ = mean outer layer thickness
$\delta_{N,\mathrm{tot}}$ = mean total thickness of the oxide layer
Δ = difference
$\Delta t(s)$ = the time for forming thickness a (meters) of oxide layer
$\Delta\delta_{\mathrm{in}}$ = increase of inner oxide layer
$\Delta\delta_{\mathrm{out}}$ = increase of outer oxide layer
$\Delta\delta_{\mathrm{tot}}$ = increase of the total oxide layer
Φ_{Lat} = local evolution rules for a lattice site
Φ_{Inte} = local evolution rules for an interstitial site
φ_{Lat} = control variables for an interstitial site
φ_{Inte} = control variables for a lattice site
ε = volume control parameter
ω = number of oxygen atoms at an interstitial site

References

[1] Park, J. J., Butt, D. P., and Beard, C. A., 2000, "Review of Liquid Metal Corrosion Issues for Potential Containment Materials for Liquid Lead and Lead-Bismuth Eutectic Spallation Targets as a Neutron Source," Nucl. Eng. Des., **196**, pp. 315–325.
[2] Spencer, B., 2000, "The Rush to Heavy Liquid Metal Reactor Coolants—Gimmick or Reasoned," ASME Paper No. ICONE-8729.
[3] Gromov, B. F., Belomitcev, Y. S., Yefimov, E. I., Leonchuk, M. P., Martinov, P. N., Orlov, Y. I., Pankratov, D. V., Pashkin, Yu. G., Toshinsky, G. I., Chekunov, V. V., Shmatko, B. A., and Stepanov, V. S., 1997, "Use of Lead-Bismuth Coolant in Nuclear Reactors and Accelerator-Driven Systems," Nucl. Eng. Des., **173**, pp. 207–217.
[4] Zhang, J. S., and Li, N., 2004, "Corrosion/Precipitation in Non-Isothermal and Multi-Modular LBE Loop Systems," J. Nucl. Mater., **326**, pp. 201–210.
[5] Zhang, J. S., Li, N., and Chen, Y., 2005, "Dynamics of High Temperature Oxidation Accompanied by Scale Removal and Implications for Technological Applications," J. Nucl. Mater., **342**, pp.1–7.
[6] Tan, T., Chen, Y., and Chen, H., 2007, "Theoretical Modeling and Numerical Simulation of the Corrosion and Precipitation in Non-Isothermal Liquid Lead Alloy Pipe/Loop Systems," Heat Mass Transfer, **44**(3), pp. 355–366.
[7] Tan, T., Chen, Y., and Chen, H., 2008, "A Diffusion Controlling Oxidation Model With Scale Removal in Oxygen Containing Liquid Flow," Comput. Mater. Sci., **44**, pp. 750–759.
[8] Tan, T., 2007, "Modeling of the Protective Oxide Layer Growth in Non-Isothermal Lead-Alloys Coolant Systems," Ph.D. thesis, University of Nevada, Las Vegas.
[9] Müller, G., Heinzel, A., Konys, J., Schumacher, G., Weisenburger, A., Zimmermann, F., Engelko, V., Rusanov, A., and Markov, V., 2002, "Results of Steel Corrosion Tests in Flowing Liquid Pb/Bi at 420–6000 °C after 2000 h," J. Nucl. Mater., **301**, pp. 40–46.
[10] Zhang, J. S., Li, N., and Elson, J. S., 2008, "Review of Studies on Fundamental Issues in LBE Corrosion," J. Nucl. Mater., **373**, pp. 351–377.
[11] Tan, T., Chen, Y., and Tan, X., 2009, "Buoyancy Enhanced Oxygen Transport in the Experimental Liquid Lead Bismuth Eutectic Container," J. Nucl. Sci. Technol., **46**(2), pp. 109–131.
[12] Chen, Y., Tan, T., and Chen, H., 2008, "Oxidation Companied by Scale Removal: Initial and Asymptotical Kinetics," J. Nucl. Sci. Technol., **45**(7), pp. 662–667.
[13] Eden, M., 1961, "A Two-Dimensional Growth Process," *Biology and Problems of Health, Proceedings of the Fourth Berkeley Symposium on Mathematics, Statistics and Probability*, F. Neyman, ed., University of California Press, Berkeley, Vol. 4, pp. 223–239.
[14] Witten, T. A., Jr., and Sander, L. M., 1981, "Diffusion-Limited Aggregation: A Kinetic Critical Phenomenon," Phys. Rev. Lett., **47**, pp. 1400–1403.
[15] Witten, A., Jr., and Sander, L. M., 1983, "Diffusion-Limited Aggregation," Phys. Rev. B, **27**, pp. 5686–5697.
[16] Saunier, J., Chausse, A., Stanfiej, J., and Badiali, J. P., 2004, "Simulations of Diffusion Limited Corrosion at the Metal/Environment Interface," J. Electroanal. Chem., **563**, pp. 239–247.
[17] Sazou, D., and Georgolios, C., 1996, "Morphological Surface Changes of the Fe Electro-Dissolution in 2M H_2SO_4 During Bursting Oscillations Induced by Br," Electrochim. Acta, **41**, pp. 144–158.
[18] Schultze, J. W., and Schweinsberg, M., 1998, "From pm to km: Scaling Up and Scaling Down of Electrochemical Systems With TiO_2 and ZrO_2 Passive Films as an Example," Electrochim. Acta, **43**, pp. 2761–2772.
[19] Zhang, J. S., 2005, "Oxidation Mechanism of Steels in Liquid-Lead Alloys," *Oxidation of Metals*, Vol. 63, pp. 353–381.
[20] Chang, Y. A., Fitzner, K., and Zhang, M.-X., 1988, "The Solubility of Gases in Liquid Metals and Alloys," Prog. Mater. Sci., **32**, pp. 97–259.
[21] Lai, G. Y., 1990, *High Temperature Corrosion of Engineering Alloys*, ASM International, Materials Park, OH.

[22] Firth, D. C., 1969, *Elementary Chemical Thermodynamics*, Oxford University Press, Oxford.
[23] Smeltzer, W. W., Hearing, R. R., and Kirkaldy, J. S., 1961, "Oxidation of Metals by Short Circuit and Lattice Diffusion of Oxygen, pp. 795–915 (September 1961)," Acta Metall., **9**, pp. 880–885.
[24] Dieckmann, R., and Schmalzried, H., 1977, "Defects and Cation Diffusion in Magnetite (II)," Ber. Bunsenges. Phys. Chem., **81**, pp. 414–419.
[25] Brieger, L., and Bonomi, E., 1991, "A Stochastic Cellular Automaton Model of Non-Linear Diffusion and Diffusion With Reaction," J. Comput. Phys., **94**, (2), pp. 467–486.
[26] http://cell-auto.com/neighbourhood/index.html.
[27] Zhang, J. S., Li, N., and Chen, Y., and Rusanov, A. E., 2005, "Corrosion Behaviors of US Steels in Flowing Lead-Bismuth Eutectic (LBE)," J. Nucl. Mater., **336**, pp. 1–10.
[28] Wagner, C., 1969, "The Distribution of Cations in Metal Oxide and Metal Sulphide Solid Solutions Formed During the Oxidation of Alloys," Corros. Sci., **9**, pp. 91–109.

Swirling Annular Flow in a Steam Separator

Hironobu Kataoka
Yusuke Shinkai
Shigeo Hosokawa
Akio Tomiyama

Graduate School of Engineering,
Kobe University,
Rokkodai, Nada,
Kobe 657-8501, Japan

Effects of pick-off ring configuration on the separator performance of a downscaled model of a steam separator for a boiling water nuclear reactor are examined using various types of pick-off rings. The experiments are conducted using air and water. Pressure drops in a barrel and a diffuser and diameters and velocities of droplets at the exit of the barrel are measured using differential pressure transducers and particle Doppler anemometry, respectively. The separator performance does not depend on the shape of the pick-off ring but strongly depends on the width of the gap between the pick-off ring and the barrel wall. The pressure drop in the barrel is well evaluated using the interfacial friction factor for unstable film flows. Carry-under can be estimated using a droplet velocity distribution at the exit of the separator. [DOI: 10.1115/1.3078701]

1 Introduction

Boiling water nuclear reactors (BWRs) are equipped with steam separators for splitting a two-phase mixture into steam and water before feeding steam to dryers and turbines. The steam separator consists of a standpipe, a diffuser with a swirler, and a barrel with several pick-off rings (PORs). Stationary vanes of the swirler apply a large centrifugal force to the flow, and thereby, most of water rapidly migrates toward the barrel wall. An annular swirling flow with negligible droplet flow rate in the gas core is, therefore, formed in the barrel. The liquid film flow is removed by the PORs from the gas core flow. However we have little knowledge on the annular swirling flow in the separator [1,2]. Hence, in our previous study [3,4], flow patterns, liquid film thickness, and the ratio of the flow rate of the separated liquid to the total liquid flow rate in air-water annular swirling flows in a one-fifth scale model of the steam separator were measured to understand the characteristics of the swirling flow and to establish an experimental database applicable to the modeling and verification of numerical methods for predicting the two-phase flow in the steam separator.

In the present study, the effects of POR configuration on the performance of a separator are examined by carrying out experiments using various PORs. Pressure drops in the barrel and the diffuser are measured and compared with available correlations. Velocities and diameters of droplets at the exit of the separator are also measured. Droplet velocities are utilized to evaluate the carry-under of the gas phase flowing into the separated flow and the carry-over, i.e., the unseparated liquid.

2 Experimental Setup

Figure 1 shows the experimental apparatus. It consists of the upper tank, the barrel, the diffuser, the standpipe, the plenum, the gas-liquid mixing section, the water supply system, and the air supply system. The barrel, the diffuser, and the standpipe were made of transparent acrylic resin for observation and optical measurements of two-phase flows. The size was one-fifth of the actual steam separator used in BWR. Air was supplied from the oil-free compressor (Oil-free Scroll 11, Hitachi Ltd. (Japan)), the regulator (R600-20, CKD, Ltd. (Japan)), and the flowmeter (FLT-N, Flowcell, Ltd. (Japan)) to the mixing section. Tap water at room temperature (293 K) was supplied from the magnet pump (MD-40RX, Iwaki, Ltd. (Japan)) and the flowmeter to the mixing section. The two-phase flow formed in the mixing section flowed up through the plenum of 60 mm in inner diameter D and 300 mm long, the standpipe of $D=30$ mm and 200 mm long, the diffuser of 33 mm long, and the barrel of $D=40$ mm and 270 mm long.

The swirler shown in Fig. 2, which was made of acrylonitrile butadiene styrene (ABS) resin, was installed in the diffuser to form a swirling flow in the barrel. Its shape was based on an actual swirler. Experiments without the swirler were also conducted to examine its effects on pressure drop and the separator performance. As will be discussed later, most of the flow patterns observed in the barrel were annular flows consisting of liquid film flow, gas flow, and droplet flow.

Figure 3 shows the upper part of the barrel. In an actual steam separator, the so-called POR is utilized for the separation. An inner pipe was inserted in the upper part of the barrel to simulate POR. The lower end of the inner pipe was located 220 mm above the bottom of the barrel. The mass flows, W_{Gs} and W_{Ls}, of the gas and liquid phases entering into the gap between the outer surface of the inner pipe and the barrel wall were separated from the two-phase flow in the barrel. The mass flows, W_{Gus} and W_{Lus}, of the gas and liquid phases were unseparated and flowed through the inner pipe.

Five types of pick-off rings listed in Table 1 were used to study the effects of POR configuration (see Fig. 4) on the separator performance. Most of the liquid film entered into the gap between the barrel wall and the outer wall of the POR, while most of the air and droplets did not. The separated liquid and the droplets carried over returned to the tank through independent pipelines.

A reference experimental condition was determined by adjusting the values of the flow quality and the two-phase centrifugal force to cover those in the nominal operating condition of the BWR separator. The values of the quality x and the gas and liquid volume fluxes J_G and J_L corresponding to the nominal operating condition were $x=0.18$, $J_G=14.6$ m/s, and $J_L=0.08$ m/s, respectively [3]. Hence, the present experiments were carried out under the conditions of $J_G=4.0-24.1$ m/s and $J_L=0.05-0.14$ m/s, including the reference point.

The mass flow rates, W_{Ls} and W_{Lus}, of the separated and unseparated liquids were measured using a timer and a graduated cylinder. Each measurement was conducted for 50 s to make the uncertainty in measured W 3%. The ratio W_s^* of the flow rate of the separated liquid to the total liquid flow rate,

$$W_s^* = \frac{W_{Ls}}{W_{Ls} + W_{Lus}} \tag{1}$$

was used as an index of the separator performance.

The film thickness δ was measured using a laser focus displacement (LFD) meter (LT-9030, Keyence, Ltd. (Japan)) [5]. The sampling period was 0.64 ms, and the measurement time was 30 s.

Manuscript received August 21, 2008; final manuscript received August 22, 2008; published online February 18, 2009. Review conducted by Dilip R. Ballal. Paper presented at the 16th International Conference on Nuclear Engineering (ICONE16), Orlando, FL, May 12–15, 2008.

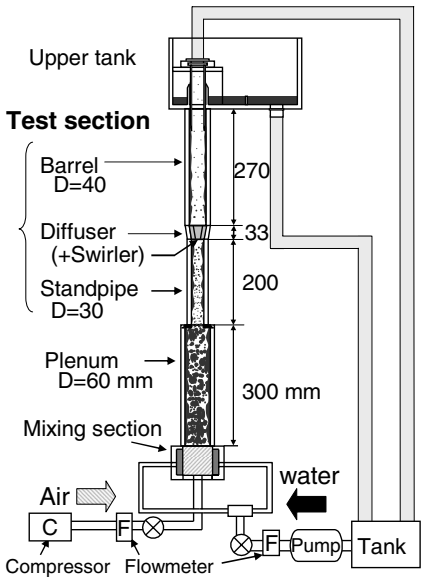

Fig. 1 Experimental apparatus

The sampling number was, therefore, more than 46,000, which was sufficient to obtain accurate time-averaged film thicknesses δ_{avg}. The uncertainty in measured δ_{avg} was 2.0%.

Pressure drops in the diffuser and the barrel were measured using differential pressure transducers (DP45, Validyne Eng. Co. (USA)). As shown in Fig. 5, six holes of 1 mm diameter were made at six elevations to measure pressure drops between two elevations. The sampling period was 1.0 ms, and the measurement

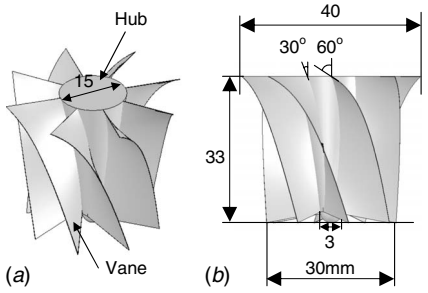

Fig. 2 Swirler with a hub and stationary vanes: (*a*) bird's-eye view and (*b*) side view

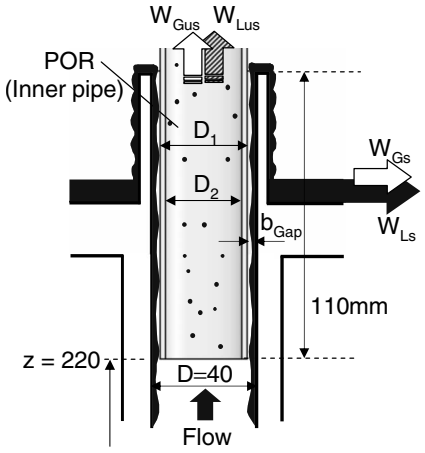

Fig. 3 POR

Table 1 Specifications of pick-off rings

Type	b_{gap} (mm)	t (mm)	Shape	D_1 (mm)	D_2 (mm)
1	2	2	Flat	36	32
2	2	1	Flat	36	34
3	2	0.5	Flat	36	35
4	2	2	Taper	36	32
5	4	2	Taper	32	28

time was 50 s, which was long enough to obtain accurate time-averaged pressure drops. The uncertainty in the measured pressure drop was less than 0.5%.

To measure droplet flow, we made use of an alternative POR section shown in Fig. 6. The diameters and velocities of droplets in the gas core flow were measured using a phase Doppler anemometry (PDA) system (58N series, DANTEC Dynamics, Ltd. (Denmark)). The gap width b_{gap}, thickness t, and inner diameter D_2 of the POR were 4, 2, and 28 mm, respectively. The measurement was conducted at 246 mm downstream of the swirler. The uncertainties in measured diameters and velocities of droplets were 1% and 0.5%, respectively.

Flow patterns in the barrel and standpipe were recorded using a high-speed video camera (Redlake Motion Pro HS-1, frame rate $=2000-2500$ fps (frames/s), and exposure time$=100$ μs).

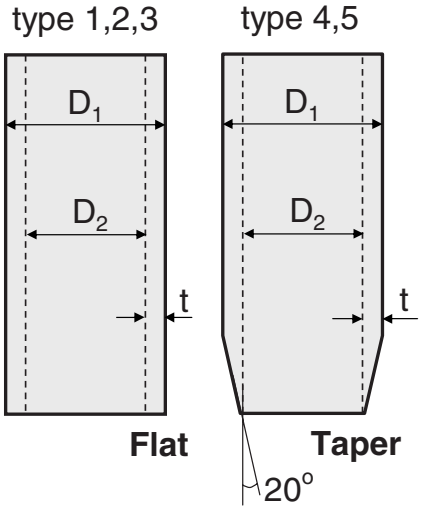

Fig. 4 POR shapes

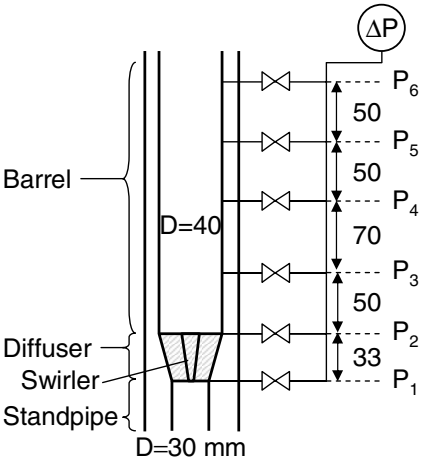

Fig. 5 Pressure drop measurement

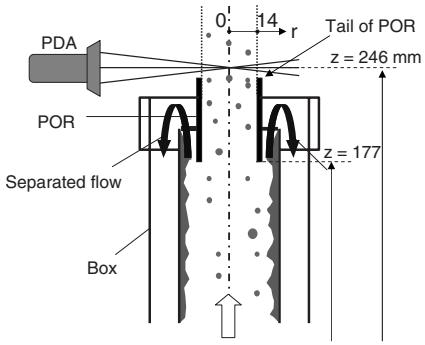

Fig. 6 POR section for PDA

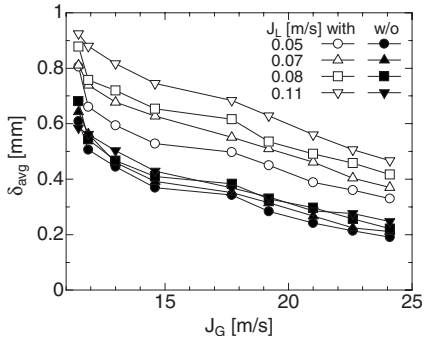

Fig. 8 Effects of J_G and J_L on δ_{avg} (z=170 mm)

3 Results and Discussion

3.1 Flow Pattern. Images of annular flow patterns without and with the swirler are shown in Figs. 7(*a*) and 7(*b*), respectively. Without the swirler, the droplet deposition takes place all over the barrel. In the case of swirling flow, the rotational speed of the flow increases with J_G, and as shown in Fig. 7(*b*) spiral streaks are formed from the swirler vanes in the annular flow condition. Most of the liquid in the streak might be made of liquid deposited on the swirler vanes; that is, the liquid transfer from droplets to the film is caused not only by the direct droplet deposition but also by the collection of droplets and film on the vanes [6]. As for the direct deposition, most of the droplets deposit on the liquid film within a short distance from the swirler (about 150 mm) due to a large centrifugal force generated by the swirling flow. This, in turn, implies that the droplet flow rate in the gas core flow is negligible in far downstream of the swirler.

3.2 Film Thickness. The mean film thickness δ_{avg} at 170 mm above the swirler is shown in Fig. 8, which clearly shows that δ_{avg} in swirling flows takes a higher value and depends more strongly on J_L than that in nonswirling flows. The strong dependence on J_L is in accordance with the fact that the film flow rate is close to the total liquid flow rate in swirling flows; i.e., the increase in J_L directly reflects the increase in the film flow rate. On the other hand, the droplet flow rate in nonswirling flows increases with J_L, and therefore, δ_{avg} does not depend on J_L so much in nonswirling flows. As shown in Fig. 9, the maximum film thickness δ_{max} is slightly higher in swirling flows than in nonswirling flows and is about three times as large as δ_{avg}. It should be noted that δ_{max} is larger than b_{gap} of types 1–4 PORs (2 mm) at low J_G.

3.3 Flow Separation. Figure 10 shows W_s^* for swirling and nonswirling flows measured by using type 4 POR (b_{gap}=2 mm, t=2 mm). The W_s^* with the swirler is larger than that without it, which implies that the swirler is an effective device for the flow separation. The difference between the two is marked especially in annular flow conditions (J_G>13 m/s). Without the swirler, W_s^* increases with J_G in churn flow, while it decreases with increasing J_G in annular flow due to the enhancement of droplet entrainment at high J_G. In annular swirling flow, W_s^* increases with J_G. This is due to the increase in the liquid film flow rate resulting from the large deposition rate caused by the strong centrifugal force.

The effects of POR configuration on W_s^* are shown in Fig. 11. Experimental data obtained by Nakao et al. [1] are also plotted in Fig. 11(*b*). Their data show a similar trend to the present data, though the size of the experimental apparatus is 2.5 times larger than the present apparatus. The W_s^* of type 5 POR (b_{gap}=4 mm) is larger than that of the other PORs (b_{gap}=2 mm), which implies

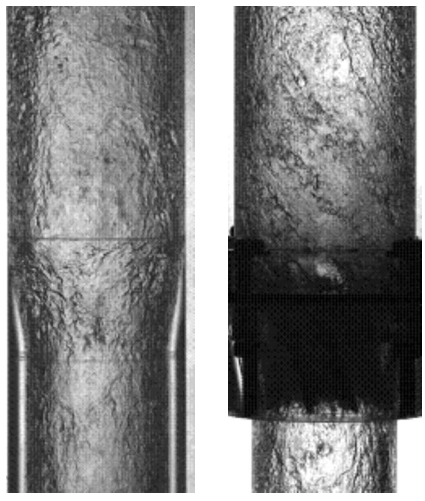

(*a*) (*b*)

Fig. 7 Annular flow in the diffuser and barrel (J_G=14.6 m/s and J_L=0.08 m/s): (*a*) without a swirler and (*b*) with a swirler

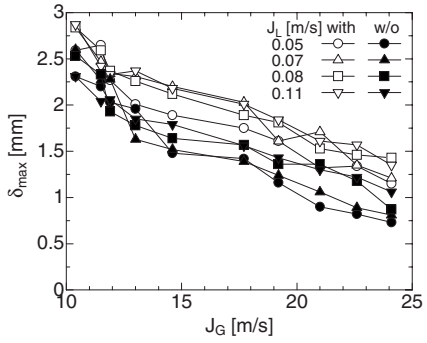

Fig. 9 Effects of J_G and J_L on δ_{max} (z=170 mm)

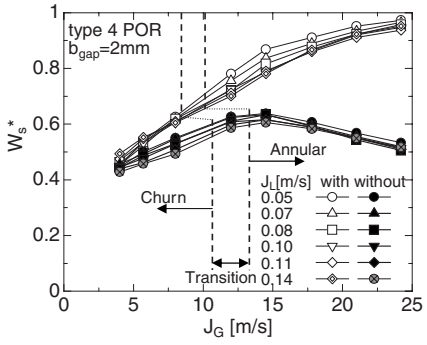

Fig. 10 Effects of the swirler on W_s^*

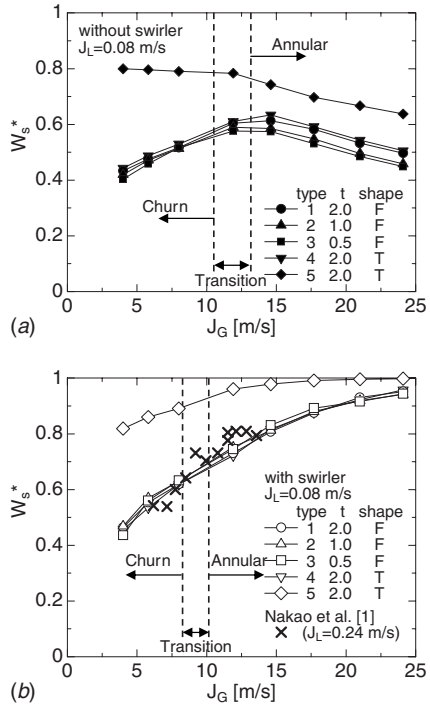

Fig. 11 Effects of the POR shape on W_s^*: (*a*) nonswirling flow and (*b*) swirling flow

the existence of liquid in the region between 2 nm and 4 mm from the barrel wall, which clearly shows that the separator performance strongly depends on the gap width. It also implies that POR configuration cannot be determined without taking into account the relationship between the liquid film thickness and the gap width. On the other hand, in the case of 2 mm gap (types 1–4), the effects of POR configuration under churn flow conditions are negligible since the maximum film thickness is larger than b_{gap}. The W_s^* for annular nonswirling flow is affected by the POR shape; that is, W_s^* takes a larger value with the tapered POR or with thicker PORs since the droplet flow rate in the POR gap is large in these cases. The W_s^* for swirling flow is not affected by POR shape because the droplet flow rate is reduced by a large centrifugal force.

3.4 Pressure Drop. Figure 12 shows pressure gradients $-dP/dz$ in the diffuser and barrel. As shown in Fig. 12(*a*), pressure recovery due to deceleration increases with J_G. On the other hand, $-dP/dz$ in swirling flow is larger than that in nonswirling flow since the swirler causes a singular pressure drop. In nonswirling flow, the region of the pressure recovery extends downstream of the diffuser as J_G increases. This must be due to the enlargement of the region of a separated recirculating flow. As shown in Fig. 12, the swirler increases the pressure drop in the barrel especially near the swirler, and the pressure drop near the swirler increases with J_G. The increase may be caused by a large centrifugal force, strong interfacial shear stress acting on the film surface roughened by the spiral streaks, and an enhanced droplet deposition.

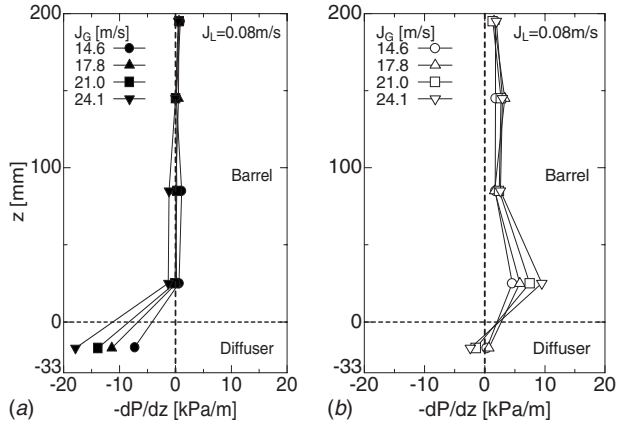

Fig. 12 Pressure gradient: (*a*) nonswirling flow and (*b*) swirling flow

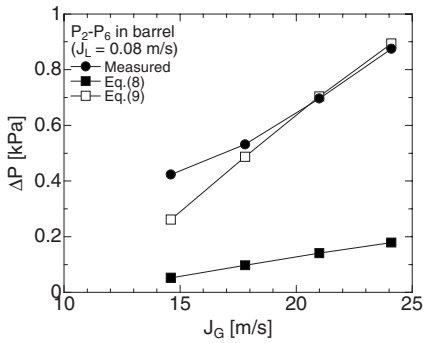

Fig. 13 Pressure drops of swirling flows in the barrel

Pressure drops can be estimated by the sum of the frictional and static pressure drops,

$$\Delta P = \frac{4}{D}\tau_w \Delta z + \rho_m g \Delta z \tag{2}$$

where τ_w is the wall shear stress, Δz is the axial distance, ρ_m is the mixture density, and g is the acceleration of gravity. Since the droplet volume fraction in swirling flow is negligible, ρ_m is estimated by

$$\rho_m = \rho_G(1-\alpha_F) + \rho_F \alpha_F \tag{3}$$

Here α is the volume fraction, ρ is the density, and the subscripts G and F denote the gas and liquid films, respectively. The film volume fraction is given by

$$\alpha_F = 4A_F/(\pi D^2) \tag{4}$$

where

$$A_F = \pi \delta_{\text{avg}}(D - \delta_{\text{avg}}) \tag{5}$$

The balance of the forces acting on the film flow yields

$$\tau_w = \tau_i - \rho_L g \delta_{\text{avg}} \tag{6}$$

where τ_i is the interfacial shear stress acting on the liquid film,

$$\tau_i = f_i \tfrac{1}{2} \rho_G u_G^2 \tag{7}$$

where f_i is the interfacial friction factor and u_G is the gas velocity. For stable films f_i can be evaluated by the Wallis correlation [7],

$$f_{iW} = 0.005\left(1 + 300\frac{\delta_{\text{avg}}}{D}\right) \tag{8}$$

whereas f_i for unstable films is given by [8]

$$f_{iU} = \max\{5f_{iW}, f_{iH}\} \tag{9}$$

where f_{iH} is the friction factor proposed by Henstock and Hanratty [9]. Note that $5f_{iW} > f_{iH}$ in the present experimental conditions, and therefore, f_{iU} is equal to $5f_{iW}$

The pressure drop ΔP ($=P_2 - P_6$) of annular swirling flow in the barrel is shown in Fig. 13. The Wallis correlation, Eq. (8), for stable films underestimates ΔP, whereas $5f_{iW}$ for unstable films agrees well with the measured ΔP.

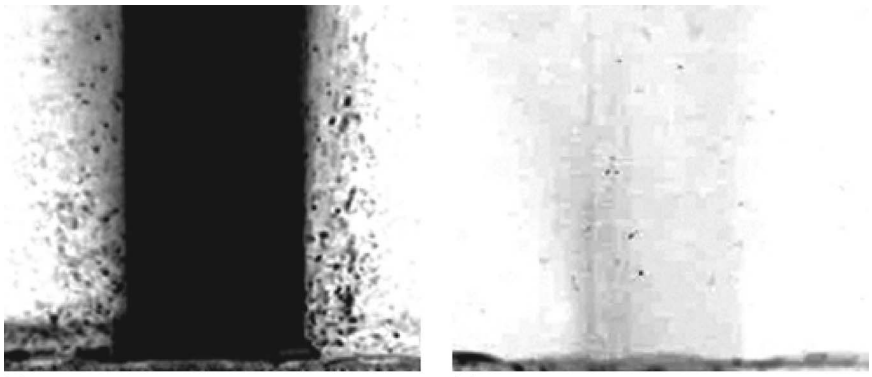

(*a*) (*b*)

Fig. 14 Gas core flows at the exit of the barrel (J_G=14.6 m/s and J_L=0.08 m/s): (*a*) nonswirling flow and (*b*) swirling flow

3.5 Droplet Diameter and Velocity. Images of gas core flows discharged from the alternative POR section are shown in Fig. 14. There are a number of droplets in nonswirling flows, whereas the number density of droplets is much smaller in swirling flows.

PDA measurement was carried out for swirling flows. Though the measurement was done for $0 \le r \le 14$ mm (the definition of radial coordinate r is shown in Fig. 6), the accuracy of the measured droplet diameter for $r > 8$ mm is low because of the presence of large droplets formed by the breakup of thin films at the tail of POR.

Figure 15 shows distributions of droplet diameter for J_G =14.6 m/s and J_L=0.08 m/s measured at the barrel center (r =0 mm and z=246 mm) and in the middle (r=7 mm and z =246 mm). Some of the large droplets (droplet diameter d >40 μm) remain at the center. This might be because the centrifugal force vanishes at r=0.

Figures 16(*a*) and 16(*b*) show effects of J_L and J_G on the Sauter mean diameter d_{32}, respectively. Here d_{32} is defined by

$$d_{32} = \sum_{i=1}^{N} d_i^3 \Big/ \sum_{i=1}^{N} d_i^2 \tag{10}$$

where d_i is the diameter of the ith droplet and N is the total number of droplets. The Sauter mean diameter is not affected by J_L but decreases with increasing J_G.

Radial distributions of mean streamwise velocity u_D of droplets in swirling flows are shown in Fig. 17. The broken line in Fig. 17(*a*) is the one-seventh power law based on the assumption of no carry-under. Although u_D shows a similar trend to the power law, the former is smaller than the latter due to carry-under. The u_D increases with J_L, which is caused by the decrease in carry-under due to the increase in film thickness at larger J_L. Since the droplet slip velocity is negligible (about 0.05 m/s), u_D is approximately equal to the gas velocity. It can also be understood from Fig. 17(*b*), which clearly shows that the increase rate of u_D is proportional to that of J_G.

3.6 Evaluation of Carry-Under and Carry-Over. The carry-under CU is defined by

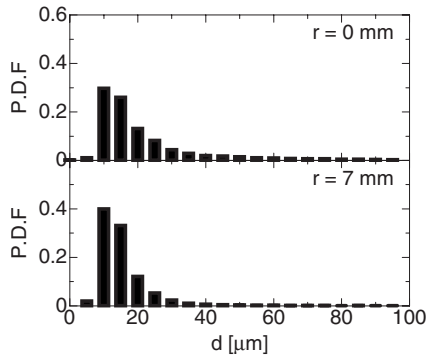

Fig. 15 Distribution of droplet diameter in swirling flow (z =246 mm, J_G=14.6 m/s, and J_L=0.08 m/s)

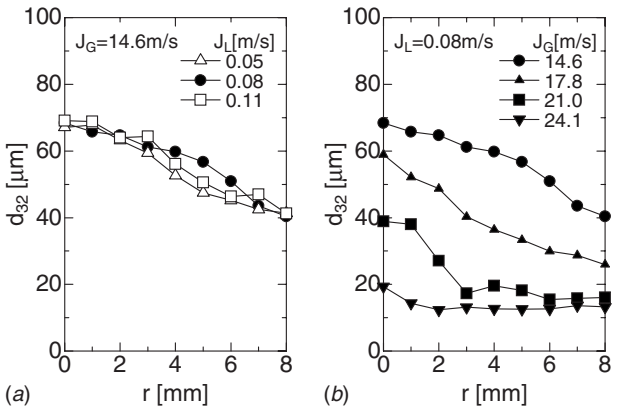

Fig. 16 Sauter mean diameter d_{32}: (*a*) influence of J_L and (*b*) influence of J_G

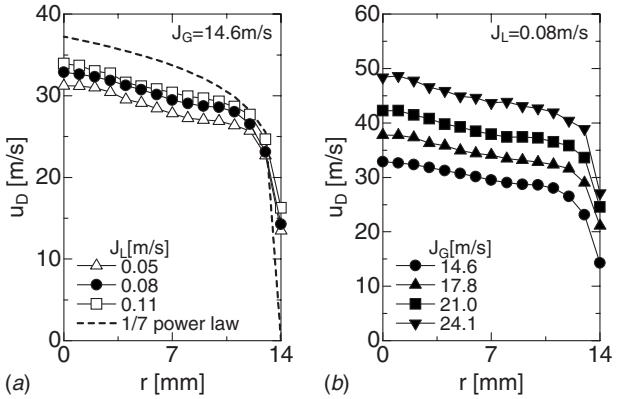

Fig. 17 Mean vertical velocity u_D of droplets: (*a*) influence of J_L and (*b*) influence of J_G

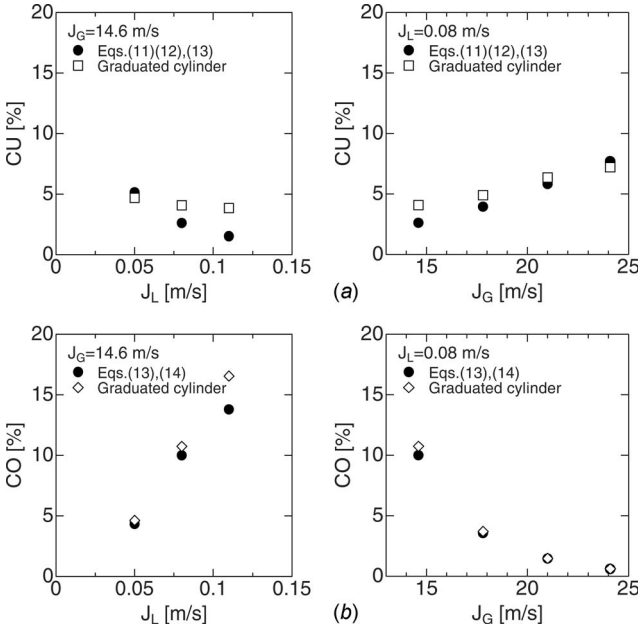

Fig. 18 Carry-under *CU* and carry-over *CO*: (*a*) carry-under and (*b*) carry-over

$$CU = \frac{W_{Gs}}{W_{Gs} + W_{Ls}} \tag{11}$$

It is not easy to measure CU because of the difficulty in measuring W_{Gs}. The separated gas flow rate *is* given by

$$W_{Gs} = W_G - W_{Gus} \tag{12}$$

where W_G is the total mass flow rate of the gas. The droplet velocity u_D is nearly equal to u_G, and the droplet volume fraction α_D is negligible. Hence W_{Gus} is estimated by

$$W_{Gus} = \rho_G \int_0^{D/2} u_D 2\pi r dr \tag{13}$$

The carry-over CO is defined by

$$CO = \frac{W_{Lus}}{W_{Gus} + W_{Lus}} \tag{14}$$

Equations (11)–(14) can be utilized to estimate CU and CO by making use of u_D.

Figures 18(*a*) and 18(*b*) show CO and CU of type 5 POR, respectively. The decrease in J_L or increase in J_G causes the decrease in film thickness, which, in turn, increases CU. This tendency is well captured in CU evaluated by using Eqs. (11)–(13). The carry-under and carry-over were also measured by using a graduated cylinder and a timer. Although there might be nonnegligible errors in this measurement, the CU and CO evaluated by using Eqs. (11)–(14) agreed well with those measured by the graduated cylinder.

4 Conclusion

The effects of the POR configuration on the separator performance of a downscaled model of a steam separator for a boiling water nuclear reactor are examined using various types of PORs. The experiments are conducted using air and water. Pressure drops in a barrel and a diffuser are measured using differential pressure transducers. Droplet velocities are measured using a PDA system, which are utilized to evaluate carry-under and carry-over. As a result, the following conclusions are obtained.

(1) The separator performance does not depend on the shape and thickness of POR but strongly depends on the gap width.
(2) The pressure drop in the barrel is well predicted by using the interfacial friction factor, $5f_{iW}$, where f_{iW} is the Wallis correlation of the interfacial friction factor for annular flow with stable films.
(3) The carry-under and carry-over are well estimated by making use of the radial distribution of droplet velocity at the exit of the separator.

Acknowledgment

The authors gratefully acknowledge the financial support by the "Innovation and Viable Nuclear Energy Technology Development Project" of the Ministry of Economy, Trade and Industry, Japan and the assistance in experiments by Mr. D. Nishiwaki.

Nomenclature

A = area (m^2)
b_{gap} = gap width (m)
CO = carry-over
CU = carry-under
D = pipe diameter (m)
d_{32} = Sauter mean diameter (m)
f = friction factor
G = mass flux (kg/m^2 s)
g = acceleration of gravity (m/s^2)
J = volume flux in a barrel (m/s)
r = radial coordinate (m)
t = POR thickness (m)
u = velocity (m/s)
W = mass flow rate (kg/s)
W_s^* = ratio of separated flow to total flow
x = quality

Greek Letters

α = volume fraction
ΔP = pressure drop (Pa)
δ = film thickness (m)
ρ = density (kg/m^3)
τ = shear stress (N/m^2)

Subscripts

avg = average
D = droplet
F = film
G = gas phase
i = interface
L = liquid phase
m = gas-droplet mixture
us = unseparated
s = separated
w = wall

References

[1] Nakao, T., Murase, M., Ishida, N., Kawamura, T., Minato, A., and Moriya, K., 2001, "Decrease of Pressure Loss in BWR Steam Separator (1) (Evaluation Method of Gas-Liquid Separation)," Jpn. J. Multiphase Flow, **15**(4), pp. 382–389.
[2] Ikeda, H., Shimizu, T., Narabayashi, T., Kondo, T., Nishida, K., and Fukuda, T., 2003, "Improvement of BWR Steam Separator With Three-Dimensional Gas-Liquid Two-Phase Flow Simulation Method," 11th International Conference on Nuclear Engineering (ICONE-11), Paper No. 36486, CD-ROM, pp. 1–9.
[3] Kataoka, H., Tomiyama, A., Hosokawa, S., Sou, A., and Chaki, M., 2008, "Two-Phase Swirling Flow in a Gas-Liquid Separator," J. Power Energy Syst., **2**(4), pp. 1120–1131.
[4] Kataoka, H., Tomiyama, A., Hosokawa, S., Sou, A., and Chaki, M., 2008, "Effects of Pick-Off-Ring Configuration on Separation Performance of a Gas-Liquid Separator," Prog. Multiphase Flow Res., **3**, pp. 67–74.

[5] Takamasa, T., and Hazuku, T., 1998, "Measuring a Film Flowing Down a Vertical Wall Using Laser Focus Displacement Meters (1st Rep.)," Trans. Jpn. Soc. Mech. Eng., **64**(617), pp. 128–135.
[6] Hills, J. H., Azzopardi, B. J., and Barhey, A. S., 1996, "Spatial Unsteadiness: A Way Towards Intensive Gas-Liquid Reactors," Trans. Inst. Chem. Eng., **74**, pp. 567–574.
[7] Wallis, G. B., 1969, *One Dimensional Two-Phase Flow*, McGraw-Hill, New York, pp. 318–322.
[8] Thurgood, M. J., Kelly, J. M., Guidotti, T. E., Kohrt, R. J., and Crowell, K. R., 1983, "COBRA/TRAC—A Thermal-Hydraulics Code for Transient Analysis of Nuclear Reactor Vessels and Primary Coolant Systems. Volume 1: Equations and Constitutive Models," Report No. NUREG/CR-3046, PNL-4385.
[9] Henstock, W. H., and Hanratty, T. J., 1976, "The Interfacial Drag and the Height of the Wall Layer in Annular Flows," AIChE J., **22**, pp. 990–1000.

G. F. Naterer
Canada Research Chair Professor
Faculty of Engineering and Applied Science,
University of Ontario Institute of Technology,
2000 Simcoe Street North,
Oshawa, ON, L1H 7K4, Canada

K. Gabriel
Professor
Associate Provost
Research,
University of Ontario Institute of Technology,
2000 Simcoe Street North,
Oshawa, ON, L1H 7K4, Canada

L. Lu
Assistant Professor
Faculty of Energy Systems and Nuclear Science,
University of Ontario Institute of Technology,
2000 Simcoe Street North,
Oshawa, ON, L1H 7K4, Canada

Z. Wang
Hydrogen Research Laboratory Manager

Y. Zhang

Faculty of Engineering and Applied Science,
University of Ontario Institute of Technology,
2000 Simcoe Street North,
Oshawa, ON, L1H 7K4, Canada

Recent Advances in Nuclear Based Hydrogen Production With the Thermochemical Copper-Chlorine Cycle

This paper presents a review of recent advances in nuclear-based hydrogen production with a thermochemical copper-chlorine cycle. Growing attention has focused on thermochemical water decomposition as a promising alternative to steam-methane reforming for a sustainable future method of large-scale hydrogen production. Recent advances in specific processes within the Cu–Cl cycle will be presented, particularly for overall heat requirements of the cycle, preferred configurations of the oxygen cell, disposal of molten salt, electrochemical process of copper electrowinning, and safety/reliability assessment of the systems. An energy balance for each individual process is formulated and results are presented for heat requirements of the processes.
[DOI: 10.1115/1.3078787]

1 Introduction

The growing shortfall between worldwide demand and supply of oil will have a major impact on future prices of fossil fuels. Rising oil prices have adverse impact on the manufacturing, automotive, aerospace, and other industries, due to their dependence and vulnerability to rising prices of petroleum products. It will be advantageous for countries to gradually shift to energy sources not solely dependent on oil and natural gas, while at the same time reducing air pollution and mitigating climate change. Unlike fossil fuels, hydrogen is a sustainable and clean energy carrier, which is widely believed to be the world's next-generation fuel. The purpose of this paper is to present recent advances in a promising new method of efficient hydrogen production by thermochemical water decomposition with a copper-chlorine cycle. By developing new technologies for hydrogen production, important progress can be made towards one of the key challenges of the emerging hydrogen economy, namely, lower-cost sustainable production of hydrogen.

Adoption of fuel cell vehicles will be one of several key driving forces for hydrogen demand in the future. Although it is difficult to predict when fuel cell vehicles will achieve a significant market share, it is widely believed that hydrogen will gradually become a prominent fuel in the future transportation sector. This paradigm shift will require a large-scale sustainable method of hydrogen production, wherein nuclear energy has a promising role. Nuclear-based hydrogen production would not emit greenhouse gases that contribute to climate change. Nuclear heat can be supplied abundantly for large-scale capacities of hydrogen production. The nuclear industry and power plants could eventually have commercial opportunities to sell hydrogen fuel as well as electricity.

Over 200 cycles have been identified previously to produce hydrogen by thermochemical water decomposition from various heat sources including nuclear and solar energy [1]. Lewis and Taylor [2] reported that a survey of the open literature between 2000 and 2005 did not reveal any new cycles. Very few have progressed beyond theoretical calculations to working experimental demonstrations that establish scientific and practical feasibility of the thermochemical processes. The sulfur-iodine cycle is a leading example that has been scaled up to a pilot plant level, with active work conducted by the Sandia National Laboratory (Albuquerque, New Mexico), Japan Atomic Energy Agency (JAEA, Tokai, Japan), CEA (France), and others [3,4]. JAEA demonstrated a pilot facility up to 30 l/h of hydrogen with the S-I cycle. JAEA aims to complete a large S-I plant to produce 60,000 m^3/h of hydrogen by 2020; enough for about 1×10^6 fuel cell vehicles. Japan has a goal to have 5×10^6 fuel cell vehicles on the road by 2020 [5]. Korea (KAERI Institute), China, and Canada [6] are also progressing toward hydrogen production from nuclear reactors.

After considering factors of availability and abundance of materials, simplicity, chemical viability, thermodynamic feasibility, and safety issues, the following seven cycles (in addition to the S-I cycle) were identified in a nuclear-hydrogen initiative [2] as the most promising cycles: copper-chlorine (Cu–Cl) [7], cerium-chlorine (Ce–Cl) [8], iron-chlorine (Fe–Cl) [8], magnesium-iodine (Mg–I) [9], vanadium-chlorine (V–Cl) [10], copper-sulfate

Manuscript received August 16, 2008; final manuscript received August 21, 2008; published online February 19, 2009. Review conducted by Dilip R. Ballal. Paper presented at the 16th International Conference on Nuclear Engineering (ICONE16), Orlando, FL, May 12–15, 2008.

Table 1 Chemical reaction steps in the Cu–Cl cycle

Step	Reaction	Temperature range (°C)		Feed/output
1	$2Cu(s)+2HCl(g)\rightarrow CuCl(l)+H_2(g)$	430–475	Feed:	Electrolytic Cu+dry HCl+QH_2+CuCl(l) salt
			Output:	Powder/granular CuCl and HCl+V
2	$2CuCl(s)\rightarrow 2CuCl(aq)\rightarrow CuCl_2(aq)+Cu(s)$	Ambient (electrolysis)	Feed:	Cu and slurry containing HCl and $CuCl_2$
			Output:	Slurry containing HCl and $CuCl_2$+Q
3	$CuCl_2(aq)\rightarrow CuCl_2(s)$	<100	Feed:	Powder/granular $CuCl_2+H_2O$/HCl vapors
			Output:	Powder/granular $CuCl_2+H_2O(g)+Q$
4	$2CuCl_2(s)+H_2O(g)\rightarrow CuO*CuCl_2(s)+2HCl(g)$	400	Feed:	Powder/granular $CuO*CuCl_2+2HCl(g)$
			Output:	Powder/granular $CuO*CuCl_2(s)+Q$
5	$CuO*CuCl_2(s)\rightarrow 2CuCl(l)+1/2O_2(g)$	500	Feed:	Molten CuCl salt+oxygen
			Output:	

Q=thermal energy and V=electrical energy.

(Cu–SO_4) [8], and hybrid chlorine [8]. Proof-of-principle demonstrations have been completed for these cycles and chemical viability has been proven.

However, most of the cycles require process heat over 800°C. Due to lower temperature requirements of 500°C (associated with an endothermic reactor of the highest temperature process), the Cu–Cl cycle is a promising alternative that could be eventually linked with Canada's nuclear reactors, particularly the supercritical water reactor (SCWR). Granovskii et al. [11] examined heat pumps to upgrade heat from low to higher temperatures needed by the Cu–Cl cycle. Advantages of the Cu–Cl cycle include minimal demands on materials of construction, inexpensive chemical agents, and reactions going to completion without side reactions. The cycle has been identified by Atomic Energy of Canada Limited (AECL, Chalk River, Ontario) (Chalk River Laboratories (CRL)) as the most promising cycle for thermochemical hydrogen production with SCWR. Current collaboration between UOIT, AECL, and the Argonne National Laboratory is focusing on enabling technologies for the Cu–Cl cycle, through the international Nuclear Energy Research Initiative (INERI [7]). Unlike the small test-tube Cu–Cl experiments in the INERI collaboration, this paper focuses on predicted product yields in laboratory experiments for each of the steps in the Cu–Cl cycle, which scale up the flow capacities by about 100 times larger than a test-tube scale.

Hydrogen is expected to be an important alternative energy carrier in the future. The current market for hydrogen is growing rapidly, due to needs in the petrochemical, fertilizer production, and other industries. Nuclear-based hydrogen generation is promising because it eliminates greenhouse gas emissions and other pollutants, at a potentially low cost in a large-scale capacity. The two main processes of hydrogen production using nuclear energy and heat are electrolysis and thermochemical methods. This paper focuses on a copper-chlorine (Cu–Cl) cycle, which has been identified by AECL and belongs to the category of themochemical processes. UOIT and AECL have been collaborating with the Argonne National Laboratory (ANL) in studies of the Cu–Cl cycle. ANL developed enabling technologies for the Cu–Cl thermochemical cycle and created a flowsheet of the hydrogen plant by using Aspen Plus® simulations [2]. The SCWR is able to provide the required high temperature steam for the four main reactions. In this paper, fault-tree models will provide mathematical and graphical representations of combinations of events, which can lead to system failure. Fault-trees will be constructed for the four reactors in the conceptual hydrogen generation plant.

2 Thermochemical Copper-Chlorine Cycle

The Cu–Cl thermochemical cycle uses a series of intermediate reactions to achieve the overall splitting of water into hydrogen and oxygen. It forms a closed cycle with water being the only input substance, while hydrogen and oxygen are the only two products: $H_2O\rightarrow H_2+1/2O_2$. Steps in the Cu–Cl cycle are summarized in Table 1, and a conceptual schematic of the cycle is illustrated in Fig. 1.

2.1 Heat Required by the Copper-Chlorine Cycle. To split water into hydrogen and oxygen implies that sufficient energy must be provided to break the chemical bond of hydrogen and oxygen atoms. From a thermodynamic perspective, the minimum energy is equal to the formation energy of water, i.e., 286 kJ/mol, denoted as ΔH_f (if water, hydrogen, and oxygen are all at a standard state and 25°C). However, a series of intermediate processes is adopted to split water. As a consequence, the energy required to split water will also be a function of the processes, and not solely the state alone. Therefore, to evaluate the total energy required by the copper-chlorine cycle, it is of vital importance to evaluate the energy performance of the cycle, e.g., thermal efficiency, system optimization, and complexity of the heat-exchanger network. The energy required by the copper-chlorine cycle includes heat, mechanical energy, and electric energy. In Secs. 2.1.1 and 2.1.2, a thermodynamic analysis is performed to determine the heat released or absorbed by each step of the Cu–Cl cycle.

2.1.1 Thermal Analysis of Cu–Cl Cycle Processes. The following steps I–V are the individual chemical reactions of the Cu–Cl cycle. A brief summary of the heat requirement for each process is listed thereafter.

Step I.

Major process:

$$2Cu(s) + 2HCl(g) = 2CuCl(l) + H_2(g) \text{ at } 450\,^\circ C \quad (1)$$

- Exothermic chemical process, $\Delta H=-46.8$ kJ

Auxiliary processes:

$$2CuCl(l,450\,^\circ C) \rightarrow 2CuCl(s,25\,^\circ C) \quad (2)$$

- Exothermic physical process, $\Delta H=-80.8$ kJ

$$H_2(g,450\,^\circ C) \rightarrow H_2(g,25\,^\circ C) \quad (3)$$

- Exothermic physical process, $\Delta H=-12.2$ kJ

$$2Cu(s,25\,^\circ C) \rightarrow 2Cu(s,450\,^\circ C) \quad (4)$$

- Endothermic physical process, $\Delta H=23.4$ kJ

$$2HCl(g,400\,^\circ C) \rightarrow 2HCl(g,450\,^\circ C) \quad (5)$$

- Endothermic physical process, $\Delta H=3.0$ kJ

Step II.

Major processes:

$$4CuCl + 4Cl^- = 4CuCl_2^-(\text{in solution at } 25\,^\circ C) \quad (6)$$

- Endothermic chemical process, $\Delta H=0.3$ kJ

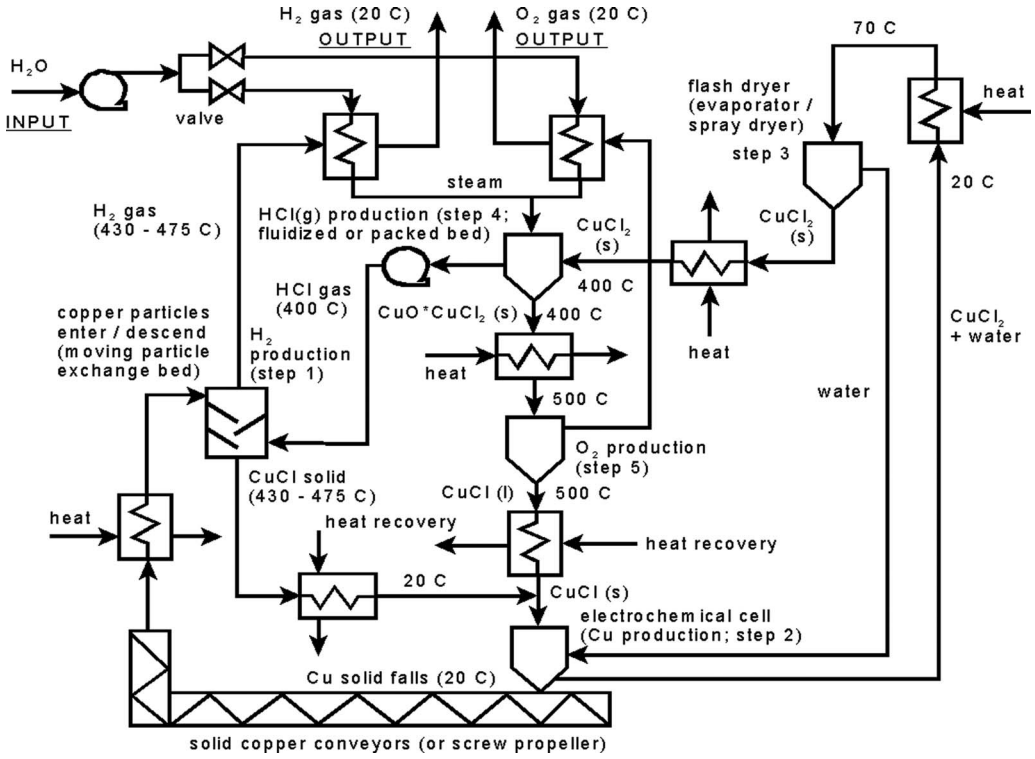

Fig. 1 Conceptual layout of the Cu–Cl cycle

$$4CuCl_2^- = 2CuCl_2 + 2Cu(s) + 4Cl^- \text{ in solution at } 25\,^\circ C \quad (7)$$

- Endothermic chemical process, $\Delta H = 12.2$ kJ

Auxiliary process:

$$\text{water(liquid, 25 °C) in Cu slurry} \rightarrow \text{vapor(gas, 100 °C)} \quad (8)$$

- Endothermic physical process, $\Delta H = 55-110$ kJ, depending on the water quantity. The maximum value 110 kJ is associated with the assumption of a worst case scenario where each Cu atom is surrounded by two water molecules.

Step III.
Major process:

$$2CuCl_2(aq, 25\,^\circ C) \rightarrow 2CuCl_2(s, 25\,^\circ C) \quad (9)$$

- Endothermic process, dissolution heat $\Delta H = 83.2$ kJ

Auxiliary processes:

$$\text{water(liquid, 25 °C) in } CuCl_2 \text{ slurry/solution} \rightarrow \text{vapor(gas, 100 °C)} \quad (10)$$

- $\Delta H = 30-300$ kJ, depending on the water quantity. The maximum value of 300 kJ occurs for the worst case scenario of drying the $CuCl_2$ solution, rather than a $CuCl_2$ slurry.

$$2CuCl_2(s, 25\,^\circ C) \rightarrow 2CuCl_2(s, 400\,^\circ C) \quad (11)$$

- Endothermic physical process, $\Delta H = 54.2$ kJ

Step IV.
Major process:

$$2CuCl_2(s) + H_2O(g) = CuO * CuCl_2(s) + 2HCl(g) \text{ at } 400\,^\circ C \quad (12)$$

- Endothermic chemical process, $\Delta H = 116.6$ kJ

Auxiliary process:

$$H_2O(25\,^\circ C, \text{liquid}) \rightarrow H_2O(400\,^\circ C, \text{vapor}) \quad (13)$$

- Endothermic physical process, $\Delta H = 57.8$ kJ
- If water source is steam, then $\Delta H < 11.2$ kJ

Step V.
Major process:

$$CuOCuCl_2(s) = 2CuCl(l) + 1/2O_2(g) \text{ at } 500\,^\circ C \quad (14)$$

- Endothermic chemical process, $\Delta H = 129.2$ kJ

Auxiliary processes:

$$CuOCuCl_2(s, 400\,^\circ C) \rightarrow CuO * CuCl_2(s, 500\,^\circ C) \quad (15)$$

- Endothermic physical process, $\Delta H = 13.0$ kJ

$$2CuCl(l, 500\,^\circ C) = 2CuCl(s, 25\,^\circ C) \quad (16)$$

- Exothermic physical process, $\Delta H = -85.4$ kJ

$$1/2O_2(g, 500\,^\circ C) \rightarrow 1/2O_2(g, 25\,^\circ C) \quad (17)$$

- Exothermic physical process, $\Delta H = -7.4$ kJ

In order to determine the previous heating values, the following enthalpy data (Figs. 2 and 3 [12]), as well as past analysis from

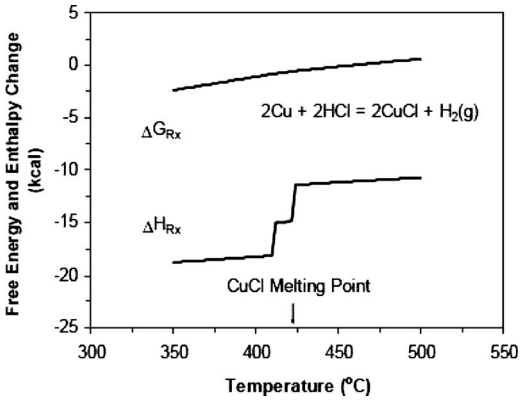

Fig. 2 Enthalpy change in hydrogen reaction

Ref. [13], are utilized. For example, to calculate the enthalpy change in H_2 from 450°C to 25°C, an isobaric processes is assumed and the maximum heat provided by 1 mol of hydrogen is

$$(\Delta H_{H_2})_{400}^{25} = n_{H_2} \int_{400}^{25} C_P^{H_2} dT \tag{18}$$

where c_p is the specific heat of hydrogen and n is the number of moles. Then,

$$(\Delta H_{H_2})_{400}^{25} = \int_{25}^{400} C_P^{H_2} dT \tag{19}$$

when $n_{H_2}=1$ mole, where $C_P^{H_2}$ (J mol^{-1} K^{-1}) is the constant pressure specific heat of hydrogen. From data on $C_P^{H_2}$, $(\Delta H_{H_2})_{25}^{400} \approx 10{,}800$ J, when $n_{H_2}=1$ mole.

2.1.2 Results of Thermal Analysis. From the previous calculations, the following heat requirements of the Cu–Cl cycle are obtained (note: further details of calculation procedures in Ref. [13]).

- The heat released by processes within the cycle is $\Delta H_{released} = -233$ kJ.
- The heat required by processes within the cycle is $\Delta H_{required} = 578 - 903$ kJ.
- The net heat required by the Cu–Cl cycle is then $\Delta H_{Cu\text{-}Cl} = 345 - 670$ kJ.

The maximum value, 670 kJ, occurs when a higher portion of water is dried in the copper-chlorine cycle. The range of ΔH_{Cu-Cl} can then allow us to evaluate the thermal efficiency of the cycle: $E_{thermal} = \Delta H_f / \Delta H_{Cu-Cl} \times 100\% = 43 - 83\%$. This efficiency is much higher than the traditional water electrolysis efficiency. When combined with the efficiency of producing electricity, the Cu–Cl cycle has a significant margin of superior overall conversion efficiency of more than one-third over electrolysis [13].

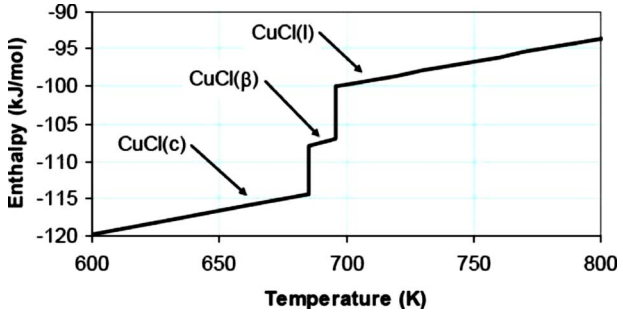

Fig. 3 Enthalpy of CuCl at varying temperatures

From the heating values, it can also be concluded that up to 40% of the heat required by the Cu–Cl cycle can be provided through exothermic processes within the cycle. The primary exothermic processes are the step I reaction and cooling of molten CuCl in step V. These processes can supply heat to other endothermic reactions in the Cu–Cl cycle. This opportunity of heat recovery is a major advantage of the Cu–Cl cycle, provided heat is recycled internally and matched with endothermic reactors. The highest temperature of the Cu–Cl cycle is about 500°C, which is much lower than most of the other thermochemical cycles (for example, the highest temperature of the S-I cycle is 900°C).

2.2 Oxygen Production Process (Step 5). The oxygen producing process occurs in step 5 of the Cu–Cl cycle, which is listed in Table 1. A schematic of the oxygen step within the Cu–Cl cycle is shown in Fig. 1. This section examines the recent advances and challenges with this step of the cycle.

2.2.1 Input and Output Across Interface of Reactor. The inputs and outputs across the interface surrounding the oxygen reactor are listed as follows.

- Gas species leaving the oxygen reactor:

(1) oxygen gas
(2) CuCl vapor
(3) chlorine gas
(4) HCl gas (trace amount)
(5) H_2O vapor (trace amount)

- Substances in molten CuCl stream leaving the reactor:

(1) molten CuCl
(2) solid $CuCl_2$ from upstream reaction 5 and side reaction accompanying reaction 5
(3) reactant particles entrained by the flow of molten CuCl

The heat supply to the reactor is $\Delta H > 129.2$ kJ/mol reactant.

The inputs and outputs across the interface surrounding the oxygen cooler are listed below.

- Substances entering the cooler:

(1) oxygen gas
(2) CuCl vapor
(3) chlorine gas
(4) HCl gas (trace amount)
(5) H_2O vapor (trace amount)

The heat removed from the oxygen is $\Delta H > 14.7$ kJ/mol oxygen.

The inputs and outputs across the interface surrounding the molten CuCl disposal cell are listed as follows:

(1) molten CuCl
(2) solid $CuCl_2$ from upstream reaction 5 and side reaction accompanying reaction 5
(3) reactant particles entrained by the flow of molten CuCl

The heat recovered from molten CuCl is $\Delta H = 42.7$ kJ/mol CuCl.

2.2.2 Material Requirements for Each Cell. Some of the key material challenges associated with this step of the Cu–Cl cycle are summarized as follows:

(1) Oxygen reactor:

(a) must be resistant to molten CuCl corrosion at 450–550°C
(b) resistant to O_2 oxidization at 450–550°C
(c) resistant to dry HCl corrosion at 450–550°C

(2) Oxygen cooler:

Table 2 Material inventory for oxygen reactor

H_2		$CuOCuCl_2$		O_2		CuCl (molten)		T	P(abs)	Operating time
kg/day	moles/h	kg/h	moles/h	N m^3/h	moles/h	kg/h	moles/h	(°C)	(atm)	(h)
3.0	62.5	13.375	62.5	0.7	31.25	12.375	125	450–550	1–4	2

(a) resistant to O_2 oxidization at 450–550°C
(b) resistant to dry HCl corrosion at 450–550°C

(3) Molten salt disposal cell:

(a) resistant to molten CuCl corrosion at 450–550°C
(b) resistant to O_2 oxidization at 450–550°C

2.2.3 Molten Salt Reactor. The reaction is given by $CuOCuCl_2(s)=2CuCl(molten)+0.5O_2(gas)$ at 500°C. This unit will serve as the reactor in which particles of $CuOCuCl_2(s)$ will decompose to molten salt and oxygen. The reactant particles gain the decomposition heat from the surrounding molten bath. Within the reactor, heat is transferred from the reactor wall to molten CuCl, and then transferred to reactant particles. The particles will descend in the molten CuCl bath. While the particles are descending, as one of two products, oxygen ascends to the molten salt free surface and then leaves the reactor. Simultaneously, as the other product, some molten CuCl is removed from the reactor.

Heat is transferred from liquid (molten CuCl) to solid (reactant particles), which is usually more efficient than from gas/solid to solid. The molten bath can be created by the reaction product itself. The product, oxygen, after being produced, will leave the reactant particles immediately due to buoyancy of gas in the molten salt. This fast separation will increase the reaction rate. For either a horizontal or vertical setup, the lifetime of reactant and the mass ratio of reactant to its surrounding molten salt can be commonly shared in different directions and scale-up.

The design of the reactor requires a high efficiency of heat exchange and separation of reactant from products, as well as product (oxygen) from product (molten salt). Key parameters for equipment scale-up are the lifetime and maximum ratio of the reactant and its surrounding molten bath. The process is less influenced by the particle size and structure. The required parameters for scale-up are the lifetime of reactant particles and the most effective mass ratio of reactant to its surrounding molten salt, provided that heat transfer requirements are satisfied. Table 2 shows the required material inventory for 3 kg of hydrogen production per day. Additional challenges and issues associated with the oxygen reactor are the reactor material (corrosion resistance to O_2 and molten CuCl at 450–550°C), and supply of reactants, which depends on the reactant particle size.

2.2.4 Molten Salt Disposal Cell. This disposal processes refers to 2CuCl (molten, 450–550°C)=2CuCl (solid, 20–90°C), and the condensation of water (<60°C) from water vapor. These processes are designed to quench the molten salt produced from the decomposition of reactants, so it is an auxiliary process of step 5 in the Cu–Cl cycle. The quenching unit will serve as the equipment by which molten CuCl product is quenched to solid at a low temperature. The molten CuCl descends into liquid water and then it is cooled to solid. Simultaneously, part of the liquid water absorbs the heat released from molten CuCl to evaporate to steam.

The quenching cell should operate on processes as simple as possible. Rapid cooling and solidification of molten CuCl are desired. The process is similar to existing technologies used in quenching of other molten materials such as liquid metals. A particular challenge is plugging of solid CuCl in the nozzle, if the equipment is insufficiently insulated. For 3 kg/day of hydrogen production in the Cu–Cl cycle, the operating parameters of a quenching cell are indicated in Table 2.

A secondary auxiliary process is condensation of steam generated from the quenching cell, i.e., water vapor (<120°C) =water(<60°C). This process is designed to cool the steam to liquid water. Within the quenching cell, all materials are recycled within the closed cell; hence little or no potential toxic gas (such as CuCl vapor) is released to the environment. In the fluids equipment, vapor flowing down through a pipe of a vertical heat-exchanger is cooled to liquid that flows up through the shell side of the heat-exchanger. The condenser should permit simple operation, rapid cooling of the vapor, and prevention of any toxic gas release to the environment. Table 3 indicates the flows and material capacities that correspond to 3 kg/day of hydrogen in the Cu–Cl cycle.

2.2.5 Oxygen Cooling and Disposal. This process refers to $O_2(450–550°C)=O_2(<60°C)$. The process is designed to cool the exiting O_2 to a relatively low temperature, for heat recovery and reduced oxidization and degradation of materials. Hot oxygen flowing within a pipe through a heat-exchanger is cooled down to a lower temperature by cooling water that is flowing in the shell side of the heat-exchanger. In addition, CuCl vapor will also be cooled to a solid. The unit must be designed to prevent any escape of toxic CuCl vapor to the environment. If N_2 is introduced as an auxiliary gas for O_2 detection, then the cell will also cool N_2. A main parameter needed for scaling up the equipment to larger capacities is the overall heat transfer coefficient within the heat-exchangers. Typical operating parameters are summarized in Table 4. If N_2 is introduced as an auxiliary gas for O_2 detection, then additional cooling water is needed. The process requires material that is oxidization resistant.

2.3 Electrochemical Process. Step 2 of the Cu–Cl cycle may be implemented by means of an electrochemical cell, which produces solid copper particles as input for step 1 via the process $2CuCl(s)\rightarrow CuCl_2(aq)+Cu(s)$. CuCl(s) enters the unit and copper particles exit on a moving conveyer. Important parameters include the chemical kinetics in the electrochemical cell, as a function of temperature, pressure, and compositions. Incoming solid CuCl streams from steps 1 and 5 pass through heat-exchangers, before entering the electrochemical cell under ambient conditions. Due to the high temperature and corrosive fluids, new innovations in conventional heat-exchanger technologies are needed to permit fluid

Table 3 Material inventory of heat recovery from molten salt

H_2		Vapor 120°C(vapor)→60°C(liquid)		Cooling water 30°C(vapor)→60°C(liquid)		P(abs)	Run time
kg/day	moles/h	kg/h	moles/h	kg/h	m^3/h	(atm)	(h)
3.0	62.5	2.449	136.0	974.6	0.9746	1–2	2

Table 4 Material inventory for oxygen cooling

H_2		Oxygen 450–550°C→30–60°C		Cooling water 30°C(vapor)→60°C(liquid)		P(abs) (atm)	Run time (h)
kg/day	moles/h	N m^3/h	moles/h	kg/h	m^3/h		
3.0	62.5	0.7	31.25	781	0.781	1–2	2

processing in the extreme operating conditions. Extensions of conventional heat-exchangers to relevant operating conditions are needed.

In the electrochemical process, an aqueous CuCl solution reacts in an electrochemical cell to produce solid copper and aqueous $CuCl_2$. Solid particles exiting from the base are collected and transported by a copper conveyer or screw propeller to the hydrogen reactor. As an adaptation of silver-refining technology, a possible realization of the electrochemical device is based on a Moebius cell, although this would be expensive, large, and energy intensive. In practice, production of copper particles is notably different from a Moebius cell developed originally for the silver-refining industry. However, the existing Moebius technology serves as a useful basis, upon which new developments can lead to alternative equipment with better performance.

Atomic Energy of Canada Limited is investigating a modification of the electrochemical process, in order to eliminate solid handling by direct electrolysis of CuCl(aq) and HCl(aq) to produce hydrogen, as per the following reaction:

$$2CuCl(aq) + 2HCl(aq) \rightarrow H_2(g) + 2CuCl_2(aq) \tag{20}$$

This would replace steps 1 and 2 of the Cu–Cl cycle. In Sec. 3, safety and reliability of the previous thermochemical and electrochemical devices in a conceptual nuclear-hydrogen plant will be examined.

3 Safety and Reliability Assessment by Fault-Tree Construction

3.1 Fault-Tree Analysis. Over the past few decades, probabilistic risk assessment (PRA) and its related techniques, including fault-tree analysis (FTA), have become useful methodologies for safety assessment of nuclear plants. Because of their systematic and comprehensive approach, PRA and FTA have been repeatedly proven capable of exposing design and operational weaknesses. Today, FTA is one of the most important logic and probabilistic techniques used in PRA and system reliability assessment. A main objective of PRA is to determine the probability and consequences of risks. Therefore, risk assessment, which is an important management tool for making critical decisions, and in some cases, meeting regulatory requirements, has an important role in PSA. Risk assessment is a three-part process: identify the hazards and their causes, determine the consequences of the hazards, and calculate the probability of their occurrence.

FTA starts with the undesired events, such as failure of a main component, and then deduces its causes using a systematic, backward-stepping process. In determining the causes, a fault-tree (FT) is constructed as a logical illustration of the events and their relationships that are necessary and sufficient to result in the undesired event, or top event. Through these steps in FTA, hazards and their causes are identified, and the consequences of the hazards are determined by risk assessment. In addition, FTA can be applied to both existing systems and a system that is being designed [14]. When FTA is applied to a system being designed, it can provide an estimate of the failure probability and the important contributors. In this step, the probability of the hazards' occurrence is calculated, which is the last process of risk assessment. The method of FTA can be used to outline the importance of the contributors to the undesired event. It assists decision-making in the design of a nuclear-based hydrogen plant.

FTA is generally divided into two stages: qualitative analysis and quantitative analysis. Qualitative analysis aims at finding the combinations of events that can cause system failure (minimal cut sets). A quantitative analysis focuses on calculating what probabilities or frequencies will cause system failure. Currently, a widely used method in FTA is binary decision diagrams (BDDs) [15,16]. BDD can deal with both qualitative and quantitative analyses in most cases. However, if a system has repairable components, such as components within the Cu–Cl cycle, BDD cannot be used to calculate the system reliability. In order to solve this problem, traditional Markov models can be used, but they are time consuming for a large system.

In the following analysis, a new approximation will be used to evaluate the system reliability, R, with repairable components, in terms of the Vesely failure rate, $\lambda_V(t)$. The following assumptions will be adopted in the analysis.

(1) The system is composed of s-independent components, with a structure function that is s-coherent (s implies statistically).
(2) There are two states in the system and its components, which are "working" and "failed."
(3) The components' failure and repair rates are constant.
(4) Components can be repaired, and repaired components are as good as new.

The Vesely failure rate is defined by

$$\lambda_V(t) = \frac{v(t)}{A(t)} \tag{21}$$

The Vesely failure rate, λ_V, is defined only for nonrepairable systems. Using it for an approximation to λ of a repairable system, R, then f can be calculated as follows:

$$R(t) \approx R_V(t) = \exp\left\{ - \int_0^t \lambda_V(u)du \right\} \tag{22}$$

$$f(t) \approx f_V(t) = \lambda_V(t) \cdot R_V(t) \tag{23}$$

Once the Vesely failure rate, $\lambda_V(t)$, is known, the equations for MTTFF, MTTF, MTTR, and MTBF can be derived.

$$\text{MTTFF} \approx \int_0^\infty R_V dt \tag{24}$$

$$\text{MTTF} = \frac{1}{\lambda_V(\infty)} \tag{25}$$

$$\text{MTTR} = \frac{U(\infty)}{A(\infty) \cdot \lambda_V(\infty)} \tag{26}$$

$$\text{MTBF} = \frac{1}{A(\infty) \cdot \lambda_V(\infty)} \tag{27}$$

Compared with two other popular reliability approximations, reliability without repair and the Murchland approximation [17], the reliability obtained from the Vesely failure rate is always closest to the real system reliability. Typical calculation results were presented by Amari and Akers [17]. The reliability measures calculated by the Vesely failure rate, such as MTTFF, MTTF, MTTR, and MTBF, are also more accurate.

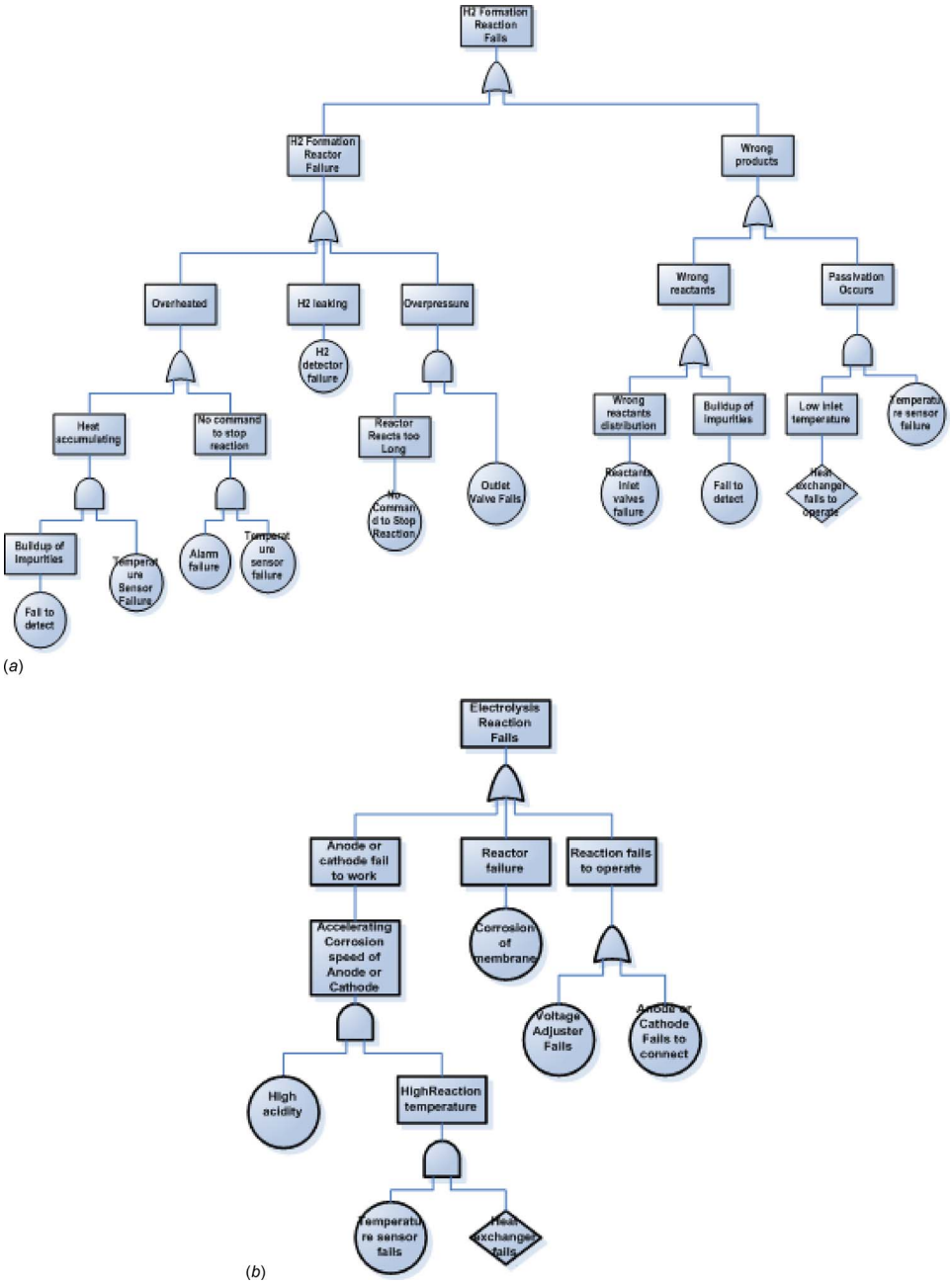

Fig. 4 Fault-tree of the (*a*) hydrogen and (*b*) electrochemical cell

3.2 Fault-Tree Construction for Cu–Cl Cycle. These parameters require the fault-tree construction for a particular system (Cu–Cl cycle in this paper). Fault-tree construction is a method of top-down analysis for reliability and safety assessment of engineering equipment and plant operations [17,18]. It starts with an unfavorable operational outcome at a top level (top event). System functional and architectural structures are represented by fault-trees. As discussed previously, step 1 of the Cu–Cl cycle is the process of hydrogen generation as follows:

$$2Cu(s) + 2HCl(g) = 2CuCl(l) + H_2(g) \quad (28)$$

An operating temperature between 425°C and 450°C is preferred to avoid the formation of solid CuCl passivating the copper metal surface [19].

Since hydrogen is a flammable gas without odor and color, monitoring leakages of H_2 will be an important safety issue. If a leakage happens, the hydrogen generation reactor must stop operating, which would influence the operation of the whole system. Other potential accident scenarios related to the hydrogen generation process are overheating and overpressurization of the reactor, since it is an exothermic reaction and buildup of impurities will influence the release of heat inside. Figure 4(*a*) shows a fault-tree for this step. HCl(g) mixes with particles of Cu to produce H_2. The flow of the HCl stream and the size of Cu particles affect the fault-tree analysis.

Since the fault-tree construction is a top-down process, we define the "H_2 formation reaction fails" as the top event in this fault-tree. Two main scenarios could cause the top event to occur. These are the failure of the H_2 formation reactor, and generating other side products through incomplete reactions or improper conditions. In terms of the reaction requirements mentioned previ-

ously, the temperature and pressure of the reactor, and the leakage of hydrogen, are the subevents if the reactor fails. Based on previous examples and practical experience, the lower levels of the fault-tree can be built until the basic events are determined, when the reliability data can be obtained. In another branch, either wrong reactants or passivation could cause the event of wrong products (side reactions) to occur. Subevents and basic events for this branch are listed in Fig. 4(*a*).

Step 2 is an electrochemical reaction, which is disproportionation of CuCl, from steps 1 and 4.

$$4\mathrm{CuCl(s)} \rightarrow 4\mathrm{CuCl(aq)} = 2\mathrm{CuCl_2(aq)} + 2\mathrm{Cu(s)} \tag{29}$$

CuCl(s) enters the electrochemical cell and Cu particles exit by a conveyer and return back to step 1. Past studies [19] have indicated that the voltage for depositing copper on the cathode varied between 0.4 V and 0.6 V. There are two main challenges to accomplish this electrochemical reaction. The first is electrochemical equipment development and scale-up, including the identification of appropriate membranes and materials of the electrode. Another challenge is to determine operating parameters that will produce small dendritic copper particles at the cathode and a concentrated $CuCl_2$ solution at the anode. Figure 4(*b*) shows the fault-tree for the electrochemical process.

In the top event, the electrolysis reaction fails in the fault-tree. The three subevents occur if the anode or cathode fail to work, the reactor fails, or the reaction fails to operate properly. It is straightforward to determine the basic events in terms of the subevents. Either high acidity or high temperature will accelerate the corrosion speed on the anode and cathode, which will result in the failure of the anode and cathode. Because of the importance of the working voltage, the voltage adjuster and the connections for the anode and cathode will influence the reaction directly.

Consider the following endothermic hydrolysis reaction (step 4):

$$2\mathrm{CuCl_2(s)} + \mathrm{H_2O(g)} = \mathrm{CuO \cdot CuCl_2(s)} + 2\mathrm{HCl(g)} \tag{30}$$

Temperatures between 300 and 400°C will give reasonable kinetics [19]. Past results showed that the rate of reaction was 2–2.5 times faster at 350°C, when compared with 300°C. In addition, the generation rate of an undesirable by-product, CuCl, strongly relates to the temperature. Another important issue in this reaction is the contact between $CuCl_2(s)$ and $H_2O(g)$, which means that the water vapor concentration is important for the reaction. The fault-tree for this process is shown in Fig. 5(*a*).

The fault-tree is built by focusing on the temperature, which is a main parameter for this reaction to achieve a higher efficiency and fewer by-products. A special gate is used on the right side of this fault-tree, which is called an "inhibit gate," and the event on its right is called a conditional event. When the temperature sensor and alarm fail in a condition of failure of the heat-exchanger, then the product distribution will be impacted.

The other remaining step of the Cu–Cl cycle is the oxygen generation reaction. The reactant comes from the third step, which is Cu_2Cl_2O (equimolar mixtures of $CuCl_2$ and CuO).

$$\mathrm{CuO \cdot CuCl_2(s)} = 2\mathrm{CuCl(l)} + 0.5\mathrm{O_2(g)} \tag{31}$$

It is an endothermic reaction and oxygen is produced in a temperature range from 450°C to 530°C. This process is represented in the fault-tree of Fig. 5(*b*).

The four isolated fault-trees are a part of the entire fault-tree of the Cu–Cl system. Heat-exchangers have an important role in the overall cycle. They connect reactors and pipelines to transport reactants and products. They are also responsible for heat input and heat recovery. The fault-tree for oxygen generation is similar to the one derived earlier for hydrogen generation. Since the reactant is solid, the impurity left in the reactor will be one of the main issues, which could cause either wrong products (side reactions) or overheating.

3.3 Failure of System Components. To apply the evaluation method of the Vesely failure rate to the Cu–Cl cycle, the system availability and system failure frequency must be identified. If the failure of a system is represented by the top event of a fault-tree, then the system unavailability is equivalent to the top event probability [17], i.e.,

$$U = P_T \tag{32}$$

Then the system availability becomes

$$A = 1 - U = 1 - P_T \tag{33}$$

In order to calculate the system failure frequency, the component availabilities and failure rates are used. If the failure distribution of components is exponential, the component failure frequency is determined by

$$v_i = A_i \cdot \lambda_i \tag{34}$$

If the events represent component failures, the component unavailability equals the probability of this event, which is represented by

$$U_i = \Pr\{E_i\} \tag{35}$$

The component availability equals 1 minus its unavailability.

Most of the failure rates of components can be determined from manufacturer's data, for different types of events, while some may need to be identified by predictive simulations, analysis, or past experience. The events in the fault-trees are usually divided by the level of components. Otherwise, the failure rate of the overall product or equipment can be determined by adding all of the component failure rates. For example, the failure rate of the electronic parts in the Cu–Cl equipment can be estimated from the data of MIL-HDBK-217 [20]. This handbook defines an equation of the following form to estimate failure rates of various electronic components:

$$\lambda_C = \lambda_b f_q f_e \cdots \tag{36}$$

where λ_b is a base failure rate, which is normally determined from a model relating the temperature and electrical influences on the component failure. It can be predicted by

$$\lambda_b = C \exp\left[-\frac{e_a}{kT_a}\right] \tag{37}$$

Reference [21] presented rules for predicting system failure frequencies in terms of the known component failure frequencies. When the system availabilities and failure frequencies are known, the Vesely failure rate can be determined for each component in the Cu–Cl cycle. In future studies, these methods will be further applied to examine the safety and reliability of nuclear-based hydrogen production via the thermochemical copper-chlorine cycle.

4 Conclusions

This paper has presented recent advances in the Cu–Cl cycle for thermochemical production of hydrogen. The heat requirements and system configuration of individual components within the cycle were analyzed. The cycle contains an oxygen producing reactor, which generates molten CuCl for a subsequent electrochemical process of copper electrowinning. This paper has summarized various thermal, materials, and chemistry challenges associated with improving the overall efficiency of the cycle. Future work will involve performing further experiments for different processes within the Cu–Cl cycle to better understand the reaction kinetics and performance of various reactor configurations. Also, reliability and probabilistic safety assessments of a conceptual nuclear-hydrogen plant were analyzed in the paper. Four fault-trees were constructed for potential risk scenarios. Based on the results from the FTAs, the risk levels of the hydrogen plant under different accident scenarios can be calculated. Based on the re-

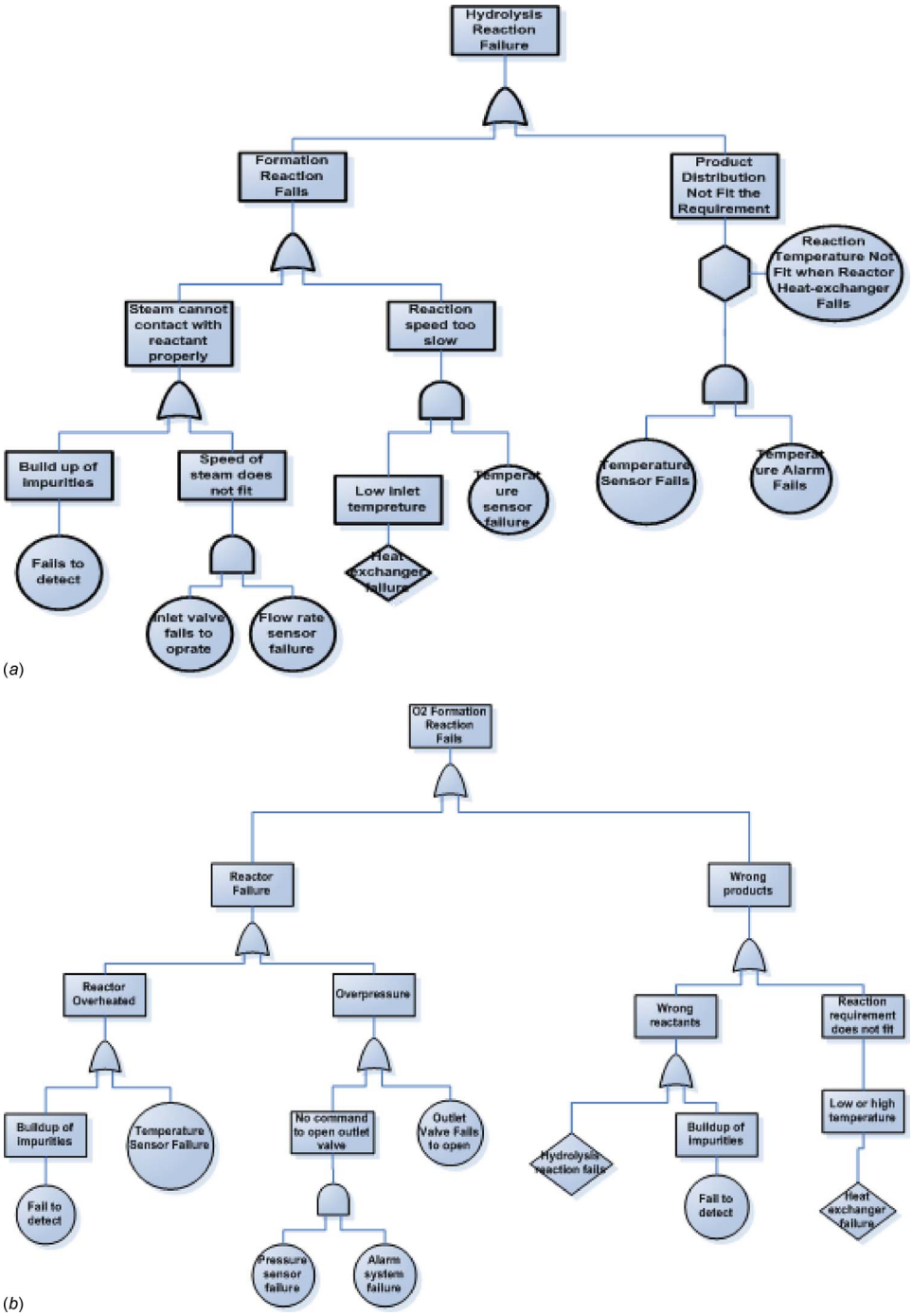

Fig. 5 Fault-tree of the (*a*) hydrolysis and (*b*) oxygen reactor

sults, potential problems encountered in the Cu–Cl cycle are identified and possible solutions will be recommended for future improvements.

Acknowledgment

Financial support of this research from Atomic Energy of Canada Limited (particularly Dr. S. Suppiah and Dr. A. Miller) and the Ontario Research Excellence Fund is gratefully acknowledged.

Nomenclature

A, A_i = system availability, unavailability of component i
e_a = activation energy for the process
E_i = event i in the fault-tree
f = actual probability density function of the system
f_e = factor that accounts for the influence of the use environment
f_q = factor that accounts for component quality level

f_V = Vesely probability density function of the system
k = Boltzmann's constant
MTBF = mean time between failures
MTTFF = mean time to first failure
MTTF = mean time failure
MTTR = mean time to repair
P_T = top event probability
R = system reliability
R_V = system reliability (using a Vesely failure rate)
T_a = absolute temperature
U, U_i = system unavailability, unavailability of component i

Greek

λ_b = base failure rate
λ_C = component failure rate
λ_V, λ_i = Vesely system failure rate, failure rate of component i
v, v_i = system failure frequency, failure frequency of component i

References

[1] McQuillan, B. W., Brown, L. C., Besenbruch, G. E., Tolman, R., Cramer, T., Russ, B. E., Vermillion, B. A., Earl, B., Hsieh, H. T., Chen, Y., Kwan, K., Diver, R., Siegal, N., Weimer, A., Perkins, C., Lewandowski, A., "High Efficiency Generation of Hydrogen Fuels Using Solar Thermochemical Splitting of Water: Annual Report," General Atomics, Report No. GA-A24972.

[2] Lewis, M., and Taylor, A., 2006, "High Temperature Thermochemical Processes," DOE Hydrogen Program.

[3] Sakurai, M., Nakajima, H., Amir, R., Onuki, K., and Shimizu, S., 2000, "Experimental Study on Side-Reaction Occurrence Condition in the Iodine-Sulfur Thermochemical Hydrogen Production Process," Int. J. Hydrogen Energy, **25**, pp. 613–619.

[4] Schultz, K., 2003, "Thermochemical Production of Hydrogen From Solar and Nuclear Energy," Technical Report for the Stanford Global Climate and Energy Project, General Atomics.

[5] 2002, *Fuel Cell Vehicles: Race to a New Automotive Future*, US Department of Commerce, Washington, DC.

[6] Sadhankar, R. R., Li, J., Li, H., Ryland, D., and Suppiah, S., 2005, "Hydrogen Generation Using High-Temperature Nuclear Reactors," 55th Canadian Chemical Engineering Conference, Toronto, Canada, Oct.

[7] Lewis, M. A., and Miller, A., 2004, "Lower Temperature Thermochemical Hydrogen Production," Project No. 2004–007-C, International Nuclear Energy Research Initiative, U.S. Department of Energy, Washington, DC.

[8] Carty, R. H., Mazumder, M., Schreider, J. D., and Panborn, J. B., 1981, "Thermochemical Hydrogen Production," Gas Research Institute for the Institute of Gas Technology, GRI Report No. 80–0023.

[9] Hakuta, T., Haraya, K., Sako, T., Ito, N., Yoshitome, H., Todo, N., and Kato, J., 1980, "A Study on the Magnesium-Iodine Thermochemical Cycle for the Production of Hydrogen," *Hydrogen Energy Conference*, Vol. 1 (A81-42851 20-44), Pergamon Press, Oxford, pp. 311–324.

[10] Knoche, K. F., Schuster, P., and Ritterbex, T., 1984, "Thermochemical Production of Hydrogen by a Vanadium/Chlorine Cycle. II: Experimental Investigation of the Individual Reactions," Int. J. Hydrogen Energy, **9**, pp. 473–482.

[11] Granovskii, M., Dincer, I., Rosen, M. A., and Pioro, I., 2007, "Exergy Analysis of a System Using a Chemical Heat Pump to Link a Supercritical Water-Cooled Nuclear Reactor With a Thermochemical Water Splitting Cycle," 13th International Conference on Emerging Nuclear Systems, Istanbul, Turkey, Jun. 3–8.

[12] Mathias, P., 2006, "Modeling of the Copper Chloride Thermochemical Cycle," Argonne National Laboratory, Argonne, IL.

[13] Wang, Z., Naterer, G. F., and Gabriel, K., 2007, "Hydrogen Production With a Cu-Cl Cycle: Analysis of Thermal Efficiency," Canadian Hydrogen Workshop on Hydrogen Production From Non-Fossil Sources, Oshawa, ON, Canada, May 30.

[14] Stamatelatos, M., and Vesely, W., 2002, *Fault Tree Handbook With Aerospace Applications, Version 1.1*, NASA Headquarters, Washington, DC.

[15] Sinnamon, R. M., and Andrews, J. D., 1997, "New Approaches to Evaluating Fault Trees," Reliab. Eng. Syst. Saf., **58**, pp. 89–96.

[16] Sun, H., and Andrews, J. D., 2004, "Identification of Independent Modules in Fault Tree Which Contain Dependent Basic Events," Reliab. Eng. Syst. Saf., **86**, pp. 285–296.

[17] Amari, S. V., and Akers, J. B., 2004, "Reliability Analysis of Large Fault Tree Using the Vesely Failure Rate," IEEE Reliability and Maintainability, 2004 Annual Symposium-RAMS, Jan., Vol. 26, pp. 391–396.

[18] Billinton, R., and Allan, R., 1983, *Reliability Evaluation of Engineering Systems*, Plenum, London.

[19] Lewis, M. A., Masin, J. G., and Vilim, R. B., 2005, "Development of the Low Temperature Cu-Cl Thermochemical Cycle," International Congress on Advances in Nuclear Power Plants, Korea, May 15–19.

[20] Dhillon, B. S., 2000, *Medical Device Reliability and Associated Areas*, CRC, Boca Raton, FL.

[21] Amari, S. V., 2000, "Generic Rules to Evaluate System-Failure Frequency," IEEE Trans. Reliab., **49**, pp. 85–89.

Experimental Study on Effects of Slot Hot Blowing on Secondary Water Droplet Size and Water Film Thickness

Chunguo Li

Xinjun Wang[1]
e-mail: xjwang@mail.xjtu.edu.cn

Daijing Cheng

Bi Sun

Institute of Turbomachinery,
School of Energy and Power Engineering,
Xi'an Jiaotong University,
Xi'an 710049, China

The effects of the slot hot blowing of the hollow stator blades on the size of secondary water droplets and the thickness of the water film were experimentally investigated in this paper. The experiment was carried out on the turbine blade cascades in a wet air tunnel with an inlet air wetness fraction of 7.9%, an outlet air velocity of 170 m/s, a slot width of 1.0 mm, and a slot angle of 45 deg to blade surface. The Malvern droplet and particle size analyzer was utilized to measure the secondary water droplet size and distribution downstream of the hollow stator blades in the experimental tests. The experimental results show that the maximum diameter and Sauter mean diameter of the secondary water droplets were reduced greatly, and the water droplet size distribution became narrower. The larger blowing pressure difference resulted in the smaller secondary water droplets and the narrower water droplet size distributions. In addition, the efficiency of water separation from the hollow stator blade surfaces was higher for slot on the suction side than that of the pressure side case. Another simplified experimental test was also carried out on the flat plate to investigate the effect of slot hot blowing on the thickness of the water film downstream of the slot. The conductivity probes were used to measure the thickness of the water film downstream and upstream of the blowing slot. The results show that the slot hot blowing reduced the thickness of the water film downstream of the slot, which was affected by the blowing pressure difference and temperature difference between the hot blowing air and the main airflow. In conclusion, the slot hot blowing of the hollow stator blades has reduced the size of the secondary water droplets and secondarily has evaporated a little water film on the blade surfaces. Both effects are beneficial to reduce the erosion damage to the rotor blades. [DOI: 10.1115/1.3030877]

Keywords: slot hot blowing, secondary water droplet, hollow stator blade

1 Introduction

When superheated steam expands through the turbine's steam path and turns into wet steam, at some stage, spontaneous nucleation takes place and large numbers of fog droplets are produced within the flowing steam. By inertial or diffusional mechanism, a small percentage of the droplets deposits on the internal surfaces of the flow path, in particular on the blade surfaces. The water deposited on the blade surfaces coalesces into films or rivulets, which are drawn toward the blade trailing edges by the viscous drag of the steam and stripped from the trailing edges in the form of large secondary or coarse water droplets of up to 400 μm diameter. These large water droplets fail to accelerate to steam velocity before impact with the leading edges on the suction side of the rotor blades, as indicated by the velocity triangle in Fig. 1, and cause severe mechanical erosion damage to the blades. The presence of water in the flow passage also leads to the decrease in the turbine stage efficiency. Baumann [1] suggested that a 1% mean wetness fraction leads to a decrease of about 1% stage efficiency.

The erosion is due to the transfer of kinetic energy during the impact of the water droplets on the rotor blades, which depends on the density of the water, the impact velocity, and the impact number [2]. To reduce the water erosion damage to the rotor blades and secondarily to improve the turbine efficiency, it is desirable to reduce the size of the water droplets and to remove as large a portion of the moisture from the steam flow as possible. The methods of moisture removal will be reviewed in Secs. 2–5.

External moisture separators and reheaters are widely applied in almost all modern wet-steam turbines, which are located after the high-pressure cylinders, before intermediate-pressure cylinders, or low-pressure cylinders of the turbines. They can provide a moisture separation efficiency of up to 98% [3], although there is a negative performance effect in additional pressure losses in the reheater piping and increased plant complexity and cost [4]. However, with increased volumetric flow and wetness fraction, the final stages of low-pressure turbines still suffer from erosion.

Some water on the rotor blade surfaces is drawn out to the stage periphery under the action of centrifugal force, and captured and gathered in the water trap belts between the stator and rotor blades of the stage. To enhance the separation efficiency, turbine manufacturers make the rotor blades with special radial furrows on the suction surface near the leading edge. The experimental data show that the separation efficiency for the furrowed rotating blades is 0.1–0.3%, depending on the steam pressure and wetness fraction [3]. The separation efficiency is defined as the ratio between the amount of the removed water and the total water contents in the steam flowing through the stage.

The water film on the stator blade surfaces can be extracted through the suction slots of the hollow stator blades. Plenty of experimental researches on the use of suction slots have been carried out by Reley and Parker [5], Tanuma [6], and Wang et al. [7–10]. The separation efficiency of water film extraction depends on the geometric shape and location and number of the suction

[1]Corresponding author.

Manuscript received June 25, 2008; final manuscript received June 26, 2008; published online February 12, 2009. Review conducted by Dilip R. Ballal Paper presented at the ASME Power 2008 (Power2008), July 22–28, Orlando, FL.

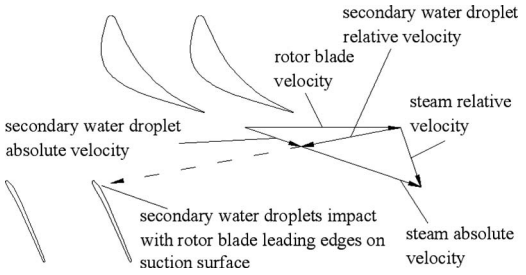

Fig. 1 Secondary water droplet's impact with leading edges on the suction side of the rotor blades

slots, slot angle relative to the blade surface, main steam velocity, and pressure difference of extraction. Hollow stator blade with suction slot along the trailing edge shows a high efficiency of water removal, which has been demonstrated by a fivefold reduction in weight loss of the rotor blades [4].

Blade heating is used to evaporate the water film on the stator blade surfaces and so to reduce the amount of moisture. This method can also inhibit the deposition of the fog droplet on the blade surfaces [11]. Blade heating has been demonstrated to give very good control on last blade erosion, but in supplying the high temperature heating system, the cycle efficiency is slightly worsened [4].

The above stated methods reduce erosion damage to the rotor blade by means of moisture separation. Caldwell [12] and Smith et al. [13] proposed a special countermeasure to prevent erosion of the rotor blades by reducing the size of the droplets reaching the rotor blades, which is the slot hot blowing of the hollow stator blades. By this means, a large portion of the water film is stripped from the stator blade surfaces by blowing high-pressure steam through the slots and re-enters main steam flow in the form of secondary water droplets. The maximum stable size of the secondary water droplets is given by $d_{\max}=\sigma(\mathrm{We})_{\mathrm{cr}}/\rho(\Delta u)^2$, where σ is the surface tension, $(\mathrm{We})_{\mathrm{cr}}$ is the critical Weber number, ρ is the steam density, and Δu is the relative velocity between the droplet and the steam. In the higher density flow the maximum stable size of the water droplets will be less than that in the main flow and it should also be possible to accelerate the water droplets to higher velocity before they reach the rotor blades. Both effects would tend to reduce erosion damage to the rotor blades [13], as indicated by the velocity triangle in Fig. 1. Secondarily, higher-temperature blowing steam will evaporate a little water film on the stator blade surfaces, which is also beneficial to reduce erosion. However, detailed researches have seldom been carried out on slot hot blowing of the hollow stator blades. In this paper, an experiment has been carried out on turbine blade cascades in a wet air tunnel to investigate the effect of the slot blowing on the size of the secondary water droplets, and another simplified experiment has been also made on the flat plate to observe the effect of slot hot blowing on the thickness of the water film downstream of the slot.

2 Tearing of Water Film at the Blade Trailing Edge

The water film on the blade surfaces flows toward the blade trailing edges and then is stripped from the trailing edges. Wang et al. [10] and Zhu [14] found that the water film stripped from the trailing edges is a periodical process, which consists of water film accumulation, stretching, tearing, and tear declining.

The water film flows toward the blade trailing edges and accumulates into water blocks at the trailing edges by its surface tension, beyond a certain size limit, which will stretch outside of the blade and flutter at a frequency. The stretched part of the water film is completely exposed in the gas flow and maintains at the blade trailing edges only by its surface tension. When the length of the stretched film increases to a certain limit, its surface tension cannot overcome the viscous drag force of the gas. Then, the water film is torn off the blade trailing edge with three modes: film tearing, spindle tearing, and silk rivulet tearing, as indicated by photos of the tearing modes in Fig. 2. Finally, the tearing declines and finishes, and enters the next accumulation. The water film re-enters the main flow in the form of secondary water droplets. Some factors, such as high gas velocity, pressure, and density, small water film flow rate, and silk rivulet tearing mode, will contribute to small-sized droplets.

3 Secondary Water Droplet Size

3.1 Experimental Equipment. The air-water two-phase flow test equipment is shown in Fig. 3, which consists of an air source, a pressure maintaining section, a water supply system, a heating system, and some measurement instruments. Compressed air from the C80 air compressor flows through the control valve and the water supply section, and enters the pressure maintaining section. In this process the water from the water pump is atomized into water droplets through the five atomizers and mixes with the airflow. Then the wet air, at the given pressure and speed, flows through experimental cascade and enters the atmosphere. The water supply system consists of a water pump, five atomizers, and some control valves and pipelines, which provides water droplets and makes air have a required wetness fraction of 7.9%. The wet fraction was measured through the two side windows in the experimental section by using the Malvern droplet and particle size analyzer. The hot air is provided by the heating system, which consists of an air pump, an electric heater, a little pressure maintaining section, and some control valves and pipelines.

The Malvern 2604Lc droplet and particle size analyzer was

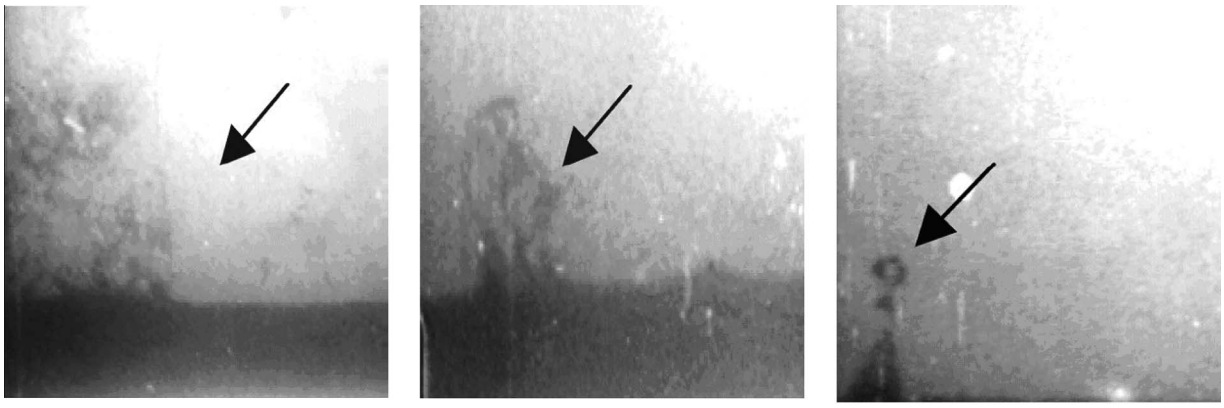

Fig. 2 Tearing modes of the water film [10]: (*a*) film tearing, (*b*) spindle tearing, and (*c*) silk rivulet tearing

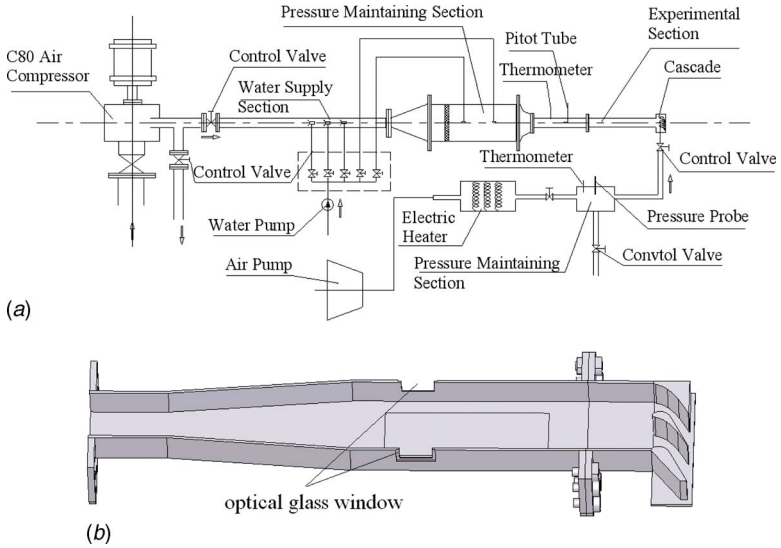

Fig. 3 Sketch of air-water two-phase flow test equipment: (*a*) sketch of air-water two-phase flow test equipment and (*b*) experimental section

used to measure the size and distribution of the water droplets, applying the principle of Fraunhofer diffraction. A parallel monochromatic laser beam illuminates a continuous flux of particles passing through the measurement area. The light incident on these particles produces a diffraction pattern regardless of the movement of the particles, reflecting the size and distribution of the particles in the measurement area at that particular instant. Thus by integrating the diffraction patterns at a given interval, an average droplet size and distribution for the total particles passing through the beam can be determined [15].

The blowing slots are 1 mm in width. The slot on the suction or pressure side is at an angle $\alpha=45$ deg to the blade surface and at a relative blade chord $x=0.691$. The parameter x is defined as the ratio of the local blade chord L to the blade chord B. A thick trailing edge was used for slot along the trailing edge of the stator blade. Figure 4 shows the blowing slots of the hollow stator blade.

In the experiment, the compressed water from the water pump is atomized into a lot of water droplets through the five atomizers. The water droplets follow the air and enter the experimental cascade. A small percentage of the droplets deposits on the blade surfaces by inertial or diffusional mechanism, and coagulates into films or rivulets. A large portion of the films or rivulets is stripped from the blade surfaces under the action of the hot air from the blowing slots, atomized into water droplets with size less than that of the droplets in the main airflow. The other water films or rivulets on the blade surfaces flow over the blowing slots, which are drawn toward the blade trailing edges by the drag of the air and torn off the trailing edge in the form of droplets. On the other hand, the hot air evaporates a little portion of the water films or rivulets on the blade surfaces.

3.2 Experimental Tests. The experiment was carried out on turbine blade cascades in a wet air tunnel with an inlet air wetness fraction of $y=7.9\%$, an outlet air velocity of $U_e=170$ m/s, a main airflow temperature of $t_1=25\,^\circ$C, and a hot air temperature of $t_2=75\,^\circ$C. The inlet air wetness fraction is obtained according to the following expression:

$$y=\frac{\rho_w\psi_w}{\rho_w\psi_w+\rho_a(1-\psi_w)}$$

where ρ_w indicates the density of the water, ρ_a indicates the density of the air, and ψ_w indicates the volume density of the water measured through the two side windows in the experimental section by using the Malvern droplet and particle size analyzer.

The Malvern droplet and particle size analyzer was also utilized to measure the size and distribution of the secondary water droplet about 100 mm away from the blade trailing in the flow direction, where the secondary atomization of the water droplet stripped from the blade trailing has been finished.

Three kinds of blowing slots were employed: the slot on the suction side, the slot on the pressure side, and the slot along the trailing edge, as shown in Fig. 4. For each kind of blowing slot, we obtained the experimental results for blowing difference $\Delta p=2.94$, 8.82, and 14.7 kPa, respectively.

3.3 Results and Discussion

3.3.1 Slot on the Suction Side. As to the slot on the suction side, the measured maximum diameters of the secondary water droplets are shown in Fig. 5(*a*). Without blowing ($\Delta p=0$), the maximum diameter is 420 μm. When the blowing pressure dif-

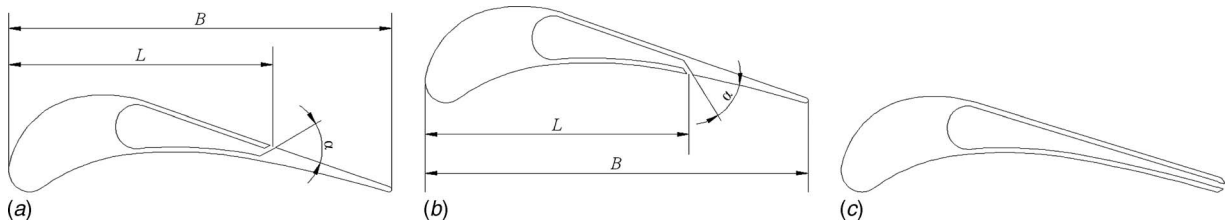

Fig. 4 Slots in the stator blade (relative blade chord $x=L/B=0.691$ and $\alpha=45$ deg): (*a*) slot on the suction side, (*b*) slot on the pressure side, and (*c*) slot along the trailing edge

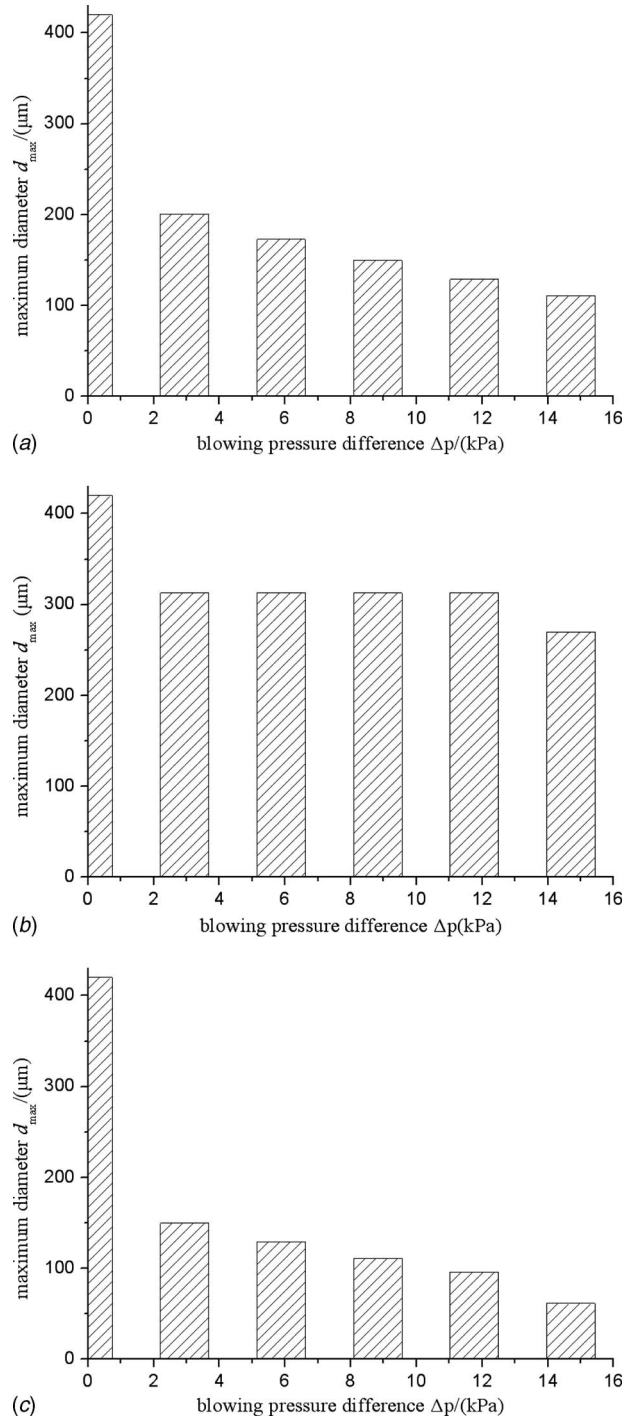

Fig. 5 Measured maximum droplet diameters: (*a*) slot on the suction side, (*b*) slot on the pressure side, and (*c*) slot along the trailing edge

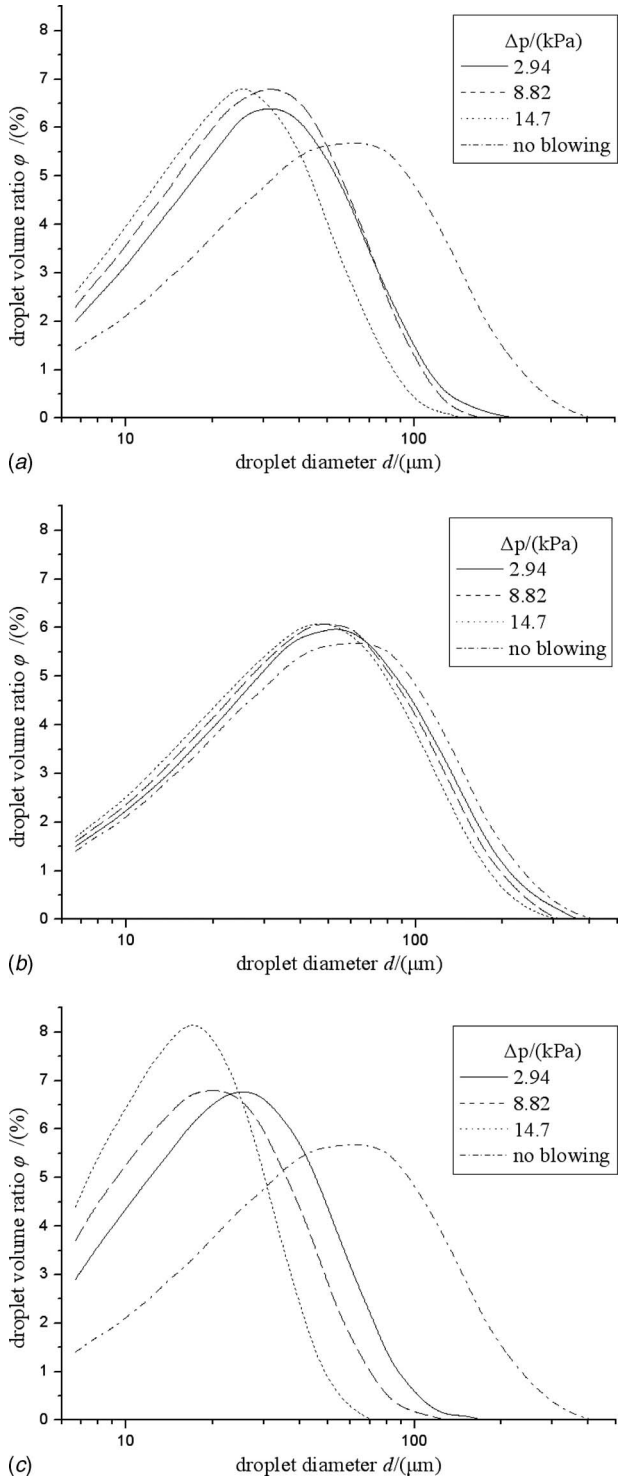

Fig. 6 Measured diameter distributions: (*a*) slot on the suction side, (*b*) slot on the pressure side, and (*c*) slot along the trailing edge

ference increases from 2.94 kPa to 14.7 kPa, the maximum diameter has a decrease from 201 μm to 111 μm. The detailed diameter distributions are given in Fig. 6(*a*), from which we can see that slot blowing makes the diameter distribution narrower, and the larger the blowing pressure, the narrower the diameter distribution.

3.3.2 Slot on the Pressure Side. Compared with slot blowing on the suction side, slot blowing on the pressure side shows a lower efficiency to reduce the size of the secondary water droplet. The measured maximum diameter decreases from 313 μm to 270 μm until the pressure difference Δp increases to 14.7 kPa, as shown in Fig. 5(*b*). A further insight into the effect of Δp is given in Fig. 6(*b*) that the diameter distributions are very approximate to that of no blowing.

These results are unexpected that the blowing pressure difference has no obvious effect on the maximum diameter of the secondary water droplets for slot on the pressure side and that it shows a low performance to reduce the size of the secondary

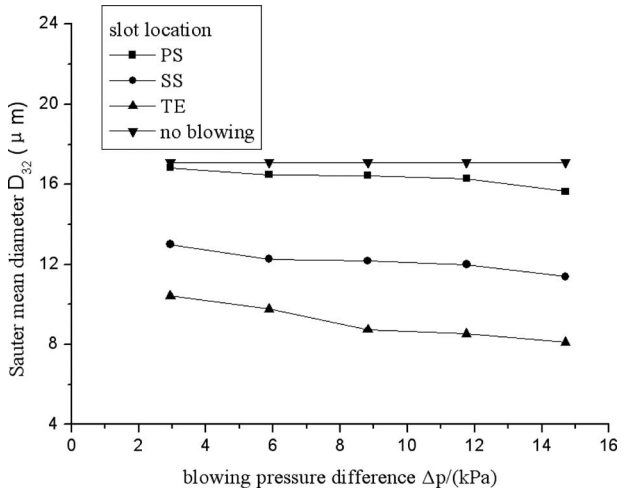

Fig. 7 Sauter mean diameter

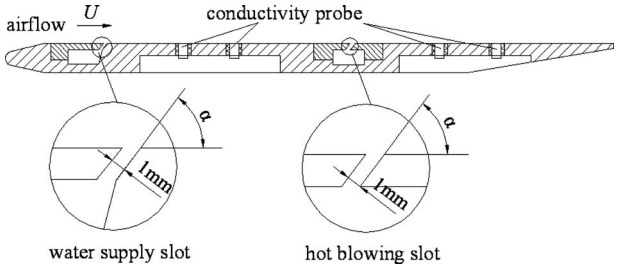

Fig. 8 Experimental flat plate (α=45 deg)

water droplets. Although some water is stripped from the pressure surface in the form of droplets under the action force of blowing, a considerable percentage of these water droplets may fail to follow the stream flow and deposit on the pressure surface again because of the concave pressure surface. It does not occur for slot on the suction side. Moreover, the pressure is higher on the pressure side than that on the suction side at the same relative blade chord x=0.691, so at the same blowing pressure ratio, slot blowing on the pressure side requires larger blowing pressure difference. Therefore the experimental results show a lower efficiency to reduce the size of the secondary water droplet for blowing slot on the pressure side than that on the suction side, even though the water film is thicker on the pressure surface than that on the suction surface. The redeposition could be weakened or eliminated if the blowing slot is much closer to the trailing edge or along the trailing edge, which requires a thick trailing edge.

3.3.3 Slot Along the Trailing Edge. The size of the secondary water droplets is reduced greatly for blowing slot along the trailing edge, although it requires a thick trailing edge and leads to a little decrease in stage efficiency. We can see from Figs. 5(*c*) and 6(*c*) that the blowing pressure difference has a distinct effect on the size and distribution of the secondary water droplets. The measured maximum diameter decreases from 150 μm to 61.5 μm when Δp increases from 2.94 kPa to 14.7 kPa and the diameter distributions become narrower with the increase in Δp.

3.3.4 Performance Comparison of the Slot Blowing. Blowing slot along the trailing edge of the hollow stator blade is more efficient to reduce the size of the secondary water droplets than that of the suction or pressure side cases. As shown in Fig. 5, when the blowing pressure difference increases from 2.94 kPa to 14.7 kPa, compared with no blowing, the measured maximum diameter has a decrease from 52% to 74% for slot on the suction side, from 64% to 85% for slot along the trailing edge, and from 25% to 36% for slot on the pressure side. The measured diameter distributions in Fig. 6 provide a further insight into the performance comparison of the slot blowing. At the same blowing pressure difference, it shows narrower diameter distributions for slot along the trailing edge than that on the suction or pressure side. Increasing blowing pressure difference leads to a quicker reduction in the maximum diameter and a sharper narrowing of the size distribution for slot along the trailing edge than that on the suction or pressure side.

The Sauter mean diameter of the secondary water droplets is a significant parameter to evaluate the performance of the hot blowing slot. Figure 7 shows the effect of the blowing pressure on the Sauter mean diameters. Without blowing, the Sauter mean diameter D_{32} is 17.1 μm. When blowing pressure difference Δp =14.7 kPa, D_{32} is 15.65 μm for slot location on the pressure side, decreased by 8.5%, 11.39 μm for slot location in the suction surface, decreased by 33.4%, and 8.10 μm for slot location along the trailing edge, decreased by 52.6%. Therefore, it is more efficient to reduce the mean diameter of the secondary water droplets for slot along the trailing edge than on the pressure or suction side.

4 Water Film Thickness

4.1 Experimental Equipment. To investigate the effect of slot hot blowing on the thickness of the water film downstream of the slot, another simplified experiment has been carried out on the

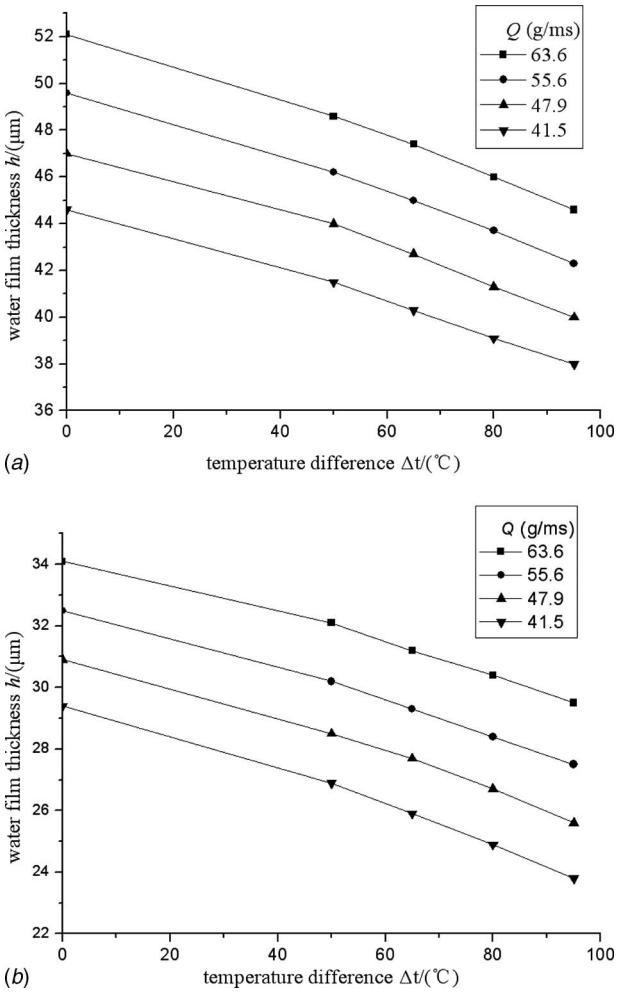

Fig. 9 Effect of temperature difference on the thickness of the water film (Δp=2.1 kPa): (*a*) *U*=110 m/s and (*b*) *U*=150 m/s

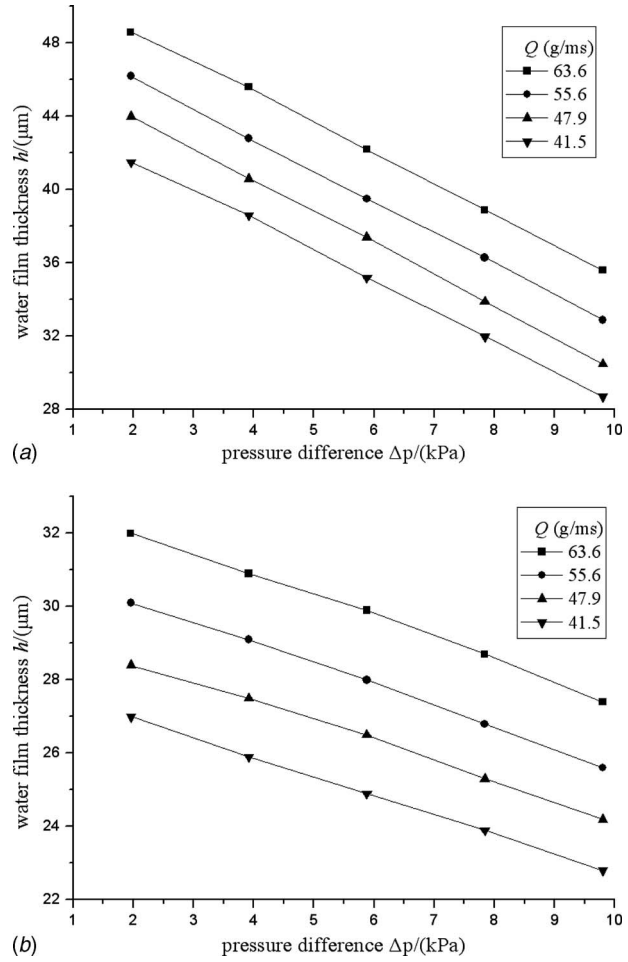

Fig. 10 Effect of pressure difference on the thickness of the water film (Δt=53°C): (*a*) U=110 m/s and (*b*) U=150 m/s

flat plate, as shown in Fig. 8. The water flows through water supply slot and forms water film on the flat plate. Under drag force of the airflow, the water film flows toward the hot blowing slot. A little portion of the water film is evaporated by the hot air, a large portion of the water film is stripped from the flat plate by slot blowing, and the other water film flows over the blowing slot by the viscous drag of the main airflow. Four conductivity probes were used to measure the thickness of the water film both upstream and downstream of the blowing slot.

4.2 Results and Discussion

4.2.1 Temperature Difference. Figure 9 indicates the effect of temperature difference on the thickness of the water film downstream of the blowing slot on the flat plate. The hot air evaporates a little water film and reduces the thickness of the water film. When the temperature difference increases from 0°C to 94°C, the water film thickness has a decrease of 15% for U=110 m/s and 17% for U=150 m/s. The airflow velocity U shows a slight help to accelerate the evaporation of the water film. It seems that we can ignore the effect of the water film flow rate Q on the decrease ratio of the water film thickness.

4.2.2 Pressure Difference. The blowing pressure difference between hot air and the main airflow exerts a great influence on the thickness of the water film downstream of the slot, as shown in Fig. 10. When the pressure difference increases from 1.96 kPa to 9.8 kPa, the water film thickness decreases by about 30% at different water film flow rate for U=110 m/s and about 15% for U=150 m/s. More water film flows over the slot under the drag force of the main airflow for higher airflow velocity. The effect of airflow velocity on evaporation ratio of the water film is comparatively slight and can be ignored.

5 Conclusions

The experimental study on the slot hot blowing of the hollow stator blades has revealed some expected characteristics that both the size of secondary water droplets and the thickness of the water film downstream of the slot have been reduced. Slot blowing from the trailing edge would be most effective, while slot blowing from the pressure side in this study is shown to be generally ineffective. The larger blowing pressure difference leads to the smaller secondary water droplets. The hot blowing also evaporates a little water film on the blade surfaces. This study provides an insight into the slot hot blowing and gives a significant suggestion for stator blade design to reduce erosion damage to the rotor blades.

Acknowledgment

The research work was supported by Hi-Tech Research and Development Program of China (Contract No. 2007AA05Z251) and by the National Natural Science Foundation of China (Contract No. 50336050).

Nomenclature

d = diameter of the water droplet
d_{max} = maximum diameter of the water droplet
D_{32} = Sauter mean diameter
Δp = blowing pressure difference
Δt = blowing temperature difference
y = wetness fraction
α = slot angle to the blade surface
x = relative blade chord
L = local blade chord
B = blade chord
ρ_a = density of the air
ρ_w = density of the water
ψ_w = volume fraction of the water
U_e = air velocity at the outlet of the cascade
t_1 = main airflow temperature
t_2 = hot air temperature
U = main airflow velocity along the flat plate
Q = water film flow rate
h = thickness of the water film
φ = droplet volume ratio

References

[1] Baumann, K., 1921, "Some Recent Developments in Large Steam Turbine Practice," J. Inst. Electr. Eng., **111**, pp. 435–453.
[2] Dehouve, J., Nardin, P., and Zeghmati, M., 1999, "Erosion Study of Final Stage Blading of Low Pressure Steam Turbines," Appl. Surf. Sci., **144–145**, pp. 238–243.
[3] Alexander, S., 2005, *Wet-Steam Turbines for Nuclear Power Plants*, Penn Well Corporation, Tulsa, OK, pp. 191–216.
[4] Hesketh, J. A., and Walker, P. J., 2005, "Effect of Wetness in Steam Turbines," Proc. Inst. Mech. Eng., Part C: J. Mech. Eng. Sci., **219**(12), pp. 1301–1314.
[5] Reley, D. J., and Parker, G. J., 1970, "The Removal of Water From Low-Pressure Steam Turbine Blades by Trailing-Edge Suction Slots," Proc. Inst. Mech. Eng., **182**(3), pp. 94–103.
[6] Tanuma, T., 1991, "The Removal of Water From Steam Turbine Stationary Blades by Suction Slots," *Proceedings of IMechE Conference on Turbomachinery*, IMechE, London, pp. 179–199.
[7] Wang, X. J., Mao, J. R., Li, Y. F., and Xu, T. X., 1999, "Experimental Investigation on the Water Removal Efficiency From Steam Turbine Stationary Blades by Suction Slot," Journal of Turbine Technology, **41**(3), pp. 164–168.
[8] Wang, X. J., Gao, T. Y., and Xu, T. X., 2004, "Experimental Study on Effects of Suction on Secondary Water Droplet Diameter and Its Distribution," Journal of Turbine Technology, **46**(6), pp. 444–446.
[9] Wang, X. J., Gao, T. Y., and Xu, T. X., 2005, "Study of the Moisture Removal Slot Structure in the Hollow Stationary Blades of a Steam Turbine," Journal of Engineering for Thermal Energy and Power, **20**(1), pp. 14–17.
[10] Wang, X. J., Xu, T. X., and Li, Y. F., 2005, "Effects of Water Suction on Water Film Tearing at Trailing Blade Edges," Heat Transfer Asian Res., **34**(6), pp. 380–385.

[11] Ryley, D. J., and Ai-Azzawi, H. K., 1983, "Suppression of the Deposition of Nucleated Fog Droplets on Steam Turbine Stator Blades by Blade Heating," Int. J. Heat Fluid Flow, **4**(4), pp. 199–215.
[12] Caldwell, J., 1966, "Description of the Damage in Steam Turbine Blading Due to Erosion by Water Droplets," Philos. Trans. R. Soc. Lond. A, **260**(1110), pp. 204–208.
[13] Smith, A., Caldwell, J., Pearson, D., McAllister, D. H., and Christie, D. G., 1966, "Physical Aspects of Blade Erosion by Wet Steam in Turbines [and Discussion]," Philos. Trans. R. Soc. London, Ser. A, **260**(1110), pp. 209–219.
[14] Zhu, G. R., 1990, "The Liquid Film Tearing on the Stationary Trailing Edges," MS thesis, Xi'an Jiaotong University, Xi'an, China, in Chinese.
[15] Walton, D., Spence, M. K., and Reynolds, B. T., 2000, "The Effects of Free Stream Air Velocity on Water Droplet Size and Distribution for an Impaction Spray Nozzle," Proc. Inst. Mech. Eng., Part A, **214**(5), pp. 531–537.

Creep Degradation of Thermally Exposed IN738C Superalloy

M. Aghaie-Khafri[1]
Associate Professor
e-mail: maghaei@kntu.ac.ir

S. Farahany
Graduate Student

Faculty of Mechanical Engineering,
K.N. Toosi University of Technology,
P.O. Box 19395-1999,
Tehran, 1999143344, Iran

Creep degradation of an IN738C superalloy after long-term thermal exposure in an atmospheric furnace was investigated by means of accelerated creep tests. Experimental observation showed that the minimum creep rate increased by increasing the exposure time or exposure temperature and is a key factor for predicting creep life during long time, high temperature service. Concerning the exposure temperature and time, an empirical equation has been presented to estimate the creep lives of the pre-exposed specimens. Furthermore, the accuracy of the Monkman–Grant (Proceedings of ASTM, Vol. ***56****, pp. 593–620) relationship has been verified by experimental results.*
[DOI: 10.1115/1.3019056]

1 Introduction

Hot sections of gas turbines are exposed to high temperatures and stresses during service and, for this reason, are usually made from heat-resistant investment cast Ni-based superalloys [1]. Prolonged operation under these conditions can severely damage critical components of gas turbine engines. These components are expensive, and there is considerable incentive to accurately assess and maximize their service lives [2].

At the high operating temperatures within a gas turbine, creep damage is a major life limiting factor. Therefore, the correlation between rupture life and creep characteristics was the subject of a number of studies conducted in the past, which suggested some accurate methods for predicting creep life during long time, high temperature service [3–5].

IN738C is an investment casting superalloy, which is frequently used for high temperature applications, especially for blades and vanes in gas turbines. This study focuses on the effect of long-term thermal exposure on the high temperature properties of IN738C samples. The degradation of mechanical properties with the exposure temperature and time has been examined and correlated with the phenomenological variables such as steady state creep rate and creep lives of specimens [6–8].

2 Experimental Procedures

The materials used in this investigation was the cast Ni-based polycrystalline superalloy IN738C containing (in wt %) 16.7 Cr, 0.16 C, 2.14 Mo, 3.02 W, 4.28 Ti, 1.17 Nb, 2.04 Ta, 9.71 Co, and 3.89 Al. The raw material was produced by the vacuum melting process. Samples were prepared from the materials and then subjected to standard heat treatment (SHT) consisting of 1200°C/4 h and 1120°C/2 h air cool followed by aging at 845°C/24 h air cool. In order to examine the effect of thermal exposure, samples were isothermally aged at 800°C and 860°C in an atmospheric furnace for 100 h, 500 h, and 1000 h.

To evaluate the stress rupture properties, the specimens were prepared from the heat treated and pre-exposed materials according to the ASTM-E8 and then tested under the conditions 650°C and 310 MPa. The creep strains in the gauge section were measured by a linear variable differential transformer attached to an extensometer frame, which was also attached to the creep specimen. The creep tests were performed until the rupture of the specimens. The temperature was monitored by three type K thermocouples and maintained within about ±2°C. The average stress rupture properties obtained on three test specimens for each experimental condition were reported, and the standard error of the mean was considered as a measure of the experimental random error.

3 Results and Discussion

3.1 Creep Behavior. The creep curve of the pre-exposed IN738C sample, like most Ni-based superalloys, shows three distinct regions, shown in Fig. 1. After the instantaneous strain, ε_0, a decelerating strain rate stage (primary creep) leads to a steady minimum creep rate, $\dot{\varepsilon}_s$ (secondary creep), which is finally followed by an accelerating stage (tertiary creep) that ends in fracture at a rupture time, t_r [3].

The variations in creep rupture life and minimum creep rate versus exposure time for IN738C at different exposure temperatures are shown in Fig. 2. It is clear that (Fig. 2(*a*)) the rupture lives of the samples decrease linearly with increasing exposure time. It is worth noting that the slope of the lines is steeper at higher temperatures, causing accelerated rupture at 850°C. It is generally accepted that the minimum creep rate is a key factor responsible for different creep rupture lives of thermally exposed samples [3,9]. The relation between the minimum creep rate and the pre-exposure temperature and time (Fig. 2(*b*)) can be expressed as

$$\dot{\varepsilon}_s = a \exp\left\{-0.5\left[\left(\frac{T-T_0}{b}\right)^2 + \left(\frac{t-t_0}{c}\right)^2\right]\right\} \tag{1}$$

where T and t are pre-exposure temperature and time, respectively, and $T_0=858.6$, $t_0=2869$, $a=3.898\times10^{-4}$, $b=70.59$, and $c=2519$ are constants. A plot of Eq. (1) is shown in Fig. 3. It is worth noting that the minimum creep rate increased by increasing either the exposure time or the exposure temperature, resulting in a shorter creep rupture life.

3.2 Modeling. Many equations relating the secondary or steady state creep rate to rupture life have been proposed to analyze data from constant load accelerated uniaxial creep tests. Consequently, if for a given material the constants related to each equation are determined, then the rupture time can be predicted just by measuring the steady state creep rate. However, there is a lack of equations to correspond the estimated rupture life to the pre-exposure temperature and time based on the steady state creep rate.

Monkman and Grant [9] found that for many alloy systems, the relation between the minimum creep rate ($\dot{\varepsilon}_s$) and time to rupture (t_r) can be expressed as follows:

$$(\dot{\varepsilon}_s)^m \cdot t_r = C \tag{2}$$

where m and C are material constants. The logarithmic form of Eq. (2) is graphically represented in Fig. 4 for aged samples based on the experimental data obtained in the present analysis. It can be observed that the experimental data have a fair agreement in the case of IN738C. Combining Eqs. (1) and (2) results in

[1]Corresponding author.

Manuscript received October 31, 2007; final manuscript received September 20, 2008; published online January 29, 2009. Review conducted by Dilip R. Ballal.

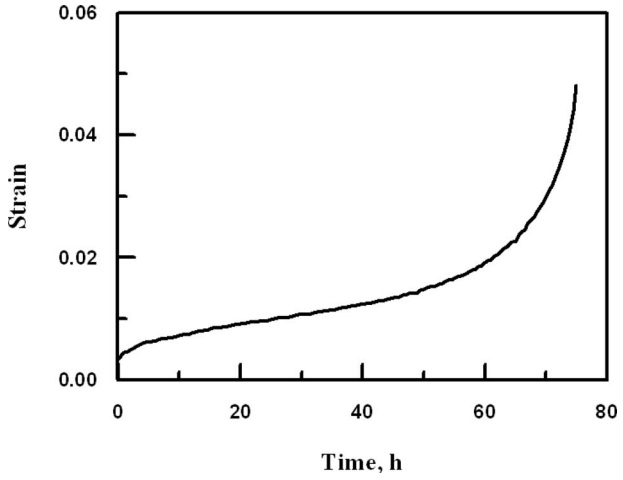

Fig. 1 Typical creep curve of the IN738C sample after aging for 100 h at 800°C

$$t_r = C\left(a \exp\left\{-0.5\left[\left(\frac{T-T_0}{b}\right)^2 + \left(\frac{t-t_0}{c}\right)^2\right]\right\}\right)^{-m} \quad (3)$$

Equation (3) can be used to estimate the creep rupture life of pre-exposed samples on the basis of exposure time and temperature.

During an investigation on the creep life predictions, Koul and co-workers [10,11] claimed that in the case of complex alloys, stress rupture data exhibit high scatter and that the Monkman–Grant relationship is unable to distinguish degenerative effects caused during service. They proposed a modified equation, which isolates the tertiary stage of creep life and creep strain from creep data. The modified Monkman–Grant equation is written as

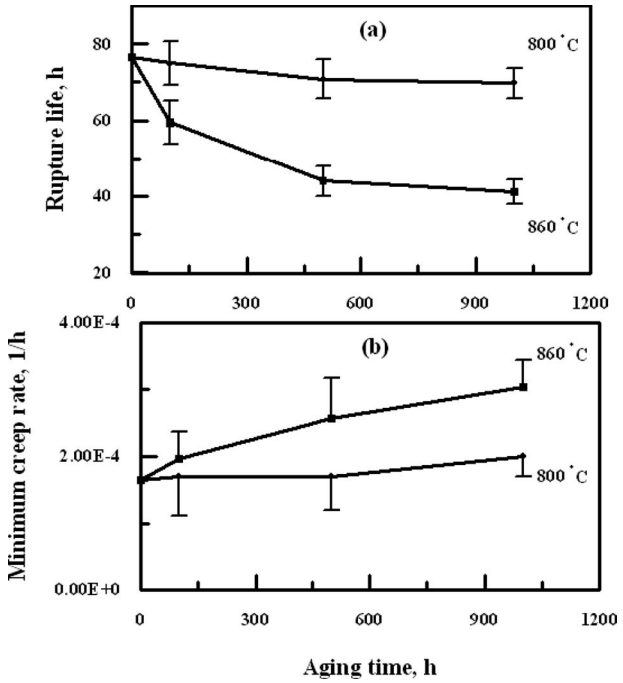

Fig. 2 Variation of (*a*) stress rupture life and (*b*) minimum creep rate of IN738C samples with exposure time at different exposure temperatures

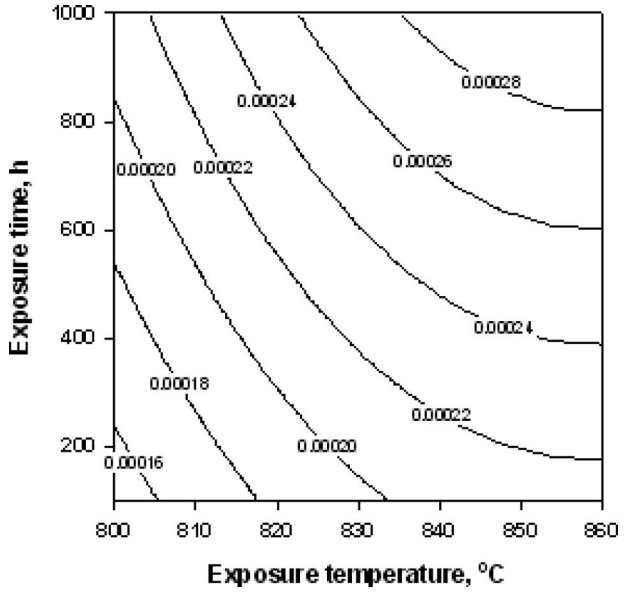

Fig. 3 A plot of Eq. (1) where contour numbers represent minimum creep rates (1/h) at different pre-exposure temperatures and times

$$t_t = K\dot{\varepsilon}_s^m \quad (4)$$

The time to tertiary creep, t_t, is the sum of the primary and secondary creep lives (t_p+t_s); m and k are material constants. Concerning the experimental result of the present investigation, time to tertiary creep versus minimum creep rate for aged samples is shown in Fig. 5. It is clear that the modified Monkman–Grant equation is in good agreement with experimental data.

Considering the normalizing parameter of strain to fracture proposed by Dobes–Milicka [12], a new creep relationship based on the sum of the primary creep life, t_p, and the secondary creep life, t_s, normalized by the sum of the primary creep strain, ε_p, and the secondary creep strain, ε_s, varying as a function of secondary creep rate $\dot{\varepsilon}$, has been developed [10]. The relationship is described by

$$\frac{t_p + t_s}{\varepsilon_p + \varepsilon_s}\dot{\varepsilon}^M = K \quad (5)$$

where M and K are constants. A logarithmic representation of the normalized parameter versus steady state creep rates is shown in

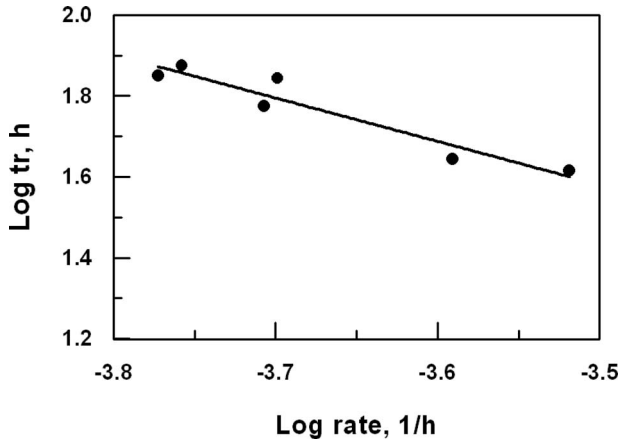

Fig. 4 Graphical representation of the Monkman–Grant equation for IN738C

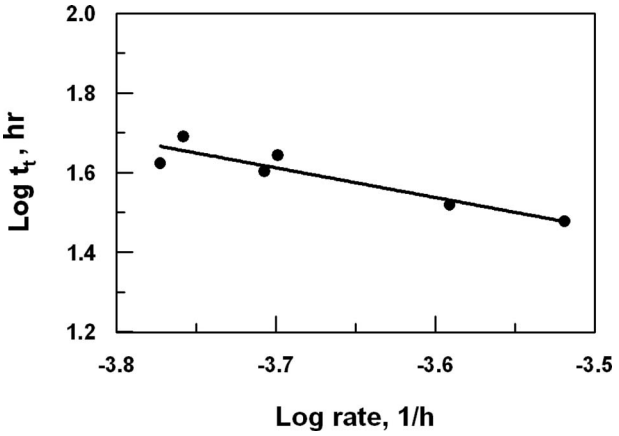

Fig. 5 Time to tertiary creep versus minimum creep rate in IN738C

Fig. 6. It is clear that normalizing by the $\varepsilon_p+\varepsilon_s$ leads to increased scatter in the results.

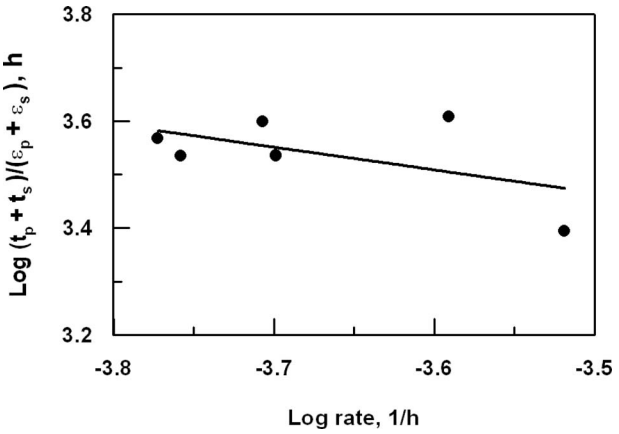

Fig. 6 A plot of log (strain rate) versus $(t_p+t_s)/(\varepsilon_p+\varepsilon_s)$ for exposed IN738C samples

4 Conclusions

The following conclusions from high temperature accelerated creep testing of prior thermally exposed Ni-based superalloy can be drawn.

- The long-term thermal exposure of IN738C reduced the creep lifetime of the alloy and was effective in increasing creep strain rate.
- The effect of exposure time and exposure temperature on the minimum creep rate of the pre-exposed samples has been described by an empirical equation. This equation together with the Monkman–Grant equation can be used to estimate the creep life of pre-exposed samples on the basis of exposure time and temperature.
- Both the original and modified Monkman–Grant equations are suitable for life assessment of a thermally exposed Ni-based superalloy.

References

[1] Maccagno, T. M., Koul, A. K., Immarigeon, J. P., Cutler, L., Allem, R., and Lesperance, G., 1990, "Microstructure, Creep Properties, and Rejuvenation of Service-Exposed Alloy 713C Turbine Blades," Metall. Trans. A, **21**, pp. 3115–3125.
[2] Brown, J. A., Freer, R., and Rowley, A. T., 2001, "Reconditioning of Gas Turbine Components by Heat Treatment," ASME J. Eng. Gas Turbines Power, **123**, pp. 57–61.
[3] Viswanathan, R., 1989, *Damage Mechanisms and Life Assessment of High-Temperature Components*, ASM International, Materials Park, OH, pp. 59–105.
[4] Orr, R., Sherby, O. D., and Dorn, J. E., 1954, "Correlation of Rupture Data for Metals at Elevated Temperatures," Trans. ASME, **46**, pp. 113–118.
[5] Larson, F. R., and Miler, J., 1952, "A Time-Temperature Relationship for Rupture and Creep Stress," Trans. ASME, **74**, pp. 756–775.
[6] Zrnik, J., Strunz, P., Vrchovinsky, V., Muransky, O., Novyc, Z., and Wiedenmann, A., 2004, "Degradation of Creep Properties in a Long-Term Thermally Exposed Nickel Base Superalloy," Mater. Sci. Eng., A, **387–389**, pp. 728–733.
[7] Lifshitz, M., and Slyozov, V. V., 1961, "The Kinetics of Precipitation From Supersaturated Solid Solution," J. Phys. Chem. Solids, **19**, pp. 35–50.
[8] Wagner, C., 1961, "Theorie der Alterung von Niederschlagen Durch Umlosen," Z. Elektrochem., **65**, pp. 581–591.
[9] Monkman, F. C., and Grant, N. J., 1956, Proceedings of ASTM, Vol. 56, pp. 593–620.
[10] Koul, A. K., Castillo, R., and Willett, K., 1984, "Creep Life Predictions in Nickel-Based Superalloys," Mater. Sci. Eng., **66**, pp. 213–226.
[11] Castilo, R., Koul, A. K., and Toscano, E. H., 1987, "Lifetime Prediction Under Constant Load Creep Conditions for a Cast Ni-Base Superalloy," ASME J. Eng. Gas Turbines Power, **109**, pp. 99–106.
[12] Dobes, F., and Milicka, K., 1976, "The Relation Between Minimum Creep Rate and Time to Fracture," Met. Sci., **10**, pp. 382–384.

Carbon Capture for Automobiles Using Internal Combustion Rankine Cycle Engines

Robert W. Bilger
School of Aerospace, Mechanical and Mechatronic Engineering,
The University of Sydney,
New South Wales 2006, Australia
e-mail: bilger@aeromech.usyd.edu.au

Zhijun Wu
School of Automotive Studies,
Tongji University,
Shanghai 201804, P. R. China
e-mail: zjwu@mail.tongji.edu.cn

Internal combustion Rankine cycle (ICRC) power plants use oxy-fuel firing with recycled water in place of nitrogen to control combustion temperatures. High efficiency and specific power output can be achieved with this cycle, but importantly, the exhaust products are only CO_2 and water vapor: The CO_2 can be captured cheaply on condensation of the water vapor. Here we investigate the feasibility of using a reciprocating engine version of the ICRC cycle for automotive applications. The vehicle will carry its own supply of oxygen and store the captured CO_2. On refueling with conventional gasoline, the CO_2 will be off-loaded and the oxygen supply replenished. Cycle performance is investigated on the basis of fuel-oxygen-water cycle calculations. Estimates are made for the system mass, volume, and cost and compared with other power plants for vehicles. It is found that high thermal efficiencies can be obtained and that huge increases in specific power output are achievable. The overall power-plant system mass and volume will be dominated by the requirements for oxygen and CO_2 storage. Even so, the performance of vehicles with ICRC power plants will be superior to those based on fuel cells and they will have much lower production costs. Operating costs arising from supply of oxygen and disposal of the CO_2 are expected to be around 20 c/l of gasoline consumed and about $25/tonne of carbon controlled. Over all, ICRC engines are found to be a potentially competitive option for the powering of motor vehicles in the forthcoming carbon-controlled energy market. [DOI: 10.1115/1.3077657]

Keywords: internal combustion engines, carbon dioxide capture, vehicle power plants

1 Introduction

Carbon capture and sequestration is one of the most promising approaches to the control of greenhouse gas (GHG) emissions [1]. Capture using oxy-fuel combustion methods is considered to be one of the most promising approaches to carbon capture [1]. In these methods oxygen rather than air is used to combust the fuel with recycled carbon dioxide and/or water used to limit combustion temperatures so leaving the products as mostly CO_2 and H_2O. On condensation of the H_2O, the CO_2 not recycled can be exhausted for compression and subsequent sequestration. Several realizations of this general method are reviewed in Ref. [1] with the direct heating steam turbine cycle being pursued by Clean Energy Systems [1–3] being of relevance here. This cycle recycles only H_2O and is capable of achieving very high cycle efficiencies with power-plant costs lower than those for gas turbine combined cycle (GTCC) plants [2,3]. The facts that it is much cheaper in both energy and equipment cost terms to compress the recycled H_2O to high pressures than it is to compress nitrogen are the main reasons for the high efficiencies and low plant costs that are attainable. For this reason, oxy-fuel combustion power-plant cycles of this type have been called internal combustion Rankine cycles (ICRCs) [3]. High cycle efficiency is very significant for oxy-fuel combustion power plants as the energy cost of separating oxygen from air is about 900 kJ/kg and results in a deduction of 0.07 or more in efficiency so that an oxy-fuel firing for a conventional type of steam power-plant results in the basic efficiency of, say, 42% being reduced to an overall efficiency of 35% [3]. Basic efficiencies for the ICRC steam turbine cycle of 65% or more are possible [2,3] and so the overall efficiency is only reduced to about 58%, still a very high figure. The Graz cycle studied by Sanz et al. [4] recycles mainly H_2O, but it is not an ICRC as it uses a heat recovery steam generator and a significant amount of the recycled fluid undergoes compression as a gas. Although high cycle efficiencies are obtained, equipment costs are much higher than those for the Clean Energy Systems cycle.

Reciprocating engine versions of the ICRC cycle have been studied [3] and may be suitable for low power output applications such as for combined heat and power units for buildings and industrial processes and for use in automobiles. Oxy-fuel combustion in reciprocating engines has been used for many years in submarines and systems are commercially available. These engines recycle incondensable exhaust products (CO_2 and N_2) and do not benefit from the much higher efficiencies and power outputs per unit size that are achievable using the ICRC. Here we focus on the feasibility of ICRC reciprocating engines for automotive applications.

In automotive applications of this technology, the vehicle will carry its own supplies of liquid hydrocarbon fuel and of oxygen and have the capacity for temporary storage of the carbon dioxide captured from the engine exhaust. On visits to a service station, the vehicle will off-load its captured CO_2 and on-load fresh supplies of oxygen and fuel.

2 Cycle Performance

The performance of any reciprocating engine cycle is limited by the laws of thermodynamics. For conventional engines, the thermodynamic limitations to performance are most realistically predicted by calculations using the fuel-air (FA) cycle as described by Taylor [5] and Heywood [6]. Achievable actual performance is better than 80% of predictions based on FA cycle calculations [5]. The performance of reciprocating ICRC engines can be estimated by carrying out fuel-oxygen-water (FOW) cycle calculations. Achievable actual performance can then be expected to be better than 80% of these ideal calculations at the maximum efficiency operating point for the engine.

The ideal "indicator" P-V diagram for the in-cylinder part of a specimen ICRC cycle is shown, schematically, in Fig. 1. The cycle shown has a two-stroke cycle, mechanically, that differs considerably from conventional two-stroke engines, it being assumed that the oxygen is available at high pressure. The exhaust-compression stroke 7-2 comprises an exhaust component, 7-8 with the exhaust valve open and the inlet valve closed; an inlet component, 8-1, during which the exhaust valve is closed and the inlet valve is open admitting fresh oxygen and fuel; and a compression component 1-2 during which adiabatic compression of the fuel/oxygen/end-gas mixture occurs. During the process 2-5, combustion of the fuel/oxidant/end-gas mixture occurs with the injection and mixing of preheated water (from an inlet state 3) being controlled so as to limit the maximum pressure in the cycle, $P_4 = P_5$, as in the so-called "limited-pressure cycle" used for modeling compression ignition engines [5]. The process 5-6 is assumed to be a reversible adiabatic (isentropic) expansion of com-

Manuscript received April 10, 2008; final manuscript received September 30, 2008; published online February 10, 2009. Review conducted by James S. Wallace.

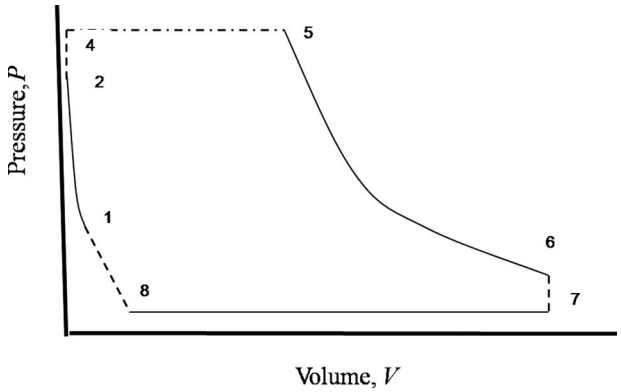

Fig. 1 Ideal indicator diagram for a specimen ICRC engine

bustion products in full chemical equilibrium. The segment 2-4 of the process is assumed to occur at constant volume as is the exhaust process 6-7. In the analysis of many of the processes in the cycle, we use the STANJAN software of Reynolds [7].

The results are presented in Table 1 for a series of ideal cycle calculations for the ideal cycle shown in Fig. 1 using iso-octane, C_8H_{18}, as the fuel. The results are presented for various values of the pressure, P_1, at the end of oxygen and fuel admission. They are for fixed values of the parameters e_2, e_8, e_1, P_8, T_8, T_1, P_3, T_3, P_5, n, and x: The values of these parameters are given in the caption to Table 1. Here, $e_2=V_2/V_S$, $e_8=V_8/V_S$, $e_1=V_1/V_S$, V_S =the swept volume$=V_7-V_2$, n=moles of water injected per mole of fuel, and x=excess moles of oxygen injected per mole of fuel. The results are insensitive to the water pump inlet state, outlet pressure, and pump efficiencies, but these were assumed at 1 atm, 300 K, 14 MPa, and 50%. The intensive data shown in Table 1 are not dependent on V_S since the cycle is ideal. In Table 1, $e_5=V_5/V_S$, and η is the thermal efficiency. The mean effective pressure (MEP), P_{MEP}, is given by $P_{\text{MEP}}=W_{\text{net}}/V_S$, where W_{net} is the net work output per operating cycle of the engine.

The data shown in Table 2 are for so-called "extensive" quantities that are dependent on the size of the engine. They are given for $V_S=500$ cm^3 and, for the ideal cycle, will scale linearly with V_S. The mass of oxygen, fuel, and water used per cycle are given by m_O, m_F, and m_W, respectively. The various $W_{j,j+1}$ are the work output per cycle for that part of the process, with W_{net} being the resulting net work per cycle. The engine torque, **T**, is given by $\mathbf{T}=W_{\text{net}}/2\pi$ for the two-stroke cycle. Although this specimen set of cycle calculations is not likely to be the optimum for any particular application, it is seen that the numbers involved are reasonably practical. It is seen that the amount of water injected is enough to limit the peak temperature, T_5, to about 2700 K, much the same as the peak temperature in limited-pressure fuel-air cycle calculations for diesel engines [5].

It is seen that the cycle is capable of achieving ideal MEPs at full load of around 5.4 MPa at an efficiency above 30%. At 6000 rpm, this corresponds to a power output of over 1000 kW for a 2 l engine. This is an order of magnitude higher than the actual power output for fuel-air cycle engines of this size. Of course, cycle losses will reduce actual performance compared with the calculated ideal, but it can be expected that such losses will have a less important effect than for conventional engines. This is because the compression work is small and many of the apparent heat losses during expansion are, in fact, regenerative. It is evident that there is a huge potential for great increases in specific power output, kW/kg of engine mass, from this cycle compared with conventional engines. Thermodynamically, much of this comes from the low work requirement of compressing water rather than nitrogen, but the "supercharging" effect of being able to supply the oxygen at elevated pressure is also a major factor.

It is noted that the ideal FOW cycle efficiency predictions at high outputs, ~40%, are similar to those for ideal FA cycle predictions for Otto (constant-volume cycle) and diesel (limited-pressure cycle) engines [5]. Of great significance are the high efficiencies obtainable at part loads for this cycle, obtained here by reducing the pressure at the end of fuel-oxygen admission, P_1. While these are not quite as large as those for the diesel [5], they are a huge improvement on those for the Otto cycle engine. This is of immense significance for automotive applications where most of the operation is at less than 30% of maximum power output. Conventional spark-ignition (Otto cycle) engines have poor efficiency at low loads and this is a major factor in their poor fuel consumption performance. Engines employing this cycle should have part-load fuel economy comparable to those of current diesel engines, but with much higher specific power output.

A parametric study of the sensitivity of ideal FOW cycle performance of the values of the various parameters listed in the caption of Fig. 1 has been carried out for a fixed value of $P_1=0.6$ MPa. Based on this sensitivity analysis, a calculation was carried out for $e_2=0.045$, $n=60$, $P_5=90$ atm, $P_8=0.15$ MPa, $T_1=750$ K, $T_3=600$ K, and $x=2$: An ideal thermal efficiency of

Table 1 Specimen ideal FOW cycle calculations for various pressures, P_1. Assumed parameters: $e_2=0.05$, $e_1=0.1$, $e_8=0.25$, $P_3=14$ MPa, $T_3=600$ K, $P_8=0.12$ MPa, $T_8=600$ K, $T_1=600$ K, $P_5=80$ atm, $n=20$, and $x=2$.

P_1, MPa	0.4	0.6	0.8	1.2	1.5
T_2, K/P_2, MPa	770/1.54	757/2.27	750/3.00	745/4.47	743/5.57
T_5, K/e_5	2493/0.00	2628/0.044	2671/0.087	2718/0.175	2722/0.373
T_6, K/P_6, MPa	1429/0.219	1757/0.479	1934/0.760	2163/1.37	2260/1.84
P_{MEP}, MPa	0.781	1.66	2.40	3.60	5.39
η	0.50	0.47	0.44	0.38	0.34

Table 2 Extensive quantities for the cycles of Table 1 for $V_S=500$ cm^3

P_1, MPa	0.4	0.6	0.8	1.2	1.5
m_O; m_F; m_W, g	0.072; 0.0177; 0.056	0.162; 0.029; 0.126	0.252; 0.062; 0.196	0.432; 0.106; 0.336	0.567; 0.140; 0.44
$W_{1\text{-}2}$, J	−37	−56	−74	−110	−137
$W_{2\text{-}5}$, J	0	177	354	711	1510
$W_{5\text{-}6}$, J	476	759	970	1250	1380
$W_{7\text{-}8}$, J	−45	−45	−45	−45	−45
$W_{8\text{-}1}$, J	−20	−27	−35	−50	−61
W_{net}, J	391	832	1200	1800	2700
T, Nm	61	131	190	285	427

Table 3 Power-plant mass and volume estimates for 50 kW maximum power and 500 km range

Quantity	SI mass, kg	ICRC mass, kg	SI volume, l	ICRC volume, l
Engine	120	50	200	50
Fuel	40	30	50	40
O_x/CO_2 storage	0	190	0	170
Radiator	10	25	25	75
Miscellaneous	10	25	25	45
Total	180	320	300	380

56% was obtained. It is expected that even higher thermal efficiencies can be obtained with further optimization.

3 System Characteristics

In Sec. 2, we have focused on the performance characteristics of the reciprocating engine component of what is, in reality, a larger power-plant system that includes tanks for the fuel, oxygen, and CO_2, a condenser radiator for condensing the steam in the engine exhaust, and several other components including a water/CO_2 separator, feed water pumps, feed water heaters, CO_2 compressors, and controls. From the viewpoint of the vehicle designer, it is the characteristics of the complete power-plant system that are important. These characteristics include the mass, volume, and costs (equipment and operating) of the overall system, together with issues associated with the integration of the power plant into the vehicle and with maintainability, etc. The mass and volume of the ICRC power-plant system is dominated by the tankage requirements for the oxygen and CO_2. Table 3 provides estimates made for the system mass and volume of an ICRC-engined vehicle power plant in comparison with estimates made for a vehicle power-plant system using a conventional spark ignition (SI) engine with the same maximum power output and vehicle range of 50 kW and 500 km, respectively. These estimates are based on the assumption that the fuel consumption of the ICRC-engined vehicle will be comparable to current automotive diesel engines. The mass of oxygen required for this amount of fuel is calculated from stoichiometry for a hydrocarbon fuel of C:H ratio of 1:2. The oxygen storage is assumed to be in a 70 MPa carbon-fiber composite pressure vessel identical to the tanks already certified for use at these pressures for hydrogen storage for fuel-cell powered vehicles [8]. Carbon dioxide storage is assumed to be accomplished in the same pressure vessel using an internal bladder. The large reductions in engine mass and volume for the ICRC engine arise from its greatly increased specific work output as has been demonstrated from the cycle calculations. The condenser-radiator sizing is based on the premise that almost all of the heat rejection for the ICRC engine is via this means whereas in a conventional SI engine most of the heat rejection occurs from the exhaust and engine surfaces. The size of the subsystem needed for compression of the CO_2 could be significant. It has been found, however, that it is possible to use the expansion of the high pressure oxygen to carry out most of this expansion in a small subsystem.

Although the estimates in Table 3 are in most cases quite crude, they are much less so for the O_x/CO_2 storage where hard data are available [8]. The O_x/CO_2 storage is the dominant component of both the ICRC mass and volume estimates. Accordingly, the estimates for the total mass and volume of the ICRC system can be expected to be accurate to within about 20%. The estimates for conventional spark-ignition engines are based on a limited survey and could have a similar range of error. The estimates for the ICRC engine power-plant amount to a specific power of about 160 W/kg and a specific energy of about 1 kW h/kg. These figures are below those for conventional engines that do not provide CO_2 capture but are considerably better than those for fuel-cell and battery powered vehicles.

A major consideration for high pressure gas storage is that of equipment cost. A fundamental underlying component of this is that of the carbon fiber. Carbon fiber production is a relatively mature industry with only modest cost reductions likely for massively increased market demand. For the above 35 MPa and 70 MPa tanks, the IEA [8] estimate is for a carbon fiber cost of \$650 per tank with a mass-produced tank production cost of about \$2700.

Based on a bulk oxygen cost of 4 c/kg, it is estimated that the extra operating cost of oxygen supply and CO_2 sequestration will amount to about 20 c/l of fuel consumed, giving a total cost of controlling carbon emissions in this way of about \$25/tonne of carbon saved or \$7/tonne of CO_2 saved. It seems that these costs could be bearable and that the system could be economically competitive with other technologies for controlling or offsetting carbon emissions from automobiles.

Implementation of this ICRC engine power plant will be aided by the fact that it will use existing technology in its development and facilities for mass production. Development problems with regard to lubrication can be expected but metal temperatures can be controlled by conventional cylinder block, cylinder head, and sump cooling and also by judicious use of the in-cylinder water injection—both processes being essentially regenerative if the block and head cooling are part of the water feed-heating system. A more challenging problem may be to overcome freezing of the water when operating in cold climates.

4 Conclusions

It is concluded that vehicles with ICRC engine power plants could be inherently competitive in carbon-controlled markets in many countries. Their acceleration and hill climbing performance will be much superior to vehicles using fuel cells and their production cost much lower. Their range and fuel economy will be comparable with current gasoline-engine vehicles. The costs of oxygen supply and CO_2 disposal are estimated to amount to about \$0.20/l of fuel consumed and so operating costs could be much less than the costs of using biofuels. The total cost of sequestering fossil carbon in this way is expected to be about \$25/tonne of carbon saved, or \$7/tonne of CO_2 saved, which seems bearable and could be less than that for carbon trading and so make operating costs less than for vehicles using fossil fuels in conventional power plants and paying for carbon credits.

Market entry for this new system will be eased by the fact that it uses existing technology in its development and mass production.

Acknowledgments

The first author gratefully acknowledges the support of Tongji University that provided for him to spend a month at their Clean Energy Automotive Engineering Center in the School of Automotive Studies to initiate collaboration on this study. The contributions of the following Tongji research students to the project are gratefully acknowledged: Wei Ava Feng, Tangtang Bao, Zhuo Alan Liao, Jia Liu, Xiao Yu, Chengjie Huang, Yonglong Chen, Yunhai Zhang, Zhilong Li, Haiping Hu, Jun Li, and Yongzheng Sun.

Nomenclature

e_j = normalized volume $\equiv V_j/V_S$

m_F, m_O, m_W = masses of fuel, oxygen, and water, respectively, consumed per operating cycle of the engine

n = number of moles of injected water per mole of fuel

P_j = pressure at state j

P_{MEP} = mean effective pressure $\equiv W_{net}/V_S$

$\mathbf{T}$ = engine torque

T_j = temperature at state j

V_j = volume at state j
V_S = swept volume
$W_{j,j+1}$ = work output for process from state j to state $j+1$
W_{net} = net work output per operating cycle of the engine
x = number of moles of excess oxygen per mole of fuel
η = thermal efficiency

Subscripts

$j=1,2,4,5,\ldots,8$ = states in the ideal indicator diagram of Fig. 1
$j=3$ = state of liquid water at water injector inlet

References

[1] Metz, B., Davidson, O., deConinck, H. C., Loos, M., and Meyer, L. A., eds., *IPPC 2005: IPCC Special Report on Carbon Dioxide Capture and Storage*, prepared by Working Group III of the Intergovernmental Panel on Climate Change, Cambridge University Press, Cambridge, 442 pp.

[2] Marin, O., Bourhis, Y., Perrin, N., Di Zanno, P., Viteri, F., and Anderson, R., 2003, "High Efficiency Zero Emission Power Generation Based on a High Temperature Steam Cycle," 28th International Technical Conference on Coal Utilization and Fuel Systems, Clearwater, FL, Mar.

[3] Bilger, R. W., 1999, "Zero Release Combustion Technologies and the Oxygen Economy," Fifth International Conference on Technologies and Combustion for a Clean Environment, Lisbon, Portugal, Jul. 12–15, pp. 1039–1046.

[4] Sanz, W., Jericha, H., Bauer, B. and Gottlieb, E., 2008, "Qualitative and Quantitative Comparison of Two Oxy-Fuel Power Cycles for CO_2 Capture," ASME J. Eng. Gas Turbines Power, **130**, p. 031702.

[5] Taylor, C. F., 1966, *The Internal Combustion Engine in Theory and Practice, Vol. 1: Thermodynamics, Fluid Flow, Performance*, 2nd ed., Wiley, New York.

[6] Heywood, J. B., 1988, *Internal Combustion Engine Fundamentals*, McGraw-Hill, New York.

[7] Reynolds, W. C., 1987, "STANJAN Chemical Equilibrium Solver", Version 3.94, Department of Mechanical Engineering, Stanford University, Stanford, CA.

[8] IEA, 2005, *Prospects for Hydrogen and Fuel Cells*, International Energy Agency, Paris, France.

Numerical Simulation of Aero-Engine Lubrication System

Yaguo Lu

Zhenxia Liu

Shengqin Huang

School of Power and Energy,
Northwestern Polytechnical University,
Xi'an 710072, China

Tao Xu
Military Representatives Office of NDMMP,
Xi'an 710025, China

A software, general analysis software of aero-engine lubrication system (GASLS), for simulating aero-engine lubrication system is presented. The software is capable of analyzing the flow, pressure, and temperature distribution in the lubrication system. The network theory and mathematical model of flow resistance for elements that include pipes, elbows, thick orifice, reductions, expansions, and nozzles are presented first. Second, the special element and combined element are introduced for treating the bearing chamber, heat exchanger, and gearbox and simplifying the calculation network, respectively. Lastly, a case study for an aero-engine lubrication system is illustrated. The distribution of oil flow, pressure, and temperature is calculated, and the oil flow results in different branches of lubrication system are compared with the experimental data. The comparison indicts that computational results agree well with the measured data. The software may be helpful in designing and analyzing aero-engine lubrication system. [DOI: 10.1115/1.3026573]

Keywords: aero-engine lubrication system, software, mathematical model, special element, combined element

1 Introduction

The aero-engine lubrication system is required to provide oil to the engine for lubricating and cooling system components and ensuring safety and life demands of engine. While designing or analyzing a lubrication system, detailed distributions of oil flow, pressure, and temperature in the lubrication system at various flight states are needed. But measuring these parameters is extremely difficult under high temperature, pressure, and rotational speed conditions while the aero-engine is working, so numerical simulation technology plays an important role in the lubrication system design and analysis. At present, some famous aero-engine research institutes or companies have developed their own software and program for simulation of complex system, such as GFSSP [1] and FLOMODL [2], but present literatures have not mentioned the application of these softwares and programs for simulating aero-engine lubrication system whereas all of them have been proved useful in many fields.

In this paper, a software, general analysis software of aero-engine lubrication system (GASLS), developed in Northwestern Polytechnical University is presented. The GASLS is the special software whose chief aim is to simulate the various aero-engine lubrication systems different from GFSSP and FLOMODL. First, the network theory and the mathematical model for oil flow through the flow resistance elements are described. The lubrication system contains many special elements such as bearing chamber, heat exchanger, and gearbox. Furthermore the lubrication system is very complicated. Second for treating the special elements and simplifying the simulation network, the special element model and combined element model are introduced. Lastly a case study for an aero-engine lubrication system is illustrated. The analysis results show that the software is helpful for the efficient design and analysis of an aero-engine lubrication system.

Manuscript received April 14, 2008; final manuscript received May 15, 2008; published online February 10, 2009. Review conducted by Dilip R. Ballal.

2 Flow Network Theory

The lubrication system has multiple branches. We use the flow network theory [3,4] to calculate oil flow, pressure, and temperature distribution in the flow complex lubrication system.

First, the theory of mass conservation may be imposed at each junction of the flow network. Therefore, the algebraic summation of all flow entering a junction is zero. For the incompressible flow, at a node, the continuity equation is

$$\sum Q = 0 \tag{1}$$

Second, the continuity of energy per unit mass may be applied along the same branch. The energy potential between two nodes in certain pipe is equal. For the incompressible flow on the same streamline, the energy balance equation is

$$\frac{P_a}{\gamma} + \frac{V_a^2}{2g} + Z_a = \frac{P_b}{\gamma} + \frac{V_b^2}{2g} + Z_b + h_w \tag{2}$$

where P_a, P_b, V_a, V_b, and Z_a, Z_b represent pressure, velocity, and elevation from data at certain points, a and b. h_w is the frictional head loss. g is the acceleration of gravity.

3 Element Model

In the GASLS, it divided the elements into three classes. The first type is the flow resistance element including pipes, elbows, thick orifices, expansions, reductions, nozzles, etc. The second type is the pressurization elements including oil pumps. The last type is the special element including bearing chamber, heat exchanger, and gearbox.

3.1 Flow Resistance Elements.

3.1.1 Pipe

$$\Delta P = \frac{fL}{D} \cdot \frac{\rho Q^2}{2A^2} + \gamma \cdot \Delta Z \tag{3}$$

where f is the friction factor.

For $\mathrm{Re} \leqslant 2300$,

$$f = \frac{64}{\mathrm{Re}} \tag{4}$$

for $\mathrm{Re} > 2300$, calculate from the Colebrook equation

$$\frac{1}{\sqrt{f}} = -2\log\left(\frac{\varepsilon}{3.7D} + \frac{2.51}{\mathrm{Re}\sqrt{f}}\right) \tag{5}$$

where ε is the absolute roughness.

3.1.2 Local Resistance Element. In the pipelines of the lubrication system, there are many local resistance elements such as elbows, expansions, reductions, thick orifices, and so on. The mathematical model is presented below.

$$\Delta P = K\frac{\rho Q^2}{2A^2} \tag{6}$$

where K is the dimensionless experimental coefficient that accounts for head losses, which could be obtained from Table 1. The Reynolds number and friction factor that are utilized within eqs.

Table 1 Dimensionless coefficient *K* calculate relationship

Elements	Dimensionless coefficient, K	
General elbow	$K=0.5$	(1)
Thick orifice [5]	For upstream $\mathrm{Re}\leqslant 2500$: $K=\left[2.72+\left(\frac{d_o}{D}\right)^2\left(\frac{120}{\mathrm{Re}}-1\right)\right]\left[1-\left(\frac{d_o}{D}\right)^2\right]\left[\left(\frac{D}{d_o}\right)^4-1\right]\left[0.584+\frac{0.0936}{(L_o/d_o)^{1.5}+0.225}\right]$	(2)
	For upstream $\mathrm{Re}>2500$: $K=\left[2.72+\left(\frac{d_o}{D}\right)^2\left(\frac{4000}{\mathrm{Re}}\right)\right]\left[1-\left(\frac{d_o}{D}\right)^2\right]\left[\left(\frac{D}{d_o}\right)^4-1\right]\left[0.584+\frac{0.0936}{(L_o/d_o)^{1.5}+0.225}\right]$	(3)
Reductions [5]	For upstream $\mathrm{Re}\leqslant 2500$: $K=\left[1.2+\frac{160}{\mathrm{Re}}\right]\left[\left(\frac{D_1}{D_2}\right)^4-1\right]$	(4)
	For upstream $\mathrm{Re}>2500$: $K=[0.6+0.48f]\left(\frac{D_1}{D_2}\right)^2\left[\left(\frac{D_1}{D_2}\right)^2-1\right]^2$	(5)
Expansions [5]	For upstream $\mathrm{Re}\leqslant 4000$: $K=2\left[1-\left(\frac{D_1}{D_2}\right)^4\right]$	(6)
	For upstream $\mathrm{Re}>4000$: $K=[1+0.8f]\left[1-\left(\frac{D_1}{D_2}\right)^2\right]^2$	(7)

(4)–(7) in Table 1 are based on the upstream conditions. D_1 represent the upstream pipe diameter and D_2 represent the downstream pipe diameter. d_o is the orifice throat diameter and L_o is the orifice length.

The thick orifice model should be used under the condition of $L_o/d_o\leqslant 5$; if $L_o/d_o>5$ the reduction and expansion model could be used to simulate the orifice.

3.1.3 Oil Nozzle. The flow through oil nozzle could be described using the method referenced in literature [4]. It treated the oil nozzle flow as the incompressible noncavitating fluid through an orifice.

$$Q=\frac{C_d A_n}{(1-m^2)^{1/2}}\left(\frac{2\Delta P}{\rho}\right)^{1/2} \tag{7}$$

where $m=d_n^2/D^2$ and $A_n=\pi d_n^2/4$. C_d is the discharge coefficient. d_n is the diameter of the nozzle.

3.2 Pressurization Element. The gear pump used in the aero-engine lubrication system is treated as the pressurization element; the relationships between oil flow rate and pressure difference can be expressed as

$$\Delta P=P_1-P_2=\alpha+\beta Q^k \tag{8}$$

where α, β, and k are constants decided by the pump characteristic curves.

3.3 Special Element. When oil flows through the bearing chamber and gearbox, it not only lubricates the system components but also absorbs the heats generated by the component friction, transferred from the walls, leaked via the seals, and so on. So the oil temperature increases when oil flows through the bearing chamber and gearbox. In the lubrication system, the oil temperature at the inlet of the bearing chamber and gearbox should be limited in a certain range that could ensure that the system operates safely. For the purpose of recycling the used oil, the oil heat exchangers are assembled in the lubrication system.

When simulating the lubrication system, the heat exchange characteristics of oil flow through the bearing chamber, gear box, and heat exchanger are considered chiefly.

In GASLS, these three elements are treated as a special element. The special element is a type of general-purpose element that only represents the parameter correlations between the two nodes (element inlet and outlet). The characteristic correlation style might be specific equations, data tables, or curves. Usually, the characteristic equations, which could be used for direct calculation, are desired. But the characteristic data tables and curves are often used because the characteristic equations are difficult to provide. The data tables and curves could be used by interpolation while the system is simulating.

The special element could be used in the software once the correlations have been defined. The methods for obtaining the correlations are thermal analysis and experiment. At present, the thermal analysis research for these three elements has been done extensively all over the world [6–10].

The GASLS software still has a thermal analysis submodule for calculating the characteristic of the bearing chamber, gearbox, and heat exchangers. The user could use this module to gain the characteristic correlations for special elements.

3.4 Combined Element. The lubrication system is very complex, which consists of a group of flow branches. It makes the lubrication system calculating network complicated and difficult to solve. In order to resolve this problem the combined element is introduced.

The combined element is one element that you group together to perform an overall function within a network. For example, the sub-branch of the lubrication system could be treated as a combined element. Thus, if we use the combined elements to replace the sub-branches of the lubrication system, the whole network of the lubrication system could be simplified and the solution of the network becomes easy.

With system simulation, we should use the software to calculate the flow characteristics of sub-branches individually at first, and then define the characteristics to the combined element.

4 Simulation Example

The lubrication system of a specific aero-engine was numerical–simulated in GASLS.

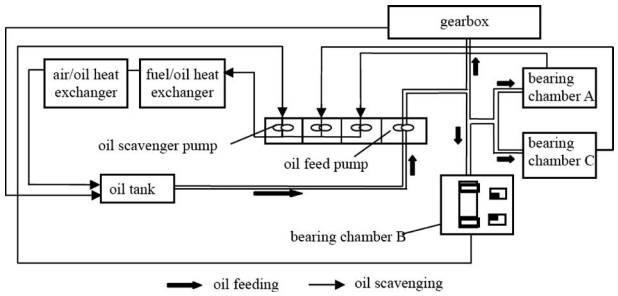

Fig. 1 Schematic of the lubrication system

4.1 Introduction of Lubrication System. The system simulated in the GASLS consists of three bearing chambers, two heat exchangers, and one gearbox. As shown in Fig. 1, the oil in the system is circulatory. The oil flows from the oil tank to the bearing chambers and gearbox through respective pipelines. The used oil pumped from the different bores flows through fuel/oil heat exchanger, and air/oil heat exchanger, and finally flows into the oil tank.

The purpose of the system simulation is to predict the distributions of the oil pressure, flow, and temperature.

4.2 Simulation.

4.2.1 Model Building. The software has a visual interface, and the lubrication system was modeled in GASLS, as shown in Fig. 2. In this model the oil supply sub-branches for all the chambers and gearboxes were modeled using combined elements. Figure 3 showed the real oil supply branch network of bearing chamber B. It can be seen from Fig. 2 that the combined elements could simplify the calculation network actually.

4.2.2 Element Characteristic for the Special Element. Before the lubrication system simulation the characteristic should be defined in the special element. The heat exchange characteristic of bearing chamber B, which is calculated by the thermal analysis module of the software, is partly given by the curves shown in Fig. 4. The fuel/oil heat exchanger characteristics obtained by experiment are given in Fig. 5.

4.3 Results. This simulation aims at detailed oil flow rates and temperature and pressure distributions. The simulation results are given below. The flow comparison between calculation results in GASLS and experimental data is given in Table 2, the oil temperature distribution of main nodes in the system is given in Table 3, and the pressure distribution is given in Table 4.

According to Tables 2–4, it indicts that the GASLS could simulate the oil flows, pressures, and temperatures in the aero-engine lubrication system. The comparison in Table 2 shows that the calculated results agree well with the experimental data.

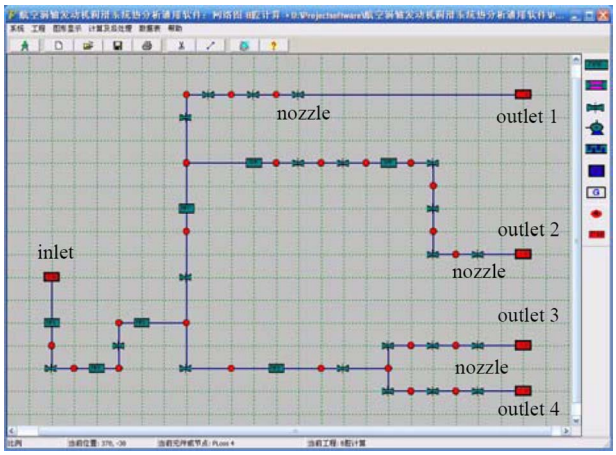

Fig. 3 Network of oil supply branch of bearing chamber B

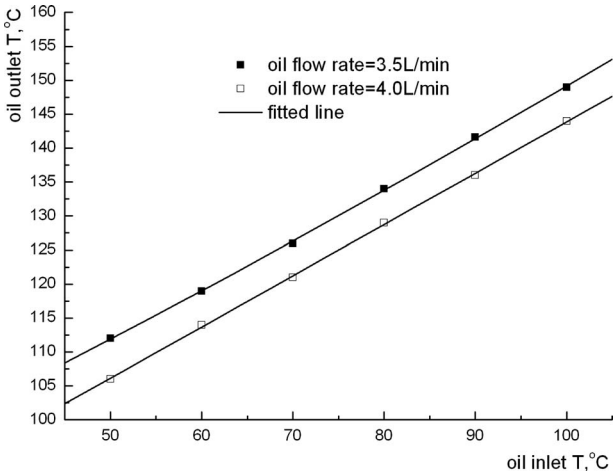

Fig. 4 Heat exchange characteristic of bearing chamber B

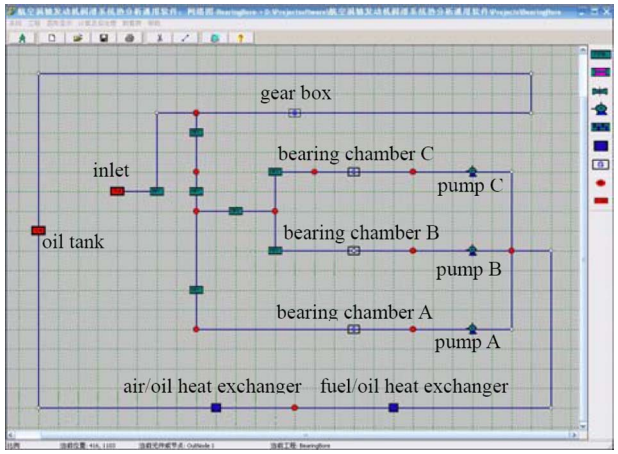

Fig. 2 The whole lubrication system calculation model in GASLS

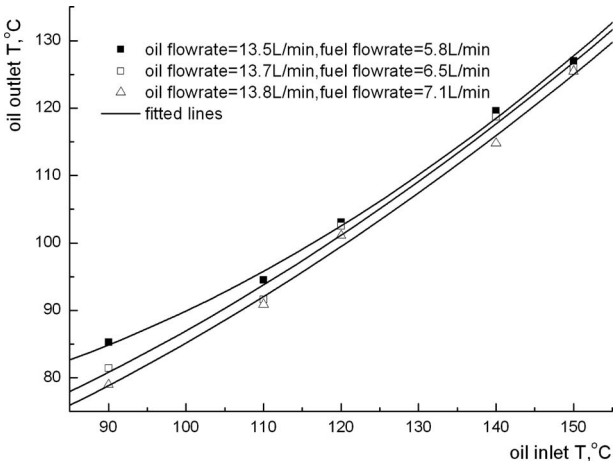

Fig. 5 Fuel/oil heat exchange characteristics with the inlet fuel temperature of 35°C

Table 2 Oil flow rate comparison between calculation results in GASLS and experimental data

Oil flow rate (l/min)	Expt.	Simulation result
Gearbox	1.5–1.8	1.5665
Bearing chamber A	6.5–7.5	6.3290
Bearing chamber B	3.5–4	3.6238
Bearing chamber C	3.8	3.6993

Table 3 Oil temperature distribution in the lubrication system

Node name	Simulation result (°C)
Oil tank	67.6
Bearing chamber A outlet	73.2
Bearing chamber B outlet	124.7
Bearing chamber C outlet	71.2
Fuel/oil heat exchanger inlet	86.4
Air/oil heat exchanger inlet	78.9

Table 4 Oil pressure distribution in the lubrication system

Node name	Simulation result (Pa)
Oil tank	113,225
Oil pressure at pipe inlet of bearing chamber A	471,791
Oil pressure at pipe inlet of bearing chamber B	485,232
Oil pressure at pipe inlet of bearing chamber C	472,897
Oil pressure at pipe inlet of gearbox	503,810

5 Conclusions

A software, GASLS, for simulating the aero-engine lubrication system is presented based on the flow network theory.

The combined element could be used to replace the subbranches of the lubrication system and could simplify the calculating network and improve calculation efficiency.

The case simulation for an aero-engine lubrication system proves that the software could calculate the distribution of oil flow, pressure, and temperature in the aero-engine lubrication system and might be helpful for the aero-engine lubrication system design and analysis.

Nomenclature

Q = volumetric flow rate (m^3/s)
P = pressure at points a and b (N/m^2)
ΔP = pressure difference between element inlet and outlet (N/m^2)
V = velocity (m/s)
Z = elevation from data (m)
A = area (m^2)
D = diameter (m)
d = diameter of orifice and nozzle (m)
L = length (m)
ρ = density of fluid (kg/m^3)
g = acceleration of gravity (m/s^2)
γ = ρg
Re = Reynolds number
f = friction factor
K = dimensionless coefficient
ε = absolute roughness (m)
h_w = frictional head loss (m)
C_d = discharge coefficient
α, β, k = constants

Subscripts

a, b = points in the pipeline
o = orifice
n = nozzle
1 = element upstream
2 = element downstream

References

[1] Majumdar, A. K., Bailey, J. W., Schallhorn, P. A., and Steadman, T., 1998, "A. Generalized Fluid System Simulation Program to Model Flow Distribution in Fluid Networks," AIAA Paper No. 98-3682.
[2] McAmis, R. W., Miller, J. T., Burdette, R. R., and Milleville, D. E., 1996, "Modeling Fluid Flow Networks," AIAA Paper No. 96-3120.
[3] Wu, D., 1996, "Network Algorithm of Internal Flow System," Biomed. Microdevices, **17**(6), pp. 653–657.
[4] Chun, S. M., 2003, "Network Analysis of an Engine Lubrication System," Tribol. Int., **36**(8), pp. 609–617.
[5] Hopper, W. B., 1988, "Calculate Head Loss Caused by Change in Pipe Size," Chem. Eng. (New York, NY), **95**(16), pp. 89–92.
[6] Ge, Z., Han, Z., Zhang, E., Li, G., and Xing, J., 2005, "Thermal Analysis of Aeroengine Bearing Compartment," Journal of Aerospace Power, **20**(3), pp. 483–486.
[7] Coe, H. H., Schuller, F. T., 1981, "Calculated and Experimental Data for a 118-mm Bore Roller Bearing to 3 Million DN," ASME J. Lubr. Technol., **103**, pp. 274–281.
[8] Flouros, M., 2005, "The Impact of Oil and Sealing Air Flow, Chamber Pressure, Rotor Speed, and Axial Load on the Power Consumption in an Aeroengine Bearing Chamber," ASME J. Eng. Gas Turbines Power, **127**, pp. 182–186.
[9] Changenet, C., Oviedo-Marlot, X., and Velex, P., 2006, "Power Loss Predictions in Geared Transmissions Using Thermal Networks-Applications to a Six-Speed Manual Gearbox," ASME J. Mech. Des., **128**, pp. 618–625.
[10] Zhang, Y., Su, H., Liu, Z., and Shen, Y., 2000, "Steady State Thermal Analysis of Planetary Transmission Systems," ACTA Aeronaut. Astronaut. Sinica, **21**(5), pp. 431–433.

Description of a Semi-Independent Time Discretization Methodology for a One-Dimensional Gas Dynamics Model

J. Galindo
e-mail: galindo@mot.upv.es

J. R. Serrano

F. J. Arnau

P. Piqueras

CMT-Motores Termicos,
Universidad Politecnica de Valencia,
Valencia 46022, Spain

Modeling has become an essential technique in design and optimization processes of internal combustion engines. As a consequence, the development of accurate modeling tools is, in this moment, an important research topic. In this paper, a gas-dynamics modeling tool is presented. The model is able to reproduce the global behavior of complete engines. This paper emphasizes an innovative feature: the independent time discretization of ducts. It is well known that 1D models solve the flow through the duct by means of finite difference methods in which a stability requirement limits the time step depending on the mesh size. Thus, the use of small ducts in some parts of the engine reduces the speed of the calculation. The model presented solves this limitation due to the independent calculation for each element. The different elements of the engine are calculated following their own stability criterion and a global manager of the model interconnects them. This new structure provides time saving of up to 50% depending on the engine configuration.
[DOI: 10.1115/1.2983015]

1 Introduction

Modeling is an important technique for the optimization of internal combustion engines (ICEs). The use of calculation models together with experimental tests are producing unquestionable successes due to the fact that both techniques complement each other [1,2]. Calculation models can be classified on the basis of their complexity as mean value or quasisteady models, filling and emptying models, one-dimensional (1D) wave-action models, and the three-dimensional calculation codes [3].

The reasonable computational cost of 1D codes allows for the calculation of whole internal combustion engines with all of their components [4]. Computational fluid dynamics (CFD) codes, which consider the three spatial dimensions, are only used to model single engine components in spite of their accuracy in comparison with 1D codes. Usually, the results of CFD codes are used as boundary conditions in 1D models when the one-dimensional hypothesis cannot be applied.

1D wave-action models [5] simplify the engine by means of ducts, where only one dimension is considered, and volumes where there can be considered mass accumulation and their properties are uniform in the entire element. Finally, nondimensional models are used to solve the connection between 1D and 0D elements.

Generally, these codes calculate every element (1D, 0D, and connections) of the engine at the same time step; only the cylinders are usually decoupled during the closed-cycle calculation. The time step must be fixed using stability criteria for each element. Usually the most restrictive elements from stability point of view are the ducts. When finite difference schemes are used, the Courant, Friedrichs and Lewy (CFL) stability condition represented by the following is enough to obtain stable results:

$$\Delta t < \frac{\Delta x}{a + |u|} \tag{1}$$

where Δt is the time step, Δx is the mesh size, a is the speed of the sound and u is the flow velocity.

It is well known that reducing the mesh size increases the accuracy of the results until convergence and stability limits are reached. However, the computational cost is also increased due to the complexity of engines, where the ducts' length can be very different. Thus, some ducts can require smaller meshes than others. Therefore, if all the ducts are set to the minimum time step, most of them are calculated with a smaller time step than that required by their stability criterion. This may cause an important waste of computational resources that does not lead to a significant accuracy improvement.

This paper presents a 1D gas-dynamics code, which includes a new methodology that calculates the engine ducts with a time step closer to their stability criteria limit. This new methodology reduces considerably the wasted time and does not damage the global accuracy.

2 Air Path Calculation

This section describes the different elements of the model that form the air path. Depending on the spatial dimensions considered the elements can be grouped in zero-dimensional elements (all properties are constant along the entry element) and one-dimensional elements (thermofluid dynamics properties vary versus the length of the element). Finally, boundary conditions complete the air path connecting the 0D and 1D elements.

2.1 1D Elements. Unsteady flow occurring in engine pipes can be considered to be, essentially, one dimensional in nature. This happens when the length to diameter (L/D) ratio of the pipes are large enough and thus the turbulent flow is fully developed. Even assuming that the fluid is inviscid, i.e., that the gas is sufficiently "dilute" for the internal stresses to be ignored, the equations defining unsteady flow in one dimension do not have general analytical solution and numerical techniques are needed. If the viscosity is not considered, the one-dimensional governing equations for unsteady flow form a nonhomoentropic hyperbolic system as follows:

$$\frac{\partial \mathbf{W}}{\partial t} + \frac{\partial \mathbf{F}}{\partial x} + \mathbf{C}_1 + \mathbf{C}_2 = 0 \tag{2}$$

where $\mathbf{W}$ is the array of field variable, $\mathbf{F}$ is the flux array, $\mathbf{C}$ is the source array, x is the spatial coordinate, and t is the time.

Governing equations forming the system represented by Eq. (2) include the mass, the momentum, and the energy conservation equations. Besides, if chemical species tracking is considered, new mass conservation equations must be added. The total number of equations is three plus the number of chemical species minus one. The last chemical specie is calculated by an additional equation, Eq. (3), due to the fact that the total mass fraction has to be equal to one.

Contributed by the Internal Combustion Engine Division of ASME for publication in the JOURNAL OF ENGINEERING FOR GAS TURBINES AND POWER. Manuscript received April 8, 2008; final manuscript received July 9, 2008; published online February 10, 2009. Review conducted by Dilip R. Ballal. Paper presented at the 2008 Spring Conference of the ASME Internal Combustion Engine Division (ICES2008), Chicago, IL, April 27–30, 2008.

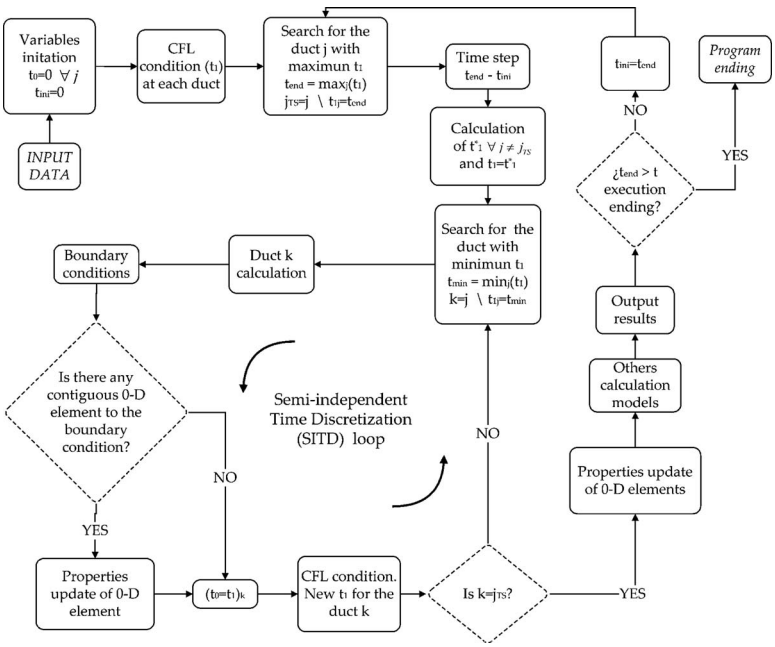

Fig. 1 SITD calculation loops

$$Y_N = 1 - \sum_{j=1}^{N-1} Y_j \tag{3}$$

The gas-dynamics model presented in this work uses finite difference schemes [6] to solve Eq. (2).

2.2 0D Elements. If the thermofluid dynamics properties of an engine element can be considered constant in all its volume at every time step, it is solved as a zero-dimensional element. 0D elements are solved as thermodynamic open systems using a filling and emptying model. When no chemical species tracking is considered, two equations are needed to solve them [7]. The first equation represents the mass conservation as a function of the flow through inlets and outlets. The second equation governing the fluid dynamics of a 0D element is the first law of thermodynamics for open systems as follows:

$$d(m_e e_e) = \delta q_e + \delta w_e + \sum \left(h_{\text{in}} + \frac{u_{\text{in}}^2}{2} \right) dm_{\text{in}} - \sum \left(h_{\text{out}} + \frac{u_{\text{out}}^2}{2} \right) dm_{\text{out}} \tag{4}$$

where the subscript e represents the 0D element, e_e is the internal energy of the element, q_e is the heat transfer, w_e is the mechanical work produced, h is the inlet or outlet enthalpy, and u is the inlet or outlet gas velocity. The chemical species tracking calculation only increases the number of mass conservation equations considered. Plenums, volumetric compressors, and engine cylinders are solved as 0D elements.

2.3 Boundary Conditions. The model assumes that the boundaries behave in a quasisteady manner and respond instantaneously to changes in incident conditions. The ducts, ends are solved, as proposed by Benson [5], using the method of characteristics. The method of characteristics uses the following well-known Riemman variables to solve the properties of the gas at the end of the ducts:

$$\lambda_{\text{in}} = A - \frac{\gamma - 1}{2} U, \quad \lambda_{\text{out}} = A + \frac{\gamma - 1}{2} U \tag{5}$$

where $A = a/a_{\text{ref}}$ and $U = u/a_{\text{ref}}$. Subscript in refers to the characteristic coming from the boundary (inlet flow) and out the characteristic coming from the duct (outlet flow). The flow is considered to be positive if it flows out of the pipe. When nonhomentropic flow is considered, an energy equation in addition to the wave characteristics given by Eq. (5) is required. This extra equation introduces an additional characteristic called a pathline as follows:

$$\frac{p}{p_{\text{ref}}} = \left(\frac{A}{A_A} \right)^{2\gamma/(\gamma-1)} \tag{6}$$

where a parameter $A_A = a_A/a_{\text{ref}}$ is introduced to define the entropy level in the duct. The parameter a_A represents the speed of sound, which would be reached at the arbitrary reference pressure due to an isentropic change of state from the pressure, p. The boundary condition is solved when the parameters λ_{in}, λ_{out}, and A_A are known at the end of the pipe. When an outflow boundary is calculated, λ_{out} and A_A are obtained from the duct. In case of inflow, only λ_{out} is known. In both cases the other parameters are obtained depending on the boundary.

3 SITD

Most of the existing commercial codes are characterized by a program layout that sets the time step to the most restrictive time discretization. It is called hereinafter common time discretization (CTD). This approach generates high time consumption when very short pipes are calculated in the engine layout or the mesh size is reduced in some particular ducts. To prevent the calculation time from increasing when spatial mesh size in some particular pipes of the engine layout is reduced the gas-dynamics model presented enables an independent time discretization (ITD) for each duct. This new calculation approach allows the spatial mesh size reduction in specific ducts without noticeably damaging the global calculation time and achieving a greater accuracy.

This new approach follows the flowchart presented in Fig. 1. The model calculates all the ducts, the boundary conditions, and the 0D elements connected to the duct according to their CFL stability criterion at least once at every time step. This is represented by the inner loop in Fig. 1, which is named as "independent time discretization loop." The main loop controls the well-running of the execution.

Two different time scales are used to control the execution of the model. On the one hand, t_0 and t_1 represent the initial and the

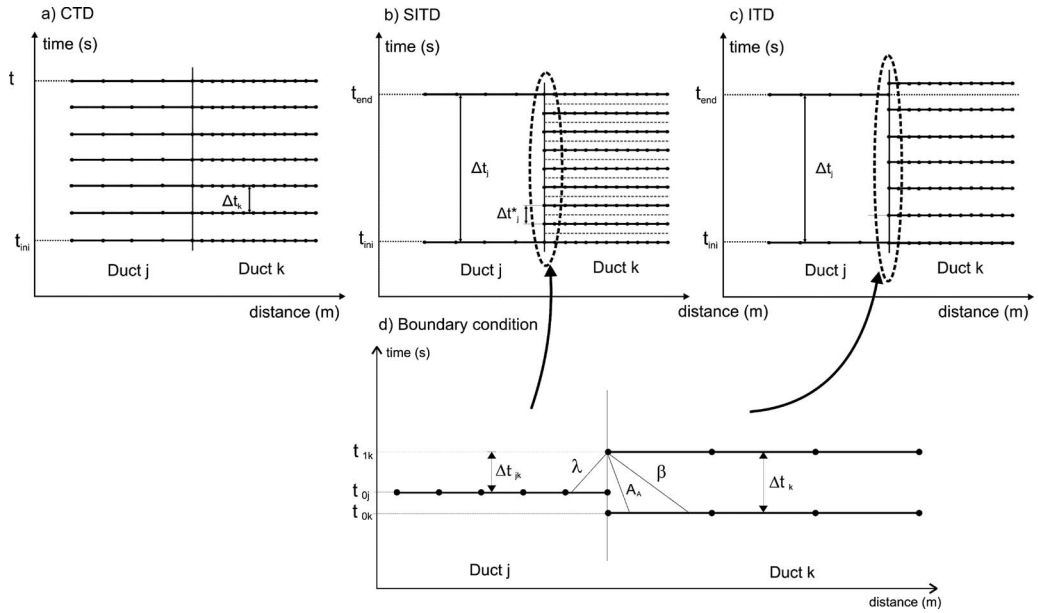

Fig. 2 Comparison of time marching between CTD, ITD and SITD calculation approaches. Boundary condition resolution.

final calculation time of each duct of the engine. On the other hand, t_{ini} and t_{end} represent the initial and the final time of the simulation time step, respectively. At the beginning of the simulation, t_{end} is obtained as the maximum t_1, which guarantees that all ducts will be calculated once during one simulation time step. Each element must divide the time step $(t_{end}-t_{ini})$ according to its own stability criteria.

The duct with the minimum t_1 is calculated first. In order to obtain the most uniform time marching a new t_1^* will be calculated as follows:

$$t_1^* = t_0 + (t_{end} - t_{ini})/2^n \tag{7}$$

where n is the smallest integer that ensures $t_1^* < t_1$ a 2-base has been chosen to minimize the differences between t_1 and t_1^*. Due to these small differences the approach with t_1^* is preferred to be called semi-independent time discretization (SITD) to distinguish between the purely ITD that calculates t_1 directly from the CFL criterion. Moreover, its boundary conditions and the 0D elements connected to it are solved, assuming that the flow conditions of the other ducts connected to the 0D element have not changed since the last time that they were calculated. Finally, $t_0 = t_1^*$ and t_1 is updated using the CFL stability criterion. Figure 2 shows a comparison between CTD, SITD, and ITD respectively. In the case of SITD, duct k shows a time discretization that results from the application of Eq. (7) with $n=3$. The time marching to be applied when $n=4$ is plotted with a dotted line.

Next, the model searches the duct with the minimum t_1 (it can be the same duct) and repeats the process until all ducts are solved once. At this moment the independent time discretization loop is finished, all the elements are updated at t_{end}, and the main loop checks if the simulation has reached the time set as calculation end. On the contrary, if the simulation has not finished, the model searches the duct with the maximum t_1 in order to establish the new time step. At this moment the SITD loop begins again and the process is repeated until the calculation end is reached.

As it was explained before, the boundary conditions are solved applying the method of characteristics. The boundary conditions can be classified into two different groups.

The first group represents connections between several different ducts or 1D elements. This group includes boundary conditions such as sudden area changes, multipipe junction, or adiabatic pressure loss. In this case, the boundary conditions belong to several ducts. Thus, every time the boundary condition is solved, it has to be taken into account that each duct connected to it is at a different calculation time. Therefore, the Riemann variables and the entrophy level coming from the ducts to the boundary condition must be calculated at the time corresponding to its duct. This situation is represented at the bottom of Fig. 2, which shows the resolution of the case in which two ducts are connected. Every point represents a node of the duct; a gas velocity from right to left is assumed in the pipe.

Figure 2 represents the solution of the duct k. Its calculation time is t_{0k} and the aim is to advance the calculation until the time t_{1k}. Once the internal nodes of the duct are calculated, the boundary conditions need to be solved.

In order to solve the boundary condition, the origin of the three characteristic lines has to be found, so that at the calculation time t_{1k} they all are passing through the extreme node of the duct k. The boundary condition between the ducts needs the information from the entropy level and β provided by the solution of duct k at time t_{0k} and information from λ, which is provided by duct j at the calculation time t_{0j}.

The second group includes those boundary conditions in which a duct is connected to a 0D element. The boundary condition in the pipe end of a duct discharging flow into a plenum, cylinder, or any other 0D engine element is solved from the characteristic lines, λ, β, the entropy level, and the output and input mass flows. There is no difference in the way the boundary condition is solved with regard to the original program layout, CTD. However, a difference arises from the calculations carried out to get the thermodynamic properties in the 0D element. Every time a duct contiguous to the 0D element is solved, the 0D element has to be updated to the current time of this duct. In order to carry out the energy and mass balances in the 0D element, every pipe end connected to the 0D element has to be considered. This is done using the last calculated results for every boundary condition, assuming the information is frozen since the last time which all were calculated until the current time, which is set by the last calculated boundary condition connected to the 0D element.

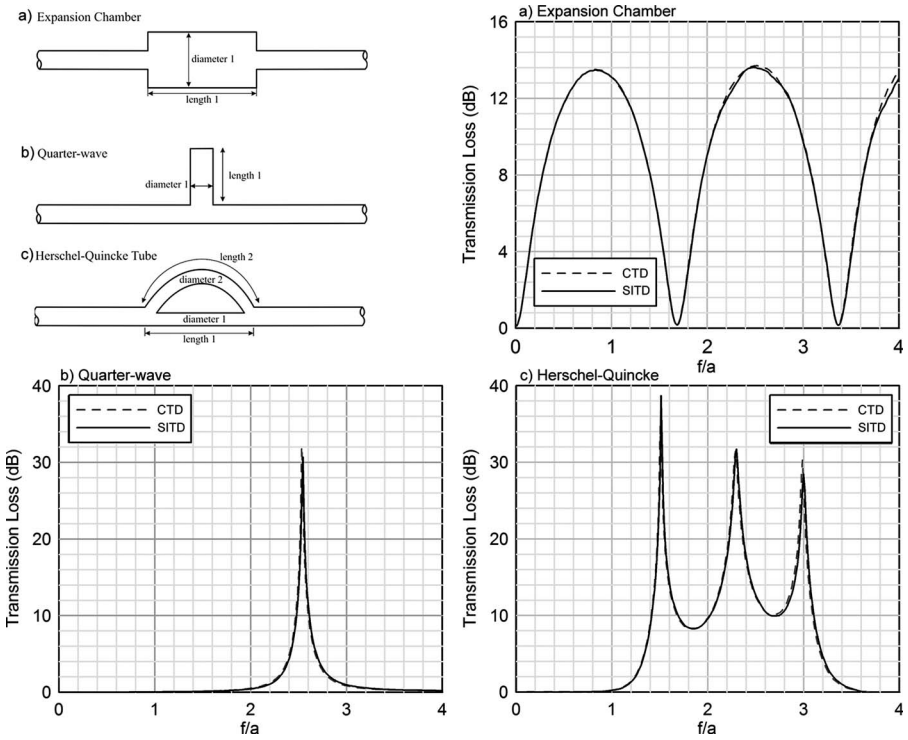

Fig. 3 Frequency response of three different silencers

4 Results

This section shows some application examples. The results of this new methodology presented (SITD) are compared to those obtained with the old one, which calculates all the elements of the engine with the most restrictive time step (CTD).

In order to validate the new methodology without external interferences three simple but representative geometries with well-known acoustic behavior have been calculated with both methodologies: (i) expansion chamber, in which the influence of the muffler volume and the effects associated with transmission and reflection at area discontinuities are present, (ii) quarter wave, and (iii) Herschel–Quincke ducts, where phenomena related with wave interference between parallel branches may be studied.

The transmission loss has been chosen as a suitable magnitude representative of the frequency response of a given muffler. It is defined in terms of a logarithmic ratio between the acoustic power incident on the muffler and the acoustic power transmitted by the muffler. In order to compute this magnitude, an impulsive excitation has been assumed at the inlet of the upstream duct and an anechoic termination has been considered at the outlet [8].

The mesh size of the ducts that form each geometry is 5 mm. The ducts upstream and downstream of the element have 51 mm of diameter, 500 mm of length, and the mesh size is 20 mm. The results shown in this paper have been obtained using a total variation diminishing (TVD) scheme to solve conservation laws in the ducts.

In Fig. 3 the transmission loss of the three elements, computed by both methodologies, is shown as a function of the ratio of the frequency f to the speed of sound a. It is apparent that both methodologies provide substantially the same results in the $f/a < 4\ \mathrm{m}^{-1}$ range. Only for the expansion chamber (Fig. 3(a)) at frequencies above $f/a \sim 3.8\ \mathrm{m}^{-1}$ (that corresponds to the cut-off frequency of the first transversal mode) 3 shows some differences.

The results obtained with the quarter-wave and with the Herschel–Quincke tube confirm the previous comments. Calculating the elements at different time steps does not introduce interferences in the results and below reasonable frequencies for engine analysis the frequency response is similar.

In order to remark the real benefits in time saving of the new methodology a complete engine has been modeled. The validation has been carried out with a 2.0 liter, four cylinder turbocharged high speed diesel engine with four valves per cylinder, intercooler, and cooled exhaust gas recirculation (EGR).

The engine has been modeled using common time discretization and independent time discretization in order to compare time consumption. The calculation has been carried out at a steady state operation considering both the transport of two chemical species and a more complex configuration with eight chemical species transport. The mesh size has been chosen according to the pipes' length. Smaller mesh sizes have been used in ducts with more critical conditions such as intake and exhaust ports.

The pressure at some locations in the engine has been compared to experimental data. Figure 4 shows a comparison of pressure in the intake port, exhaust port, and exhaust manifold (dash) versus experimental data at 2500 rpm (solid) for both methodologies and a good agreement can be observed between the modeled and measured pressure traces.

Finally, in this example, the new methodology consumes half-time (both with two and eight chemical species) but the reduction is not always the same and it depends on the variety of mesh sizes used in the model.

5 Conclusions

In this model a 1D gas-dynamics code has been described. This model is able to calculate the different elements that can appear in an engine (cylinders, turbocharger, intercooler, etc.). The model uses explicite finite difference techniques to solve the flow through the pipes and the method of characteristics to calculate the boundaries. The most remarkable feature of the presented code is the new methodology that calculates each element with its own

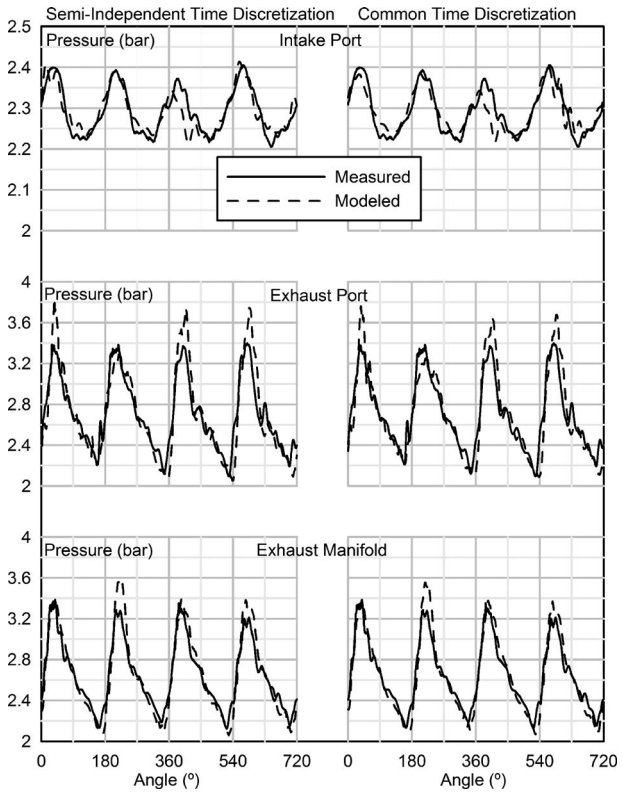

Fig. 4 Modeled versus measured using CTD and SITD methodologies

time step according to the stability criterion. In most 1D codes the time step is common for all the pipes and it is calculated as the smallest time step among the pipes. This leads to high computation time if there are very different time steps. The performance of this new methodology, for the gas-dynamics modeling of internal combustion engines, has been tested and compared to the results obtained using the most restrictive time step for all the elements.

The methodology has been tested with simple geometries in order to see if the interaction between element at different times could introduce interferences in the frequency domain. It has been demonstrated that the new code does not introduce any interference inside the frequency range analyzed. As a conclusion, the main objective of this methodology has been achieved. In engine modeling, where the length of the ducts can be very different, the computational time can be reduced considerably, without damaging the accuracy. Furthermore, this technique can be applied to any explicit 1D scheme and this would increase the productivity in engine development.

Acknowledgment

This work has been partially supported by the European Project "Innovative particle trap system for future diesel combustion concepts" Contract No. FP6-031410.

References

[1] Morel, T., Fleming, M. F., and Lapointe, L. A., 1990, "Characterization of Manifold Dynamics in the Chrysler 2.2 si Engine by Measurements and Simulation," SAE Technical Paper No. 900678.
[2] Silvestri, J., and Morel, T., 1994, "Study of Intake System Wave Dynamics and Acoustics by Simulation and Experiment," SAE Technical Paper No. 940206.
[3] Ramos, J. I., 1989, *Internal Combustion Engine Modelling*, Hemisphere, New York.
[4] Winterbone, D. E., and Pearson, R. J., 2000, *Theory of Engine Manifold Design*, Professional Engineering, London, UK.
[5] Benson, R. S., 1982, *The Thermodynamics and Gas Dynamics of Internal Combustion Engines*, Vol. 1, Clarendon, Oxford.
[6] Payri, F., Galindo, J., Serrano, J. R., and Arnau, F. J., 2004, "Analysis of Numerical Methods to Solve One-Dimensional Fluid-Dynamic Governing Equations Under Impulsive Flow in Tapered Ducts," Int. J. Mech. Sci., **46**, 981–1004.
[7] Payri, F., Desantes, J. M., and Corberán, J. M., 1988, "A Quasi-Steady Model on Gas Exchange Process, Some Results," *Motor Sympo'88*, Praha.
[8] Broatch, A., Serrano, J. R., Arnau, F. J., and Moya, D., 2007, "Time-Domain Computation of Muffler Frequency Response: Comparison of Different Numerical Schemes," J. Sound Vib., **305**, pp. 333–347.

Application of Exhaust Gas Recirculation in a DLN F-Class Combustion System for Postcombustion Carbon Capture

Ahmed M. ElKady

Andrei Evulet

Anthony Brand

General Electric,
Global Research Center,
Niskayuna, NY 12309

Tord Peter Ursin

Arne Lynghjem

StatoilHydro ASA,
Technology and New Energy,
N-4035 Stavanger, Norway

This paper describes experimental work performed at General Electric, Global Research Center to evaluate the performance and understand the risks of using dry low NO_x (DLN) technologies in exhaust gas recirculation (EGR) conditions. Exhaust gas recirculation is viewed as an enabling technology for increasing the CO_2 concentration of the flue gas while decreasing the volume of the postcombustion separation plant and therefore allowing a significant reduction in CO_2 capture cost. A research combustor was developed for exploring the performance of nozzles operating in low O_2 environment at representative pressures and temperatures. A series of experiments in a visually accessible test rig have been performed at gas turbine pressures and temperatures, in which inert gases such as N_2/CO_2 were used to vitiate the fresh air to the levels determined by cycle models. Moreover, the paper discusses experimental work performed using a DLN nozzle used in GE's F-class heavy-duty gas turbines. Experimental results using a research combustor operating in a partially premixed mode include the effect of EGR on operability, efficiency, and emission performance under conditions of up to 40% EGR. Experiments performed in a fully premixed mode using a DLN single nozzle combustor revealed that further reductions in NO_x could be achieved while at the same time still complying with CO emissions. While most existing studies concentrate on limitations related to the minimum oxygen concentration (MOC) at the combustor exit, we report the importance of CO_2 levels in the oxidizer. This limitation is as important as the MOC, and it varies with the pressure and firing temperatures. [DOI: 10.1115/1.2982158]

1 Introduction

In order to capture and sequester the CO_2 emitted from natural gas based power-generation plants, three different main concept categories can be considered [1,2]. Postcombustion carbon capture is viewed as a short-term plan with low risk to capture CO_2 produced in gas-fired power plants. In this case, separation from the exhaust gas of a standard gas turbine combined cycle (CC) can be achieved with a direct contact between exhaust gas and absorbent, e.g., 30% mono-ethanolamine (MEA).

The CO_2 separation process results in significant penalties associated with the efficiency of the plant. It is important therefore to minimize the energy (work) consumed for CO_2 capture. Today's state-of-the-art amine separation systems rely on gas separation processes with operational and capital costs dependent on the concentration of the CO_2 in the flue gas and its volumetric flow. A significant reduction in CO_2 separation work results from increasing the CO_2 concentration in the flue gas. EGR can reduce the capital cost of CO_2 separation units by decreasing the flow of flue gases for treatment while increasing the CO_2 concentration. Further promising advanced postcombustion capture concepts, which are favored by EGR, have been identified [3].

The combustion risks associated with EGR for gas turbines are the changes in operability, emissions (NO_x,CO) in low-oxygen air, heat transfer with the altered working fluid, and possible combustion efficiency penalties associated with combustion completion. Unfortunately very little data exist to quantify the assumed risks associated with EGR for combustion, particularly at the elevated temperatures and pressures representative of gas turbines. Existing data are limited to experiments performed at atmospheric pressures and ambient temperatures or with diffusion flames (e.g., boiler burners) or models and simulations of low-oxygen combustors. Pressure effects are very evident and important, yet omitted in most of the previous studies.

A detailed discussion about literature work can be found in Ref. [4]. It is apparent that there is a need for experiments at representative pressures and temperatures utilizing premixed combustion systems such as GE's DLN or dry low emission (DLE) systems. One can thus determine the effects of EGR on combustor operability. To eliminate the coupling between EGR and flame temperature, experiments reported here are at a fixed flame temperature rather than at fixed fuel mass flow rates. Such conditions are also representative of the most likely operating conditions of an EGR combustor.

2 Experimental Setup

A research combustion premixer rig was developed for the experimental evaluation of combustion with EGR, as described in Fig. 1. The DLN premixer is a research nozzle, which is slightly modified from the version used in a gas turbine combustor. The nozzle has the capability of operating in partially and fully premixed modes via two independent fuel supply systems (pilot and premix). The ability to operate in diffusion partially premixed (or piloted) or fully premixed modes allows an investigation of the operability of this combustor in various conditions of pressure, temperature, and oxygen content. The experimental facility used in this study was a high-pressure single-nozzle combustor. The test section of the combustor is housed within a pressure vessel. The combustor test section is a square section at the upstream end to facilitate the attachment of flat viewing ports for optical access.

Preheated air and natural gas fuel are supplied to the test cell by facility systems. The exhaust is directed into the facility exhaust tunnel. Sample gases are collected from the end of the metallic liner at a single position and directed to the emission analyzer where NO_x, O_2, CO_2, and CO measurements are performed after samples are cooled and dried. All critical pressures, temperatures, and flows are measured within the test cell. The inlet oxidizer ($air/CO_2/N_2$) conditions for this experiment were $T_{inlet} \approx 700$ K and $P_{inlet} \approx 10$ atm.

A gas blending station was utilized for this test to provide a constant flow of a mixture of N_2 and CO_2 to the fresh preheated air supply in order to mimic the EGR oxidizer composition into the combustor. The fresh air was overheated before being mixed with the N_2/CO_2 mixture such that the overall oxidizer inlet tem-

Contributed by the International Gas Turbine Institute of ASME for publication in the JOURNAL OF ENGINEERING FOR GAS TURBINES AND POWER. Manuscript received April 7, 2008; final manuscript received July 31, 2008; published online February 19, 2009. Review conducted by Dilip R. Ballal. Paper presented at the ASME Turbo Expo 2008: Land, Sea and Air (GT2008), Berlin, Germany, June 9–13, 2008.

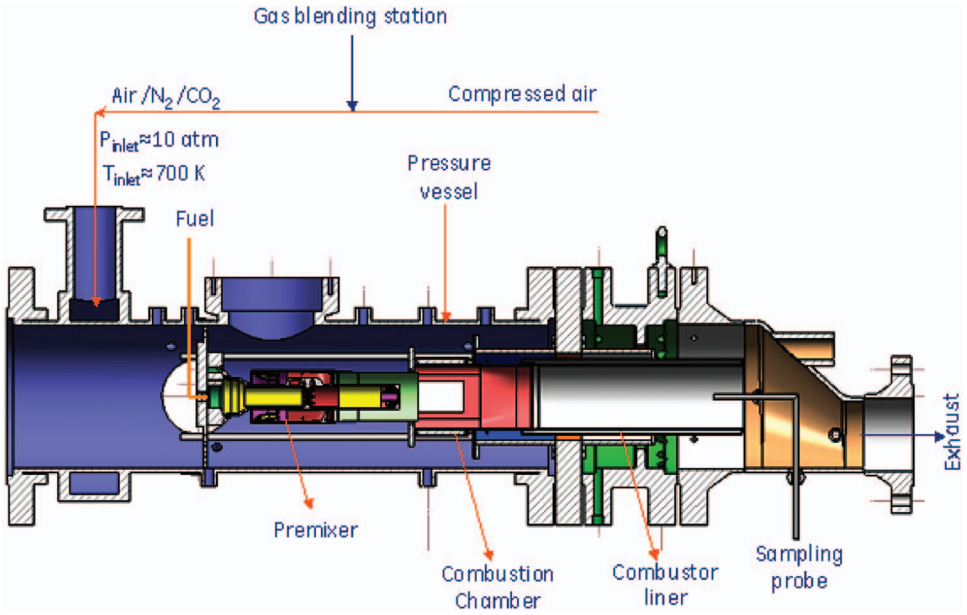

Fig. 1 Experiment setup

perature remain at 700 K. Results presented will focus on the case of 35% EGR, which corresponds to an oxidizer composition of 3% CO_2 and 17% O_2 balanced with N_2. In this paper we do not discuss the effect of the addition of minor species such as CO and NO_x to the oxidizer mixture. Here we attempted to isolate the kinetics of these species when added to the oxidizer from the effect of EGR on the production/destruction of CO and NO_x. This study, using only CO_2/N_2 as the recycled gases, will serve as a baseline for kinetics modeling validation and development. In addition, this baseline study will serve in the quantification of NO_x reburn and CO destruction in the flame zone when these minor species are added in a later study. Those experiments at pressure with minor species will be discussed in another publication. All tests were performed under the assumption that water is condensed out of the exhaust gas, which is cleaned before recirculation. This is commonly referred to as a "cold EGR."

Ignition of the combustor is achieved via a H_2 fueled torch placed upstream of the premixer. Once the correct fuel and airflows are established, the torch is ignited for a short period, enough to ignite the downstream primary zone mixture of fuel and oxidizer. At the exit from the rig, exhaust gases are quenched using water sprays, and a backpressure valve is used to control the pressure drop across the rig. After stabilization of the flame, a sweep of fuel-to-air ratios is performed to determine baseline emissions and performance; the gas blending system is then used to add the required amount of inerts to the combustion air, e.g., 15–21% O_2 balanced by N_2/CO_2.

3 Results and Discussions

Flame temperatures reported are based on O_2 levels measured at the probe. These values were compared with the thermodynamic equilibrium temperatures, and good agreement was found. In addition, flame temperatures based on the flows of air and natural gas (equivalence ratios) and airflow-splits (combustion versus bypass/cooling) also show good agreement. Temperatures at the inlet of the combustor varied somewhat due to the addition of the inerts, which were generally much colder than the main air stream. As a countermeasure the fresh air preheater was set at higher temperatures in order to obtain the correct temperatures at the inlet of the premixer after being mixed with the inerts in the head end of the rig. Since the percentage of EGR is also a function of the flame temperature, it is too difficult to compare results for a wide range of temperatures on an equal basis. Thus, we selected to present the data in the relative flame temperature range of 0.95–1.05, in which the change in EGR percentage in the oxidizer due to the change in flame temperature could be neglected. In the following pages, all data are reported at flame temperatures relative to a predetermined reference temperature, typical of F-class combustor flame temperature.

3.1 Flame Stability. Flame stability limits narrow with EGR utilized in a DLN combustor system operating in a fully premixed mode. To keep flame stability margins similar to the baseline engine (running with 21% O_2), in some cases, a pilot (diffusion) fuel was added in a small percentage of the total fuel mass flow. In this case the flame was stable even with the low levels of O_2 tested. The lean blow-out (LBO) varied with the percentage pilot, and it worsened, as expected, in a fully premixed operation as O_2 levels extremely decreased. With any amount of pilot, the vitiated air operation remained highly operable with highly improved turndown.

3.2 CO_2 Emissions. The main goal of this work was to explore the technology operability and efficiency of the DLN premixed combustion with EGR. At the same time, the goal was to demonstrate that high levels of CO_2 may be achieved in the combustor, thus enabling a CO_2 capture plant to operate with minimum losses in a postcombustion CO_2 capture scenario.

Figure 2 compares experimental data (symbols) with equilibrium calculations (curves). The good agreement between experimental data and equilibrium calculations indicates that the emissions were accurately measured and the sampling was representative of the combustor exhaust. This good agreement is also an indication of complete combustion in this flame temperature range at 35% EGR. Experimental data demonstrate that measured CO_2 levels of more than 8% are achievable in the primary zone of the combustor for large EGR%. This, as well as the achievement of low levels of O_2 resulting from combustion with EGR, was successfully demonstrated. Moreover it confirms the CO_2 levels expected as a function of flame temperatures, where clearly the levels of EGR more than 35% will achieve the 10% CO_2 level at a flame temperature greater than 1900 K. In addition, the 40% EGR at temperatures greater than 1870 K would also exceed 10% CO_2.

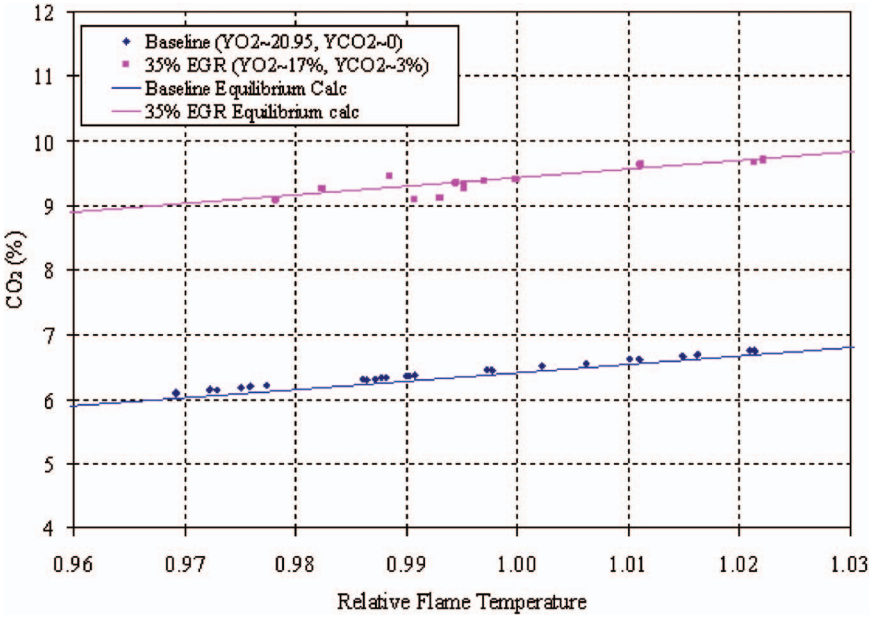

Fig. 2 Exhaust CO_2 as a function of flame temperature

3.3 O_2 Levels. From Fig. 3, it can be seen that there is good agreement between the O_2 levels measured (symbols), compared with the equilibrium calculations (curves). This demonstrates very reliable emission measurements at the analyzers.

Figure 3 also shows the lower oxygen levels obtained with increasing flame temperature and EGR levels. It can be seen that the lowest oxygen levels, which correspond to more complete oxygen depletion, correspond to higher fuel to oxidizer ratios and therefore high temperatures to below 4% O_2 concentration by volumes at 40% EGR. It should, however, be noted that these low levels also result in less consumption of CO, and therefore emissions of CO are higher due to the oxygen starvation of these flames. This changes for the better at higher pressures due to the fact that CO_2 dissociation is suppressed at higher pressures.

3.4 NO_x Emissions. According to previous literature, it is expected that NO_x emissions will be reduced with EGR. However there is a concern about presenting the NO_x data corrected to 15% oxygen; the question about the reality of NO_x reduction arises: is it because of the NO_x correction or is this a real reduction in NO_x due to the effect of EGR? The correction of NO_x to 15% oxygen using CH_4 as the fuel could be written as

$$NO_x|_{@15\%O_2} = NO_x|_{\text{dry-measured}} \cdot \left(\frac{0.2095 - 0.15}{0.2095 - X_{O_2}|_{\text{dry}}} \right) \quad (1)$$

where "dry" refers to measured gases in a dry basis, and X_{O_2} is the measured O_2 in the combustor exit. Utilizing EGR and using the above-mentioned equation indicates more benefit in NO_x reduc-

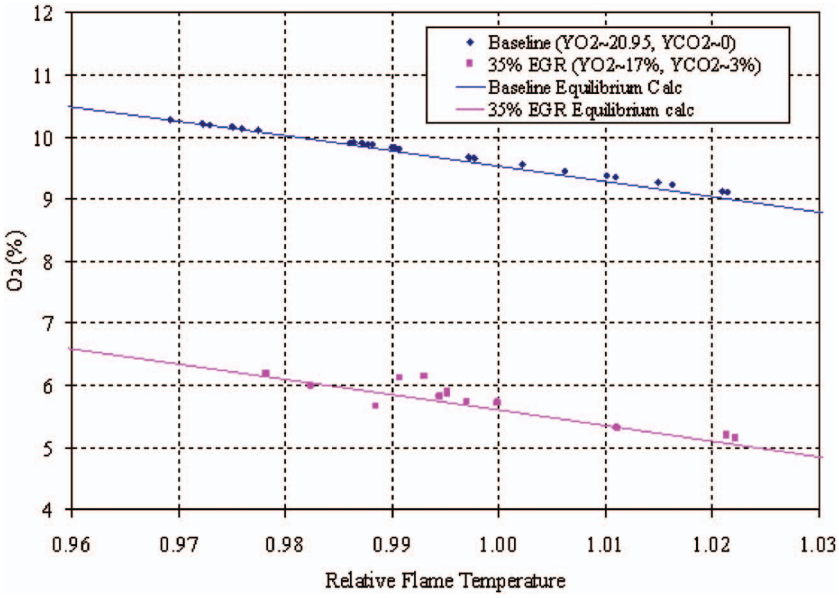

Fig. 3 Exhaust O_2 as a function of flame temperature

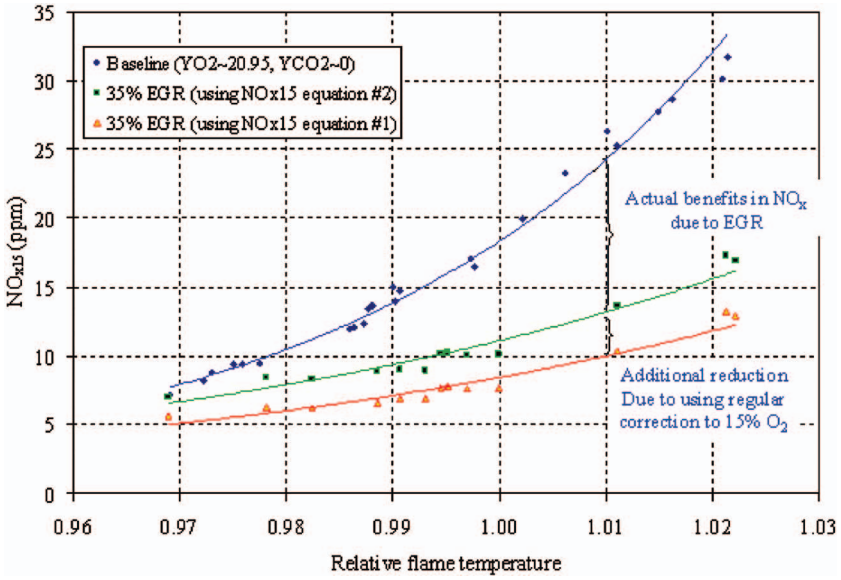

Fig. 4 Effect of EGR on NO_x as a function of flame temperature

tion just by vitiating the air. Since the term X_{O_2} will be reduced for EGR cases, the denominator will be larger than that of air combustion and will thus lead to an obvious reduction in NO_x corrected to 15% O_2 by just applying this formula. Also it is worth mentioning that this formula was derived based on air as the oxidizer. The authors thought about using the NO_x emission index based on the mass of fuel burned in the combustion process, which is defined as the ratio of the mass of NO_x to the mass of fuel burned by the combustion process,

$$\mathrm{EI}_{\mathrm{NO_x}} = \frac{\dot{m}_{\mathrm{NO_x emitted}}}{\dot{m}_{\mathrm{fuel,burned}}} (\mathrm{gm/kg\ \ fuel})$$

However, the selection of emission index was omitted in this study for the following reason: at fixed fuel mass flow burned in the combustion process, the flame temperature in the EGR mode will be reduced due to the change in the oxidizer specific heats and EGR will act partly as a diluent, so that the thermal effect on NO_x production cannot be isolated [4]. To keep the flame temperature fixed, the required fuel to be burned will need to increase to match the flame temperature in both cases, namely, the baseline and EGR cases, in which the denominator will increase in the EGR case.

To the authors' knowledge, one of the best ways to represent NO_x or CO in gas turbine combustion applications utilizing EGR could be the mass specific emissions based on the net power output, but since our focus is on the combustor performance the net power could not be quantified. As an alternative, to eliminate the effect of vitiating the air on NO_x correction, Eq. (1) was rederived based on an oxidizer composed of α O_2, β N_2, and γCO_2 (instead of air) for a hydrocarbon fuel C_xH_y,

$$\mathrm{C_xH_y} + a\left(\mathrm{O_2} + \frac{\beta}{\alpha}\mathrm{N_2} + \frac{\gamma}{\alpha}\mathrm{CO_2}\right) \rightarrow \left(x + a\frac{\gamma}{\alpha}\right)\mathrm{CO_2} + \frac{y}{2}\mathrm{H_2O} + b\mathrm{O_2} + a\frac{\beta}{\alpha}\mathrm{N_2} + \mathrm{trace\ \ species}$$

where α, β, and γ are mole fractions of O_2, N_2, and CO_2, respectively. For a hydrocarbon fuel C_xH_y and an oxidizer generally composed of $O_2/CO_2/N_2$, the NO_x correction to 15% O_2 is presented as

$$\mathrm{NO_x}|_{@15\%\mathrm{O_2}} = \mathrm{NO_x}|_{\mathrm{dry\text{-}measured}} \cdot \left(0.0595 \frac{\left[\dfrac{x + \frac{y}{4}(1 - X_{\mathrm{O_2}}|_{\mathrm{dry}})}{\alpha - X_{\mathrm{O_2}}|_{\mathrm{dry}}} - \frac{y}{4} \right]}{\left[\dfrac{x + \frac{y}{4}(1 - 0.15)}{0.2095 - 0.15} - \frac{y}{4} \right]} \right) \quad (2)$$

For CH_4 as a fuel, the above equation reduces to

$$\mathrm{NO_x}|_{@15\%\mathrm{O_2}} = \mathrm{NO_x}|_{\mathrm{dry\text{-}measured}} \cdot \left(0.033231 \frac{[2 - \alpha]}{(\alpha - X_{\mathrm{O_2}}|_{\mathrm{dry}})} \right) \quad (3)$$

Comparing Eqs. (1) and (3), it is obvious that Eq. (3) is more generalized for any oxidizer containing different compositions of $O_2/CO_2/N_2$, and it takes into account how much oxygen is consumed from the oxidizer, while Eq. (1) shows results based on how much O_2 was consumed from the air (which is a special case of Eq. (3)); this could still be valid for a cycle to cycle comparison but not for just studying the combustor as a control volume (separately).

The comparison between baseline operation (i.e., using air as the oxidizer) and operation with 35% EGR is presented in Fig. 4. It clearly shows a significant reduction in NO_x with EGR especially at higher flame temperatures. Using Eq. (1), lower NO_x is obtained due to the combined benefit of EGR and the correction to 15% O_2. Using Eq. (3) as a correction for NO_x represents the real reduction in NO_x using EGR. The results indicate that NO_x reduction is nonlinear with flame temperature. At higher flame temperatures, NO_x can be reduced by roughly 47% with EGR at temperatures of interest. This result indicates that EGR could be a major path for NO_x reduction when integrated to DLN combustion systems. NO_x emissions are strongly reduced via the reduction of oxygen in the combustion air. This can be explained by analyzing the thermal NO mechanism formed by the elementary reaction of O and N_2 ,

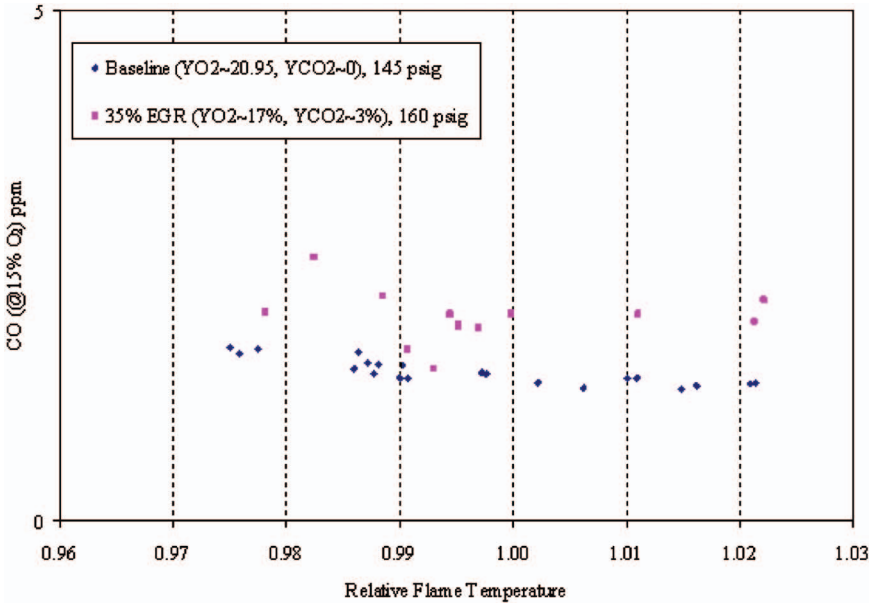

Fig. 5 Effect of EGR on CO as a function of flame temperature

$$O + N_2 \rightarrow NO + N \quad (4)$$

This reaction has very high activation energy due to the strong triple bond in the N_2 molecule, and it is sufficiently fast only at high temperatures [5]. Because of its small rate, this reaction is the rate-limiting step of the thermal mechanism. Another aspect of the NO_x reduction is the equilibrium calculated [O] atom. This radical, typically measured to be at superequilibrium in flames, affects the NO_x production, as described by the thermal mechanism. As a result of the addition of inerts to the incoming air and decreasing O_2 levels, the peak temperatures in the flame will be reduced. These results show that NO_x emissions strongly depend not only on the flame temperature but also on the concentration of O_2 in the combustion air.

It is important to mention that this experiment did not take into account any recycled NO_x, which might lead to a decrease in the total reduction in NO_x when EGR is deployed on a gas turbine. The upstream NO_x is not inert, and it will react in the flame zone and a portion of it could be burnt by the so-called NO_x reburn or NO_x destruction mechanism. Here we selected not to introduce these minor species as part of the oxidizer in order to perform a baseline study in which the effect of minor species addition could be eliminated. Hence, we concentrate on the effect of EGR alone on the production of these species. This study will be of paramount importance to help quantify the effect of the addition of these species, an analysis that will be reported in a future paper. It will provide important information also for the purpose of kinetic modeling and its validations and improvements.

3.5 CO Emissions. Experimental data (with fully premixed operation) of CO emissions, corrected to 15% O_2 based on Eq. (3), are presented as a function of flame temperature in Fig. 5. Generally in the presence of EGR, at constant flame temperature, larger amounts of CO are expected. This may be due to (a) the dissociation of CO_2, as a constituent of the oxidizer, to CO in the flame zone; (b) the additional fuel needed to maintain a fixed flame temperature in the EGR case as compared with baseline combustion case due to the changes in the specific heat of the oxidizer; or (c) the lack of oxygen to complete the oxidation reaction to CO_2.

It has been determined that at high reacting temperatures, the principal CO oxidation reaction in hydrocarbon flames is

$$CO + OH \rightarrow CO_2 + H \quad (5)$$

When EGR is utilized, for this case about 3% CO_2 is present in the oxidizer. It is believed that this oxidizer, CO_2, does not only act as inert or diluent but may also participate in the reaction through the reversal of reaction (5) or may act as a third body for other reactions. A similar experiment (to be published) has been performed utilizing a premixed combustion system to study the effect of CO_2 as a constituent of the oxidizer. In this experiment the O_2 concentration was kept fixed, while the CO_2/N_2 ratio changed. The results of this experiment showed a pronounced effect of CO_2 in the oxidizer on CO emissions. This result coincides with previous literature, for example, Masri et al. [6], who investigated the chemical kinetic effects in diffusion flames of H_2/CO_2 fuel. They stated that CO_2 is not a passive diluent, and at low mixing rates, CO is formed mainly due to the reversal of Eq. (5). Numerical simulations by Liu et al. [7,8] showed that CO_2 added to either the fuel or the oxidizer side participates in chemical reactions. They also concluded that reactions $CO_2+H \rightarrow CO+H$ and $CO_2+CH \rightarrow HCO+CO$ were found to be responsible for the chemical effects of carbon dioxide addition.

3.6 Combustion Efficiency. The gas turbine combustor needs to operate at high combustion efficiency. The combustion efficiency can be measured based on the levels of unburnt hydrocarbons (e.g., methane) as well as on the incomplete burnout of CO, etc. Due to oxygen starvation and specific conditions, a gas turbine combustor designed for 21% O_2 air may not perform toward a complete oxidation reaction to CO_2 when operating in EGR conditions. Clearly this represents a concern when compared with the baseline case due to possible requirements to comply with the CO emissions. For this experiment CO emissions did not deviate much from the baseline case, and generally the combustion efficiency was almost the same as compared with the baseline case. It is expected that the combustion efficiency will be improved with increased pressure and/or lower levels of CO_2 in the oxidizer.

3.7 Combustion Dynamics. The acoustic instabilities were monitored during the test. When EGR is applied, dynamics was abated within the window of flame temperatures considered (hot tones.) Figure 6 presents the pressure fluctuation power spectral density function in both the baseline and EGR cases. The pressure

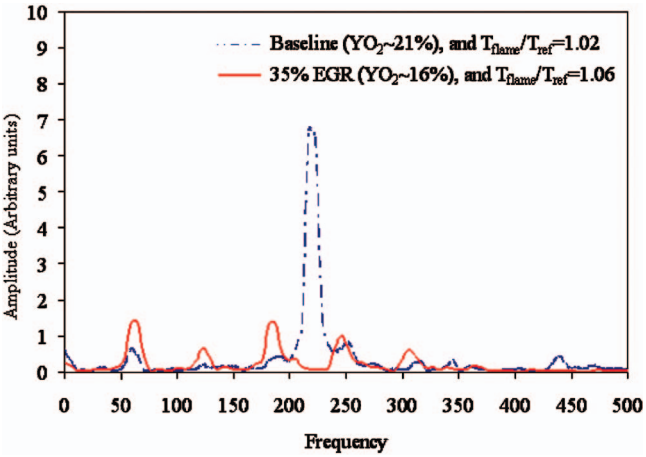

Fig. 6 Pressure fluctuation power spectrum in baseline and EGR cases

spectrum indicates a dominant hot tone dynamics mode near 240 Hz for the baseline case. When EGR is applied, this dynamics mode was eliminated. It is to be noted that the peaks at 60 Hz, 120 Hz, and 180 Hz represent line noise. During the course of the experiments, EGR demonstrated the benefit of reducing dynamics in the flame temperature range tested with or without pilot under vitiated air operation. This behavior could be attributed to changes in the heat release distribution zone as a result of oxygen starvation.

4 Summary

In summary, the presence of EGR leads to low-oxygen concentrations, which play a role in shifting as well as reducing the reaction rates, allowing for combustion to spread over a large region and to reduce the peak flame temperature, which is not in favor of the oxidation of CO to CO_2. On the contrary, reduction in oxygen levels combined with supplementary CO_2 in the oxidizer leads to changes in the heat release process via CO_2 dissociation.

The question to be asked is: from the emission point of view, what is the maximum acceptable EGR level for a gas turbine combustor? For the current lean premixed gas turbine research combustor, the emissions of concern are NO_x, CO, and unburned hydrocarbon (UHC). It has been demonstrated that NO_x emissions decrease with increasing EGR levels by more than 50% with 35% EGR. On the other hand, CO emissions increase with EGR but could be reduced further at elevated pressures. UHC usually follows the same trends as CO, and if we keep CO levels to minimum levels, this in turn will keep the UHC minimum. Thus it is apparent that the CO emissions remain the main concern when EGR is applied, and higher EGR levels could be achieved at increased combustion pressures while complying with CO emissions.

5 Conclusions

Combustion tests in exhaust gas recirculation conditions at representative pressures and temperatures have been executed. They confirm the feasibility of using current combustion technologies in low-oxygen conditions determined by EGR levels of up to 35%. Under carefully chosen conditions and with some design changes, gas turbine combustors can operate with high efficiencies and can determine CO_2 levels of more than 10% by volume in the gas products. The consumption of oxygen with EGR can be down to as low as less than 4%, associated with good NO_x emission behavior comparable to current levels. CO levels are found to be the significant limiting factor for EGR. Current models may be updated with our current findings and may allow for optimization of the EGR cycles for carbon capture. The following recommendations are made:

- Existing GE technology DLN gas turbine combustors may accept up to 35% EGR levels without major modifications.
- The minor modifications needed for an EGR operation involve change in premixedness, appropriate controls, and, depending on the machine, introduction/optimizations of pilots; this can push the acceptable levels to beyond 40% EGR while maintaining LBO margins.
- The larger the operating pressure, the lower the MOC that could be achieved while still complying with CO, and therefore the higher potential to increase the EGR percentage.

References

[1] Shilling, N. Z., and Jones, R. M., 2003, "The Response of Gas Turbines to a CO_2 Constrained Environment," *Proceedings of the Gasification Technology Conference*, San Francisco, CA, Oct. 13–14.
[2] Shilling, N. Z., and Jones, R. M., 2004, "Gas Turbine Experience With High Hydrogen Fuels," *Proceedings of the Power Gen Europe Conference*, Barcelona.
[3] Finkenrath, M., Ursin, T. P., Hoffmann, S., Bartlett, M., Evulet, A., Bowman, M. J., Lynghjem, A., and Jakobsen, J., 2007, "Performance and Cost Analysis of a Novel Gas Turbine Cycle With CO_2 Capture," ASME Paper No. GT2007-27764.
[4] Elkady, A. M., Evulet, A. T., Brand, A., Ursin, T. P., and Lynghjem, A., 2008, "Exhaust Gas Recirculation in DLN F-Class Gas Turbines for Post-Combustion CO_2 Capture," ASME Paper No. GT2008-51152.
[5] Bowman, C. T., 1991, "Chemistry of Gaseous Pollutant Formation and Destruction," *Fossil Fuel Combustion*, W. Bartok and A. F. Sarofim, eds., Wiley, New York, pp. 215–260.
[6] Masri, A. R., Dibble, R. W., and Barlow, R. S., 1992, "Chemical Kinetic Effects in Nonpremixed Flames of H_2/CO_2 Fuel," Combust. Flame, **91**(3–4), pp. 285–309.
[7] Liu, F., Guo, H., Smallwood, G. J., and Gulder, O. L., 2001, "The Chemical Effects of Carbon Dioxide as an Additive in an Ethylene Diffusion Flame: Implications for Soot and NO_x Formation," Combust. Flame, **125**(1–2), pp. 778–787.
[8] Liu, F., Guo, H., Smallwood, G. J., and Gulder, O. L., 2003, "The Chemical Effect of CO_2 Replacement of N_2 in Air on the Burning Velocity of CH_4 and H_2 Premixed Flames," Combust. Flame, **133**(4), pp. 495–497.

Development of an Improved Desiccant-Based Evaporative Cooling System for Gas Turbines

Amir Abbas Zadpoor[1]
Faculty of Aerospace Engineering,
Delft University of Technology,
Kluyverweg 1,
Delft 2629HS, The Netherlands
e-mail: a.a.zadpoor@tudelft.nl

Ali Asadi Nikooyan
Faculty of Mechanical, Maritime and Materials Engineering,
Delft University of Technology,
Mekelweg 2,
Delft 2628CD, The Netherlands

The evaporative inlet cooling systems do not work well in humid areas. However, desiccant wheels can be used to dehumidify the air before passing it through the evaporative cooler. A previous study of combined direct and indirect evaporative coolers showed that a single desiccant wheel does not offer much higher effectiveness compared with the multistage evaporative systems. In this paper, additional dehumidification and indirect evaporative cooling stages are added to increase the effectiveness of the desiccant-based inlet cooling. A typical gas turbine cycle along with an industrial gas turbine with actual performance curves are used to study the performance of the proposed system in three different climatic conditions. It is shown that the added stages substantially improve the effectiveness of the desiccant-based inlet cooling.
[DOI: 10.1115/1.3030875]

1 Introduction

The generated power of the gas turbines installed in tropical locations significantly decreases during hot months when the demand for electricity is normally higher. One remedy to this problem is to use some sort of inlet cooling system and direct the inlet air through it before the air is introduced to the gas turbine. Evaporative cooling systems, vapor compression refrigerators, absorption chillers, and thermal storage systems are examples of the inlet cooling systems, which can be used for this purpose [1].

Even though there is no limit for inlet cooling achieved by the refrigeration systems, the energy consumption of the power augmentation system rapidly increases up to a point where further cooling is not feasible. The energy consumption of the evaporation cooling systems is much less than the refrigeration systems. Furthermore, the initial investment of the evaporation cooling systems is limited and there are few or no moving parts in the system. Although it has been shown that evaporation-based systems have significant economic advantage over refrigeration systems [2], the performance of the evaporative cooling systems is limited by the psychometric properties of the installation site. The dehumidification techniques can be applied to overcome this limitation of the evaporative cooling. In a previous paper [3], we studied the performance of the desiccant-based cooling systems for inlet cooling of gas turbines and showed that the advantages of a single-stage dehumidification inlet cooling system over a combined direct and indirect evaporative cooling system are marginal. A new multistage configuration of the desiccant-based inlet cooling system is proposed in the current paper. A typical gas turbine cycle along with an industrial turbine with actual performance curves are considered to study the thermal performance of the turbines when the proposed inlet cooling system is applied in three different climatic conditions. The performance of the proposed cooling system is compared with that of the direct, indirect, combined indirect and direct, and single-stage desiccant-based evaporative cooling systems, and it is shown that the proposed system can significantly improve the performance of the desiccant-based systems.

2 Desiccant-Based Cooling Systems

In the solid-desiccant systems, the adsorptive material is used in fabrication of the so-called desiccant wheels where the adsorptive material is formed into a honeycomblike pattern. The processing air flows through this honeycomblike pattern and comes in contact with the adsorptive material. The humidity of the air is adsorbed and its temperature rises due to the evaporation enthalpy of the adsorbed humidity. The wheel has to rotate at a relatively low rotational speed to make the process continuous. While the processing air is directed through the upper part of the wheel, the lower part is exposed to a hot airflow (regeneration air), which sheds off the adsorbed humidity. A typical desiccant-based system uses a combination of direct and indirect evaporative coolers such that the wheel's outlet is first passed through a cooling coil fed by a cooling tower and is then introduced to a direct evaporative cooler where demineralized water is sprayed into the airstream. The air moves along an isenthalpic line toward saturation and cools down. In this study, the effectiveness of the indirect and direct evaporative coolers are assumed 70% and 90%, respectively.

As already discussed, we have previously [3] shown that the performance of a single stage desiccant-based system is not much different from combined direct and indirect evaporative cooling. In the current paper, a multistage version of the desiccant-based system with up to five wheels is proposed. Figure 1 schematically represents the five-stage desiccant-based system. Each wheel is followed by an indirect evaporative cooler. When the number of the desiccant wheels is less than five, the remaining wheels and associated indirect evaporative coolers are skipped and the air coming from the last wheel is introduced to the direct evaporative cooler. In the most general case, the regeneration air is a mixture of the regeneration air coming from the previous wheel and fresh air. Two extreme conditions are when the regeneration air is 100% fresh regeneration air option (FRAO) and when 100% of the regeneration air comes from the previous wheel non-fresh regeneration air option (NFRAO). While the former scenario has the highest dehumidification effectiveness and energy consumption, the latter consumes less energy and offers less dehumidification effectiveness. These two extreme cases are studied in this paper. The specifications of the desiccant wheels are given in Table 1. NovelAire desiccant wheel simulation program is used for simulation of the thermodynamic evolutions of the process and regeneration airs. The program is found by several researchers to provide accurate results [3–5]. For a comprehensive review of the desiccant-based systems, see Refs. [3,6].

3 Gas Turbine Model and Climatic Conditions

A typical gas turbine (T1) consisted of one compressor, two combustors, two turbines, and one generator is used for simulation of the performance of the gas turbine under the effect of different inlet cooling scenarios. Design parameters of the gas turbine are listed in Table 2. The efficiency of the turbines, η_t, and compressor, η_c, are determined by using two following relationships [2]:

[1]Corresponding author.

Manuscript received June 20, 2008; final manuscript received July 22, 2008; published online February 19, 2009. Review conducted by Dilip R. Ballal. Paper presented at the ASME Turbo Expo 2008: Land, Sea and Air (GT2008), June 9–13, 2008, Berlin, Germany.

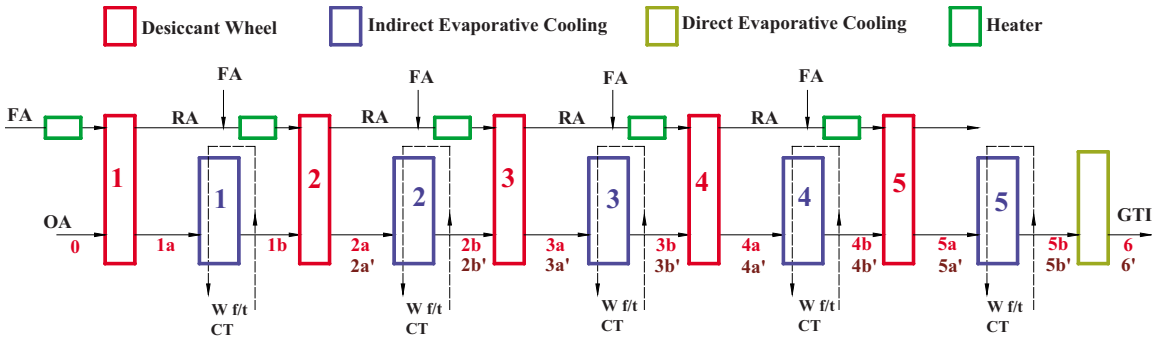

OA: Outdoor Air, FA : Fresh Air, RA: Regeneration Air, GTI: Gas Turbine Inlet, W f/t CT: Water from and to Cooling Tower

Fig. 1 Schematic of the proposed desiccant-based inlet cooling system

$$\eta_t = 1 - \left(0.03 + \frac{r_c - 1}{180}\right), \quad \eta_c = 1 - \left(0.04 + \frac{r_c - 1}{150}\right) \qquad (1)$$

where r_c is the compressor's pressure ratio. A code is developed for simulation of the performance of the gas turbine cycle. The governing thermodynamic equations of the model [3] were solved by numerical techniques. An empirical correlation describing the NO_x emissions (ppmv) of the gas turbine as a function of combustion temperature, T_c (K), and combustion pressure, P (atm) [7], was used as follows:

$$NO_x = 3.32 \times 10^{-6} e^{0.008 T_c} \sqrt{P} \ \text{ppmv}$$

The model was validated against analytical and experimental studies and it was shown that it can accurately predict the thermodynamic behavior of the cycle [3]. In addition to the typical gas turbine, a frame-5 industrial gas turbine (T2) with rated power of 16.6 MW and actual performance curves (as detailed in Ref. [8]) was considered. Three different locations, namely, Qom, Chabahar, and Siri, respectively, representing hot and dry, hot and moderately humid, and hot and humid climates, were considered to study the effects of the climatic conditions on the performance of the proposed system. The specifications and climatic conditions of these three different locations, as well as the parameters showing the performance of the gas turbines in these three default climates, are listed in Table 3. For a more detailed explanation of the gas turbine cycle, see Ref. [3].

Table 1 Parameters of the desiccant-based cooling system

Desiccant media	Silica gel
Regen./proc. air ratio	0.333
Wheel diameter (m)	3.050
Wheel depth (m)	0.20
Regen. portion (%)	25
Wheel speed (rph)	24
Regen. side face velocity (m/s)	1.823
Hub diameter (m)	0.254
Cassette height (m)	3.352
Cassette width (m)	3.352
Cassette depth (m)	0.452
Heater temp.	100
Airflow (m^3/s)	10
Process side face velocity (m/s)	1.823

Table 2 Gas turbine's (T1) design parameters

Inlet air volume (m^3/s)	10
LHV (kJ/kg)	43×10^3
Pressure ratio of the first turbine to ambient pressure	20
Pressure ratio of turbines	2
First combustor's outlet temp. (°C)	1600
Second combustor's outlet temp. (°C)	1500
Regenerator's effectiveness (%)	95
First combustor's efficiency (%)	97
Second combustor's efficiency (%)	97

4 Simulation Results and Discussion

The performance of the multistage desiccant system was simulated for the three aforementioned climatic conditions and the two different regeneration air options, i.e., FRAO and NFRAO. Figures 2(*a*) and 2(*b*) show the pressure drops of the individual wheels of the proposed system calculated by NovelAire program for T1 and T2. As is clear from these figures, the accumulated pressure drop becomes quite significant as the number of the wheels increases. This pressure drop adversely affects the performance of the gas turbine and needs to be taken into account so that a realistic estimation of the performance of the system can be obtained. It is suggested that for each 25.4 mmH_2O of pressure drop, the output power decreases by 0.3–0.48% [9]. The upper value of 0.48% was used to calculate the loss of the output power due to the pressure drop caused by the desiccant wheels. Figures 3(*a*)–3(*c*) show the net output power, and NO_x emission of the typical turbine (T1) and the output power of the industrial turbine (T2) when the above-mentioned inlet cooling schemes are applied. All of the values are normalized with respect to the case where no inlet cooling system was applied (i.e., the values given in Table 3 for T1 and the rated power of 16.6 MW for T2). In Fig. 3, DEC stands for direct evaporative cooling, IDEC stands for combined direct and indirect evaporative cooling (IEC), and "*i* Desc." ($i \in \{1,2,\ldots,5\}$) stands for the inlet cooling system with *i* desiccant wheels. Figure 3 shows that as the direct evaporative cooler is combined with the indirect evaporative cooler and the number of the desiccant wheels increases, the specific NO_x emission decreases. However, the percentage of the change in these

Table 3 The climatic conditions and the performance of the gas turbine in these default conditions

	Qom	Chabahar	Siri
Dry bulb (°C)	42	40	37
Wet bulb (°C)	23	32	32
Altitude (m)	918	6	17
Relative humidity (%)	20	58	71
Humidity ratio (g/kg)	11.4	27.7	29.1
Dew point (°C)	14.2	30.3	31.1
Specific volume (m^3/kg)	1.02	0.93	0.92
Enthalpy (kJ/kg)	71	111	112
NO_x (g/kW h)	0.723	0.759	0.755
Output power (OP) (W)	9.16×10^6	1.04×10^7	1.06×10^7

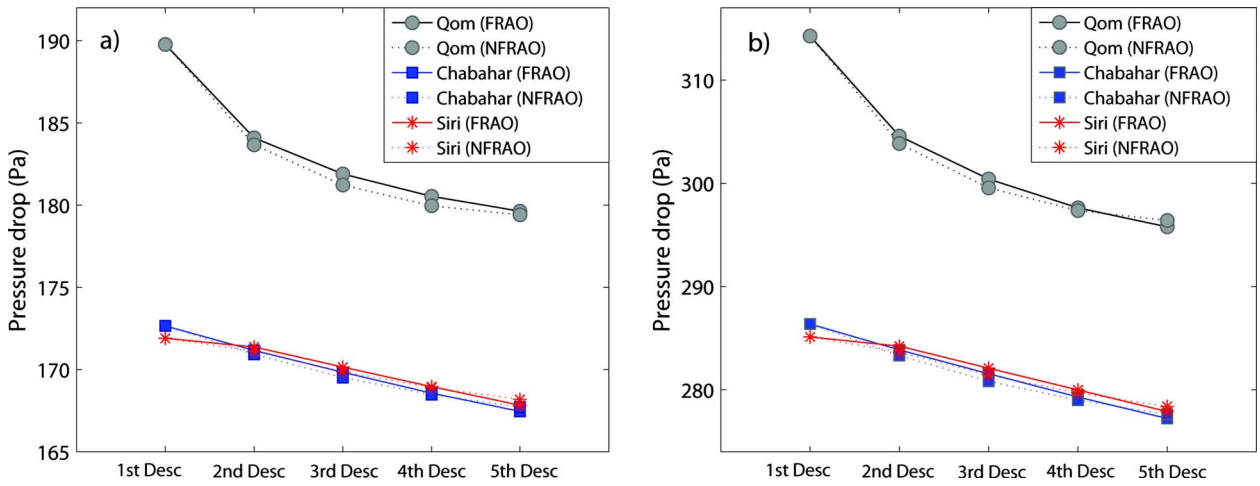

Fig. 2 Pressure drop of the process air for different wheels (per wheel) for T1 (*a*) and T2 (*b*)

parameters is much dependent on the climatic conditions. The best improvement is achieved for dry and humid climate, i.e., Qom. The next best improvement is for hot and moderately humid climate, i.e., Chabahar, and the worst performance is for Siri. This is not surprising given the fact that the desiccant-based inlet cooling systems work on the basis of evaporation and the drier the climate, the more effective the evaporative cooling. While in Qom the output power is increased between 14.4% (NFRAO) and 16.1% (FRAO) for T1 and between 20.8% (NFRAO) and 23.3% (FRAO) for T2, the output power of a similar gas turbine package installed in Chabahar is increased between 5.7% (NFRAO) and 7.9% (FRAO) for T1 and between 9.0% (NFRAO) and 12.6% (FRAO) for T2. In Siri, the output power increase is between 3.9% (NFRAO) and 6.0% (FRAO) for T1 and between 6.3% (NFRAO) and 9.7% (FRAO) for T2. Therefore, the power output increase in the dry climate (Qom) is more than double of the power output increase in the humid climate (Siri). Figures 3(*a*)–3(*c*) show that the first desiccant wheel does not have a significant impact on the performance of the inlet cooling system. Therefore, desiccant-based systems with just one wheel are not feasible and at least two wheels should be used in the system. The second point is that the performance improvements achieved by FRAO and NFRAO are almost the same for the systems with up to two desiccant wheels. For three and more wheels, the improvements achieved by FRAO and NFRAO are remarkably different and the difference keeps increasing as the number of the wheels increases. The relative difference between FRAO and NFRAO is higher for the more humid climates, which makes sense because the already humid regeneration air saturates sooner than in the dry climates. Considering only the desiccant-based systems, a line was fitted to the simulation results giving the output power as a function of the number of the desiccant wheels. The parameters of the fitted line as well as the R^2 values of the fittings are listed in Table 4. This table shows that for the humid climates, Chabahar and Siri, the power output fits well to the linear function, $R^2 = 0.84-1.00$. However, the power output versus the number of the desiccant wheels does not fit well to the linear function for the dry climate, $R^2 = 0.56-0.89$ for Qom. These trends can be seen in Figs. 3(*a*)–3(*c*) as well. For Qom, the power output versus the number of the wheels shows an asymptotic behavior and does not change much by adding, for example, the fifth wheel. Besides the dependency of the output power on the climatic conditions, one can see that the coefficient of determination is dependent on the composition of the regeneration air. The coefficient of determination of the FRAO is more than that of the NFRAO regardless of the climatic condition, because the regeneration air in the NFRAO option moves toward saturation and looses its dehumidification capability causing the final wheels to be not as efficient as the first ones. Figures 3(*a*)–3(*c*) show some sort of the asymptotic in the power output of the NFRAO option, which is reflected in Table 4 as well. As is clear from Table 4, the intercept of the linear equations, which describes the performance of the IDEC system, is

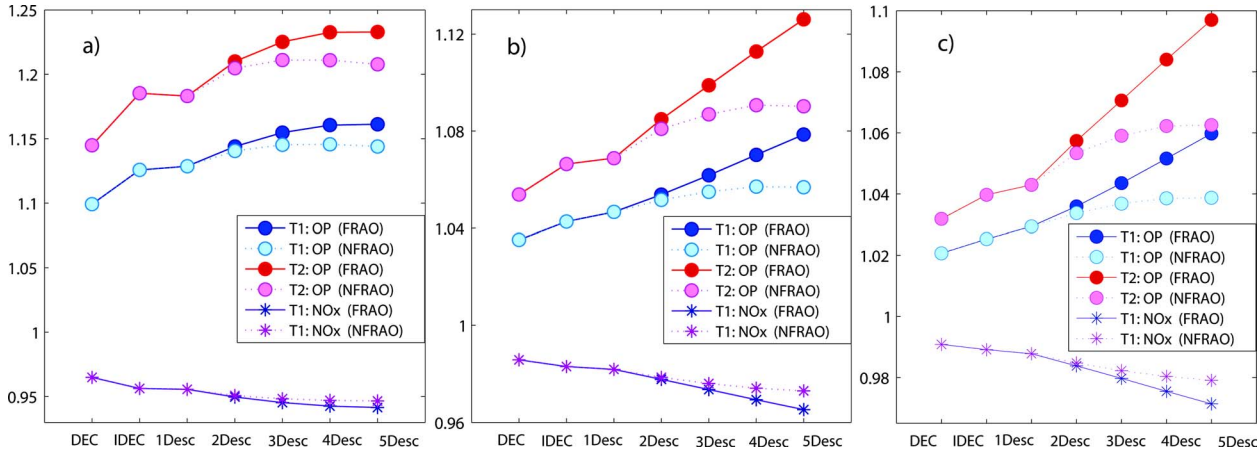

Fig. 3 The performance of the turbines versus the type of the inlet cooling system for Qom (*a*), Chabahar (*b*), and Siri (*c*)

Table 4 Parameters of the linear functions fitted to the power outputs of the studied turbines in different climates

	p_1		p_2		R^2	
$f(x)=p_1x+p_2$	T1	T2	T1	T2	T1	T2
Qom, FRAO	0.0082	0.0122	1.125	1.180	0.889	0.847
Qom, NFRAO	0.0036	0.0056	1.130	1.187	0.634	0.562
Chabahar, FRAO	0.0080	0.0142	1.038	1.056	0.999	0.999
Chabahar, NFRAO	0.0026	0.0053	1.046	1.068	0.872	0.837
Siri, FRAO	0.0076	0.0135	1.021	1.030	0.998	1.000
Siri, NFRAO	0.0023	0.0048	1.028	1.042	0.891	0.861

greater for the dry climate and decreases as the humidity of the climate increases. The slopes of the linear equations show the power output increase per desiccant wheel.

5 Power Analysis of the Cooling System

The feasibility of implementation of the inlet cooling systems depends on the additional power generated by the gas turbine compared with the power consumed by the inlet cooling system. The power consumed by a desiccant-based inlet cooling system can be expressed as

$$P_{\text{cooling}} = P_{\text{heater}} + P_{\text{tower}} + P_{\text{fans}} + P_{\text{misc}} \tag{3}$$

where P_{heater}, P_{tower}, P_{fans}, and P_{misc} are, respectively, the powers consumed by the heaters, cooling towers, processing and regeneration air fans, and the miscellaneous power consumptions such as the power consumed by the electromotor used to rotate the desiccant wheels. The power consumption of the heaters was calculated by the NovelAire desiccant wheel simulation program based on the temperature of the regeneration air. In order to calculate the power consumed by the cooling tower, the volumetric rate of the cold water's flow was calculated based on the heat exchanged during the course of the indirect evaporative cooling. Given the volumetric flow rate of the cold water and by assuming the cold water's temperature about 2 °C above the outdoor's wet bulb temperature, the cooling tower was selected from the range of the available industrial cooling towers. The power consumptions of the water pump and fan were summed up to calculate the power consumption of the cooling tower. The power consumptions of the fans were determined by using the pressure drops shown in Fig. 2 and assuming a fan efficiency of 54%. The miscellaneous power consumptions were neglected. The three last terms of Eq. (3) were summed up to calculate a parameter called P_{other} standing for all of the power consumptions expect for that of the heaters. Figures 4(*a*)–4(*c*) compare the additional power generated by the gas turbine and the power consumed by the inlet cooling system for different climatic conditions and different configurations of the inlet cooling system. The power consumption of the inlet cooling system is given only for the first turbine (T1) because the data needed to calculate the values for the second turbine (T2) were not available. Note that the values of the output power increase are not given per wheel and refer to the whole value of the additional generated power when the corresponding inlet cooling system is applied. However, the values of the power consumptions of the inlet cooling system are given per desiccant wheel. Figures 4(*a*)–4(*c*) show that the power consumed by the heater is the largest part of the power consumption of the inlet cooling system and the power consumed by the other processes, P_{other}, is negligible compared with that. Furthermore, the power consumed by the heaters is different for the FRAO and NFRAO options. While the power consumption of the FRAO is almost the same regardless of the number of the desiccant wheels, the power consumption of the desiccant wheels in the NFRAO decreases as the number of the wheels increases. This is because of the fact that the temperature of the air passed through the last heaters is higher than that of the air passed through the first ones. Although the regeneration air cools down as it regenerates the wheel, it is still warmer than the fresh air. Comparing the power consumptions of the heaters and the additional power generated by the gas turbine in Figs. 4(*a*)–4(*c*), one can see that the additional power generated by using additional desiccant wheels is either less or almost the same as the power consumed by the heater. However, the important point is that, in contrast to the cooling towers and fans, the power consumption of the heaters should not be considered as a power load. Dependent on the type of the power plant, the hot water needed for heaters can be provided through different sources. If the gas turbine is not working in combination with a steam turbine, the high-temperature exhaust of the gas turbine is more than enough to provide the hot water needed for the heaters. In case the gas turbine is being used in combination with a steam turbine, the exhaust of the steam generator is in most cases hot enough to be used for generation of the hot water particularly when the steam turbine operates in the supercritical conditions. In most cases, the temperature of the hot water needed for the heaters of the cooling system is much less than the temperature of the interheaters and, thus, operation of the inlet cooling system does not adversely affect the performance of the steam turbine. Even in cases where the exhaust of the steam generator is used in cogeneration systems, the operation of the inlet cooling system is possible without side-effects; because the inlet cooling system has to be used only in the hottest days of the year when the cogeneration systems, which are mostly used for heating, are not on duty. Besides that, the temperature of the heater can be adjusted by adjusting the ratio of the regeneration portion of the desiccant wheel to

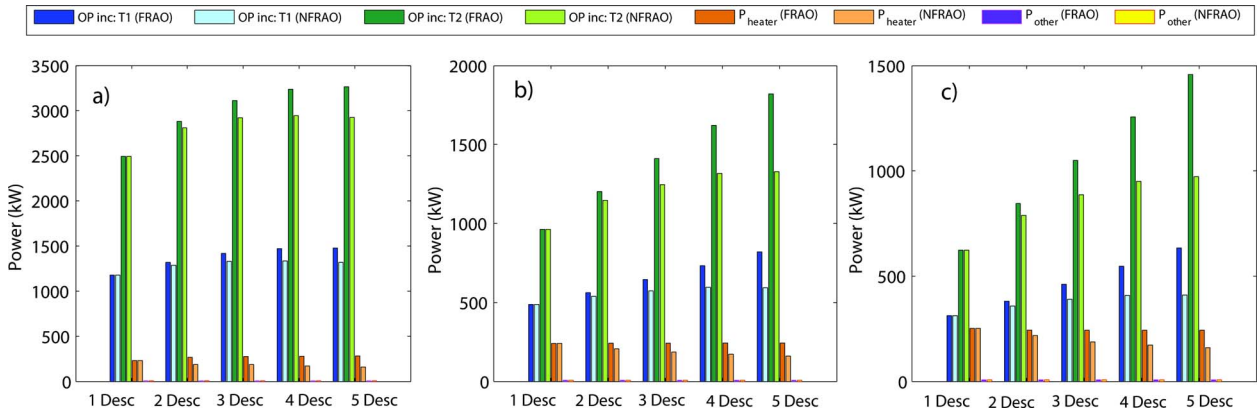

Fig. 4 Analysis of the power consumption and power output increase for different cooling systems: Qom (*a*), Chabahar (*b*), and Siri (*c*)

its process portion (R/P). A greater ratio of the regeneration portion to the process portion is normally needed for lower heater temperatures to preserve the performance of the wheel. Aside from the power needed for the heaters, the power consumption of the desiccant-based inlet cooling system is negligible compared with the additional power generated by the gas turbine.

6 Practical Issues

In addition to the pressure drop, which was taken into account in the analysis of the proposed system, air leakage and heat gain of the air while passing through the system adversely affect the performance of the turbine. Therefore, the actual performance improvement values would be less than the theoretically calculated ones. Moreover, even though application of the desiccant-based systems is theoretically possible and is even suggested for relatively large turbines (i.e., >50 MW [10]), design of such large system is somewhat challenging particularly given that the current commercialized technology mainly concerns small size wheels used for thermal conditioning purposes.

From engineering economics standpoint, the evaporative inlet cooling systems, which are based on the desiccant systems, have a clear advantage over the other cooling systems wherever the climatic conditions are appropriate for such systems. Gareta et al. [11] compared absorption, vapor compression, and thermal storage systems with evaporative cooling systems and showed that the payback duration of the evaporative cooling systems is 4–11 times less than heat absorption systems, 6–18 times less than vapor compression systems, and about 15 times less than thermal storage systems. Some comparative cost analyses can be found in literature for small- and medium-size desiccant systems. For example, Mazzei et al. [12] showed that the desiccant systems offer a 35% saving of the life-cycle cost compared with the traditional refrigeration systems, if gas-fired heaters are used and a saving of 87% life-cycle cost, if waste heat is used for the heaters. The initial investment needed for single-stage desiccant cooling is estimated between 100 USD per m^3/min and 280 USD per m^3/min (3–8 USD/cfm) [13]. This specific price is less for the systems with a higher volumetric flow rate such as the case of the inlet cooling systems. The price of multiple-stage desiccant systems is obviously higher than this value and depends on several factors including the number of the wheels. According to some initial speculations, the specific price grows less than proportionally with the number of the wheels.

7 Conclusions

A multistage desiccant-based inlet cooling system with up to five desiccant wheels was proposed and analyzed in this paper. The following conclusions can be drawn from the study.

(1) The performance of the system becomes significantly better than the IDEC only when two or more desiccant wheels are used in the system.
(2) The performance of the desiccant-based system is much better in the dry climates compared with the humid climates as the desiccant-based systems still work on the basis of the evaporation cooling.
(3) The difference between the performances of the FRAO and NFRAO systems is negligible for up to two desiccant wheels. Therefore, it is advisable to use NFRAO for the systems with up to two desiccant wheels because it is easier to design and manufacture and cheaper to operate.
(4) The difference between the performance improvements achieved with the FRAO and NFRAO is significant regardless of the climatic conditions. Nevertheless, the difference is even greater for more humid climates.
(5) The performance improvement achieved using the proposed multistage system shows an asymptotic behavior versus the number of the desiccant wheels for dry climate. However, the additional output power increases linearly with the number of the desiccant wheels in humid climates. Therefore, application of a system with three or more desiccant wheels is not feasible in dry climates while relatively larger number of desiccant wheels seem to be feasible in humid climates.
(6) The power consumption of the cooling system can be divided into the power consumed by the heater and the other power consumptions. The other power consumptions are negligible compared with the heater's consumption. The heater's power consumption should not be considered as power load as it can be provided through different sources depending on the type of the power plant.

Acknowledgment

A.A.Z. and A.A.N. contributed equally to this work and are, thus, considered as joint first authors.

References

[1] Boyce, M. P., 2002, *Gas Turbine Engineering Handbook*, 2nd ed., Gulf Professional, Boston, MA.
[2] Alhazmy, M. M., and Najjar, Y. S. H., 2004, "Augmentation of Gas Turbine Performance Using Air Coolers," Appl. Therm. Eng., **24**(2–3), pp. 415–429.
[3] Zadpoor, A. A., and Golshan, A. H., 2006, "Performance Improvement of a Gas Turbine Cycle by Using a Desiccant-Based Evaporative Cooling System," Energy, **31**(14), pp. 2652–2664.
[4] Camargo, J. R., Ebinuma, C. D., and Silveira, J. L., 2003, "Thermoeconomic Analysis of an Evaporative Desiccant Air Conditioning System," Appl. Therm. Eng., **23**(12), pp. 1537–1549.
[5] Liu, W., Lian, Z., Radermacher, R., and Yao, Y., 2007, "Energy Consumption Analysis on a Dedicated Outdoor Air System With Rotary Desiccant Wheel," Energy, **32**(9), pp. 1749–1760.
[6] Daou, K., Wang, R. Z., and Xia, Z. Z., 2006, "Desiccant Cooling Air Conditioning: A Review," Renewable Sustainable Energy Rev., **10**(2), pp. 55–77.
[7] Lefebvre, A. H., 1998, *Gas Turbine Combustion*, Taylor & Francis, London.
[8] Ameri, M., Hejazi, S. H., and Montaser, K., 2005, "Performance and Economic of the Thermal Energy Storage Systems to Enhance the Peaking Capacity of the Gas Turbines," Appl. Therm. Eng., **25**(2–3), pp. 241–251.
[9] Chaker, M., Meher-Homji, C. B., Mee, T., and Nicholson, A., 2003, "Inlet Fogging of Gas Turbine Engines Detailed Climatic Analysis of Gas Turbine Evaporation Cooling Potential in the USA," ASME J. Eng. Gas Turbines Power, **125**(1), pp. 300–309.
[10] Corporation, R. D., 2003, *Cooling, Heating, and Power for Industry: A Market Assessment*, U.S. Department of Energy, Vienna, Austria.
[11] Gareta, R., Romeo, L. M., and Gil, A., 2004, "Methodology for the Economic Evaluation of Gas Turbine Air Cooling Systems in Combined Cycle Applications," Energy, **29**(11), pp. 1805–1818.
[12] Mazzei, P., Minichiello, F., and Palma, D., 2002, "Desiccant HVAC Systems for Commercial Buildings," Appl. Therm. Eng., **22**(5), pp. 545–560.
[13] Wilson, A., 2003, *Greening Federal Facilities*, U.S. Department of Energy, Brattleboro, VT.